Automating delineation and classification of alluvial fans by the use of object-based geomorphometry and machine learning

Von der Fakultät für Georessourcen und Materialtechnik der
Rheinisch-Westfälischen Technischen Hochschule Aachen

zur Erlangung des akademischen Grades einer

Doktorin der Naturwissenschaften

genehmigte Dissertation

vorgelegt von

M.Sc. Isabel Pipaud

aus Düren

Berichter: **Univ.-Prof. Dr. rer. nat. Frank Lehmkuhl**
Univ.-Prof. Florian Wellmann, Ph.D.
PD Dr. rer. nat. Georg Stauch

Tag der mündlichen Prüfung: 10.07.2020

Diese Dissertation ist auf den Internetseiten der Universitätsbibliothek online verfügbar

© 2021 Isabel Pipaud



This work is licensed under the Creative Commons Attribution-ShareAlike 4.0 International License.
To view a copy of this license, visit http://creativecommons.org/licenses/by-sa/4.0/

The very nature of science is discoveries, and the best of those discoveries are the ones you don't expect.

– *Neil deGrasse Tyson*

Table of Contents

List of Figures vii

List of Tables ix

List of Supplements x

List of Abbreviations and Acronyms xii

1 Introduction 1
- 1.1 Background . . . 1
- 1.2 Challenges . . . 4
- 1.3 Research questions and objectives . . . 6
- 1.4 Outline of this thesis . . . 7

2 State of research 9
- 2.1 Definitions and differentiation . . . 9
  - 2.1.1 Fan-building processes . . . 9
  - 2.1.2 Autogenic dynamics . . . 13
  - 2.1.3 Fanhead entrenchment . . . 14
  - 2.1.4 Scale . . . 14
  - 2.1.5 Landforms grading into alluvial fans . . . 15
- 2.2 Environmental controls . . . 16
  - 2.2.1 Evolution of paradigms . . . 16
  - 2.2.2 Climatic conditions . . . 17
  - 2.2.3 Tectonic activity . . . 20
  - 2.2.4 Bedrock lithology . . . 22
  - 2.2.5 Base level . . . 23
- 2.3 Geomorphometric research . . . 24
  - 2.3.1 Fan–catchment relationships . . . 24
  - 2.3.2 Geomorphometry of fan surfaces . . . 27
  - 2.3.3 Exploratory data analysis and clustering . . . 29
  - 2.3.4 Automatic delineation and object-based geomorphometry . . . 30
- 2.4 Conclusions and incentives . . . 31

3 Evaluation of TanDEM-X elevation data 33
- 3.1 Introduction . . . 33
- 3.2 Data . . . 35
  - 3.2.1 TanDEM-X CoSSC dataset . . . 35
  - 3.2.2 SRTM dataset . . . 36
  - 3.2.3 ASTER GDEM dataset . . . 37
- 3.3 Current state of research . . . 37
- 3.4 Regional setting . . . 39
- 3.5 Methods . . . 41
  - 3.5.1 DEM generation from TanDEM-X CoSSC data . . . 41
  - 3.5.2 DEM quality parameters . . . 42
  - 3.5.3 Morphometric DEM analysis . . . 43
  - 3.5.4 Geomorphological mapping and visual evaluation . . . 46
- 3.6 Results . . . 47
  - 3.6.1 Exploratory visual DEM analysis and DEM quality parameter assessment . . . 47

3.6.2 Morphometric DEM analysis . . . 49
3.6.3 TanDEM-X DEM landscape representation . . . 55
3.7 Discussion . . . 63
3.7.1 DEM quality assessment . . . 63
3.7.2 TanDEM-X DEM advantages and drawbacks . . . 67
3.7.3 Perspectives toward geomorphological applications of TanDEM-X DEMs . . . 67
3.8 Conclusions . . . 68

4 Regional Setting **69**
4.1 Overview . . . 69
4.2 North America . . . 71
4.2.1 Tectonic setting . . . 71
4.2.2 Modern environmental setting . . . 76
4.2.3 Formation phases . . . 79
4.3 Asia . . . 84
4.3.1 Tectonic setting . . . 84
4.3.2 Modern environmental setting . . . 85
4.3.3 Formation phases . . . 86

5 Mean-shift segmentation and support vector machines **89**
5.1 Introduction . . . 89
5.2 Morphological characteristics of alluvial fans . . . 91
5.3 Regional setting . . . 93
5.4 Data . . . 94
5.4.1 SRTM dataset . . . 94
5.4.2 DEM preparation . . . 95
5.5 Methods . . . 95
5.5.1 Segmentation . . . 96
5.5.2 Classification . . . 100
5.6 Results . . . 109
5.6.1 Reference fans . . . 109
5.6.2 OBMA result – exploratory analysis . . . 112
5.6.3 OBMA – relationship between morphometric parameters and SVM scores . . . 117
5.6.4 OBMA – relationship between segmentation parameters and SVM scores . . . 120
5.7 Discussion . . . 121
5.7.1 Segmentation approach assessment . . . 121
5.7.2 Classification approach assessment . . . 122
5.7.3 Perspectives and challenges . . . 124
5.8 Conclusions . . . 125

6 One-Class Random Forests **127**
6.1 Introduction . . . 127
6.2 Data . . . 129
6.2.1 SRTM1 . . . 129
6.2.2 ALOS World-3D DEM . . . 129
6.2.3 State of research . . . 130
6.2.4 DEM assessment . . . 131
6.2.5 DEM preparation . . . 133
6.3 Methods . . . 133
6.3.1 Channel infilling . . . 133
6.3.2 Morphometric formalization of alluvial fans . . . 135

6.3.3 Classification . . . 144
6.4 Results . . . 152
6.4.1 Classification performance . . . 152
6.4.2 OCRF parametrization . . . 157
6.4.3 Attribution analysis . . . 157
6.5 Discussion . . . 162
6.5.1 Classifier assessment . . . 162
6.5.2 DEM assessment . . . 163
6.5.3 Assessment of morphometric parameters . . . 163
6.5.4 Feature importance metrics . . . 164
6.5.5 Perspectives and incentives . . . 165
6.6 Conclusions . . . 166

7 Morphometric expression of environmental controls 167
7.1 Introduction . . . 167
7.2 Data and Methods . . . 169
7.2.1 Geomorphometric Analysis . . . 169
7.2.2 Trend removal . . . 170
7.2.3 Mean-shift clustering . . . 171
7.2.4 Principal component analysis . . . 173
7.3 Results . . . 174
7.3.1 Scaling relationships with alluvial fan area . . . 174
7.3.2 Clustering . . . 179
7.3.3 Principal Component Analysis . . . 181
7.4 Discussion . . . 185
7.4.1 Scaling relationships . . . 185
7.4.2 Feature space structure . . . 186
7.5 Conclusions . . . 187

8 Synthesis 189

Acknowledgments 205

A Supplements, Evaluation of TanDEM-X elevation data 207

B Supplements, Mean-shift segmentation and support vector machines 221

C Supplements, One-Class Random Forests 233

D Supplements, Morphometric expression of environmental controls 271

Bibliography 277

Summary 337

Zusammenfassung 341

List of Figures

2.1 Schematic plan view of elementary fan types. . . . 10
2.2 Schematic cross sections of alluvial fans abutting fault-bounded mountain ranges. . . . 21

3.1 Regional overview of the central eastern Nyainqêntanglha Range in southeastern Tibet. 40
3.2 Topographical overview of the study area in the Bodui Tsangpo valley as depicted in the self-processed TDX DEM. . . . 48
3.3 Classified slope angles calculated from TDX, ASTER and SRTM1 DEMs for Details 2 and 4. . . . 50
3.4 Classified absolute general curvatures calculated from TDX, ASTER and SRTM1 DEMs for Details 2 and 4. . . . 51
3.5 Vector ruggedness measure calculated with a 3×3 moving window (scaling factor 1000) from TDX, ASTER and SRTM1 DEMs for Details 2 and 4 52
3.6 Results of grayscale morphological filtering (White Top Hat – Black Top Hat) calculated from TDX, ASTER and SRTM1 DEMs for Details 2 and 4. . . . 53
3.7 Results of the moving window zero-mean sum of absolute differences algorithm calculated from TDX, ASTER and SRTM1 DEMs for Details 2 and 4. . . . 54
3.8 Histograms of morphometric parameters for Details 2 and 4 calculated from TDX, ASTER and SRTM1 DEMs 56
3.9 Detail 1 in the uppermost part of the Bodui Tsangpo valley included in the TanDEM-X footprint. . . . 59
3.10 Detail 2 in the center part of the Bodui Tsangpo valley. . . . 60
3.11 Detail 3 at the outflow of Baiyu valley into Bodui Tsangpo valley. . . . 62
3.12 Detail 4 at the valley head of Baiyu valley. . . . 64

4.1 Regional overview of the American greater study area. . . . 70
4.2 Regional overview of the Gobi Altai study area (Region 7). . . . 72
4.3 Subunits of the Basin-and-Range taphrogen according to Dickinson (2006). . . . 74
4.4 1900 to 2013 averages of monthly precipitation during meteorological winter (A) and summer (B), and major synoptic-scale atmospheric circulation patterns, depicted for the greater American study area. . . . 78
4.5 Wisconsin-stage glacial and pluvial features (according to Orme, 2008), and extent of NAM/tropical currents during the early and middle Holocene (according to Barron et al., 2012). . . . 82
4.6 1900 to 2013 averages of monthly precipitation during the meteorological winter (A) and summer (B) season, and major synoptic-scale atmospheric circulation patterns, depicted for the greater Asian study area. . . . 87

5.1 Regional overview of the study area in north-western Mongolia. . . . 93
5.2 Flowchart of the segmentation procedure conducted in this study. . . . 97
5.3 Location of the manually delineated reference fans. . . . 102
5.4 Flowchart of the classification procedure conducted in this study. . . . 103
5.5 Illustration of the specific morphometric parameters exploiting the conical shape of alluvial fans. . . . 106
5.6 Perspective view on reference fan TID 0, located at the eastern flank of the Tsagaan Shuvuut Massif. . . . 111
5.7 Final OBMA objects and their SVM scores, after merging and topological cleansing with area weighting. . . . 113

5.8 Location of details depicted for in-depth geomorphological analysis. 115
5.9 Perspective view on a large alluvial fan located at the south-western shore of the Uureg Nuur Lake. 116
5.10 Scatter plots of SVM score plotted against morphometric classification parameters. . . 118
5.11 SVM score arithmetic means and standard deviations for bins of the morphometric classification parameters. 119

6.1 Perspective view on a large alluvial fan abutting the Sarcobatus Flat, SW Nevada, as depicted by versions of AW3D30 and SRTM1 differing in the degree of mesh denoising filtering applied. 132
6.2 The result of the channel infilling procedure, depicted for fan TID 241 and the lightly filtered (t=.995, i=3) AW3D30 dataset. 134
6.3 Schematic drawing of the global gradient convergence apex point estimation (GGC) method. 137
6.4 Comparison of apex points obtained with different methods. 138
6.5 Comparison of RAD and GAD rasters for training fan TID 241. 141
6.6 Schematics of calculation for the DGD and the LGD. 143
6.7 Comparison of ROC curves obtained for the evaluation dataset, using the respective hyper-parameter set which maximizes AUC_{EV}. 153
6.8 Comparison of ROCs obtained from one-class support vector machine (OCSVM) and one-class random forest (OCRF) instances for the evaluation dataset. 154
6.9 OCRF membership likelihoods obtained for the evaluation dataset, using the AW3D30 DEM with light mesh denoising applied (t=.995, i=3). 156
6.10 MDI scores obtained for OCRF instances which were configured to fully randomize feature selection (mtry=1), and inverse Bhattacharyya coefficients obtained for the evaluation dataset. 158

7.1 Scatter plots of the incorporated morphometric variables prior and after de-trending, and the corresponding regression function yielding the minimal MSE, or the stipulated linear regression function, respectively. 176
7.2 Product-moment correlation matrix of the de-trended dataset. 178
7.3 Average silhouette values in relation to the number of clusters, obtained via mean-shift clustering and iterative increase of bandwidths. 179
7.4 Projections of morphometric variables on principal components. 181
7.5 Scatter plots of component scores in the two-dimensional space spanned by PC0 and PC1. 183
7.6 Scatter plots of component scores in the two-dimensional space spanned by PC1 and PC2. 184

8.1 Fundamental differences between object-based image analysis (OBIA) and object-based morphometric analysis (OBMA). 192
8.2 Synopsis of the OBMA workflow developed in this doctoral dissertation. 194

List of Tables

3.1 Interferometric geometry of CoSSC dataset 1032207_002. 36
3.2 Mean elevations for Details 1–4 calculated from TDX, SRTM1 and ASTER DEMs. . . 50
3.3 Mean slope angles for Details 1–4 calculated from TDX, ASTER and SRTM1 DEMs. 51
3.4 Mean absolute general curvatures for Details 1–4 calculated from TDX, ASTER and SRTM1 DEMs. 52
3.5 Mean vector ruggedness measure values for Details 1–4 calculated from TDX, ASTER and SRTM1 DEMs. 53
3.6 Mean grayscale morphological filtering (White Top Hat – Black Top Hat) values for Details 1–4 calculated from TDX, ASTER and SRTM1 DEMs. 54
3.7 Mean moving window zero-mean sum of absolute differences algorithm values for Details 1-4 calculated from TDX, ASTER and SRTM1 DEMs. 55
3.8 Landform cognoscibility in TDX, SRTM1 and ASTER GDEM v2 DEMs. 57

5.1 Weightings applied to slope and cross-sectional curvature before multiband dataset creation. 99
5.2 Bandwidth parameters used for mean-shift segmentation and total number of runs. . . 101
5.3 Morphometric parameter values and SVM scores for the reference fan dataset. 110
5.4 LOOCV morphometric parameters (Z-standardized) and LOOCV SVM score values obtained for the reference dataset. 112
5.5 Relationships between mutual overlaps and SVM scores for the reference fans. 114

6.1 Evaluated hyper-parameter sets. 149
6.2 Terminology of metrics used for the evaluation of machine learning algorithms. 150
6.3 OCRF parameter sets yielding the best performance for the respective DEM versions. . 155

7.1 Morphometric variables used for alluvial fan feature space analysis. 171
7.2 Set of non-linear regression functions considered for trend removal. 172
7.3 Regression functions and function coefficients applied to remove the relationship with fan planimetric area (km^2). 175
7.4 Obtained clusters from mean-shift clustering of the raw morphometric data with silhouette-optimal bandwidth selection. 179
7.5 Obtained clusters from mean-shift clustering of the de-trended morphometric data with silhouette-optimal bandwidth selection. 180

List of Supplements

A.1 Workflow conducted to process the experimental DEM, geocoded SAR amplitude, and geocoded interferometric coherence from TanDEM-X CoSSC data. 207
A.2 Interferometric coherence depicted for the four Details. 208
A.3 Position of pixels which were identified as outliers in the intermediate 1.5 m DEM. . . 209
A.4 Data voids present in the SRTM1 product. 210
A.5 Filled voids in ASTER GDEM v2 data and number of stereometric scene pairs incorporated into the generation of the DEM. 211
A.6 Classified values of aspect slope in the four Details, as depicted by TDX (15 m), ASTER GDEM v2, and SRTM1. 212
A.7 Classified absolute values of general curvature in the four Details, as depicted by TDX (15 m), ASTER GDEM v2, and SRTM1. 213
A.8 Classified values of VRM (3×3 kernel) in the four Details, as given by TDX (15 m), ASTER GDEM v2, and SRTM1. 214
A.9 Classified values of the BTH-WTH filter obtained for TDX (15 m), ASTER GDEM v2, and SRTM1. 215
A.10 Values yielded by the MWZSAD using juxtapositions of TDX (15 m) with ASTER GDEM v2, SRTM1, and TDX30. 216
A.11 Topographical overview of the study area in the Bodui Tsangpo valley, as depicted by SRTM1. 217
A.12 Topographical overview of the study area in the Bodui Tsangpo valley, as depicted by ASTER GDEM v2. 218
A.13 Rendition of forest clearings in the self-processed TanDEM-X DEM. 219

B.1 Effects of the selection of *hs* and *hr* on object delineation. 221
B.2 Outlines of all segmentation objects passing the exclusion routine described in Section 5.5.2. 222
B.3 Reference fan (manual delineation) SVM scores. 223
B.4 Outlines of all OBMA objects exhibiting a SVM score of −2 or better. 224
B.5 Workflow conducted for all classified polygons to yield a final OBMA dataset. 225
B.6 Final OBMA dataset computed with area weighting, compared to the final OBMA objects produced with no area weighting applied. 226
B.7 SVM scores of the OBMA dataset which was computed without area weighting (NAW dataset). 227
B.8 Morphometric parametrization (Z-standardized values) and classification results for the final OBMA dataset (with area-weighting applied). 228
B.9 Arithmetic means and standard deviations of the segmentation parameters for bins of the SVM score 231

C.1 Workflow conducted to infill prominent incised channels. 233
C.2 Matrix of product-moment correlation coefficients for the AW3D30 DEM with no filtering applied. 234
C.3 Matrix of product-moment correlation coefficients for the AW3D30 DEM with light filtering applied (t=.995, i=3). 235
C.4 Matrix of product-moment correlation coefficients for the AW3D30 DEM with strong filtering applied (t=.99, i=10). 236
C.5 Matrix of product-moment correlation coefficients for the SRTM1 DEM with no filtering applied. 237

C.6 Matrix of product-moment correlation coefficients for the SRTM1 DEM with light filtering applied (t=.995, i=3). . . . 238
C.7 Matrix of product-moment correlation coefficients for the SRTM1 DEM with strong filtering applied (t=.99, i=10). . . . 239
C.8 ROC plots obtained for the *training dataset* via 10-fold cross-validation. . . . 240
C.9 TPRs, FPRs, and corresponding ACC scores, as obtained for the *training dataset* via 10-fold cross-validation. . . . 241
C.10 TPRs, FPRs, and corresponding ACC scores, as obtained for the *evaluation dataset*. . . . 242
C.11 OCRF scores and morphometric parameter values (Z-standardized) for the *evaluation dataset*, as yielded by the best-performing AW3D30 variant (t=.995, i=3). . . . 243
C.12 OCRF scores and morphometric parameter values (Z-standardized) for the *evaluation dataset*, as yielded by the best-performing SRTM1 variant (t=.99, i=10). . . . 244
C.13 Membership likelihoods obtained for the evaluation dataset, using a OCRF being trained with morphometric data derived from the SRTM1 DEM with strong filtering applied (t=.99, i=10). . . . 245
C.14 Membership likelihoods obtained for the evaluation dataset, using a OCSVM being trained with morphometric data derived from the SRTM1 DEM with strong filtering applied (t=.99, i=10). . . . 246
C.15 TPRs, FPRs, and corresponding ACC scores, as obtained for the training dataset via reverse 10-fold cross-validation, that is, a k-fold cross-validation where one fold is used for training and all remaining folds are used for evaluation. . . . 247
C.16 AUC scores obtained for all evaluated OCRF instances, sorted in descending order. . . . 248
C.17 Empirical probability density plots for all morphometric variables, as depicted by the AW3D30 DEM with no filtering applied. . . . 252
C.18 Empirical probability density plots for all morphometric variables, as depicted by the AW3D30 DEM with light filtering applied (t=.995, i=3). . . . 255
C.19 Empirical probability density plots for all morphometric variables, as depicted by the AW3D30 DEM with strong filtering applied (t=.99, i=10). . . . 258
C.20 Empirical probability density plots for all morphometric variables, as depicted by the SRTM1 DEM with no filtering applied. . . . 261
C.21 Empirical probability density plots for all morphometric variables, as depicted by the SRTM1 DEM with light filtering applied (t=.995, i=3). . . . 264
C.22 Empirical probability density plots for all morphometric variables, as depicted by the SRTM1 DEM with strong filtering applied (t=.99, i=10). . . . 267

D.1 Product-moment correlation matrix of the raw dataset. . . . 271
D.2 Clustering result obtained for the raw dataset and feature-specific bandwidth values estimated via CVML bandwidth estimation. . . . 272
D.3 Clustering result obtained for the de-trended dataset and feature-specific bandwidth values estimated via CVML bandwidth estimation. . . . 273
D.4 Clustering result obtained for the raw dataset with scaling factors adjusted to yield ten clusters. . . . 274
D.5 Clustering result obtained for the de-trended dataset with scaling factors adjusted to yield ten clusters. . . . 274
D.6 Empirical density distribution of the local outlier factor. . . . 274
D.7 Eigenvalues (in percent of total variance) and eigenvectors of the PCA applied on the de-trended dataset. . . . 275
D.8 Empirical density distribution of planimetric fan area for samples identified as outliers and the remaining alluvial fan dataset. . . . 275

List of Abbreviations and Acronyms

ACC Accuracy 150, 154, 155, 241, 242, 247

ADF Apex distance factor 144, 160, 161, 169, 171, 175, 178–181, 185, 186, 196, 272–275

AF Alluvial fan 243, 244

ALOS Advanced Land Observing Satellite 2, 129, 152, 190

ANN Artificial neural network 30, 197

AP Alluvial plain 243, 244

API Application programming interface 105, 108, 136

AR Aspect ratio 169, 171, 175, 178–182, 185, 272–275

AS Alluvial slope 243, 244

asl Above sea level 39, 40, 55, 58, 61, 73, 79, 85, 86, 94

ASTER Advanced Spaceborne Thermal Emission and Reflection Radiometer 2, 6, 7, 30, 33–35, 37–39, 42, 46, 47, 49–68, 189, 211–216, 218

AUC Area under curve 149, 150, 152, 154, 155, 157, 248

AUROC Area under the receiver operating characteristic (curve) 149

AW3D30 ALOS World-3D DEM with 1″ (~30 m) posting 2, 6, 7, 129–134, 144, 152–166, 169, 189, 190, 193, 234–236, 240–243, 245, 247–252, 255, 258

AW3D5 ALOS World-3D DEM with 0.15″ (~5 m) posting 2, 130, 163

BAS Bilateral asymmetry 105, 106, 109, 110, 118–120, 123, 135, 228–230

BC Bhattacharyya coefficient 152, 157–160, 164, 193

BFS Bogd Fault system / Valley of the Lakes fault system 71, 84

BP Before present (used irrespective of dating method) 41, 73, 75, 76, 80, 81, 83, 84, 86, 88

BTH Black Top Hat 45, 54, 66, 98, 133–135, 215

CART Classification and Regression Tree 144, 146, 150

CCurv Cross-sectional curvature 96, 98, 99, 104, 109, 110, 117–119, 121, 160, 161, 171, 175, 178–182, 185, 228–230, 272–275

CCW Cross-sectional curvature weighting 99, 221, 228–231

CGIAR-CSI Consultative Group on International Agricultural Research – Consortium for Spatial Information 36, 37, 210

CNN Convolutional neural network 197–204

CoSSC Coregistered Single look Slant range Complex 7, 35, 36, 40–42, 67, 68, 190, 207

CVML Cross-validated maximum likelihood 148, 152, 157, 170, 172, 176, 248–251, 272–274

DEM Digital elevation model 1–7, 30, 31, 33–39, 41–68, 70, 90, 95, 96, 101, 105, 116, 121, 122, 124, 128–133, 135, 136, 140, 144, 149, 152–166, 182, 186, 189, 190, 193, 195, 202, 203, 207, 209, 211, 215, 219, 234–242, 245–247, 252, 255, 258, 261, 264, 267

DGD Distal gradient difference 142, 143, 160, 164, 171, 174, 175, 178–182, 185, 272–275

DLR Deutsches Zentrum für Luft- und Raumfahrt 35, 67, 190

DTED Digital terrain elevation data 35, 67, 68

EASM East Asian Summer Monsoon 86
ECSZ Eastern California Shear Zone 75
EGM Earth Gravitational Model 36, 37, 130
EID Evaluation dataset ID 155, 156, 243–246
ELA Equilibrium-line altitude 41, 79, 86, 94

FCN Fully convolutional neural network 200, 201, 204
FPR False positive rate 149, 154, 241, 242, 247

GAD Gradient–apex divergence 104–106, 109–111, 113, 118–120, 123, 135, 139, 141, 155, 157, 159–161, 164, 169, 171, 174, 175, 178–182, 185, 186, 195, 196, 228–230, 272–275
GDEM Global digital elevation model 2, 6, 7, 30, 34, 37–39, 46, 47, 53, 57–60, 62, 64–66, 189, 211–216, 218
GeoTIFF Tagged Image File Format with embedded geospatial metadata 1, 42
GGC Global gradient convergence 136–138, 141, 144, 159, 160, 164, 165, 169, 171, 175, 195, 196
GIS Geographic information system 1, 28, 33
GMTED2010 Global Multi-resolution Terrain Elevation Data 2010 70, 82
GPCC Global Precipitation Climatology Centre 78, 87
GPS Global Positioning System 28, 74
GPU Graphics processing unit 198
GRS Geodetic Reference System 130
GTSFS Gobi-Tian Shan fault system 71, 84

HRTI High-resolution terrain information 35, 67, 68
HSA Half-splay angle 105, 106, 109, 110, 118–120, 123, 135, 169, 170, 228–230

ICESat Ice, Cloud and Land Elevation Satellite 37
IDL Interactive Data Language 41, 42
IMSE Integrated mean squared error 148
IRLS Iteratively re-weighted least squares 140

JAXA Japanese Aerospace Exploration Agency 2, 129, 130

ka Thousand years 41, 80, 81, 83, 86, 88
KDE Kernel density estimation 129, 147, 149, 157, 162, 164, 166, 174, 179, 186, 192, 252, 255, 258, 261, 264, 267

LCurv Longitudinal curvature 104, 109, 110, 117–119, 171, 175, 178–181, 228–230, 272–275
LGD Lateral gradient difference 142, 143, 160, 164, 171, 175, 178–182, 185, 272–275
LGM Last Glacial Maximum 83, 88
LiDAR Light detection and ranging 34, 39, 124
LOF Local outlier factor 174, 181, 197, 274
LOOCV Leave-one-out cross validation 110, 112

LRD Local reachability density 174

M Million 100, 130, 149, 202
Ma Million years 73, 75, 76, 84
MD Mean absolute difference 140
MDA Mean decrease of accuracy 150, 151
MDI Mean decrease of impurity 150–152, 157–160, 164, 193
METI Ministry of Economy, Trade and Industry 2, 37
MIS Marine Isotope Stage 88
MLP Multilayer perceptron 198, 199, 202
MRS Multi-resolution image segmentation 30, 31, 39, 90, 121, 125
MS COCO Microsoft Common Objects in Context 202, 203
MSE Mean squared error 148, 170, 172, 175, 176
MTJ Mendocino triple junction 73, 74
MWZSAD Moving window zero-mean sum of absolute differences algorithm 46, 54, 55, 65, 66, 216

NAM North American Monsoon 77, 79, 81, 82
NASA National Aeronautics and Space Administration 37
NED National Elevation Dataset 31
NIR Near infrared 189
NNLS Non-negative least squares 139, 140
NPH North Pacific High 76, 77, 82
NR Normal reference 148, 149, 157, 162, 248–252, 255, 258, 261, 264, 267

OBIA Object-based image analysis 3, 4, 30, 89–91, 127, 142, 189, 191, 192, 200–202
OBMA Object-based morphometric analysis 91, 107–109, 111–114, 118–121, 124, 149, 165, 166, 191–197, 224–228, 231
OCRF One-class random forest 8, 129, 132, 144, 147–149, 152, 154–160, 162, 164–166, 192–195, 243–245, 248, 252, 255, 258, 261, 264, 267
OCSVM One-class support vector machine 7, 91, 107, 109, 125, 129, 152, 154, 156, 162, 164, 192, 193, 243, 244, 246
OID Object ID 243, 244
OOB Out-of-bag 150, 151
OSL Optically stimulated luminescence 88

PC Principal component 29, 173, 181–187, 196, 197, 275
PCA Principal component analysis 8, 29, 173, 174, 181, 186, 275
PFD Polygon fractal dimension 101
PRISM Panchromatic Remote-Sensing Instrument 2, 129, 130
PVCH Paleovegetation-change hypothesis 81

R-CNN Region-based convolutional neural network 201–203
RAD Radial approximation divergence 141, 155, 159–161, 164, 169, 171, 174, 175, 178–182, 185, 186, 195, 196, 272–275

RBF Radial basis function 107, 108, 129, 192
RMSE Root mean squared error 130
ROC Receiver operating characteristic 149, 150, 152–154, 240
RTJ Rivera triple junction 73, 75, 76

SA Splay angle 170, 171, 175, 178–182, 185, 272–275
SAD Sum of absolute differences algorithm 46
SAR Synthetic aperture radar 1, 2, 4, 35, 36, 42, 67, 128, 129, 163, 189, 190, 207
SAW Slope area weighting 99, 221, 228–231
SIR-C Shuttle Imaging Radar with Payload C 1, 67, 129, 163, 190
SNAPHU Statistical-cost, Network-flow Algorithm for Phase Unwrapping 41, 65
SOM Self-organizing map 29, 30, 196
SRTM Shuttle Radar Topography Mission 1, 2, 33, 34, 36–39, 46, 49–51, 54, 63, 66–68, 91, 94, 95, 101, 111, 115, 116, 121, 122, 129, 155, 157, 190
SRTM1 Shuttle Radar Topography Mission DEM with 1″ posting 1, 2, 6, 7, 34–39, 42, 46, 47, 49–67, 129–133, 144, 152–166, 190, 193, 210, 212–217, 237–242, 244–247, 249–251, 261, 264, 267
SRTM3 Shuttle Radar Topography Mission DEM with 3″ posting 1, 38, 39, 210
SST Sea surface temperature 81
STK Number of scene stacks 161, 163
SVM Support vector machine 5, 91, 107–123, 193, 200, 223, 224, 227–231

TanDEM-X TerraSAR-X add-on for Digital Elevation Measurement 2, 6, 7, 33, 35, 40, 41, 49, 55, 58, 63, 65, 67, 68, 131, 165, 189–191, 207, 219
TDX Self-processed DEM from TanDEM-X CoSSC dataset (1032207_022) (15 m posting, other versions are named explicitly) 35, 46–62, 64–68, 212–216
TDX30 Version of TDX downscaled to 30 m 46, 55, 216
TID Training dataset ID 102, 106, 109–114, 132, 134, 141
TIN Triangular irregular network 1
TPI Topographic position index 2
TPR True positive rate 149, 154, 155, 157, 241, 242, 247

UTM Universal Transverse Mercator 37, 95, 129, 130

VRM Vector ruggedness measure 44, 52, 53, 66, 144, 161, 163, 165, 214

WGS World Geodetic System 36, 37
WTH White Top Hat 45, 54, 66, 98, 215

X-SAR X-band Synthetic Aperture Radar 2
XML eXtensible Markup Language 41, 42

ZGC Zonal gradient convergence 138, 141, 159, 164, 169
ZSAD Zero-mean sum of absolute differences 46

1 Introduction

1.1 Background

Since terrain is the time-integrated product of geological, tectonic, climatic, geomorphic, hydrological and ecological processes, a conception of land surface via quantitative terrain analysis (cf. e.g., Wood, 1996; Rodriguez et al., 2002; Schmidt and Hewitt, 2004; Iwahashi and Pike, 2007; Minár and Evans, 2008; Siart et al., 2009; Frey and Paul, 2012) offers valuable insights into the spectrum of geomorphodynamic processes at work (MacMillan and Shary, 2009). Geomorphometry is the science of quantitative land surface analysis by means of digital modeling the bare-earth topography (Pike, 1995, 2000; Rasemann et al., 2004). While research into the quantitative assessment of land surface has a long history (cf. Pike et al., 2009, for a review on the evolution of the discipline), geomorphometry matured with the growing availability of digital computers in the late 20th century (cf. Wood, 1996).

Near-global digital elevation models

In its most common conception, the term digital elevation model (DEM) refers to a gridded representation of the continuous variation of relief over space (Burrough, 1986)[1]. Since DEMs directly translate into array data structures, their processing can be easily handled in programming languages (cf. e.g., Evans, 1972). Furthermore, the regular lattice enables their storage in common image data formats such as GeoTIFF, facilitating their integration into geographic information systems (GIS's) and remote sensing software (cf. Weibel and Heller, 1991). Owing to these beneficial characteristics, gridded digital elevation data became the de facto standard for digital terrain modeling.

During the past two decades, DEMs and geomorphometric techniques found steadily increasing use in the field of geomorphology and related sciences. A major impetus for this development was the growing availability of near-global medium resolution DEM products that the scientific community can access at no or little cost. Enabling the unbiased comparative analysis of landscapes or a single type of landform over spatially extensive regions, near-global digital elevation datasets foster the synoptic analysis of landscapes. In doing so, they also facilitate the transfer of knowledge gained locally through field campaigns to larger study areas (Smith and Pain, 2009; Gonga-Saholiariliva et al., 2011; Schlummer et al., 2014).

Prior to 2003, global digital elevation data was only available with a posting of 30″ (GTOPO30; cf. EROS et al., 1997), limiting its scope to continental-scale applications. The Shuttle Radar Topography Mission (SRTM) was the first project to implement spaceborne single-pass SAR interferometry. The SRTM DEM was processed from data acquired by the bistatic C-Band system SIR-C. The sensor produced interferometric imagery with spatial resolutions between 13 m and 26 m in slant range, and 30 m in azimuth (Jordan et al., 1995; Bamler and Hartl, 1998; Rott, 2009; Freeman et al., 2019). The SRTM DEM was first released in 2003 with a posting of 1″ for U.S. territories (SRTM1) and 3″ (SRTM3) worldwide (Smith et al., 2006; Farr et al., 2007; Reuter et al., 2009).

[1] In a more general sense, irregular elevation data such as triangular irregular networks (TINs) and contour data is referred to as DEM as well.

In 2009, the Ministry of Economy, Trade and Industry (METI) of Japan released the initial version of the ASTER GDEM, a near-global DEM which was generated from near-infrared 15 m-posting ASTER imagery via automatic along-track stereometry (Tachikawa et al., 2011a). In September 2014, the U.S. government announced the release of global SRTM1 data, which successively became available. In the year 2016, the Japanese Aerospace Exploration Agency (JAXA) published AW3D30, a free-of-charge 1″ version of the commercial product ALOS World-3D 5 m-DEM (AW3D5). AW3D5 was stereometrically processed from panchromatic triplet stereo imagery with a posting of 2.5 m, acquired by the Panchromatic Remote-Sensing Instrument (PRISM) onboard the spacecraft ALOS (Tadono et al., 2004, 2009; Shimada et al., 2010; Tadono et al., 2014).

Building upon the experience gained with the X-SAR payload of SRTM, the still ongoing TanDEM-X mission utilizes two X-band SAR satellites flying in a helix-like formation to create a bistatic interferometer with adjustable baseline geometry (Krieger et al., 2007; Freeman et al., 2019). A high spatial resolution of the X-band imagery (<2 m and 2.3 m for ground range and azimuth, respectively) as well as state-of-the-art radar technology, such as multibaseline phase unwrapping, enabled the generation of a near-global DEM with a posting of 12 m (Lachaise et al., 2008; DLR, 2011b; Rossi et al., 2012). The operative DEM was published in 2016 (Rizzoli et al., 2017; Zink et al., 2017).

Geomorphometry and object-based analysis

Evans (1972) established the differentiation in *generic* and *specific* geomorphometry. Generic geomorphometry covers the generic conceptualization of the land surface by measuring characteristics which are obtainable from any continuous surface. In contrast, the field of specific geomorphometry tackles the morphometric formalization of landforms (cf. Evans and Cox, 1974; Minár and Evans, 2008; Pike et al., 2009; Wilson, 2012). In this context, landform is defined as any discrete physical feature on terrestrial surfaces (cf. MacMillan and Shary, 2009), and geomorphometric studies are performed using land surface parameters (morphometric parameters). Land surface parameters can be chiefly differentiated into (1.) variables which quantify the local geometry (*local* land surface parameters), and (2.) variables which provide information on the relative topographic position within the landscape (*regional* land surface parameters; cf. Speight, 1974; Shary, 1995; Shary et al., 2002; MacMillan and Shary, 2009; Olaya, 2009).

Since geometric information on a local surface patch is reflected in the spatial contexts of altitude values, the quantification of local relationships between pixel values is performed by computing partial derivatives (Arrell et al., 2008; Gallay, 2009; Reuter et al., 2009). Discrete datasets are not differentiable, so that the DEM data needs to be locally approximated (Evans, 1980; Zevenbergen and Thorne, 1987; Schmidt et al., 2003; Reuter et al., 2009). Calculation of the topographical position is most commonly performed by taking the difference between the DEM and a low pass-filtered grid as a measure of local topographic context, the topographic position index (TPI), or by exploiting grayscale mathematical morphology (Rodriguez et al., 2002; Schmidt and Hewitt, 2004; Wilson et al., 2007; Tagil and Jenness, 2008).

Automatic approaches to generic morphometric classification involve the formalization of heuristic rules for combinations of local and/or regional land surface parameters, or the application of classification algorithms (cf. e.g., Florinsky, 2012; Gruber et al., 2017, for concise overviews of techniques in use).

Yielding morphometric primitives (cf. Dikau, 1989; Schmidt and Dikau, 1999; Shary et al., 2005), this approach is generally well-suited for a generic perspective on landscape. Computation of both local and regional morphometric parameters entails the use of a moving calculation window. In conjunction with the posting of the DEM under consideration, these search windows determine the scale on which the morphometric modeling is performed, and the window size thus must be adapted to the surface features of interest and the methodology applied (cf. Shary et al., 2002; MacMillan and Shary, 2009). As an alternative, multi-scale approaches enable a comprehensive landscape evaluation (cf. Wood, 1996; Schmidt and Hewitt, 2004; Schmidt and Andrew, 2005).

Since landform boundaries are not necessarily pronounced discontinuities (cf. Evans, 2012), specific geomorphometry involves a form of semantic conception which incorporates a-priori expert knowledge (cf. e.g., Argialas and Miliaresis, 1997; Dehn et al., 2001). In the context of specific geomorphometry, generic land surface parameters function as *atomic* morphometric information. By treating landforms as discrete entities, specific geomorphometry imposes an object-based view on the land surface (cf. Drăguţ and Eisank, 2011). In modern medium-resolution DEMs, many real-world objects cover a multitude of pixels. These so called H-res scenarios (Strahler et al., 1986; Woodcock and Strahler, 1987) are generally desired, because the altitude field contains valuable information on geospatial context within a landform (Strahler et al., 1986; Woodcock and Strahler, 1987). Pixel-neighborhoods with predefined shape can, however, not account for the irregular boundaries of landforms. Conversely, specific geomorphometry requires a complete delimitation of the landform of interest (Evans, 1987, 2010). Manual approaches to landform delineation are, however, tedious and bear the risk of user-induced inaccuracies, if not performed with care by an expert in the field (cf. Smith and Clark, 2005; Smith, 2011; Smith et al., 2013).

Object-based image analysis (OBIA) is a two-stage methodological framework, which evolved in the field of remote sensing as a response to the increasing incidence of H-res scenarios and the concomitant issue of salt-and-pepper effects in pixel-based classification workflows (cf. Blaschke et al., 2000). First, a segmentation algorithm is applied to the gridded data, yielding objects based upon one or more criteria of homogeneity (Blaschke et al., 2004; Blaschke, 2010). Subsequently, a classification routine is applied to the obtained set of segments (Benz et al., 2004). In doing so, the methodological framework of OBIA holds the promise of improving research tasks within the field of specific geomorphometry by enabling segment-level morphometric analysis, the incorporation of geospatial topology, and the consideration of thematic neighborhood relationships (cf. Blaschke, 2003; Burnett and Blaschke, 2003; Blaschke et al., 2004). Object-based analysis frameworks were soon successfully adopted for geomorphometric research, with applications being demonstrated for the fields of generic (cf. e.g., Drăguţ and Blaschke, 2006; Gerçek et al., 2011; Mashimbye et al., 2014) and specific geomorphometry (Saha et al., 2011; Van Den Eeckhaut et al., 2012; Eisank et al., 2014; Pedersen, 2016). In the case of object-based analysis of alluvial fans, however, approaches either predate the emergence of modern object-based methodologies (cf. Miliaresis, 1999; Miliaresis and Argialas, 2000; Miliaresis, 2001) or are deficient with respect to the delimitation of adjoining fans (cf. Argialas and Tzotsos, 2004, 2006; Norini et al., 2016; Argyridis and Argialas, 2017).

1.2 Challenges

Although studies applying the concept of object-based image analysis to morphometric data show auspicious results, multiple challenges hamper scientific progress in this research field. These challenges fall within the scope of the object-based methodology per se, or they are caused by the peculiarities of geomorphometric data. In what follows, it is shown that concepts established in the field of remote sensing cannot be directly adopted into the field of specific geomorphometry.

Challenge 1 – DEM properties

DEM base data and production methods are inherently limited by the quality of terrain representation, most notably caused by SAR phase noise and limitations in the accuracy of co-registration algorithms (cf. Hannah, 1981; Zebker and Villasenor, 1992; Geudtner, 1995; McGlone, 2007). Resulting in undulations with moderate to high frequency, these interferences have the potential to substantially impair the rendition of local altitude fields and consequently affect generic morphometric variables (Weibel, 1990; Oksanen, 2006; Wechsler and Kroll, 2006; Reuter et al., 2009; Gonga-Saholiariliva et al., 2011).

In comparison to the assessment of absolute accuracy metrics, the evaluation of relative accuracy of DEM products gained, however, surprisingly little emphasis. As a consequence, studies adopting OBIA methodologies for geomorphometric research tasks mostly do not critically assess how the incorporated DEM depicts the terrain. This issue goes in hand with the fact that the majority of studies do not consider filtering techniques for the improvement of terrain rendition for the application task at hand (cf., however, Eisank et al., 2014; Mashimbye et al., 2014).

Challenge 2 – Segmentation of geomorphometric data

Segmentation algorithms need to be parametrized with a scaling factor or bandwidth value in order to control their susceptibility to discontinuities in the altitude field or derived morphometric parameters. Segmentation is considered an ill-structured problem, in the sense that it has no unique solution, and is mostly tackled using an expert-driven tentative approach (Hay and Castilla, 2008; Arvor et al., 2013). Research done hitherto focused on global optimization of this scaling problem, yielding appropriate solutions only in cases where the objects of interest display only a small range of sizes (Drăguţ et al., 2009, 2011; Ming et al., 2012; Drăguţ et al., 2014; Ming et al., 2015; Louw and van Niekerk, 2019). These conditions are clearly not met in the field of geomorphometry (cf. Evans, 2003).

Challenge 3 – Classification concepts

For classification, OBIA frameworks often rely heavily on expert knowledge being utilized to define rule sets (cf. Flanders et al., 2003; Benz et al., 2004; Bishop et al., 2012). For geomorphometric tasks, this conventional approach is problematic in two respects: Firstly, morphometric variables are strongly affected by DEM posting and properties (cf. Challenge 1, Weibel, 1990; Florinsky, 1998; Shary et al., 2002). It follows that the specification of thresholds must be tailored towards the dataset in use, hampering the transfer of *feature ontologies* (cf. Arvor et al., 2013) between different DEM products. Secondly, the geomorphometric properties of many landforms show strong relationships with scale (cf. Challenge 5). As a consequence, a set of static thresholds in principle cannot appropriately reflect the

complex feature spaces going along with this situation.

In the field of remote sensing, increasing emphasis has been given to data-driven classification approaches, involving discriminatory classifiers such as support vector machines (SVMs) and random forests (cf. e.g., Stumpf and Kerle, 2011; Ghosh and Joshi, 2014). With respect to geomorphometric analysis, these algorithms learn to differentiate between the landform types that are present in the geomorphic inventory of a study area, but they do not formalize a morphometric signature (cf. Challenge 4). This entails that the results of the classification are case-specific and allow no universally valid inferences on the significances of incorporated morphometric variables for the identification of the considered landforms. While data-driven classification approaches found sporadic use in combined approaches incorporating remote sensing data and digital terrain data (cf. Guan et al., 2013; Juel et al., 2015), they are yet to be used in geomorphometric research.

Challenge 4 – Morphometric signatures and incorporation of specific geomorphometry

The concept of *spectral signatures* is pivotal to the field of remote sensing. There, a spectral signature is defined as a characteristic multi-spectral pattern of reflectance and/or emittance, enabling the identification of surface types in remote sensing datasets (Jensen, 1986; Lillesand et al., 2004). In contrast, the term (geo-) morphometric signature is not widely established in geomorphometric research (cf., however, Pike, 1988; Giles, 1998; Schmidt and Hewitt, 2004) and to this day neglected in object-based geomorphometry. This manifests itself in research done hitherto being based upon generic geomorphometric parameters. Since informative value emerges from spatial context, geomorphometric variables need to be appropriately designed and combined to be able to represent a signature pattern. Morphometric variables specifically formalizing the geometry of a landform can be expected to minimize intra-class heterogeneity and maximize inter-class heterogeneity (cf. Dikau, 1989), optimizing the identification of a landform within a diverse geomorphologic inventory.

Challenge 5 – Controlling factors of alluvial fan morphogenesis

Geomorphometric applications in alluvial fan research predate the widespread availability of DEMs, which to this day is reflected in the spectrum of techniques applied. Giving emphasis to the juxtaposition of planimetric areas of fans and corresponding catchments, as well as average fan gradient, early research elaborated on scale relationships of alluvial fan geomorphometry. In this context, only those morphometric variables were used which could be retrieved from topographic map data or measured in the field (cf. e.g., Stock, 2013; Bowman, 2018). Although this research unveiled the generally negative allometry of fan–catchment systems (cf. Church and Mark, 1980), as well as the related decrease in fan gradients, it mostly neglected that sediment retention and sediment reworking in catchments are not merely a function of catchment size (cf. Fryirs et al., 2007; Mather and Stokes, 2018). Metrics of fan–catchment relationships thus show scatter which bears no informative value with regard to the respective fan surfaces.

A pivotal research question in alluvial fan research is to what extent different environmental controls—most notably climatic and tectonic boundary conditions—affect the geomorphology of alluvial fans (cf. Lecce, 1990). During the last two decades, this research question has been primarily tackled from a geomorphodynamic perspective, and it has been shown that Quaternary aggradation phases are

predominantly linked with rapid climatic shifts (cf. e.g., Bull, 1991; Harvey et al., 1999a,b). Although geomorphological footprints of controlling factors have been elaborated via multivariate statistical analysis (cf. Silva et al., 1992; Calvache et al., 1997; Sorriso-Valvo et al., 1998; Viseras et al., 2003; Bahrami, 2013; Šilhán, 2014), this research considers controlling factors under relatively constrained conditions, i.e., it focuses on single study areas where differences in geomorphic expression are driven by one dominant controlling factor. This situation comes along with the fact that these studies do not take scale relations into account. In research done hitherto, approaches to cluster the alluvial fan feature space received little attention (cf. Crosta and Frattini, 2004; Karymbalis et al., 2018).

The disentanglement of environmental controls from morphometric data of a large and diverse set of alluvial fans entails that the problem can be *inverted*, i.e., a supposed prevalence of controlling factors must be expressed as an unequivocal morphometric signature within the alluvial fan property space (cf. Ellis et al., 1999; Tarantola, 2005). Equifinality (also denoted convergence)—the phenomenon of a disparate set of processes creating similarly shaped landforms (cf. Beven, 2006)—is, however, a well-known problem in alluvial fan research (cf. e.g., Clarke et al., 2010; Clarke, 2015; de Haas et al., 2016, 2018).

1.3 Research questions and objectives

These challenges give rise to the following research questions (RQs) and research intents, which will be addressed in this doctoral thesis.

Objective 1

RQs How do near-global DEM products compare to each other with respect to their intrinsic resolution and consistency of terrain rendition?
What improvements are made by the recently released DEM products TanDEM-X and AW3D30?

We will evaluate non-commercial near-global DEM datasets, that is TanDEM-X, ASTER GDEM, SRTM1, and AW3D30, with respect to their ability to provide a consistent representation of terrain. In this context, we define consistent terrain rendition as the approximation of the in-field situation in such a way that landforms can be identified, accurately delineated, and described via visual analysis (cf. Smith and Wise, 2007; Smith, 2011) and geomorphometric methods (cf. Wood, 1996; Drăguţ and Eisank, 2011, 2012). We will assess how the respective base data and DEM production methods affect terrain rendition and in particular the high-frequency components of the modeled altitude field.

Objective 2

RQs Which combination of morphometric variables allows for an accurate delineation and classification of alluvial fans, including adjoining fans?
Can the problem of bandwidth selection for segmentation be addressed on a per-feature basis and in an objective, data-driven manner?
How can machine learning approaches facilitate the object-based analysis of landforms? What are the advantages over rule-based techniques and which challenges need to be addressed?
What inferences can be drawn for the future development of object-based geomorphometry?

The core research objective of this thesis is to design an object-based morphometric workflow which is able to delineate and classify alluvial fans in a robust data-driven manner by utilizing supervised machine learning algorithms. In order to perform a formalization of a morphometric signature rather than to train disparities between different thematic classes, one-class classifiers are, for the first time, introduced into an object-based framework. We will evaluate if a classifier can be used to guide the upstream processing steps. I.e., we will assess if the parametrization of the segmentation algorithm can be governed by fuzzy classification scores derived from a supervised machine learning algorithm, and if the object-based workflow can be made scale-adaptive. Furthermore, we will assess if classifier metrics can be used to guide DEM selection, DEM preprocessing, as well as the conception and selection of morphometric parameters.

Objective 3

RQ To which extent is variability in environmental controls reflected in the geomorphometry of fan surfaces?

As an addendum to these primary research objectives, we will utilize the morphometric features developed within the scope of Objective 2 to address the question whether the alluvial fan feature space allows for an inversion of controlling factors.

1.4 Outline of this thesis

This doctoral dissertation commences with an in-depth discussion of the state of research on controlling factors of alluvial fan development and their impact on alluvial fan geomorphology. Chapter 2 also reviews paradigms of the geomorphometric analysis of alluvial fans, summarizes previous approaches to infer controlling factors from morphometric properties, and outlines prior approaches to the automatic mapping of fans.

Tackling Objective 1, Chapter 3 presents an experimental TanDEM-X DEM which was self-processed from CoSSC imagery, and juxtaposes it with ASTER GDEM and SRTM1. Since AW3D30 was not available at this time, an ad hoc analysis of AW3D30 is given in Chapter 6.

Chapter 4 introduces the reader into the different study areas wherein alluvial fans have been delineated to incorporate them into a reference dataset of 306 fans. To provide a foundation to address Objective 3, we will summarize and discuss the state of research with respect to the significance of tectonic and climatic boundary conditions in the respective regions.

Focusing on a single study area located in the Mongolian Altai, Chapter 5 attends to Objective 2 by presenting a novel object-based morphometric framework for the identification and classification of alluvial fans. The framework utilizes a spatial variant of mean-shift clustering to segment multiband rasters of morphometric variables which were derived from filtered SRTM1 elevation data. A one-class support vector machine (OCSVM) is used to formalize a morphometric signature for alluvial fans and to identify alluvial fans within the set of segmentation objects. Specifically, segmentation is performed repeatedly for different bandwidths, and class membership likelihoods are used to control the conflation of the single segmentation layers into a final vector dataset.

Chapter 6 builds upon the results obtained in Chapter 5, now using the full reference dataset for

classification. It introduces a one-class random forest (OCRF) algorithm whose robust characteristics and non-parametric nature facilitate the unbiased, data-driven processing of object-based data. In Chapters 5 and 6, we will introduce and evaluate new morphometric variables, which use tailored linear algebra to model the alluvial fan geometry, so that they can be expected to minimize the intra-class heterogeneity within sets of alluvial fans, but maximize the disparities to the remaining geomorphological inventory.

In Chapter 7, we will then consider a subset of the morphometric parameters introduced in the previous two sections, to address the question whether signals indicating the impact of certain boundary conditions can be inferred from the property space of alluvial fans (Objective 3). For this purpose, we will first work out whether the alluvial fan feature space as defined by the morphometric variables is amenable to a clustering into thematically significant classes. Subsequently, a principal component analysis is performed to figure out which signals contribute most to dataset variance, and whether these signals allow inferences to be drawn about environmental controls. For both tasks, the morphometric data is cleared of scale-related variance via linear or non-linear regression.

Eventually, a synthesis of the quintessential results of this dissertation and incentives for future research are given in Chapter 8.

2 State of research – The alluvial fan–catchment system

2.1 Definitions and differentiation

Alluvial fans are composite sedimentary landforms resembling a segment of a cone radiating from a point—the apex—where a feeder channel emerges from an upland basin and becomes unconfined (Drew, 1873; Bull, 1977; Schumm et al., 1987). They are generally arcuate in plan view, with aperture angles (splay angles) governed by the degree of coalescence with other fans or neighboring environments (Viseras et al., 2003; Blair and McPherson, 2009; Bahrami, 2013). Alluvial fans thus can be differentiated into unconfined and confined fans, and confinement can occur both laterally and distally (cf. Fig. 2.1; Sorriso-Valvo et al., 1998; Crosta and Frattini, 2004; Cavalli and Marchi, 2008). Their distinctive conical shape evolves from cyclic radial avulsions which lead the feeder stream to explore the entire fan surface, hence establishing and maintaining an approximate radial symmetry (Field, 2001; Sinha, 2009; Delorme et al., 2017, 2018).

While active mountain ranges abutting valleys or basins represent the most prevalent setting for alluvial fan morphogenesis, its primary precondition is topographic contrast (Ventra and Clarke, 2018). Common examples for alluvial fan development at tectonically stable positions are (1.) tributary junction fans (cf. e.g., Gómez-Villar et al., 2006; Stokes and Mather, 2015), as well as, (2.) fans located at margins of recently deglaciated valleys (paraglacial fans; cf. Ryder, 1971; Church and Ryder, 1972; Lehmkuhl and Haselein, 2000; Giles, 2010; Berger et al., 2011). Although strong emphasis has been given to the study of arid and semi-arid settings where alluvial fans are most abundant, alluvial fans occur in a wide array of climatic conditions (cf. e.g., Kesel and Spicer, 1985; Kostaschuk et al., 1986; Saito and Oguchi, 2005; de Haas et al., 2015b).

2.1.1 Fan-building processes

Sourcing catchment and depositional basin are dynamically linked by a sediment routing system, whose hydraulic conditions exert a strong control on alluvial fan geometry (Armitage et al., 2011). The end-members of the process spectrum of fan-building processes are sediment-gravity-driven debris flows and fluid-gravity-driven (watery) streamflows. Furthermore, the term hyperconcentrated flow is used to depict flows exhibiting intermediate rheological behavior between the two ends of the spectrum (Costa, 1988; Scott et al., 1995; Pierson, 2005; North and Davidson, 2012; Ouellet and Germain, 2014).

Streamflows exhibit relatively small sediment concentrations up to approximately 4 % by volume or 10 % by weight and behave as turbulent Newtonian fluids (Leeder, 1982; Whipple et al., 1998; Pierson, 2005). The local transport capacity of a fluvial system is given by its stream power per unit downstream length and channel width (Petit et al., 2005):

$$\omega = \frac{\rho g Q S}{b}, \tag{2.1}$$

where ω is the stream power per unit downstream length and channel width (W m^{-2}), ρ denotes the fluid

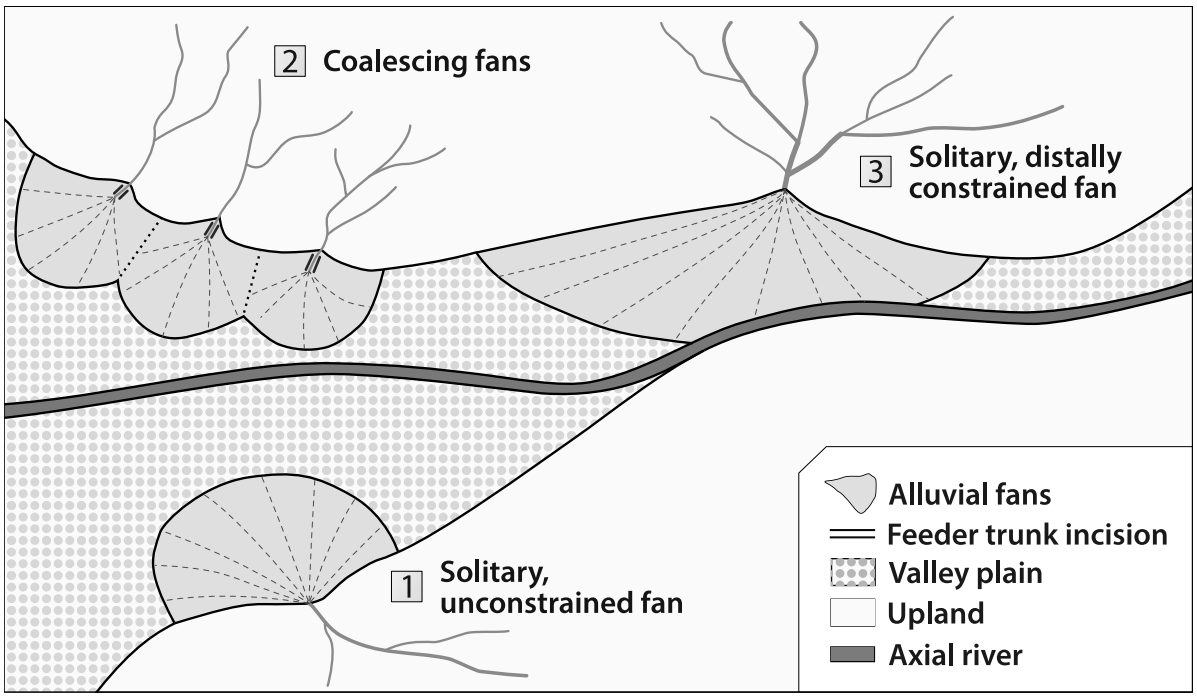


Figure 2.1: Schematic plan view of elementary fan types. (1) Solitary, unconstrained fans are facilitated by ample accommodation space being generated by proximal synsedimentary tectonic activity. (2) Laterally coalescing fans are instigated by pronounced sediment evacuation and/or deficient accommodation space. Failure to accommodate sediment proximal to the mountain front results in a downstream shift of radial deposition, denoted progradation. Progradation can be accompanied by feeder trunk incision. (3) Solitary fan, distally constricted by an axial river.

density (1000 kg m^{-3}), g defines the gravitational acceleration (9.81 m s^{-2}), Q is the discharge (m^3 s^{-1}), S defines the channel slope (m m^{-1}), and b defines the channel width (m). The erosional or depositional response of a fluvial system is governed by the threshold of critical power (Bull, 1979):

$$\frac{\omega}{\omega_{\text{crit}}} = 1, \tag{2.2}$$

where ω denotes the actual in-situ stream power, and ω_{crit} denotes the stream power required for the considered channel to be in equilibrium. Another aspect to consider is stream competence, which defines the maximum grain size that can be mobilized by the stream. The critical power to transport a uniform grain size D is defined by the Shields criterion (Shields, 1936):

$$\tau_{\text{crit}} = \tau^*_{\text{crit}}(\rho_s - \rho_w)gD, \tag{2.3}$$

where τ_{crit} (Pa) defines the critical fluid shear stress required for initial motion, τ^*_{crit} is the non-dimensional Shields number and defines resistance to motion, ρ_s and ρ_w (kg m^{-3}) denote particle and fluid density, and D is the grain size (m). Values for the Shields number depend on the roughness of the natural stream and consequently vary, but values around 0.045 are generally accepted as good approximation

(cf. Knighton, 2014). Furthermore, bed shear stress (τ_b) can be approximated by (Wohl, 2000):

$$\tau_b = \rho g h S, \tag{2.4}$$

where h denotes the depth of flow (m). It is a common misconception that alluvial fans aggrade due to a reduced channel slope (Ventra and Clarke, 2018). From equations (2.1) and (2.4), however, it is easily apparent that aggradation is essentially forced by the loss of confinement.

Since the granular phase is free to settle out of suspension, streamflow-fed alluvial fans will adjust their slope to the in-situ critical stream power. This so-called equilibrium slope shows an inverse log-log-linear relationship with (1.) the ratio of granular (Q_s) and fluid phase (Q_w) of the total discharge (sediment load factor; cf. Blair and McPherson, 1994; Parker et al., 1998; Milana and Ruzycki, 1999; Rohais et al., 2012) and (2.) is positively dependent on grain size (Hooke, 1967; Hooke and Rohrer, 1979). Compared to fans on which debris flows are the prevalent formative process, gradients of predominantly streamflow-fed alluvial fans are generally small and vary up to about 6° in apex proximity (cf. e.g., Bull, 1977; Jackson et al., 1987; Stock et al., 2008; Stock, 2013)

Studies conducted in the North American Southwest indicate that alluvial fans in this region display minimum slopes above 1.5°, whereas the adjoining floodplain exhibits gradients well below 1° (Blair and McPherson, 1998; Blair, 1999c; Saito and Oguchi, 2005). In this context, Blair and McPherson (1994) conjectured the existence of a universal *slope gap* between the fluvial regime of rivers and those of alluvial fans, which they attributed to the widespread occurrence of supercritical flow conditions on fan surfaces (cf. Blair and McPherson, 1998). Since then, it has been shown that streamflow-fed fans can exhibit gradients way below 1° and display gradual transitions from the toe zone to the adjacent floodplain, indicating that the alleged slope gap emerged from the impact of the semi-arid to arid environmental conditions of the North American Southwest on hydraulic conditions (Harvey, 2002b; Saito and Oguchi, 2005; Hashimoto et al., 2008).

Owing to the downstream decrease of stream power, streamflow-fed alluvial fans exhibit concave-upward longitudinal profiles (cf. e.g., Bull, 1964; Denny, 1965; Hooke and Rohrer, 1979; Parker et al., 1998; Miller et al., 2014). The prevalent mechanism of this basinward slope decrease is, however, subject to debate. The *transport hypothesis* claims that the gradient decrease is essentially a function of the Q_s/Q_w ratio, which successively decreases downslope due to a decreasing hydraulic radius. This, in turn, forces the alluvial fan surface to constantly readjust to the critical stream power (cf. Whipple et al., 1998; Powell et al., 2012; Guerit et al., 2014). Conversely, the *threshold hypothesis* claims that the in-situ slope is set by the coarsest grain fraction that can be entrained according to the Shields criterion (cf. Miller et al., 2014). Laboratory experiments verify that downstream fining coincides with concave long-profiles (cf. e.g., Paola et al., 1992a,b; Smith and Ferguson, 1996; Whipple et al., 1998) but also indicate that longitudinal concavity occurs for a singe grain size (Clarke et al., 2010; Guerit et al., 2014). Based on field measurements of hydraulic geometry on four alluvial fans in the North American Southwest, Stock et al. (2008) assert that fan gradients exhibit a stronger correlation with hydraulic radius and concomitant stream power than with median grain size.

Debris flows are muddy slurries composed of a disorganized mixture of cobbles, gravels and finer material embedded into a clay-water matrix, whose buoyancy is sufficient to keep the coarse

compartments in suspension (Major, 2003; Bowman, 2018). The slurries move *en masse* as a liquified viscoplastic mass in a non-Newtonian laminar manner (Dasgupta, 2003; Sattler, 2016) and typically exhibit between 20 and 60 % water by volume (Costa, 1988; Pierson, 2005). Mass movement is instigated by transient stress, which increases granular pore water pressure, brings coarse material into suspension, and mediates basal friction below a critical threshold (Iverson, 1997). In debris flows, pore pressure dissipation is impeded by clay and silt particles, and a minimum concentration of fine-grained material is thus essential for the persistence of liquefaction (Costa, 1984).

Debris flows initiate at the interface of high pore pressure, steep terrain, and abundant sediment (Iverson, 1997; Bovis and Jakob, 1999). Common scenarios are (1.) initiation of shallow landslides arising from oversaturated soil after heavy rainfalls or rapid snowmelt (Major, 2003) and (2.) the generation of concentrated overland flows as part of a process known as *sediment bulking*, that is, the progressive entrainment of water-saturated material into drainage channels (Blair and McPherson, 2009; Borga et al., 2014).

The plasticity of debris flows shows a complex non-linear dependency on multiple controlling factors. Specifically, the critical slope for net deposition is set by the volume and the grain size distribution of the debris flow, and the degree of flow confinement (Rickenmann, 2005; Davies and McSaveney, 2008; Rickenmann and Scheidl, 2013). Debris flows undergo a longitudinal sorting, which ends in large clasts being moved to the front of the debris flow and the eventual development of a terminal lobe (Takahashi, 1980). By exhibiting a high permeability, the terminal lobe raises marginal friction and promotes the escape of pore water, which in turn increases internal grain contact friction (Major and Iverson, 1999). Once the debris flow debouches into the depositional basin, this process extends to the flanks of the flow. The resulting *levées* hinder the following flow from spreading sidewards and therefore *increase* the runout distance (Iverson, 2004). De Haas et al. (2015a) produced scaled laboratory fans built up from debris flows and evaluated the relative importance of material properties for the mobility of debris flows. The authors were able to show that the runout potential of debris flows is optimal for intermediate values of both clay content and coarse clasts by balancing yield strength, pore water retainment, and terminal friction. Upper limits on debris flow runout distances involve that debris flows triggered in large catchments exhibit a low probability of reaching the fan surface. In this context, several studies showed that debris flows are unlikely to reach the fan surface if the corresponding catchment is larger than approximately 25 km^2 (cf. Marchi and Brochot, 2000; Marchi and D'Agostino, 2004; Scheidl and Rickenmann, 2010)

In accordance with these remarks, alluvial fans primarily built by debris flow show a wide range of slope values, with angles varying between 4° and 18° (cf. e.g., Jackson et al., 1987; Harvey, 1992; de Scally et al., 2001; de Scally and Owens, 2004; Blair and McPherson, 2009). Lacking mechanisms of preferential deposition, debris flows tend to produce straight longitudinal profiles (Blair and McPherson, 1994; Williams et al., 2006). Note however, that concave radial profiles can be caused by secondary redeposition in the distal parts of the fan (cf. Marchi and Tecca, 1995). Furthermore, debris flows with relatively little clay content (so called non-cohesive debris flows; cf. Scott et al., 1995) can induce longitudinal concavity via flow transformation (cf. Deangeli et al., 2013).

Since the rheological characteristics of the conveyed sediment control depositional slopes, and catchment characteristics may vary on a small scale, even neighboring fans can be dominated by

contrasting processes and thus exhibit different morphometric properties (Blair and McPherson, 1994; Blair, 1999b, 2003). That said, the continuum of processes potentially acting on alluvial fan surfaces entails that a continuum of fan gradients should exist for large sample datasets covering a variety of boundary conditions (cf. Saito and Oguchi, 2005). The geomorphometric differentiation of alluvial fans with respect to their prevalent primary process is hampered by the fact that equifinal solutions can emerge from variable combinations of sediment load factor and grain size distribution. Furthermore, a substantial proportion of fans experiences variable contributing primary processes (Harvey et al., 1999b). While pure streamflow-fed fans may result from environmental controls impeding the generation of debris flows (cf. Section 2.2.4), pure debris flow fans are not the norm (Davies and McSaveney, 2008).

Some authors were able to unambiguously differentiate between streamflow-fed fans and debris flow-fed fans using a slope threshold of 4° (cf. Marchi et al., 1993; Marchi and Brochot, 2000). It is, however, generally accepted that a transition zone exists between streamflow fans and fans built by hyperconcentrated flows and debris flows (cf. Kostaschuk et al., 1986; Jackson et al., 1987; Marchi and Tecca, 1995; de Scally and Owens, 2004; Rickenmann and Scheidl, 2013).

2.1.2 Autogenic dynamics

The construction and maintenance of the characteristic semi-conical form of alluvial fans is induced by cyclic radial shifts of runoff and concomitant sediment distribution around an avulsion node, which is not necessarily the topographic apex (Bull, 1964; Denny, 1967; Blair and McPherson, 1994; Field, 2001). For fans constructed via Newtonian fluid mechanics, cyclical *lateral* avulsions are accompanied by a *vertical* oscillation pattern characterized by alternations between channel entrenchment, channel backfilling, and aggradation. These alternations in turn instigate a cyclical change between prevalent channelized flow and unconfined sheetflow (Whipple et al., 1998; Reitz and Jerolmack, 2012; Delorme et al., 2017, 2018)[1].

An avulsion cycle is initiated by a collapse of flow into a single channel, with abrupt scouring resulting from the enhanced stream power in the confined environment (cf. Section 2.1.1). As a consequence, the incised channel is able to transport sediment at a lower equilibrium slope, and thus will eventually emerge at the fan surface. The resulting mid-fan or distal lobation drives fan progradation, the distal growth of the fan, but also promotes the gradual backfilling of the incised channel. Once backfilling has substantially reduced the channel depth, initial overbank flow eventually switches to sheetflooding, with substantial parts of the fan surface being activated (cf. Bryant et al., 1995; Martin et al., 2009). A subsequent cycle is initiated by preferential flow initializing a self-reinforcing collapse into a new channel. Selection of a new flow path is guided by small differences in radial gradient, but is essentially a stochastic process (Slingerland and Smith, 2004; Reitz et al., 2010).

Debris flow avulsion dynamics differ from streamflow dynamics in that vertical autogenic processes are not fundamentally governed by intermittent erosion (cf. de Haas et al., 2016). Conversely, debris flows gradually generate their own lateral constriction via levées (cf. Section 2.1.1). This phenomenon

[1] Note that the term *sheetflow* is used for any sheetlike overland flow over the alluvial fan surface. This does not strictly correspond to the original definition of sheetflow as high-frequency, low-magnitude overland flow, but our usage is common practice within in the field of geomorphology. Furthermore, we will refer to widespread sheetflows on the fan surface as *sheetflooding*. For more information on this matter, please refer to North and Davidson (2012).

causes subsequent debris flows to be progressively funneled over the preferential flow path, resulting in enhanced runout distances. The process is eventually reversed by terminal lobe blockage, causing the debris flows at the end of an avulsion cycle to gradually fill the conveyor path, culminating in a new path being selected (Davies and McSaveney, 2008; de Haas et al., 2016, 2018).

With avulsion sequences exhibiting cycle times between 10^2 and 10^4 years (cf. Heward, 1978; Bowman, 2018), digital elevation data is unlikely to depict alluvial fans in a state of fan-wide sheetflooding (cf. Clarke et al., 2010).

2.1.3 Fanhead entrenchment

Fanhead entrenchment is a common phenomenon on mature alluvial fans. These incised channels are downslope extensions of the feeder trunk stream onto the fan and attain the fan surface at a point in the proximal or intermediate section of the fan—the intersection point (Hooke, 1967; Bowman, 1978; French, 1987). In case of fanhead entrenchment, the intersection point rather than the apex is the locus of potential active aggradation, with lobes emanating from the intersection point being referred to as active depositional lobes (Calvache et al., 1997; Viseras et al., 2003).

If existing, active depositional lobes promote the distal growth of the fan surface. In this context, alluvial fans can be differentiated into fan systems displaying a strong tendency for progradation, as opposed to fans whose growth in volume occurs via simple aggradation, i.e., vertical stacking (cf. Clevis et al., 2003; Densmore et al., 2007; Rohais et al., 2012; Bowman, 2018). As we will discuss in detail in Section 2.2.3, the propensity of a fan–catchment system for progradation is chiefly controlled by available accommodation space (cf. Paola et al., 1992a).

It is important to emphasize that the differentiation between systems tending to aggradate and prograde, respectively, must not be understood in the sense that entrenchment is an unambiguous indicator for a progradation-dominated system. Conversely, the fact that alluvial fans having some degree of entrenchment is the norm rather than the exception during an autocyclic avulsion casts some doubt on approaches taking channel entrenchment as indicator for (changes of) allogenic boundary conditions (cf. Section 2.1.2; Ritter et al., 1995; Viseras et al., 2003). Furthermore, the proximal dissection may be related to regolith depletion at the end of a climatically induced aggradational phase, i.e., time-transgressive morphodynamics which do not require a second climatic change (cf. e.g., Bull, 1964; Harvey and Wells, 2003; Eppes and McFadden, 2008).

2.1.4 Scale

Trapping at least the vast majority of the sediment evacuated from the upland catchment, alluvial fans generate a disconnectivity between their source area and the downstream landscape (cf. Rohais et al., 2012; Delorme, 2017; Bowman, 2018). Hence, the volume of alluvial fan bodies is coercively linked to the size of the corresponding catchment. Alluvial fans consequently show a large variety of scales, with high-end members being *megafans*[2] with up to 60 km in length (Gohain and Parkash, 1990; Horton and DeCelles, 2001; Zani et al., 2012). Small debris cones with down to ~50 m in length and slopes up to 30° (cf. Wells and Harvey, 1987; Harvey and Wells, 2003) are precursors to the development of mature

[2]Note that the term *megafans* is loosely applied to fluvial fans with radii in excess of 30 km (cf. Gohain and Parkash, 1990).

fan–catchment systems (Blair and McPherson, 2009). While they are subsumed under the spectrum of fans by some authors (cf. e.g., Gómez-Villar et al., 2006), they lack some fundamental features of mature fan–catchment systems. Specifically, their sourcing basin is limited to a short gullied slope, entailing that they are generated by rockfall and colluvial slips rather than the channelized sediment conveyance inherent to alluvial fan morphogenesis (Stock, 2013; Bowman, 2018). Development of a mature fan from such a juvenile system is a gradual process by nature, and consequently no hard lower bound can be given for alluvial fan size.

Alluvial fan morphodynamics and morphology are strongly characterized by scale-related variability, and the quantification of scaling relationships is consequently a primary subject of geomorphometric alluvial fan research (cf. Section 2.3.1). Since evacuation of sediment from the catchment in the form of debris flows imposes constraints on runout length, there is a tendency for streamflow deposits to show growing relevance with increasing scale, with large fans being built exclusively by streamflows (Stanistreet and McCarthy, 1993; Harvey, 2003a). Growing catchment sizes also entail a gradual change of hydrologic conditions from episodic discharge with strongly peaked hydrographs to intermittent and perennial discharge (Ventra and Clarke, 2018). In addition, the increase of sediment path lengths, i.e., the mean distance traveled by entrained sediment before reaching the fan surface (cf. Church, 2006), involves decreasing sediment connectivity, growing retention times, and enhanced disintegration by weathering and fluvial reworking (cf. e.g., Roehl, 1962; Fryirs et al., 2007; Church, 2017). In concert, these aspects cause average slope values to decrease with increasing catchment area (cf. Section 2.3.1; Blissenbach, 1952; Bull, 1962; Harvey, 2011).

The question whether the spectrum of subaerial fans actually represents a continuum is subject to a long-standing controversy, with some authors suggesting to differentiate between alluvial and fluvial fans (cf. e.g., Stanistreet and McCarthy, 1993; Blair and McPherson, 2009; Ventra and Clarke, 2018). This distinction is primarily motivated by morphodynamic peculiarities of megafans, specifically a tendency to display enduring braided or low-sinuosity channel patterns enabled by very low slopes and long avulsion cycles (cf. Ventra and Clarke, 2018). Furthermore, avulsion dynamics are progressively attained on the fan platform, whereas avulsions on smaller alluvial fans are distinct events induced by sudden loss of confinement (cf. e.g., Clarke et al., 2010; Reitz et al., 2010; Reitz and Jerolmack, 2012). With respect to the gradual nature of morphometric transition (cf. Saito and Oguchi, 2005), the proposition to differentiate between alluvial and fluvial fans is insufficiently substantiated. Therefore, this nomenclature is not used in this thesis.

2.1.5 Landforms grading into alluvial fans

As will become apparent later, a critical point in object-based alluvial fan delineation is the differentiation between alluvial fans and landforms exhibiting a limited degree of diverging alluvial sedimentation. In this context, we will refer to a valley-wide divergent sedimentation pattern as *alluvial (valley) plain*. In contrast to fans, alluvial plains lack nodal alluviation but rather show a linear divergent sedimentation pattern. Note that this definition of alluvial plains is geared towards the environmental settings and landforms encountered during the work presented in this thesis, whereas alluvial plains sensu stricto are defined as level or gently sloping planar land surfaces produced by extensive deposition of alluvium (cf. Kolb, 1984),

A second type of landform to be differentiated are *alluvial slopes*, which we define as segments of alluvium-veneered mountain fronts which show a limited degree of radial sedimentation. This superclass includes (1.) pediments, i.e., degradation-affected alluvial surfaces (French, 1987; Löhrer, 2008) with fan-shaped sheets potentially generated from sediment conveyed by small low-order channels and lateral demarcations accentuated by interfluves (Bowman, 2018). Furthermore, the superclass involves (2.) debris cones—gravimetric-triggered talus composed of colluvium and rockfall scree (Blair and McPherson, 1994).

2.2 Environmental controls

2.2.1 Evolution of paradigms

The prevalent control of alluvial fan formation has been subject to a long-standing and controversial debate. In this section, the reader is provided with an outline of paradigms impelling research in the field. For an in-depth discussion on this matter, please refer to Lecce (1990).

During the 20th century, several geomorphological models were suggested with the intent of providing a conceptual framework for alluvial fan development. The *evolutionary model* of Davis (1905) regards alluvial fans as a transient phenomenon being indicative for the *youthful stage* of the *geographic cycle*, which was the dominant geomorphological paradigm of the first decades of the 20th century (cf. Bull, 1977; Oldroyd, 2013). The geographic cycle—also called the cycle of erosion—is an idealized concept postulating that landforms evolve through evolutionary stages driven by vertical erosion (Orme, 2013). Assuming tectonic stability, it is supposed that a landform evolves through the stages of youth, maturity, and old age (Kamp and Owen, 2013; Sack, 2013). Penck (1924) postulated a refined evolutionary model incorporating syntectonic geomorphic development.

Equilibrium models regard fans as syntectonic and essentially time-independent landforms which are in a steady state equilibrium after a juvenile growth phase (Hack, 1960; Denny, 1965, 1967; Schumm, 1977). Specifically, Denny (1965, 1967) defines the steady state condition as a dynamic mass equilibrium given by the rate of sediment discharge to the fan and the rate of erosion from the fan to the floodplain. For the playa to not encroach the fan, this concept requires the playa to be in a dynamic equilibrium as well—a constraint which is conflicting for depositional basins with interior discharge like those situated in the Great Basin (SW USA, see Chapter 4). Alternatively, a steady-state condition between regolith supply to the fan and to the playa was suggested (Hooke, 1968b; Jansson et al., 1993).

As pointed out by Schumm and Lichty (1965), accepting steady state conditions does not preclude longterm evolutionary change. The integration of equilibrium concepts into an evolutionary setting implies, however, that the dimension of time cannot be excluded from the analysis of landforms. Since steady state balance implies a balance between landform and process, any disturbances of environmental controls like climatic change and intermittent uplift must lead to changes in the geomorphic expression and the sedimentary record of fans (cf. Hack, 1960; Lecce, 1990). The pivotal question is therefore whether alluvial fans are able to reach a dynamic equilibrium at all, which even then was strongly contested by several researchers (cf. Lecce, 1990).

In the following years, the focus of research shifted towards environmental controls of fan *morphodynamics*, which were considered as *complications* of the equilibrium hypothesis (cf. Lecce, 1990).

This new paradigm emphasized climate change and tectonic activity as major variable environmental boundary conditions. Motivated by the widespread occurrence of fanhead entrenchment throughout the North American Southwest, Lustig (1965) proposed that humid periods induce fluvial aggradation, whereas dry periods are associated with proximal entrenchment induced by *erosive* debris flows. Since debris flows were already identified as fan-constituting processes, Lustig's view of debris flows as erosional agents was called into question (Hooke, 1967; Beaty, 1970). In contrast, Schumm (1977) proposed to assign the prevalent primary process according to hygric conditions. Debris flows were exclusively associated with arid and semi-arid climates, and fans displaying debris flows as their prevalent constituting process were referred to as *dry fans*. Conversely, fans primarily built by fluvial processes were referred to as *wet fans* and linked with humid conditions. Although conflicting evidence has been found early on (cf. Baker, 1977; Harvey et al., 2005), this wet–dry fan dichotomy was widely accepted for more than a decade (cf. Leeder, 1982).

Focusing on tectonic activity, Bull (1972, 1977) emphasized that differential uplift along the mountain front affects the locus of deposition and the thickness of the alluvial fan deposit. The author suggested two fundamental tectonic boundary conditions for alluvial fan development. If uplift is greater than the rate of stream channel downcutting, deposition takes place adjacent to the mountain front, resulting in a thick wedge-like sedimentary body. Conversely, if the rate of channel downcutting exceeds differential uplift, the fanhead tends to get entrenched, the locus of deposition progrades, and the sedimentary body is eventually modified into a more lenticular shape (cf. Fig. 2.2).

While modern research is still dominated by the fan dynamics paradigm, it greatly profited from the proliferation of absolute dating methods such as optical luminescence and cosmogenic radionuclides. Enabling the derivation of absolute ages on fan surfaces and within the sedimentary body for which derivation of ^{14}C ages is regularly unfeasible due to the lack of organic material (cf. Blisniuk et al., 2012; Cesta and Ward, 2016), alluvial fans became increasingly regarded as important archives for paleoenvironmental research (cf. e.g., Robinson et al., 2005; Vassallo et al., 2005; Quigley et al., 2007; Miller et al., 2010). Valuable insights into the interplay of environmental controls on fan development have also been achieved by using numerical modeling and laboratory alluvial fan models (cf. e.g., Schumm, 1977; Clevis et al., 2003; Densmore et al., 2007; Nicholas et al., 2009; Rohais et al., 2012). Conversely, little emphasis has been given to the question to what extent environmental conditions are reflected in fan geometries.

2.2.2 Climatic conditions

Climate exerts control on the alluvial fan–catchment system in two principal aspects. Firstly, by providing the agents of erosion and sediment transfer, the frequency-magnitude relationship of precipitation governs whether unconsolidated material can be removed from the catchment, i.e., whether the process-response system is transport-limited or limited by weathering and hydraulic detachment (Pope et al., 1995; Whipple and Tucker, 1999, 2002). In concert with readily transportable material, the hydrograph of runoff establishes the sediment load ratio and therefore influences the equilibrium slope. As elaborated in Section 2.1.1, the slope of alluvial fans displays an inverse log-log-linear relation with the ratio of sediment flux (Q_s) and water supply (Q_w; Milana and Ruzycki, 1999; Rohais et al., 2012).

Under ceteris paribus conditions, an increase in precipitation rate will reduce the fan slope and thus

cause a toe progradation of the fan. By increasing the sediment load factor, a decrease in precipitation rate induces higher slopes, fan backstepping (retrogradation), and the concomitant development of a downlap geometry (Bonnet and Crave, 2003; Densmore et al., 2007; Rohais et al., 2012). Detachment limitation negatively affects fan gradients, but also increases the susceptibility of the alluvial fan–catchment system towards overshoots of the geomorphic threshold, i.e., a transition from deposition to erosion due to sediment depletion (cf. Section 2.1.1).

Hygric and thermal constraints jointly govern the potential for vegetation development. Vegetation growth reduces the runoff component of the water balance via evapotranspiration, decreases the susceptibility of the colluvium to erosion, and facilitates the infiltration capacity under arid conditions (cf. Vandenberghe, 2002; Thompson et al., 2010). The corollary is that for sites with thermal conditions conducive to substantial vegetation growth, a high transport efficiency (cf. Milana and Ruzycki, 1999) is given in the case of episodic high-intensity discharge events under otherwise arid conditions (Mack and Leeder, 1999; Leier et al., 2005).

The second principal aspect of climatic control is given with respect to overall weathering intensity, soil development, and concomitantly the rate of regolith replenishment (Bull, 1991). Furthermore, the local climatic regime controls the differentiation between physical and chemical/biological weathering, and thus affects alluvial fan geomorphometry via its effect on grain size (cf. Marshall and Sklar, 2012; Riebe et al., 2015). Planetary-scale differences in weathering and discharge result in a gross differentiation of alluvial fan morphology (cf. e.g., Pope et al., 1995; Goudie and Viles, 2008), with fans in humid regions displaying lower gradients in average than fans located in semi-arid and arid settings (cf. Section 2.1.1; Saito and Oguchi, 2005; Hashimoto et al., 2008).

Sedimentary sequences of alluvial fan deposits can often be ascribed to distinct climatic impulses (cf. e.g., Ritter et al., 1995; Owen et al., 2014; Cesta and Ward, 2016). Alluvial fan morphodynamics is thus strongly impacted by time-transgressive processes (cf. e.g., Brunsden, 1993), that is, periods characterized by little transport capacity act as a primer for substantial catchment erosion during subsequent high-intensity precipitation events, because they facilitate the accumulation of regolith on hillslopes (cf. e.g., Bull, 1964; Eppes and McFadden, 2008; Mason and Romans, 2018). A distinctive example for the significance of time-transgressive morphodynamics are *paraglacial* environments, i.e., settings where post-glacial processes are directly conditioned by glaciation and the release of the glacially generated sediment (Ballantyne, 2002; Dorn, 2009; Slaymaker, 2011). Notably, paraglacial response has been found to be the primary driving factor for fan aggradation in deglaciated u-shaped valleys (cf. e.g., Ryder, 1971; Church and Ryder, 1972; Kostaschuk et al., 1986; Hinderer, 2001).

The comprehensive absolute chronological record obtained throughout the last two decades strongly suggests that Quaternary alluvial fan *morphodynamics* in semi-arid to arid settings is predominantly linked with rapid climatic shifts of the late Pleistocene and the early Holocene, inducing regionally synchronous aggradation episodes (see Chapter 4; cf. e.g., Bull, 1991; Ritter et al., 1995; Harvey et al., 1999b; Ritz et al., 2003; Vassallo et al., 2005; Quigley et al., 2007; D'Arcy et al., 2017; Lehmkuhl et al., 2018b). Conversely, only a few studies suggest tectonically driven alluvial morphodynamics (cf. Goswami et al., 2009; Gray et al., 2014). Essentially two process-response models were proposed to explain these climatically induced sedimentation impulses. The *arid model* suggests that aggradation phases are linked with a transition from a relatively humid to a more arid climatic regime (Wells et al.,

1987; Bull, 1991; Pope and Wilkinson, 2005). Contrastingly, the *humid model* assumes that major phases of alluvial fan aggradation are synchronous with an increase of precipitation (Harvey et al., 1999a).

The *arid model* is widely accepted for the North American Southwest (cf. Spelz et al., 2008; Owen et al., 2014), where major alluviation phases lag behind pluvial lake level highstands (cf. Section 4.2.3; Wells et al., 1987; Benson et al., 1990; Anderson and Wells, 2003; Benson, 2003; Miller et al., 2010). Increased sediment supply is attributed to a general moisture deficit in conjunction with episodic high-intensity rainfall, and particular emphasis has been given to the concomitant decline in vegetation density (cf. Knox, 1984; Reheis et al., 1996; Harvey et al., 1999b; Spelz et al., 2008; Miller et al., 2010; Pelletier, 2014). Recent research critically reviewed the impact of vegetation density and emphasized the role of precipitation effectiveness for late Pleistocene and early Holocene aggradation. This criticism is chiefly based on the lack of temporal agreement between main aggradation and the transition from late Pleistocene woodlands to Holocene desert scrub, i.e., an alleged underestimation of ecotone resilience (Koehler et al., 2005; Antinao and McDonald, 2013a,b). Notably, the arid model nicely illustrates how time-transgressive processes can cause the deposition–erosion threshold to be crossed without further climatic interference. If the sediment buffers on the hillslopes become exhausted, sediment supply eventually decreases and the deposition–erosion threshold can be crossed, resulting in proximal entrenchment and redeposition in the distal portions of the fan (Bull, 1979, 2000).

Fundamental to the *humid model* of alluvial fan aggradation is that sediment supply is transport-limited, i.e., aggradation is controlled by variations in frequency and magnitude of precipitation. It is straightforward to deduce that an increase of precipitation facilitates hillslope erosion and debris mobilization under ceteris paribus conditions. Given that thermal boundary conditions support a considerable vegetation density, a prolonged increase of total moisture will, however, facilitate vegetation growth and thus stabilize the colluvium (cf. Blum and Törnqvist, 2000; Bogaart and van Balen, 2000).

Hence, three scenarios are conceivable for major aggradation to occur within the framework of the humid model. Under (hyper-) arid and temperate or warmer transport-limited conditions, (1.) short aggradation phases can be concomitant with a transition to a more humid climatic regime. Enhanced vegetation growth will eventually stabilize the hillslopes and decrease the sediment load factor, so that aggradation will transition into proximal entrenchment. Alternatively, (2.) aggradation pulses can be caused by climatic boundary conditions promoting episodic high-magnitude precipitation events under otherwise (hyper-) arid conditions, so that the impact on average moisture is negligible (cf. Spelz et al., 2008; Bowman, 2018). Furthermore, (3.) aggradation can be triggered by medium- to high-magnitude rainfall events in cold environments which are not conducive to a protective vegetation cover but are affected by intense physical weathering (cf. Owen et al., 1997; Harvey et al., 1999a; Lehmkuhl et al., 2018b).

Importantly, the finding that sedimentary sequences of alluvial fans can often be ascribed to pronounced climatic impulses does not imply that the geomorphometry of said fans does not reflect a tectonic signature. An increase of the precipitation rate affects the whole catchment simultaneously, whereas tectonic uplift involves a very gradual increase in sediment flux (cf. Section 2.2.3; Paola et al., 1992b; Densmore et al., 2007; Rohais et al., 2012). The sedimentary record thus merely displays sequences which are to be expected from theoretical considerations and numerical modeling.

2.2.3 Tectonic activity

Providing (1.) accommodation space and (2.) the potential energy for geomorphic agents to become effective, tectonic activity is widely recognized as a primary controlling factor for the morphogenesis of alluvial fans (Denny, 1965; Whipple and Trayler, 1996; Allen and Densmore, 2000; Densmore et al., 2007). It follows that the impact of tectonic activity differentiates into processes effective at the sediment *source* and the sediment *sink* of the fan–catchment system.

At the sediment source, tectonic uplift involves a hypsometric change of climatic and related environmental conditions. In response to this change, the significance of physical weathering in comparison to chemical and biological weathering regularly grows with altitude, resulting in a tendency for increasing grain sizes (cf. Riebe et al., 2004, 2015; D'Arcy et al., 2017). Furthermore, the shift towards dominantly physical weathering in mountainous settings is facilitated by increasing relief (von Blanckenburg, 2005). Specifically, relief negatively affects the residence time of rock fragments, reducing the potential exposure for weathering processes to substantially alter the substrate (Dixon et al., 2012; Allen et al., 2015; Attal et al., 2015; D'Arcy et al., 2017). Owing to rupturing or subcritical crack growth, historic stresses reduce the in-situ rock strength and thus facilitate bedrock deterioration (Molnar et al., 2007). By triggering landslides, modern seismicity increases regolith availability in the system, and facilitates the occurrence of debris flows (cf. Section 2.1.1; Allen and Hovius, 1998). In addition, tectonic shearing can crush catchment rocks and contribute to high regolith production rates, which in turn promote alluvial fan growth because sediment supply is limited merely by hydraulic transport capacity (cf. Blair, 2003).

Interestingly, the strong focus on climatic conditions in geomorphologic and sedimentologic research is contrasted by the geological literature on alluvial fans, which mostly stresses tectonic activity as primary driver of alluvial sedimentation (cf. e.g., Harvey et al., 2005; Nichols, 2005; Harvey, 2011). When juxtaposing the significance of climate and tectonic activity, it must be borne in mind that both environmental controls operate over timescales which differ in several decadal powers (Harvey, 2002a). While sediment flux increases with growing relief, the geomorphic response occurs with a substantial time lag (cf. Paola et al., 1992b). For instance, Densmore et al. (2007) illustrate that a sudden increase in uplift rate initiates a very gradual increase in sediment flux, and the timespan needed to reach a new equilibrium after doubling or halving the slip rate was found to be be in excess of $5 \cdot 10^5$ years. Since an increase in precipitation rate affects the sediment flux instantaneously, tectonic and climatic signatures can, *in principle*, be distinguished in the *stratigraphic* record (cf. Densmore et al., 2007; Rohais et al., 2012). That said, tectonic variability on climatic timescales is not distinctively reflected in the sedimentologic stacking pattern (cf. e.g., Ritter et al., 1995; Allen and Densmore, 2000; Whittaker et al., 2008; Armitage et al., 2011).

Climate and tectonics are characterized by contrasting behavior with respect to their control on fan slope, i.e., fan–catchment systems adjust to an increase in tectonic offset rate by increasing the sediment load factor and average grain size, which in turn increases fan gradients and consequently reduces relative radial lengths. Due to convergent large-scale fan geometries, perturbations of either controlling factor cannot be differentiated via geomorphometry (cf. Densmore et al., 2007; Rohais et al., 2012).

As a consequence, a geomorphometric fingerprint of tectonic activity is established mainly by its

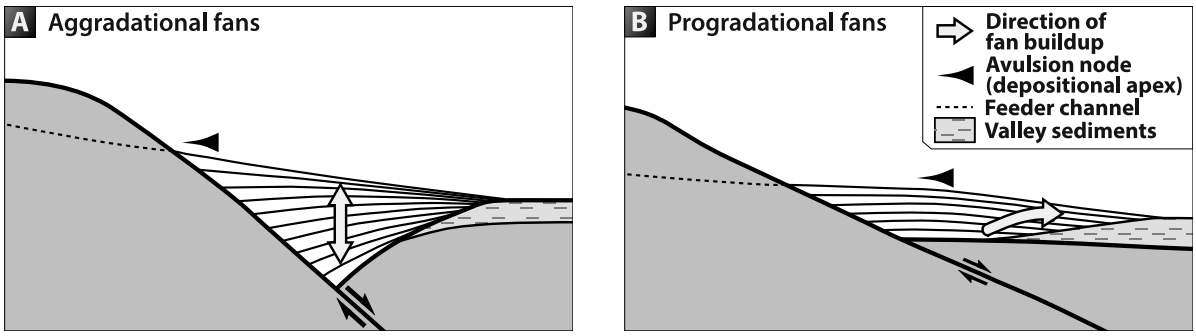


Figure 2.2: Schematic cross sections of alluvial fans abutting fault-bounded mountain ranges. The ratio between sediment evacuation from the catchment and generation of accommodation space by tectonic rejuvenation results in two fundamental modes of alluvial fan morphogenesis. (A) Accommodation space matches sediment conveyance. Sediment is accommodated proximal to the mountain front. After a juvenile growth phase, fans do not tend to grow in planimetric area. (B) Sediment evacuation exceeds recreation of accommodation space, resulting in a progressive onlap on basement and valley sediments. The locus of radial sedimentation shifts in downstream direction.

impact on the space available for fan accommodation. As already noted by Bull (1972, 1977), relative uplift affects the locus of deposition and the thickness of the fan deposit, which in turn determines the planimetric size of the fan. If accommodation space generation balances the sediment flux, the fan will build up proximal to the mountain front by vertical stacking (cf. Paola et al., 1992a; Silva et al., 1992; Parker et al., 1998; Clevis et al., 2003; Viseras et al., 2003; Dade and Verdeyen, 2007; Bahrami, 2013). These *aggradational* fans exhibit comparably high slopes and, consequently, small planimetric areas (cf. Fig. 2.2A; Whipple and Trayler, 1996; Weissmann et al., 2005). The abundance of proximal accommodation space will also decrease the probability of lateral confinement, and fans in tectonically dominated settings will thus tend to exhibit simple radial shapes with large splay angles (cf. Fig. 2.1; Bahrami, 2013).

If the formation of accommodation space lags behind sediment supply, the alluvial fan is forced to prograde into the depositional basin to maintain its equilibrium slope, i.e., the locus of deposition is shifted in downstream direction (Clevis et al., 2003; Densmore et al., 2007; Salcher et al., 2010; Armitage et al., 2011). The resultant increase in radial lengths also elevates the probability of fans to adjoin, with a bajada representing the end-member. *Progradational* fans thus exhibit an elongated fan footprint, a small splay angle, and lower-than-average values of fan slope (cf. Fig. 2.2B; Clevis et al., 2003; Viseras et al., 2003; Densmore et al., 2007).

Note that these assertions presuppose that the center of relative subsidence is located proximal to the mountain range. This assumption is valid for mountain ranges bounded by normal and reverse faults, but does not necessarily apply to pull-apart basins and restraining bends (Heller et al., 1993; Salcher et al., 2010). Furthermore, care must be taken when interpreting progradation signals, because a basinward shift of the depositional apex by itself does not necessarily indicate that the respective fan is *progradational* in the system sense. For fans featuring an active depositional lobe emerging from an incised channel, the proximal dissection may be related to regolith depletion at the end of a climatically induced aggradation phase. In such cases, progradation results predominantly from a redeposition of

fan material (Harvey, 2003b). Moreover, transient proximal incision and distal progradation occur as part of autogenic avulsion (cf. Section 2.1.2). To quantify accommodation-related progradation, the full spectrum of morphometric indicators must be taken into account.

2.2.4 Bedrock lithology

Bedrock lithology is generally not regarded as a first-order environmental control for alluvial fan evolution (cf. Quigley et al., 2007). The lack of emphasis on influential factors related to lithology is understandable, because these controls are challenging to constrain on a regional or supra-regional scale. Specifically, fragmentation of bedrock is controlled by a plethora of factors, such as mineralogy, crystal or grain size, bedding, foliation, and fracturing—which operate in conjunction with environmental controls such as water availability, cyclical changes of air temperature, wetting-drying cycles, freeze-thaw cycles, and transport-related physical disintegration (Selby, 1980; Pye, 1995; Smith et al., 2002; Goode and Wohl, 2010; Allen et al., 2015). As a consequence, apparently subtle lithologic differences, e.g., in mineralogy and fracturing, can result in substantial differences in erodibility (cf. Pye et al., 1986; Hill, 1995).

The impact of lithology on fan geometry is given by four major points: (1.) The source material must yield sufficient clay and fine silt to enable the generation of debris flows. A lack of fine material will restrict the primary process spectrum to hyperconcentrated flows or streamflows, and consequently lower equilibrium slopes (cf. e.g., Calvache et al., 1997; Blair, 1999b; Griffiths, 2004; Sattler, 2016). For instance, Blair (1999b) points to the case of two adjoining fans located in the Death Valley, California, which show substantially different fan gradients induced by dominance of debris flows and streamflows, respectively. The author was able to show that the sudden change of the prevalent primary process emerges from a lithological transition from a suite of sedimentary rocks to granite and andesite, which produce insufficient amounts of clay and silt to support debris flows.

In addition, (2.) the average grain size and the grain size distribution of sediment conveyed to the fan will affect the equilibrium slope of the alluvial deposit both in the case of streamflows and debris flows. As elaborated in Section 2.1.1, the relationship between fan slope and grain size is a monotonically increasing function for streamflows, whereas it is a complex relationship for debris flows (cf. de Haas et al., 2015a). Under arid conditions, fragmentation of felsic magmatic rocks is, for instance, dominated by inter-crystal granular disintegration, yielding fine pebbles and sand (grus; Bull, 1979; Eppes and McFadden, 2008; Blair and McPherson, 2009). Conversely, production of clay-sized sediments is limited to tight tectonic shearing and hydrolysis of feldspar, which requires sufficient residence time in a colluvial mantle (Blair, 1999b, 2003). Furthermore, modal slope inclinations values of hillslopes in tectonically active terrain are controlled by in-situ rock strength, which in turn varies in accordance with bedrock geology and the degree of fracturing (cf. Selby, 1982; Korup, 2008). Since a more pronounced terrain results in shorter residence times, lithologies with higher rock strengths yield coarser regolith (Selby, 1980; Allen et al., 2015; Sklar et al., 2017; Roda-Boluda et al., 2018).

Furthermore, (3.) the susceptibility of the source rock to weathering and physical disintegration influences whether a catchment is predominantly transport-limited or limited by weathering and detachment (cf. Whipple and Tucker, 2002; West et al., 2005; Wobus et al., 2006; Eppes and McFadden, 2008). From a general perspective, sedimentary rocks show approximately twice as large erosion rates

than igneous rocks, whereas sediment yield for metamorphic rocks is only slightly higher than for igneous bedrock (cf. Portenga and Bierman, 2011). Interestingly, conflicting evidence is given with respect to the impact a resistant lithology exerts on alluvial fan size. Since a predominantly detachment-limited catchment lags behind in terms of erosional adjustment, it is intuitive to assume that highly resistant rocks induce comparably smaller fans (cf. Bull, 1962, 1964; Hooke, 1968a; Marchi and Tecca, 1995).

Lecce (1991) investigated the interrelation between bedrock weathering resistance, catchment area, and fan area for a set of fans located in the White Mountains, California/Nevada. In contrast to the authors just mentioned, Lecce found that relatively large fans are associated with resistant magmatic rocks, and proposed that the smaller specific sediment supply for weaker lithologies is induced by facilitated sediment retention (cf. Mills, 2000; Ventra and Clarke, 2018). This finding exemplifies that in addition to the control on primary sediment production, (4.) bedrock geology potentially affects the routing of the sediment to the fan (cf. Fryirs et al., 2007; Mather and Stokes, 2018). For a study area located in the High Atlas Mountains, Morocco, Mather and Stokes (2018) found sediment connectivity to be controlled by the dip orientation of limestone interbedded with mudstones in respect to catchment orientation. In the case of strike-oriented catchments, resistant bedrock causes the main trunk stream to adjust its orientation to the structural strike, which induces local backfilling of sediment due to a decreased gradient. Conversely, syn-dip catchments show enhanced sediment conveyance.

2.2.5 Base level

The base level is defined as the local or global altitude level where the hydraulic gradient becomes zero and to which fluvial systems thus strive to adjust (Leopold and Bull, 2008). With the majority of fans toeing to stable base levels, base levels effects are regularly not considered as a principal factor for alluvial fan geomorphology (Harvey, 2003a).

Scenarios with partial hydraulic coupling are given for alluvial fans adjacent to axial rivers and lacustrine or marine coasts (cf. Fig. 2.1; Harvey, 2002c, 2005, 2011; Giles et al., 2018). In such settings, base level dynamics are a significant controlling factor which by itself is governed by a spectrum of tectonic, climatic, or autogenic dynamics, such as regional uplift and concomitant river incision, formation of pluvial lakes and lake level changes, eustatic sea level changes, stream piracy, or axial river meandering (cf. e.g., Jackson et al., 1987; Leeder and Mack, 2001; Bowman, 2018). Fans directly adjoining axial rivers or open water bodies with lateral currents exhibit basal trimming, resulting in a foreshortening and steepening of the fan body (Harvey et al., 1999a; Harvey, 2003a; Giles et al., 2018).

In the case of rapid base level lowering, alluvial fans often fail to keep contact with the retreating coast line, hence becoming uncoupled (Bowman, 2018). Fan response to the distally extended accommodation space depends, however, on the gradient of the exposed surface. Specifically, the effect of a surface which is more gently inclined than the equilibrium slope of the fan system facilitates simple distal aggradation (cf. Ritter et al., 2000; Harvey and Wells, 2003; Harvey, 2005). Conversely, a comparably steeper surface induces up-fan entrenchment (cf. Holbrook and Schumm, 1999; Muto and Steel, 2004; Harvey et al., 2005; Storz-Peretz et al., 2011), as well as a basinward shift of alluvial sedimentation, resulting in a telescopic fan pattern (cf. Harvey et al., 1999b; Harvey, 2002c, 2005, 2011).

Base level-related basinward shifts of alluviation are connected with autogenic dynamics in a complex

fashion. If pronounced, the basal dissection can link up-fan with a fanhead trench, inducing a complete sediment bypass and fan surface abandonment (Harvey, 2018). Muto and Steel (2004) demonstrated empirically that base level-related basinward fan development is characterized by an autogenic cyclical alternation between aggradational and progradational phases. Different magnitudes of basin slope and Q_s/Q_w lead to different manifestations of this *autoincision* process. In the event of high sediment load ratios and moderate basin slopes, the system shows simple autogenic dynamics, i.e., channels are restricted to the proximal fan section and tend to get backfilled (cf. Section 2.1.2).

Within the scope of a geomorphometric evaluation of fan surfaces, base level effects act as an uncertainty factor potentially hampering the differentiation of environmental settings. Alluvial fans experiencing basal trimming by axial rivers are, for instance, comparably small and steep, mimicking the morphometric expression of vertical stacking associated with accentuated tectonic activity.

2.3 Geomorphometric research

2.3.1 Fan–catchment relationships

Fan area vs. catchment area

Consideration of fan–catchment scaling interrelations is the traditional focus of alluvial fan research in the field of geomorphometry, with particular emphasis being given to area relationships (cf. Church and Mark, 1980; Stock, 2013). Provided that no sediment bypasses the fan, the sedimentary fan body is the sink for all sediment evacuated from the catchment plus potential changes in net porosity (cf. Delorme, 2017). If we suppose a radial geometry with a straight longitudinal profile and a splay angle of 180°, the fan volume V (km^3) is given by:

$$V = \frac{\pi \cdot r^3 \cdot S}{6} = \frac{A_f \cdot r \cdot S}{6} = \frac{A_f \cdot h}{6}, \tag{2.5}$$

where r is the fan radius (km), S denotes the fan gradient (km km^{-1}), A_f (km^2) defines the planimetric fan surface, and h (km) is the height of the half-cone.

As can be seen from equation (2.5), planimetric surface increases linearly with evacuated sediment *if* the cone height stays constant. Bull (1962) was the first to suggest that planimetric fan area can be used as a proxy for fan volume, and proposed a log-log-linear relationship in the form of:

$$A_f = a_1 \cdot {A_c}^{b_1}, \tag{2.6}$$

where A_c is the planimetric catchment area (km^2). Reported values for the scaling exponent b_1 vary between 0.24 (Hooke, 1968a) and slightly above 1 (cf. e.g., Mills, 2000) but are generally below unity. Axis intercept values are commonly below unity as well, indicating that sediment connectivity is relatively low in juvenile catchments (cf. Brardinoni et al., 2012; for an overview of obtained coefficients in the literature, please refer to Stock, 2013).

As indicated by equation (2.5), an evident cause for this negative allometric relationship is syntectonic deposition (cf. Whipple and Trayler, 1996; Dade and Verdeyen, 2007). Investigations carried out in study areas with pronounced relative subsidence at the mountain front report low scaling exponents

(cf. Hooke, 1968b). Then again, Giles (2010) also derived scaling exponents below unity for a set of paraglacial fans, indicating that negative allometry is related to catchment-intrinsic controls. This result is, however, to be expected, because it is established in fluvial geomorphology that the *sediment delivery ratio*—i.e., the proportion of eroded material evacuated from the basin—tends to decrease with increasing drainage area as a result of declining sediment connectivity (cf. e.g., Roehl, 1962; Fryirs et al., 2007; Church, 2017). In addition, numerous other factors can induce deviations from an overall allometric trend, such as variances in *trap efficiencies* (i.e., the rate of conveyed sediment bypassing the fan; cf. Whipple and Trayler, 1996; Dade and Verdeyen, 2007; Bowman, 2018), sedimentological processes (cf. Section 2.1.1), lithology (cf. Section 2.2.4; Bull, 1962, 1964; Lecce, 1991), stream piracy (cf. Mather et al., 2000), or distal constriction by axial rivers (cf. Marchi and Tecca, 1995; Sorriso-Valvo et al., 1998; Giles et al., 2018).

Product-moment correlation coefficients calculated for A_f and A_c consequently show strong variations, with low ($r^2 < 0.5$; cf. e.g., Marchi and Tecca, 1995; Sorriso-Valvo et al., 1998; Löhrer, 2008; Karymbalis et al., 2018), medium (cf. e.g., Calvache et al., 1997; Crosta and Frattini, 2004; Karymbalis et al., 2010), and high coefficients of determination ($r^2 > 0.8$; cf. e.g., Harvey et al., 1999a; Viseras et al., 2003; Giles, 2010) being reported.

Fan gradient vs. catchment area

Another pivotal scaling metric is the negative power law relation between fan gradient ($\mathrm{km\,km^{-1}}$) and basin area (Bull, 1962; Harvey, 1987):

$$S_f = a_2 \cdot {A_c}^{b_2}, \tag{2.7}$$

where S_f is the average gradient of the fan surface. Values for b_2 commonly vary between −0.15 and −0.4 (cf. Harvey, 2011; Stock, 2013), whereas values for the axis intercept show greater variations between approximately 0.03 (cf. Saito and Oguchi, 2005) and 0.18 (cf. Crosta and Frattini, 2004).

The reason for the negative correlation between fan gradient and catchment area is that growing catchment sizes entail intrinsic changes to processes affecting regolith production and transport to the fan. Specifically, water discharge increases with drainage area, resulting in higher bed shear stress and lower equilibrium slopes (cf. Section 2.1.1; Hooke, 1968a). Furthermore, increased average residence times of substrate facilitate its disintegration, so that median grain sizes of evacuated sediment tend to decrease with growing catchment size (cf. e.g., Dixon et al., 2012; Allen et al., 2015; Attal et al., 2015; Riebe et al., 2015). Also recall that debris flows exhibit a finite runout distance (cf. Section 2.1.1). For study areas exhibiting favorable conditions for debris flow initiation, increasing catchment area thus also entails a gradual transition from debris flow fans into mixed flow fans and eventually pure streamflow-fed fans (cf. Wells and Harvey, 1987; de Scally and Owens, 2004). Another potential contributing factor is distal constriction by, e.g., axial rivers, which involves a steepening of the fan profile (cf. Section 2.2.5; Harvey et al., 1999a; Harvey, 2003a).

While some studies obtain high coefficients of determination (cf. e.g., Milana and Ruzycki, 1999; Ritter et al., 2000; Viseras et al., 2003; Giles, 2010), coefficients are generally below 0.5 (cf. e.g., Silva et al., 1992; Crosta and Frattini, 2004; Al-Farraj and Harvey, 2005; Saito and Oguchi, 2005).

Fan gradient vs. fan area

Since fan area is allometrically related with basin area, it is readily apparent that fan gradient scales inversely with the planimetric area of the fan (Al-Farraj and Harvey, 2005; Saito and Oguchi, 2005; Hashimoto et al., 2008):

$$S_f = a_3 \cdot {A_f}^{b_3} \tag{2.8}$$

There is little empirical data on the coefficients of equation (2.8). Available study results indicate, however, that coefficients of determination are only slightly lower (Al-Farraj and Harvey, 2005; Saito and Oguchi, 2005; Lin et al., 2009) or even higher (Löhrer, 2008) than those obtained for the fan gradient–catchment area relationship.

Bivariate residual analysis

Bivariate scatter plots of the residuals obtained from performing a regression between catchment area and the dependent variables fan area and fan gradient have been investigated to differentiate controlling factors of alluvial fan geomorphology (Harvey, 1987; Silva et al., 1992; Harvey et al., 1999a; Al-Farraj and Harvey, 2005).

For a set of 61 fan–catchment systems located in Southeast Spain, Silva et al. (1992) identified four non-overlapping clusters which they could trace back to differences in the primary depositional process and variable tectonic activity, specifically a distinction between stacked and prograding fans. Other studies did not yield spatially separated clusters, but still showcase shifts in the residual plot attributable to distinct environmental controls. The role of lithology is emphasized by Harvey (2002c), who found that lithologies conducive for debris flow generation result in systematically steeper fans. Harvey et al. (1999a) and Al-Farraj and Harvey (2005) demonstrate that distally constrained fans exhibit both subpar fan areas and above-average gradients.

Superimposed influences on fan processes and resulting geometric characteristics can, however, completely obfuscate environmental controls, and pinpointing single controlling factors is thus not always successful (cf. Crosta and Frattini, 2004). Hence, controlling factors can only be delineated under relatively constrained settings where geometric differentiation of fans is caused by a prevalent mechanism.

Catchment ruggedness

Motivated by the potential geohazard coming along with debris flow activity, another focus of geomorphometric research has been on the significance of catchment relief for sedimentary processes and the associated geomorphologic characteristics of fan surfaces (cf. e.g., de Scally and Owens, 2004; Wilford et al., 2004; Davies and McSaveney, 2008; Bertrand et al., 2013).

Steep terrain is a necessary prerequisite for debris flow instigation, and it is thus indicated to consider catchment relief. A widely suggested metric for a quantification of terrain conditions and debris flow susceptibility is the ruggedness number, originally proposed by Melton (1965):

$$R = \frac{A_{\max} - A_{\min}}{\sqrt{A_c}}, \tag{2.9}$$

where R is the dimensionless ruggedness number (also denoted Melton's R), and A_{min} (km) and A_{max} (km) are the minimum and maximum altitude values of the catchment, respectively. Melton's R figures have been mostly used in conjunction with average fan slopes, leading to substantial improvements for the differentiation between streamflow-fed and debris-flow fed fans (cf. e.g., Kostaschuk et al., 1986; Bertrand et al., 2013; Rickenmann and Scheidl, 2013). Then again, threshold values vary substantially between approximately 0.3 (cf. e.g., Jackson et al., 1987; Marchi et al., 1993; Wilford et al., 2004) and 0.75 (cf. e.g., de Scally and Owens, 2004), indicating that thresholds are case-specific.

Emphasizing that the probability for debris flows to reach the fan surface is chiefly given by both catchment relief and runout distance, some authors advocate to use watershed length as an alternative to juxtaposing Melton's R with fan gradient (Wilford et al., 2004; Welsh and Davies, 2011; Stolle et al., 2015). Utilizing multiple statistical and machine learning approaches such as discriminant analysis and tree-based classification, Stolle et al. (2015) compared various morphometric variables including, among others, planimetric catchment area, catchment length, and Melton's R. While they obtained the best discrimination by juxtaposing Melton's R and catchment length, they found watershed length to be even more indicative than Melton's R.

Since Melton's R is essentially a generalized measure for catchment steepness (cf. Church and Mark, 1980), it is indicated to juxtapose the obtained values with average fan slope (in degrees; Melton, 1965; French, 1987):

$$S_f = a_4 \cdot R^{b_4} \tag{2.10}$$

For fan–catchment systems located in (semi-) arid regions, regression coefficients for this functional relationship were found to be around unity (cf. Melton, 1965; Church and Mark, 1980; Giles, 2010; Bertrand et al., 2013) or above (cf. Kostaschuk et al., 1986; Karymbalis et al., 2018). Furthermore, coefficients of determination are often higher than 0.8 (Kostaschuk et al., 1986; Giles, 2010), indicating that catchment steepness exerts a strong control on fan gradient by reducing the residence time of debris within the catchment. Melton's R is, in turn, relatively strongly correlated with catchment area (cf. Stolle et al., 2015), corroborating the pivotal impact of scaling relationships on fan geometry. In contrast to studies addressing (semi-) arid regions, Lin et al. (2009) evaluated 55 fans located in the humid mountain ranges of Taiwan. By finding that alluvial fan gradients show relatively little linkage with catchment steepness, the authors point to a potentially larger role of climatic control.

While studies focusing on a small number of fan–catchment systems were able to achieve sound classification accuracy by identifying thresholds or discriminant functions, studies involving a large number of fan–catchment systems show a gradual transition of fan gradient, Melton's R, catchment length, and corresponding primary sedimentary processes (cf. Wilford et al., 2004; Bertrand et al., 2013; Stolle et al., 2015). These results therefore complement the finding of Saito and Oguchi (2005) that the alluvial fan property space is gradual in nature.

2.3.2 Geomorphometry of fan surfaces

In contrast to the consideration of fan–catchment relationships, the geomorphometric formalization of alluvial fan surfaces received relatively little emphasis. This issue can be seen as a repercussion of the lack of digital elevation data in early morphometric analysis, and the resultant scope on metrics

which are readily deducible from topographic contour maps or can be surveyed in the field (cf. e.g., Blissenbach, 1952; Hooke and Rohrer, 1979). A pioneering contribution to alluvial fan geomorphometry was made by Troeh (1964, 1965), who suggested to model conical landforms by approximating them as a longitudinally concave radial body:

$$Z_i = Z_a + s\left(\sqrt{(X_i - X_a)^2 + (Y_i - Y_a)^2}\right) + \ell\left((X_i - X_a)^2 + (Y_i - Y_a)^2\right), \tag{2.11}$$

where Z_i denotes the elevation at a point i on the cone surface, Z_a is the elevation at the apex, s is the coefficient defining the altitude change in relation to radial distance (i.e., aspect slope), ℓ denotes the coefficient defining the change of slope in relation to radial distance (i.e., curvature), X_i and Y_i are the cartesian coordinates of the point considered, and X_a and Y_a are the cartesian coordinates of the apex.

Although the potential of Troeh's approach for alluvial fan geomorphometry has been acknowledged (cf. Bull, 1977; Farr, 1995), it has not yet attracted much attention, and has not been applied in the context of modern GIS analysis to this day. A related methodology is to estimate the coefficients of a general quadratic polynomial trend surface (cf. Clarke, 1995; Florinsky, 2012), which was used by Zani et al. (2012) to obtain the high-frequency components of a megafan in Brasil. Its fundamental drawback is, however, that it does not impose a conical body on the fan surface under consideration. Hence, this approach neither can be used to detect alluvial fans among a diverse set of landforms, nor does it help in differentiating distinct types of fans.

During the last two decades, emphasis has been mostly given to augmenting the analytical framework of fan–catchment relations with additional metrics of alluvial fan surfaces. Notably, morphometric data acquisition still relies heavily on traditional labor-intensive approaches involving topographic contour map data, GPS, and in-field geodetic survey (cf. e.g., Viseras et al., 2003; de Scally and Owens, 2004; Williams et al., 2006; de Scally et al., 2010; Bahrami, 2013; Karymbalis et al., 2018), limiting the analytical scope in terms of investigable geomorphometric metrics. The potential of contextual relationships of the fan surface and adjoining land surface patches is also yet to be fully exploited. A first approach to consider contextual statistics was carried out by Hashimoto et al. (2008), who—aiming at demonstrating morphometric differences between fans in the North American Southwest and in Japan—juxtaposed aspect slope at the distal fan zone with aspect slope of the adjoining playa, and showed that Japanese fans lack a distinct knickpoint at the toe due to their low equilibrium slopes.

The explanatory potential of longitudinal curvature for the differentiation between primary processes (cf. Section 2.1.1) was demonstrated both in the context of fan–catchment relations (cf. de Scally and Owens, 2004; de Scally et al., 2010) and as a standalone measure (cf. Williams et al., 2006). Importantly, fan elongation (width-length ratio; cf. Sorriso-Valvo et al., 1998; Viseras et al., 2003; Bahrami, 2013; Šilhán, 2014) and fan splay angle (cf. Calvache et al., 1997; Viseras et al., 2003; Bahrami, 2013) were—in conjunction with fan slope and basin metrics—recognized as indicative for the magnitude of relative tectonic uplift and concomitant generation of accommodation space. Specifically, these empirical studies show unanimously that the vertical aggradation inherent to tectonically active mountain fronts entails steep fans with width-length ratios greater than unity and large splay angles, and vice versa (cf. Section 2.2.3).

It was further suggested that the occurrence of incised channels and the proportion of channel length

related to the total fan length are indicators for progradation inherent to low tectonic activity (cf. Calvache et al., 1997; Viseras et al., 2003). With regard to autogenic and time-transgressive processes, however, the potential of generalizing these study results must be viewed with some skepticism. For instance, Bahrami (2013) noticed no agreement between the presence of an incised channel and low tectonic uplift rates and attributed incision to decreased sediment loads after transitioning to the current arid climate given for the author's study area in western Iran.

2.3.3 Exploratory data analysis and clustering

It can be inferred from the preceding sections that the juxtaposition of environmental boundary conditions involves complex process-response systems which are challenging to disentangle with respect to prevalent environmental controls. This issue in conjunction with the large number of potentially informative morphometric variables calls for exploratory data analysis via dimensionality reduction methods. Although research done hitherto strongly points to a gradual nature of morphometric properties (cf. Saito and Oguchi, 2005), the incorporation of clustering approaches might still help in gaining further insights into the morphometric expression of environmental controls.

Approaches to cluster the fan–catchment feature space have received little attention so far, with research being restricted to agglomerative clustering (Crosta and Frattini, 2004) and the application of self-organizing maps (SOMs; cf. Karymbalis et al., 2010, 2018). A fundamental issue of said studies is that dimensionality reduction or clustering is conducted on the raw morphometric data, and thus also reflects variability related solely to scaling relationships (cf. Section 2.3.1). Furthermore, fan surface parametrization in these studies is limited to planimetric area, slope, total relief, or longitudinal curvature.

Crosta and Frattini (2004) performed both principal component analysis and agglomerative hierarchical clustering on a set of 36 variables quantifying basin morphometry, fan morphometry, geology, and land cover. For the first principal component (PC), which accounted for 18 % of the total variance, they identified highly negative component loadings for variables expressing catchment size and high positive loadings for fan slope. Notably, component loadings for Melton's R in PC0 and PC1 are very similar to fan slope (cf. Section 2.3.1). Although both principal fan types showed a substantial amount of overlap, differentiation between streamflow- and debris flow-fed fans was still found to be substantially reflected in the first principal component—i.e., to be fundamentally scaling-related.

Conducting agglomerative clustering, the authors obtained groups of fans which they were able to semantically link with primary depositional processes and fan size. Agglomerative hierarchical clustering involves recursive pairwise aggregation of samples and proto-clusters, joining those clusters whose distance is minimal. The linkage criterion, the metric used to compute the distances between proto-clusters, strongly affects the structure of the constructed binary tree (cf. Hastie et al., 2009). The algorithm imposes a hierarchical structure on the data, irrespective of whether such a structure actually exists. Owing to the fact that cluster mergers at a certain level inherit their structure from all prior aggregations, the algorithm yields, by principle, a suboptimal overall solution (cf. Kaufman and Rousseeuw, 1990; Agarwal and Skupin, 2008). As a consequence, the generated clusters need to be carefully evaluated via consistency measures such as silhouette coefficients (cf. Chapter 7; Rousseeuw, 1987; Hastie et al., 2009). Regrettably, Crosta and Frattini, 2004 did not quantitatively validate the

obtained clustering result, and their study thus does not allow definite assertions on whether the alluvial feature space is actually conducive to a hard partition.

The self-organizing map approach, originally proposed by Kohonen (1982), is a special kind of artificial neural network (ANN). The algorithm generates a commonly two-dimensional discrete representation of a continuous Euclidean ($\mathbb{R}^p$) feature space in such a way that the two-dimensional neural map preserves the intrinsic topology of the high-dimensional feature space (cf. Kohonen, 2001; Agarwal and Skupin, 2008). By doing so, SOMs yield a map that is conducive to the assessment of spatial organization trends by visual means. For in-depth information on the SOM algorithm, please refer to Kohonen (2001).

Karymbalis et al. (2018) used a SOM-based workflow to cluster alluvial fans in Peloponnese, Greece, with agglomerative clustering applied to the neuronal grid to obtain thematic clusters. While only incorporating the traditional set of fan and catchment variables discussed in Sections 2.3.1, they were able to verify the results obtained by Calvache et al. (1997) and Viseras et al. (2003), that fan gradient and relative fan size are fundamentally related to the rate of tectonic uplift.

2.3.4 Automatic delineation and object-based geomorphometry

Although initial approaches of automatic fan delineation date back to the late 1990s, the application of object-based approaches to fan delineation has received little attention so far. Significantly predating the emergence of OBIA frameworks in geomorphometry, Miliaresis (1999, 2001) and Miliaresis and Argialas (2000) applied a region-growing algorithm relying on seed points extracted from drainage networks. This pioneering approach was deficient in that it took a slope threshold of 2° as solitary stop criterion for the iterative region-growing, and therefore was incapable of accurately delineating distal parts without incorporation of auxiliary data such as satellite imagery. While the algorithm showed a decent performance in delineating solitary fans and bajadas as a whole, the pixel-wise thresholding of slope prevented the differentiation of adjoining fans.

Norini et al. (2016) suggested an algorithm which essentially is an application of region growing to radial profiles emanating from apex seed points. Apexes are located by applying manually-set thresholds on slope and curvature grids and intersecting the mask grids with drainage networks. The radial profiles are then trimmed by defining thresholds on profile slope and slope change. Eventually, fan objects are delineated by deriving interpolated surfaces from the trimmed radial profiles, and intersecting these surfaces with the DEM. While generally enabling the delineation of coalescing fan bodies, the algorithm yields overlapping fan boundaries even in cases where lateral demarcation is distinctly given by a change of aspect (cf. Norini et al., 2016, p. 151). By honoring the radial nature of alluvial fan geomorphology, the algorithm exploits specific geomorphometry to yield a sound delineation. Then again, the method completely lacks the classification component inherent to the OBIA methodology.

An early implementation of an OBIA workflow sensu stricto was presented by Argialas and Tzotsos (2004, 2006), who suggested a multistage analysis scheme based on the multi-resolution image segmentation (MRS) algorithm (cf. Section 5.1; Baatz and Schäpe, 2000; Blaschke et al., 2004) and incorporating both ASTER GDEM and ASTER imagery. However, their technique also did not enable a discrimination of adjoining fans—presumably due to the fact that only elevation and slope values were included in the segmentation.

Only recently, Argyridis and Argialas (2017) suggested a refined multistage MRS-based procedure incorporating the US-specific 10 m National Elevation Dataset (NED) and Landsat 8 imagery, and applied the workflow to a study area located in Death Valley, California. In their approach, the playa is differentiated from all elevated areas by using a pixel-based index of valley bottom flatness (cf. Gallant and Dowling, 2003). Thereafter, a piedmont zone is separated from the highlands by using MRS and performing a fuzzy slope and curvature thresholding on the obtained objects. Furthermore, spatial reasoning is performed by assessing whether candidate piedmont zones are located between playa and mountain zone. Subsequently, piedmont objects are considered appurtenant to an alluvial fan if they exhibit a dichotomic drainage network, and adjoining objects fulfilling this condition are merged. Differentiation between solitary and coalescing fans or bajadas was carried out by evaluating the level of agreement between the fan footprint and a circular sector, constructed from an apex point found by intersecting the fan surface with the drainage network. Eventually, a fan toe refinement procedure was carried out by incorporating satellite imagery. While Argyridis and Argialas present a well-reasoned object-based framework for alluvial fan identification, the authors did not attempt to separate adjoining fans. In addition, their approach involves a multitude of hard and fuzzy thresholds, which cannot be readily applied to other study areas and elevation datasets.

2.4 Conclusions and incentives

Although considerable progress has been made in recently published studies on object-based workflows for the delineation of alluvial fans, all suggested approaches are still deficient in delineating laterally constricted fans. As lateral coalescence is a common scenario for piedmont surfaces abutting mountain ranges, this issue impedes the operative applicability for unattended generation of alluvial fan inventories in geomorphology and all other cases where interest lies in identification of individual landforms. While inability to differentiate between coalescing landforms is to be anticipated if segmentation is conducted on the basis of altitude and slope gradient, incorporation of curvature values apparently did not improve segmentation in the study of Argyridis and Argialas (2017). A re-consideration of potential morphometric variables for alluvial fan segmentation is thus indicated.

In the context of object-based morphometric analysis, we are interested in identifying one or several types of landforms among a diverse set of objects obtained via segmentation. Notably, landform types contained in this raw dataset may vary for different study areas. Object-based workflows proposed hitherto tackle this problem via semantic modeling with user-defined (fuzzy) rule sets (cf. Argyridis and Argialas, 2017). This approach, however, makes these techniques tedious to set up, prone to user-induced bias or inaccuracies, and specific with respect to the applied DEM. In the dissertation at hand, it is conjectured that object-based morphometry can be made both more robust and flexible by conducting a data-driven classification via supervised one-class classification techniques. This approach involves finding a set of morphometric variables defining a *morphometric signature* for the landform of interest. Given the large variability of alluvial fan surfaces with respect to generic morphometric variables, such as slope and directional curvatures, these variables have insufficient discriminatory potential to be exclusively used for classification. With a fundamental characteristic of alluvial fans being radial sedimentation, the classification should instead be based on algorithms quantifying deviations from an

ideal conical body (cf. Troeh, 1964, 1965).

There is ever growing consensus that in the vast majority of cases, Quaternary climatic variability and concomitant cyclical regolith replenishment and depletion chiefly control the sequence stratigraphy of alluvial fans. From a geomorphometric perspective, the fundamental question is, however, how climatic control is reflected in fan geometry. Climatic boundary conditions chiefly affect the degree of regolith disintegration, and the frequency–magnitude characteristics of runoff exert a pivotal control on the hydraulic conditions of the catchment outflow and the resultant threshold stress for transport. A climatic signature is indeed clearly evident in large-scale morphometric data, which point out that fans located in humid regions exhibit *in average* lower gradients than fans built up under more arid conditions (cf. Saito and Oguchi, 2005; Hashimoto et al., 2008). The climatic impact is, however, closely intertwined with tectonic and lithologic influences, rendering a full disentanglement of climatic signals unfeasible.

Bearing the complex juxtaposition of controlling factors within the sourcing catchment in mind, the most promising approach for a partial disentanglement of controlling factors is to focus on the role of the piedmont zone as a sediment sink. Under many fault-bounded tectonic settings, relative subsidence is most pronounced in vicinity to the mountain front, and tectonic activity thus essentially controls the accommodation of evacuated sediment. Studies augmenting catchment-related morphometric variables and fan gradient with additional parametrizations of fan surface indicate that aggradation and progradation bear specific morphometric signatures (cf. Viseras et al., 2003; Crosta and Frattini, 2004; Karymbalis et al., 2018). Then again, all these studies have a local scope of analysis and completely refrain from considering scaling relationships.

With scale being a major controlling factor of fan morphology, the consideration of scale-related changes is pivotal for any comparative morphometric assessment of datasets involving fans with substantially different sizes. Goodness of fit values for fan–catchment relationships show, however, strong variations, and tend to decrease for large and diverse sets of fans (cf. e.g., Saito and Oguchi, 2005; Lin et al., 2009). In this doctoral thesis, therefore, an approach is pursued that conducts exploratory statistical analysis of the alluvial fan feature space using alluvial fan planimetric area as exclusive reference for the de-trending of scale-related changes in morphometric expression. By taking a diverse set of fan-related morphometric variables into consideration, we will assess if scale-independent morphometric signals are identifiable within the alluvial fan feature space, and in what respect they can be linked to environmental controls of fan morphogenesis.

3 Evaluation of TanDEM-X elevation data for geomorphological mapping and interpretation in high mountain environments – A case study from SE Tibet, China

Isabel Pipaud*†, David Loibl*†, Frank Lehmkuhl*† (2015)
Geomorphology 246, 232–254. doi:10.1016/j.geomorph.2015.06.025

3.1 Introduction

During the past decades digital elevation model (DEM) have gained increasing importance for many different applications in the field of geomorphology, such as terrain visualization and mapping (e.g., Spark and Williams, 1996; Fraser et al., 2002; Smith and Clark, 2005; Jones et al., 2007), quantitative terrain analysis (e.g., Wood, 1996; Rodriguez et al., 2002; Schmidt and Hewitt, 2004; Iwahashi and Pike, 2007; Siart et al., 2009; Frey and Paul, 2012) as well as numerical modeling for land evolution studies and process simulation approaches (e.g., Montgomery, 2003; Jain et al., 2004; Martin and Church, 2004; Dymond and De Rose, 2011; Hancock et al., 2011; Chen et al., 2014; Pohjola et al., 2014). With the DEMs provided by the Shuttle Radar Topography Mission (SRTM) and the Advanced Spaceborne Thermal Emission and Reflection Radiometer (ASTER), two medium resolution datasets of near-global coverage became available since 2003 and fostered the use of digital topographic elevation for geomorphological analysis (Smith et al., 2006; Suwandana et al., 2012). GIS-based application of digital topographic information incorporating qualitative and quantitative analysis techniques allows synoptic landscape analysis and facilitates the transfer of field research results exclusively provided on a local scale to larger investigation areas, thus helping to overcome the classic geographic problem of upscaling (Smith and Pain, 2009; Gonga-Saholiariliva et al., 2011; Schlummer et al., 2014). Moreover, remote topographic analysis approaches are of particular relevance for study areas where access is restricted, e.g., by topography, remoteness, lack of infrastructure or for political reasons. The applicability of DEMs for geomorphological research is strictly depending on data quality, particularly the DEM's effective resolution and proneness to errors. High mountain environments pose considerable challenges to DEM generation, resulting in adverse effects in DEMs (Bamler and Hartl, 1998; Small, 1998; Fisher and Tate, 2006; Hensley et al., 2007; McGlone, 2007; Nelson et al., 2009; Richards, 2009; Mukherjee et al., 2013). A detailed comparative evaluation of DEM quality in high mountain environments is, however, still lacking.

Topographic height values given by a rasterized DEM are discrete samples of the earth surface (Wechsler, 2007; Hebeler and Purves, 2009). As the earth's surface possesses fractal properties and is

*RWTH Aachen University, Department of Geography, Templergraben 55, 52056 Aachen, Germany

†**Author contributions:** Isabel Pipaud conceived the study, programmed all tools required for the interferometric processing of the TanDEM-X DEM, designed and performed the geomorphometric analysis, conducted the geomorphological assessment in cooperation with David Loibl, and wrote the manuscript. David Loibl carried out the geomorphological mapping, and jointly performed the geomorphological interpretation with Isabel Pipaud. Frank Lehmkuhl acted as supervisor.

consequentially non-differentiable, a landform's shape cannot be reproduced in full detail by a rasterized DEM (Wood, 1996; Albani et al., 2004). Visual and geomorphometric landform analysis both implicate continuity between elevation data points, inevitably ignoring the DEM's discrete characteristics. This is feasible because terrain height also possesses a high level of positive autocorrelation for small distances, sufficiently reflecting the assumption of continuity (Hunter and Goodchild, 1997; Ehlschlaeger, 1998; Gallay, 2009; Haining et al., 2010). According to the Nyquist-Shannon sampling theorem, the intrinsic resolution of a raster DEM is twice the sampling distance of the height values actually measured for DEM generation, whereas the double of the DEM posting represents the nominal resolution (Robinson, 1994; Florinsky, 1998; Fisher and Tate, 2006; Arrell et al., 2008). The effective resolution and, consequentially, the minimum footprint for a surface element to be unambiguously sampled, are thus given by the smaller of the two values (cf. Pike, 1988). If the Nyquist-Shannon criterion is not satisfied for the sampling distance and/or the DEM posting, topographic features with footprints below the critical value may still be visible in the DEM but are rendered ambiguously because of aliasing effects (cf. Cumming and Wong, 2005).

The principal quality criterion of a DEM in geomorphological terms is its ability to represent the in-field topography consistently. Consistent terrain representation can be defined as the DEM's capacity to contain surface information in a way that the image reflects the in-field situation sufficiently to be meaningfully interpretable via visual analysis (cf. Smith and Wise, 2007; Smith, 2011) or extractable via geomorphometric methods (cf. Wood, 1996; Drăguţ and Eisank, 2011, 2012; Mashimbye et al., 2014). The representation quality of the altitude field is determined by the relation between terrain shape complexity, the effective resolution of the incorporated elevation model and the influence of errors potentially harming the representation of the altitude field (Oksanen, 2006; Wechsler, 2007; Arrell et al., 2008; Gallay, 2009; Hebeler and Purves, 2009; Reuter et al., 2009). Terrain shape complexity can be defined by feature size relative to the DEM's effective resolution, feature slope and sharpness of breaks in the slope (Kervyn et al., 2008). In practical terms, the quality of terrain representation is also defined by the desired scale on which a landform of interest will be addressed.

At present time, near-global elevation information is available with a posting of 1″ by the Shuttle Radar Topography Mission (SRTM) DEM (referred to as *SRTM* or *SRTM1 DEM* hereafter) and by the ASTER GDEM v2 (referred to as *ASTER* or *ASTER GDEM* hereafter), both free of charge. However, their posting limits geomorphological mapping to landforms of the uppermost microscale[1] and larger. Geomorphological studies on a regional scale are still often based on DEMs derived from contour lines that have been digitized from topographic maps (Ruszkiczay-Rüdiger et al., 2009; Shi et al., 2012; Le Bris and Paul, 2013; Thomas et al., 2014). Although the posting of these data may indicate adequate resolution, a microscale-oriented morphological analysis based on these DEMs may produce questionable results because the topographic variability in areas between contour lines is inevitably underestimated and the contour lines itself are generalized (Weibel, 1990; Gallay, 2009; Reuter et al., 2009; Florinsky, 2012). light detection and ranging (LiDAR) and photogrammetric processing of high-

[1] Scale definitions used in this thesis follow Barsch and Stäblein (1978) and Brunsden (1996).
Microscale: landforms with a basal footprint between 1 and 100 m
lower microscale: 1–10 m, upper microscale: 10–100 m
Mesoscale: landforms with a basal footprint between 100 m and 10 km
lower mesoscale: 100–1000 m, upper mesoscale: 1–10 km

resolution airborne image data allow the generation of DEMs with sufficient resolution and data quality to carry out geomorphological analysis on a microscale level (Liu, 2008; Loibl and Lehmkuhl, 2013). However, coverage is strictly limited to smaller study areas because of technical limitations (Smith, 2002; McGlone, 2007; Nelson et al., 2009). The yet unreleased operative TanDEM-X (TerraSAR-X add-on for Digital Elevation Measurement) global DEM promises to alleviate these problems through high-quality radar interferometric measurement and processing that result in a posting of 12 m and supposedly low error-proneness, reducing the resolution gap between (near-) global and local datasets (Krieger et al., 2005; DLR, 2011b; Rossi et al., 2012). However, the achievable DEM quality from this new dataset and its applicability toward geomorphological investigations still have to be demonstrated, particularly for high mountain environments. Even though the final TanDEM-X DEM products are not yet available, access to coregistered Single look Slant range Complex (CoSSC) scenes is possible for scientific users by submitting a proposal to German Aerospace Center (DLR, https://tandemx-science.dlr.de/).

The Nyainqêntanglha Range is an extensively glaciated high mountain range in southeastern Tibet, China (Wang et al., 2012), providing challenging conditions for DEM generation from remote sensed data. In this study, a TanDEM-X CoSSC scene depicting a section of the eastern Nyainqêntanglha Range was used to process an experimental DEM (referred to as *TDX* or *TDX DEM* hereafter) using standardized radar interferometric processing schemes. The dataset is thus providing a preview of the level of detail of the future TanDEM-X operational DEM and also of possible challenges regarding artifacts. A qualitative and quantitative assessment was carried out by interpreting hillshaded relief maps, DEM quality measures and morphometric parameters of TDX, SRTM1 and ASTER data. Manual geomorphological mapping of three sections within the Bodui Tsangpo valley and one high-mountain valley head area was then conducted to evaluate the quality of landscape rendering for different geomorphic settings on a large scale. We explicitly evaluated which landforms are detectable in the respective DEM.

3.2 Data

3.2.1 TanDEM-X CoSSC dataset

The TanDEM-X mission is based on the utilization of the two X-band radar satellites TerraSAR-X and TanDEM-X flying in a helix-like formation. Thus, a flexible single-pass interferometer is generated which is unprecedented in the history of SAR interferometry (Krieger et al., 2005, 2007). The primary objective of the mission is the generation of a global DEM compliant to the digital terrain elevation data (DTED)/high-resolution terrain information (HRTI)-3 specification (DLR, 2010). The final operative TanDEM-X DEM is planned to have a planar resolution of 12 m, a relative vertical accuracy within 2 m and an absolute vertical accuracy within 10 m, both for 90 % confidence (DLR, 2011b). TanDEM-X CoSSC datasets are an intermediate product of the Integrated TanDEM-X Processor which will also be used by DLR to generate the operative TanDEM-X DEM. Each dataset comprises one coregistered interferometric image pair in radar geometry, processing parameters and georeferencing information (DLR, 2012).

For the study at hand, the ascending scene 1032207_002 taken on July 19, 2011 was used (details on the imaging parameters are provided in Table 3.1). During the time frame of the data take, all descending

Table 3.1: Interferometric geometry of CoSSC dataset 1032207_002.

Parameter	Value
Acquisition mode	bistatic
Incidence angle [°] [a]	38.285
Height of ambiguity [m]	40.945
Ground range resolution [m] [b]	1.907
Effective baseline [m]	148.304
Azimuth resolution [m]	2.300

[a] For center pixel of master satellite
[b] Resolution in range projected on ground

acquisitions were characterized by small perpendicular baselines, resulting in low interferometric sensibility. Therefore, descending scenes were not incorporated into this study.

3.2.2 SRTM dataset

The SRTM was the first project to utilize a spaceborne single-pass SAR interferometer and enabled near-global DEM generation by the use of radar interferometry. For this purpose, the C-band system SIR-C was extended by a passive antenna mounted on a 60 m long boom to establish a bistatic interferometer with a fixed perpendicular baseline (Bamler and Hartl, 1998; Hancock et al., 2006; Hensley et al., 2007; Rott, 2009). During an 11-day mission of the space shuttle Endeavour in February 2000, imaging of 99.97 % of the terrestrial surface between 60° N and 56° S was possible (Sun et al., 2003; Rodríguez et al., 2006; Smith and Pain, 2009; Wang et al., 2012; Mukherjee et al., 2013).

At least two interferometric pairs with opposite viewing perspectives were used for DEM generation (Rabus et al., 2003; Smith and Sandwell, 2003; Hensley et al., 2007). Because SRTM is derived from C-band radar without subsequent height correction, the DEM represents a near-canopy surface (Nelson et al., 2009; Mukherjee et al., 2013). As part of the postprocessing, a 3×3 boxcar filter was used to attenuate phase noise (Rodríguez et al., 2006; Stevenson et al., 2010). The geodetic reference is WGS 1984 and vertical reference is the EGM 1996 geoid (Smith and Sandwell, 2003; Thomas et al., 2014). The data is provided with plate carrée projection.

Until September 2014, SRTM data were provided with a posting of 1″ for all territories of the United States of America and 3″ for the rest of the world (Nikolakopoulos et al., 2006; Arrell et al., 2008; Reuter et al., 2009). On September 23, 2014, the U.S. government announced the release of global 1″ data, which successively became available.

In high mountain areas, the initial version of the SRTM DEM was characterized by extensive data gaps originating from distinct layover and shadowing effects. These voids were filled by auxiliary lower resolution data in later versions (Rott, 2009). In the case of the recently released SRTM1 data, void-filled datasets are, however, not yet available. In this study, the seamless SRTM 3″ dataset provided by the CGIAR-CSI was used to fill the gaps present in the SRTM1 DEM (Dowding et al., 2004; Jarvis et al., 2008). The CGIAR-CSI applied interpolation algorithms incorporating auxiliary DEMs for filling of larger gaps, resulting in lower accuracy in the regions concerned (Reuter et al., 2007). Gap filling

of the SRTM1 DEM was conducted by first establishing a fine coregistration between both datasets and resampling the CGIAR-CSI fill-up data to 1″ posting using cubic convolution. To account for the different resolutions and data inaccuracies, both datasets were merged with boundary blending applying a bicubic spline interpolation.

For this study, the seamless 1″ DEM was projected to UTM Zone 46 N and resampled to a posting of 30 m using a cubic convolution algorithm.

3.2.3 ASTER GDEM dataset

The ASTER sensor, a multispectral imager on NASA spacecraft Terra, is run by NASA and the Ministry of Economy, Trade and Industry (METI) of Japan. Its near-infrared bands 3N (nadir looking) and 3B (backward looking, 27.7° along-track inclination) have a posting of 15 m and allow a generation of along-track stereo images suitable for stereometric DEM processing (Yamaguchi et al., 1998; Abrams, 2000; Reuter et al., 2009; Tachikawa et al., 2011a).

For generation of the ASTER GDEM, automatic image matching by stereo correlation was applied to the stereo image pairs (Reuter et al., 2009; Mukherjee et al., 2013). Processing of a seamless DEM was conducted by stacking of several base DEMs, whereby the number of grids incorporated varies owing to the variable influence of cloud cover (Reuter et al., 2009; Jacobsen, 2010). As ASTER is an optical imager, the ASTER GDEM strictly models the canopy. ASTER GDEM has a posting of 1″ and is available for all land surfaces between 83° N and 83° S. Analogous to SRTM, the geodetic reference is WGS 1984 and the vertical reference is the EGM 1996 geoid (Nelson et al., 2009; Smith and Pain, 2009; Wang et al., 2012). The first version was released in June 2009 (Reuter et al., 2009; Tachikawa et al., 2011b,c; Zhao et al., 2011; Frey and Paul, 2012). For the study at hand, the current version 2 was used (Wang et al., 2012). Primary modifications compared to the initial version are a reduction of correlation window size from 9×9 to 5×5 pixels and incorporation of stereo image pairs acquired after September 2008 (Tachikawa et al., 2011a,b,c; Mukherjee et al., 2013; Mashimbye et al., 2014). For this study, the ASTER dataset was projected to UTM Zone 46 N and resampled to a posting of 30 m using cubic convolution.

3.3 Current state of research

The vertical accuracy of the SRTM DEM is specified to 16 m (mean absolute error) at 90 % confidence (Rabus et al., 2003; Berry et al., 2007; Farr et al., 2007). A large number of studies investigated the numerical accuracy of the SRTM DEM by comparing SRTM values to high precision measurements. The overall result of these statistical analyses was that the SRTM DEM performs better than its specifications in most cases (Sun et al., 2003; Gorokhovich and Voustianiouk, 2006; Hofton et al., 2006; Rodríguez et al., 2006; Slater et al., 2006; Mouratidis et al., 2010; Shortridge and Messina, 2011; Mukherjee et al., 2013). An exception is given by Carabajal and Harding (2006), who conducted a worldwide evaluation of SRTM data by comparing it to ICESat altimeter measurements. They found that for Asian regions with extreme topography, most notably the Himalaya, the numerical accuracy of the SRTM DEM degrades substantially and the accuracy specifications are not met.

The ASTER GDEM has been thoroughly evaluated by U.S. and Japanese ASTER science teams

(Fujisada et al., 2005; ASTER GDEM Validation Team, 2009). According to their results, the ASTER GDEM v1 has a vertical accuracy (mean absolute error) of 20 m at 95 % confidence. Version 2 of the ASTER GDEM was assessed to have an accuracy of 17 m at 95 % confidence (Tachikawa et al., 2011c). Other studies come to somewhat contradictory results. In the studies for version 1 (Hirt et al., 2010; Miliaresis and Paraschou, 2011) and version 2 (Li et al., 2013; Mukherjee et al., 2013), ASTER GDEM accuracy matches or is better than the accuracy level specified by the ASTER science teams. Hirt et al. (2010) state, however, that the 3″ SRTM performed superior to ASTER GDEM v1. On the contrary, Mukherjee et al. (2013) reported that ASTER GDEM v2 provided better numerical performance than the 3″ SRTM (SRTM3). In opposition to the studies listed above, Chrysoulakis et al. (2011) found that ASTER GDEM v1 performs inferior to the level stated by the ASTER science teams for their study site in Greece.

Until now, little emphasis has been given to the effective resolution of both products, the resulting cognoscibility of landforms in both DEMs, and the consequences for geomorphological interpretation and mapping. Smith et al. (2006) investigated the SRTM3 DEM with regard to the delineation of linear glacial features such as drumlins, eskers and glacial erosion channels. They concluded that SRTM3 provides a poor basis for detecting these landforms as a consequence of the 3″ posting.

Tachikawa et al. (2011b,c) evaluated the effective resolution of the 1″ and 3″ versions of SRTM and both ASTER GDEM releases. According to their results, ASTER GDEM v1 yields an effective resolution equivalent to a ~114 m posting and ASTER GDEM v2 has an effective resolution equivalent to ~72 m posting. SRTM1 and SRTM3 were found to exhibit an effective resolution equivalent to ~75 and ~100 m pixel size, respectively. Consequently, the effective resolution of all DEMs is considerably lower than their posting theoretically allows (cf. Section 3.1). The significant resolution improvement from ASTER GDEM v1 to v2 is primarily a result of a smaller correlation kernel (5×5 instead of 9×9 pixels; Tachikawa et al., 2011b).

Several studies attest ASTER GDEM increased capabilities for landform detection and analysis in comparison to SRTM3 whereas the majority of studies negate improvements or even find ASTER inferior to SRTM3. Bubenzer and Bolten (2008) analyzed the cognoscibility of a Pleistocene megadune (draa) located in the eastern Sahara. Exhibiting an altitudinal variation of ~40–50 m, this distinct landform could be clearly detected and morphometrically analyzed using ASTER GDEM v1, but not using SRTM3.

Kervyn et al. (2008) conducted an assessment of the potential of SRTM1, SRTM3 and a self-processed ASTER DEM (15 m posting) to retrieve quantitative morphometric data for uppermost microscale and lower mesoscale volcanic features. They found that DEMs generated from ASTER images provide substantially more fine-scale irregularities than SRTM1, which could be traced back to inaccuracies of the stereo correlation process. Therefore, the detection of microscale topographic features such as gullies can be considerably hindered. The SRTM3 DEM renders topography in a very smooth way. On the downside, lower mesoscale key features such as craters are partly not detectable in SRTM data. Concluding, Kervyn et al. (2008) see SRTM1 as suitable for quantitative geomorphological studies of uppermost microscale and lower mesoscale landforms. In contrast, ASTER DEMs, in spite of their 1″ posting, are only considered as an equivalent alternative to SRTM3.

Examining the applicability of SRTM3 and a self-processed ASTER DEM (15 m posting) for

detection and mapping of Mediterranean Karst, Siart et al. (2009) found that neither of the two DEMs independently qualifies for detection of landforms with footprints less than ~40 m. The SRTM3 DEM was applicable for questions concerning the mesoscale, as large depressions were clearly highlighted by clusters of low resolutions. As opposed to that, the ASTER model generated a high amount of sinks, which could not be related to visible dolines in high-resolution satellite imagery. This is again an indicator for high-frequency undulations resulting from the image matching process. It has to be kept in mind that these results, in the first instance, only apply to the respective ASTER DEM product generated within the framework of these studies. However, Tachikawa et al. (2011c) note that ASTER GDEM v2 is affected by considerable high-frequency undulations, which worsened from version 1 to version 2 as a result of the smaller correlation kernel.

Comparing ASTER GDEM v1 and SRTM3 with LiDAR data downscaled to 30 and 90 m, respectively, Shafique et al. (2011) found that a higher product-moment correlation is evident between LiDAR data and SRTM1 in comparison to the LiDAR DEM and ASTER GDEM v1. Mashimbye et al. (2014) used a multi-resolution image segmentation (MRS) algorithm to perform an object-based land component classification of ASTER GDEM v2, SRTM3 and a DEM derived from Geoeye stereo images (5 m posting), the latter serving as reference. They found that SRTM produces shapes similar to the ones derived from the Geoeye DEM, just deviating in less sensitivity to morphological discontinuities as a consequence of lower resolution. In contrast, ASTER GDEM v2 differs substantially and fails to identify many major morphological discontinuities. As a consequence, SRTM3 is considered suitable for delineation of sufficiently large landforms whereas ASTER GDEM v2 is not.

3.4 Regional setting

The study area is located at the southeastern fringe of the Tibetan Plateau in the eastern Nyainqêntanglha Range. Geologically it is part of the southernmost terrane of the Tibetan tectonic collage, the Lhasa Terrane, and adjacent to the eastern Himalayan syntaxis (Dewey et al., 1988; Zhang et al., 2012). The regional topography is characterized by a distinct gradient from high-altitude plateau to foreland morphologies, reaching from ~4700 m asl base level altitude on the southern plateau down to ~150 m asl at the mountain front. As a consequence of the interplay of this pronounced altitudinal gradient, external drainage, and high precipitation, the region is characterized by remarkably deeply incised valleys, presenting a sharp contrast to the widely plain landscape of the inner Tibetan Plateau (Armijo et al., 1989; Peng et al., 2000; Clark et al., 2004). The highest peaks in the region are the summits of Namche Barwa and Gyala Peri, reaching altitudes of 7782 and 7294 m asl, respectively (Fig. 3.1; Burg et al., 1998; Seward and Burg, 2008). Summits >6000 m asl are abundant in the region. Floor altitudes of the major valleys range from 2050 m asl at the confluence of Parlung Tsangpo and Yigong Tsangpo to ~3000 m asl in the Bodui valley. Thus, local relief >3000 m over less than 10 km horizontal distance is evident in many local settings, yielding steep slopes and providing high energy regimes for geomorphologic processes (Korup et al., 2010).

The study area's climate is predominantly characterized by the Indian Monsoon and to a lesser extent by currents of the Southeastern Asian monsoonal system (Benn and Owen, 1998; Böhner, 2006; Cai et al., 2012; Loibl et al., 2014; Maussion et al., 2014). Intraannual climate variability is dominated by

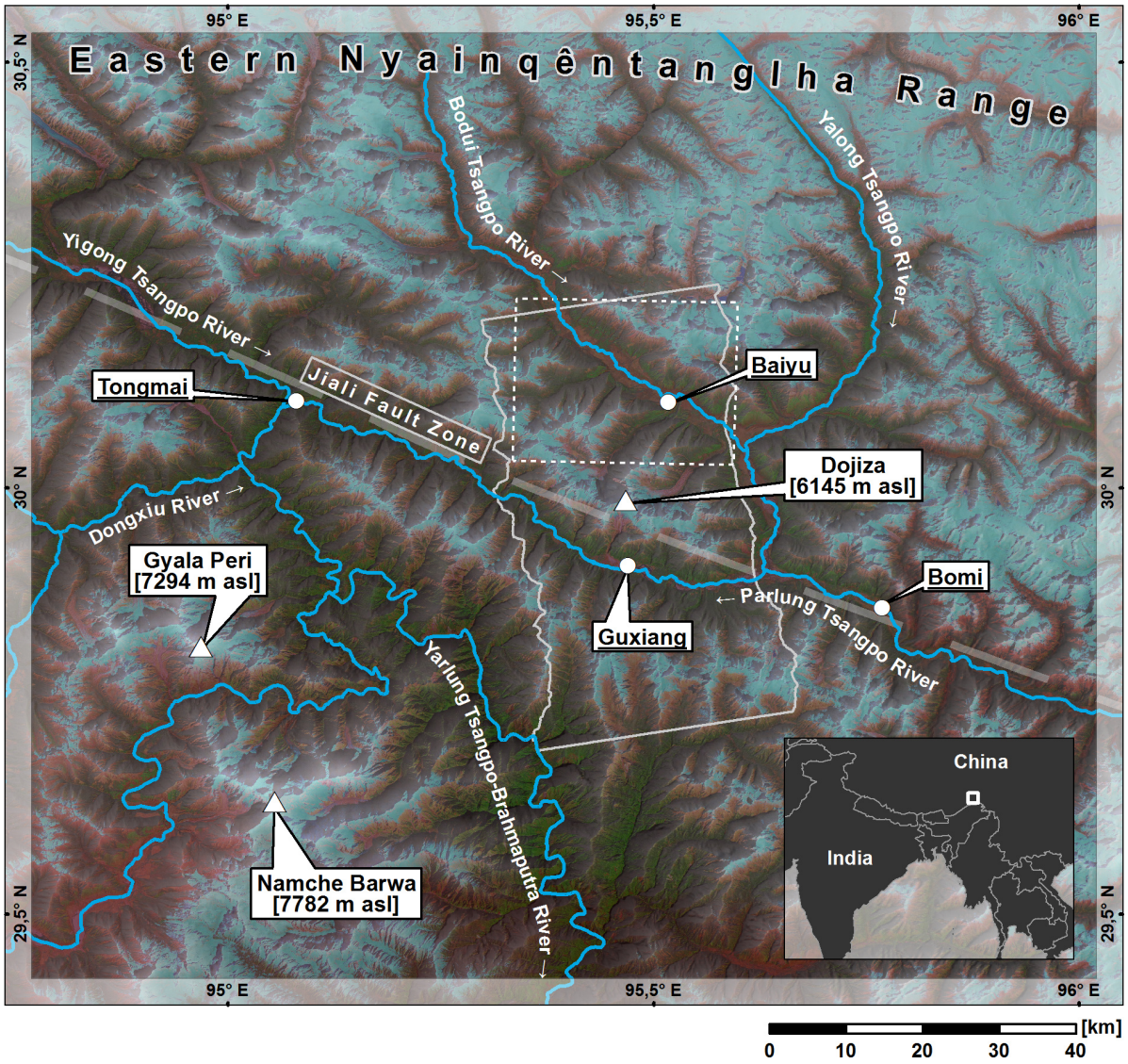


Figure 3.1: Regional overview of the central eastern Nyainqêntanglha Range in southeastern Tibet. Included are the footprint of the TanDEM-X CoSSC scene (solid white line) and the outline of the study area (Fig. 3.2, dashed white line).

an extremely humid summer season and an extratropical winter season characterized by considerably reduced precipitation (Molnar et al., 2010). The deeply incised valleys of the Yarlung Tsangpo-Brahmaputra river system and its tributaries act as a prominent transmission path for monsoonal vapor saturated air masses and, consequently, for sensible and latent heat (Yang et al., 2008). Monsoonal precipitation, associated release of latent heat, sensible heat flow and a lower mean altitude than the central Tibetan Plateau induce positive anomalies of annual precipitation and mean air temperature (Peng et al., 2000; Yang et al., 2008; Zhou et al., 2011; Zhu et al., 2013). As a result of its comparably low mean altitude and its favorable climatic conditions, the southeastern rim of the Tibetan Plateau is characterized by extensive extratropical mixed forests, exhibiting a sharp contrast to the inner plateau regions (Fang et al., 1996; Peng et al., 2000; Schickhoff, 2005). According to Liang et al. (2009), the timberline is situated at an altitude level of 4200 m asl–4400 m asl.

The Nyainqêntanglha range constitutes the Pleistocene glaciation center of the southeastern Tibetan Plateau (Zhou et al., 2011). Pronounced erosion entailed that glacial deposits older than the upper middle Pleistocene are missing in the study area (Zhou et al., 2007). The Bodui Tsangpo valley is characterized by prominent lateral and terminal moraines of late Pleistocene glacial advances, representing the type localities of the Guxiang and Baiyu glacial advances (Zhou et al., 2011). Guxiang deposits have been dated to 136.4 ka BP–112.9 ka BP (Zhou et al., 2007) and are located at an altitude range from 500 to 800 m above the modern valley floor, building a lateral moraine partially preserved as far as the confluence of the Bodui Tsangpo River and the Parlung Tsangpo River. During the Guxiang glacial phase, an expanded valley glacier system was developed within Bodui Tsangpo valley and its tributary valleys (Zhou et al., 2007, 2010). Baiyu deposits are located at an altitude level of 100 to 300 m above the modern valley floor and build considerably smaller moraines which were dated to 18.5 ka BP–11.1 ka BP (Zhou et al., 2007). The terminal moraines of the tributary Baiyu valley and Zhuxi valley are also to be subsumed under the Baiyu glacial phase (Zhou et al., 2010, 2011). According to Zhou et al. (2010), the equilibrium-line altitude (ELA) depressions during the Guxiang and Baiyu advances were ~800 and ~600 m, respectively.

3.5 Methods

3.5.1 DEM generation from TanDEM-X CoSSC data

The following section is a brief description of the processing scheme that was applied for DEM generation from CoSSC data. A flowchart of the processing routine is presented in Suppl. A.1.

With few exceptions, all data preparation and interferometric processing was performed with a routine using Interactive Data Language 7.1 (IDL). For the extraction of the CoSSC image data, the IDL-based data preparation routine 'TerraSAR-X/TanDEM-X SSC/CoSSC Reader for IDL and ENVI' ('tdx_openfile.sav') was integrated into the main routine (Exelis and DLR, 2012). Parameters necessary for interferometric processing were extracted from the appended XML files (see DLR, 2012 for comprehensive information on the TanDEM-X CoSSC data structure).

A high precision geodetic approach was used for flat earth extraction, i.e., extracting the interferometric phase evident on the ellipsoid chosen as projection reference. The coordinates of a specific image pixel on the reference ellipsoid are given by the point in which range equation, Doppler equation and ellipsoid equation intersect (Curlander, 1982; Schwäbisch, 1995, 1998). Because the intersection points cannot be determined via an analytical solution, the iterative Newton-Raphson approach is appropriate (cf. Geudtner, 1995). Interferogram filtering was applied prior to unwrapping the topographic phase because additive phase noise resulting from interferometric decorrelation, i.e., a partial loss of coherence due to disturbing influences like thermal noise, increases the error proneness of the phase unwrapping process (Zebker and Villasenor, 1992; Bamler and Hartl, 1998; Richards, 2009). The adaptive filter of Goldstein and Werner (1998) with the modification suggested by Baran et al. (2003) was used.

The iterative algorithm SNAPHU was used for phase unwrapping (Chen and Zebker, 2000; Chen, 2001). This algorithm first applies a 'minimum cost flow path following' approach and improves the phase unwrapping solution by incorporating probability density functions derived from radar imaging geometry and coherence/amplitude data. To derive topographic information from the absolute

interferometric phase, the 'empirical lookup table' approach was used (Geudtner, 1995; Schwäbisch, 1995; Small et al., 1996). Determination of the phase offset was conducted by using the reference points provided in the XML annotation data of the CoSSC dataset. Owing to the steep topography in our study area, considerable local phase aliasing was expected. To take this into account and minimize the influence of such inaccuracies, all 6440 reference points listed in an XML file were used to calculate a regression between topographic phase and phase offset. As no nonlinear trend could be found in the data, linear regression was considered sufficient for this task.

The final processing steps were transforming the raw DEM into a projected coordinate system and subsequent gridding. Initially, geocentric coordinates of the DEM were calculated by applying the Newton-Raphson approach again. The integrated geocoding functions of IDL, 'mapprojstruct' and 'map_proj_forward', were utilized to geocode the DEM into the Universal Transverse Mercator system. As these functions expect geographic position data as input, geographic coordinates were calculated by the common iterative approach (IOGP, 2014). Delaunay triangulation on the basis of a 1.5 m grid was carried out with the IDL functions 'triangulate' and 'trigrid'. Eventually, DEM, geocoded amplitude, and geocoded coherence were exported as GeoTIFF files.

As the intermediate high resolution DEM is noisy, outlier filtering and subsequent local pixel aggregation were conducted. For outlier filtering, a modification of the statistical filtering method presented by Felicísimo (1994) was applied with an error probability of 0.01. Geocoded coherence information was incorporated by using a kernel size of 5×5 pixels and a weighting matrix derived by multiplication of a quadratic inverse distance kernel and the local coherence matrix. To deal with anisotropy inevitably induced by coherence, separated calculations for eight azimuth directions were performed and the results were averaged afterwards. Finally, a pixel aggregation to a posting of 15 m was carried out using arithmetic averaging.

3.5.2 DEM quality parameters

All three DEM datasets incorporated into the study provide parameters giving information about DEM processing conditions. These parameters were addressed prior to morphometric analysis and geomorphological mapping, because they allow statements about the potential in-situ DEM quality and thus help to differentiate between general and local DEM characteristics.

The interferometric coherence (Suppl. A.2) is the primary quality measure of SAR interferometric data. Decorrelation causes random noise within the topographic phase and thus induces high roughness values within the DEM (Zebker and Villasenor, 1992; Geudtner, 1995). The position of pixels interpolated by the extreme value filter was also included in the analysis, as it indicates outliers induced by low correlation (Suppl. A.3).

Consideration of void-filled data positions (Suppl. A.4) and the number of image pairs incorporated into stereometric processing (Suppl. A.5) is mandatory for the assessment of SRTM1 and ASTER, respectively, as both parameters entail consequences on the achievable quality of surface representation (cf. Section 3.2).

3.5.3 Morphometric DEM analysis

Geomorphometry is the science of quantitative land surface analysis, essentially conducted by deriving parameters from DEMs (Pike, 1995, 2000; Rasemann et al., 2004). As the information on a local surface is chiefly given by the topologic relationships of the altitude values, most geomorphometric parameters quantify the local relationship between pixel values (Arrell et al., 2008; Gallay, 2009; Reuter et al., 2009). As a consequence of their high sensitivity to variability in the local altitude field, these point attributes are also an important element of DEM evaluation (Weibel, 1990; Florinsky, 1998; Gonga-Saholiariliva et al., 2011).

Essential quantitative information on a local surface is given by mathematical derivatives. As the earth surface as depicted by the DEM is not differentiable (cf. Section 3.1), calculation of mathematical derivatives can only be carried out by a local parametrization of the DEM. For this purpose, a mathematical function is fitted to the local altitude field and derivatives are calculated thereafter (Wood, 1996).

Commonly, a polynomial is calculated for a 3×3 cell moving window, whereby two common approaches exist. Evans (1980) proposed the use of a quadratic polynomial, thus providing six parameters. Being overdetermined for the 3×3 cell neighborhood, this function filters out small random errors possibly evident in the DEM (Irvin et al., 1997; Florinsky, 1998; Schmidt et al., 2003; Albani et al., 2004; Oksanen, 2006). Zevenbergen and Thorne (1987) proposed, in contrast, the usage of a partial quartic (nine parameter) polynomial:

$$z = ax^2y^2 + bx^2y + cxy^2 + dx^2 + ey^2 + fxy + gx + hy + i, \tag{3.1}$$

where variables x, y and z are the (local) three-dimensional grid coordinates and a to i are the coefficients to be derived.

As this function is determined when using the common 3×3 cell neighborhood, it provides the best possible fit to the local neighborhood and thus is the preferable approximation function for DEM evaluation (cf. Thorne et al., 1987). Consequentially, the partial quartic was used for the study at hand.

The DEM's local gradient determines the gravitational potential energy for geomorphological work (Arrell et al., 2007; Fig. 3.3 below, Suppl. A.5). The slope (in degrees) of the steepest path down the polynomial surface is calculated as:

$$\text{Slope} = \arctan \sqrt{\left(\frac{\partial z}{\partial x}\right)^2 + \left(\frac{\partial z}{\partial y}\right)^2} \cdot \frac{180}{\pi}, \tag{3.2}$$

where $\frac{\partial z}{\partial x}$ is the first partial derivative of z with respect to x, and $\frac{\partial z}{\partial y}$ is the first partial derivative of z with respect to y.

A single measure for the second order derivative of the local approximation surface can be calculated by deriving the second order derivative from an intersecting plane (Wood, 1996). Several alternative curvature values are applicable for geomorphometric analysis and DEM assessment (for detailed information please refer to Gallant and Wilson, 2000; Shary et al., 2002; Schmidt et al., 2003; De Smith et al., 2007; Olaya, 2009).

The most commonly used curvature values are (i) the profile curvature, which describes the curvature parallel to the direction of maximum slope and therefore is a parameter for acceleration or deceleration of flow processes across the surface, and (ii) the planform curvature, describing the surface curvature perpendicular to the direction of the maximum slope. Planform curvature indicates convergence or divergence of flow processes across the surface (Irvin et al., 1997; Gallant and Wilson, 2000; Wilson et al., 2007; Olaya, 2009).

In this study, the general curvature was applied as it reflects both profile and planform curvature. It is calculated as (Moore et al., 1991):

$$\text{General Curvature} = -200\left(\frac{\partial^2 z}{\partial x^2} + \frac{\partial^2 z}{\partial y^2}\right), \tag{3.3}$$

where $\frac{\partial^2 z}{\partial x^2}$ is the second partial derivative of z with respect to x and $\frac{\partial^2 z}{\partial y^2}$ is the second partial derivative of z with respect to y.

Please note that the scaling factor of 100 is commonly applied to express curvature as percent gradient per unit length as well as to scale the curvature values to a more convenient value range (Albani et al., 2004). In this study, the absolute value of the general curvature was used in order to facilitate display (Fig. 3.4, Suppl. A.7).

The term roughness intuitively refers to the local irregularity of a surface (Mark, 1975). The concept of roughness is, however, generally ambiguous. Consequentially, various methods for calculating roughness measures exist (cf. Grohmann et al., 2011; Smith, 2014). Pronounced local scale surface roughness necessarily results in high curvature values and is thus already reflected by (general) curvature. Nevertheless, incorporation of surface roughness parameters can be beneficial for DEM evaluation. The main reason for this is the high dependency of curvature on DEM resolution, with DEMs exhibiting higher effective resolutions generally showing higher curvature values because of the fractal characteristics of the earth surface (cf. Gallay, 2009, Section 3.1). Roughness parameters are, however, generally less sensitive to different postings, allowing quantitative comparisons between DEMs having different postings to a certain degree (cf. Grohmann et al., 2011).

For this study, we used the *vector ruggedness measure (VRM)* after Sappington et al. (2007). Being a vector dispersion measure, VRM is derived from the slope and aspect variability within a defined neighborhood. Because aspect is defined in polar space, a direct calculation of its variability does not give meaningful results. Therefore, the VRM is determined as:

$$\text{VRM} = 1 - \|\vec{r}\|/n, \tag{3.4}$$

where $\vec{r}$ is the sum vector of all surface normal (unit) vectors within the calculation window and n is the pixel count of the calculation window. A 3×3 pixel calculation window was used for the study at hand to indicate high-frequency irregularities of the altitude field as modeled by each DEM (Fig. 3.5, Suppl. A.8).

Parameters reflecting local topology do not provide any information about the terrain context. The incorporation of terrain context into DEM evaluation is, however, essential for understanding how a DEM models the topographic surface. A method suitable for quantifying the topographic position of

a raster is the application of grayscale mathematical morphology. Rodriguez et al. (2002) have shown the benefit of grayscale morphological operations in the field of geomorphology by applying a Top Hat function to quantify watershed incision rates. Schmidt and Hewitt (2004) proposed the use of Top Hat functions as part of a fuzzy landform classification framework.

The basic idea behind mathematical morphology is that a grid consists of groups of pixels representing *structures* and that these structures are manipulated using a morphological operation (cf. Serra, 1986; Sternberg, 1986; Pratt, 2001). The pattern affected by the morphological operation is defined by a binary structuring element which is scanned over the grid. The basic operations in mathematical morphology are *dilation* in which a structure is extended according to the structuring element, and *erosion* in which a structure is shrunken according to the given structuring pattern (Pratt, 2001):

$$D(x, y) = G(x, y) \oplus S(x, y) \qquad \text{(Dilation)} \tag{3.5}$$

$$E(x, y) = G(x, y) \ominus S(x, y) \qquad \text{(Erosion),} \tag{3.6}$$

where G is the grid to be manipulated, $\oplus/\ominus$ indicate morphological dilation/erosion, and S is the structuring element.

In the case of mathematical morphology applied to grayscale images like DEMs, the dilation and erosion operators represent local maximum and minimum operations, respectively (Sternberg, 1986). All further morphological operations are based on dilation and erosion. *Closing* is defined as dilation followed by erosion while using the same structuring element. It causes the join of high value zones. Erosion followed by dilation, called *opening*, induces the opening of high value zones (Pratt, 2001):

$$C = [G \oplus S] \ominus S \qquad \text{(Closing)} \tag{3.7}$$

$$O = [G \ominus S] \oplus S \qquad \text{(Opening)} \tag{3.8}$$

Top Hat functions are subtractions between the original grid and it's closed or opened version and thus can be used to delineate the local topographic position in relation to the size of the structuring element (cf. Rodriguez et al., 2002; Schmidt and Hewitt, 2004). The White Top Hat (WTH) function delineates antiforms and is determined as:

$$\text{WTH} = G - O \tag{3.9}$$

The Black Top Hat (BTH) function delineates synforms and is determined as:

$$\text{BTH} = C - G \tag{3.10}$$

For this study, the approach taken by Schmidt and Hewitt (2004) was modified by first calculating WTH and BTH using a circular structure element. Both grids were then combined by subtracting the BTH grid from the WTH grid, creating a raster showing both antiforms and synforms.

The scale of the morphological operation is defined by the size of the structuring element so that the filter of WTH – BTH generally allows a delineation of the topographic position independent from the DEM posting, thus facilitating the comparative evaluation of DEMs exhibiting different pixel sizes. As

the structuring element needs to exhibit an odd size to ensure isotropic filtering, a diameter of 19 pixels (equivalent to 285 m) was used for the TDX DEM and a diameter of nine pixels (equivalent to 270 m) was applied for both the ASTER GDEM and the SRTM1 DEM (Fig. 3.6, Suppl. A.9).

Since no reliable sources of absolute heights such as geodetic measurements, high-resolution DEMs and small-scale topographic maps are available for the study area, a quantitative assessment of absolute DEM accuracy was not applicable. Thus, a quantitative approach to compare relative differences between the DEMs was developed. The applied algorithm is based on the *sum of absolute differences algorithm (SAD)* which is a simple difference measure used in the field of image processing for matching of two raster images and analyzing image motion (Aschwanden and Guggenbuhl, 1992; Giachetti, 2000). The parameter is given by summing up all absolute differences of corresponding pixels within a defined calculation window. For computing the *zero-mean sum of absolute differences (ZSAD)*, both grids' arithmetic means are adjusted to zero before difference calculation by using:

$$\mathrm{ZSAD} = \sum_{x,y=1}^{n} \left| \left(\mathrm{G}_{1;x,y} - \overline{G_1} \right) - \left(G_{2;x,y} - \overline{G_2} \right) \right|, \tag{3.11}$$

where G_1 and G_2 are the details of the first and second grid, respectively, $\overline{G_1}$ and $\overline{G_2}$ their respective mean values, x and y are the local grid coordinates, and n denotes the pixel count of the local window.

Applied to elevation data, this zero-mean adjustment implies that only differences in the local relief representation are factored in the difference measure, thus providing a quantitative measure of the local degree of dissimilarity of two DEMs.

For this study, the zero-mean sum of absolute differences (ZSAD) was implemented with a moving window method (MWZSAD) so that the considered surface is centered over each pixel, generating a smooth raster of numerical surface differences (cf. Fig. 3.7, Suppl. A.10). The TDX DEM served as reference for both SRTM and ASTER. A circular neighborhood with a 150 m diameter was found to be appropriate to show microscale differences. An expedient computation of the MWZSAD parameters requires the DEMs to exhibit identical postings. Therefore, SRTM and ASTER were resampled to the TDX grid by using cubic convolution. This approach is in accordance with the implication of continuity between DEM data points, which is intrinsic to visual and geomorphometric DEM analysis (cf. Section 3.1). Furthermore, the TDX DEM was compared with a downscaled version (30 m, referred to as *TDX30* hereafter) of itself to illustrate the effect of DEM posting.

3.5.4 Geomorphological mapping and visual evaluation

The processed TDX DEM was applied as data basis for expert-driven manual geomorphological mapping. Specifically, the DEM was analyzed regarding the feasibility of detecting and interpreting landforms by a trained geomorphologist who is familiar with the regional setting (cf. Smith, 2011). The case study focuses on the Bodui valley which exhibits manifold heterogeneous landforms of different sizes, originating from various geomorphological processes. The aim of this approach was to test how far the shapes of different landforms can be determined from this new DEM dataset and where the limits of such mapping are in terms of scale and, possibly, artifacts or noise. Furthermore, the possibility of assigning landforms to different geomorphological processes was assessed. Thus,

all mapping was performed solely using the DEM and the basic derivatives, i.e., hillshade, slope and curvature raster datasets. Satellite imagery (Google Earth, Landsat ETM+) was exclusively used to evaluate the results after the mapping process was finished. Subsequently, the feasibility of delineating the landforms from the ASTER GDEM and SRTM1 DEM datasets was assessed in order to comparatively evaluate the benefits of the new dataset. The mapping approach adapts concepts of the classic German 'Geomorphologische Karte 1:25,000' (Barsch and Liedtke, 1980; Barsch et al., 1987) and the 'Geomorphologische Karte Hochgebirge' (Kneisel et al., 1998) frameworks, such as the colors for different dominant sedimentological processes and the symbols for linear features including drainageways and steps/rims. In order to assess the upper limits of landform cognoscibility achievable with the TDX DEM, several small landforms were located from high-resolution Google Earth imagery and measured by cross sections in the DEM.

3.6 Results

In the following, the results of the comparative evaluation of the processed TDX DEM with the SRTM1 DEM and the ASTER GDEM are presented. Section 3.6.1 provides a general assessment of the performance of the three DEMs regarding the display of local topography, conducted by qualitatively interpreting hill-shaded relief images and incorporating the DEM quality parameters. For convenient visualization, the study area was limited to the northern part of the TDX footprint, as shown in Figs. 3.1 and 3.2. In Section 3.6.2, the DEMs are evaluated by visually and statistically analyzing the geomorphometric parameters (Figs. 3.3 and 3.7) for four core study areas (called *Details* hereafter) located within the Bodui Tsangpo valley (cf. Figs. 3.9–3.11, see Fig. 3.2 for locations) and the Baiyu valley's upper catchment (cf. Fig. 3.12, see Fig. 3.2 for location). In Section 3.6.3, an assessment of the TDX DEM data's potential for high-resolution geomorphological exploitation is carried out by analyzing the geomorphological inventory of the four Details (Figs. 3.9 and 3.12).

3.6.1 Exploratory visual DEM analysis and DEM quality parameter assessment

In general, the SRTM1 DEM provides a moderate level of detail. It exhibits, however, visible blurring causing a smooth landscape representation and is also characterized by a homogeneous low-wavelength grainy texture (cf. Suppl. A.11). Potential differences in roughness are detectable by visual interpretation only in the case of data voids, which are clearly cognizable by a heavily blurry, low detailed representation. This is clearly visible in the northeastern part of the study area, where a bulk of SRTM1 data is missing and the substitute provides a very limited level of detail. Within the core study areas, however, data voids are sparse (cf. Suppl. A.5). With ~5 %, only Detail 4 shows a considerable number of voids. Concerning the whole study area, the proportion of voids is slightly above 6 %.

The ASTER GDEM scene is characterized by a peculiar bumpy texture which exhibits a relatively homogeneous distribution (cf. Suppl. A.12). Each texture element extends over several pixels, indicating local autocorrelation. The number of image pairs incorporated into the stereometric processing exhibits a considerable local variation, ranging from one to 12 image pairs with an arithmetic mean of 6.6 (cf. Suppl. A.5). According to Tachikawa et al. (2011c), a significantly decreasing quality of topographic representation has to be expected when less than 10 stereo image pairs are applied, becoming severe at

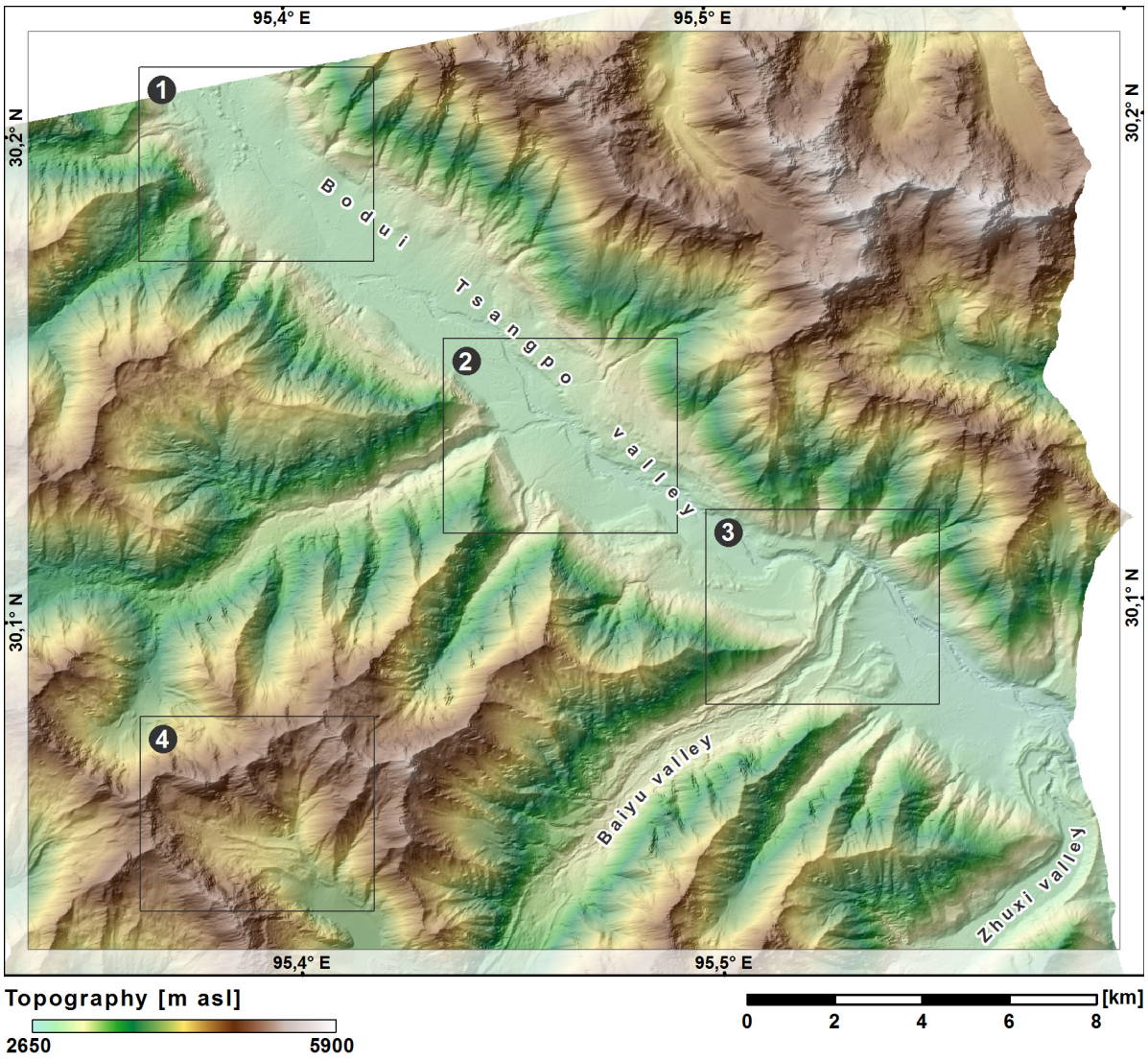


Figure 3.2: Topographical overview of the study area in the Bodui Tsangpo valley as depicted in the self-processed TDX DEM. Black outlines indicate the locations of the Details.

less than three image pairs. Approximately 95 % of the study area was processed from ten stereo image pairs or less but only ~1.5 % was derived from fewer than three stereo pairs.

In the case of the three Details located within the Bodui Tsangpo valley, the arithmetic means of the number of image pairs incorporated into the stereometric processing vary between 7.8 and 9 and are thus higher than the regional average. Only Detail 4 (Fig. 3.12), which incorporates the high-alpine valley and ridge setting, matches the map average. The proportion of areas processed from less than 10 image pairs varies between 57 % and 100 % with maxima of 100 % and 95 % in Details 3 (Fig. 3.11) and 4 (Fig. 3.12), respectively. Image pair counts below three scenes amount to below 0.05 % for all Details within the Bodui Tsango valley and 1.8 % for Detail 4. It has to be emphasized that although the number of image pairs incorporated into the processing varies considerably, this does not induce visible texture heterogeneity. A large batch of filled voids is evident south of Detail 2 (Fig. 3.10) which is characterized by slightly reduced roughness (cf. Suppl. A.5 and A.12). No filled voids are present

within the Details.

In comparison to the ASTER and SRTM1 DEMs, the overall level of detail of TDX is notably higher (cf. Fig.3.2, Suppl. A.11 and A.12). The TDX DEM is characterized by perspicuous facets on the hillsides faced towards the radar system, leading to low roughness values in the upper reaches of large west-oriented slopes. On steeper slopes facing leeward from the radar sensor (referred to as leeward slopes hereafter), an accentuated roughness and decreased level of topographic detail is evident. These conspicuities are clearly reflected in the positions of filtered outliers, which predominantly concentrate on the leeward slopes (cf. Suppl. A.3). A total of 2.23 % of all pixels located within the study area were filtered. All Details within the Bodui Tsangpo valley exhibit percentages of filtered pixels <1 %, whereas Detail 4 shows an above average value of 3.23 %.

The study area's arithmetic mean of interferometric coherence is 0.56. As expected with regard to characteristic decorrelation processes (cf. Zebker and Villasenor, 1992), montane zone, streams and leeward slopes exhibit low interferometric correlation. Flat valley floors with shallow vegetation cover and nival areas exhibit substantially higher correlation values (cf. Suppl. A.2). Average coherence values of the Details are in accordance with this general statement. Varying between 0.65 and 0.72, coherence means of the Details located within the Bodui Tsangpo valley are above average, indicating comparably favorable processing conditions. Detail 4, characterized by a rugged topography with abundant steep leeward slopes, exhibits a coherence average of 0.53. Forest clearings are generally detectable in the TanDEM-X data, showing a smooth surface and transition to woodland (cf. Suppl. A.13).

The phase offset locally applied was determined using linear regression between interferometric phase and phase reference data from georeferencing points (cf. Section 3.5.1). The calculation resulted in a regression factor of 1.011 indicating that the applied phase offset slightly rises with increasing topographic height.

3.6.2 Morphometric DEM analysis

In all Details, TDX mean elevations show a negative bias when compared to ASTER and SRTM1 (cf. Table 3.2). Within the Bodui Tsangpo valley, the bias exhibits a conspicuous variation between −22.7 m (Detail 3) and −65.3 m (Detail 1). In the high mountain-environment, the elevation bias amounts to −114.1 m. Accordingly, TDX exhibits the lowest mean elevation increase from Detail 3 to Detail 4, whereas ASTER shows the greatest one. When looking at the frequency distributions of Detail 2, the absolute maximum indicating the average elevation level of the valley bottom is much less pronounced in the case of ASTER (Fig. 3.8A).

In Detail 2, TDX and SRTM1 slope grids display consistent slope angle distributions (Fig. 3.3). Bumpy artifacts are well visible in the ASTER slope grid of Detail 2, particularly in the valley floor. In Detail 4, this bumpy texture is accompanied by a banding structure. Striped and noisy artifacts are visible in TDX's representation of the ridge areas in Detail 4. Intermediate slopes are, however, displayed relatively homogeneously and the valley bottom shows a clear and consistent slope distribution. With the exception of Detail 4, ASTER exhibits the highest average slope values and the lowest standard deviation of slope (cf. Table 3.3). SRTM shows the lowest slope means in all Details. Examination of the frequency distributions of slope as modeled by SRTM1 shows a considerable variation below 8° in the case of Detail 2 (Fig. 3.8B). In the case of ASTER, the proportion of low slope values is strikingly

Table 3.2: Mean elevations for Details 1–4 calculated from TDX, SRTM1 and ASTER DEMs (see Fig. 3.2 for locations). Values in brackets are standard deviations.

Detail	TDX (15 m)	SRTM 1″	ASTER GDEM v2
1 (Fig. 3.9)	3149.83 [290.83]	3213.33 [295.72]	3215.09 [303.14]
2 (Fig. 3.10)	3075.87 [229.48]	3101.39 [230.27]	3103.56 [238.80]
3 (Fig. 3.11)	3036.54 [221.39]	3053.52 [202.94]	3059.20 [205.04]
4 (Fig. 3.12)	4602.18 [292.04]	4685.53 [305.16]	4698.10 [314.21]

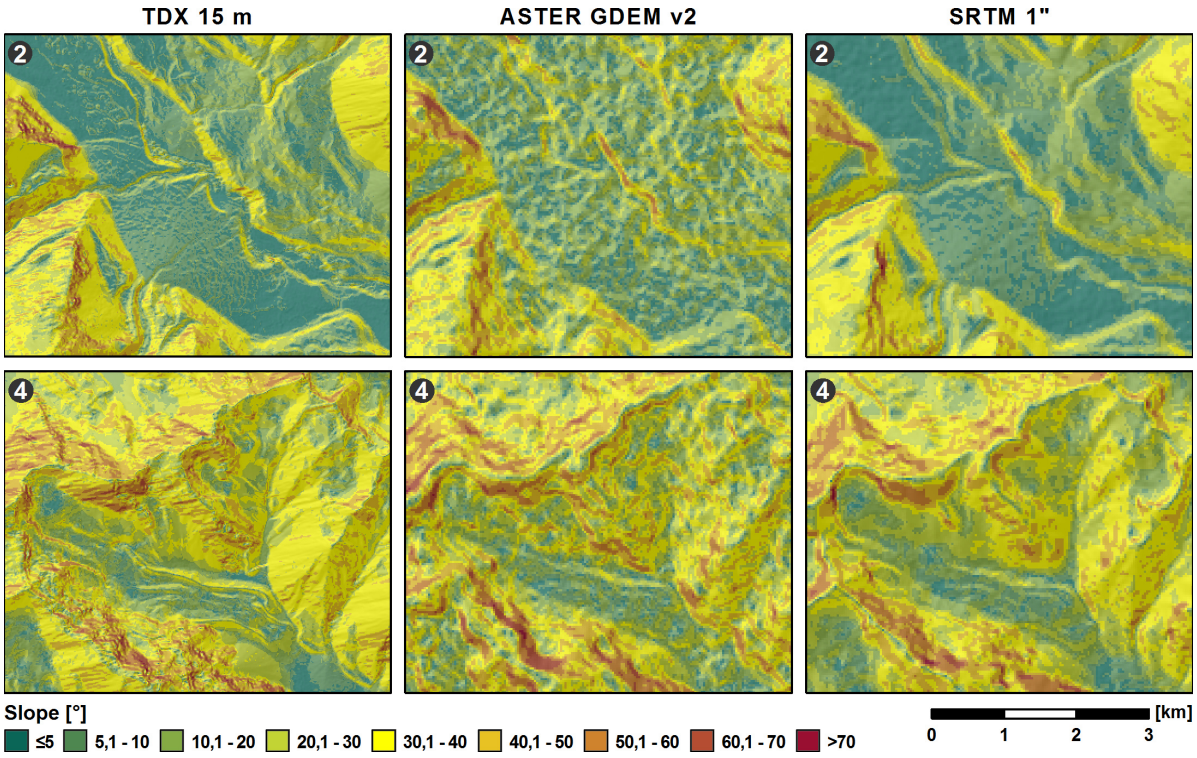


Figure 3.3: Classified slope angles calculated from TDX, ASTER and SRTM1 DEMs for Details 2 and 4 (see Fig. 3.2 for locations, Suppl. A.5 for a display of all Details).

low. TDX and SRTM both exhibit a second peak between 35° and 40°, representing the average angle of adjacent slopes. In the SRTM1 histogram, this peak is, however, much less pronounced than in TDX. When looking at the slope histograms for Detail 4, this peak is displayed in a very clear manner in the case of TDX, whereas SRTM1 and ASTER show flat distributions. Besides, the slope histograms of TDX show less variability between neighboring value classes.

The fractal characteristics of the earth surface entail that DEM curvature values inevitably increase with increasing effective resolution (cf. Section 3.1). Consequentially, TDX exhibits the highest average curvature values in all Details. In accordance with the results presented for slope, the TDX curvature grid of Detail 2 exhibits a clear spatial differentiation, showing planar surfaces as well as breaks in slope, thus clearly delineating the geomorphological inventory (Fig. 3.4). In Detail 4, however, high curvature values prevail in the upper slopes and particularly on steeper leeward slopes. SRTM1 generally resembles the spatial curvature distribution as shown by TDX. The predominantly planar zones evident

Table 3.3: Mean slope angles for Details 1–4 calculated from TDX, ASTER and SRTM1 DEMs (see Fig. 3.2 for locations). Values in brackets are standard deviations.

Detail	TDX (15 m)	SRTM 1″	ASTER GDEM v2
1 (Fig. 3.9)	19.87 [14.78]	18.93 [14.29]	22.37 [13.14]
2 (Fig. 3.10)	18.14 [14.50]	17.03 [13.49]	20.37 [13.20]
3 (Fig. 3.11)	22.24 [14.75]	21.14 [13.88]	23.06 [13.59]
4 (Fig. 3.12)	30.52 [12.69]	29.65 [12.99]	30.34 [13.93]

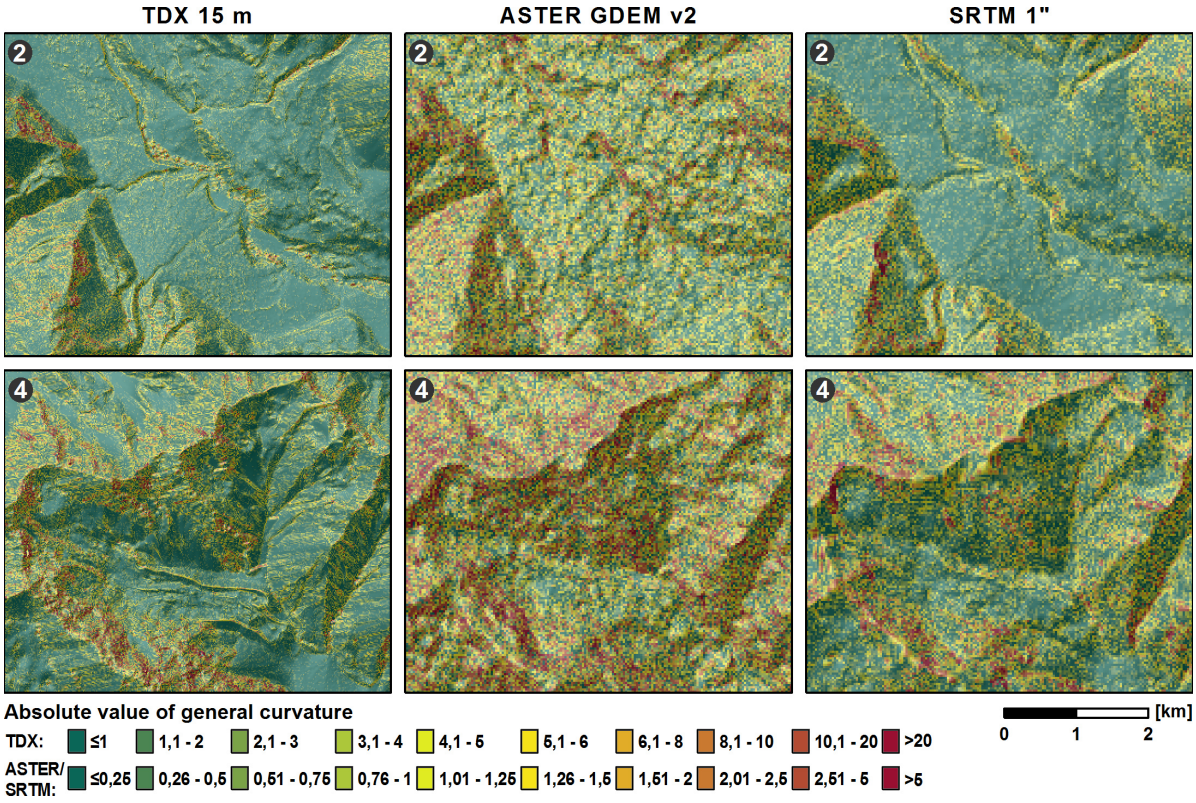


Figure 3.4: Classified absolute general curvatures calculated from TDX, ASTER and SRTM1 DEMs for Details 2 and 4 (see Fig. 3.2 for locations, Suppl. A.7 for a display of all Details). To facilitate visual comparability, ASTER and SRTM classes are four times smaller than those of TDX.

Table 3.4: Mean absolute general curvatures for Details 1–4 calculated from TDX, ASTER and SRTM1 DEMs (see Fig. 3.2 for locations). Values in brackets are standard deviations.

Detail	TDX (15 m)	SRTM 1″	ASTER GDEM v2
1 (Fig. 3.9)	1.821 [2.523]	0.541 [0.640]	1.116 [0.996]
2 (Fig. 3.10)	1.639 [2.199]	0.520 [0.631]	1.048 [0.946]
3 (Fig. 3.11)	1.650 [2.092]	0.649 [0.693]	1.144 [1.045]
4 (Fig. 3.12)	2.636 [3.405]	0.926 [1.089]	1.513 [1.385]

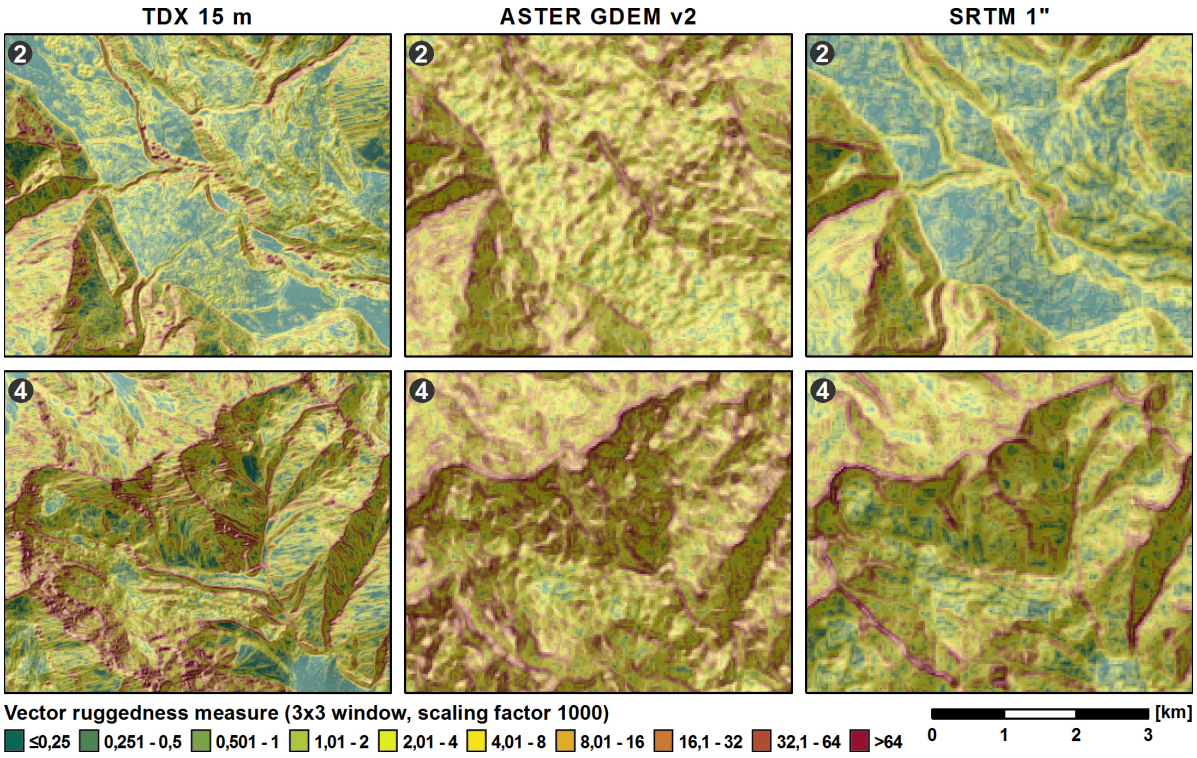


Figure 3.5: Vector ruggedness measure calculated with a 3×3 moving window (scaling factor 1000) from TDX, ASTER and SRTM1 DEMs for Details 2 and 4 (see Fig. 3.2 for locations, Suppl. A.8 for a display of all Details).

in Detail 2 are characterized by a homogeneous texture of moderate curvature values whereas TDX shows more differentiation here. SRTM1 exhibits the lowest average curvature values for all Details (Table 3.4, Fig. 3.8C). Average curvature values of ASTER are much higher in comparison to SRTM1. The striking feature of ASTER curvature is its spatial distribution, which predominantly shows moderate to high curvature values and thus allows no differentiation between different geomorphological units in the valley bottoms.

TDX and SRTM1 show a clear differentiation between zones exhibiting different VRM amplitudes and patterns so that different morphological domains like terraces, slopes, alluvial fans and channels are clearly reflected in the VRM grids (Fig. 3.5). In Detail 4, TDX exhibits high VRM values on upper leeward slopes. The VRM grid of SRTM1 appears smooth and generally shows lower amplitudes. As a consequence, SRTM1 exhibits the lowest mean VRM values (Table 3.5). Contrastingly, ASTER

Table 3.5: Mean vector ruggedness measure values for Details 1–4 calculated from TDX, ASTER and SRTM1 DEMs (see Fig. 3.2 for locations). Values in brackets are standard deviations.

Detail	TDX (15 m)	SRTM 1″	ASTER GDEM v2
1 (Fig. 3.9)	0.0061 [0.0116]	0.0045 [0.0097]	0.0113 [0.0091]
2 (Fig. 3.10)	0.0056 [0.0106]	0.0041 [0.0076]	0.0103 [0.0089]
3 (Fig. 3.11)	0.0072 [0.0139]	0.0066 [0.0115]	0.0119 [0.0117]
4 (Fig. 3.12)	0.0116 [0.0174]	0.0097 [0.0146]	0.0140 [0.0119]

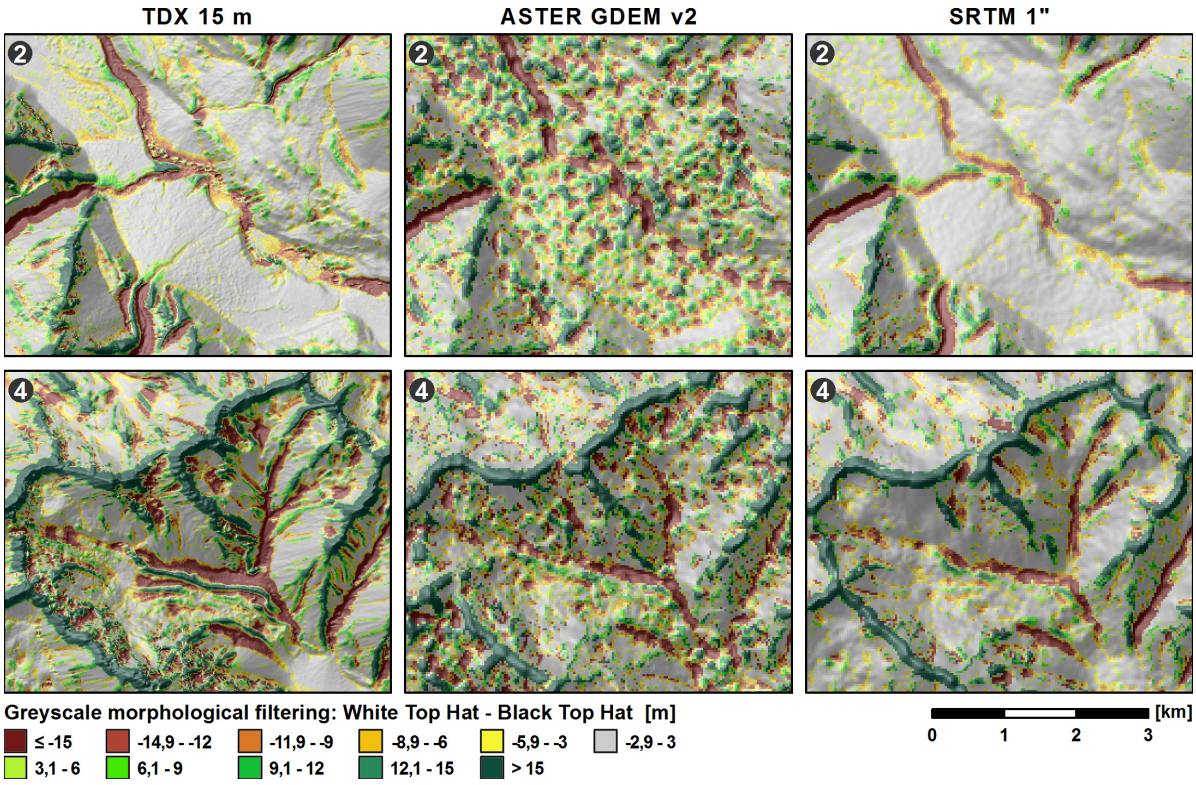


Figure 3.6: Results of grayscale morphological filtering (White Top Hat − Black Top Hat) calculated from TDX, ASTER and SRTM1 DEMs for Details 2 and 4 (see Fig. 3.2 for locations, Suppl. A.9 for a display of all Details).

shows high VRM values throughout all Details and consequentially models a rugged and undifferentiated surface. In accordance, ASTER exhibits the highest average VRM values whereas the standard deviation of the ASTER VRM shows the lowest values or is just slightly above that of SRTM1. In the histogram, ASTER exhibits a pronounced long-tailed frequency distribution with low percentages of the lowermost classes (Fig. 3.8D).

SRTM1 is capable of displaying landforms down to the uppermost microscale, but exhibits noticeable smoothing (Fig. 3.6). TDX additionally shows many more details beyond the uppermost microscale, e.g., hummocky surfaces and incised channels in the northwestern part of Detail 2 are clearly displayed. Furthermore, TDX is the only DEM capable of representing lineaments of the glacier tongue and adjacent areas evident in Detail 4. In the case of ASTER GDEM, a bumpy texture conceals real landforms and renders delineation of lower mesoscale landforms nearly impossible. With the exception

Table 3.6: Mean grayscale morphological filtering (White Top Hat – Black Top Hat) values for Details 1–4 calculated from TDX, ASTER and SRTM1 DEMs (see Fig. 3.2 for locations). Values in brackets are standard deviations.

Detail	TDX (15 m)	SRTM 1″	ASTER GDEM v2
1 (Fig. 3.9)	-0.576 [11.783]	-0.559 [9.322]	-0.633 [13.404]
2 (Fig. 3.10)	-1.222 [12.082]	-0.719 [8.525]	-0.735 [12.925]
3 (Fig. 3.11)	-2.112 [18.401]	-1.735 [15.047]	-0.970 [17.528]
4 (Fig. 3.12)	3.602 [20.379]	3.541 [16.987]	2.656 [17.236]

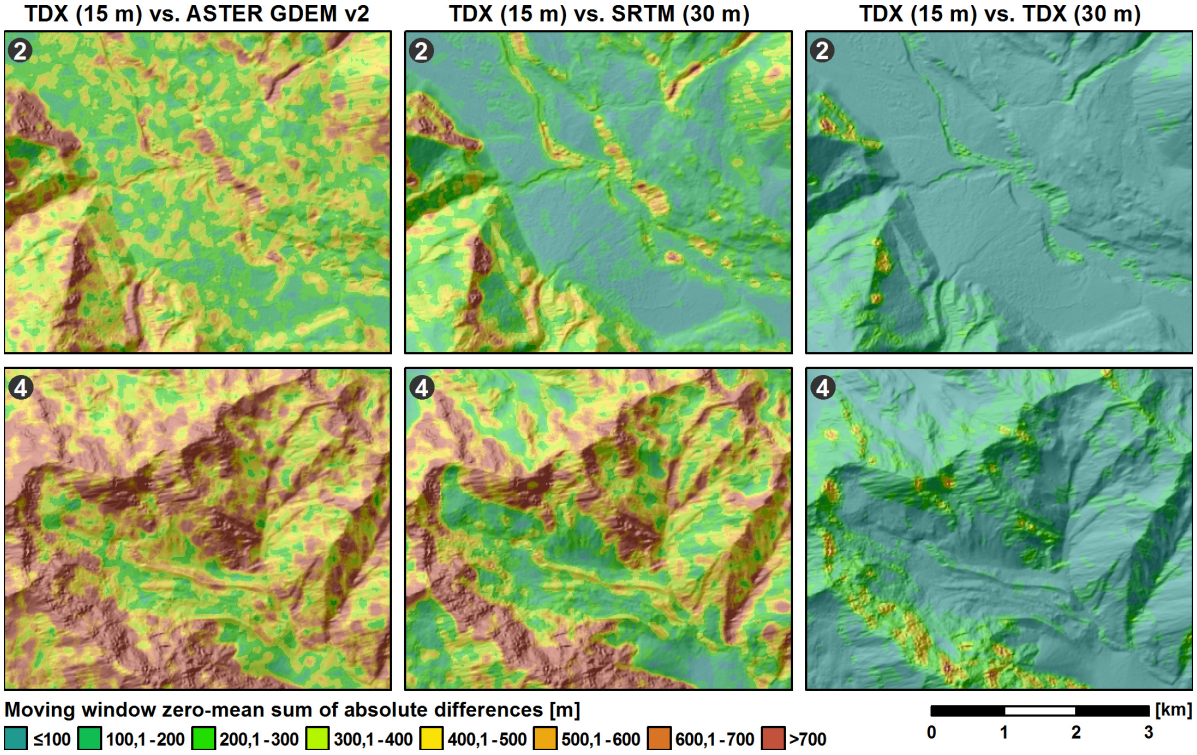


Figure 3.7: Results of the moving window zero-mean sum of absolute differences algorithm calculated from TDX, ASTER and SRTM1 DEMs for Details 2 and 4 (see Fig. 3.2 for locations, Suppl. A.10 for a display of all Details).

of the riverbed of the Bodui Tsangpo, which is displayed discontinuously, no landforms within the Bodui Tsangpo valley can be delineated in Detail 2. In Detail 4, where landforms with larger wavelengths prevail, the bumpy structure is less destructive for landscape rendering. Consequentially, the frequency distribution of the WTH-BTH grid in Detail 2 is more long-tailed in comparison to TDX and SRTM1 (Fig. 3.8E). This conspicuity of the ASTER dataset is, however, much less evident in Detail 4.

As shown in Fig. 3.7, the MWZSAD grid of SRTM exhibits a strong positive relationship with relief. With the exception of discontinuities like hummocks, terrace edges and moraine bodies, valley plains show low values. On the hillsides, differences are generally much higher. High values are evident in the summit areas, over mountain ridges and small v-shaped mountain valleys. Particularly high values occur on leeward slopes, where TDX exhibits high roughness values (cf. Fig. 3.5). These areas match

Table 3.7: Mean moving window zero-mean sum of absolute differences algorithm values for Details 1-4 calculated from TDX, ASTER and SRTM1 DEMs (see Fig. 3.2 for locations). Values in brackets are standard deviations.

Detail	TDX (15 m) vs. TDX (30 m)	TDX (15 m) vs. TDX (30 m	TDX (15 m) vs. ASTER GDEM v2
1 (Fig. 3.9)	81.22 [68.19]	245.18 [203.82]	414.09 [178.64]
2 (Fig. 3.10)	73.12 [53.48]	215.99 [156.04]	377.04 [174.11]
3 (Fig. 3.11)	74.21 [50.88]	302.51 [196.40]	420.11 [188.97]
4 (Fig. 3.12)	120.28 [83.35]	456.62 [261.78]	579.17 [232.93]

patches of moderate MWZSAD values in the MWZSAD grid of TDX30, indicating the influence of roughness induced by high-frequency topography or random noise. Moreover, small zones of high MWZSAD values are present on hillsides facing toward the radar sensor. Mean MWZSAD values of the Details are in agreement with these general statements because they increase in accordance with relief intensity (Table 3.7). Correspondingly, the frequency distribution of SRTM1 is longer tailed than that of TDX30, but shows a strong deviation only in the case of Detail 4 (Fig. 3.8F).

In agreement with ASTER's representation of topography, the MWZSAD grid of ASTER exhibits a distinctive bumpy texture (cf. Fig. 3.7, Suppl. A.10). Overall, MWZSAD values for ASTER are much higher than those for SRTM1. While the spatial distribution of high- and low-value zones generally agrees with that of SRTM1, the bumpy texture superimposes the local topography. Accordingly, the degree of similarity between the MWZSAD grids of ASTER and TDX30 is low. MWZSAD averages of the Details increase with relief intensity. However, the percent increase from the minimum, given by Detail 2, and the maximum, given by Detail 4, is substantially lower for ASTER than for SRTM1 (cf. Table 3.7). In accordance with this aspect, the ASTER MWZSAD histograms are flat both in the case of Detail 2 and Detail 4 (Fig. 3.8F).

3.6.3 TanDEM-X DEM landscape representation

The TDX DEM data's potential for geomorphological exploitation was evaluated by analyzing geomorphological features within the Bodui Tsangpo valley where prominent sculptural landforms are preserved. Four core study areas exhibiting different key landforms were chosen for detailed geomorphological mapping, all of which are located in the Bodui Tsangpo catchment (Fig. 3.2). Details 1–3 (Figs. 3.9–3.12) are located within the valley and comprise a complex association of glacial and fluvial landforms, including moraines of Baiyu and Guxiang glacial stages, a cascade of fluvial terraces, kame terraces, alluvial fans and debris cones. Detail 4 (Fig. 3.12) additionally encompasses the southern main ridge with summit elevations >5250 m asl. In this area, several active glaciers and Little Ice Age moraines occur (cf. Loibl et al., 2014; Loibl and Lehmkuhl, 2015). In the following, landforms will be described as mapped from the TDX DEM and subsequently be evaluated regarding their cognoscibility in ASTER and SRTM1 (Table 3.8).

Detail 1 (Fig. 3.9) is located at the northeastern edge of the TanDEM-X footprint, displaying the upper part of the Bodui Tsangpo valley. The valley floor is ~2 km wide and framed by relatively steep

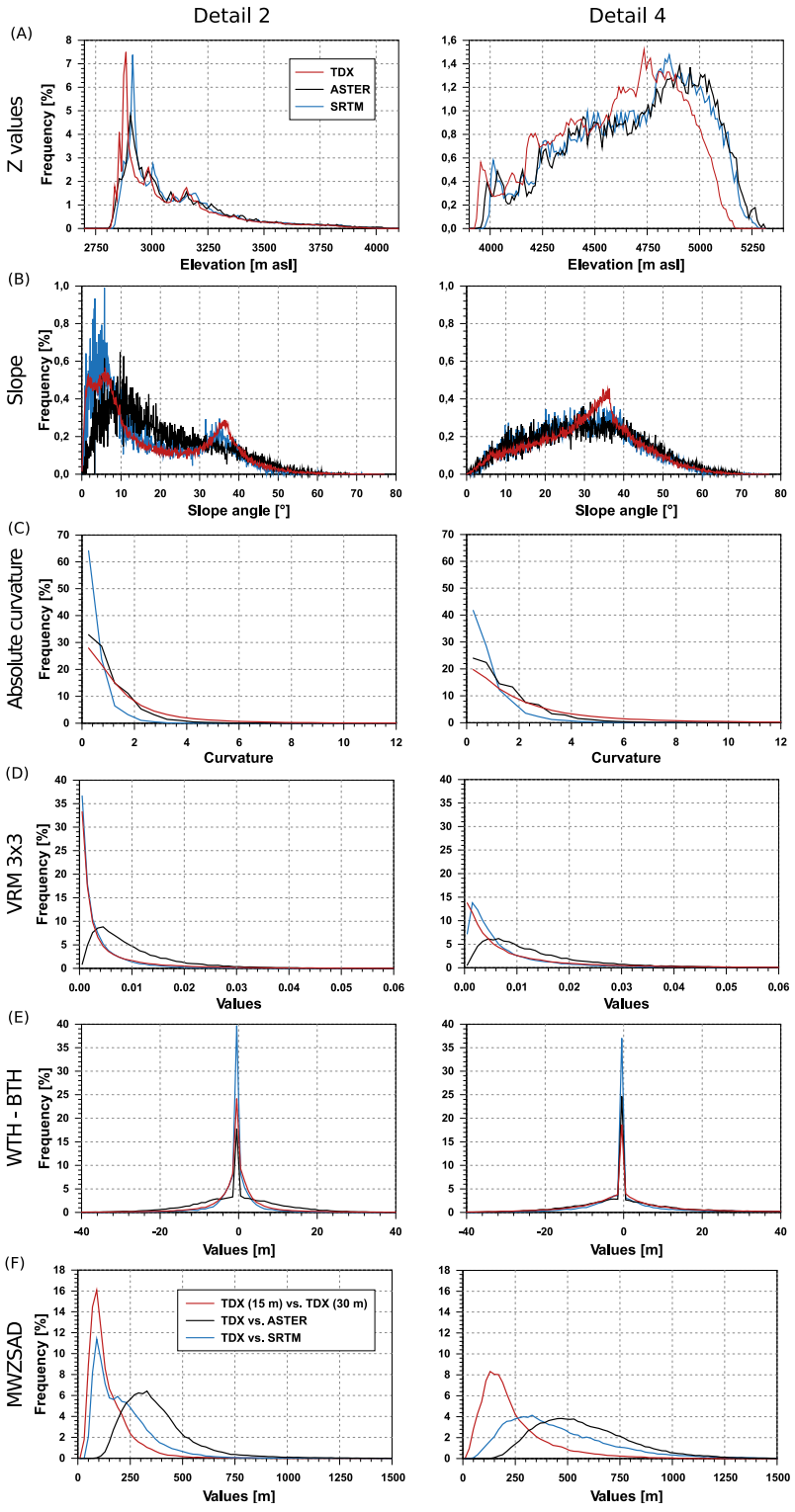


Figure 3.8: Histograms of morphometric parameters for Details 2 and 4 calculated from TDX, ASTER and SRTM1 DEMs (see Fig. 3.2 for location). (A) Elevation, (B) slope, (C) absolute general curvature, (D) vector ruggedness measure, (E) grayscale morphological filtering (White Top Hat – Black Top Hat), (F) moving window zero-mean sum of absolute differences.

Table 3.8: Landform cognoscibility in TDX, SRTM1 and ASTER GDEM v2 DEMs.

Objects	TDX	SRTM1	ASTER GDEM v2
Mesoscale relief (valleys, slopes, ridges)	true	mostly true	mostly true
Large moraines (> 500 m width)	true	true	mostly true
Medium moraines (200–500 m width)	true	mostly true	mostly false
Small moraines (< 200 m width)	true	mostly false	false
Kame terraces	true	mostly true	mostly false
Hummocky terrain from basal till	true	mostly true	false
Large alluvial fans (> 2000 m diameter)	true	true	mostly true
Medium alluvial fans (500–2000 m diameter)	true	true	mostly false
Small alluvial fans (< 500 m diameter)	true	mostly false	false
Distinguish alluvial fans from debris cones	true	true	mostly false
Large fluvial terraces (> 50 m drop or > 5 km long)	true	true	mostly true
Medium fluvial terraces (20–50 m drop or l–5 km long)	true	mostly true	mostly false
Small fluvial terraces (< 20 m drop and < 1 km long)	true	mostly false	false
Erosional channel structures	true	mostly false	mostly false
River course	mostly true	mostly true	false
Complex microscale landform cascades	true	mostly false	false

True	Landform(s) can be clearly identified using only the DEM and its derivatives.
Mostly true	Like "true", except that cognoscibility is hampered in areas of strong artifacts or filled voids.
Mostly false	Landform(s) generally visible but so unclear that a correct interpretation is hardly possible from the DEM.
False	Landform(s) not visible in DEM or not cognoscible without prior knowledge.

slopes (30° to 60° in most parts). Several steep v-shaped channels are incised into these slopes. Alluvial fans of different sizes were accumulated at the end of most of these channels and also at the outflows of tributary valleys. Glacial sediments at the termination of the largest valley can be clearly distinguished from the alluvial fans by the rugged and asymmetric topography. Additionally, two erosional channels incised into this moraine body. These indications of a relatively young age of formation and the position at the outflow of a medium size tributary catchment support an assignment of this moraine to the Baiyu glaciation. In the northwestern part of the valley floor, a set of distinct bumps with variable diameter, ranging from ~30 to ~250 m, surrounded by hummocky terrain can be clearly observed, presumably consisting of basal till relicts from the Guxiang glacier advance. This set of landforms provides suitable features to test the effective resolution of the TDX DEM, because the general relief is moderate and the average coherence is high (cf. Suppl. A.2). Incorporating high-resolution Google Earth imagery shows that the minimum diameter of hummocks generally detectable in the DEM is ~20 m. These hummocks are, however, not unambiguously identifiable when solely using the DEM.

In comparison, land surfaces in the southeastern part of the valley floor are much smoother, indicating that fluvial processes were the dominant sediment accumulation mechanism here. The active river incised ~5–10 m into these surfaces, resulting in a shallow but well defined terrace edge. Small hummocky structures are also visible immediately adjacent to the riverbed in several places. Even though the morphologically nonsensical pattern clearly indicates that these are artifacts related to low interferometric correlation (cf. Section 3.5.1, Suppl. A.2), they render a precise determination of the river course impossible in the areas concerned. Flat downvalley-dipping surfaces at ~3300 m asl, i.e., ~460 m above the modern valley floor, are evident on the true left side of the valley. Their size and the relatively smooth slope surfaces toward the valley neither support fluvial origin. Further, terraces of this size have not been reported in the wider region so far. Their topographic position rather indicates a correlation to the terminal moraine of the Guxiang glacial advance which is located in the Parlung Tsangpo valley, close to the entrance to Bodui valley. Steep slopes of erosional rims in the terrace structures indicate that they consist of consolidated glacial till. Consequently, these landforms are interpreted as kame terraces. At the highest level of detail achievable from the TanDEM-X dataset, anthropogenic dam structures of ~15 m width can be observed in the southwestern part of Detail 1. Checking these linear structures in high resolution satellite imagery revealed that they exhibit a true width of ~10 m.

Most major landforms, such as the large alluvial fans and the kame terraces, can easily be allocated in SRTM1 (Fig. 3.9A). This is also true for the river course and, to some extent, for the basal moraine relicts in the northwestern part of the Detail. The relatively smooth yet overall good terrain representation is of advantage here. For small structures, however, the grainy texture introduces considerable uncertainties regarding landform cognition. The ASTER GDEM does not allow determining microscale landforms owing to abundant bumpy artifacts (Fig. 3.9B). Linear structures such as the Bodui Tsangpo river bed are particularly affected by these artifacts, resulting in a discontinuous representation. Additionally, planar surfaces can hardly be identified as such and hummocky features cannot be distinguished from bumpy artifacts.

Detail 2 (Fig. 3.10) shows a similar set of landforms, encompassing kame terraces, fluvial terraces, alluvial fans, moraines, and erosional channels. The setting is, however, much more complex owing to

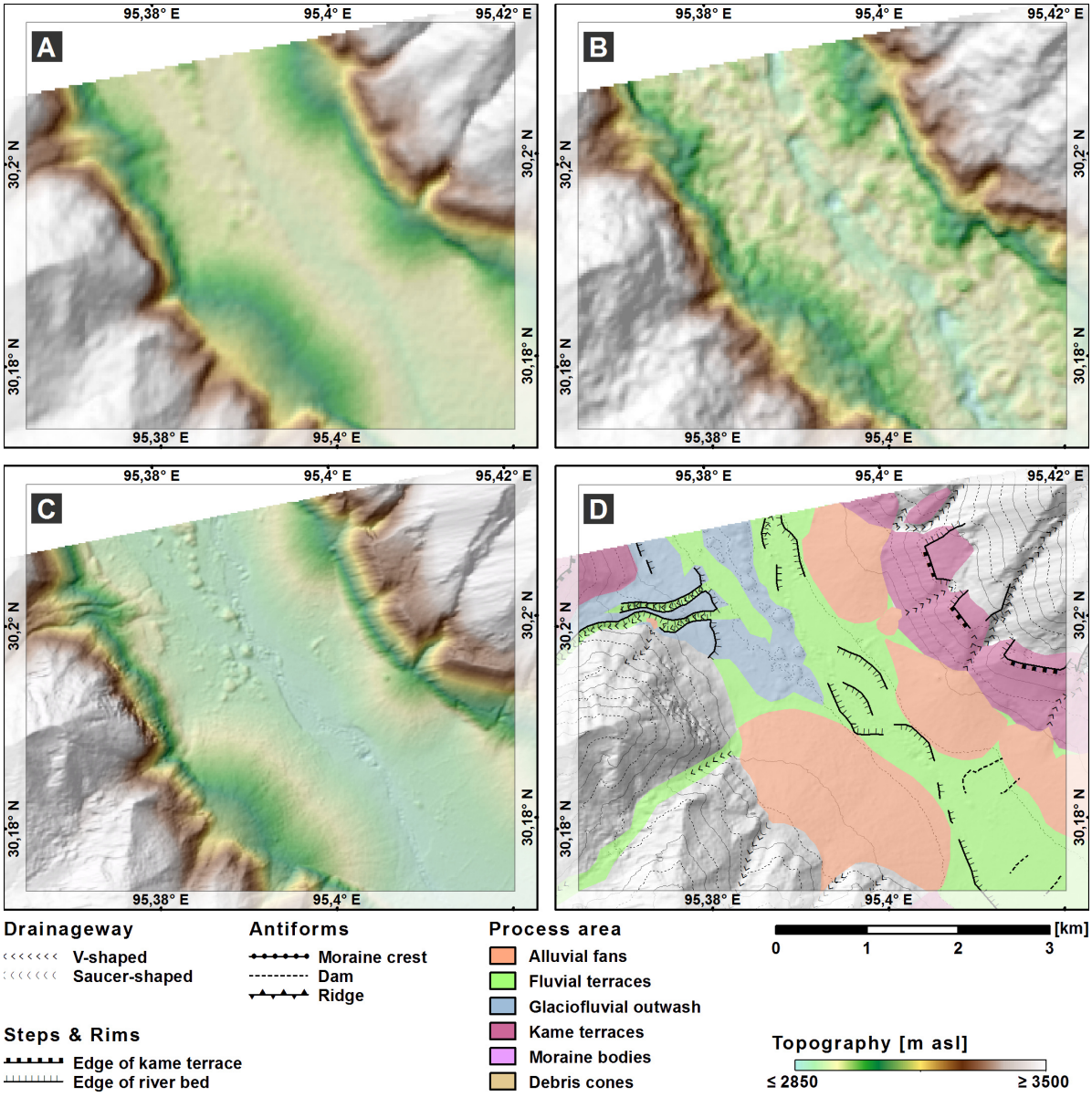


Figure 3.9: Detail 1 in the uppermost part of the Bodui Tsangpo valley included in the TanDEM-X footprint (see Fig. 3.2 for location). (A) Detail in SRTM1, (B) Detail in ASTER GDEM, (C) Detail in TDX DEM, (D) geomorphological map based on TDX DEM.

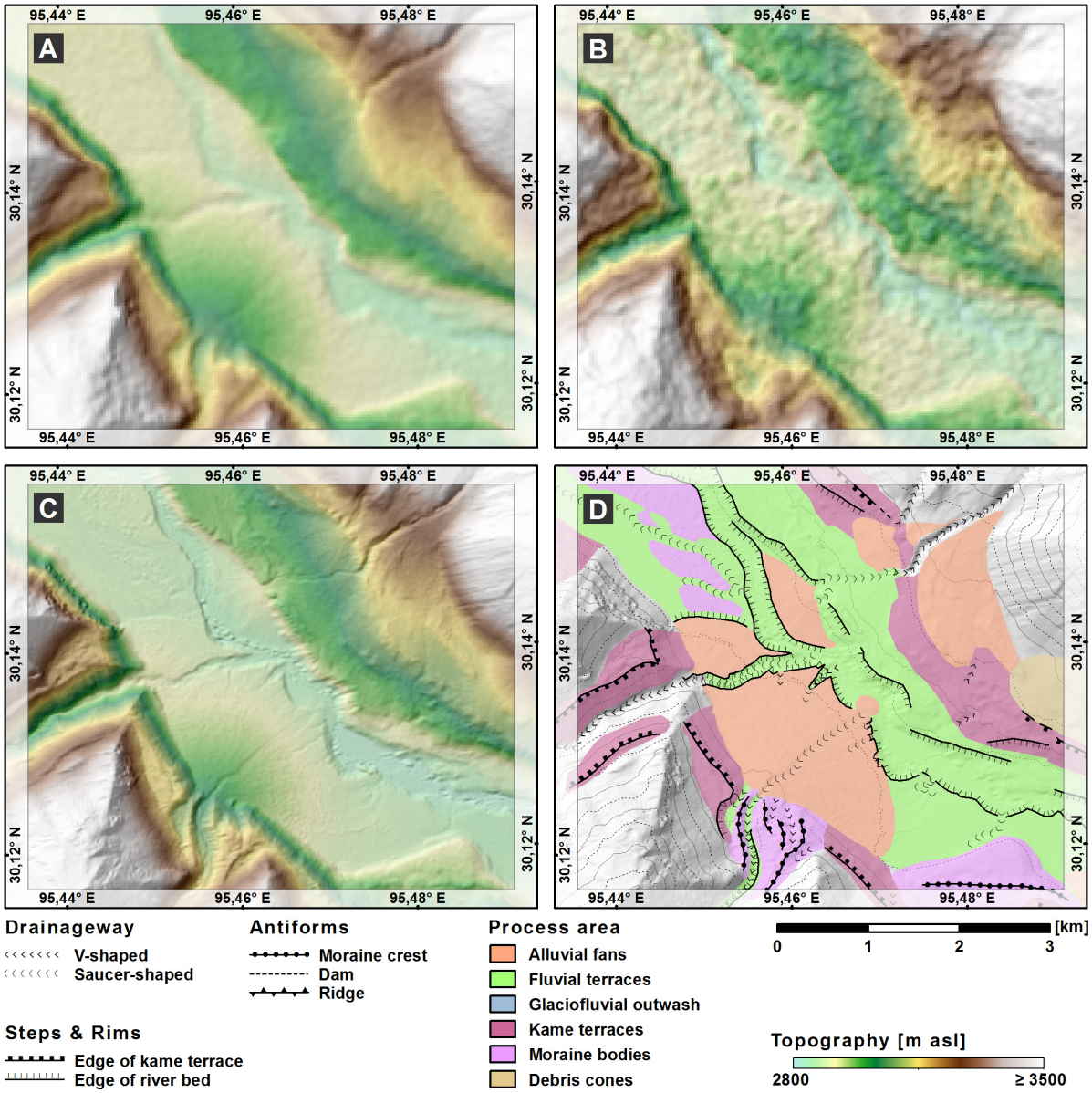


Figure 3.10: Detail 2 in the center part of the Bodui Tsangpo valley (see Fig. 3.2 for location). (A) Detail in SRTM1, (B) Detail in ASTER GDEM, (C) Detail in TDX DEM, (D) geomorphological map based on TDX DEM.

more interaction between different landform types. In the southern part of the Detail, a moraine body similar to the one observed in Detail 1 cut through the kame terrace, supporting the relative age concept presented before. The front of the terminal moraine is apex to a large alluvial fan which is, in turn, exhibiting a distinct erosional channel in its center part. The footslopes of this fan are cut by a ~30 m deep channel originating from the next valley upstream. On the true left valley side, alluvial fan and debris cone material – both easily distinguishable by slope angles – is deposited on top of the kame terrace. The alluvial fan and the kame terrace are cut by a v-shaped channel which can be traced further down to the fluvial terrace below. There, the channel cut through again and deposited another small alluvial fan on the lowest terrace. Additionally, four different terrace levels can be distinguished in the western part of the Detail: the lowest at ~2830 m asl, a few meters above the modern river, the second at ~2850 m asl, the third at ~2915 m asl, and the fourth at ~2980 m asl. Without prior knowledge of the setting, none of these details can be derived from ASTER (Fig. 3.10B). In SRTM1, most upper microscale landforms are vaguely perceptible but limited posting and the abundant grainy texture considerably exacerbate disentangling their relationships (Fig. 3.10A).

The dominant landform feature in Detail 3 (Fig. 3.11) is the Baiyu moraine body, consisting of a major and several subordinate crests. Similar to the previous examples, deeply incised channels cut through the glacial sediments. At the outer slopes of the moraine body, relatively smooth surfaces softly declining toward the fluvial terraces are evident. These can be interpreted as glaciofluvial outwash material. Two further moraine ridges are situated in the western part: one is well-defined and directly adjacent to the true right slope, and the other is bumpy and ~400 m further to valley center. Even though noticeably less pronounced than in Detail 2, up to four fluvial terraces can be distinguished in this Detail as well. Elevations of terrace surfaces on the western side of the Baiyu moraine are ~90 m higher than their pendants on the eastern side. Even though this difference in altitude level may show the effect of damming by the moraine body, a phase discontinuity in the TDX data is also evident at the contact between the Baiyu terminal moraine and the Bodui Tsangpo river bed. The phase discontinuity itself is indicated by a step within the river bed.

Similar to the former Details, SRTM1 renders the overall topography well but lacks many details visible in TDX, such as subordinate moraine crests and terraces (Fig. 3.11A). Even though ASTER's terrain representation is better than in the other maps, the DEM exhibits several major artifacts in this scene, particularly evident in striking depressions at the moraine crests and terrace surfaces (Fig. 3.11B). Notably, these blunders coincide with local patches of low image pair count used for stereometric processing (cf. Suppl. A.5). As a consequence, even major landforms can hardly be delineated from ASTER in this scene. Additionally, the bumpy texture hampers a correct interpretation of planar surfaces, e.g., the bumpy basal moraine and different fluvial terraces are lost in noise.

The high mountain environment of Detail 4 (Fig. 3.12) poses the greatest challenge to all sensors, leading to the strongest DEM artifacts in this comparative study. Despite the abundant stripes on west facing and grainy textures on east facing slopes, the TDX DEM still offers a sufficiently good terrain representation to delineate the key morphological features. As such, the tongue of an active glacier as well as Little Ice Age moraines, medial moraines and glacier foreland can be mapped (cf. Loibl et al., 2015). Furthermore, the front of the modern glacier terminus is visible as a convex feature and debris cover on the lower tongue is indicated by higher surface roughness (cf. Figs. 3.4 and 3.5). A

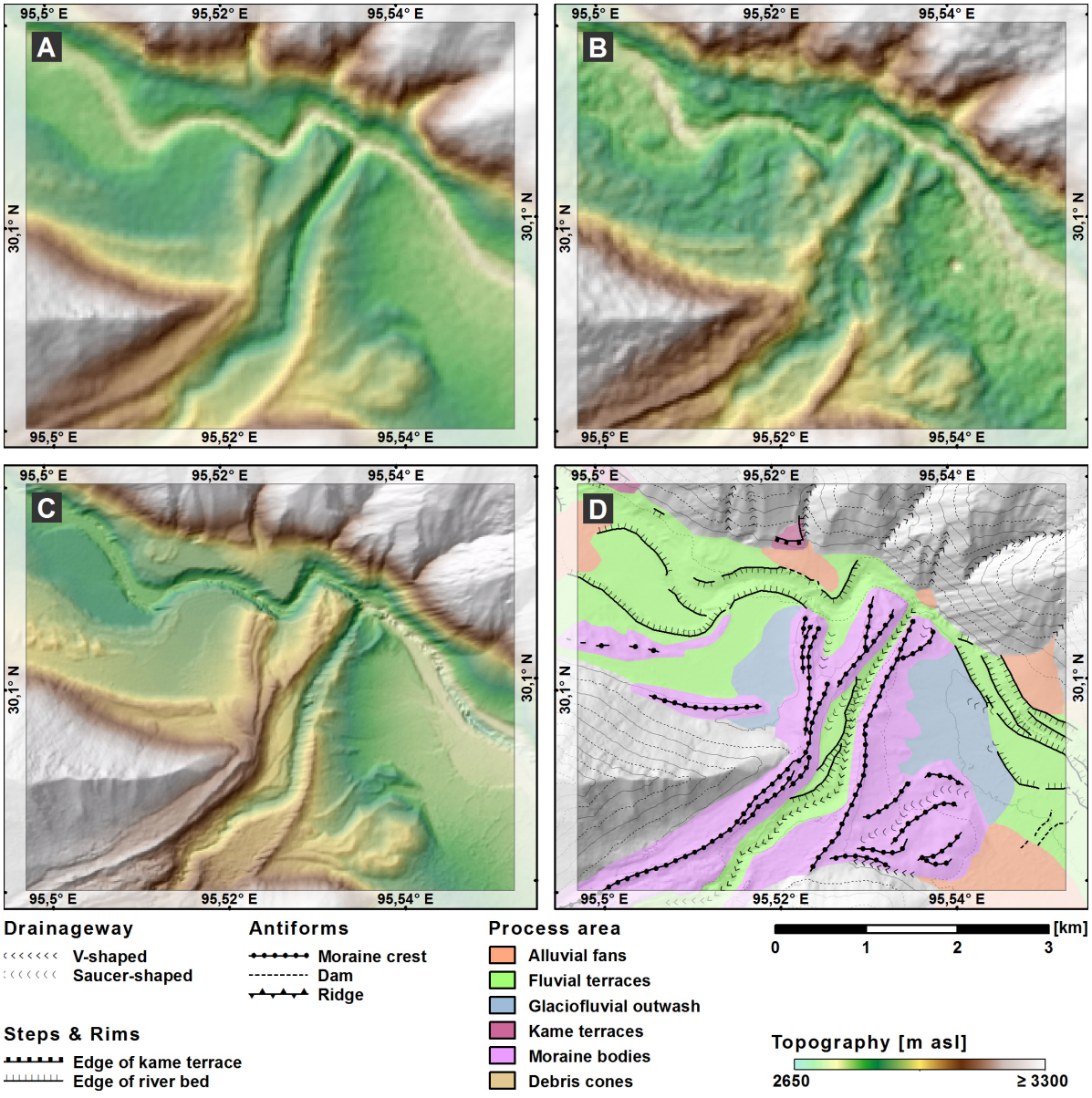


Figure 3.11: Detail 3 at the outflow of Baiyu valley into Bodui Tsangpo valley (see Fig. 3.2 for location). (A) Detail in SRTM1, (B) Detail in ASTER GDEM, (C) Detail in TDX DEM, (D) geomorphological map based on TDX DEM.

relatively flat surface between the glacier tongue and the Little Ice Age terminal moraine suggests that the proglacial depression was filled with glaciofluvial sediments. Smaller moraines are also evident in the upper reaches of the northern tributary valleys. In the southern part of the Detail, a debris cone with linear surface textures is visible. The opposite side of the valley floor exhibits another alluvial fan cutting through a kame terrace. However, this Detail also includes the only artifact found in the TanDEM-X data that cannot be easily identified by typical noise characteristics and thus has a potential to be misinterpreted as a landform: Located on the lowest part of the spur at the confluence of the main valley and the northern tributary (95.398° E / 30.055° N), an almost vertical linear convex form is visible which turns to the west in its lower part and continues as a dam-like structure crossing the outflow of the tributary valley. This dam is particularly suspicious because it crosses the drainage way without showing signs of dammed-up material upstream. Checking this locality in satellite imagery confirmed that no such landform exists there. Despite several minor void fills, SRTM1 is capable of representing this Detail's ridgelines and basic valley configuration consistently. However, microscale linear antiforms, such as the Little Ice Age moraines and terraces, are hardly recognizable. Again, much detail is lost through SRTM's grainy texture. ASTER, characterized by a prevailing bumpy texture, does not show the terrain in sufficient detail for convenient delineation of any of the relevant landforms. The bumpy terrain representation leads the glacier forefield to be erroneously displayed as a hummocky surface.

3.7 Discussion

The study area provides challenging conditions for DEM generation from remotely sensed radar data. The rugged topography leads to significant geometric distortion, resulting in shadowing and layover effects. Moreover, the lower and middle parts of the slopes are covered with dense forests, leading to volume decorrelation and, consequently, low coherence values on such positions (Zebker and Villasenor, 1992). On leeward slopes, coincidence of thermal decorrelation, i.e., a low signal to noise ratio due to low backscatter intensity, and volume decorrelation causes particularly low coherence values (Goldstein et al., 1988; Small, 1998). In valley floor positions, however, abundant unforested land surfaces and moderate topography facilitate processing of high-quality topographic information. The comprehensive inventory of distinct glacial landforms located in the Bodui Tsangpo valley yields a suitable setting for assessing the topographic sensibility of the generated DEM. Regarding the stereometric generation of DEMs from optical imagery, the abundant cloud cover poses further challenges.

3.7.1 DEM quality assessment

Several challenges apply for deriving DEMs from X-band radar data in the rugged topography of the eastern Nyainqêntanglha range. Interferometric decorrelation causes random noise in the interferogram, propagating into the processed DEM and inducing areas showing high local roughness (cf. Figs. 3.4 and 3.5). The study area has a mean coherence of 0.56, indicating that the area is substantially affected by decorrelation. The amplitude of the noise induced by decorrelation depends on the height of ambiguity, i.e., the range of altitude values reflected by a single phase cycle (cf. Geudtner, 1995). Regarding the whole study area, the low height of ambiguity of scene 1032207_022 thus results in a moderate degree

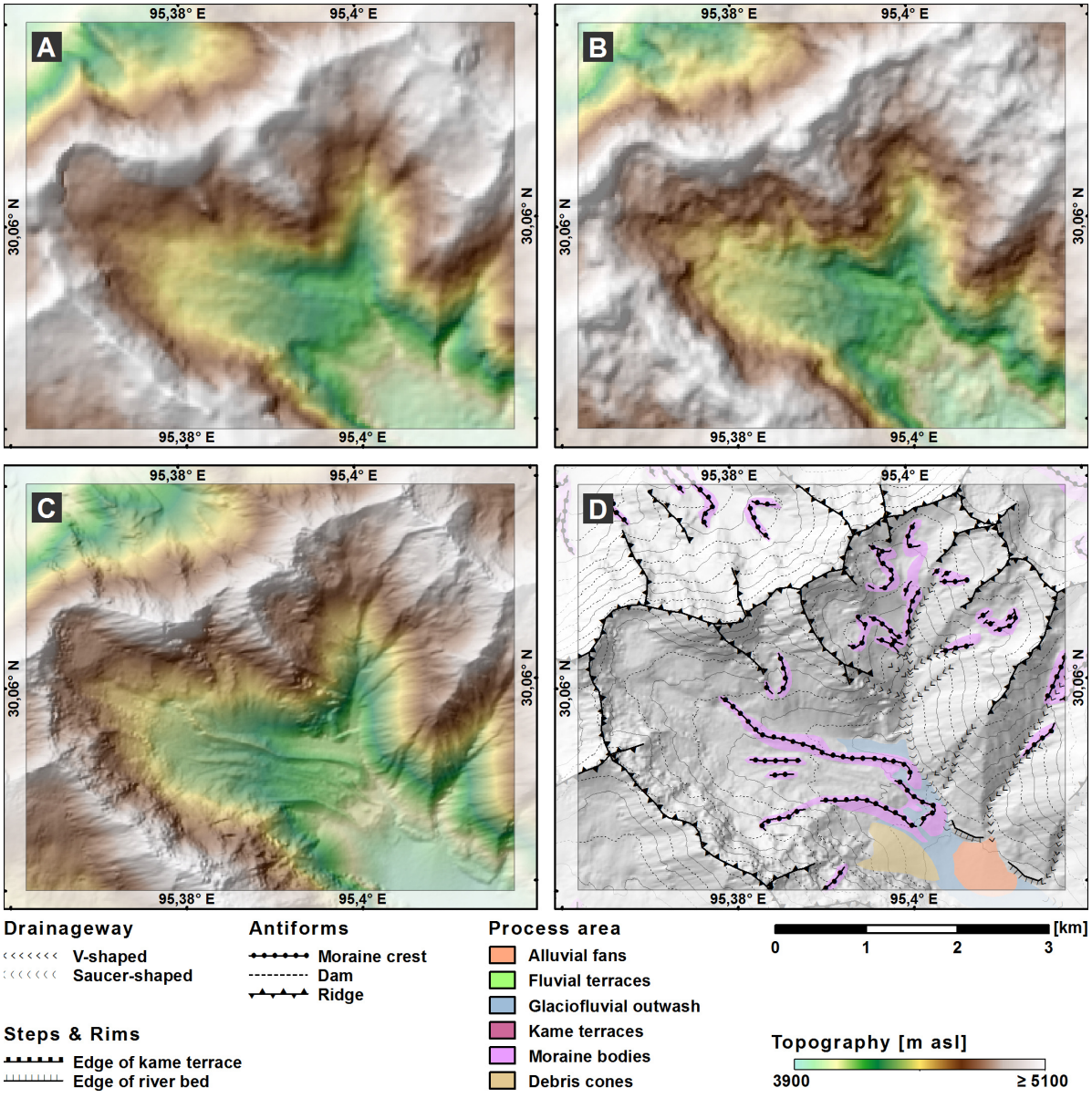


Figure 3.12: Detail 4 at the valley head of Baiyu valley (see Fig. 3.2 for location). (A) Detail in SRTM1, (B) Detail in ASTER GDEM, (C) Detail in TDX DEM, (D) geomorphological map based on TDX DEM.

of roughness. Areas with high interferometric coherence, e.g., large parts of the Bodui Tsangpo valley floor, exhibit a smooth and highly detailed representation of topography, indicating sufficient filtering. In areas of high decorrelation, however, the noisy texture remains visible, and morphometrically detectable even after the application of several smoothing filters as described in Section 3.5.1.

High average roughness and low detail of topographic information are evident on leeward slopes, impairing geomorphological interpretation and morphometric analysis (cf. Figs. 3.5 and 3.12C). This striking feature is induced by low signal to noise ratios, local shadowing, and the abundant forest vegetation, leading to predominantly low coherence values (cf. Small, 1998; Suppl. A.2). The rendering of the Bodui Tsangpo river bed is likewise affected because of characteristic interferometric decorrelation over water surfaces (cf. Schwäbisch, 1995; Richards, 2009; Fig. 3.9C). Layover effects occur on moderate to steep radar-faced slopes, resulting in missing topographic information. Due to the Delaunay triangulation routine used for projecting data from radar to map space, this inevitably leads to facets visible in the final DEM (cf. Fig. 3.12). Taking the topographic information provided by SRTM1 as correct, the small zones of high MWZSAD values on hillsides facing toward the radar sensor in the case of the SRTM1 grid may indicate this missing topographic information (cf. Fig. 3.7). The distinct peak evident in the TDX slope histogram between 35° and 40° has partly to be tied back to this effect, as slope variability cannot be displayed on slopes affected by layover (cf. Fig. 3.8B).

The phase unwrapping algorithm SNAPHU allowed a complete and mostly consistent unwrapping of the topographic interferogram. The absolute phase offset regression coefficient of 1.011 implies, however, an underestimation of topographic variability within the original unwrapped data. With regard to the increasing negative elevation bias from low to high elevations, an underestimation of total relief is still evident in the TDX DEM (cf. Table 3.2). In a few cases, potential integration paths for phase unwrapping were fully dissected by discontinuities, impeding a flawless solution using the single baseline approach carried out for this study. For example, the discontinuity found in Detail 3 at the contact of Baiyu terminal moraine and Bodui Tsangpo river bed, both inducing phase discontinuities, renders an error-free phase unwrapping of the Bodui Tsangpo river floor impossible (cf. Fig. 3.12C).

The effective resolution is equivalent to the posting of 15 m in areas of moderate topography and high coherence. Though the posting limits the effective resolution to 30 m (cf. Pike, 1988; Section 3.1), the DEM displays anthropogenic dams with a true width of ~10 m as ~15 m wide structures. This conspicuity results from the inherent resolution defined by the TDX X-band radar data being much higher than the posting of the processed DEM. If a topographic feature is pronounced enough, it remains visible in the pixel-aggregated DEM, but exhibits an apparent width matching the DEM posting.

Because the TDX DEM is derived from X-band radar data, the DEM models a surface practically coinciding with the canopy surface (cf. Bamler and Hartl, 1998; Hensley et al., 2007; Richards, 2009). With respect to the high resolution of the X-band radar data and the small posting of the TDX DEM, forest clearings are generally visible in TanDEM-X data, in contrast to SRTM1 and ASTER (see also Suppl. A.13). A potential influence of the canopy on surface rendering has to be kept in mind when conducting geomorphological evaluations applying TanDEM-X data in areas with abundant woodland.

The most striking feature of the ASTER GDEM is its bumpy texture, exhibiting considerable amplitude and a conspicuous local autocorrelation, superimposing the actual topography (cf. Tachikawa et al., 2011c). Interestingly, this texture pattern is, except for blunders like the trough evident in the Baiyu

terminal moraine, independent of the amount of image pairs incorporated into stereometric processing. The texture is distinctly reflected in the morphometric data, e.g., by showing the highest average slope and VRM values and flat distributions of both parameters. Regarding the isotropy of this effect, the texture seems to be a result of high frequency undulation in the underlying elevation point network, indicating inaccurate parallax calculation by the image matching routine. Conversely, vegetation cover seems not to be of major relevance (cf. Kervyn et al., 2008). The intrinsic resolution of ASTER GDEM is thus substantially lower than its potential effective resolution of 2″, which is in general agreement with the results of Tachikawa et al. (2011b,c). As a consequence of the abundant bumpy artifacts, landforms are not visualized consistently and are partly concealed. Because of the approximately constant magnitude of the pattern, the destructive influence on earth surface modeling increases with decreasing actual topographic variability. This issue is clearly reflected by the BTH-WTH grid of Detail 2, which shows no meaningful delineation of landforms (Fig. 3.6). Conversely, the influence of the bumpy texture is less destructive in Detail 4. This can also be exemplified by the low MWZSAD average increase in Detail 4 in comparison to the Details located within the Bodui Tsangpo valley (Figs. 3.7 and 3.8F, Table 3.7). Considerable misinterpretation of the geomorphological inventory might result from the bumpy texture (cf. Siart et al., 2009). The effect is particularly problematic in the cases of (i) planar surfaces such as fluvial or kames terraces, (ii) linear features such as rivers and dams, and (iii) landforms that are not approximately a magnitude larger than average artifacts in the surrounding. Therefore, ASTER GDEM has to be considered unsuitable for landform delineation at a spatial scale of the same magnitude as the DEM's nominal resolution (cf. Mashimbye et al., 2014). However, it has to be emphasized that ASTER provides the largest range of the Details' elevation means, which presumably indicates the best representation of total relief (Table 3.2).

The SRTM1 DEM provides a smooth, moderately detailed surface representation with an abundant grainy texture which exhibits relatively low amplitude and visible blur. The abundance of the grainy texture indicates that the random noise induced by interferometric decorrelation could not be filtered out successfully in SRTM1. Morphometrically, this effect is indicated by the considerable variation of the SRTM1 slope histogram below 8° inclination (Fig. 3.8B). SRTM's smoothness has to be interpreted as a result of low pass filtering within the postprocessing (cf. Rodríguez et al., 2006). The effects are widely visible in the DEM and morphometrically expressed by the lowest average slope (Table 3.3), curvature (Table 3.4) and VRM values (Table 3.5) as well as visible blur within the WTH-BTH grid (Fig. 3.6). The predominant positioning of high MWZSAD values in areas of strong topographic contrasts and the low to moderate values in the valley bottom demonstrate that SRTM's surface modeling is essentially comparable to TDX (Fig. 3.7). However, the TDX DEM provides a considerably higher level of detail, originating from its superior base data and smaller posting.

As SRTM's grainy texture exhibits low amplitude values, its negative effect on surface representation is much smaller in comparison to the undulations evident in ASTER GDEM. Therefore, this texture does not substantially impair the delineation of landforms. With the exception of studies focusing or depending on local roughness, the applicability of SRTM1 data in the field of geomorphology is thus, in contrast to ASTER, predominantly limited by its effective resolution. The effective resolution of SRTM1 is, however, also considerably lower than its potential maximum of 2″. Consequentially, the SRTM1 DEM can be considered consistent regarding lower mesoscale landforms with footprints above

~150 m (cf. Tachikawa et al., 2011b,c).

This result agrees with other studies dealing with SRTM surface representation, consistently demonstrating that the applicability of SRTM is primarily limited by its posting and that artifacts are not substantial (cf. Smith et al., 2006; Kervyn et al., 2008; Siart et al., 2009; Mashimbye et al., 2014). In the study area, the external data used for void-filling exhibit very little topographic information and the transition to data derived from SIR-C is not smooth in some parts. As the void-filled areas are mostly located in the summit areas, this is not a severe issue for the majority of potential geomorphological applications in the study area.

3.7.2 TanDEM-X DEM advantages and drawbacks

The processed TDX DEM exhibits a detailed surface representation which is consistent in an overall view. Its main advantages, particularly in comparison to SRTM and ASTER, are the relatively high planar resolution of 15 m and the relatively low proneness to errors. In addition, errors are limited to certain parts of the landscape, i.e., steep slopes facing toward or away from the radar sensor, and water bodies. Distinguishing artifacts from real landforms is thus feasible in the vast majority of studied situations. The only exception that was encountered during DEM analysis and mapping is the dam perpendicular to the drainage way in the high alpine environment of Detail 4 (Fig. 3.12). Conversely, surface representation of the TDX DEM is particularly good in low-relief areas as demonstrated in Details 1–3 (Figs. 3.9–3.11). Here, the overall quality of the DEM is sufficient to map landforms down to footprints of ~30 m and to identify even complex landform sequences including conclusions regarding the relevant depositional processes. In comparison to ASTER and SRTM1, total relief is underestimated in the TDX DEM. A conclusive investigation of this effect is, however, impossible within the scope of this investigation because reliable geodetic measurements are lacking in the study area. Ultimately, it has to be stressed that the TDX DEM used in this study was self-processed from a single CoSSC dataset and is not representative for the final DEM product.

3.7.3 Perspectives toward geomorphological applications of TanDEM-X DEMs

Even in this premature state, the TanDEM-X data demonstrates its vast potential for DEM-based geomorphological applications, such as spatial analysis, landform mapping and identification of key settings for field work. Compared to SRTM1 and ASTER, it constitutes a step forward on the path to DEM-based mapping of microscale landforms, fostering the application of digital geomorphological mapping in regions where regional high-resolution topographic data are yet unavailable.

The extremely rugged topography of the study area poses a great challenge for DEM processing. Regions with less pronounced relief will presumably have a noticeably higher quality in the raw data and thus allow an even better representation of topography. Processing a DEM with homogeneous quality is always problematic for areas with pronounced relief and, in the case of SAR interferometry, requires the combination of ascending and descending CoSSC scenes. Furthermore, incorporation of several interferograms can significantly reduce the influence of phase noise.

To comply with DTED/HRTI-3 specifications, the DLR is planning to use at least two interferograms per viewing side in order to provide topographic information independent of aspect and to reduce

the influence of phase noise by averaging different datasets (Krieger et al., 2005, 2007). Applying a multibaseline approach, at least two interferograms with slightly deviating perpendicular baselines are simultaneously incorporated into the phase unwrapping process, vastly reducing the ambiguity inherent to integration jumps because the direction of the phase jump can be clearly detected (Rossi et al., 2012). Chances are high that the influence of phase noise and the likelihood of integration errors will be much lower in operative TanDEM-X data and that operative TanDEM-X DEMs will indeed be capable of providing consistent high-qualitative topographic information even in regions with pronounced relief.

3.8 Conclusions

This study investigated a DEM processed from a single TanDEM-X CoSSC scene regarding its potential for geomorphological applications. The results showed that the self-processed TDX DEM yields a detailed and widely consistent landscape representation and thus fosters geomorphological analysis by visual and quantitative means, allowing delineation of landforms down to footprints of ~30 m. Even in this premature state, the TDX DEM is widely superior to the ASTER and SRTM datasets, primarily owing to its significantly higher resolution and its lower susceptibility to artifacts that hamper landform interpretation. Most errors in the TDX DEM were clearly attributable to certain properties of the CoSSC dataset that caused problems in different steps in the processing procedure. These are (i) layover resulting in missing topographic information on steep slopes facing toward the radar sensor, (ii) low signal to noise ratio on leeward slopes, (iii) decorrelation effects over water bodies, and (iv) challenges for phase unwrapping in settings of strong topographic contrasts. Most of these artifacts can, however, be clearly identified as errors and thus be well distinguished from real landforms. The final DTED/HRTI-3-compliant DEM product will presumably have better geometrical properties and be less prone to errors than the experimental dataset used for this study, yielding a great potential to become a global DEM with high relevance for geomorphological investigations.

4 Regional setting

4.1 Overview

A training dataset comprising 306 fans in total was compiled from an American (cf. Fig. 4.1) and an Asian greater study area. In what follows, we will briefly introduce all single study areas, which will thereafter be discussed in greater detail and set into context.

Region 1 – Absaroka Range

Encompassing parts of the Shoshone Valley (109.7° W to 109.4° W, 44.1° N to 44.4° N), this study area is situated in the Absaroka Range—a sub-range of the Rocky Mountains located in north-western Wyoming. A total of 13 alluvial fans were incorporated into the training dataset. During the last glacial period, the area was part of the Yellowstone ice complex, with the Shoshone Valley containing a major outlet glacier (Pierce, 2003). At present, the study area hosts no glacial inventory, but shows periglacial features (cf. Ackert, 1998). The paraglacially induced alluvial fans abut the flanks of the u-shaped valley, and exhibit planimetric areas between 0.16 and 3.28 km^2 (cf. Giles, 2010).

Region 2 – Northern Great Basin

This 75-sample study area is mostly located in the Great Basin segment of the Numic subtaphrogen, but also covers peripheral regions of the Walker Line Fault Zone (119.7° W to 113.2° W, 38° N to 40.9° N). It features the classic basin-and-range setting of north-south-trending mountain ranges bounded by high-angle normal faults (cf. Ellis et al., 1999). It is understood that fans in this part of the greater American study area are prevalently built up by streamflows (cf. Reheis et al., 1996) and aggradation phases presumably accord with the humid model of alluvial fan morphodynamics (cf. Section 2.2.2; Harvey et al., 1999b).

Region 3 – Walker Lane Fault Zone

This study area, containing 71 fans, encompasses valleys strongly affected by the transtensive setting of the Walker Lane Fault Zone (118.7° W to 116.5° W, 35.8° N to 38.0° N). It hosts classic alluvial fan study areas such as Death Valley and Owens Valley (cf. e.g., Denny, 1965; Beaty, 1970). Due to ample accommodation space, solitary fans are relatively frequent, and coalescing fans still display clear lateral demarcations. It is understood that aggradation occurs in agreement with the arid model of alluvial fan aggradation (cf. Section 2.2.2; Bull, 1991), with debris flows instigation being facilitated by high-intensity storms (cf. e.g., Harvey and Wells, 1994; Reheis et al., 1996).

Region 4 – Baja California

The Baja California study area stretches from 117.0° W to 114.4° W, and from 30.0° N to 34.0° N. It comprises 72 fans which are mostly located at the eastern slope of the Peninsular Ranges of Baja California, but also includes fans located within the Transverse Ranges of southern California (U.S.A.). An outstanding characteristic of the western Gulf escarpment segment is its great aridity (Peinado et al., 2006; Holmgren et al., 2011), which presumably entails a further transition of environmental triggering

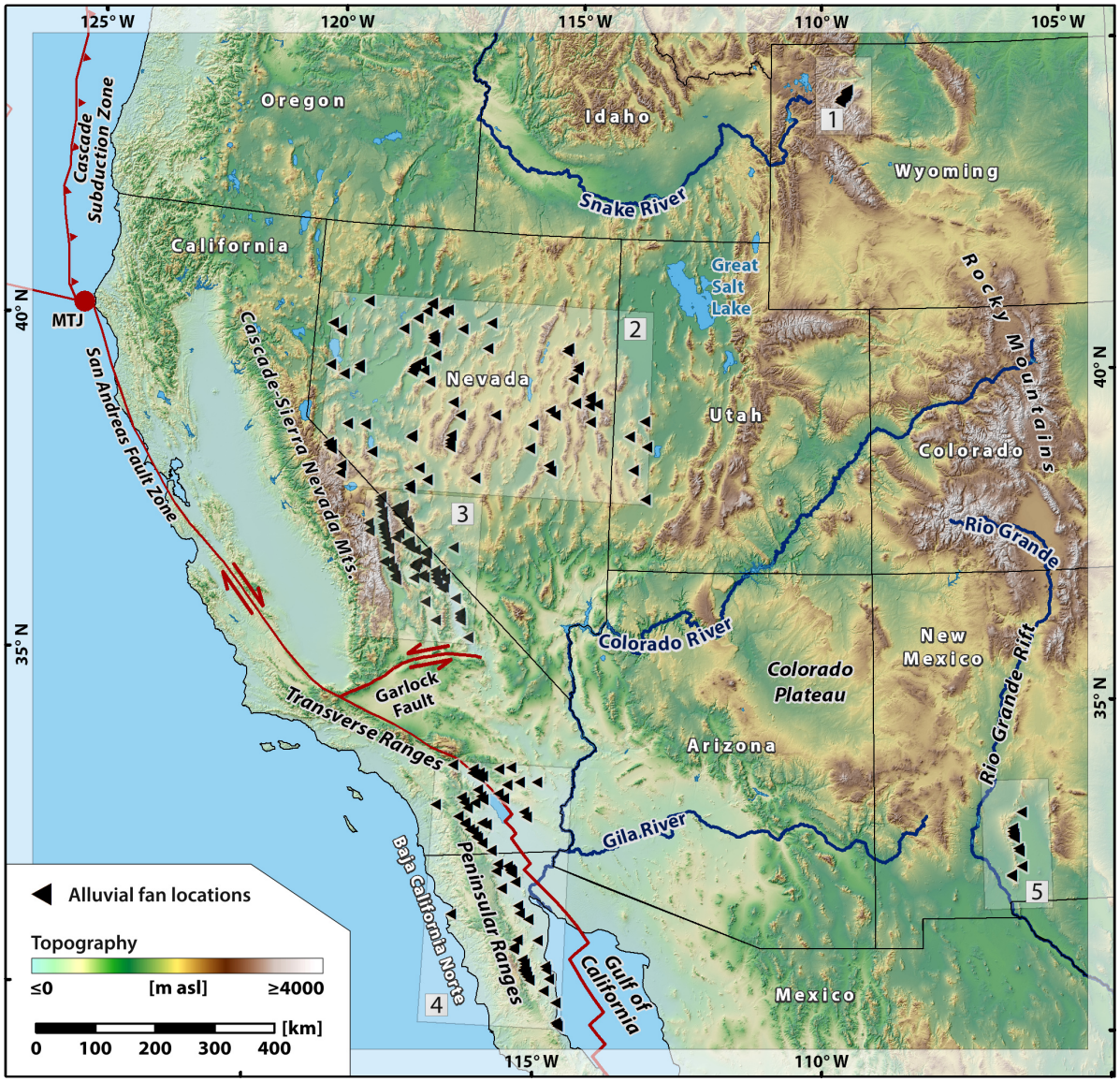


Figure 4.1: Regional overview of the American greater study area. The individual investigation areas are marked with semi-transparent rectangles. (1) Absaroka Range, (2) Northern Great Basin, (3) Walker Lane Fault Zone, (4) Baja California, (5) Rio Grande Rift. Elevation data provided by the GMTED2010 DEM with 7.5″ posting (Danielson and Gesch, 2011).

mechanisms for alluvial fan aggradation towards a purely transport-limited regime (cf. Spelz et al., 2008).

Region 5 – Rio Grande Rift

This subset (106.7° W to 106.3° W, 32.3° N to 33.4° N) represents the second dataset located within the Piman subtaphrogen. It encompasses 11 fans abutting the west-tilted half-horst of the San Andres Mountain range, which is situated in southern New Mexico (Seager, 1981; Sonder and Jones, 1999). The fans are mostly located at the eastern slope of the range, where the block tilt entails relatively high amounts of accommodation space.

Region 6 – Mongolian Altai

The study area stretches from 90.4° E to 91.7° E, and from 49.8° N to 50.5° N. It comprises the alluvial fan inventory next to the Uureg Nuur Basin (cf. Fig. 5.1). The Tsagaan Shuvuut Range borders the Uureg Nuur Basin to the north and is characterized by an abrupt rise of the mountain front, providing high energy regimes for geomorphologic processes (Baljinnyam et al., 1993). To the south, the Uureg Nuur Basin is bounded by the Turgen-Kharkiraa Massif and its foothills. The altitudinal gradient is, however, more gradual than on the northern side of the basin. In accordance, boundary conditions for fan formation are relatively diverse, with accommodation space being abundant along the northern shore, but limited accommodation space is available at the southern shore. From this region, 11 and 14 fans have been used in Chapter 5 and Chapters 6 and 7, respectively. This study area will be discussed in further detail in Section 5.3.

Region 7 – Gobi Altai

Alluvial fans form in great numbers along the lenticular mountain ranges which line up along the two major transpressional fault systems of the Gobi Altai—the Bogd Fault system / Valley of the Lakes fault system (BFS) and the Gobi-Tian Shan fault system (GTSFS; cf. Fig. 4.2; Owen et al., 1999b; Cunningham, 2010). For the training dataset, 50 alluvial fans were delineated (95.0° E to 103.9° E, 43.4° N to 47.0° N). Many ranges of the Gobi Altai experience a structural widening, manifesting itself in foreberg zones with up to 100 m in relative relief (Bayasgalan et al., 1999). In conjunction with the fact that the development of transtensional elements is impeded by the structural grain, the structural widening involves that the proximal space for accommodation of alluvial sediments is generally limited. The specific situation along the mountain ranges depends, however, on the degree of development of foreberg zones, as well as the sediment connectivity between proximal and distal foreland. A major alluviation phase can be narrowed down to the Late Glacial, thereby conforming to the humid model of alluvial aggradation (cf. Ritz et al., 2003; Vassallo et al., 2007; Lehmkuhl et al., 2018a).

4.2 North America

4.2.1 Tectonic setting

The modern plate tectonic configuration of western North America emerges from the mesozoic-cenozoic subduction of the Farallon plate and several microplates at the Pacific margin of the North American

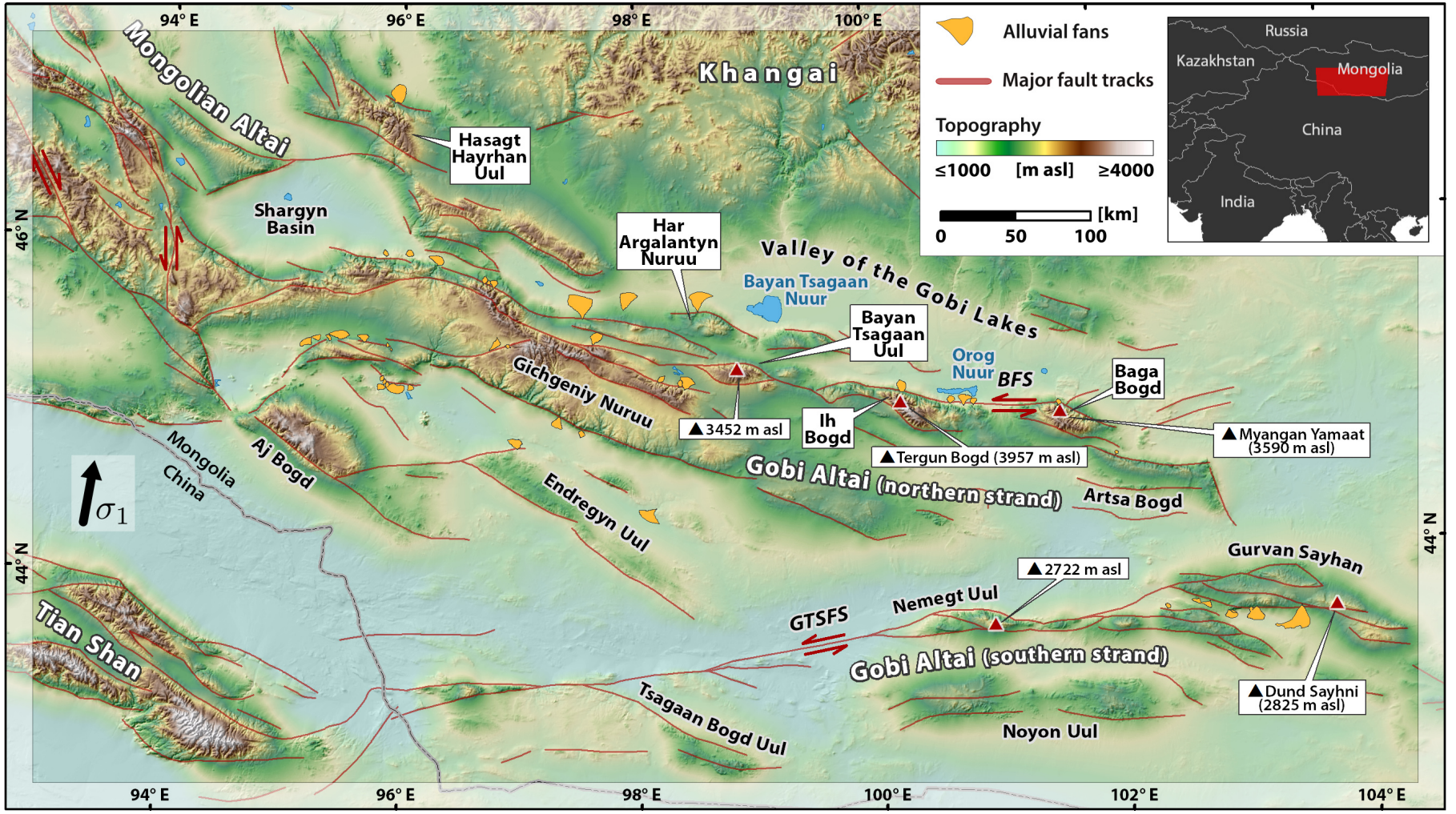


Figure 4.2: Regional overview of the Gobi Altai study area (Region 7). Fault data was taken from Cunningham (2007).

continent, accompanied by accretion of pre-assembled microcontinents and oceanic allochthons (DeCelles, 2004; Dickinson, 2004; Goes, 2013; Sigloch and Mihalynuk, 2013). In this context, the late Cretaceous to Eocene-time *Laramide* orogeny induced thick-skinned block uplift tectonics leading to the formation of the Rocky Mountains fold-and-thrust belt (cf. e.g., Livaccari et al., 1981; Sonder and Jones, 1999; English and Johnston, 2004; Liu et al., 2010).

Initial subduction of the East Pacific Rise below southern California during the late Oligocene (28 Ma BP to 25 Ma BP) led the Farrallon plate to split into several fragments (Atwater, 1970; Dickinson and Snyder, 1979; Calmus et al., 2003). Owing to subparallel motion of the Pacific plate with respect to North America, the plate boundary between Pacific and North American plate developed as a dextral transform fault with two triple junctions—the Mendocino (MTJ) and Rivera triple junctions (RTJ) to the north and south, respectively. In this context, the triple junctions straddled the transition between the still active subduction zones of the American Cordillera and a translational segment represented by the precursor of the modern San Andreas transform (Atwater, 1970; Dickinson and Snyder, 1979; Powell and Weldon, 1992). Concomitant with consecutive subduction of the East Pacific rise, both triple junctions progressively migrated in opposite directions. Seafloor spreading within the Guadalupe and Magdalena microplates, which adjoined the RTJ to the south, eventually ceased around 12 Ma BP (Nicholson et al., 1994; Calmus et al., 2003), inducing a sudden shift of the coastal transform system southward of Baja California (Tosco-Abreojos fault zone; cf. Stock and Hodges, 1989; Michaud et al., 2007).

Subsequently, transition to transtensive conditions caused an initial diffuse extension in the *Gulf Extensional Province* (Stock and Hodges, 1989; Umhoefer, 2000; Plattner et al., 2009). Starting with 7 to 8 Ma BP, accommodation of transtensive offset eventually stepped inward to the Gulf of California (Sea of Cortez) area, inducing the restraining *Big Bend* of the San Andreas transform (Powell and Weldon, 1992; Calmus et al., 2003; Seiler et al., 2010; Dorsey et al., 2011). Production of oceanic crust within the Gulf of California commenced around 5 Ma BP, and induced the transfer of the Baja California peninsula from the North American to the Pacific plate (Stock and Hodges, 1989; Plattner et al., 2009). Providing up to 1500 m offset and a maximum height of 3095 m asl, the western rift shoulder is marked by high topographic contrasts and favorable conditions for alluvial fan morphogenesis (Axen, 1995; Mueller et al., 2009; Bonini et al., 2017).

The Basin-and-Range taphrogen is a widespread region of Cenozoic foreland extension stretching from the Snake River Plain in Idaho to central Mexico (cf. Fig. 4.3; Stewart, 1998; Dickinson, 2006). Its eponymous feature are subparallel, approximately north-south-trending mountain ranges, emerging from footwall uplift at high-angle normal faults (Ellis et al., 1999). The taphrogen is subdivided into a northern (*Numic*) section mostly coinciding with the endorheic *Great Basin*, and a southern (*Piman*) section encompassing, from west to east, the Gulf of California escarpment, the Sonoran desert, and the Rio Grande rift (cf. Sonder and Jones, 1999; Thatcher, 1999; Dickinson, 2002, 2006). The northern and southern section are separated by the Mojave block, which is delimited by the sinistral Garlock fault to the north and the San Andreas fault and the Eastern Transverse ranges to the south (Walker and Glazner, 1999; Glazner et al., 2002).

In the Numic subtaphrogen, two successive extension phases relating to distinct geodynamic settings can be differentiated. Specifically, an Eocene to Oligocene extension phase led to the exhumation

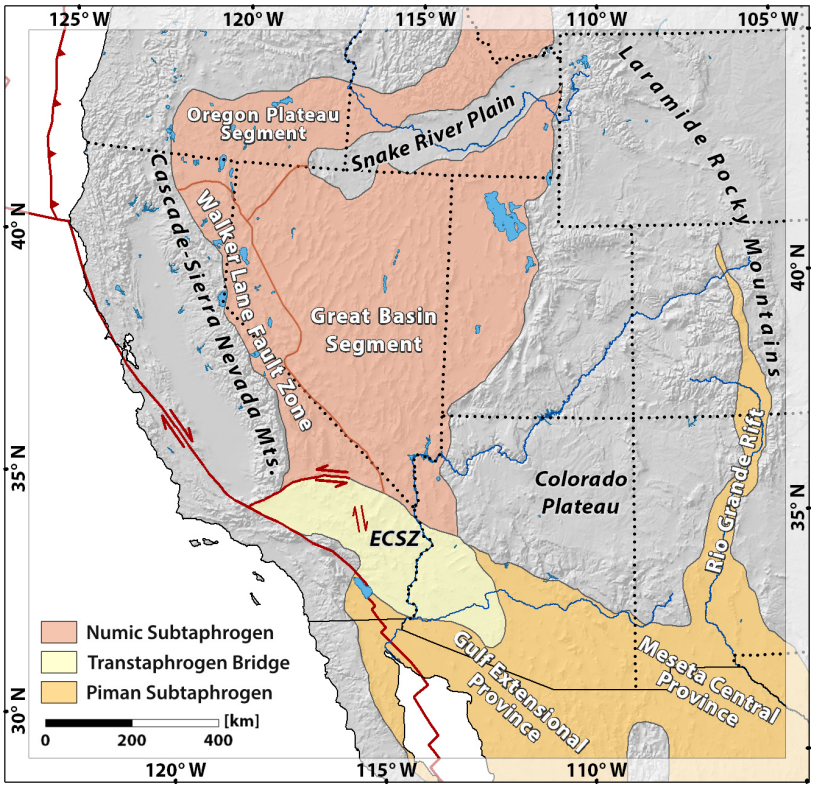


Figure 4.3: Subunits of the Basin-and-Range taphrogen according to Dickinson (2006).

of metamorphic core complexes, i.e., ductily deformed high-grade metamorphic footwalls juxtaposed against brittlely deformed hanging-wall rocks along low-angle detachment faults (Dickinson, 2006; Henry et al., 2011). This early phase of tectonic denudation is commonly attributed to (1.) slab rollback after cessation of Laramide compression, (2.) gravitational collapse of the thickened crust, potentially facilitated by (3.) asthenospheric heat flows (cf. Jones et al., 1996a; Liu and Shen, 1998; Sonder and Jones, 1999; Dickinson, 2002; Schellart et al., 2010).

The modern topography of the taphrogen was, however, induced by a second extension phase which was characterized by widespread brittle extension along high-angle normal faults. This period, which commenced in late Miocene and is still active today, led to an overall extension by a factor of two (Stewart, 1998; Colgan et al., 2006). It is assumed that this phase is geodynamically linked to the passage of the MTJ northward along the coast of California and the establishment of a transtensional regime at the developing San Andreas fault (Nicholson et al., 1994; Atwater and Stock, 1998; Glazner et al., 2002; Dickinson, 2006). According to GPS measurements, the Numic subtaphrogen currently experiences WNW-ESE- to NW-SE-directed expansion (Dixon et al., 2000). GPS velocities vary between $2.5 \pm 0.5\,\mathrm{mm\,yr^{-1}}$ and $6.5 \pm 0.7\,\mathrm{mm\,yr^{-1}}$, with movement being most pronounced in the westernmost parts of the northern Basin and Range segment (Thatcher, 1999).

The 100 to 200 km wide *Walker Lane* fault zone, which adjoins the Cascade-Sierra Nevada Mountains to the east, is a zone of transtensional shear accommodating approximately 25 % of the total translative displacement of the Pacific plate in relation to stable North America (Dixon et al., 2000; Dickinson, 2002; Unruh et al., 2003; Wesnousky, 2005; Carlson et al., 2013). It is diffusely connected with the

San Andreas fault via the Eastern California Shear Zone (ECSZ; Dolan et al., 2007; Mann, 2007). Transtensive stress is expressed by an extended releasing stepover structure composed of numerous individual (asymmetric) grabens and pull-apart basins, with maximum extension given for the pull-apart basin of the Death Valley (Unruh et al., 2003; Frankel et al., 2007). Due to this peculiar stress pattern, topographic contrasts are in average the highest among all studies areas, with ample accommodation space enabling the generation of morphologically distinct fans with no or little lateral constriction (cf. Section 2.2.3). The Walker Lane zone consequently hosts some classic study areas of alluvial fan research in the North American Southwest (cf. e.g., Denny, 1965; Lustig, 1965; Hooke, 1967; Beaty, 1970).

In contrast to the northern Basin and Range region, the Piman subtaphrogen experienced a single extension phase starting around 25 Ma BP, which was strongly tied to the southward migration of the RTJ along the Pacific coast and the establishment of transtensional stress along the nascent Tosco-Abreojos fault zone (Sonder and Jones, 1999; Dickinson, 2002; Ferrari et al., 2013). Following the cessation of subduction around 12.5 Ma BP, the southern Basin and Range region was subjected to a widespread extension (Stock and Hodges, 1989; Dickinson, 2002; Michaud et al., 2007). The establishment of the San Andreas fault system past Baja California and rifting within the Gulf of California constitute a change from diffuse crustal extension to focused extension within the gulf. Extension within the (remaining) Piman subtaphrogen consequently waned after approximately 6 Ma BP, and there is little evidence for a recent extension (Stock and Hodges, 1989; Stewart, 1998; Sonder and Jones, 1999). Consequently, topographic contrasts within the Piman subtaphrogen are generally low.

The Rio Grande rift is a N-S-oriented series of en echelon horsts, west-tilted blocks, and grabens stretching across southern Colorado, New Mexico, and northern Mexico, where it segues into the Piman subtaphrogen (Christiansen and Lipman, 1972; Seager, 1981; Sonder and Jones, 1999). Mountain ridges rise about 1200 to 1700 m above the valley level (Stewart, 1998). Although the Rio Grande rift is considered part of the southern Basin and Range section, it shows a geodynamically distinct two-stage evolution. By late Oligocene to early Miocene time, initial extension occurred within a post-Laramide extensional setting with increased heat flows. This setting was characterized by distributed pure-shear rifting that resulted in broad and shallow basins (Wilson et al., 2005). Modern block faulting commenced around 13 Ma BP and was associated with the broader evolution of the Piman subtaphrogen (Ingersoll et al., 1990; Dickinson, 2002), but was potentially facilitated by clockwise rotation of the Colorado Plateau (Chapin and Cather, 1994; Atwater and Stock, 1998). While the Rio Grande rift overall displays little recent tectonic activity, range-bounding faults at the San Andres fault block have been reported to show Holocene-time offsets (cf. Seager, 1981).

The Mojave block experienced a minor extension during the latest Oligocene and early Miocene, which waned around 18 Ma BP (Stewart, 1998; Glazner et al., 2002). Lacking basin-and-range-style structural configuration, it is considered a *transtaphrogen bridge* (Dickinson, 2002). In conjunction with the establishment of transpressive tectonics at the Big Bend of the San Andreas fault, the Mojave region was subjected to transpressional stress along mostly north-west striking dextral faults (Glazner et al., 2002). Sinistral strike-slip at the Garlock fault commenced around 11 to 10 Ma BP, thereby occurring contemporaneously to the onset of block faulting within the Numic subtaphrogen (Walker and Glazner, 1999). The Garlock fault is consequently assumed to balance the strain between extensional tectonics

within the Great Basin and the transpressive setting of the Mojave Block (Stewart, 1998).

The California Transverse Ranges are a series of restraining bends adjoining the southern strand of the San Andreas fault system (cf. Sonder and Jones, 1999; Dickinson, 2002, 2006). The ranges experienced the most recent exhumation of all study areas, and are characterized by a polyphase evolution closely intertwined with the development of the Pacific-North American plate boundary. Initial development starting around 18 Ma BP saw the clockwise vertical-axis rotation and translation of the western Transverse Ranges (San Gabriel Mountains) as a response to dextral shear induced by the southerly passage of the RTJ. During this first phase, the western Transverse Ranges where shifted more than 200 km in northwesterly direction (Powell and Weldon, 1992; Nicholson et al., 1994; Ingersoll and Rumelhart, 1999). Transtensional conditions prevailed until initiation of the modern transpressional stress regime at approximately 6 Ma BP, concomitant with the evolution of the Big Bend (Atwater, 1970; Dickinson, 2002). For the central Transverse Ranges, it has been shown, e.g., via fission track analysis and provenance analysis, that the majority of exhumation is younger than 3 Ma BP (cf. e.g., Blythe et al., 2000; Binnie et al., 2007, 2008).

4.2.2 Modern environmental setting

Fundamental to the climatic differentiation of the North American greater study area are (1.) its large meridional extent (~1300 km), which involves a hydroclimatic variation with variable impacts of the semipermanent features of the polar front jet and the subtropical North Pacific High (NPH), (2.) infrequent incursions of tropical cyclone remnants into the southern parts of the greater study area, as well as (3.) the meridional strike of the North American Cordillera, causing strong lee effects and a concomitant moisture deficit (cf. Fig. 4.4; Davis and Walker, 1992; Mock, 1996; Sheppard et al., 2002; Antinao and McDonald, 2013a). The meridional strike of the taphrogenic mountain ranges and the forced advection of extratropical air masses give rise to a regional nesting of arid basins and semiarid to semihumid ranges (cf. Whitlock and Bartlein, 1993).

Low average vapor contents result in a radiation-intensive paraautochthonous climate with high intradiurnal and interseasonal temperature variability in the continental interior of the North American Southwest (Weischet, 1996; Osborn, 2004). In the basins of the northern parts of the Basin and Range province, mean annual temperatures amount to approximately 10 °C, with a strong seasonal variability reflected in January means of approximately 0 °C and July means of circa 20 °C (Harvey et al., 1999b; Ritter et al., 2000). To the south, mean temperatures gradually increase (cf. Sheppard et al., 2002), but the propensity for large temperature variability persists—with the notably exception of the mediterranean areas of the Transverse Ranges. In the leeward situation east to the Peninsular Ranges of Baja California, average annual temperatures in the lowlands reach higher than 19 °C, with January averages reaching more than 11 °C and July averages reaching more than 30 °C (cf. Holmgren et al., 2011; Joo et al., 2016).

The hydroclimate of the northern Numic subtaphrogen is governed by the incursion of polar-front cyclones during winter terms, which is facilitated by the comparably low elevations of the Cascade-Sierra Nevada Mountains to the west of northern Nevada and Oregon (cf. Fig. 4.4A). Consequently, northern Nevada shows a clear winter precipitation maximum, with annual precipitation amounting to slightly lower than 200 mm in the basins and around 500 mm within the ranges (Harvey et al.,

1999b; Ritter et al., 2000; Osborn, 2004; Grayson, 2011). To the south, the extratropical dominance of hydroclimate gradually changes into a climate which is increasingly affected by subtropical high pressure and convective precipitation events. This latitudinal transition is accordingly characterized by a growing relevance of summer precipitation. In the case of the Walker Lane fault zone, it is further enhanced by accentuated lee effects to the east of the Sierra Nevada (cf. Sheppard et al., 2002).

For instance, Reheis et al. (1996) report a mean annual precipitation of approximately 120 mm and a mostly even intraannual distribution of precipitation for the Fish Lake valley (cf. Weischet, 1996). The adjoining White Mountains are reported to receive 250 to 400 mm of annual precipitation (Rush and Katzer, 1973). Since the Mojave desert is located east to an area of moderate elevations which is situated between the high massifs of the Sierra Nevada and the Transverse Ranges of southern California, advection into the desert is only moderately impeded. Here, extratropical winter precipitation still contributes the major share to the annual moisture supply (Hereford, 2004; Kirby et al., 2015).

In contrast, the southern part of the Basin and Range region (i.e., the Piman subtaphrogen) shows a dominance of summer precipitation. The summer maximum is related to the onset of the North American Monsoon (NAM) in July and the potential incursion of tropical cyclone remnants, which are moving into the North American Southwest from the tropical East Pacific Ocean and the Gulf of California in late summer and early fall (cf. Fig. 4.4B; Sheppard et al., 2002). The NAM is chiefly governed by the establishment of a pressure disequilibrium between the Gulf of California coastal area and the Sonoran desert lowlands. Summertime sea surface temperatures in the Gulf of California reach values of over 28 °C, involving local convection and therefore comparably cooler, showery air masses. Concurrently, strong heating over the lowlands of the Sonoran desert induces the development of a thermal low. Furthermore, convective activity is augmented by the convergent airflow of the low-level maritime tropical air into the uplands of Sonora and Arizona (Adams and Comrie, 1997).

Advection from the Gulf of Mexico is considered a secondary source of moisture which is significant for monsoonal activity in New Mexico and western Texas (Burnett, 1994; Weischet, 1996; Comrie and Glenn, 1998). The NAM is a mesoclimatic convective phenomenon displaying complex interactions with synoptic-scale dynamics and local atmospheric instability. Monsoonal precipitation thus tends to be short-lived, regionally patchy, and also exhibits a high interannual variability (Carleton et al., 1990; Cerezo-Mota et al., 2011; Kirby et al., 2015). High precipitation intensities entail a high risk of flash flooding, rendering the convective thunderstorms a very effective agent for sediment mobilization (Corrigan et al., 1999; Bieda, 2012). As a corollary of the southward shift of the polar front during the winter months, the northern parts of the Piman subtaphrogen receive some precipitation from extratropical cyclones entering the continental interior (Sheppard et al., 2002). In this part of the study area, higher amounts of extratopical precipitation are contingent upon an anomalously southerly track of cyclones. Rainy weather is regularly associated with troughing over the American Southwest, entailing extended meridional advection of moisture-ladden Pacific air masses (Woodhouse, 1997).

Southwestern California and northern Baja California exhibit a Mediterranean climate, characterized (1.) by the seasonal alternation of high pressure which is associated with the NPH, and (2.) advection of moisture-ladden air masses which are associated with the polar front reaching the region during the winter months (Weischet, 1996). The Transverse Ranges consequently show a strongly seasonal climate with long dry summers followed by mild wet winters, and maximum precipitation being reached in

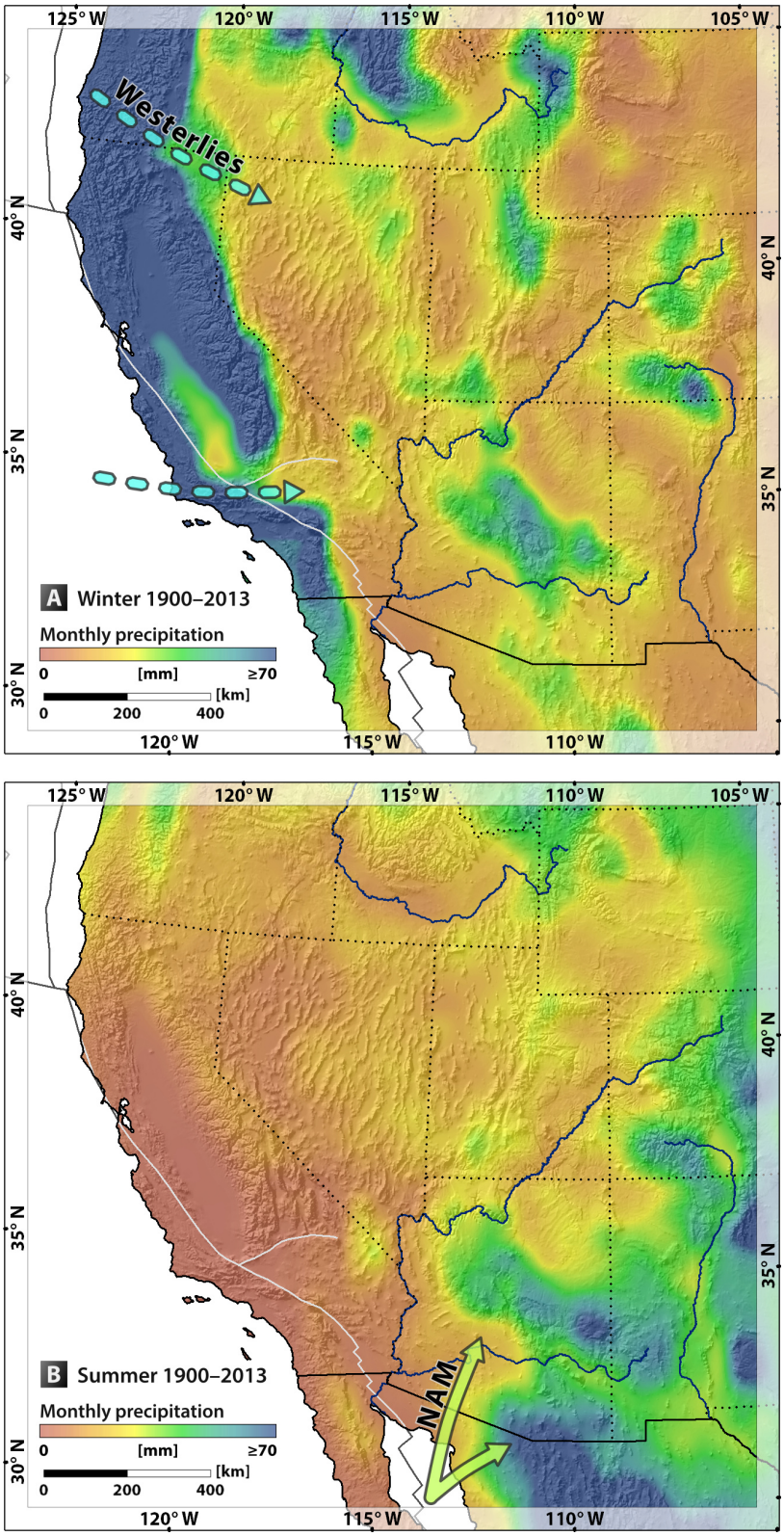


Figure 4.4: 1900 to 2013 averages of monthly precipitation during meteorological winter (A) and summer (B), and major synoptic-scale atmospheric circulation patterns, depicted for the greater American study area. Precipitation data compiled from the GPCC full reanalysis dataset (Version 7.0; Schneider et al., 2015).

January (Bull, 1991). Advection of cyclonal air masses involves strong orographic effects, and annual precipitation quantities are thus reported to vary between 100 mm in low areas located within the rain shadow of ranges (Stokes et al., 1997) and higher than 1300 mm in the mountain ranges (Bull, 1991; Owen et al., 2014).

While northern Baja California is located at the southernmost fringe of wintertime extratropical circulation, precipitation amounts are strongly conditioned by orographic effects imposed by the meridional strike of the Peninsular Ranges (Hastings and Turner, 1965). Specifically, orographic rainfall at the western slope of the Sierra Juarez is reported to bring about around of 450 mm of annual precipitation (Markham, 1972). Conversely, foehn effects and the blockage of cool Pacific air induce a hot and arid weather at the eastern slope of the Peninsular Ranges (Peinado et al., 2006; Holmgren et al., 2011). What is more, the region is located at the western limit of the NAM and therefore receives very limited moisture supply throughout the year. In accordance, reported values for annual precipitation are approximately 60 mm at sea level and still less than 200 mm at 1700 m asl (Spelz et al., 2008; Holmgren et al., 2011), rendering the western Gulf Escarpment the most arid of all American study areas.

4.2.3 Formation phases

The growth of the Laurentide ice shield during the late Pleistocene and the concomitant increase of latitudinal temperature gradients led to strengthening and equatorward deflection of the westerlies (Grayson, 2011; Bartlein et al., 2014; Barth et al., 2016). Intensified troughing over the North American Southwest is indicated by general circulation models parametrized with Late-Pleistocene boundary conditions (cf. Mock and Bartlein, 1995). The more meridional storm track facilitated incursion of extratropical lows into the deeper continental interior, resulting in more humid conditions and a dominance of winter-season precipitation even beyond the modern core domain of the NAM, i.e., Arizona and New Mexico (cf. Weischet, 1996; Spelz et al., 2008; Holmgren et al., 2011; Lyle et al., 2012).

Equilibrium-line altitude (ELA) depressions are estimated to be around 500 m at 37° N, increasing to circa 900 m at 43° N (cf. Dohrenwend, 1984). Corresponding full-glacial ELA values of 3500 and 2500 m at 37° N and 43° N, respectively, indicate a limited potential for Pleistocene glaciations in the Great Basin. Evidence for Pleistocene glaciation is shown by 40 ranges. This evidence is, however, mostly limited to cirques and terminal moraines at high altitudes, pointing to glacial advances below 1 km (Osborn and Bevis, 2001; Osborn, 2004). Glaciation was most extensive in the Ruby and East Humboldt Mountains of north-eastern Nevada, where numerous cirques, terminal moraines, and several u-shaped valleys can be related to both the Last (Wisconsian) Glacial—the Angel Lake glacial advance—and the penultimate (Illinoian) glaciation—the Lamoille glacial advance (Grayson, 2011). Evidence for substantial Angel Lake glacial advances are also found in the Sweetwater Mountains and White Mountains of eastern California (Walker Lane fault zone; Osborn and Bevis, 2001).

With respect to the abundance of alluvial deposits irrespective of summit elevations, however, it is clearly apparent that glacial deposits bear little relevance for alluvial morphodynamics in the Great Basin beyond locally providing unconsolidated (paraglacial) material. Sedimentological studies conducted in the White Mountains by Reheis et al. (1996) show, for instance, that aggradation phases are neither temporally related to Angel Lake advances, nor spatially constrained to glacial deposits. A notable

exception is given by the bajada at the eastern slope of the Sierra Nevada, whose morphogenesis is clearly related to glacial outwash of the Sierra Nevada, and whose alluvial lobes partly emanate from breached terminal moraines (cf. Blair, 2001; Benn et al., 2006). Note that this bajada is *not* part of the Walker Lane subset used in this thesis. Although receiving little emphasis in research done hitherto, it can be assumed that periglacial processes enhanced regolith supply in the North American Southwest (cf. Péwé, 1983; Dohrenwend, 1984; Löhrer, 2008) and consequently facilitated major aggradations during the Pleistocene-Holocene transition or the early Holocene.

As a result of the southward deflection of the polar front and the decline in temperature, the North American Southwest hosted extensive Last Glacial pluvial lakes within its endorheic basins (cf. Fig. 4.5; Benson et al., 1990; Benson, 2003; Orme, 2008; Reheis et al., 2014; Barth et al., 2016). In this context, a causal link between a sinuous polar front track and rising lake levels is strongly indicated by robust correlations and fast response between δ^{18}O time series derived from speleothems in two caves in Nevada and lake levels (cf. Lachniet et al., 2014). Importantly, this finding precludes monsoonal moisture sources as contributing factor for last glacial lake highstands (also cf. Wendt et al., 2018). The two largest pluvial lakes were Lake Lahontan and Lake Bonneville—located in north-western Nevada and western Utah, respectively—which incorporated multiple tectonic basins at their highest levels, and reached highstands between 17 and 14.5 ka BP (cf. e.g., Harvey et al., 1999b; Harvey, 2003a, 2005; Reheis et al., 2014).

With regard to a subsequent polarward remigration of the jet stream, a meridional time-transgressive development of lake levels has been discussed (cf. Grayson, 2011; Lyle et al., 2012). The current state of research suggests, however, that lakes located in the southern parts of the Great Basin desert and the Mojave desert reached maximum lake levels only slightly earlier than pluvial lakes in the northern parts of the Great Basin, corroborating a substantial meridional component of the extratropical cyclone track (Orme and Orme, 2008; Lyle et al., 2012; Reheis et al., 2014, and citations therein). Importantly, hydrological modeling suggests that the increase in precipitation was relatively moderate, i.e., the decline of evapotranspiration contributed a major part to the formation and maintenance of the pluvial lake systems (cf. Hostetler and Benson, 1990; Matsubara and Howard, 2009; Ibarra et al., 2018). In accordance, this pluvial period is a phase of terrain stability for many parts of the greater study area.

The southwest of North America arguably received the most emphasis in alluvial fan research, a fundamental result being that aggradation of alluvial fans took place episodically, and that it was decisively governed by climatic boundary conditions (cf. e.g., Ritter et al., 1995; Miller et al., 2010; Owen et al., 2014). A striking feature is that a first phase of major alluvial aggradations occurred between 13 and 9.5 ka BP (Wells et al., 1987; Bull, 1991; Harvey et al., 1999b; McDonald et al., 2003; Miller et al., 2010) at a time where lake levels were already in decline (Wells et al., 1987; Benson et al., 1990; Li et al., 1996; Anderson and Wells, 2003; Benson, 2003).

Mostly owing to the occurrence of fossilized packrat (Neotoma) middens, the paleobotanical evolution of the North American Southwest is relatively well constrained. In the northern Mojave desert, the northward backshift of the polar front was accompanied by a transition to a more arid environment, as indicated by Pinus woodland giving way to a Juniperus-Yucca woodland at around 11.5 ka BP. Starting from 10 ka BP, the Juniperus-Yucca woodland then eventually retreated in favor of modern Mojave desert scrub (Spaulding and Graumlich, 1986; Koehler et al., 2005).

The parallelism between fan aggradation and the timing of these ecotone changes gave rise to the assumption that alluvial fan aggradation in this area is associated with and strongly facilitated by a decrease in vegetation density—the *arid model* of alluvial fan aggradation (cf. Section 2.2.2; Bull, 1991; Reheis et al., 1996). Although the arid model is widely accepted for the North American Southwest, there is no consensus on which environmental controls played a decisive role for fan aggradation during an aridification phase.

Recent research critically reviews the impact of vegetation density and suggests that high precipitation intensities are the primary driver for alluvial fan aggradation during the Late Pleistocene-Holocene transition and the early Holocene. On the basis of 18 studies on paleoecology and fan aggradation, Antinao and McDonald (2013b) deduce that aggradation predates the transition from late Pleistocene woodlands to Holocene desert scrub by more than 2 ka. Pelletier (2014) objects this assertion by putting emphasis on the altitude differences between midden sites and alluvial fans, proposing that if time-transgressive ecotone changes along the hydrologically induced lower timberline are taken into account, aggradation patterns are in line with the paleovegetation-change hypothesis (PVCH, arid model sensu stricto). A further issue of the PVCH hypothesis is that alluvial fan aggradation in the North American Southwest shows a second aggradation phase between 6 and 2.5 ka BP (cf. e.g., Wells et al., 1987; Mahan et al., 2007; Bacon et al., 2010; Fuchs et al., 2015), an empirical evidence which is difficult to reconcile with paleovegetation-change being the primary driver of aggradation (cf. Miller et al., 2010).

Irrespective of the relative impact of changes in vegetation density and precipitation intensity, sediment conveyance to fans requires sediment paths to become highly connected (Reid et al., 1999; Pierson et al., 2007; Mayor et al., 2008; Parsons et al., 2009). A scrutiny of the hypothesis of alluviation during aridification thus needs to involve a critical assessment of potential sources for heavy rainfall (cf. Bull, 1991, p. 114). With respect to the Mojave desert and the southern parts of the Great Basin, an important observation is that sediment yield increased primarily through debris-flow transport, corroborating the involvement of high-intensity storms (cf. Section 2.1.1; Harvey and Wells, 1994; Reheis et al., 1996; Keefer et al., 2007).

Aggradation during the Pleistocene-Holocene transition is habitually associated with the onset of the NAM at approximately 12 ka BP, and with its intensification between 10 and 8 ka BP (Bull, 1991; Mock and Bartlein, 1995; Adams and Comrie, 1997; Spelz et al., 2008; Roy et al., 2014). The inception of the NAM was predominantly driven by precession-related increases of summer insolation, which peaked around 12 ka BP and declined since then (Kutzbach, 1981; Bartlein et al., 2014). For the northern marginal region of the NAM, the nature of the transition into the Holocene is, however, insufficiently established (cf. Metcalfe et al., 2015), and the impact of monsoonal precipitation is subject to critical debate (cf. e.g., Miller et al., 2010; Pelletier, 2014; Kirby et al., 2015).

A key argument for the significance of the NAM for fan aggradation is its generally good correlation with sea surface temperatures (SSTs) within the Gulf of California (cf. Miller et al., 2010), which are understood to be a good proxy for monsoon intensity (cf. e.g., Mitchell et al., 2002). While Gulf of California SSTs show excellent correlation with the younger aggradation phase between 6 and 2.5 ka BP, they correlate relatively poorly with the first aggradation period (cf. Barron et al., 2005). As an alternative to a hypothetical modern-style NAM, i.e., a monsoonal system predominantly driven

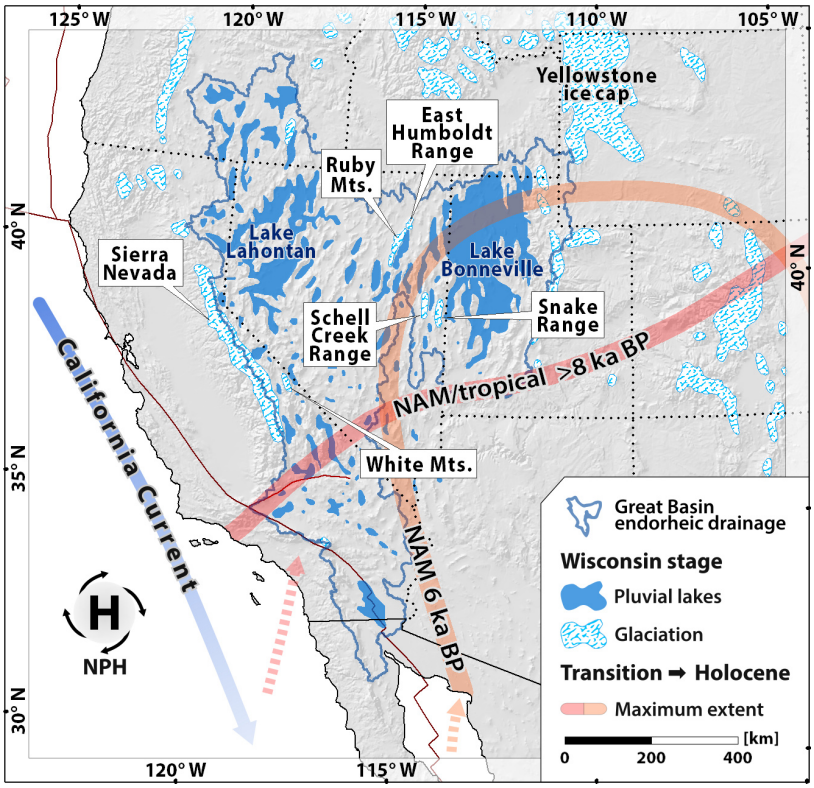


Figure 4.5: Wisconsin-stage glacial and pluvial features (according to Orme, 2008), and extent of NAM/tropical currents during the early and middle Holocene (according to Barron et al., 2012). Extent of the Great Basin endorheic drainage modeled from GMTED2010 elevation data with 7.5″ posting (Danielson and Gesch, 2011).

by moisture surges advecting from the Gulf of California, Antinao and McDonald (2013a,b) suggest that this first aggradation phase was linked to the NPH being located further to the north, so that the resultant onshore air flow impeded upwelling at the coast of California. Attenuation of the California Current induced semi-permanent El Niño-like conditions off Coastal California, enabling the incursion of moist tropical air masses (cf. Fig. 4.5; Thompson et al., 1993; Barron et al., 2012).

Importantly, such a scenario would support all potential moisture sources for SW North America, i.e., it (1.) enables mesoscale convective systems in southern California and southern Nevada (cf. Kirby et al., 2015), (2.) facilitates the incursion of tropical cyclone remnants into the North American interior (cf. Larson et al., 2005), and (3.) allows for the incorporation of tropical air masses into winter-season extra-tropical systems (cf. Lyle et al., 2012).

Unlike this core region of the Basin and Range province, the other areas of the taphrogen received relatively little attention in alluvial fan research, and phases of alluvial fan aggradation are therefore much less constrained. As discussed in detail in Section 4.2.2, the greater American study area displays a general transition from dominantly winter-time advective precipitation to summer-time convective precipitation, which is concomitant with a transition from extratropical towards subtropical synoptical-scale patterns. Albeit it is assumed that the late Pleistocene to early Holocene NAM reached further to the north (cf. Thompson et al., 1993; Barron et al., 2012), northern Nevada remained largely unaffected by subtropical moisture and consequently shows only little evidence for summer-season thunderstorms

(cf. Harvey et al., 1999b; Wigand and Rhode, 2002).

In accordance, the majority of fans in the northern parts of the Basin and Range province were mostly fed by streamflows, indicating a moderate-intensity moisture source (Reheis et al., 1996). Furthermore, the limited data available suggest that the main phase of aggradation took place during the Last Glacial, preceding the highstands of Lake Lahontan and Lake Bonneville or occurring shortly afterwards (cf. Reheis, 1987; Harvey et al., 1999b; Ritter et al., 2000). Unlike the North American Southwest, there are no indicators for a substantial causal relationship between vegetation changes and alluvial fan aggradation. According to dated packrat middens, juniper woodland disappeared from the lower parts of the Lake Lahontan area after the Younger Dryas, i.e., after approximately 10.5 ka BP (Ritter et al., 2000; Wigand and Rhode, 2002).

No evidence is, however, given for any considerable sediment mobilization during the Pleistocene-Holocene transition (cf. Harvey et al., 1999b). Available data indicates a strong interlink between sediment mobilization and synoptical-scale changes in atmospheric circulation, specifically the passage of the polar front over the northern Great Basin (Benson et al., 1995). The northern parts of the Basin and Range province thus generally seem to exhibit a transport-limited process-response system for alluvial fan aggradation, thereby complying with the *humid* model of fan aggradation (cf. Section 2.2.2; Harvey et al., 1999b). Paleobotanical proxies as well as lake level records point to a wet onset of the last glacial stage (cf. Negrini et al., 2000; Negrini, 2002), concomitant with a rapid lake level rise of Lake Lahontan (Benson et al., 1997) and fan aggradation (Pierce and Scott, 1982; Reheis, 1987; Ritter et al., 2000; Kenworthy et al., 2014). A second major aggradation phase was associated with the back-shift of the westerlies and concomitantly increased wetness after the Last Glacial Maximum (Hostetler and Benson, 1990; Ritter et al., 2000; Kenworthy et al., 2014). In addition, this second aggradation phase might have been facilitated by seasonal snowmelt being enhanced by increasing temperatures under still periglacial conditions (cf. Pierce and Scott, 1982; de Vries, 1994; Vandenberghe, 2002).

With respect to the southernmost parts of the study area, there is evidence that suggests a transport-limited process-response system as well. For their study area located to the east of the Sierra Juarez (northern Peninsular Ranges), Spelz et al. (2008) yielded ^{10}Be ages of 15.0 ± 2.2 ka BP, which approximately match aggradation phases stated by Antinao et al. (2016) for southern Baja California, and are also in agreement with lake level highstands within the Baja California peninsula and continental northern Mexico (cf. Roy et al., 2012, 2014). In this context, Spelz et al. (2008) propose that the humid model is valid for hyperarid settings, because increased runoff instantly drives the system toward aggradation. However, it should be noted that the radionuclide measurements of Spelz et al. are challenged by Pelletier (2014) for their large variances, indicating inheritance issues.

In summary, the American greater study area displays a complex picture, with diverse changes in environmental conditions facilitating aggradation (cf. Antinao and McDonald, 2013a). As already noted by Bull (1991), transitions zones are to be expected between areas where systems aggraded mainly during glacial and interglacial climates, respectively. These transition zones are, however, yet to be unveiled.

4.3 Asia

4.3.1 Tectonic setting

In what follows, we will focus on the Gobi Altai, and the reader is referred to Pipaud and Lehmkuhl (2017 / Chapter 5) for further information on the Mongolian Altai. Like the Mongolian Altai, the Gobi Altai is an intracontinental transpressional orogen and part of the Central Asian Orogenic Belt (the Altaids; Cunningham, 2005). The Altaids are a system of late Proterozoic to early Mesozoic orogens composed of island-arc complexes and continental blocks, which became amalgamated due to the closure of the Paleo-Asian Ocean (Şengör et al., 1993; Cunningham et al., 1996; Badarch et al., 2002; Dobretsov and Buslov, 2007).

In the Gobi Altai area, the progressive accretion of terranes south to Precambrian blocks resulted in a WNW-ENE to WSW-ESE structural grain (Cunningham, 2007, 2010). After consolidation of the Central Asian Orogenic Belt during the Permian, the area remained under compressive stress and experienced significant erosion. The compressive setting emerged from collisions at the southern margin of Asia (Dewey et al., 1988; Hsü and Chen, 1999; Yin and Harrison, 2000; Kapp et al., 2005). Subsequently, a transition into a tensive stress environment induced orogenic collapse and concomitant Basin-and-Range-style taphrogenesis (Johnson et al., 2015). During the late Cretaceous to early Tertiary, the region was subjected to peneplanation (Cunningham et al., 1997; Jolivet et al., 2007).

The initiation of the Himalayan-Tibetan orogeny is dated to the lower Eocene (~50 Ma BP; Yin, 2010; Gloaguen and Ratschbacher, 2011). Indentation of the rigid Indian plate into the weaker crust of South Asia (cf. Molnar and Tapponnier, 1975) caused a far-field roughly SW-NE-oriented σ_1 within Central Asia, which, on a continental scale, is accommodated by both compression and extrusion (cf. Tapponnier and Molnar, 1979; Yin, 2010). In Central Asia, compressive stress induces localized shear of the comparably weak Altaid lithosphere located to the south of a passive indenter formed by the Khangai dome (Cunningham, 2005; van Hinsbergen et al., 2008).

Deformation is partitioned into sinistral deformation in the Gobi Altai and conjugate dextral transpressional deformation in the Mongolian Altai (Baljinnyam et al., 1993; Bayasgalan et al., 2005). According to Calais et al. (2003), approximately 15 % of the total India-Eurasia convergence is terminally accommodated in the Altaid corridor between the Khangai dome in the north and the Qilian Shan to the south. Apatite fission track measurements (Vassallo et al., 2007), as well as paleoclimatic proxy data (Caves et al., 2014) indicate that major uplift of the Gobi Altai is constrained to the Late Miocene and Pliocene. Ongoing deformation is indicated by seismic activity such as the M_s 8.3 earthquake occurring in 1957 along the Bogd Fault, which had a sinistral oblique-reverse focal mechanism and produced about 260 km of surface ruptures (Baljinnyam et al., 1993; Bayasgalan et al., 2005).

The Gobi Altai is characterized by sinistral transpression along two major approximately east-west-striking translational fault systems (Owen et al., 1999b). A gross differentiation can be made into a northern strand, which is connected with the Mongolian Altai to the west (Bogd Fault system / Valley of the Lakes fault system, BFS), and a southern strand, which passes into the Tian Shan mountains to the west (Gobi-Tian Shan fault system, GTSFS; Cunningham et al., 1996; Cunningham, 2010). Along these fault systems, neotectonic uplift of individual ranges occurs in the form of oblique thrusting, right-stepping restraining bends, or along right-stepping fault stepovers, where compression is accommodated

by WNW-ESE-striking thrust faults following the basement grain. Conversely, left-stepping is strongly impeded by the structural grain, which entails that the Gobi Altai lacks any larger transtensional elements (Cunningham, 2007). Both range fronts and intermountain basins are thus remnant lows lacking down-dropping.

In cross section, the lenticular Gobi Altai bends exhibit positive half-flower or full-flower (bivergent) structure geometries (Bayasgalan et al., 1999; Owen et al., 1999b). Structural asymmetry is common in both cases and is matched by a topographic asymmetry which is reflected by tilted peneplain surfaces forming the core of many ranges (Baljinnyam et al., 1993; Jolivet et al., 2007). In part, these peneplains are made up of inverted Mesozoic basin infill, providing an easily erodible sediment source for alluviation (Cunningham et al., 1997; Cunningham, 2010). Kinematics along strike-slip faults vary throughout the range. Transpression dominates in the western section of the orogen, resulting in elongated mountain chains. Conversely, translation prevails to the east of the range, where strike-slip faults are subordinate transfer zones between offset thrust ridges (Cunningham, 2005, 2007). Maximum elevations (up to 3957 m asl, approximately 2000 m above the surrounding piedmonts) are found in the Ih Bogd, a sigmoidal-shaped restraining bend in the eastern part of the Bogd Fault System (cf. Fig. 4.2; Owen et al., 1999a).

Many ranges of the Gobi Altai are characterized by the occurrence of deeply routed frontal reverse faults, which generate small ridges in the range foreland with a relief of up to 100 m (Bayasgalan et al., 1999; Owen et al., 1999a). These *forebergs* signify structural widening of flower structures, with transpression being progressively transferred to the outer faults (Cunningham, 2007; Vassallo et al., 2007; Cunningham, 2010). Conducting luminescence dating of uplifted lacustrine deposits of Ih Bogd forebergs, Owen et al. (1999a) estimated high uplift rates of 1 to 5 mm yr^{-1}. The proximal foreland, i.e., the foreland located between mountain front and the foreberg zone, is progressively involved into this uplift, albeit at a much lower rate than the forebergs themselves (Owen et al., 1997, 1999a; Vassallo et al., 2007).

Local morphodynamics are multifaceted and chiefly depend on whether the foreberg zone got dissected by a larger feeder stream or not (Carretier et al., 2002). Scenarios for alluvial fan morphodynamics at foreberg zones are (1.) alluvial fan surfaces interrupted by initial foreberg development, (2.) dissected alluvial fans at locations where the foreberg zone got intersected and where sediment connectivity is established, or (3.) uninterrupted foreberg segments, where alluvial fans can become distally constrained (cf. Owen et al., 1997, 1999a,b; Lehmkuhl, 2000; Carretier et al., 2002). From a general perspective, the specific transpressive setting of the Gobi Altai provides very limited proximal accommodation space for alluvial deposits, and the high potential for cascaded sediment deposition is casting serious doubt on the explanatory potential of fan–catchment area relationships (cf. Section 2.3.1).

4.3.2 Modern environmental setting

Being part of wider *Arid Central Asia*, Southwestern Mongolia is characterized by an arid continental climate, showing large intraannual variations both in temperature and precipitation (An et al., 2008; Chen et al., 2010; Lehmkuhl et al., 2016, 2018b). In the Basin of the Gobi Lakes, mean annual temperatures of −2 to 5 °C are contrasted by January mean temperatures of below −20 °C and July averages of up to 20 °C (Felauer, 2011; Gerelchuluun and Ahn, 2014). Longterm averages of annual

precipitation vary between less than 50 mm yr^{-1} in the Valley of the Gobi Lakes, and up to 200 mm yr^{-1} in the mountain areas (Gunin et al., 1999; Pyankov et al., 2000; Felauer et al., 2012). During the winter season, the area is under the influence of the Siberian-Mongolian anticyclone, which tends to be established over the Khentii Mountains of North-Eastern Mongolia (Domrös and Peng, 1988; Gong and Ho, 2002; Panagiotopoulos et al., 2005). The thermally induced Siberian-Mongolian high entails stable atmospheric conditions, concomitant with frequent inversions and severe winter dryness (cf. Fig. 4.6A; Gunin et al., 1999; Morinaga et al., 2003). Inhibiting greater snow depths, this synoptic pattern facilitates frost cracking (Kostrova et al., 2014), and slopes are thus covered by thick blankets of debris (Stolz et al., 2012; Lehmkuhl et al., 2016).

In the context of the summer relocation of the polar front to the northwest of Mongolia, moister air masses advect into the Gobi Altai region (Caves et al., 2014). Most frequently, rain is brought by extratropical depressions, typically developing over the Eastern Mediterranean and regenerating over the Caspian Sea (Lioubimtseva et al., 2005; Nicholson, 2011). Orographic precipitation along the north-easterly trajectory into southwestern Mongolia—particularly the western fringes of the Mongolian Altai—entails strong lee effects in the Gobi Altai area (cf. Fig. 4.6B). While approximately two third of precipitation occurs during the meteorological summer months (cf. e.g., Endo et al., 2006; Nandintsetseg and Shinoda, 2011; Lee et al., 2013), western Mongolia is affected by a large interannual variation of precipitation (Sato et al., 2007), and multi-year droughts are reflected in historical records and dendrochronological archives (cf. e.g., Peck et al., 2002; Davi et al., 2006; Li et al., 2009).

Under modern climatic boundary conditions, the limit of the East Asian Summer Monsoon (EASM) runs through the Helan Mountains (Inner Mongolia) in northern China (cf. Chen et al., 2010, and references therein), and the study area thus experiences only rare incursions of Pacific air masses (Sato et al., 2007; Lee et al., 2013). In accordance with low winter temperatures and limited moisture supply, vegetation is characterized by relatively sparse grass-shrub communities, with flora transitioning from Kobresia meadows and cryophytes in the summit areas, associations of juniper and grasses at intermediate altitudes, to xerophytes and petrophytes in the basin deserts (Hilbig, 1995; Gunin et al., 1999; Lehmkuhl et al., 2018a).

4.3.3 Formation phases

Well-developed cirques and terminal moraines along the slopes bordering the Ih Bogd summit plateau provide clear evidence of glacier advances during the late glacial between 20 ka BP to 15 ka BP (Batbaatar et al., 2018). Conversely, the lower ranges of the Gobi Altai lack such evidence. Accordingly, it is assumed that the Pleistocene ELA is located at an altitude of 3800 to 3900 m asl, indicating an ELA depression in the Gobi Altai of approximately 1000 m (Lehmkuhl, 1998; Lehmkuhl et al., 2011). While modern permafrost is limited to isolated patches at high elevations, extensive permafrost developed during the Last Glacial down to the piedmont surfaces, involving pronounced active layer processes and intensive frost weathering throughout the mountain ranges (Owen et al., 1998; Lehmkuhl, 2000; Lehmkuhl et al., 2018a).

Geomorphological evidence of latest-generation fan surfaces along Gobi Altai mountain flanks, e.g., deflation of fine sand and silt and the presence of involutions and ice-cast wedges in many fans, indicates that (1.) alluvial fans in the regions formed concentrated in time, and (2.) the last major alluviation phase

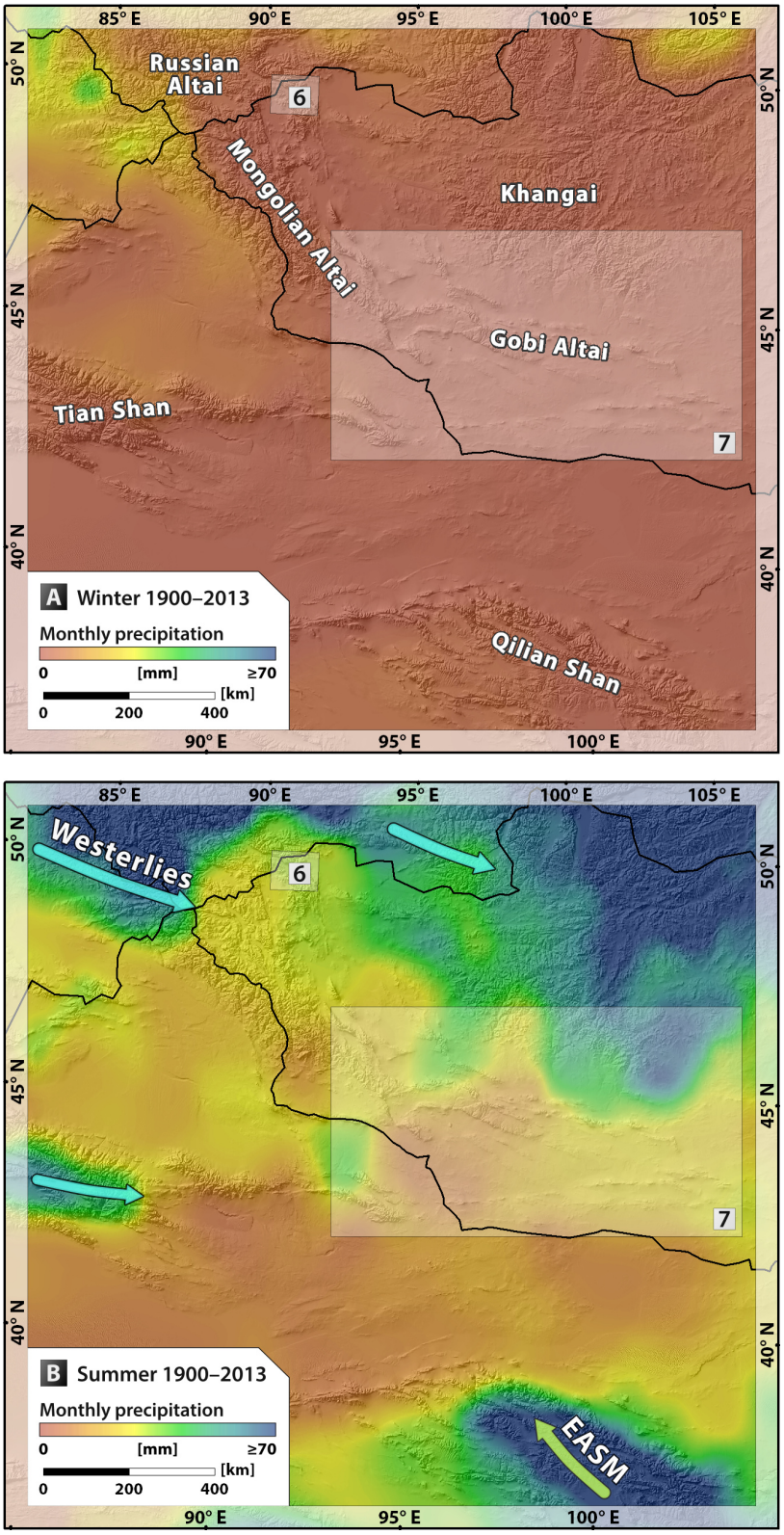


Figure 4.6: 1900 to 2013 averages of monthly precipitation during the meteorological winter (A) and summer (B) season, and major synoptic-scale atmospheric circulation patterns, depicted for the greater Asian study area. Precipitation data compiled from the GPCC full reanalysis dataset (Version 7.0, Schneider et al., 2015). Also denoted are the extents of Regions 6 and 7.

precedes the retreat of permafrost conditions from the piedmont after the Last Glacial Maximum (Owen et al., 1997, 1998). Cosmogenic radionuclides datings (^{10}Be) and optically stimulated luminescence datings of abandoned fan surfaces strongly indicate that major alluviation pulses occurred during the termination of glacial stages MIS6 and 2, with Last Glacial aggradations being dated to 20 ka BP to 12 ka BP (Ritz et al., 1995; Carretier et al., 1998; Ritz et al., 2003, 2006; Balescu et al., 2007; Gregory et al., 2014). With respect to the consistency of age clusterings for various locations of the Gobi Altai range, it is apparent that alluviation was induced by a late glacial increase in precipitation (cf. Ritz et al., 2003), and fan formation in the Gobi Altai thus generally conforms to the *humid model* of alluvial aggradation (Harvey et al., 1999a,b). It is noteworthy that alluviation pulses considerably predate early Holocene lake level highstands in western Mongolia (Lehmkuhl et al., 2018a), indicating that major alluviations occurred during a transitional late glacial period (cf. Vassallo et al., 2007) which facilitated the occurrence of flash floods (Vassallo et al., 2011).

5 Object-based delineation and classification of alluvial fans by application of mean-shift segmentation and support vector machines

Isabel Pipaud*, Frank Lehmkuhl* (2017)
Geomorphology 293A, 178–200, doi:10.1016/j.geomorph.2017.05.013

5.1 Introduction

In the field of geomorphology, (semi-) automated extraction and classification of landforms is one of the most active research areas (Evans et al., 2009). A landform is a physical feature of the land surface being perceived as a unitary entity because of its particular shape (Mark and Smith, 2004; MacMillan and Shary, 2009). Consequently, landforms are—by definition—bounded segments of the earth surface (Evans, 2012), although they do not necessarily display clear demarcations (Mark and Smith, 2004). Until the late 2000s, pixel-based analysis schemes were the de facto standard for land surface classification (cf. e.g., Irvin et al., 1997; Burrough et al., 2000; MacMillan et al., 2000; Schmidt and Hewitt, 2004; Iwahashi and Pike, 2007). By representing a field-based view of the land surface (Moore et al., 1991; Gallant and Wilson, 2000), pixel-based approaches treat the land surface as a continuous phenomenon, and can thus appropriately address scientific issues in the field of general geomorphology (Evans, 1972; Goudie, 1990). In the field of specific geomorphology, however, geomorphometry involves analyzing the geometric and topological characteristics of landforms. It therefore requires, in contrast, a complete delimitation of the landform of interest (Evans, 1987, 2010), i.e., the landform must be considered as a discrete spatial feature (Evans, 1972, 2012). Consequently, specific geomorphology requires an object-based view of the land surface (cf. Drăguţ and Eisank, 2011). Taking pixel-neighborhoods with predefined shape and (commonly) size as the sole basic entities for analysis, exclusively pixel-based approaches cannot account for the irregular boundaries of real-world objects. During the last decade, this fundamental deficiency of geomorphometric standard applications gained increasing emphasis, and an object-based methodology incorporating segmentation was proposed as an alternative (MacMillan et al., 2004; Minár and Evans, 2008; Strobl, 2008; MacMillan and Shary, 2009).

Object-based image analysis (OBIA) is a methodological framework which evolved in the field of remote sensing in the early 2000s as a response to the increasing incidence of H-res scenarios, i.e., situations in which scene elements of interest cover many pixels (Strahler et al., 1986; Woodcock and Strahler, 1987). OBIA attempts to appropriately address these scenarios by redefining the basic spatial unit from a single grid cell to a group of adjoining cells—an image object, which can be shown to represent a meaningful spatial entity (Hay et al., 2001). It is a two-step technique, which consists of initially conducting a segmentation algorithm on the gridded dataset, partitioning the raster data based on one or more criteria of homogeneity in one or several dimensions (Blaschke et al., 2004; Blaschke, 2010). Subsequent to the segmentation routine, a rule-based classification is applied on the individual segments (Benz et al., 2004). In doing so, the methodological framework of OBIA can

*RWTH Aachen University, Department of Geography, Templergraben 55, 52056 Aachen, Germany

improve landform extraction by enabling segment-level morphometric and shape analysis as well as considering geospatial topology and thematic neighborhood relationships (Blaschke, 2003; Burnett and Blaschke, 2003; Blaschke et al., 2004).

Accompanying the growing availability of high-resolution satellite imagery, OBIA quickly gained emphasis and commercial software packages rapidly became available (Blaschke and Strobl, 2001). Specifically, the multi-resolution image segmentation algorithm (MRS) implemented into the OBIA-focused software suite eCognition facilitated the application of object-based analysis approaches (Baatz and Schäpe, 2000; Benz et al., 2004; Blaschke et al., 2004). This readily available object-based analysis framework was soon successfully adopted for geomorphometric research (Drăguţ and Blaschke, 2006; van Asselen and Seijmonsbergen, 2006; Drăguţ and Blaschke, 2008; Möller et al., 2008; Schneevoigt et al., 2008; Drăguţ et al., 2009; Anders et al., 2011; Gerçek et al., 2011; Drăguţ and Eisank, 2012). In terms of case studies focusing on individual landforms, frameworks using MRS were proposed for the delineation of drumlins (Saha et al., 2011; Eisank et al., 2014), landslides (Van Den Eeckhaut et al., 2012) and glaciovolcanic landforms (Pedersen, 2016). Alternative segmentation algorithms gained less attention, but were successfully applied as well. Stepinski et al. (2007) and Ghosh et al. (2010) extended the k-means clustering algorithm by augmenting feature vectors with pixel coordinates, and exemplified its applicability for classification of Martian landforms. Effective application of watershed transformation approaches was demonstrated by Stepinski et al. (2006), Ghosh et al. (2010) and Romstad and Etzelmüller (2012).

Until now, delineation of alluvial fans has been primarily tackled using region growing-algorithms. Significantly predating the establishment of OBIA frameworks in geomorphology, Miliaresis (1999) and Miliaresis and Argialas (2000) applied a region-growing algorithm relying on apex seed points to yield polygons delimiting alluvial fans. This early approach was, however, deficient in that it took a simple slope threshold of 2° as exclusive stop criterion for the iterative region-growing. Hence, it was incapable of delineating fan toes and satellite imagery needed to be incorporated to include these distal fan parts into alluvial fan delineation. In addition, pixel-wise slope thresholding prevented differentiation of adjoining fans. Argialas and Tzotsos (2004) presented an MRS-based analysis scheme incorporating both topographic data and satellite imagery. Yielding results equivalent to those obtained by Miliaresis (1999) and Miliaresis and Argialas (2000), their approach did as well not allow a discrimination of adjoining fans. Only recently, Norini et al. (2016) presented a new approach relying on the construction of radial profiles emanating from apex points. Apexes are located by applying manually optimized thresholds on slope and curvature grids, and intersecting these binary grids with drainage networks. Eventually, alluvial fans are delineated by deriving interpolated surfaces from the trimmed radial profiles, and intersecting these surfaces with the DEM. Enabling the differentiation between adjoining fans, their approach shows considerable improvements in terms of alluvial fan delineation but lacks the classification component inherent to the OBIA methodology.

While segmentation algorithms maximize intra-class homogeneity and inter-class heterogeneity, their parametrization still needs to be tuned to an appropriate scale level reflecting shape and dimension of the landform of interest (cf. Anders et al., 2011). Considerable effort has been undertaken to provide methods to objectively choose an appropriate global scale setting for the respective objects of interest (Drăguţ et al., 2009, 2011; Ming et al., 2012; Drăguţ et al., 2014; Ming et al., 2015). However, a landform

may exhibit considerable intra-class variation in terms of size and shape, and specifying a global scale may thus be suboptimal (cf. Ming et al., 2015). A further important aspect is that dimension and shape of terrain segments produced by segmentation are strongly dependent on selection and weighting of input terrain parameters (cf. Anders et al., 2011; Gerçek et al., 2011). In contrast to imagery, where equal band weightings are generally appropriate, terrain parameters exhibit varying statistical properties and normalization is not always feasible (cf. Evans and Cox, 1999; Csillik et al., 2015). Even if we assume normalization has been carried out, there is no reason to assume that equal weights optimally reflect object boundaries. Conversely, optimal weights have to be found for each specific object of interest. It follows that morphometric parametrization adds an additional level of complexity to the OBIA framework, and we thus propose to use the term object-based morphometric analysis (OBMA) for the adoption of OBIA in the field of geomorphometry.

In this study, we describe a novel supervised method for delineation and classification of alluvial fans, which is premised on the application of mean-shift segmentation and a one-class support vector machine (OCSVM). It takes elevation data and derived terrain parameters as exclusive input. The potential of the approach and possible challenges are assessed using a SRTM 1″ scene depicting a section of the north-eastern Mongolian Altai, which displays many alluvial fans of different dimension and shape. In trying to fully exploit the potential of segment-level morphometric analysis, we conduct geomorphometric parametrization separately for the segmentation and classification stage. By performing mean-shift segmentation repeatedly for different weightings of the incorporated morphometric parameters as well as different bandwidths, we both take account for uncertainty in terms of terrain parameter weights as well as for the spectrum of alluvial fan dimension and shape. Subsequently, manually delineated alluvial fans are used to train the support vector machine (SVM), and the trained model is used to derive hyperplane distance values for all segmentation datasets. Eventually, we obtain the final OBMA layer by merging all single classification results based on the distances to the SVM decision surface and the topological relationships between objects.

5.2 Morphological characteristics of alluvial fans

In contrast to field-based morphometry, segment-level morphometric analysis enables us to quantify unique characteristics of a landform. Consequently, morphometric parameters specifically quantifying such peculiar morphological aspects of a landform of interest are ideal for the classification of objects obtained by applying a segmentation algorithm on a topographic dataset. In this context, we now give a brief description of the morphological characteristics of alluvial fans and their differentiation.

Alluvial fans are aggradational sedimentary landforms essentially resembling a segment of a cone radiating from a point—the apex—where a feeder channel emerges from a mountainous catchment and becomes unconfined (e.g., Troeh, 1964, 1965; Bull, 1977; Oguchi and Ohmori, 1994; Viseras et al., 2003; Harvey et al., 2005). They are generally arcuate in plan view, with aperture angles depending on lateral coalescence with other fans or neighboring fluvial and lacustrine environments (Saito and Oguchi, 2005; Blair and McPherson, 2009). In this context, alluvial fans can be differentiated into unconfined and confined alluvial fans, and confinement can occur both laterally and distally (cf. Sorriso-Valvo et al., 1998; Crosta and Frattini, 2004; Cavalli and Marchi, 2008). As a result of considerable variation

in sediment delivery and prevalent fan-building sedimentation processes, alluvial fan morphology is characterized by a great range of fan radii and slopes (cf. e.g., Saito and Oguchi, 2005; Hashimoto et al., 2008). Radial sediment deposition entails that alluvial fans exhibit convex shapes in cross section (Bull, 1977). Cross-sectional relief, however, shows large variations between individual fans, and is primarily determined by the significance of lateral coalescence. Intensive coalescence eventually leads to generation of a bajada, where cross-sectional profiles can be nearly flat (cf. Sánchez-Núñez et al., 2015). Conversely, Hooke and Rohrer (1979) found that fans can exhibit increasingly steep slopes when approaching their radial margins, which they interpreted as being induced by high inertia flows on steeper fans entailing a reduced tendency to divert from the axial flow path.

Primary fan-building processes of mature fans are sediment-driven debris flows or fluid-driven streamflows radiating over the fan surface (Wells and Harvey, 1987; Blair and McPherson, 1994; Stock, 2013). Differentiation between these two transport processes is primarily established by catchment bedrock lithology, catchment shape, climate and tectonics (cf. e.g., Kostaschuk et al., 1986; Wells and Harvey, 1987; Lecce, 1991; Calvache et al., 1997; Blair, 1999a; Levson and Rutter, 2000; Ritter et al., 2000; Dorn, 2009; Bahrami, 2013). As drainage basin characteristics may vary on a small scale, even neighboring fans can be dominated by contrasting processes and thus exhibit different geomorphological properties in terms of radius, slope and curvature (Blair and McPherson, 1994).

Debris flows are characterized by a relatively large spectrum of modal grain size and grain size distribution. Alluvial fans primarily built by debris flows consequently show a wide range of slope, with slope angles varying between 18° and 4° (cf. e.g., Harvey, 1992; Marchi et al., 1993; Oguchi and Ohmori, 1994; Sorriso-Valvo et al., 1998; Milana and Ruzycki, 1999; Williams et al., 2006; Hashimoto et al., 2008). They commonly exhibit rather straight radial profiles (Blair and McPherson, 1994; Hashimoto et al., 2008). Conversely, sheetflood-dominated fans regularly exhibit concave radial profiles, with slopes varying between about 6° in apex proximity to values ranging below 1° in distal parts (cf. e.g., Bull, 1977; Sorriso-Valvo et al., 1998; Milana and Ruzycki, 1999; Saito and Oguchi, 2005; Hashimoto et al., 2008; Stock et al., 2008; Stock, 2013). In many cases, mature alluvial fans exhibit an incised channel. Incised channels are downslope extensions of the catchment feeder channel onto the fan, and terminate in a point in the proximal or intermediate section of the fan. This intersection point indicates the location of potential active aggradation—the active depositional lobe (Calvache et al., 1997; Viseras et al., 2003). In contrast to mature fans, juvenile fans commonly exhibit radii below 1 km and depositional slopes up to 30° (Blair and McPherson, 1994, 2009).

The above aspects suggest that fans primarily built by debris flows can generally be expected to exhibit systematically steeper slopes than streamflow-dominated fans. Classifying 52 alluvial fans based on sedimentologic evidence, Marchi et al. (1993) obtained average mean slope values of 10.5° for debris flow-dominated fans and 1.7° for streamflow-dominated fans. Analogously, Sorriso-Valvo et al. (1998) yielded average mean slopes of 8.3° and 3.6°, respectively. However, the prevailing fan-building process of mature fans may change through time. In this context, Saito and Oguchi (2005) analyzed the morphometry of 690 alluvial fans in Japan, Taiwan and the Philippines. They obtained a log-normal distribution of mean slope values without any significant gaps, displaying values ranged from 0.1° to 7°. Consequently, alluvial fans are often of composite character in terms of geomorphogenesis, and debris flow dominance and streamflow dominance should thus be interpreted as endmembers of a process

spectrum (cf. Saito and Oguchi, 2005; Blair and McPherson, 2009).

5.3 Regional setting

The alluvial fan inventory within and next to the Uureg Nuur Basin, which is located in the north-eastern part of the Mongolian Altai (see Fig. 5.1), provides the evaluation data for this study. The processing area stretches from 90.4° E to 91.6° E, and from 49.8° N to 50.5° N. The Mongolian Altai is part of the central Asian orogenic system and composed of several amalgamated island arc terranes of Paleozoic age (Şengör et al., 1993; Cunningham et al., 1996). Neotectonic orogenesis of the Mongolian Altai takes place as a result of the tectonic stress field caused by ongoing India-Asia convergence, which in central Asia is accommodated by means of an intracontinental oblique transpression with NNW-SSE striking dextral strike-slip faults and oblique faults (Molnar and Tapponnier, 1975; Şengör et al., 1993). Consequently, deformation is primarily taken up on discrete structures (Frankel et al., 2010).

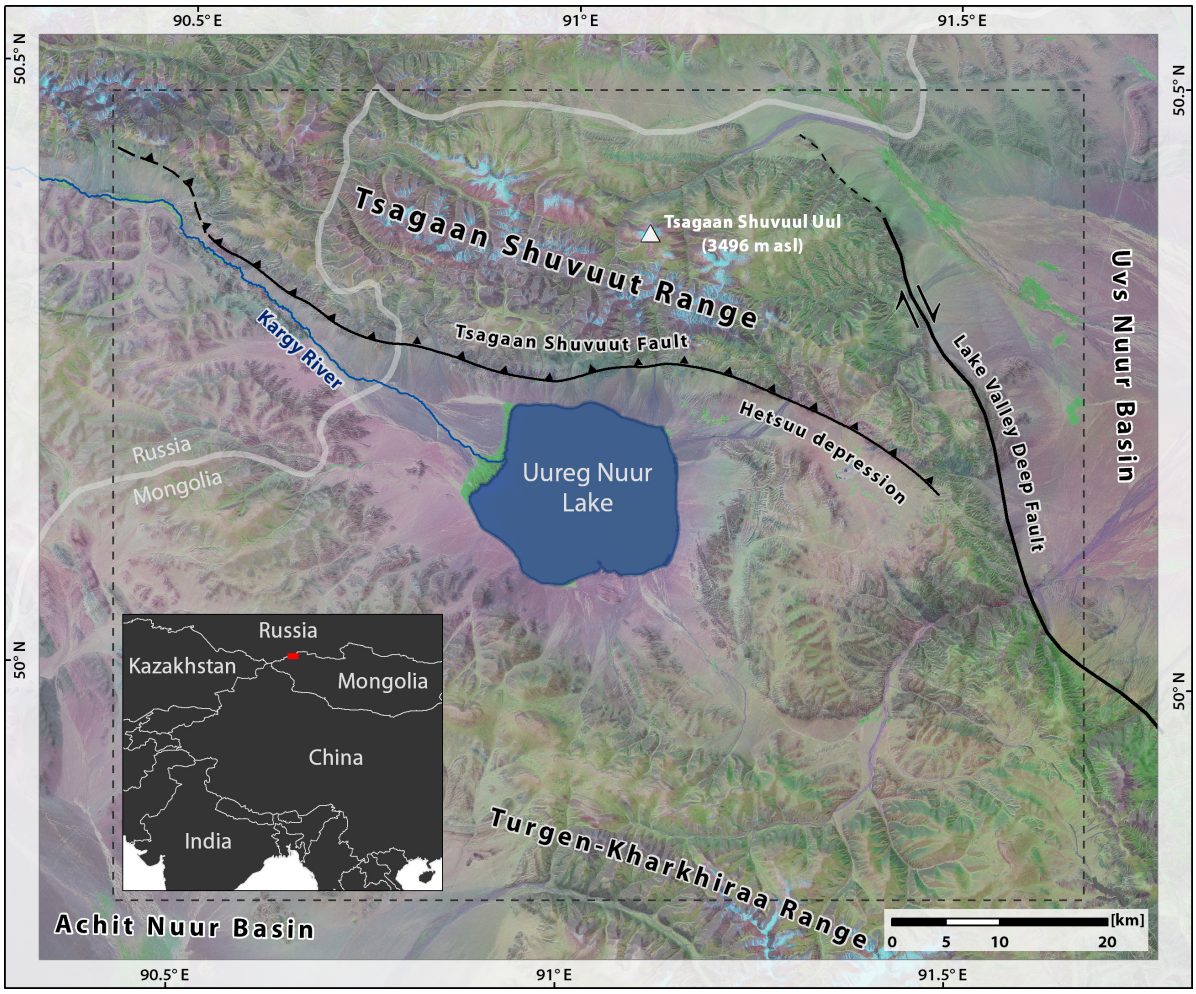


Figure 5.1: Regional overview of the study area in north-western Mongolia. The extent of the object-based processing is denoted by the dashed line.

The Lake Valley Deep Fault (Har-Uvs-Nuur) dextral strike-slip fault is the easternmost fault of the NNW-SSE oriented dextral strike-slip fault system running through the Mongolian Altai. The

termination of the fault system results in a regional compressive regime, which is supposed to be accommodated by uplift of the Tsagaan Shuvuut Range (Walker et al., 2006). The Tsagaan Shuvuut Massif—exhibiting maximum elevations of around 3500 m asl—borders the Uureg Nuur Basin to the north by an abrupt rise of the mountain front, providing high energy regimes for geomorphologic processes (Baljinnyam et al., 1993). The Uureg Nuur Basin is an uplifted endorheic intermontane basin with a saline lake in its center. A small subordinate basin—the Hetsuu Depression—is developed to the east, and connected with the Uureg Nuur Basin by a small corridor. The WNW-ESE-trending Tsagaan Shuvuut fault runs along the southern flank of the Tsagaan Shuvuut Range. Vertical offsets along the fault track are partially apparent in the alluvial fans. A pronounced offset is evident for the corridor between Uureg Nuur Basin and the Hetsuu Depression, indicating a focus of local uplift in this area (cf. Emanov et al., 2012). To the south, the Uureg Nuur Basin is bounded by the Turgen-Kharkiraa Massif and its foothills. The altitudinal gradient is, however, much less pronounced than on the northern side of the basin.

The climate of the study area is characterized by large intra-annual temperature variations, partially exceeding a mean temperature of 20 °C in July and falling below −30 °C in January (Grunert et al., 2000; Kamp et al., 2013). Annual rainfall is about 200 mm at an altitude of 2000 m asl, but may locally exceed 400 mm in the high mountain areas (Grunert et al., 2000; Khrutsky and Golubeva, 2008). The synoptic pattern during the winter season shows as dominance of the Mongolian anticyclone, leading to cold and dry conditions (Morinaga et al., 2003; Böhner, 2006; Kamp et al., 2013). Consequently, only a thin snow cover develops on mountains below 3000 m asl, favoring frost cracking. Slopes are thus covered by thick blankets of debris moving downwards by solifluction (Stolz et al., 2012; Lehmkuhl et al., 2016). In association with pronounced topographic gradients between distinctly uplifted blocks and separating basins this infers favorable conditions for alluvial fan formation (cf. Fig. 5.1).

At present, the study area is entirely unglaciated. For the neighboring Turgen-Kharkhiraa Massif, Pleistocene equilibrium-line altitude (ELA) values of 2900 to 3000 m asl are postulated, indicating a modest impact of the Pleistocene glaciations on the study area (Lehmkuhl, 1998; Grunert et al., 2000; Lehmkuhl et al., 2011). Cosmogenic nuclides datings (^{10}Be) of abandoned alluvial fan surfaces as well as luminescence ages of alluvial fan material consistently show that in the Gobi Altai and the Mongolian Altai, alluviation predominantly took place during transition phases between glacial and interglacial periods (cf. e.g., Owen et al., 1998; Ritz et al., 2003). As the Gobi Altai exhibits no considerable glacial geomorphological inventory, it can be concluded that these major alluviations were induced by an increase in rainfall magnitude and intensity associated with a low vegetation coverage (cf. e.g., Grunert et al., 2000; Ritz et al., 2003; Vassallo et al., 2005). Taking the modest glacial impact in the study area into consideration, we assume that alluvial fan formation in the Uureg Nuur Basin is predominantly related to these transitional climate regimes.

5.4 Data

5.4.1 SRTM dataset

We used digital elevation data, acquired by the Shuttle Radar Topography Mission (SRTM), for method development and evaluation. SRTM was the first project to utilize a spaceborne single-pass SAR

interferometer and enabled near-global DEM generation by the use of C-band radar interferometry (cf. Bamler and Hartl, 1998; Rott, 2009). During an 11-day mission in February 2000, imaging of nearly the complete terrestrial surface between 60° N and 56° S was achieved (Rodríguez et al., 2006; Smith and Pain, 2009). Since September 2014, SRTM data are available with a posting of 1″ for latitudes below 50°. Tiles with a latitude greater than 50° N or 50° S have, however, a posting of 2″ by 1″. As the parallel of 50° north latitude runs through the study area, this complicates the preparation of a mosaicked dataset for this study.

5.4.2 DEM preparation

To prepare a seamless DEM for the whole study area and avoid artifacts at the boundary between 1″ tiles and 2″ by 1″ tiles, the sets of tiles with 1″ posting and 2″ by 1″ posting were separately mosaicked, projected to UTM Zone 46 N and resampled to a posting of 30 m using cubic convolution. Subsequently, the two mosaicked grids were merged with a boundary blending algorithm applying bicubic spline interpolation.

The Shuttle Radar Topography Mission (SRTM) 1″ DEM generally provides decent topographic information, making it suitable for lower mesoscale morphometric analysis (Pipaud et al., 2015 / Chapter 3). Quantitative analysis of the altitude field as modeled by the DEM is, however, affected by a high-frequency texture with moderate magnitude, impairing the morphometric derivatives to be extracted from the DEM altitude values (cf. e.g., Smith et al., 2006; Kervyn et al., 2008; Siart et al., 2009). Segmentation of DEM data is essentially based on discontinuities of the altitude field (cf. Minár and Evans, 2008). Consequently, this substantial topographic signal needs to prevail over noise. To both alleviate the noise signal and simultaneously maintain as much topographic information as possible, we applied mesh denoising on the dataset. Mesh denoising, first proposed by Sun et al. (2007) and adopted for use on topographic datasets by Stevenson et al. (2010), is an adaptive filtering approach being based on transformation of the DEM data lattice into a triangular irregular network and applying a weighted local averaging based on the normal vectors of neighboring facets. The weighting is based on the inverse of the angular difference of normal vectors, assigning larger weights to facets with low angular difference to the facet considered. By defining an appropriate angular difference threshold, above which the respective facet is not considered for filtering, significant topographic information can be preserved. Choosing a threshold of 0.99 and 10 smoothing iterations, we were able both to remove the high-frequency texture and preserve substantial topographic detail.

5.5 Methods

In this section, we introduce the methodological framework developed for extraction of alluvial fan objects from SRTM 1″ data. Section 5.5.1 provides a description of the processing scheme that was applied on the DEM data to yield segmentation objects being suitable for alluvial fan extraction (see Fig. 5.2). In Section 5.5.2, we present a fuzzy classification model geared for the specific morphometric properties of alluvial fans (see Fig. 5.4), and a finalization routine for extraction of alluvial fan objects from the segmentation dataset. Unless otherwise noted, all processing was performed using own routines written in Python programming language. Computation was carried out on a single x86-64

quad-core workstation.

5.5.1 Segmentation

Morphometric parametrization for alluvial fan segmentation

Quantitative information on a surface and its discontinuities is provided by partial derivatives. Discrete datasets like gridded DEMs are, however, not differentiable, and the DEM thus needs to be locally approximated (Reuter et al., 2009). Usually, quadratic or partial quartic polynomials are derived for a 3×3 cell moving window, providing a two times differentiable surface (Evans, 1980; Zevenbergen and Thorne, 1987). As segmentation relies on discontinuities of the altitude field, these discontinuities should be completely captured by partial derivatives and morphometric parameters. Hence, we used the partial quartic for derivation of partial derivatives, as it entails no smoothing and thus fully preserves all topographic detail as modeled by the DEM (Thorne et al., 1987):

$$z = ax^2y^2 + bx^2y + cxy^2 + dx^2 + ey^2 + fxy + gx + hy + i, \tag{5.1}$$

where variables x, y and z are the local Cartesian grid coordinates, and a to i are the coefficients to be derived. The slope (in degrees) of the steepest path down the polynomial surface is calculated as:

$$\text{Slope} = \arctan \sqrt{\left(\frac{\partial z}{\partial x}\right)^2 + \left(\frac{\partial z}{\partial y}\right)^2} \cdot \frac{180}{\pi}, \tag{5.2}$$

where $\frac{\partial z}{\partial x}$ is the first partial derivative of z with respect to x, and $\frac{\partial z}{\partial y}$ is the first partial derivative of z with respect to y. The slope aspect, the direction of the steepest path down the polynomial surface, is defined by:

$$\text{Slope Aspect} = \text{arctan2}\left(\frac{\partial z}{\partial x}, \frac{\partial z}{\partial y}\right) \cdot \frac{180}{\pi} \tag{5.3}$$

Segmentation is based on calculating the differences between neighboring data samples (cf. Baatz and Schäpe, 2000). Being defined in polar coordinates, a direct calculation of local aspect differences does, however, not guarantee to provide correct results, because polar coordinates can differ substantially for small actual differences. It follows that slope aspect needs to be decomposed into its directional components using (cf. Wilson et al., 2007):

$$\text{Slope Aspect}_{\text{easting}} = \sin\left(\text{Slope Aspect} \cdot \frac{\pi}{180}\right) \tag{5.4}$$

$$\text{Slope Aspect}_{\text{northing}} = \cos\left(\text{Slope Aspect} \cdot \frac{\pi}{180}\right) \tag{5.5}$$

Directional curvatures can be calculated by computing second order directional derivatives of the polynomial approximation function. Different directions are applicable for geomorphometric surface parametrization (cf. Gallant and Wilson, 2000; Shary et al., 2002; Schmidt et al., 2003). Here, we calculated the cross-sectional curvature (CCurv), which quantifies the curvature along the line orthogonal to the line of the steepest gradient and thus indicates convergence or divergence of flow processes across the surface (Zevenbergen and Thorne, 1987; Florinsky, 1998; Florinsky et al., 2002;

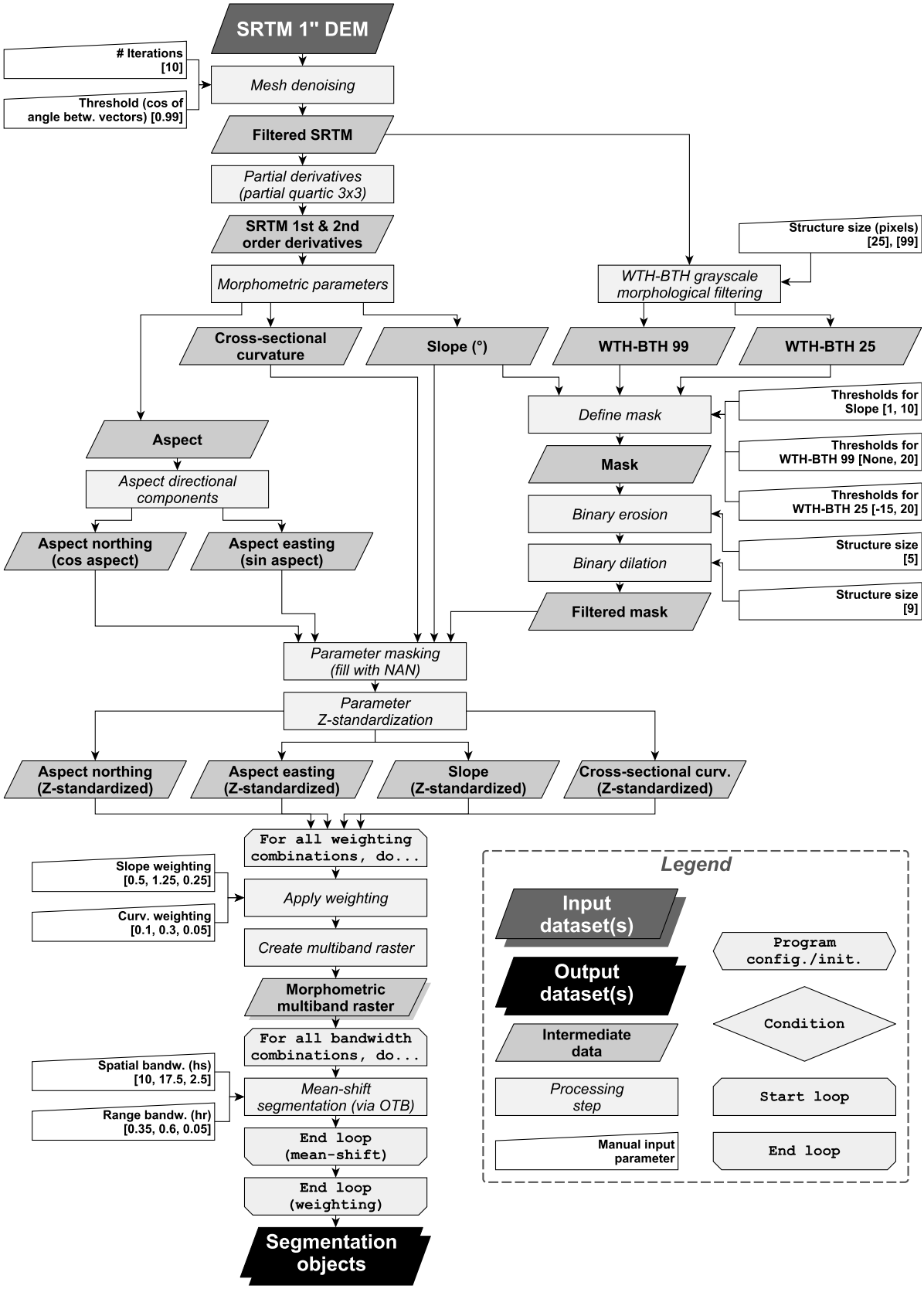


Figure 5.2: Flowchart of the segmentation procedure conducted in this study.

Schmidt et al., 2003):

$$\text{Cross-sectional Curvature} = 200 \cdot \frac{\frac{\partial z}{\partial y}^2 \cdot \frac{\partial^2 z}{\partial x^2} - \frac{\partial z}{\partial x} \cdot \frac{\partial z}{\partial y} \cdot \frac{\partial^2 z}{\partial x \partial y} + \frac{\partial z}{\partial x}^2 \cdot \frac{\partial^2 z}{\partial y^2}}{\frac{\partial z}{\partial x}^2 + \frac{\partial z}{\partial y}^2}, \tag{5.6}$$

where $\frac{\partial^2 z}{\partial x^2}$ is the second partial derivative of z with respect to x, $\frac{\partial^2 z}{\partial y^2}$ is the second partial derivative of z with respect to y, and $\frac{\partial^2 z}{\partial x \partial y}$ is the second partial derivative of z with respect to x and then y.

As we will discuss further in Section 5.5.1, mean-shift algorithms provide a single parameter defining the sensitivity of the segmentation for all features—the range bandwidth. Hence, it is assumed that all incorporated features exhibit equivalent value ranges. Morphometric parameters exhibit, however, quite different value ranges and distribution characteristics (cf. e.g., Speight, 1971; Evans and Cox, 1999; Katsube and Oguchi, 1999; Minár et al., 2013), indicating the necessity to scale them into a common value range or transform their distributions into normalized Gaussian-like distributions (cf. Speight, 1971; Csillik et al., 2015). As the directional components of aspect generally show highly scattered multi-modal density functions, such transformation functions are not feasible for the problem at hand, and we therefore refrained from applying them on any of the four parameters. Instead, we derived Z-standardized values from all morphometric parameters:

$$Z_i = \frac{M_i - \mu}{\sigma}, \tag{5.7}$$

where M_i is a morphometric parameter value of a pixel i, and Z_i is the calculated standardized value. Applying this transformation gives us unity σ for all morphometric parameters, but does not alter distribution shape.

To both mitigate the influence of extreme values and accelerate processing, we applied Z-standardization only on the subset of cells which values indicate potential occurrence of alluvial fans, and excluded all other cells from further consideration. For this purpose, we conducted a thresholding using slope as well as topological context, for which we incorporated grayscale morphological filtering. Combining White Top Hat (WTH) and Black Top Hat (BTH) filters by subtracting the BTH raster from the WTH grid, topologically high positions exhibit positive values, and vice versa (Pipaud et al., 2015 / Chapter 3). In this study, we used two white top hat-black top hat (WTH-BTH) filters with a kernel size of 99 m and 25 m, respectively. The exclusion rule is defined as follows:

$$\{M_i\} = \begin{cases} \{M_i\} & \text{if } 1° < \text{slope} < 10°, \\ & \text{WTH-BTH}_{99} < 20 \text{ m, and} \\ & \text{-15 m} < \text{WTH-BTH}_{25} < 20 \text{ m} \\ \{\text{NAN}\} & \text{otherwise,} \end{cases} \tag{5.8}$$

where $\{M_i\}$ are the values of slope, slope $\text{aspect}_{\text{easting}}$, slope $\text{aspect}_{\text{northing}}$ and cross-sectional curvature for a cell i. Here, the 99 m-sized WTH-BTH kernel was used to exclude low-sloping patches in mountainous areas from the grid passed on for Z-standardization and segmentation. This filter was supplemented by a WTH-BTH filter with a kernel size of 25 m to discard floors of deeply cut mountain

Table 5.1: Weightings applied to slope and cross-sectional curvature before multiband dataset creation.

Morphometric parameter	Minimum weighting	Maximum weighting	Increment	Parameter total
Slope	0.5	1.25	0.25	4
Cross-sectional curvature	0.1	0.3	0.05	5
Total				20

valleys, which exhibit topological low positions on a small scale. For detailed information on the application of mathematical morphology in the field of geomorphology, please refer to Rodriguez et al. (2002), Schmidt and Hewitt (2004) and Pipaud et al. (2015 / Chapter 3). Subsequently, we Z-standardized the morphometric parameters applying the respective mean and standard deviation of all cells satisfying the conditions of the exclusion routine.

We can now fuse the single parameter grids into multiband datasets to be used as input for segmentation. In contrast to segmentation based on spectral data, however, there is no canonical weighting of the input parameters (cf. Section 5.1). To account for this uncertainty, we conducted the fusion repeatedly with different weightings for slope (slope area weighting, SAW) and cross-sectional curvature (cross-sectional curvature weighting, CCW), while keeping both aspect parameters constant. Applying an empirically determined range of weightings as denoted in Table 5.1, we eventually yielded 20 datasets in total.

Mean-shift segmentation

Mean-shift—in its original conceptual design—is a single-parametric approach for locating the modes of a density function, without the necessity to calculate the gradient itself (Fukunaga and Hostetler, 1975; Cheng, 1995; Comaniciu and Meer, 1999, 2002; Wu and Yang, 2007). This essential property can be exploited to provide robust segmentation of multi-dimensional datasets (Comaniciu and Meer, 2002). The algorithm is based on calculating the mean-shift vector $\vec{m}$, which is given by the difference of a centered feature vector $\vec{p}$ and a weighted mean of all n feature vectors p_i within a non-negative and non-increasing kernel K of bandwidth h (Comaniciu and Meer, 2002; Wu and Yang, 2007):

$$\vec{m}(\vec{p}) = \frac{\sum_{i=1}^{n} \vec{p}_i \cdot K\left\{\frac{\|\vec{p}-\vec{p}_i\|}{h}\right\}}{\sum_{i=1}^{n} K\left\{\frac{\|\vec{p}-\vec{p}_i\|}{h}\right\}} - \vec{p} \tag{5.9}$$

In the simplest approach, K is defined as a uniform kernel (Cheng, 1995; Wu and Yang, 2007):

$$K = \begin{cases} 1 & \text{if } \frac{\|\vec{p}-\vec{p}_i\|}{h} \leq 1 \\ 0 & \text{otherwise} \end{cases} \tag{5.10}$$

The kernel window is then translated so that $\vec{p}^{\,(k+1)} = \vec{p}^{\,(k)} + \vec{m}(\vec{p}^{\,(k)})$ (Comaniciu and Meer, 1999). The mean-shift vector always points toward the direction of the maximum increase of the density, and the trajectory of consecutive mean-shift vectors eventually converges on positions where the gradient

$\nabla(\vec{p})$ is zero (Comaniciu and Meer, 2002). Modes for all feature vectors are determined by ensuring that initializations of the mean-shift algorithm cover the entire feature space (Cheng, 1995; Carreira-Perpinan, 2006; Einbeck, 2011). Clusters are then defined by the set of all data points converging to the same mode, i.e., clustering is inherently provided by the mean-shift method and no constraints on cluster shape and the number of clusters are required (Fukunaga and Hostetler, 1975; Cheng, 1995; Carreira-Perpinan, 2006).

This original approach only considers non-spatial attributes of a dataset. To incorporate positional data and provide a framework for segmentation of multidimensional gridded data, separate kernel bandwidths must be provided for the feature domain (range bandwidth, h_r) and the spatial domain (spatial bandwidth, h_s). Subsequently, both kernels are concatenated and the spatial coordinate values are appended to the feature values, establishing a joint domain representation (Comaniciu and Meer, 2002). In this study, we applied the mean-shift routine provided by the open source remote sensing-oriented software Orfeo Toolbox (Inglada and Christophe, 2009), which uses uniform kernel-based mean-shift segmentation.

In trying to conduct delineation of alluvial fans, it is necessary to define both bandwidth parameters in such a way that all fans are segmented along their lateral and distal demarcations, i.e., the whole fan surface must constitute a single cluster. In this context, increasing the range bandwidth increases the probability of low-magnitude feature modes to become subordinated to a more significant mode, and thus leads to a larger average size of segmentation objects. By increasing the spatial bandwidth, in turn, we increase the influence of spatial support on mode-seeking (cf. Ming et al., 2015). It may seem that increasing the spatial influence enhances the average size of segmentation objects as well. Empirical evaluation indicates, however, that increased spatial bandwidths rather cause a reduction of average object size (cf. Suppl. B.1). This counterintuitive effect can be attributed to the fact that increasing the spatial bandwidth while keeping the range bandwidth constant can cause relatively small but high magnitude features to become disconnected from their surroundings and define a separate cluster.

Alluvial fans exhibit considerable variability in terms of size, shape, internal differentiation and their distinctness of delimitation. An inspection of Suppl. B.1 indicates that fixed values for spatial and range bandwidth cannot account for this variability, and that a static parametrization thus cannot provide an accurate overall object delineation for a larger study area. Moreover, the necessity to find appropriate combinations of spatial bandwidth and range bandwidth makes the decision task nontrivial. Hence, we empirically determined an appropriate value range and a step size for both bandwidth parameters (cf. Table 5.2), and performed mean-shift segmentation on all 20 multiband datasets with all bandwidth combinations. This resulted in a total of 480 single segmentation runs.

5.5.2 Classification

Exclusion of implausible objects

All 480 segmentation runs generated approximately 5.8 M polygons in total. In order to keep processing times of the subsequent classification workflow on a feasible level, we applied a routine which excludes polygons with a very low likelihood of belonging to the semantic class alluvial fans from further consideration. Exploiting the fact that alluvial fans are arcuate in plan view (cf. Section 5.2), shape

,

Table 5.2: Bandwidth parameters used for mean-shift segmentation and total number of runs.

Bandwidth parameter	Minimum	Maximum	Increment	Total
h_s	10	17.5	2.5	4
h_r	0.35	0.6	0.05	6
Total (×20 input datasets)				480

measures being based on simple arithmetic expressions can be efficiently used to achieve this exclusion. In this study, we used the polygon fractal dimension (PFD), which is defined as follows (Wu, 2004):

$$\mathrm{PFD} = \frac{\ln\left(0.25 \cdot p_i\right)}{\ln\left(\sqrt{a_i}\right)}, \tag{5.11}$$

where p_i and a_i denote the perimeter and area of a polygon i, respectively. By thresholding the dataset choosing 1.045 and 1.1375 as minimum and maximum PFD values, respectively, and additionally setting the minimum polygon area to 6 ha, we were able to reduce the total polygon count to approximately 118 000 (see Suppl. B.2).

Training dataset preparation

Expert-driven manual geomorphological mapping was carried out to delineate eleven alluvial fans which were selected as reference data for the classification process and evaluation purposes (see Suppl. B.3). We took care to ensure that this selection reflects the variability of alluvial fans occurring throughout the study area. Geomorphological mapping provided by a trained geomorphologist being familiar with the regional setting (cf. Smith, 2011) is the principal quality indicator for unattended segmentation approaches. Given that the segmentation is carried out based on the SRTM DEM and its derivatives, segmentation quality has to be assessed in relation to the intrinsic resolution and quality of the DEM dataset. Therefore, we did not incorporate auxiliary topographical data or optical imagery, and performed the mapping solely using the DEM and basic derivatives, i.e., hillshades with different azimuthal directions of the light source, slope, and directional curvatures.

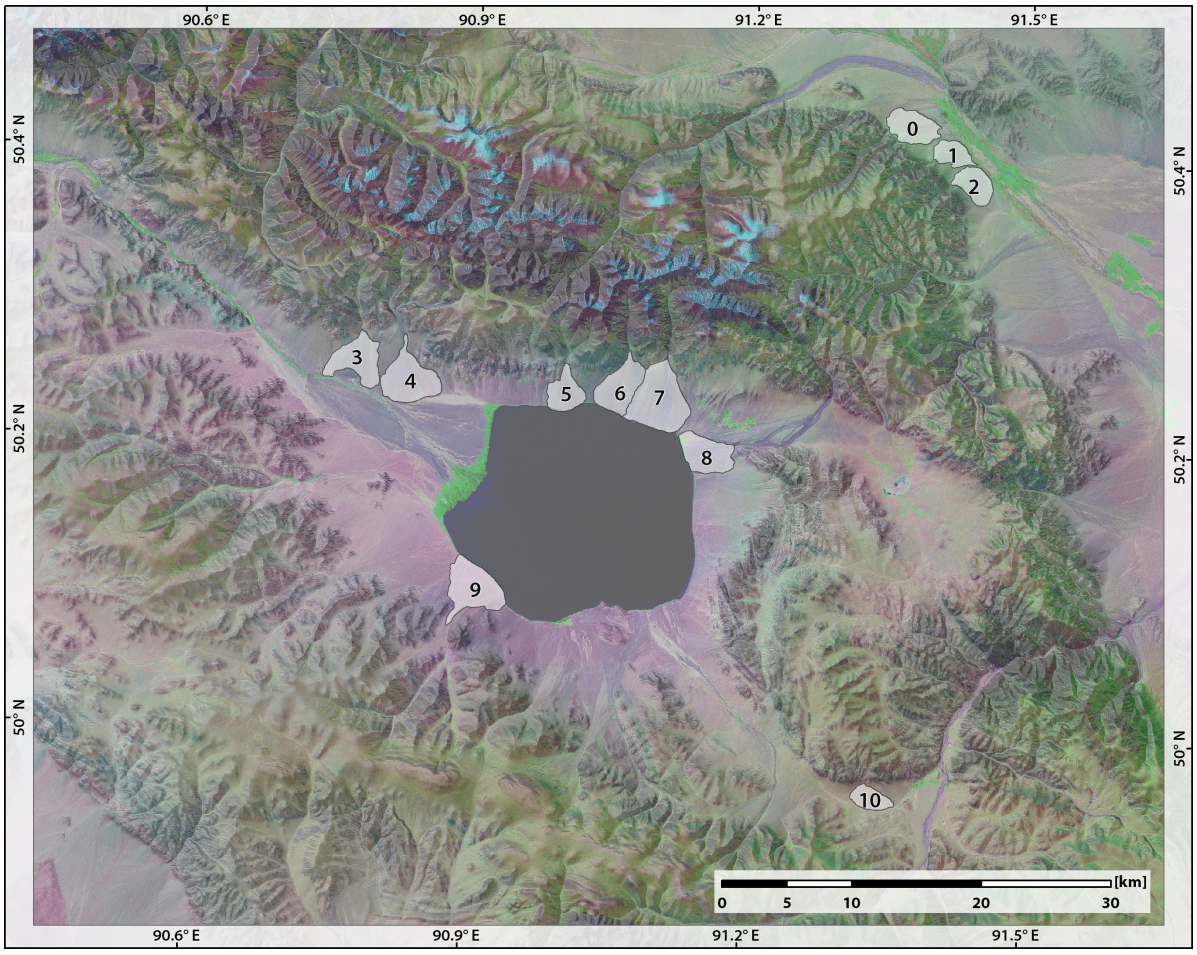


Figure 5.3: Location of the manually delineated reference fans. Reference fans are denoted by their TID.

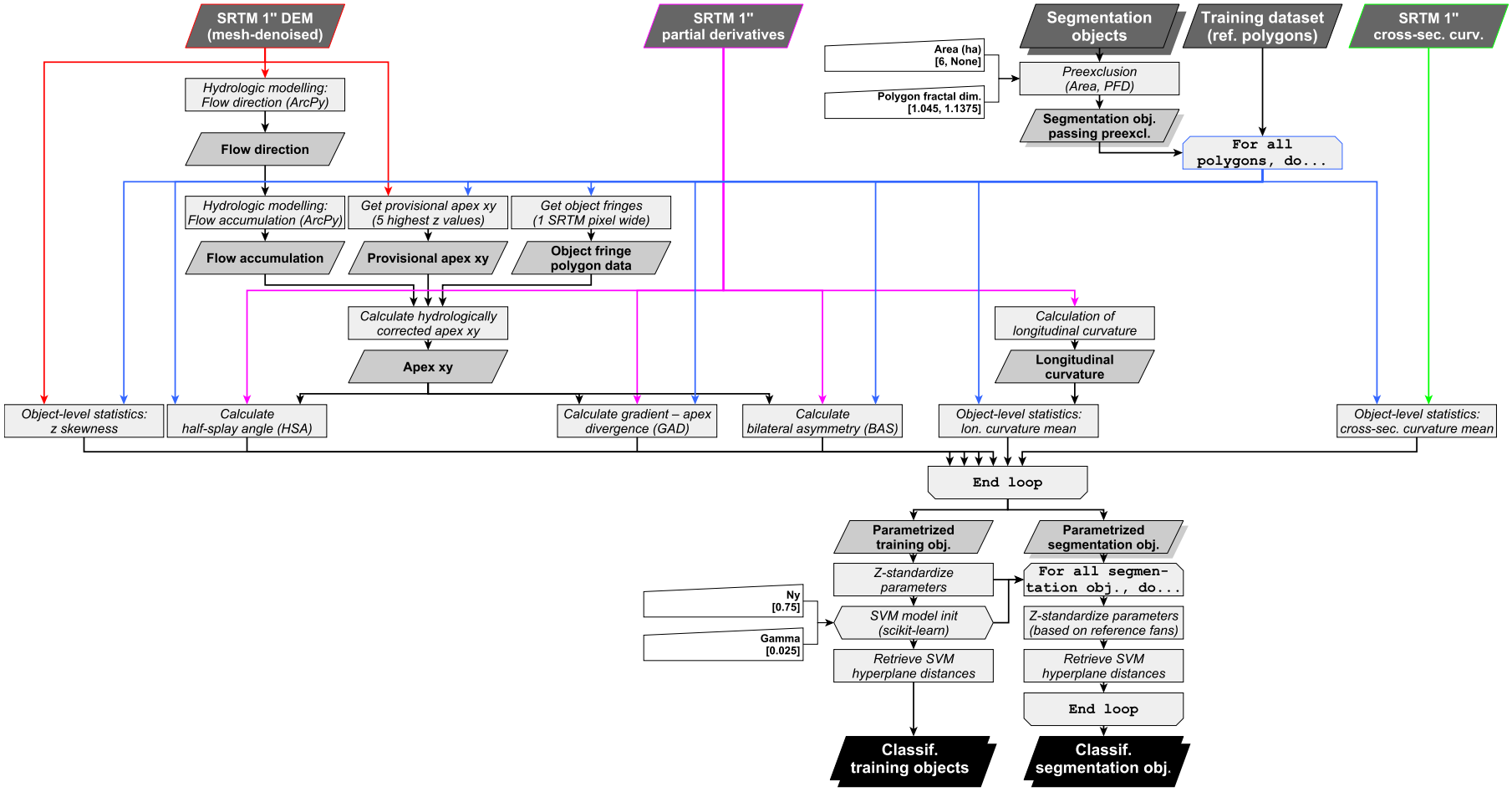


Figure 5.4: Flowchart of the classification procedure conducted in this study. For a legend, please refer to Fig. 5.2.

Morphometric parametrization of segmentation objects

In the case of morphometric parametrization of delineated shapes for classification purposes, the objective is to provide parameters allowing a differentiation between the semantic class(es) of interest—in our case alluvial fans—and the miscellaneous geomorphological features remaining. Applying parameters specifically addressing the morphometric expression of alluvial fans, we can expect alluvial fans to exhibit a low intra-class heterogeneity when compared to the remaining geomorphological inventory. Besides using generic geomorphometric parameters, we thus propose the application of parameters imposing an alluvial fan model on the segmented shapes. We used cross-sectional curvature as introduced in Section 5.5.1. Furthermore, we incorporated longitudinal curvature (LCurv), which describes the curvature along the line of maximum slope and thus indicates acceleration or deceleration of flow processes across the surface (Moore et al., 1993; Shary, 1995; Florinsky, 1998; Gallant and Wilson, 2000; Florinsky, 2012):

$$\text{Longitudinal Curvature} = -200 \cdot \frac{\frac{\partial z}{\partial x}^2 \cdot \frac{\partial^2 z}{\partial x^2} + \frac{\partial z}{\partial x} \cdot \frac{\partial z}{\partial y} \cdot \frac{\partial^2 z}{\partial x \partial y} + \frac{\partial z}{\partial y}^2 \cdot \frac{\partial^2 z}{\partial y^2}}{\frac{\partial z}{\partial x}^2 + \frac{\partial z}{\partial y}^2} \tag{5.12}$$

Note that this definition of longitudinal curvature complies with longitudinal curvature values as provided by ArcGIS, i.e., positive values represent upward-concavity. Subsequently, curvature arithmetic means were calculated for all segmentation objects. As alluvial fans widen downwards, the frequency distribution of the altitude field must be positively skewed. Hence, we also included the skewness of the altitude values (z skewness), which is defined as follows:

$$z \text{ skewness} = \frac{1}{n} \sum_{i=1}^{n} \left(\frac{z_i - \bar{z}}{\sigma_z} \right)^3, \tag{5.13}$$

where n is the pixel count of the object considered, and σ_z is the standard deviation of the altitude values z.

The principal morphometric characteristic of an alluvial fan is its conical shape, which consequently should be exploited for object parametrization (cf. Fig. 5.5A, Section 5.2). Consider a simple model, in which an alluvial fan is resembled by a partial cone with arbitrary aperture angle. Here, the directions of all gradient vectors $\nabla z(x, y)$ exactly reflect the vectors given by the apex of the cone and the respective points (cf. Fig. 5.5B). Hence, any discrepancies from this idealized model will result in an angle between both vectors, and the arithmetic mean of all angles is a measure for the average deviation from the model. We thus introduce the gradient–apex divergence (GAD) parameter, which is given by:

$$\text{Gradient–Apex Divergence} = \frac{1}{n} \sum_{i=1}^{n} \arccos \left(\frac{\overrightarrow{AP_i} \cdot \vec{g_i}}{\|\overrightarrow{AP_i}\| \cdot \|\vec{g_i}\|} \right) \cdot \frac{180}{\pi}, \tag{5.14}$$

where $\overrightarrow{AP_i}$ is the vector given by the apex A to the point $P_i(x, y)$, and $\vec{g_i}$ is the vector given by the gradient $\nabla z_i(x, y)$ in point $P_i(x, y)$. For alluvial fans, we generally can expect GAD values to be low. Most alluvial fans, however, will considerably deviate from the idealized conical shape in the proximity of the apex and in the most distal parts. In the case of the proximal areas, such deviations are mostly

induced by a channel being incised into the fan as far as the intersection point (cf. Section 5.2). In the most distal parts, lateral undercutting can induce linear incision (cf. Crosta and Frattini, 2004). Therefore, it is appropriate to exclude the proximal and distal parts from the GAD calculation. In this study, we defined minimum and maximum distance as percentage of the distance between the apex and the most distant point on the alluvial fan surface, taking 0.2 as minimum value and 0.8 as maximum.

Other characteristics of alluvial fans are that (1.) they are often symmetric, and (2.) that their aperture angles typically vary within a modest range (cf. Section 5.2). Both characteristics can be parametrized by initially calculating the mean gradient vector of the segmentation object considered and then splitting the polygon along the line given by the apex and the mean gradient vector into two halves. In this context, the next parameter we developed is the bilateral asymmetry (BAS) index being defined as follows (cf. Fig. 5.5C):

$$\text{Bilateral Asymmetry} = \frac{|A_1 - A_2|}{|A_1 + A_2|}, \tag{5.15}$$

where A_1 and A_2 define the area of the split halves. The angle between the mean gradient vectors of both halves provides an indicator of the aperture angle of the alluvial fan. The half-splay angle (HSA) is given by (cf. Fig. 5.5D):

$$\begin{aligned} \bar{\nabla}_{S_1} = \frac{1}{n} \cdot \sum_{i=1}^{n} \nabla_i \,, \quad \bar{\nabla}_{S_2} = \frac{1}{m} \cdot \sum_{j=1}^{m} \nabla_j \,, \\ \text{Half-splay Angle} = \arccos \frac{\bar{\nabla}_{S_1} \cdot \bar{\nabla}_{S_2}}{\left\|\bar{\nabla}_{S_1}\right\| \cdot \left\|\bar{\nabla}_{S_2}\right\|} \cdot \frac{180}{\pi}, \end{aligned} \tag{5.16}$$

where S_1 and S_2 denote the surface patches resulting from the split, ∇i and ∇j denote the gradients of points i and j, respectively, and n and m denote the pixel count of the split segment considered. In the case of alluvial fans, the HSA can be expected to be approximately half of the aperture angle.

When using the BAS and the HSA for object parametrization and subsequent classification, we must bear in mind that these parameters are, in comparison to the GAD, based on a more restrictive model of alluvial fan shape. Local topography may impose constraints on the direction of alluvial deposition, potentially leading to asymmetric fan growth (cf. Cavalli and Marchi, 2008), and, consequently, increased BAS values. Aperture angles can vary substantially within a study area, leading to a considerable range of HSA values. Furthermore, fans may exhibit variations of their radial slope angles. This typically occurs for alluvial fans exhibiting intensive lateral coalescence. E.g., in the case of a bajada, slope angles in direction of the radial margins are reduced, $\bar{\nabla}_{S_1}$ and $\bar{\nabla}_{S_2}$ are more influenced by gradient vectors in proximity of the central axis, and the HSA is thus lower than half of the aperture angle. In contrast, steeper fans may exhibit increasing gradients when approaching their radial margins (cf. Hooke and Rohrer, 1979, see also Section 5.2).

For the specific morphometric parameters addressed above, a correct localization of the apex is crucial, i.e., we need to exactly identify the point reflecting the emergence of the feeder channel from the mountain front. To conduct a hydrologically correct apex placement, we first calculated the mean position vector of the five pixels exhibiting the highest DEM pixel values, thus taking inaccuracies of the DEM into consideration. Subsequently, we determined the hydrological flow paths using the flow direction and flow accumulation routines provided by the ArcGIS 10.2/ArcPy API. Eventually, the

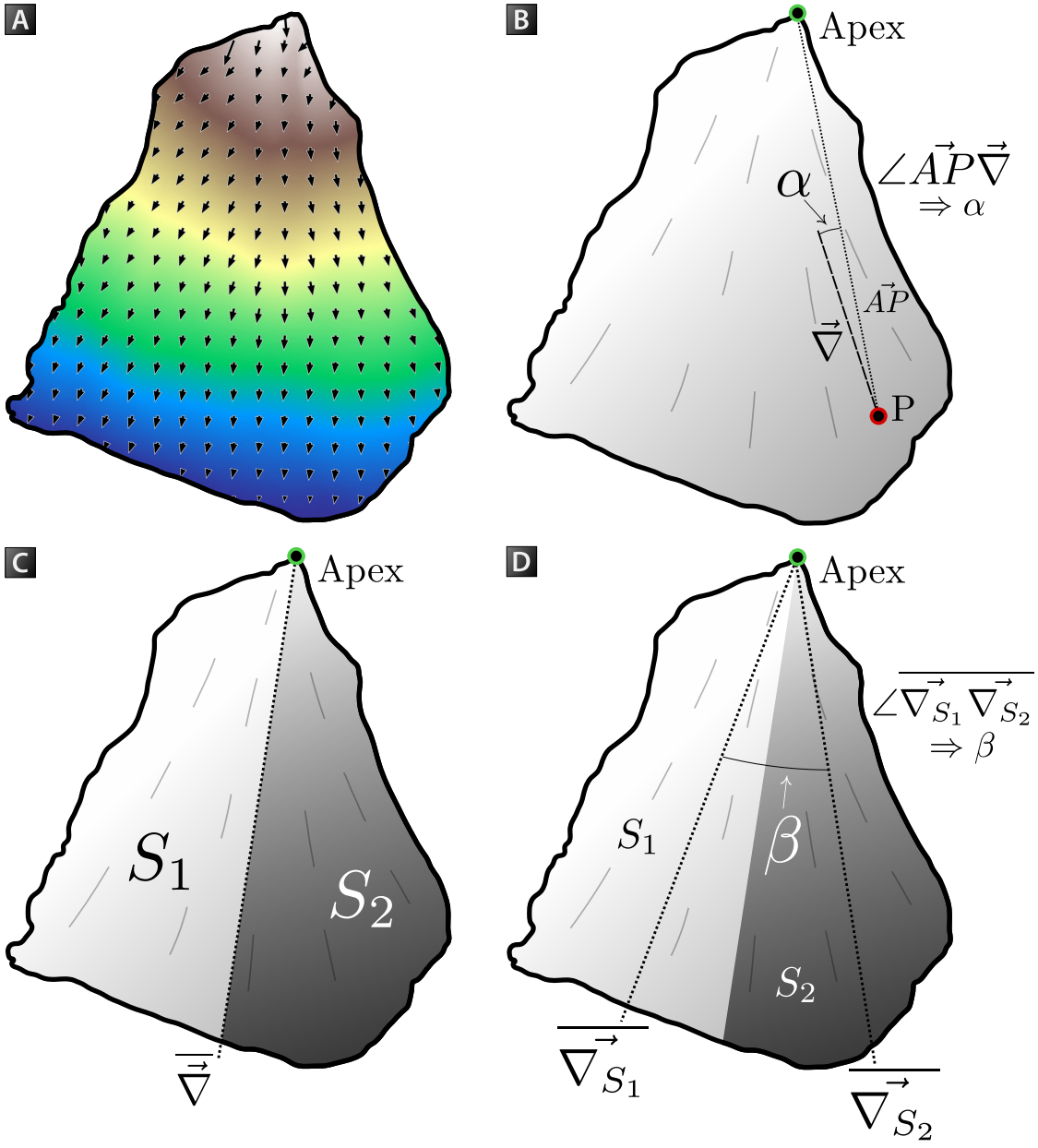


Figure 5.5: Illustration of the specific morphometric parameters exploiting the conical shape of alluvial fans. (A) Smoothed gradient field of reference fan TID 7 (cf. Fig. 5.3). (B) Principle of gradient–apex divergence (GAD) calculation. For each pixel on the fan surface, the angle between the local gradient $\nabla z_i(x, y)$ and the vector defined by pixel and fan apex is calculated. The GAD is then given by the arithmetic mean of all angles. (C) Principle of bilateral asymmetry (BAS) calculation. The mean vector of the fan gradient field is used to split the fan into two segments which are then used for area difference calculation. (D) Principle of half-splay angle (HSA) calculation. For both segments, the mean vector of the gradient field is determined. The HSA is defined as the angle between these two vectors.

preliminary apex point is shifted to that pixel lying on the outer rim of the object, which exhibits the largest flow accumulation.

One-class support vector machines

We can now use a support vector machine (SVM) algorithm to classify the segmentation dataset according to the morphometric parameters described in Section 5.5.2. An SVM is a supervised non-probabilistic binary classifier being based on calculation of a hyperplane optimally separating a training dataset into two classes (Boser et al., 1992; Vapnik, 2000). Consider a set of training samples mapped into p-dimensional feature space, where each sample vector is assigned to one of two classes. Let it be supposed that these two classes are linearly separable by a hyperplane. The optimal hyperplane is then given by maximizing the margin between these two categories (Hastie et al., 2009). This decision function is only specified by the sample vectors being critical for the hyperplane positioning, the support vectors (Cristianini and Shawe-Taylor, 2000). After being mapped into feature space, novel samples can be assigned to one class based on the SVM model prediction, i.e., based on which side of the hyperplane they are situated.

In most instances, however, real-world datasets are not linearly separable, e.g., the boundary is non-linear or noisy and the dataset may contain outliers. Two approaches were proposed to overcome this issue, making SVMs applicable to complex real-world problems. Soft margin variants introduce a slack variable to allow some training observations to be localized within the margin, preventing SVM classifiers from overfitting with noisy data (Cortes and Vapnik, 1995). Non-linear boundaries can be introduced into SVM classification by using kernels to map the data into a higher-dimensional space where the data becomes linearly separable by a hyperplane (cf. Boser et al., 1992). A common kernel is the Gaussian radial basis function (RBF) kernel, which is defined as (Vert et al., 2004; Chudzian, 2011):

$$K(\vec{v}_1, \vec{v}_2) = \exp\left(-\gamma \cdot \|\vec{v}_1 - \vec{v}_2\|^2\right) \quad \text{for} \quad \gamma > 0, \tag{5.17}$$

where $\vec{v}_1$ and $\vec{v}_2$ are two feature vectors of any dimension, and γ defines the distance dependence. As the value of K decreases with increasing Euclidean distance of the two observation vectors, distant feature vectors exhibit only a relatively slight impact on boundary determination. High values of γ lead to a pronounced local behavior potentially leading to overfitting. If γ is low, in contrast, the model may be very constrained, resulting in a strongly generalized separating boundary.

In the case of OBMA focusing on a single type of landform, it is unfeasible to provide reference data for the full geomorphological inventory of a study area. Instead, we aim to create a representational model for the landform of interest, and test if new observations represent new members of this semantic class or if they have to be defined as novelties. A modification of SVM classification for single class problems was proposed by Schölkopf et al. (2001). It is, in short, based on defining the origin as the only member of a secondary class, from which the training dataset is to be separated in an optimal manner. The objective function of a OCSVM is given by (Schölkopf et al., 2001):

$$\min_{\vec{w},\xi} \left\{ \|\vec{w}\| + \frac{1}{\nu \cdot n} \cdot \sum_{i=1}^{n} \xi + b \right\} \quad \nu, \xi \in [0,1], \tag{5.18}$$

where $\vec{w}$ is the surface normal vector of the hyperplane, b is the offset (scalar) from the origin, ξ is the slack variable, which allows feature vectors to be located within the margin, and ν defines the upper bound on the fraction of outliers. Higher values of ν allow a more generalized separating boundary at the expense of more training samples being treated as outliers.

For the study at hand, we conducted one-class SVM classification using the implementation provided by scikit-learn, an open source machine learning library for Python (Pedregosa et al., 2011). Besides the binary class value, the scikit-learn implementation of the algorithm also provides Euclidean distance values of feature vectors to the boundary of the representative model, with positive values stating that the considered features are located inside the model boundary, and vice versa. The representative model for the reference alluvial fans was obtained utilizing soft margins and an RBF kernel, and all segmentation datasets were classified accordingly. Choosing $\gamma = 0.025$ and $\nu = 0.75$, we decided for a representative model with a relatively generalized separating boundary. This conservative approach is motivated by the small number of reference fans, which involves a low statistical support. Hence, the training dataset does not allow assumptions on the detailed shape of the alluvial fan parent population in feature space, and a conservative parametrization is thus indispensable to avoid overfitting. These aspects entail, however, that objects located outside the model boundary may actually still be alluvial fans. Consequently, it is reasonable to treat the Euclidean distance to the model boundary as a fuzzy-like membership value (called SVM score hereafter), allowing an analysis of the level of similarity between sample objects and the reference fans.

Dataset fusion

The described approach of repeatedly applying mean-shift segmentation with different weightings of the morphometric input data and kernel bandwidths entails that all single segmentation results—morphometrically characterized and classified according to the procedure described in the subsection at hand—need to be fused into a final OBMA dataset. Varying the weightings of the morphometric parameters used for segmentation implies that discontinuities of the altitude field are reflected differently among the set of multiband datasets. The bandwidth parameters specify the minimum magnitude of a density maximum in spatial domain and feature domain to define a pool of attraction in the final result. These two aspects induce variable object boundaries, which, in turn, may result in segmentation objects overlapping each other. If we intend to obtain discrete objects, we have to establish the topological constraint that segmentation objects may share parts of their boundaries, but must not overlap each other.

In this study, we first applied a SVM threshold of -2 to all classified datasets, discarding all polygons exhibiting a very low likelihood of representing an alluvial fan (cf. Suppl. B.4). This thresholding reduced the total polygon count to roughly 7500 objects. We implemented overlap resolve as illustrated by the flowchart given in Suppl. B.5. Initially, all remaining polygons were merged into a single shapefile. Subsequently, we identified all overlapping polygons using the ArcGIS 10.2/ArcPy API. If the overlapping area amounts to more than ten percent of the full extent of either of the two polygons, this is considered a significant overlap and it is appropriate to assume that both polygons partly represent the same geomorphological phenomenon. In such cases, that object exhibiting the higher area-weighted score is preserved, the other one discarded. On the contrary, overlapping areas accounting for less than

ten percent of the extent of either of the two objects are considered to be caused by discontinuities being represented differently among the incorporated morphometric parameters, implying that both objects actually represent different geomorphological phenomena. Therefore, the overlapping part of the lower rated object is trimmed to match the boundary of the higher ranked object, and both objects are included in the final classification result.

By dividing the SVM scores of the objects by the respective polygon areas and using this value as quality criterion, we acknowledge that the alluvial fan model constraints defined by the classification parameters are more easily to fulfill for smaller objects. In the case of larger alluvial fans, the spatially and temporally dynamic nature of alluvial fan sedimentation more likely will induce deviations from the ideal alluvial fan model (cf. Section 5.2). Applying the finalization routine to the OBMA dataset, we eventually yielded 114 objects (see Fig. 5.7).

5.6 Results

5.6.1 Reference fans

Table 5.3 displays the results of the morphometric calculations for the reference dataset. As expected, all reference fans exhibit positive z skewness values, concave radial shapes in average and relatively low values for the gradient–apex divergence (GAD) and the bilateral asymmetry (BAS) parameters. The half-splay angle (HSA) varies between 20.7 and 39.4°. Surprisingly, reference fan TID 3 exhibits a slightly negative mean cross-sectional curvature value of −0.04, presumably being induced by the pronounced feeder channel extending up to the mid-fan area. In contrast, all other reference fans are characterized by positive CCurv values. It is noteworthy that the magnitude of mean CCurv is often lower than respective longitudinal curvature values. This may indicate that, in such cases, channels and/or levees running in gradient direction significantly lower the arithmetic means of cross-sectional curvature.

Also denoted in Table 5.3 are the mean slope angles obtained for the reference fans. Because alluvial fans show a characteristic range of slope values (cf. Section 5.2), it may seem that mean slope angles should be applicable for classification. Recall, however, that lower and upper slope thresholds of one and ten degrees, respectively, were already applied to the multiband raster passed on for segmentation (cf. Section 5.5.1). In this context, a range between 1.8° (TID 9) and 5.5° (TID 6) casts doubt on the explanatory potential slope angles can have for the SVM-based classification of the alluvial fan inventory in this study. Preliminary investigation confirmed that incorporation of slope angle actually impairs the classification quality, and the parameter was therefore not used for classification.

Training the OCSVM model with the Z-standardized parameter dataset of the reference fans, we obtained relatively low SVM scores varying between 0.22 and −1.19 (cf. Table 5.3). It is striking that the majority of training fans exhibits negative scores, and thus is situated outside of the SVM decision surface delimiting the semantic class alluvial fans. This result is to be expected, because we opted for a generalized representative model allowing such violations of the margin (cf. Section 5.5.2). Still, SVM scores are mostly above −0.5, showing that these fans lie near to the model boundary. Displaying an outstanding low SVM score of −1.19, reference fan TID 0 is a notable exception in this respect. Examining this fan more in detail, it becomes apparent that this fan is built by two feeder streams of

Table 5.3: Morphometric parameter values and SVM scores for the reference fan dataset. Numbers in brackets denote Z-standardized values. Numbers in italics indicate corresponding mean slope angles (in degrees). Due to the wide range of values, mean slope angle proved to be a poor parameter for classification of this particular study area. Hence, it was omitted for calculation of SVM scores.

TID	z skewness	LCurv	CCurv	GAD	BAS	HSA	SVM score	*Slope*
0	0.04 [−1.67]	0.08 [−1.03]	0.18 [0.26]	15.7 [2.59]	0.16 [0.17]	20.6 [−1.64]	−1.19	*3.4*
1	0.30 [−0.71]	0.09 [−0.89]	0.45 [2.24]	5.0 [−0.88]	0.20 [0.70]	39.4 [0.91]	−0.72	*4.4*
2	0.66 [0.60]	0.25 [0.71]	0.26 [0.87]	4.5 [−1.07]	0.08 [−0.90]	47.1 [1.96]	−0.45	*3.8*
3	0.35 [−0.54]	0.13 [−0.51]	−0.04 [−1.44]	10.8 [1.00]	0.08 [−0.90]	24.7 [−1.09]	−0.28	*4.1*
4	0.85 [1.30]	0.15 [−0.28]	0.16 [0.08]	6.9 [−0.26]	0.09 [−0.67]	33.1 [0.06]	0.14	*4.1*
5	0.81 [1.13]	0.38 [2.04]	0.27 [0.93]	5.2 [−0.84]	0.09 [−0.69]	34.4 [0.22]	−0.45	*5.3*
6	0.26 [−0.86]	0.15 [−0.36]	0.14 [−0.09]	6.5 [−0.41]	0.19 [0.65]	31.9 [−0.12]	0.22	*5.5*
7	0.43 [−0.23]	0.19 [0.13]	0.09 [−0.46]	7.0 [−0.23]	0.02 [−1.70]	23.4 [−1.26]	−0.17	*4.6*
8	0.42 [−0.27]	0.14 [−0.41]	0.01 [−1.05]	6.4 [−0.44]	0.22 [1.05]	32.9 [0.02]	0.00	*2.3*
9	0.97 [1.73]	0.08 [−1.06]	0.05 [−0.76]	9.0 [0.40]	0.28 [1.81]	33.0 [0.04]	−0.78	*1.8*
10	0.36 [−0.49]	0.34 [1.65]	0.07 [−0.57]	8.2 [0.14]	0.18 [0.49]	39.4 [0.90]	−0.11	*2.8*

similar dimension (cf. Fig. 5.6), whose *sub-fans* seamlessly merge at the mid section of the fan. The sedimentation pattern thus cannot be traced back to a single deposition source, leading to high GAD values. As a further consequence of the sub-fan merge, the central section is rather flat than convexly curved, inducing both low CCurv and HSA values. In the case of fan TID 1, which is directly located to the south of fan TID 0, a high cross-sectional curvature induces a relatively low SVM score of −0.72. Eventually, fan TID 9 also shows a relatively low SVM score of −0.78. Being the sole reference fan located at the southern shore of the Uureg Nuur, this fan exhibits low normalized values of longitudinal and cross-sectional curvature (cf. Section 5.3, Fig. 5.3). Moreover, it also displays a high BAS value. This peculiarity is induced by the absence of a clear apex, which results from the laterally extensive transition between the upstream alluvial plain and the fan. Consequently, the modeled apex is located off-center, having an allegedly high asymmetry as a consequence.

To provide a quantitative assessment of the robustness of the classification approach, we conducted a leave-one-out cross validation (LOOCV) by repetitively removing one polygon from the dataset and classifying it on basis of the remaining training polygons, applying the classification workflow as described in Section 5.5.2. Comparing the LOOCV SVM scores with the scores yielded as part of the model calibration run, it is noticeable that when ordered by scores, the sequence of the fans nearly remains the same. An inspection of Table 5.4 shows that differences between the calibration case and the LOOCV strongly relate to this sequence, with fans exhibiting negative scores now showing even lower values, and fans with positive SVM scores now having even higher scores. These results indicate that the model has indeed a stable, conservative behavior, because the removal of one reference polygon from the training dataset does not significantly alter the separating hyperplane of the model. Again, fan TID 0 displays an exceptionally low SVM score of −2.81. All other fans stay above SVM values of approximately −1.5.

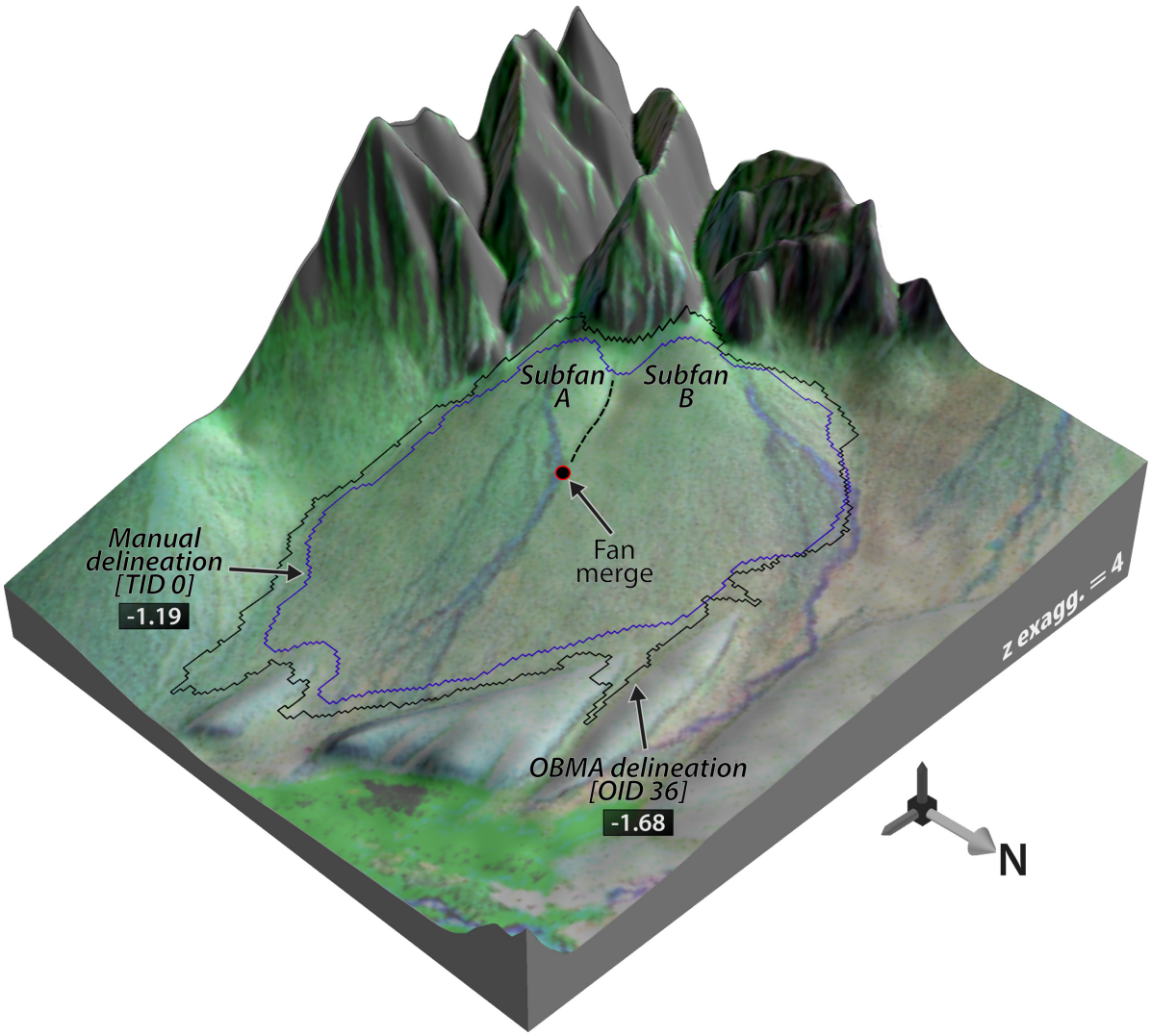


Figure 5.6: Perspective view on reference fan TID 0, located at the eastern flank of the Tsagaan Shuvuut Massif (refer to Fig. 5.7 for exact location). The manual delineation result is displayed by the blue outline. The black outline shows the segmentation result. Numbers in white font denote corresponding SVM scores. The internal subdivision of the fan entails low SVM scores for both reference fan and OBMA object. The higher score of the reference fan polygon is induced by the more conservative delineation, leading to a lower apex positioning and lower GAD values. (Data source: SRTM 1″, Landsat ETM+ pan-sharpened)

Table 5.4: Leave-one-out cross validation (LOOCV) morphometric parameters (Z-standardized) and LOOCV SVM score values obtained for the reference dataset.

TID	z skewness	LCurv	CCurv	GAD	BAS	HSA	SVM score
0	−2.06	−1.14	0.28	4.74	0.18	−2.01	−2.81
1	−0.77	−0.97	3.32	−0.96	0.75	0.99	−1.51
2	0.65	0.77	0.95	−1.19	−0.99	2.61	−1.02
3	−0.57	−0.54	−1.70	1.10	−0.98	−1.22	−0.51
4	1.49	−0.30	0.08	−0.28	−0.72	0.06	0.25
5	1.27	2.80	1.02	−0.91	−0.75	0.24	−1.05
6	−0.94	−0.38	−0.10	−0.44	0.69	−0.12	0.31
7	−0.25	0.14	−0.49	−0.24	−2.11	−1.44	−0.57
8	−0.28	−0.44	−1.16	−0.47	1.17	0.02	0.09
9	2.16	−1.18	−0.82	0.42	2.32	0.04	−1.16
10	−0.52	2.03	−0.60	0.15	0.52	0.99	−0.39
10	0.52	2.03	0.60	0.15	0.52	0.99	0.39

5.6.2 OBMA result – exploratory analysis

All reference fans were successfully delineated and classified, and the obtained shapes strongly resemble the manual delineations. Considering those segmentation objects yielding the highest degree of mutual overlap with the reference polygons, we obtained degrees of overlap between 0.78 and 0.89 (cf. OVLP_{AW}, Table 5.5). These high degrees of overlap (cf. Drăguţ et al., 2014; Eisank et al., 2014) indicate that the proposed OBMA workflow delineates the reference fans along the same major morphometric discontinuities. Considerable differences are only apparent for areas where the distal boundary is indistinct. SVM scores of the OBMA objects are—with the single exception of reference fan TID 0—higher than the respective reference polygon scores, suggesting that the objects better reflect the alluvial fan model than the manually digitized polygons. Besides, OBMA SVM scores fall in the positive range except for reference fans TID 0 and TID 2 (cf. Table 5.5).

In order to analyze the effects of area weighting conducted as part of the topological cleansing routine, we also produced a topologically cleansed dataset produced with no area weighting applied (NAW dataset), and calculated the maximum degree of mutual overlap with the reference delineation (OVLP_{NAW}). Comparing both variables, we see that OVLP_{NAW} has a tendency to exhibit lower values and a larger variability for lower SVM scores (cf. Table 5.5). In contrast, reference fans with high SVM scores display comparable values of OVLP_{AW} and OVLP_{NAW}. SVM scores of the default dataset are substantially lower than those of the NAW dataset in cases where the difference in mutual overlap is high.

As can be seen from Suppl. B.6, low values of OVLP_{NAW} are related to relatively small NAW polygon footprints. In such cases, the respective fans often exhibit one or more additional, smaller NAW polygons. These smaller polygons are regularly located at marginal positions and show low SVM scores, indicating that an exclusion of marginal zones improves SVM scores obtained for the main polygon at the expense of coverage (cf. TID 2 in Table 5.5 and Suppl. B.7). If we consider Suppl. B.6

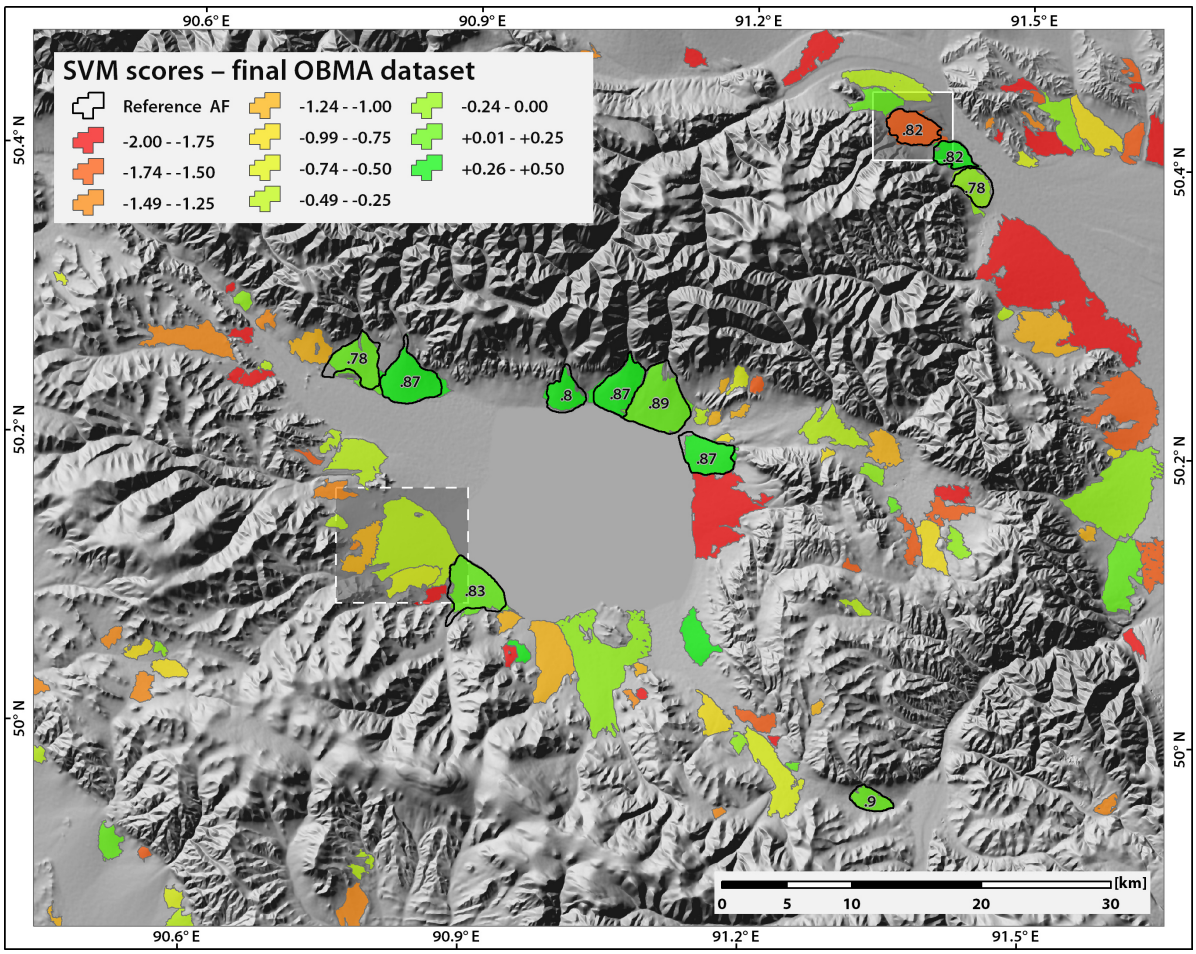


Figure 5.7: Final OBMA objects and their SVM scores, after merging and topological cleansing with area weighting. Labels denote the degree of mutual overlap between reference fans and the corresponding OBMA objects. Continuous and dashed white outlines denote the extent of Fig. 5.6 and Fig. 5.9, respectively.

in more detail, it becomes apparent that no morphologically plausible splits of segmentation objects are obtained when overlap resolve is computed without area weighting. In the case of fan TID 0, for example, the full fan surface is made up by one major and two smaller polygons, and the complete distal fan zone is assigned to the orographically left sub-fan. An inspection of Fig. 5.6 shows, however, no reasons for such a split. Still, fan TID 0 is a remarkable exception in that all NAW polygons making up the fan surface exhibit somewhat higher SVM scores than the default OBMA object (cf. Fig. 5.7 and Suppl. B.7). This is again due to fan TID 0 exhibiting two feeder channels and, consequently, a low GAD value.

The aforesaid results indicate that alluvial fan polygons with higher SVM scores are characterized by relatively homogeneous surfaces, so that the highest-scored segmentation polygon already covers the full alluvial fan surface or at least large parts of it. Conversely, alluvial fans exhibiting more complex surfaces can be subdivided into one major and one or more minor segments, the major segment showing higher SVM scores than the full fan surface. The splits between these segments occur, however, at subtle gaps in feature space, which generally do not represent clearly discernible morphological

Table 5.5: Relationships between mutual overlaps and SVM scores for the reference fans. Mutual overlaps between OBMA objects generated with area weighting and the reference fans, mutual overlaps between OBMA objects generated without area weighting and the reference fans, and SVM scores of the reference dataset, the default OBMA dataset, and the OBMA dataset produced with no area weighting applied. Reference fans are sorted by their manual delineation SVM score in descending order.

TID	Overlap with area weighting ($OVLP_{AW}$)	Overlap without area weighting ($OVLP_{NAW}$)	SVM score (manual delineation)	SVM score ($OVLP_{AW}$= default)	SVM score ($OVLP_{NAW}$)
6	0.87	0.88	0.22	0.43	0.43
4	0.87	0.81	0.14	0.36	0.37
8	0.87	0.87	0.00	0.34	0.34
10	0.90	0.89	−0.11	0.06	0.07
7	0.89	0.90	−0.17	0.17	0.17
3	0.78	0.77	−0.28	0.06	0.09
5	0.80	0.80	−0.45	0.39	0.39
2	0.78	0.62	−0.45	−0.18	0.20
1	0.82	0.79	−0.72	0.35	0.43
9	0.83	0.83	−0.78	0.18	0.18
0	0.82	0.66	−1.19	−1.68	−0.97

discontinuities. Area-weighting helps prevent such alluvial fans from getting subdivided, but can slightly worsen segmentation results in case of high SVM scores (cf. TID 1 in Table 5.5).

Visual examination of the classification result indicates that also the vast majority of all other larger alluvial fans could be successfully segmented and classified (cf. Fig. 5.7). Specifically, the delineation result consistently reflects principal morphometric discontinuities as depicted by generic morphometric parameters and hillshade maps, and our approach is thus able to reliably delimit both unconfined and confined alluvial fans. A notably exception is given for the corridor between the Uureg Nuur Basin and the Hetsuu Depression, where a distally constrained and markedly dissected alluvial fan is only partly delineated. At the southern margin of the Uureg Nuur Basin, some small-sized alluvial fans were delineated incompletely or were not delineated at all. Here, complex lateral and distal coalescence occurs in association with low slope angles, leading to scarcely marked discontinuities between fans (detail a, please refer to Fig. 5.8 for locations). Due to vague lateral boundaries, the segmentation routine was not capable of delineating two alluvial fans at the eastern shore of the Uvs Nuur, thus yielding a single polygon for both. As this *meta* object violates constraints imposed by the classification parameters, it consequently shows a low SVM score (cf. Fig. 5.7).

Pronouncedly incised feeder channels are generally excluded from segmentation, indicating that the rather sudden transition from incision to lateral deposition at the channel walls and at mid-fan section is identified as a major morphometric discontinuity (cf. detail b). In such cases, the algorithm used in this study will place the apex at a position beside the feeder channel, and calculation of morphometric parameters being dependent on correct apex placement can be negatively affected. In the study at hand, however, classification of the OBMA objects concerned does not seem to be significantly influenced by deficient apex placement. At the south-western shore, a large depositional lobe was delineated separately

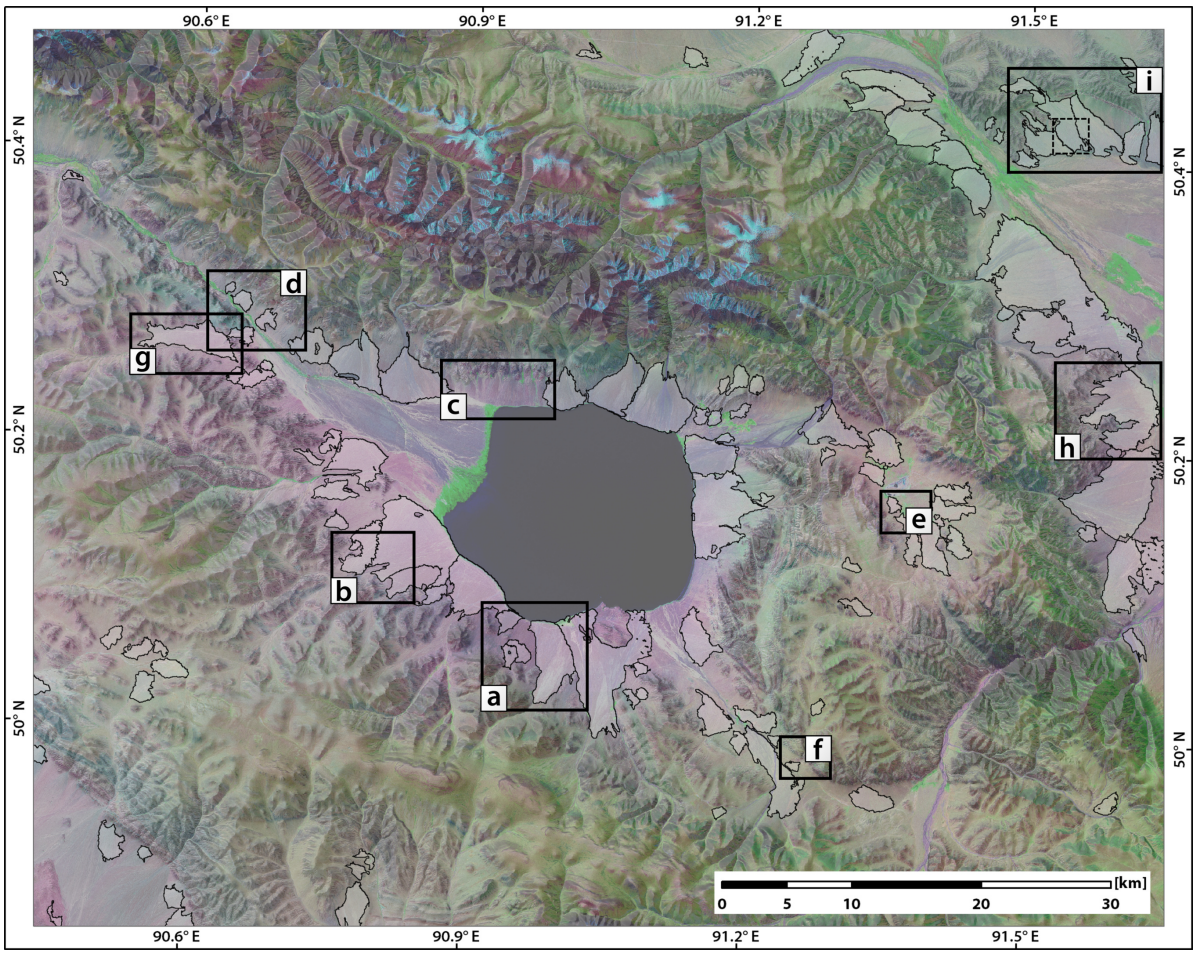


Figure 5.8: Location of details depicted for in-depth geomorphological analysis.

from the older alluvial fan surface (Fig. 5.9). If deposition at the intersection point is significant, and if the alluvial fan surface does not undergo strong fluvial resedimentation, the margins of these depositional lobes can be identified as substantial morphometric discontinuities by the mean-shift routine, and the depositional lobe is thus delineated as a separate segment. As the older alluvial fan surfaces partly do not honor the alluvial fan model—i.e., they likely exhibit low aperture angles, a lower z skewness and a relatively high bilateral asymmetry—they score low SVM values.

At the southern flank of the Tsagaan Shuvuut Range, along the northern shore of the Uureg Nuur and the Kargy River (Kharagiin-Gol) delta (cf. Fig. 5.1), substantial parts of the ramp delimiting the range from the basin were omitted from delineation. When analyzing these slopes in detail, it becomes clear that although the whole ramp as such can be generally addressed as an alluvial slope, local erosion by small ephemeral streams is co-responsible for the geomorphological shaping of such slopes (detail c). However, some smaller alluvial fans were omitted as well. Specifically, at the beginning of the Kargy River delta, two small fans were fully missed out, and one alluvial fan body could only partly be delineated (detail d). Consequently, we have to raise the question if we come across a minimum size below which we cannot expect appropriate delineation with SRTM 1″ data. Small objects (area $\leq 3\,\mathrm{km}^2$) constitute the majority of the final classification output. Among those objects, several objects yield high SVM scores and visual assessment indicates that they actually have to be addressed as alluvial

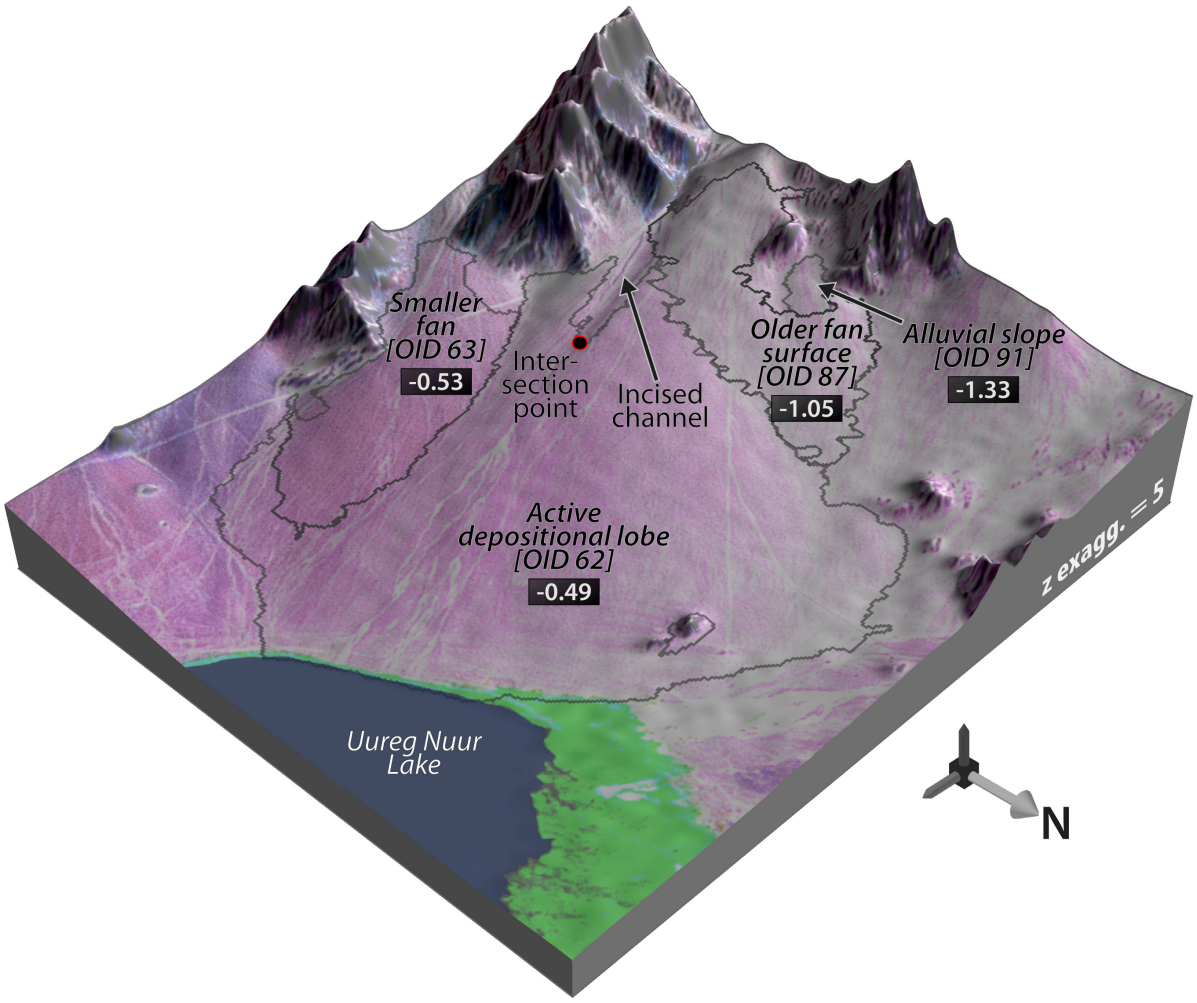


Figure 5.9: Perspective view on a large alluvial fan located at the south-western shore of the Uureg Nuur Lake (refer to Fig. 5.7 for exact location). (Data source: SRTM 1″, Landsat ETM+ pan-sharpened)

fans (detail e and f). These objects also constitute the lower bound in terms of alluvial fan size being identifiable via visual analysis of the DEM and its derivatives. Hence, small alluvial fans are generally identifiable by object-based morphometric analysis of SRTM 1″ data, but the probability of omission increases with declining alluvial fan size.

SVM scores generally fit well with visually assessed segmentation quality as well as with post-sedimentary dissections of alluvial fan bodies and alluvial fan peculiarities. The largest likelihood of confusion is evident for alluvial slopes displaying signs of incipient alluvial fan development (cf. detail c). Moreover, alluvial fans may be confused with alluvial plains (detail g). These objects have SVM scores which are comparable to alluvial fans being deficiently delineated or exhibiting peculiarities like pronounced coalescence or multiple feeder channels (detail h). If a feeder channel dissects the corresponding alluvial fan over its full length, the alluvial fan body gets delineated by two separate objects. However, these two objects will likely yield relatively low SVM scores, because they do not fully meet the constraints imposed by the classification parameters. Complex interconnection patterns with diffuse boundaries can lead to partly implausible object delineation. At the northern rim of the Uvs

Nuur Basin, alluvial slope formation is evident along a reverse fault scarp (detail i). Owing to enhanced modern slope gradients, only slight radial sedimentation occurs, and the easternmost fan got dissected. However, an old alluvial fan body is mostly preserved at a position which is located approximately 70 m below the modern fault scarp (detail i, dashed outline). Due to diffuse boundaries, mean-shift segmentation yields one single polygon for the western feeder channel and the inactive alluvial fan body, although they are not connected in terms of geomorphogenesis. It has to be stressed, however, that the overall sedimentation pattern is correctly reflected by the segmentation algorithm.

5.6.3 OBMA – relationship between morphometric parameters and SVM scores

Inspecting the scatter plots of parameter values against the respective SVM scores (Fig. 5.10), it is noticeable that objects exhibiting positive scores plot near the parameter means and on both sides of the means. Hence, large deviations from the parameter mean reliably rule out a high alluvial fan likelihood. Conversely, no significant correlation between SVM scores and the respective parameter values is apparent for any parameter. Specifically, all parameters show an increased variability with increasingly negative SVM scores, and in all cases, low-scoring objects occur near the mean. None of the incorporated classification parameters is thus able to independently quantify alluvial fan class membership.

We further analyzed the relationships between SVM scores and the classification parameters by calculating SVM score arithmetic means and standard deviations for divisions of the classification parameter value range (Fig. 5.11). Maximum SVM score mean, SVM score standard deviation and the closeness of the relationship between mean SVM score and Z-standardized parameter values are indicators for evaluating the explanatory value which the respective parameter has for alluvial fan classification. High explanatory potentials are given in case of high maximum SVM scores, low SVM score standard deviations and a monotonous decrease of SVM scores with increasing distance from the parameter mean.

As can be seen from Fig. 5.11, the altitude skewness shows two approximately equivalent peaks of SVM score means which exhibit moderate values of slightly below -0.6. These two peaks are interrupted by a drop to mean values below -0.9. Interestingly, this area of relatively high SVM scores is predominantly located in the positive range of parameter values, indicating that the majority of highly scored polygons exhibits a stronger positive skewness than the reference dataset.

Rather than showing one or several distinct maxima, the cross-sectional curvature plot (Fig. 5.11B) displays a plateau of mean SVM scores, which is centered around parameter zero and stretches roughly symmetrically to Z-standardized values of ± 1. Hence, the expected variability of alluvial fan cross-sectional curvature (cf. Section 5.2) is actually reflected in the data, indicating a limited explanatory potential for the high SVM score domain. To both sides of the plateau, however, the graph of SVM score averages exhibits a steep decline, implying that cross-sectional curvature provides explanatory value by separating objects falling into the high SVM score plateau from polygons located beyond this area. Maximum SVM score averages amount to approximately -0.7, thus being lower than those given for the altitude skewness. Since cross-sectional curvature exhibits no local minima, the explanatory potentials of both parameters are generally equivalent. Longitudinal curvature (Fig. 5.11C) closely resembles the characteristics of cross-sectional curvature, with the notable exception that it exhibits a

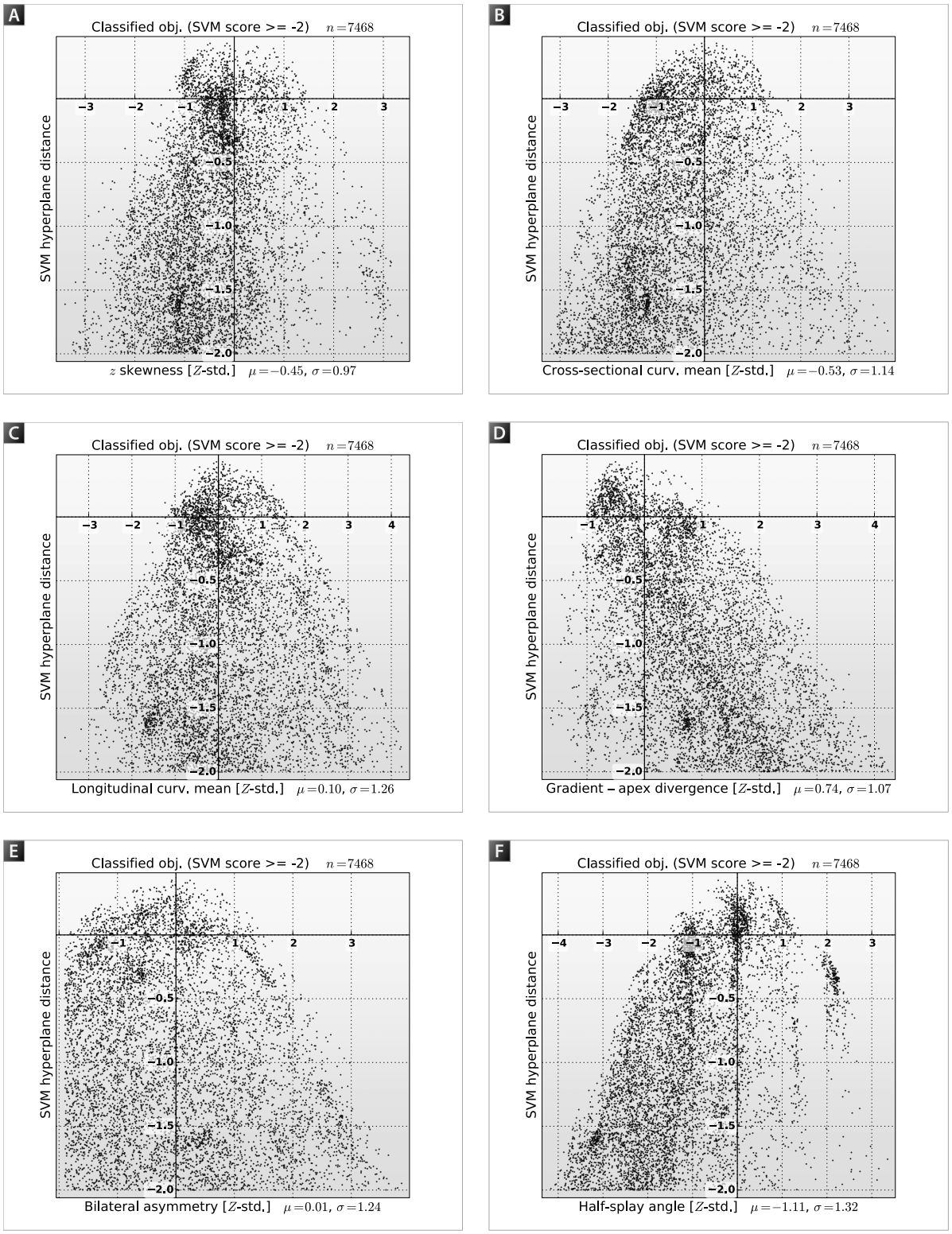


Figure 5.10: Scatter plots of SVM score plotted against morphometric classification parameters (data basis: OBMA objects yielding SVM scores of −2 or better). (A) z skewness, (B) Cross-sectional curvature (CCurv), (C) Longitudinal curvature (LCurv), (D) Gradient–apex divergence (GAD), (E) Bilateral asymmetry (BAS), (F) Half-splay angle (HSA).

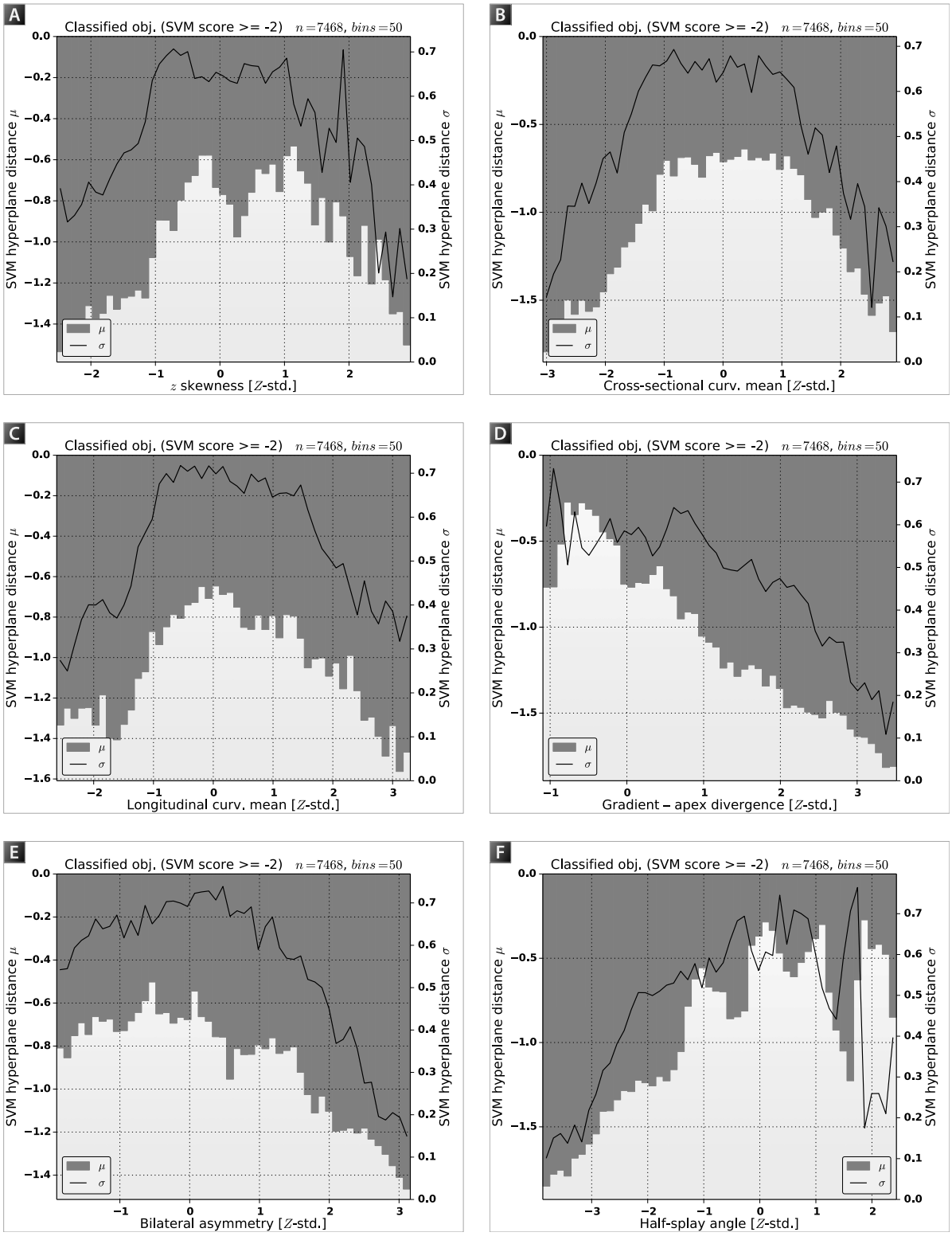


Figure 5.11: SVM score arithmetic means and standard deviations for bins of the morphometric classification parameters (data basis: OBMA objects yielding SVM scores of −2 or better). (A) z skewness, (B) Cross-sectional curvature (CCurv), (C) Longitudinal curvature (LCurv), (D) Gradient–apex divergence (GAD), (E) Bilateral asymmetry (BAS), (F) Half-splay angle (HSA).

single peak located at parameter zero. Consequently, its explanatory potential is slightly better for the high SVM score domain.

The striking feature of the gradient–apex divergence (GAD) parameter (Fig. 5.11D) is that it exhibits a high maximum SVM score average of approximately −0.25, representing the highest SVM score average of all parameters. Furthermore, this maximum occurs for GAD values slightly below zero and it is accompanied by a sudden decrease of SVM score standard deviation. The co-occurrence of maximum SVM score average and a distinct decrease of SVM score standard deviation can be interpreted as a clear signal for radial sedimentation patterns, implying that GAD has a high explanatory value for alluvial fan classification. Besides, SVM score averages decrease monotonously and with high gradient to either side of the maximum.

The bilateral asymmetry (BAS) parameter (Fig. 5.11E) displays two narrow mean SVM score peaks being located slightly below and above parameter zero, exhibiting values of approximately −0.35 and slightly above −0.4, respectively. Apart from that, a zone of relatively high SVM score values above −0.6 extends from BAS values of approximately −1.5 to 0.5, indicating that objects fulfilling the constraints of the alluvial fan model mostly exhibit a low asymmetry. The maximum SVM score mean is significantly higher than those of any generic morphometric parameter, but notably lower than those given for GAD. In comparison with GAD, the explanatory value of BAS is thus reduced, but still superior to all generic morphometric parameters.

The graph of the half-splay angle (HSA) parameter (Fig. 5.11F) is characterized by three equivalent peaks and a subordinate local maximum, which reach relatively high SVM scores of approximately −0.3 and slightly below −0.5, respectively. Analogous to GAD, three of the four peaks are accompanied by distinct minima of SVM score standard deviation. As HSA provides a measure for the aperture angle of a radially sedimented body, this multimodality indicates that we encounter different styles of radial sedimentation in the study area. The maxima are separated by significant drops of mean SVM scores. This peculiarity implies that HSA provides a limited explanatory value for alluvial fan classification, if significantly different fan aperture angles occur within a single study area.

5.6.4 OBMA – relationship between segmentation parameters and SVM scores

Examining the segmentation parameters of all final OBMA objects (Suppl. B.8), no trend is apparent for any of the segmentation parameters with regard to SVM score. Specifically inspecting the segmentation objects depicting training fans, i.e., objects yielding the highest degree of mutual overlap with the reference polygons, it is conspicuous that—with the exception of a range bandwidth of 0.6—the full value range of all segmentation parameters already occurs in this small set of eleven polygons. Bearing in mind that the reference dataset is comprised of characteristic alluvial fans which largely display high SVM scores, this finding indicates that the full spectrum of parametrizations used for mean-shift segmentation (cf. Section 5.5.1) can give us objects yielding high SVM values.

A more detailed assessment of possible relationships between the choice of segmentation parameters and SVM scores of the obtained OBMA objects was carried out by calculating arithmetic mean and standard deviation of each segmentation parameter for divisions of SVM scores. Inspecting Suppl. B.9, it becomes apparent that no relationship is evident for either of the segmentation parameters. Specifically, all segmentation parameters show moderate scatter of both arithmetic means and standard deviations,

but completely lack global or significant local trends even for high SVM scores above −0.5. If a particular value of a segmentation parameter would have been superior to other parametrizations in terms of delineation quality, it would make up a significant fraction of the high SVM score bins. This, in turn, must be reflected at least by a negative trend of parameter standard deviation against SVM score. The complete absence of trends thus verifies that high SVM scores are not limited to a certain subset of parametrizations, and consequently, the considered range of segmentation parametrizations is indeed required to ensure optimal delineation of alluvial fans.

5.7 Discussion

5.7.1 Segmentation approach assessment

By conducting object-based morphometric analysis applying mean-shift segmentation of multiband raster datasets being composed of SRTM 1″ DEM derivatives, and using a one-class SVM for fuzzy classification, we obtained a generally accurate delineation of alluvial fan bodies in the study area. With regard to the training dataset, all OBMA object boundaries closely resemble the manual delineation, and the remaining alluvial fan inventory displays a mostly consistent delineation reflecting the major morphometric discontinuities as depicted by maps of morphometric parameters. For high SVM scores, the corresponding OBMA objects yielded by topological cleansing without area weighting are largely identical to the respective OBMA objects obtained with area weighting (cf. Section 5.6.1). This coincidence implies that a higher degree of segmentation indicates substantial internal heterogeneities of the respective alluvial fan, rather than a deficient segmentation or DEM noise.

In contrast to the early MRS-based method of Argialas and Tzotsos (2004) as well as approaches being based on simpler variants of region-growing segmentation (Miliaresis, 1999; Miliaresis and Argialas, 2000), our approach is reliably capable of discriminating adjoining fans. Furthermore, the calculated apex points are accurately located with regard to the drainage network (cf. Section 5.5.2), and our method thus allows to associate the individual fans with their catchments. Consequently, our findings contradict the postulates made by Norini et al. (2016, p. 138), who have stated that object-based alluvial fan extraction is not able of providing such discrimination capabilities, and does not enable assignments to corresponding catchments. Furthermore, our proposed object-based workflow renders discrete objects which are guaranteed to not overlap each other, whereas the method of Norini et al. (2016) generates significantly overlapping polygons in most cases. In opposition to that study, we deem discretization as the generally appropriate approach for alluvial fan delineation, because discretization is inherent to the object-oriented view of specific geomorphology (cf. Section 5.1). It follows that the extraction of discrete objects is preferable to a fuzzy delineation as long as sufficiently cognizable morphometric discontinuities enable a mostly unbiased differentiation between adjoining fans.

Segmentation quality drops off in case of intensive lateral coalescence, which may lead two alluvial fans to seamlessly merge together at mid-fan section. Furthermore, segmentation quality is impaired for alluvial fans exhibiting significant fan-head trenching. In this case, the abrupt change from negative cross-sectional curvature to positive cross-sectional curvature values at the channel walls and the intersection point is interpreted as a major morphometric discontinuity, and the incised channel is thus excluded from the fan delineation. A failure of including the incised feeder channel results in incorrect

apex calculation, potentially hampering the computation of morphometric parameters relying on apex localization. Feeder channel width is, however, commonly quite low and the effect of such misplacement is thus limited. Deposition at the intersection point induces the development of a lobe superimposing the main alluvial fan body (Calvache et al., 1997; Viseras et al., 2003; Blair and McPherson, 2009). Substantial discontinuities between a younger depositional lobe emanating from the intersection point and the older alluvial fan surface may cause the alluvial fan sub-entities to be segmented as separate objects. As the older fan surface patches do not fully honor the morphometric constraints imposed by the classification workflow, such patches score relatively low SVM values. No sharp lower scale bound could be found for alluvial fan identification and delineation. In the case of small fans, however, the probability of omission increases significantly. This peculiarity can be attributed to the fact that mean magnitudes of morphometric discontinuities decrease with declining alluvial fan dimensions, so that the intrinsic resolution of the SRTM 1″ dataset (cf. Kervyn et al., 2008; Pipaud et al., 2015 / Chapter 3) as well as DEM filtering gain relevance. Consequently, distinctness and consistency of delimiting discontinuities become increasingly important with declining fan dimensions, i.e., for fans exhibiting footprints smaller than approximately 3 km^2, only those fans with prominent delimitations can be expected to be successfully delineated.

Mean-shift segmentation is known to be computationally efficient for datasets with low to medium dimensionality (cf. Comaniciu and Meer, 2002). A large spectrum of alluvial fan dimension and shape (cf. Section 5.2) entails, however, that optimal spatial and range bandwidth as well as input parameter weightings are object-specific (cf. Strobl, 2008; Anders et al., 2011; Eisank et al., 2014). It has to be stressed that variations of parameter weightings are not only related to the morphometric properties of the particular geomorphological phenomenon, but can also stem from the fact that DEM derivatives exhibit differing distribution characteristics (cf. Romstad and Etzelmüller, 2012; Csillik et al., 2015). The significance of this issue depends on the adjustment applied on the DEM derivatives in order to establish a similar distribution density function. Due to the multimodality of sine and cosine of slope aspect, we were limited to the application of Z-standardizing (cf. Section 5.5.1), and it is thus possible that the still different distributions are co-responsible for the depicted variability of parameter weightings (cf. Section 5.6.4). These points implicate that—for an optimized segmentation result—numerous mean-shift runs are necessary, making the segmentation routine computationally intensive. Methods to determine local bandwidth as a function of the local gradient field have been discussed in literature (Comaniciu et al., 2001; Comaniciu, 2003; Einbeck, 2011). Implementations are, however, not available, and the suggested approaches do not cover the issue of selecting optimal weights for input raster bands. As single segmentation runs are independent of each other, segmentation can still be vastly accelerated if computation is done on a many-core system.

5.7.2 Classification approach assessment

Distance values from the decision surface of the one-class SVM model proved to be an appropriate measure to quantify the likelihood of an object belonging to the semantic class alluvial fan. As is evident from the partially negative SVM scores for objects representing alluvial fans, our study reveals that a fuzzy classification model is indeed required for classification. We must bear in mind that the SVM decision surface is defined according to the training dataset, and that the morphometric feature space is

six-dimensional. In this context, eleven samples provide merely sparse information on the shape of the alluvial fan property space, and thus cannot be expected to fully reflect the statistical variability of the alluvial fan inventory in the study area (cf. Bellman, 1984). This low statistical support also makes the model prone to overfitting to potential irregularities of the training dataset (cf. Hastie et al., 2009), and hence, a conservative parametrization of the SVM model is mandatory (cf. Section 5.6.1). This entails, however, a relatively generalized decision surface, and it is thus to be expected that alluvial fans will be located outside the model boundary.

Still, particularly low SVM scores for alluvial fans relate to shape peculiarities, e.g., a compound morphologic character of the alluvial fan or post-sedimentary disturbances of the fan surface by, for instance, fault offsets. Consequently, there is an overlap area of SVM scores for such fans and surfaces grading into fans in terms of their morphometric characteristics. This is particularly true for alluvial slopes, which may display signs of incipient radial sedimentation. Analogously, no sharp differentiation exists between alluvial plains and alluvial fans. Given the fact that a universal slope gap between alluvial plains and alluvial fans does not exist (cf. Saito and Oguchi, 2005), a morphometric continuum exists between relatively steep alluvial plains with at least locally divergent sedimentation patterns, and alluvial fans. Consequently, objects falling into this range of fuzzy transition between different geomorphic systems eventually have to be evaluated by an experienced human interpreter, and it might be necessary to incorporate auxiliary data. Nevertheless, object-based morphometric analysis is still helpful by identifying the aforesaid objects and highlighting them for further analysis.

The variable nature of alluvial fan geomorphology (cf. Section 5.2) entails that a sufficient number of classification parameters is crucial for a robust classification. Recall that the main objective in parameter selection is concurrent maximization of intra-class homogeneity and inter-class heterogeneity (cf. Section 5.5.2). In this context, one might expect morphometric parameters specifically addressing the morphology emerging from the radial sedimentation pattern to provide more explanatory value than generic morphometric parameters. This indeed fully applies to the gradient–apex divergence (GAD) parameter, which exhibits a comparatively very high SVM score average for small GAD values. Furthermore, the abrupt decrease of standard deviation for low GAD values indicates that the parameter is actually diagnostic for fans exhibiting near-ideal cone shapes. However, substantial internal fan differentiation into distinct lobes and postsedimentary influences like tectonic offsetting can cause relatively high GAD values for objects representing alluvial fans. In such cases, medium to high absolute GAD values regularly coincide with relatively high SVM scores, indicating the robustness of the multiparameter approach. In comparison to GAD, the bilateral asymmetry (BAS) parameter exhibits a notably reduced explanatory value, but is still superior to all other classification parameters. In contrast, a large variability of alluvial fan aperture angles causes the half-splay angle (HSA) parameter to significantly fall short in terms of explanatory value. Consequently, it does not exhibit benefits over the generic morphometric parameters used in this study. If, however, the style of radial sedimentation is relatively consistent throughout a study area, the HSA can be expected to exhibit a high potential for classification.

5.7.3 Perspectives and challenges

Already providing a satisfactory delineation and classification potential when using a medium resolution DEM, the suggested approach can be improved by incorporating higher resolution topographic data, so that morphometric classification can be extended by parameters specifically addressing microscale features of alluvial fans. Doing so will presumably not only enhance the differentiation between objects representing alluvial fans and the remaining geomorphologic inventory, it furthermore enables us to differentiate between sheetflood-dominated and debris flow-dominated alluvial fans (cf. e.g., Staley et al., 2006; Frankel and Dolan, 2007; Volker et al., 2007; Cavalli and Marchi, 2008). In terms of segmentation, higher intrinsic resolutions allow identification of topographic discontinuities exhibiting low wavelengths, and thus will foster segmentation by facilitating the delineation of alluvial fans displaying a smooth coalescence with neighboring fans.

Limitations of the proposed methodology are encountered for alluvial fans displaying pronounced channel incision and accentuated composite morphologies, which can exhibit a flawed delineation impairing classification. In this context, a pre-processing routine conducting a channel infilling on the DEM may help in making the OBMA workflow more robust against channel incision, facilitating both segmentation and classification. Composite fan bodies, however, cannot be captured as a single entity by segmentation algorithms relying on internal homogeneity of segmentation units. Instead, these *atomic* fan sub-entities must first be segmented, classified as independent objects, and then conditionally merged into *functional spatial units*, based on their spatial relationships (cf. Lang, 2008; Blaschke et al., 2014). Using LiDAR data, Van Den Eeckhaut et al. (2012) demonstrated that landslides—which exhibit compound morphologies as well—can be successfully delineated by initially treating potential landslide main scarps and bodies as separate objects. Composite objects are subsequently obtained by considering the spatial relationship between a main scarp, potential landslide flanks drawn from both outer ends of the main scarp in a direction perpendicular to the principal orientation, and adjacent landslide bodies enclosed by these flanks. It remains, however, an open question if and to what extent such a concept can be applied on alluvial fans.

In this study, we introduced an object-based morphometric processing and analysis scheme specifically addressing the problem of identifying and delineating alluvial fans. The methodological framework, however, can be extended into a general object-based analysis framework potentially including various geomorphological phenomena of interest. Geomorphological phenomena are characterized by a unique set of morphometric characteristics, and consequently exhibit different optimal parametrizations both in terms of segmentation and classification. By conducting segmentation and classification for each geomorphological phenomenon separately and merging the single object layers into a final meta dataset, one can ensure that the object-based morphometric workflow is optimized for each distinct segmentation and classification problem. Consequently, we consider such a serial or *stratified* approach (cf. Anders et al., 2011) the most promising method for capturing larger portions of the geomorphological inventory of a study area by means of an unattended, object-based analysis.

5.8 Conclusions

The presented object-based workflow proved to be an effective, flexible and expandable framework for delineation and classification of a particular landform. Our results indicate that a variable, object-specific parametrization of the segmentation algorithm and a variable selection of terrain parameter weightings are crucial to take account of the intra-class variability of the landform of interest, and, in turn, for a constantly high segmentation quality. This finding has significant implications for the future development of object-based morphometric analysis, because research done hitherto has focused on a global optimization of parametrization.

Application of mean-shift segmentation resulted in a promising delineation accuracy, and the algorithm thus provides an alternative to multi-resolution image segmentation. An inherent drawback of the introduced segmentation approach is that object-specific parametrization is achieved by repeatedly running the mean-shift algorithm with different parametrizations, which is computationally intensive. Although methods to determine local bandwidth as a function of the local gradient field have been discussed in literature, practical implementations are yet missing, and the suggested approaches do not cover the issue of variable optimal weightings of the input datasets.

Object-specific distance values to the separating hyperplane of a one-class support vector machine (OCSVM) can be conveniently used as a fuzzy measure of class membership. Moreover, these membership values enable us to select, for each real-world object, the most appropriate delineation among the set of delineation layers generated with different bandwidths and weightings. To ensure an objective classification as well as a high selection accuracy, the location of the decision surface must closely reflect the specific geomorphological properties of the landform of interest. In this context, our results reveal that parameters specifically quantifying peculiar morphological aspects of the landform are essential for developing an accurate classification scheme. To fully exploit the potential of segment-level morphometric analysis, we therefore suggest to put more emphasis on design and evaluation of such parameters.

6 One-Class Random Forests as a robust approach to alluvial fan discrimination: A comparison of SRTM and ALOS World 3D

6.1 Introduction

Considering landforms as discrete spatial features (Evans, 1972, 2012), specific geomorphometry stipulates an object-based perspective on the land surface (cf. Drăguţ and Eisank, 2011). Since the vast majority of landforms covers many pixels in modern medium and high resolution digital elevation data, the implementation of specific geomorphometric analysis involves landforms to be delineated prior to an investigation of their geomorphometric properties. In this context, efforts to automate the delineation and generation of thematic maps motivated the adoption of object-based techniques being developed in the field of remote sensing as a way to tackle these scenarios (Strahler et al., 1986; Woodcock and Strahler, 1987). Object-based image analysis (OBIA) is a two-stage methodological framework consisting of initially performing a segmentation algorithm on the gridded data, yielding image objects based upon one or more criteria of homogeneity (Baatz and Schäpe, 2000; Blaschke and Strobl, 2001; Blaschke et al., 2004; Castilla and Hay, 2008; Blaschke, 2010). Subsequently, a classification routine is applied on the individual segments to identify the semantic nature of their geomorphometric properties (cf. Bishr, 1998; Lang, 2008) and assign them to corresponding thematic classes.

For classification, the common approach to OBIA relies heavily on expert knowledge being utilized to define manually set up (fuzzy) rules which are then combined into a hierarchical decision framework (cf. Flanders et al., 2003; Benz et al., 2004; Bishop et al., 2012). During the last two decades, this rule-based approach to OBIA has become the de facto standard in object-based analysis of digital terrain data, with successful applications being shown both for the derivation of multi-class thematic maps (cf. e.g., Drăguţ and Blaschke, 2006; Stepinski et al., 2006; van Asselen and Seijmonsbergen, 2006; Drăguţ and Blaschke, 2008; Möller et al., 2008; Schneevoigt et al., 2008; Drăguţ et al., 2009; Stepinski and Bagaria, 2009; Anders et al., 2011; Gerçek et al., 2011; Drăguţ and Eisank, 2012), and the extraction of individual landforms (cf. e.g., Saha et al., 2011; Van Den Eeckhaut et al., 2012; Pedersen, 2016; Argyridis and Argialas, 2017; Rahmati et al., 2017a). While feature signature libraries are suggested to formalize and store *semantic models* of landforms (cf. Anders et al., 2011; Eisank, 2013), the formalization of expert knowledge into *ontologies* (cf. Chapter 1; Gruber, 1995) is impaired by a semantic gap between the high-level semantic conceptualization of the expert and the low-level statistical information which can be extracted from the data (cf. Arvor et al., 2013; Belgiu et al., 2014).

With the morphometric information of a local surface patch being given by the altitude field on a local scale, most geomorphometric parameters are based upon a quantification of local relationships between pixel values (cf. Pipaud et al., 2015 / Chapter 3; Arrell et al., 2008; Gallay, 2009; Reuter et al., 2009). Since the earth surface possesses fractal properties (Wood, 1996; Albani et al., 2004), the effective resolution of the digital elevation data (Chapter 3) exerts a strong influence on the range of values shown by these morphometric variables. In addition, they are susceptible to high-frequency

errors coming along with common digital elevation model (DEM) processing techniques, e.g., phase noise in the case of SAR interferometry (cf. Zebker and Villasenor, 1992; Geudtner, 1995; Gonga-Saholiariliva et al., 2011), and co-registration issues in the case of image matching routines used to process stereometric optical imagery (cf. Hannah, 1981; McGlone, 2007). Hence, the morphometric expression corresponding to a semantic conception of a landform strongly depends upon the DEM in use, hampering the transfer of semantic models between different DEM products (cf. Stumpf and Kerle, 2011). Another aspect that has been completely disregarded so far is that a morphometric signature of a landform (cf. Enzmann, 1966; Pike, 1988; Giles, 1998) is not necessarily static in the sense that a singular set of statistical bounds can be expected to appropriately formalize the complete feature space of this landform. Specifically, with respect to alluvial fans, their variable nature with respect to scale (cf. Chapter 2) casts doubt on approaches to formalize the alluvial fan property space via rule sets.

Data-driven ontologies tackle these issues by identifying feature signatures in the analyzed data by means of geostatistics or machine learning techniques (Janowicz, 2012; Belgiu et al., 2014). In the field of geomorphometry, morphometric parameters act as an interface to the land surface objects of interest (cf. Eisank et al., 2014; Pipaud and Lehmkuhl, 2017 / Section 5.1). By selecting a specific set of morphometric parameters, experts compulsorily impose their own conceptual view on the data. Therefore, application of data-driven object based image analysis for geomorphometric problems involves a hybrid procedure (cf. Belgiu et al., 2014), in which the selection and parametrization of morphometric parameters is ideally guided by variable importance metrics.

During the last two decades, random forests ensemble classifiers (Breiman, 2001) received increasing emphasis due to a high classification performance, their non-parametric nature, their ability to yield measures of variable importance for the classification problem at hand, and their robustness towards features with little discriminatory potential (cf. e.g., Bostrom, 2002; Gislason et al., 2006; Rodriguez-Galiano et al., 2012; Cracknell and Reading, 2014; Belgiu and Drăguţ, 2016). Consequently, random forests found widespread use for pixel-based land cover classification (cf. e.g., Gislason et al., 2006; Chan and Paelinckx, 2008; Ghimire et al., 2012; Rodriguez-Galiano et al., 2012; Du et al., 2015), as well as for various classification tasks in the fields of geomorphology, geology, geoecology, and soil sciences (cf. e.g., Wiesmeier et al., 2011; Cracknell and Reading, 2014; Pahlavan Rad et al., 2014; Veronesi and Hurni, 2014; Messenzehl et al., 2017; Rahmati et al., 2017b; Scarpone et al., 2017). While the body of research on application of random forests within the scope of object-based analysis is still relatively limited, the adoption of random forests showed promising results for the processing of multispectral imagery (cf. Stumpf and Kerle, 2011; Shruthi et al., 2014; Jhonnerie et al., 2015; Li et al., 2016), as well as for combined workflows which utilize both imagery and DEM data (cf. Guan et al., 2013; Juel et al., 2015).

While formalization via rule sets allows for the formalization of single semantic classes, all machine learning algorithms considered hitherto are discriminatory in nature and therefore require to differentiate between different semantic classes via training data. That is, these classifiers actually learn to differentiate between semantic classes present in an area, not to identify their unique feature signature. With respect to the individual contextual setting of study areas, this property renders the training information case-specific and hampers its transferability to other areas (cf. Juel et al., 2015). Adhering to the fundamental concept of formalizing feature signatures, Pipaud and Lehmkuhl (2017 /

Chapter 5) suggested to use one-class classifiers and showcased an object-based morphometric workflow incorporating a one-class support vector machine (OCSVM) with a radial basis function kernel (Schölkopf et al., 2001) for the delineation and identification of alluvial fans. While displaying sound performance, the algorithm is very sensitive to feature selection and classifier parametrization, thereby requiring a tentative evaluation approach (cf. Chan et al., 2012; Li et al., 2015).

In this study, we introduce a one-class random forest (OCRF) classification framework which allows for a full data-driven formalization of a morphometric signature by differentiating a training dataset from synthetic outliers derived from a kernel density estimation (KDE). After training the classifier with a representative dataset of 306 fans (cf. Chapter 4), we evaluate the classification potential by considering an evaluation dataset consisting of alluvial fans and landforms grading into them, i.e., alluvial slopes and alluvial plains (cf. Chapter 2). Furthermore, we demonstrate that the algorithm can be used to perform an unbiased comparison between different DEM products and DEM filtering intensities and capitalize on this robust properties by comparing SRTM1 with the recently released AW3D30.

6.2 Data

6.2.1 SRTM1

The Shuttle Radar Topography Mission (SRTM) was the first project exploiting spaceborne single-pass SAR interferometry for near-global DEM generation. For this purpose, the C-band system SIR-C was extended by a passive antenna mounted on a 60 m long boom, to establish a bistatic interferometer with a fixed perpendicular baseline (cf. Bamler and Hartl, 1998; Rott, 2009). During an 11-day mission in February 2000, an imaging of almost the entire terrestrial surface between 60° N and 56° S was performed (Rodríguez et al., 2006; Smith and Pain, 2009).

Since September 2014, SRTM data are globally available with a posting of 1″ for latitudes below 50°, whereas tiles for latitudes greater than 50° N or 50° S are provided with a posting of 2″ by 1″ (SRTM1). For the study at hand, the DEM was projected to the respective UTM zones and resampled to a posting of 30 m using cubic convolution.

Importantly, the parallel of 50° north latitude runs through the Mongolian Altai study area (Region 6). To prepare a seamless DEM for the whole study area and avoid artifacts at the boundary between 1″ tiles and 2″ by 1″ tiles, tiles bordering the parallel were merged with a boundary blending algorithm based on bicubic spline interpolation (cf. Pipaud and Lehmkuhl, 2017 / Chapter 5). For in-depth information on SRTM1, refer to Pipaud et al. (2015 / Chapter 3).

6.2.2 ALOS World-3D DEM

The ALOS World-3D DEM is a near-global DEM compiled from archived imagery acquired by the PRISM sensor (Panchromatic Remote-Sensing Instrument) onboard the ALOS satellite (Advanced Land Observing Satellite), which was run by the Japanese Aerospace Exploration Agency (JAXA) in cooperation with commercial partners NTT Data and RESTEC (Tadono et al., 2014). The spacecraft was launched in January, 2006, and was in operational state until the end of its planned lifespan in 2011 (Shimada et al., 2010; Tadono et al., 2014). Being specifically designed for DEM generation

(Takaku et al., 2007), PRISM was a triplet stereo imager consisting of nadir, forward and backwards looking (23.8° inclination each) panchromatic (0.52 to 0.78 µm) push-broom scanners with a horizontal resolution of 2.5 m (Tadono et al., 2004, 2009).

Single-scene DEMs are processed from the fully overlapping triplets by automatic along-track stereometry, using a correlation kernel of variable size. During its operational lifespan of 5 years, PRISM acquired approximately 6.5 M scenes, from which circa 3 M scenes exhibit a cloud cover below 30 % and thus could be incorporated into DEM processing (Tadono et al., 2014, 2015, 2016). The AW3D5 is a 0.15″ (~5 m) DEM derived from this multi-temporal dataset via stacking and mosaicking. It was made commercially available in March 2016 for all land surfaces between 82° N and 82° S and is specified to exhibit a vertical root mean squared error (RMSE) of 5 m or smaller (Igarashi, 2001; Takaku et al., 2014; Tadono et al., 2016). Preliminary investigations by Takaku et al. (2014) and Tadono et al. (2014) confirm compliance with the specification with the single exception of surfaces with inclinations greater than 30°, where RMSE are slightly above 5 m.

In May 2016, JAXA published a 1″ (~30 m) version (AW3D30) which is available free of charge. It is directly derived from the commercial product by cell aggregation, using either averaging or median 7×7 processing (Tadono et al., 2016). As with SRTM1, AW3D30 is compiled with the EGM1996 geoid as vertical reference, but uses the GRS1980 as geodetic reference (Tadono et al., 2014). The data is provided with plate carrée projection. For this study, we used version 1.1 released in March 2017, for which void filling was conducted for all regions between 60° N and 60° S by incorporating adjusted values of other DEMs (Takaku and Tadono, 2017; EORC and JAXA, 2018). Furthermore, we opted for the median variant of the dataset. This choice was motivated by the fact that median aggregation can be expected to filter high frequency signals better than an unweighted low pass filter. Notably, high frequency undulations have been reported for AW3D5 (Purinton and Bookhagen, 2017). The AW3D30 DEM was projected into the appropriate UTM zone of the study areas (cf. Chapter 4) and resampled to a posting of 30 m using cubic convolution.

6.2.3 State of research

Considerable emphasis has been given to a comparison of AW3D30 with other near-global datasets. The recency of the dataset entails, however, that the body of research is still limited. In addition, research done hitherto focused on descriptive statistics by point-wise comparison of AW3D30 elevation values with high-resolution reference data. Among these studies, there is broad consensus that AW3D30 (1.) complies with the mission specifications stated for AW3D5 as well, and (2.) that AW3D30 is more accurate than SRTM1 (cf. Tadono et al., 2016; Bayburt et al., 2017; Jain et al., 2017; Purinton and Bookhagen, 2017; Alganci et al., 2018; Bayık et al., 2018; Gesch, 2018; Grohmann, 2018; Li and Zhao, 2018; Sefercik et al., 2018; Zhang et al., 2019). Studies reporting non-compliance with AW3D5 mission specifications mostly still show that AW3D30 performs better than or equivalent to SRTM1 (cf. Santillan and Makinano-Santillan, 2016; Florinsky et al., 2018, 2019), whereas a slightly lower accuracy is stated by Hu et al. (2017).

Descriptive statistics do not reflect topological relationships and therefore have limited significance for geomorphic applications (cf. e.g., Pipaud et al., 2015 / Chapter 3; Florinsky et al., 2019). Until now, only a few studies dealt with the intrinsic resolution of AW3D30 data and the consistency of terrain

rendition. Purinton and Bookhagen (2017) conducted a visual assessment of AW3D30 (version 1) data depicting parts of the southern Central Andean Plateau. With regard to numerous step-like artifacts and blunders found at hillsides, the authors discourage the use of AW3D30 for geomorphic applications. Herewith in agreement, Hu et al. (2017) state that the accuracy of AW3D30 (version 1) is slightly worse than the one observed for SRTM1 in mountainous high relief settings. Grohmann (2018) evaluated AW3D30 version 1 data of several Brazilian sites. While the author note that AW3D30 exhibits a higher intrinsic resolution than SRTM1, Grohmann also observed occasional scene mismatches indicated by crisscross patterns. Furthermore, Alganci et al. (2018) assessed AW3D30 (version not mentioned) and SRTM1 by evaluating vertical cross sections. Comparing the DEMs with a stereometrically derived 5 m reference DEM, they found AW3D30 to reflect the reference profiles more closely.

Focusing on DEM usage for fluvial landscape analysis, Boulton and Stokes (2018) assessed version 1.1 of the AW3D30 for a study area located in the High Atlas Mountains, Morocco, and conclude that AW3D30 has a higher intrinsic resolution than SRTM1. More notably, however, stream delineation based upon AW3D30 data proved to be superior even compared to TanDEM-X. Not observing degrading performance for high relief settings, the authors attribute the differences to the studies of Hu et al. (2017) and Purinton and Bookhagen (2017) to improvements made with version 1.1. Li and Zhao (2018) confirm that drainage network extraction of AW3D30 is better than in SRTM1.

AW3D30 data is provided with a stack number file denoting the pixel-specific number of triplets incorporated into DEM calculation. Regrettably, only Hu et al. (2017) evaluated the impact of the stack count on DEM accuracy, and found that accuracy statistics degrade considerably with a decreasing number of scenes. It is therefore appropriate to fathom the dependency of classification scores on fan-averaged stack counts, as well as to consider potential statistical relationships of the stack number with morphometric variables.

6.2.4 DEM assessment

In what follows, we perform an ad hoc visual assessment of AW3D30 and SRTM1 to gain preliminary insights into the quality of AW3D30 terrain rendition with focus on alluvial fans and their contextual setting. Depicted in Fig. 6.1 is a large alluvial fan (~54 km^2) bordering the Sarcobatus Flat, Nevada, a topographically closed basin at the southwestern border region to California (Hevesi et al., 2003).

The visualized alluvial fan features multi-lobation and directly adjoins an alkaline flat exhibiting virtually no relief. The study area is thus an ideal testbed for an evaluation of the textural characteristics of the considered elevation models. As elaborated in Pipaud et al. (2015 / Chapter 3), SRTM1 exhibits a blurred grainy texture attributable to interferometric decorrelation and the application of low pass filtering in the postprocessing stage (Rodríguez et al., 2006; Stevenson et al., 2010). Notably, the intrinsic resolution of SRTM1 is known to be approximately twice as large as its posting (Guth, 2006; Tachikawa et al., 2011b,c). In accordance with these constraints, high frequency information as modeled by SRTM1 is dominated by this textural grain, with microscale topography of the alluvial fan surface being completely obscured. While AW3D30 shows a grainy texture as well, this texture exhibits both a higher frequency and lower magnitude than those given for SRTM1. As a consequence, both the active lobe as well as smaller channels at the orographically left side of the fan are clearly depicted in the unfiltered DEM data, signaling a superior effective resolution and resultant landform rendition.

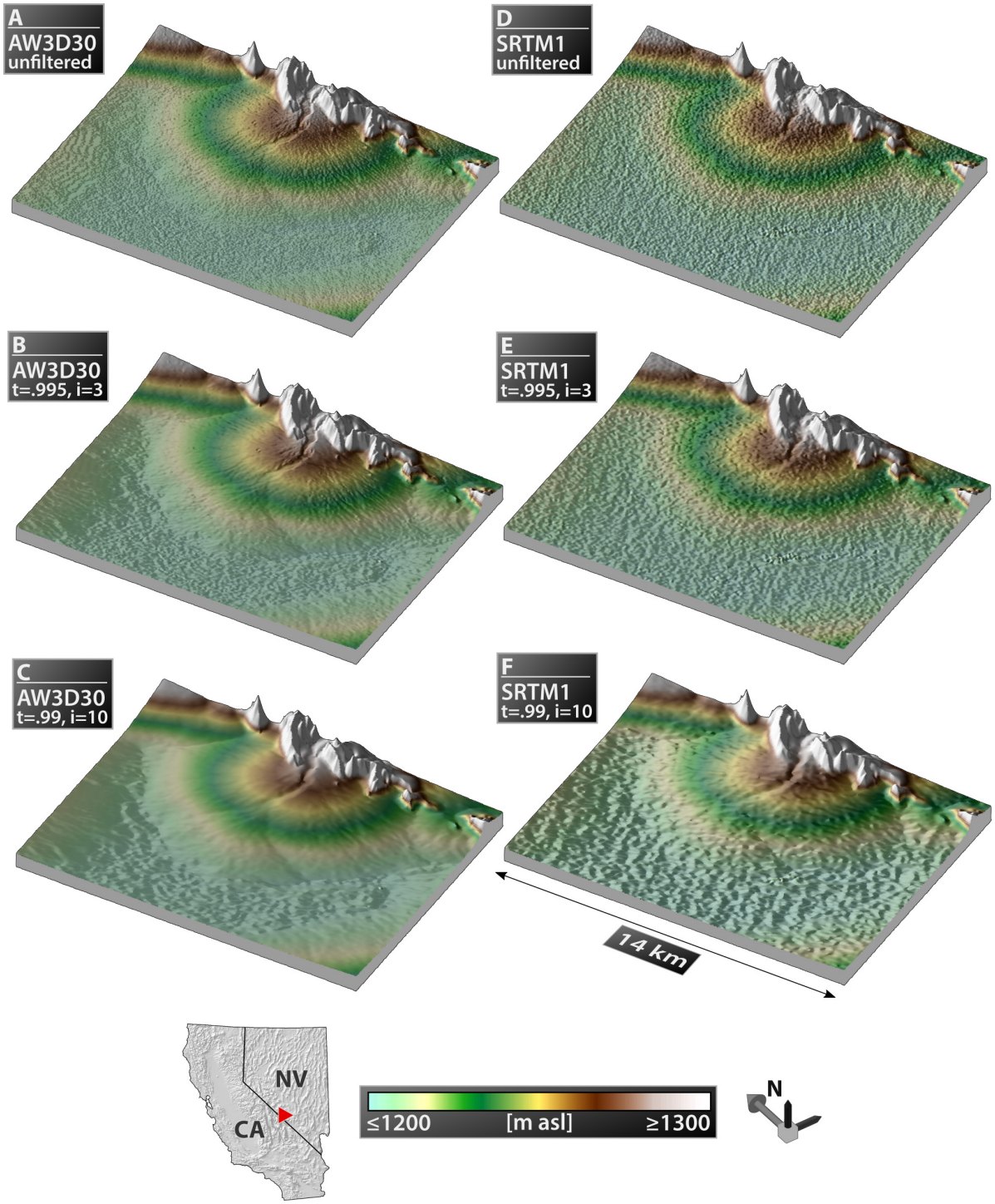


Figure 6.1: Perspective view on a large alluvial fan abutting the Sarcobatus Flat, SW Nevada, as depicted by versions of AW3D30 and SRTM1 differing in the degree of mesh denoising filtering applied. Terrain rendered with fivefold vertical exaggeration. To highlight the texture rendition of the considered DEM variants, directional components of slope aspect (cf. Pipaud and Lehmkuhl, 2017 / Section 5.5.1) were blended into an overlay of color-coded altitude values and hillshade. Note that this fan is part of the training dataset used to train the OCRF introduced in this study (Training ID 241, Training ID denoted TID hereafter).

6.2.5 DEM preparation

Since local geomorphometric parameters quantify topological relationships between local pixel neighborhoods (cf. Chapter 1), they require topographic information to prevail over noise in order to have an explanatory value for a geomorphic classification. Hence, it is indicated to assess if classification performance can be improved by DEM filtering, and if so, which filtering strength yields optimal results for the DEM at hand. We conducted filtering using mesh denoising, an adaptive filtering technique relying on transforming the DEM lattice into a triangular irregular network and performing a weighted local averaging based on the angular differences of normal vectors (refer to Section 5.5 for in-depth information on the mesh denoising algorithm; Sun et al., 2007; Stevenson et al., 2010).

In this study, two filtering intensities were applied to the elevation models: (1.) a light variant parametrized with a threshold of 0.995 and 3 smoothing iterations, and (2.) a more intense variant using a threshold of 0.99 and 10 smoothing iterations. Note that the second variant matches the filtering strength used in Pipaud and Lehmkuhl (2017 / Chapter 5), who found that this filtering strength is well suited for SRTM1. Fig. 6.1 illustrates the impact of the two filtering intensities on the altitude field. In the case of AW3D30, weak filtering is sufficient to purge noise from the altitude field depicting the alluvial fan. Conversely, the non-informative texture inherent to SRTM1 is only weakly filtered using the softer filtering variant, corroborating that noise frequencies exhibit larger magnitudes than those displayed by AW3D30. Notably, SRTM1 retains some noise even with stronger filtering.

6.3 Methods

6.3.1 Channel infilling

In what follows, we will address the infilling of major incised channels. Implying a substantial discrepancy from the model conception of alluvial fans as partial cones, we must expect trunk feeder channels to adversely affect likelihood scores of the respective fans. Notably, incised channels are a distinguishing feature for avulsion cycles, which are inherent to the autogenic morphodynamics of mature alluvial fans (cf. Section 2.1.2), but may also indicate time-transgressive morphodynamics of fan formation phases (cf. Sections 2.1.3 and 2.2.2). Therefore, the presence of incised channels potentially involves a negative bias of the classification scores obtained for these fans, which should be avoided.

For this purpose, we developed an object-based channel detection and channel infilling procedure, which is based on grayscale mathematical morphology. An illustration of the complete workflow is provided in Suppl. C.1. Initially, a Black Top Hat (BTH) algorithm is used to identify and quantify topologically low positions. A BTH filter is defined as subtraction between the original grid and its *closed* version, where closing is defined as dilation followed by erosion using the same kernel (cf. Rodriguez et al., 2002; Schmidt and Hewitt, 2004; Pipaud et al., 2015 / Chapter 3, and Pipaud and Lehmkuhl, 2017 / Chapter 5, for detailed information on the application of mathematical morphology in the field of geomorphology).

Defining the scope of pixels considered for filtering, i.e., the scale on which filtering is applied, the size and the shape of the kernel are crucial for the filtering result. Alluvial fan channels run approximately parallel to the mean local gradient, and channel detection thus involves a measurement of topological lows in cross-sectional direction. We therefore used a rectangular kernel with a pixel count

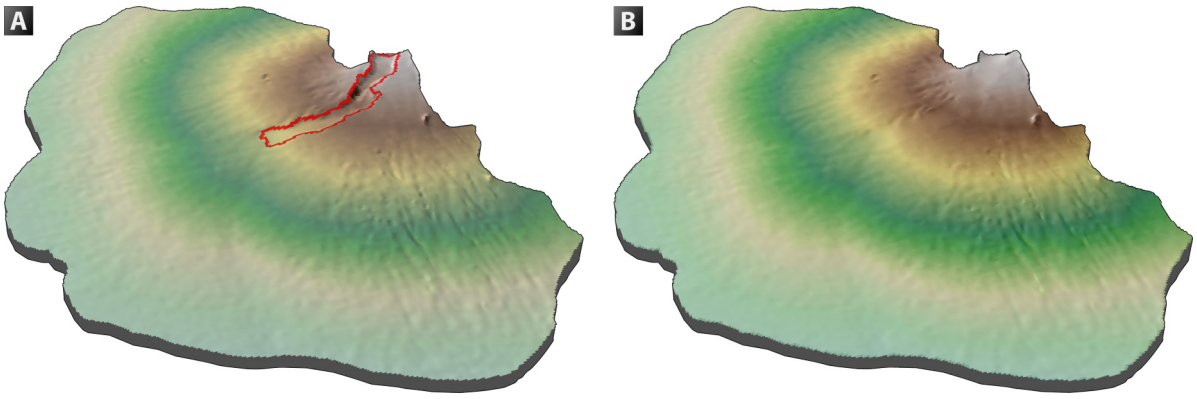


Figure 6.2: The result of the channel infilling procedure, depicted for fan TID 241 and the lightly filtered (t=.995, i=3) AW3D30 dataset. (A) Terrain rendering prior to channel infilling, and outline of the identified channel. (B) Result of the infilling procedure.

of 29 and 7 pixels, respectively, whose longer side is orientated perpendicular to the mean gradient of the alluvial fan.

Subsequently, the obtained BTH grid is thresholded using a value of 1 m, yielding a binary grid with patches of considerable incision. By converting this grid to vector data, we have a set of disjoint objects to whom we can apply an object-based morphometric analysis to identify the incised channel or to assert that no distinct channel exists on the respective fan surface. Prior to classification, we conduct a binary dilation by one pixel to incorporate edge zones of depressions with incision values below 1 m. A rule-based classification approach was used for the subsequent identification of channel objects. This choice was motivated by insufficient statistical support for channels within the dataset. In contrast, the distinct contextual setting of primary trunk channels facilitates the design of a robust rule set. Specifically, we assert that a potential channel shows (1.) an appropriate size with respect to the fan surface, (2.) emerges from the fan boundary, i.e., touches the fan perimeter, (3.) exhibits a minimum amount of incision, (4.) is located within the proximal to central parts of the fan surface, (5.) is elongated, and (6.) runs at an acute angle to the mean gradient of the fan surface:

$$C_{\mathrm{CH}} = \begin{cases} 1 \text{ if } & 0.002 \leq A_{\mathrm{CH}}/A_{\mathrm{AF}} \leq 0.1, \text{ and} \\ & \mathrm{CH} \text{ touches AF, and} \\ & 3\,\mathrm{m} \leq \max_{p \in \mathrm{CH}} \left(\mathrm{BTH}_p\right) \leq 70\,\mathrm{m}, \text{ and} \\ & 1\,\mathrm{m} \leq \overline{\mathrm{BTH}_{\mathrm{CH}}} \leq 10\,\mathrm{m}, \text{ and} \\ & \mathrm{dist}_{\overline{\nabla}}\left(\overrightarrow{c_{\mathrm{CH}}}\right) \leq 0.6 \cdot \max_{\vec{p} \in \mathrm{AF}} \left(\mathrm{dist}_{\overline{\nabla}}\left(\vec{p}\right)\right), \text{ and} \\ & M_{\mathrm{ecct}}(\mathrm{CH}) \geq 0.7, \text{ and} \\ & \measuredangle\left(\overline{\nabla_{\mathrm{CH}}}, \overline{\nabla_{\mathrm{AF}}}\right) \leq 40^\circ \\ 0 & \text{otherwise,} \end{cases} \tag{6.1}$$

where C_{CH} is the binary classification result for a potential channel object CH, A_{CH} and A_{AF} denote the planimetric area of the considered patch and the corresponding fan, respectively, $\mathrm{BTH}_{\mathrm{CH}}$ indicates the subset of all BTH grid values located under the object considered, c_{CH} is the centroid of the object under

consideration, M_{ecct} defines the eccentricity, $\text{dist}_{\overline{\nabla}}$ is a function measuring the planimetric distance in direction of the mean gradient of the fan, and $\measuredangle(\overline{\nabla_{\text{CH}}}, \overline{\nabla_{\text{AF}}})$ is defined as the angle between the mean gradient vectors of the object and the fan, respectively.

In this context, eccentricity is calculated via centralized moments of inertia. The centralized moment for a polygon is defined as (Jain, 1989; Nixon and Aguado, 2002; Gonzalez and Woods, 2008):

$$I_{pq} = \frac{1}{n_{v_{\text{CH}}}} \sum_{i=1}^{n_{v_{\text{CH}}}} (x_i - x_c)^p \cdot (y_i - y_c)^q \,, \tag{6.2}$$

where I denotes the moment, $n_{v_{\text{CH}}}$ is the number of vertices of the object boundary, (x_c, y_c) is the centroid of the polygon, and p and q define the order of the moment in x and y direction, respectively. The eccentricity is then given by (Jain, 1989):

$$M_{\text{ecct}}(\text{CH}) = \frac{\sqrt{(I_{20} - I_{02})^2 + 4 \cdot {I_{02}}^2}}{I_{20} + I_{02}} \tag{6.3}$$

Thresholds were defined in a conservative manner in order to avoid errors of commission, so that the algorithm is only sensitive to major incised channels. If, however, more than one object meets the conditions, the polygon displaying the largest incision, i.e., the largest average BTH value, is designated as incised channel. Eventually, all DEM values under the identified channel are substituted by a bicubic spline interpolate based on all surrounding border pixels, for which we used the algorithm provided by SAGA GIS (Conrad et al., 2015). A total of 22 feeder trunk channels were identified and subjected to the infilling procedure. An exemplary result of the channel infilling procedure is depicted in Fig. 6.2.

6.3.2 Morphometric formalization of alluvial fans

In the case of morphometric processing for classification purposes in the context of an object-based analysis setting, the objective is to provide parameters enabling a differentiation between the semantic class(es) of interest—in our case alluvial fans—and the miscellaneous geomorphological features remaining. Applying parameters specifically addressing the morphometric expression of alluvial fans, we can expect alluvial fans to exhibit a low intra-class heterogeneity when compared to a diverse geomorphological inventory. Besides using generic geomorphometric parameters, we build upon the findings of Pipaud and Lehmkuhl (2017 / Chapter 5) by reconsidering methods which impose a conical model on classification objects. While the gradient–apex divergence (GAD) was consequently reused in this study, the informative value of bilateral asymmetry (BAS) and half-splay angle (HSA) was found to be not substantially superior to generic morphometric parameters. Accordingly, these two variables were not taken into account in this study. For a discussion of generic morphometric variables, the reader is referred to Section 5.5.

Apex calculation

The cone-like alluvial fan morphology stems from radial sedimentation from the apex. Hence, specific morphometric parameters exploiting the location of the apex can be expected to provide high significance for alluvial fan discrimination (cf. Troeh, 1964, 1965; Pipaud and Lehmkuhl, 2017). In alluvial fan

research, the apex is uncritically defined as the emergence point of the feeder channel (cf. Section 2.1), i.e., the apex coincides with the inflow point of the delineated alluvial fan object (denoted *hydro apex* hereafter).

To perform such a hydrologically correct apex localization, we first calculated the mean position vector of the five pixels exhibiting the highest DEM pixel values, thus taking inaccuracies of the DEM into consideration. Let us denote this raw apex localization by the term *Z apex*. Subsequently, we evaluated the hydrological flow paths using the flow direction and flow accumulation routines provided by the ArcGIS 10.2/ArcPy API. Eventually, the preliminary apex point is shifted to that object boundary pixel which exhibits the largest flow accumulation (cf. Pipaud and Lehmkuhl, 2017).

With regard to mature alluvial fans, however, this hydrological perspective on apex localization is fraught with difficulties. Specifically, channel shifting is an inherent part of alluvial fan morphodynamics, so that the modern feeder channel as depicted in digital elevation data may not be representative for the sedimentary pattern of parts of the alluvial fan surface (cf. e.g., Clarke et al., 2010; Reitz and Jerolmack, 2012; Clarke, 2015; de Haas et al., 2016, 2018). Here, we introduce an alternative approach to apex localization, which is based on the convergence of lines defined by all pixel locations and the corresponding gradient vector (called gradient lines hereafter). Consider a radially symmetric, partial cone with arbitrary aperture angle. For this cone, all gradient lines intersect at a single point—the apex. In the case of real-world alluvial fans, a single intersection point does not exist, but most gradient lines should still intersect within a small area.

An expedient apex localization thus could in theory be performed by calculating the intersections of all gradient lines with each other, and deriving the point which is at a minimum distance to all intersection points. Let us name this method global gradient convergence (GGC), and this type of apex localization a *GGC apex*. The overall number of possible combinations is, however, given by the binomial coefficient for two mutually combined elements ($n!/(2(n-1)!$), where n denotes the number of pixels comprising the fan). It becomes clearly apparent that this approach is unfeasible for larger fans. We therefore propose to not consider explicit intersections of gradient lines, but to identify the point where the distance of all gradient lines to this point is at a minimum (cf. Fig. 6.3). Let the gradient vector corresponding to a pixel $\vec{p_i}$ be denoted by:

$$\nabla z(p_{i,x}, p_{i,y}) = \begin{pmatrix} \partial z/\partial x \\ \partial z/\partial y \end{pmatrix} = \vec{g_i} \tag{6.4}$$

We want to minimize the sum of the distance of an unknown apex $\vec{a}$ to all gradient lines. The gradient line of the pixel $\vec{p_i}$ is the line through the point p_i in direction of $\vec{g_i}$. The distance between the point a and the gradient line of $\vec{p_i}$ is given by:

$$\vec{d_i} = \widehat{\vec{g_{\perp,i}}} \cdot (\vec{a} - \vec{p_i}) = \widehat{\vec{g_{\perp,i}}} \cdot \vec{a} - \widehat{\vec{g_{\perp,i}}} \cdot \vec{p_i}, \tag{6.5}$$

where $\widehat{\vec{g_{\perp,i}}}$ is a unit vector perpendicular to $\vec{g_i}$. Considering $\vec{d_i}$ as an error term we shall minimize, the

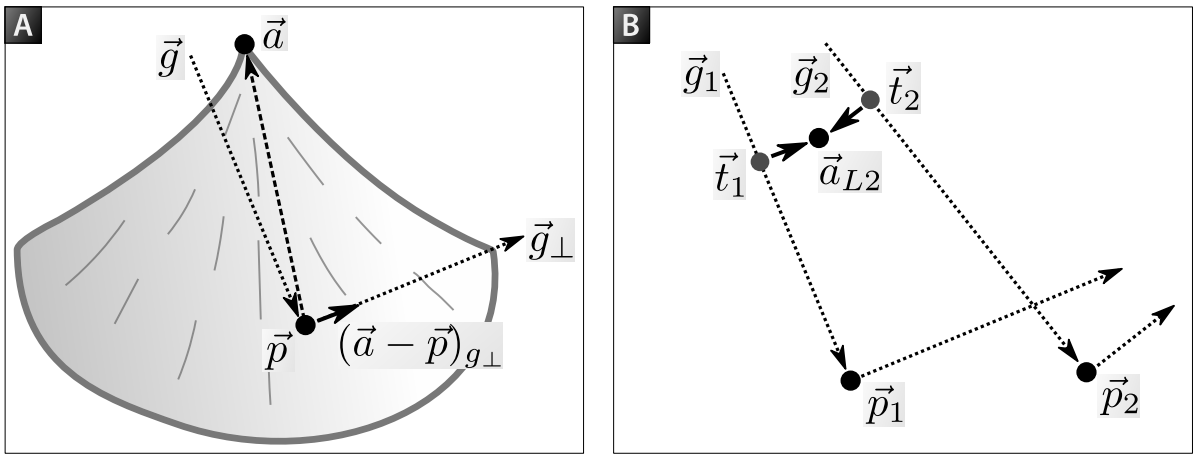


Figure 6.3: Schematic drawing of the global gradient convergence apex point estimation (GGC) method. (A) The algorithm first minimizes the squared distance of the GGC apex to all gradient lines $\vec{g_i}$. (B) For each gradient line, that point with minimum distance to the L_2-minimal apex point (t_i) is identified. All t_i points can then be used to identify the L_1-minimal point via the Weiszfeld approach.

least squares (L_2) criterion yielding the minimum distance point is given by:

$$\min \left\| \begin{pmatrix} (\widehat{\overrightarrow{g_{\perp,1}}})^T \\ \vdots \\ (\widehat{\overrightarrow{g_{\perp,n}}})^T \end{pmatrix} \vec{a} - \begin{pmatrix} (\widehat{\overrightarrow{g_{\perp,1}}})^T \cdot \vec{p_1} \\ \vdots \\ (\widehat{\overrightarrow{g_{\perp,n}}})^T \cdot \vec{p_n} \end{pmatrix} \right\|_2 \tag{6.6}$$

Equation (6.6) can now be solved using an ordinary least squares solver, which leads us to an efficient solution of the problem. However, an unfavorable property of L_2 solutions is its sensitivity to outliers, resulting in an unrobust solution (Rousseeuw and Leroy, 1987). Due to both high-frequency undulations in digital elevation data (cf. Fig. 6.1) and micromorphological features of the alluvial fan surface (Volker et al., 2007; Cavalli and Marchi, 2008; Regmi et al., 2014), a non-negligible portion of outliers is to be expected, potentially impairing the apex placement.

We thus suggest to replace the L_2-norm by the sum of absolute values (L_1 norm), which is known to be robust against outliers. Hence, we want to determine a point a such that the sum of distances to all gradient lines is minimal. Finding the point which minimizes the sum of distances to n non-collinear points in a plane is a classical locational problem—the Generalized Fermat Problem, which has no analytical solution (cf. Katz and Vogl, 2010). Weiszfeld (1937) proposed an iterative solution to the problem, and it has been shown that this algorithm is globally convergent for a set of non-collinear points. The iteration is given by:

$$\vec{a}^{(k+1)} = \frac{\sum_{i=1}^{n} \left\| \frac{\vec{t}_i^{(k)}}{\vec{a}^{(k)} - \vec{t}_i^{(k)}} \right\|}{\sum_{i=1}^{n} \left\| \frac{1}{\vec{a}^{(k)} - \vec{t}_i^{(k)}} \right\|}, \tag{6.7}$$

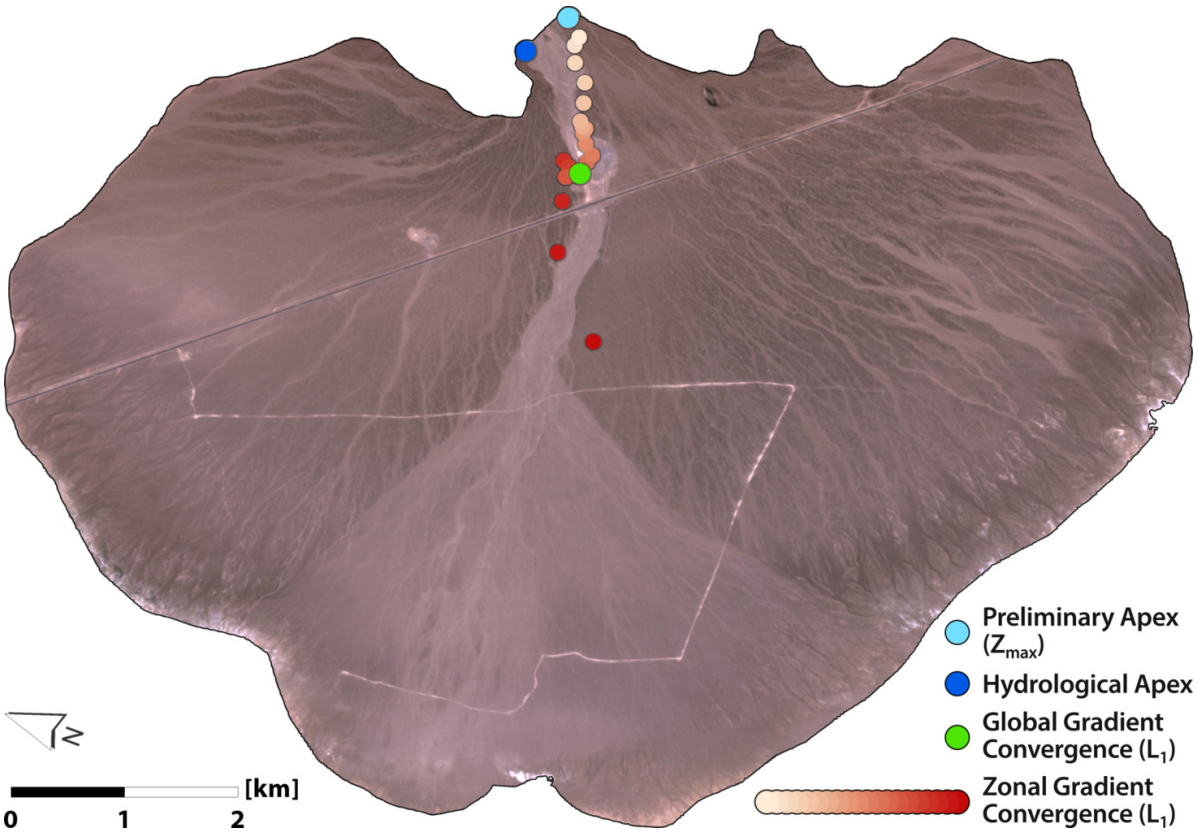


Figure 6.4: Comparison of apex points obtained with different methods. The color brightness of single ZGC points refers to the corresponding zone, with colors getting dimmer towards lower altitude zones. (Imagery source: Sentinel 2a)

where k is the iteration number, $a^{(k)}$ is the (preliminary) apex point, and $t_i^{(k)}$ are the n points for which a minimum distance is searched. In order to adapt the Weiszfeld algorithm to the problem at hand, it is, in every iteration, necessary to identify the points t_i on the gradient lines which are at minimum distance to the current apex guess $a^{(k)}$. Using the L_2-minimal apex as initial guess and recalculating all t_i after each iteration, we eventually obtain an L_1-minimal solution for the global gradient convergence (GGC) apex.

A beneficial characteristic of the gradient convergence method is that in contrast to hydrological apex placement, the calculation does not necessarily cover the whole alluvial fan surface. We may thus assert that characteristic alluvial fans do not only exhibit a plausible global apex localization, but that they also honor the radial sedimentation constraint when apex calculation is conducted separately for altitude zones of the alluvial fan surface. In doing so, this approach pays regard to the possibility that the gradient point may be different for vertical zones of the alluvial fan surface, with a prominent example being fans which display distinct active depositional lobes emerging from an intersection point (cf. Section 2.1.3). Furthermore, a zonal perspective on gradient convergence might help in cases where a fan bends towards a regional slope, as given for fans located in steep mountain valleys. Let us denote this approach by the name zonal gradient convergence (ZGC). In this study, we subdivide the alluvial fan surface into twenty overlapping vertical zones, each accounting for ten percent of the alluvial fan altitude range, and derive a separate convergence point for each of them (cf. Fig. 6.4).

In what follows, we shall be concerned with exploiting apex localization to yield morphometric parameters with high indicative and discriminatory value. In order to evaluate the suitability of the aforementioned apex localization methods for a one-class alluvial fan discrimination workflow, we will incorporate all four apex localization methods.

Gradient Apex Divergence

In the case of a partial cone with an arbitrary aperture angle, the directions of all gradient vectors $\nabla z(x, y)$ correspond precisely to the vectors given by the respective surface points to the apex of the cone. Any discrepancies from the model will thus result in an angle between both vectors, and the arithmetic mean of all angles measures the average deviation from the model—the gradient–apex divergence (GAD; Pipaud and Lehmkuhl, 2017 / Chapter 5):

$$\text{Gradient–Apex Divergence} = \frac{1}{n}\sum_{i=1}^{n} \arccos\left(\frac{\overrightarrow{AP_i} \cdot \vec{g_i}}{\|\overrightarrow{AP_i}\| \cdot \|\vec{g_i}\|}\right) \cdot \frac{180}{\pi}, \qquad \text{(5.14 revisited)}$$

where $\overrightarrow{AP_i}$ is the vector given from the apex A to the point P_i, and $\vec{g_i}$ is the vector given by the gradient ∇z_i in point $P_i(x, y)$.

Radial Approximation

As an alternative approach to the gradient–apex divergence, we can assess the discrepancy of an alluvial fan sample from the ideal partial cone model via trend surface analysis. By conducting trend surface analysis on a megafan in Brasil, Zani et al. (2012) demonstrated that a second order (bilinear) polynomial approximation is able to approximate the overall topographic trend, yielding a de-trended surface depicting smaller-scale landforms on a megafan. A second-order polynomial fits, however, to a multitude of landforms, and thus cannot provide discriminatory capabilities. We are thus interested in a function which is selective towards alluvial fans, i.e., an approximation method which yields large residuals for non-fans. In this context, Troeh (1965) already emphasized that a circular cone, which is augmented with an r^2 term, is the canonical trend surface for alluvial fan approximation:

$$z(r) = u \cdot r^2 + v \cdot r + w, \tag{6.8}$$

where r defines the radial distance of points to the apex, and u to w are the coefficients to be derived.

This function can be globally fitted using a regular least-squares solver, providing an L_2-minimal solution. By enforcing a straight or concave radial profile, we further specialize the trend surface to fit to alluvial fan surfaces, but to fail for most non-fan surfaces. A non-negative least squares (NNLS) minimizer (Lawson and Hanson, 1995) can be utilized to constrain the radial curvature—defined by u—to zero or positive values. Note that for alluvial fans, the radial slope as defined by v must be always negative. To allow a restriction to positive values for v, the coefficient must be determined for the negative value of r. Furthermore, s has been added to account for alluvial fans with apexes below sea level. It follows:

$$z(r) = u \cdot r^2 + v \cdot -r + w \cdot s \quad \text{with } s = \begin{cases} 1 & \text{if } z(0) \geq 0 \\ -1 & \text{otherwise} \end{cases} \tag{6.9}$$

As already discussed in Section 6.3.2, L_2 solutions are sensitive to outliers. Outliers of the residual between radial approximation and actual fan surface are, however, to be expected for real alluvial fans due to factors such as channel incision and progradation (cf. Chapter 2). Iteratively re-weighted least squares (IRLS) minimization allows for the derivation of other p-norms (with $1 \leq p \leq 2$) by iteratively solving a weighted least squares problems, using any kind of L_2-minimizer including the NNLS method just introduced (cf. e.g., Holland and Welsch, 1977; Björck, 1996):

$$\min \left\| \begin{pmatrix} w_1 \left(r^2(\overrightarrow{p_1}), -r(\overrightarrow{p_1}), s\right) \\ \vdots \\ w_n \left(r^2(\overrightarrow{p_n}), -r(\overrightarrow{p_n}), s\right) \end{pmatrix} - \begin{pmatrix} w_1 \\ \vdots \\ w_n \end{pmatrix} \begin{pmatrix} z(\overrightarrow{p_1}) \\ \vdots \\ z(\overrightarrow{p_n}) \end{pmatrix} \right\|_2, \tag{6.10}$$

where w_i define the respective weightings for which the L_2-minimal solution will be derived, and $z(\overrightarrow{p_i})$ denotes the corresponding altitude value for the pixel $\overrightarrow{p_i}$.

The pixel-specific weightings w_i are set to 1 in the first iteration and then calculated using:

$$w_i^{(k)} = \left|y_i - z_i\right|^{(p-2)/2}, \tag{6.11}$$

where k indicates the iteration number, p defines the norm, and y_i is the estimate of the altitude z_i obtained in iteration $k-1$. In the case of $p = 1$, we use:

$$w_i{}^{(k)} = \max\left(\delta, \frac{1}{\sqrt{|y_i - z_i|}}\right), \tag{6.12}$$

where δ is a small regularization constant precluding a division by zero.

When calculating the non-negative L_1 approximation (NNL_1) for alluvial fans, we must bear in mind that an exclusively concave or straight radial profile is a restrictive conception of alluvial fan morphology. This assertion is particularly true for prograding alluvial fans, where the proximal fan build-up can result in longitudinal convexity.

We use the mean absolute difference (MD) between the alluvial fan surface as modeled by the DEM and the respective approximation surface as the object-specific morphometric variable assigned to each fan sample:

$$\mathrm{MD} = \frac{1}{n}\sum_{i=1}^{n}\left|y_i - z_i\right| \tag{6.13}$$

It is important to point out, however, that as we measure residuals—i.e., vertical differences—the mean absolute difference is affected by surface slope. In this context, consider the hypothetical case of a small segment of the trend surface running parallel at an arbitrary offset to the alluvial fan surface it models. The mean absolute difference is then dependent on surface slope according to:

$$\mathrm{MD} = \left|\frac{d}{\cos\theta}\right|, \tag{6.14}$$

where θ denotes the slope angle of both surfaces, and d denotes the offset. It becomes apparent that by using MD on residuals, steeper fans obtain spuriously high MD values. To address this issue in

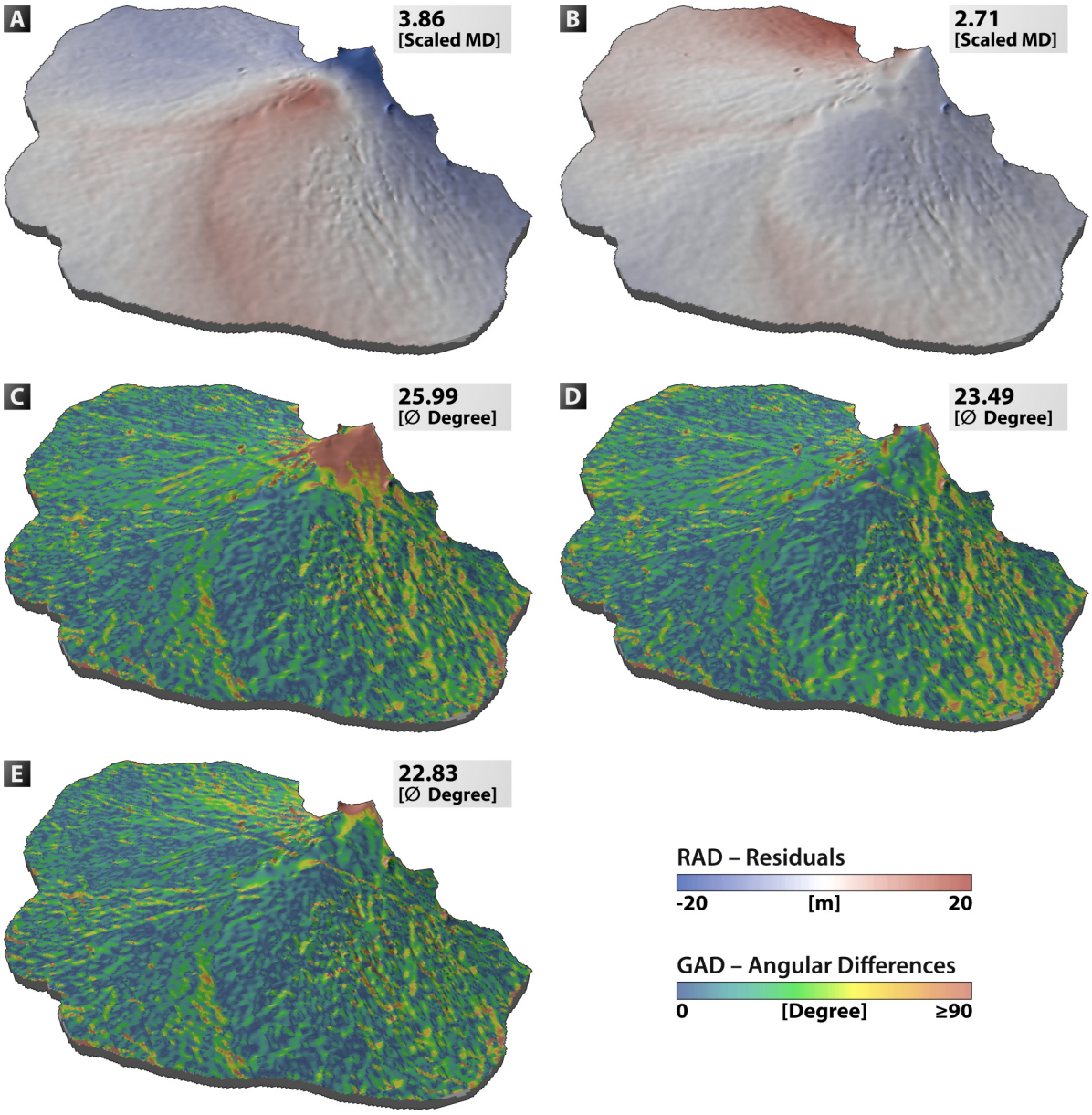


Figure 6.5: Comparison of radial approximation divergence (RAD) and gradient–apex divergence (GAD) rasters for training fan TID 241. (A) RAD calculated with the global gradient convergence (GGC) apex as reference point, (B) RAD calculated with the hydrological apex, (C) GAD calculated with the GGC apex, (D) GAD calculated with the zonal gradient convergence (ZGC) apex, (E) GAD calculated with the hydrological apex.

the simplest possible manner, we calculate the mean absolute difference for dimensionless values of altitude, i.e., we rescale both surfaces assigning 0 and 1 to the lowermost and uppermost altitude value, respectively. An exemplary display of all radial approximation divergence (RAD) and GAD measures considered is provided in Fig. 6.5.

Contextual measures

In the field of object-based image analysis, it is widely acknowledged that particular emphasis must be given to contextual measures—that is, measures that quantify the spatial context that an object is embedded in and the mutual relations between objects—to fully exploit the potential of object-based analysis (Blaschke, 2003; Benz et al., 2004; Blaschke, 2010). In geomorphometric research of alluvial fans, contextual metrics have, however, received little consideration so far. Hashimoto et al. (2008) proposed a method to measure the change of aspect slope at alluvial fan toes. After deriving representative areas above and below fan toes by conducting a polygon buffer analysis, they defined distal slope change as the ratio of mean slope of the upper area (inner zone, IZ), divided by the mean slope of the lower area (outer zone, OZ).

In this study, we will build upon this approach, but enhance it in one major point. Instead of taking the ratio of mean aspect slope of both zones, we defined the distal gradient difference (DGD) as the difference of the mean directional slope angles, where the direction is given by the mean gradient vector of the full alluvial fan surface. A valuable characteristic of this approach is that it yields negative slope values for gradient vectors opposing the average fan gradient, thereby tackling cases where the adjacent foreland is sloping towards the fan. By measuring slope in the direction of mean fan aspect, the DGD also handles peculiar geomorphological settings in which aspect changes significantly between the lowermost parts of the fan and the adjoining downstream areas. This mainly applies to alluvial fans embedded into steep mountain valleys, where the aspect tends to abruptly bend over to the longitudinal axis of the valley. The mean directional slope of a surface patch (in degrees) is given by:

$$\text{Slope}_{\bar{\nabla}} = \frac{1}{n} \sum_{i=1}^{n} \arctan\left(\hat{\bar{\nabla}} \cdot \nabla(\vec{p_i})\right) \cdot \frac{180}{\pi}, \tag{6.15}$$

where n denotes the number of pixels comprising the surface patch considered, $\nabla(\vec{p_i})$ denotes the gradient given for the pixel $\vec{p_i}$, and $\hat{\bar{\nabla}}$ is the unit vector of the mean gradient of the fan surface. Equation (6.15) is first calculated separately for the inner and outer zone. Subsequently, we obtain the DGD (in degrees) by using:

$$\text{Distal Gradient Difference} = \text{Slope}_{\bar{\nabla},\,\text{OZ}} - \text{Slope}_{\bar{\nabla},\,\text{IZ}} \tag{6.16}$$

We define the inner zone as the set of all pixels exhibiting altitude values between the lowest 5 % and 20 % of the altitude range. As depicted in Fig. 6.6A, the outer zone is given by a rectangle whose short side runs parallel to the mean gradient vector, and whose long side is specified by the width of the fan. Here, fan width is defined as the lateral extent of the fan given in the direction perpendicular to the mean gradient. The outer zone starts at 105 % of alluvial fan length as defined by the mean gradient, and the rectangle length is chosen so that the number of pixels matches that of the inner zone. In agreement with the work of Hashimoto et al. (2008), we keep a void between both zones to account for potential irregularities such as distal erosion of the fan surface (cf. e.g., Crosta and Frattini, 2004). Note that a positive and negative sign indicate divergent and convergent surface patches, respectively.

The proposed method can be easily adapted to measure the lateral gradient difference (LGD), which is illustrated in Fig. 6.6B. Specifically, we first calculate the slope in direction of the vector running

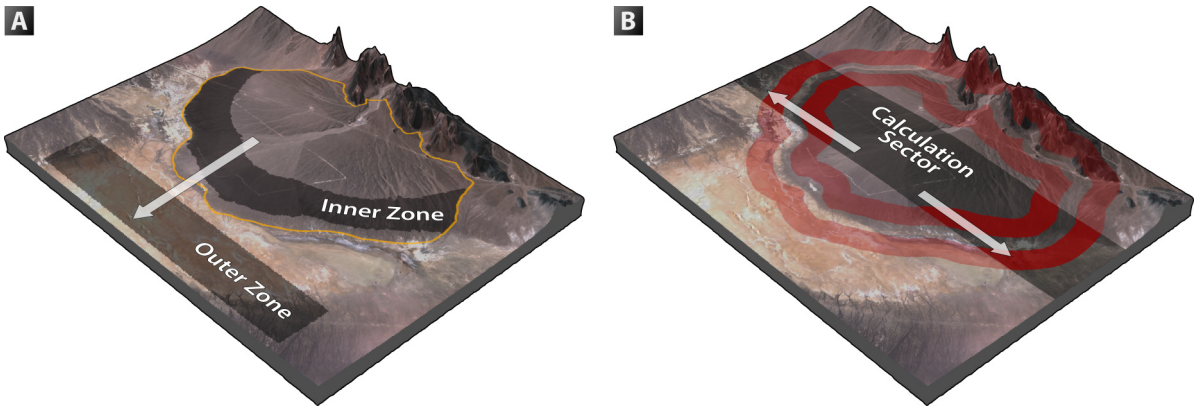


Figure 6.6: Schematics of calculation for the distal gradient difference (DGD) and the lateral gradient difference (LGD). (A) Zones derived for estimating the DGD, with the arrow denoting the direction of the mean gradient of the fan surface. While the inner zone is based on altitude zoning, the outer zone is based on distance in direction of the mean fan gradient. (B) Zones derived for the LGD calculation. The inner and outer buffer zones are intersected with a calculation sector, whose orientation is again based on the distance in direction of the mean fan gradient. (Imagery source: Sentinel 2a)

perpendicular to the mean gradient of the fan:

$$\text{Slope}_{\bar{\nabla}\perp} = \frac{1}{n}\sum_{i=1}^{n} \arctan\left(\hat{\bar{\nabla}}\perp \cdot \nabla(\vec{p_i})\right) \cdot \frac{180}{\pi}, \tag{6.17}$$

where $\hat{\bar{\nabla}}\perp$ is a unit vector orthogonal to the mean gradient of the fan surface. As shown in Fig. 6.6B, we calculate the inner and outer zone by conducting a buffer analysis on the alluvial fan boundary, obtaining circumferential zones with a width of 0.1 times the alluvial fan width. A void of 10 % of the alluvial fan width is kept to avoid potential adverse effects due to ambiguous lateral demarcations, which is to be expected in the case of strong lateral coalescence (cf. e.g., Sorriso-Valvo et al., 1998; Crosta and Frattini, 2004; Cavalli and Marchi, 2008). From these circumferential zones, we obtain the final zones by extracting the respective segments in the central area of the fan (see Fig. 6.6B). Yielding two inner and outer zones each, this computation results in the following definition for the LGD (in degrees):

$$\text{Lateral Gradient Difference} = \frac{1}{2} \cdot \sum_{\ell=1}^{2} \text{Slope}_{\bar{\nabla}\perp,\text{OZ}_\ell} - \text{Slope}_{\bar{\nabla}\perp,\text{IZ}_\ell}\,, \tag{6.18}$$

where ℓ defines the orographical side of the alluvial fan a zone pair is given for. Analogous to the DGD, positive and negative values signify divergent and convergent gradient patterns, respectively.

Auxiliary measures

In this section, we will briefly introduce metrics which bear no direct discriminatory potential for one-class fan classification, but are expected to exhibit informative value about causal factors for high or low membership likelihoods. As we discussed in detail in Chapter 2, an important internal differentiation of the alluvial fan inventory is caused by the amount of accommodation space produced by tectonic

rejuvenation. Insufficient accommodation space forces fans to prograde and coalesce, which in prior research has been measured via elongation and splay angle metrics (cf. Clevis et al., 2003; Viseras et al., 2003; Densmore et al., 2007; Bahrami, 2013).

The GGC approach introduced in Section 6.3.2 allows for a direct measurement of the concomitant downstream shift of the deposition locus. We thus introduce the apex distance factor (ADF), which is defined as the distance of the GGC point with respect to the most upstream point of the fan area in relation to the maximum distance found for the fan surface:

$$\text{Apex Distance Factor} = \frac{\text{dist}_{\bar{\nabla}}\left(P_u, P_{GGC}\right)}{\left|\max_{P \in \text{AF}}\left(\text{dist}_{\bar{\nabla}}\left(P_u, P\right)\right)\right|}, \tag{6.19}$$

where P_u denotes the most upstream point on the fan surface (with respect to $\bar{\nabla}$), P_{GGC} is the GGC apex, and $\text{dist}_{\bar{\nabla}}\left(P, P_{\text{GGC}}\right)$ denotes the planimetric distance between P_{GGC} and the point obtained from projecting P onto the line through P_{GGC} in direction of $\bar{\nabla}$, i.e., the difference between P and P_{GGC} *in direction of* $\bar{\nabla}$. Note that shifts in downstream direction receive negative signs, i.e., fans characterized by progradation display negative values for the ADF.

High-frequency undulations of the altitude field as modeled by the DEM impair the deduction of thematically significant morphometric information. Being interested in a comparative performance assessment of SRTM1 and AW3D30, as well as different DEM preprocessings, surface ruggedness shall be considered as auxiliary metric. With respect to AW3D30, we are specifically interested in potential interrelations between the number of incorporated scene stacks with surface ruggedness and membership scores. In this study, we quantified local surface ruggedness applying the vector ruggedness measure (VRM) after Sappington et al. (2007) with a 3×3 cell calculation window. For further information on the VRM algorithm, refer to Section 3.5.2.

6.3.3 Classification

Random forests

We shall now be concerned with the introduction of one-class random forests (OCRFs) for alluvial fan classification. A random forest is an ensemble meta-algorithm which utilizes random sampling and a large number of decision trees to cast a majority vote on the class membership assigned to samples, thereby averting the overfitting issues inherent to a single decision tree (Breiman, 2001; Louppe, 2014).

A decision tree is a hierarchic, non-parameteric supervised machine learning algorithm which is based on successively applying a split logic on a classification dataset to partition the data into two or more target classes. This recursive partitioning scheme results in a tree structure, consisting of a root node, an arbitrary amount of inner nodes, and two or more leaves. Without any further logic, the recursion proceeds until all leaves are pure, i.e., all leaves contain members of a single class only. Decision trees with exclusively pure nodes are referred to as being *fully built*. A Classification and Regression Tree (CART) is a common decision tree variant which identifies optimal *binary* splits by maximizing the reduction in entropy achieved by the split, performing a heuristic search (Breiman et al., 1984). In their original approach, Breiman et al. (1984) propose to use the Gini impurity as entropy

metric:

$$G = 1 - \sum_{j=1}^{J} \mathbb{P}(C_t = j)^2, \tag{6.20}$$

where J is the number of feature classes, and $\mathbb{P}(C_t = j)$ is the probability that a sample which is randomly chosen from all the samples at the considered node t belongs to the class j.

Having built a decision tree with a training dataset, a tree can be used for classification tasks by passing a sample through the tree and assigning the target value of the leaf the sample ends in.

Decision trees are widely acknowledged for their low classification bias, simplicity, and interpretability (Hastie et al., 2009). An outstanding characteristic in the context of geomorphometry is that the binary split logic also implies that no assumptions on the statistical distribution of the incorporated features need to be made (cf. Pipaud and Lehmkuhl, 2017 / Chapter 5; Chapter 7). Consequently, decision trees are able to handle a diverse set of value ranges and data distributions well, and therefore do not require any standardization techniques.

A serious shortcoming of decision trees is, however, that they show bad generalization performance, i.e., they are prone to overfit to the training dataset and show a large variance for a set of evaluation datasets (Bramer, 2007; James et al., 2013). This issue can be partially mitigated by so called pruning techniques, which are essentially based on halting the splitting process at nodes if a certain criteria is met, or pruning the tree back to nodes so that the generalized accuracy is not adversely affected (see, e.g., Quinlan, 1986; Breslow and Aha, 1997; Strobl et al., 2009).

Ensemble meta-algorithms can be utilized to improve the stability and accuracy of machine learning approaches. With respect to decision trees, the rationale is to improve the generalization performance while keeping the classification bias as low as possible. This can be achieved by generating, using randomization techniques, a set F of little correlated tree classifiers T_j, where each tree casts a single vote on the target class for a sample so that the vote of the ensemble is given by the majority of votes. For the binary case, the majority vote for a sample x is given by:

$$C_F(x) = \begin{cases} 1 & \text{if } \dfrac{1}{n_T} \displaystyle\sum_{i=1}^{n_T} C_{T_i}(x) \geq 0.5 \\ 0 & \text{otherwise,} \end{cases} \tag{6.21}$$

where C_F is the class value obtained for x, C_{T_i} is the class vote casted by a single tree T_i, and n_T is the number of tree classifiers in F. Inspecting Equation (6.21), it is readily apparent that we can also obtain a continuous score S_F providing us with a measure of membership likelihood, essentially turning an ensemble classifier into a fuzzy classification approach. For the binary classification case, it follows:

$$S_F(x) = \frac{1}{n_T} \sum_{i=1}^{n_T} C_{T_i}(x) \tag{6.22}$$

In this study, we will use continuous scores exclusively.

A common randomization technique is bootstrap aggregating (bagging), which is premised on building multiple decision trees using randomly generated tree-specific samplings D_i from a training

dataset D, both with size n (cf. Breiman, 1996). Random sampling is performed with replacement, yielding training sets which in average contain $1 - (1 - 1/n)^n \approx 63\,\%$ unique training objects, the rest being duplicates (Efron, 1979; Efron and Tibshirani, 1997). As splitting continues to be performed in a deterministic way, the trees still show considerable correlation.

Originally proposed by Breiman (2001), the random forests approach further reduces tree correlation by supplementing bagging with random feature selection. At each node, the best split is searched among a subset of randomly selected features (node-level feature bagging). Let us denote the number of features considered at each split by the term mtry. The best value for mtry depends on the problem considered, and can be assessed via cross-validation in a straightforward manner. For classification tasks, Breiman (2001) suggests to default to $\sqrt{n\ \text{features}}$, which according to Díaz-Uriarte and Alvarez de Andrés (2006) leads to optimal or close to optimal results. Since the random forest algorithm is considered to not overfit to training data, fully-built CART-like trees can be used.

A particularly advantageous feature of random forests for classification in the field of geomorphometry is that the algorithm can generally be considered to be robust against features which turn out to be irrelevant for the problem at hand, thereby facilitating the classification setup and avoiding anthropic bias (Bostrom, 2002). Due to the principle of local optimal split selection, the probability of an irrelevant feature to be selected for partitioning in upper tree nodes is low. Deeper in the tree, however, the feature will eventually be selected because it provides largest reductions of entropy by chance. Hence, the inclusion of an irrelevant feature will increase the tree depth and potentially exacerbate the overfitting characteristic of individual trees. In the case of tree ensembles, this issue is, however, mostly mitigated by bootstrapping. In the case of random forests, the robustness against irrelevant features depends on the number of irrelevant features in relation to mtry, with a degraded performance possible for low mtry values (Hastie et al., 2009).

One-class random forests

Recall that in this study, we focus on identifying a single type of landform and differentiating it from the full geomorphological inventory. Therefore, we aim at creating a representational model for the landform of interest which allows us to reliably test if new observations represent new members of this semantic class. In this context, it is unfeasible to provide reference data for the full geomorphological inventory of a study area for practical reasons. What is more important, however, is that creating a conventional multi-class dataset entails the risk of introducing user-bias into the classification model. Because CART-like trees try to establish optimal splits between two or more classes of interest, a multi-class model can serve as a universal representational model for a single landform type only if all training sets for all landforms represent the respective basic populations. This is a condition which can hardly be ensured in practice.

We thus propose the use of a one-class classification algorithm for classification tasks focusing on a single landform type. Random forests are intrinsically discriminative classifiers which require at least one other class for partitioning. Adapting them to a one-class problem thus involves simulating a null-class so that a regular binary random forest approach is applicable. While the feature space distribution of the thematic class can be utilized to seed null-class samples, one major challenge needs to be addressed. Specifically, by using the set of morphometric parameters as introduced in Section 6.3.2,

we define a relatively high-dimensional feature space. As a consequence, even a dataset of 306 alluvial fans provides only sparse information about the shape of the alluvial fan property space, and it is inviable to provide a mesh grid of outliers with reasonable sparsity (cf. *curse of dimensionality*; Bellman, 1984; Aggarwal and Yu, 2001). In this context, note that it is particularly this general uncertainty about the delimitation of the high-dimensional property space which motivates the use of continuous membership scores.

One-class random forests were first proposed by Désir et al. (2013). Their approach to tackle the curse of dimensionality consists of applying the random subspace method on a tree level (Ho, 1998; Panov and Džeroski, 2007), i.e., decision trees are trained only for subspaces of the full feature space. For null-class seeding, they examine the statistical distribution of the positive class within the selected subspace via normalized histogram calculation, and seed outliers according to the complementary histogram. This method has, however, the adverse effect that it exacerbates the susceptibility of the forest towards features bearing little relevance for the classification problem. With tree-wise feature bagging, trees can be built on uninformative features only, so that they exhibit no explanatory power for the problem at hand (cf. e.g., Xu et al., 2012; Nguyen et al., 2015). Furthermore, effects of tree-level feature bagging on feature importance measures (cf. Section 6.3.3) have, to the best of our knowledge, not yet been investigated.

In this study, we thus propose an alternative approach which refrains from feature bagging, but tries to estimate the multi-dimensional variable distribution in a more robust fashion. As histograms are intrinsically discrete—they rely on counting samples in (hyper-) bins, they cannot appropriately reflect sparse datasets in high-dimensional spaces (Wasserman, 2010). Hence, we propose kernel density estimation (KDE) as a basis for property space identification and outlier seeding. KDE—also known as Parzen-Rosenblatt window method—is a non-parametric method to estimate the true probability density distribution f of a variable from a set of samples (Rosenblatt, 1956; Parzen, 1962). KDE is premised on centering a kernel function over each sample point X_i. Here, a kernel is a non-negative, integrable smoothing function which is usually symmetric and normalized so that it integrates to unity, and whose amount of smoothing can be controlled by a bandwidth h. The kernel density estimate for a value x is then given by the local average of all centered kernels (Jones et al., 1996b):

$$\widehat{f}_{h,K}(x) = \frac{1}{n}\sum_{i=1}^{n}\frac{1}{h}K\left(\frac{x - X_i}{h}\right), \tag{6.23}$$

where $\widehat{f}$ is the estimator function for f, and K is the kernel function. Different kernels are applicable for kernel density estimation, and the reader is referred to Silverman (1986) for an overview of kernel functions. A popular kernel is the *Gaussian* kernel, which is given by:

$$K(x) = (2\pi)^{-0.5} \cdot e^{-x^2/2} \tag{6.24}$$

Another commonly used kernel is the *Epanechnikov* kernel, defined as (Epanechnikov, 1969):

$$K(x) = \begin{cases} 3/4\left(1 - x^2\right)/5 & \text{if } |x| < \sqrt{5} \\ 0 & \text{otherwise} \end{cases} \tag{6.25}$$

It can be shown theoretically and empirically that the kernel density estimate converges to the true probability density distribution for large n and an optimal bandwidth h (Nadaraya, 1965). Consequently, we search for a function $\hat{f}$ that approximates f in a globally optimal manner, i.e., that minimizes the integrated mean squared error (IMSE; Jones et al., 1996b; Li and Racine, 2009):

$$\mathrm{IMSE}\,(h, K) = E \int \left(\widehat{f}_{h,K}(x) - f(x)\right)^2 \mathrm{d}x \tag{6.26}$$

In this context, note that while the Epanechnikov kernel is optimal in the sense of minimizing the mean squared error (MSE; Hodges and Lehmann, 1956; Epanechnikov, 1969), differences between kernels tend to be small, and kernel selection is therefore not crucial for the estimation outcome (cf. e.g., Silverman, 1986; Wasserman, 2010). The problem of finding an optimal estimator thus effectively reduces to finding the bandwidth which minimizes the IMSE (Li and Racine, 2009).

A simple approach to empirical bandwidth optimization are rule-of-thumb estimators, which yield a bandwidth which minimizes, for a given sample size and standard deviation, the IMSE by assuming the true probability density function is a Gaussian (Silverman, 1986; Marron, 1988; Scott, 1992; Jones et al., 1996b). This so called normal reference (NR) estimator is defined as:

$$h_{\mathrm{NR}} = 1.059 \cdot \sigma \cdot n^{-1/(4+d)}, \tag{6.27}$$

where d is the number of dimensions, and σ is the standard deviation of the true density distribution. Note that because σ is unknown, the standard deviation of the samples is used instead. The normal reference estimator regularly overestimates the bandwidth, i.e., it yields an over-smooth estimate of the true distribution (Sheather, 1992; Jones et al., 1996b). We are thus interested in obtaining a fully data-driven density estimate which makes no a-priori assumptions on the true density distribution. For the study at hand, we incorporated likelihood cross-validation (cross-validated maximum likelihood, CVML), which maximizes the leave-one-out log-likelihood of the samples and is defined as (Stone, 1974; Rudemo, 1982; Racine, 2008):

$$h_{\mathrm{CVML}} = \max \left(\sum_{i=1}^{n} \log \widehat{f_{-i}}(X_i) \right), \tag{6.28}$$

where $\widehat{f_{-i}}$ is the leave-one-out kernel estimator of f that uses all training samples except X_i. Cross-validated maximum likelihood (CVML) estimation is a batch approach which repeatedly calculates estimates of the likelihood for the left-out samples. A numerical optimization algorithm is used to find the bandwidth which yields the maximum average value for the estimate $\hat{f}$. Here, we used the implementation of the Nelder-Mead (downhill simplex) algorithm from the SciPy project (Nelder and Mead, 1965; Millman and Vaught, 2008). Note that the above considerations do not necessarily indicate that CVML-based OCRF instances yield a higher classification performance than instances which apply the normal reference approach. Specifically, the impact of data sparsity might mask the effect of a distribution estimate which is more accurate from a statistical perspective. As the CVML method involves additional computational load, we will apply both methods to assess whether CVML offers substantial improvements over an NR-based estimation.

Table 6.1: Evaluated hyper-parameter sets. For all considered DEM variants, the most appropriate parametrization of the OCRF was evaluated by optimizing the area under curve (AUC) for the evaluation dataset via exhaustive grid search. Note that the NR approach is only valid for a Gaussian kernel, and consequently was omitted for the Epanechnikov kernel.

Kernel	mtry	Bandwidth estimation	Total
Gaussian	1–9	CVML, NR	18
Epanechnikov	1–9	CVML	9
Total (×6 DEM variants)			162

Outliers cannot be seeded from the obtained empirical probability densities in a direct manner. Conversely, we rely on predefining locations and obtaining their respective likelihoods from the validated KDE. For each tree of the OCRF ensemble, an individual set of 1 M points was seeded with random locations within the enclosing hypercube. After calculating density values using the validated KDE, the set of likelihood values is upscaled to exhibit a likelihood of 1, and inverted. Subsequently, we obtain the final outlier points by sampling from the respective cumulative density function. While random forests show moderate robustness towards imbalanced classes, they yield best results when trained with balanced data (cf. e.g., Drummond and Holte, 2003; Dittman et al., 2015). Hence, we seed a set of 306 outliers for every tree. Note that the tree-specific outlier seeding adds an additional level of randomization, leading to a more diverse set of trees than in a conventional random forest. Consequently, it is to be expected that a OCRF reaches its maximum performance and stability at a relatively high number of trees (cf. Hastie et al., 2009). Each OCRF was therefore built by 3000 trees.

By principle, an assessment of inter-class heterogeneity cannot be conducted within a one-class context. Hence, we shall compare the landform under consideration with landforms which exhibit most similar morphometric properties. Considering alluvial fans, this applies to landforms grading into alluvial fans—alluvial plains and alluvial slopes (cf. Section 2.1.5). In this study, we will evaluate classification performance by incorporating the OBMA dataset obtained by Pipaud and Lehmkuhl (2017 / Chapter 5) for a study area of the Mongolian Altai (Region 6; cf. Chapter 4). Specifically, we extracted a set of 12 characteristic alluvial fans, as well as a null-class population of 14 members, containing both alluvial slopes and alluvial plains. Note that none of the evaluation fans was used for the training dataset. We estimate optimal hyper-parameter[1] sets by employing the area under curve (AUC) obtained for the evaluation dataset as metric for the diagnostic ability of the respective OCRF instance, and performing an exhaustive grid search. For all six DEM variants considered, this results in a total number of 162 validated hyper-parameter sets (cf. Table 6.1).

In the context of binary machine learning algorithms, AUC refers to the area under the receiver operating characteristic (ROC) curve (also denoted AUROC). The ROC curve is defined as the curve made up of corresponding true positive rates (TPRs) and false positive rates (FPRs; cf. Table 6.2), obtained for all possible variations of the discrimination threshold (Bradley, 1997; Fawcett, 2006). It follows that the AUC is a measure for the average diagnostic ability of a binary classifier across the full

[1] With regard to machine learning algorithms, hyper-parameters are parameters which are not directly learned within the estimator.

Table 6.2: Terminology of metrics used for the evaluation of machine learning algorithms.

Abbreviation	Metric	Explanation / Derivation
P	Condition positive	Number of real positives in the dataset
N	Condition negative	Number of real negatives in the dataset
TP	True positive	Actual positives, correct assignments
FP	False positive	Type I errors, errors of commission
TN	True negative	Actual negatives, correct assignments
TPR	True positive rate, sensitivity	TP/P
FPR	False positive rate, fall-out	FP/N
ACC	Accuracy	(TP + TN)/(P + N)

range of selectable discrimination thresholds. For evaluation purposes, we will also consider accuracy (ACC) values, a metric which quantifies the diagnostic potential for a given discrimination threshold.

Note that while the area under the ROC curve is a popular approach to classifier evaluation, an important caveat is that an AUC yields biased estimates of classifier performance if there is a large skew in the class distribution (cf. Davis and Goadrich, 2006; Ivezić et al., 2014). Since we are concerned with balanced estimators, this issue is, however, not relevant for this study.

Variable importance measures

A beneficial characteristic of all tree-based ensemble learners is that they provide intrinsic methods to quantify the significance of a feature for the classification task at hand, i.e., the relevance of features can be evaluated without requiring a comprehensive feature-level cross-validation (Strobl et al., 2007; Conn and Ramirez, 2016). If we recall the way partitioning in CART-like decision trees is conducted, it becomes apparent that information on feature relevance can be derived from the reduction of feature entropy achieved at nodes. The mean decrease of impurity (MDI) for a variable j is the sum of the weighted (Gini) impurity decreases ΔG for all nodes t where j was used for partitioning, averaged over all n_T trees in the forest (Breiman et al., 1984; Friedman, 2001; Louppe et al., 2013):

$$\mathrm{MDI}\,(j) = \frac{1}{n_T} \sum_{i=1}^{n_T} \sum_{\substack{t \in T_i \\ v\,(s_t)=j}} \frac{N_t}{N} \Delta G\,(s_t, t)\,, \tag{6.29}$$

where N_t/N is the proportion of samples reaching a node t, and $v(s_t)$ is the variable used in split s_t.

An alternative approach to variable importance quantification is the mean decrease of accuracy (MDA, also denoted permutation importance), which is exclusive to bootstrapping ensembles. The MDA exploits the fact that approximately one third of training samples is not used to train a tree. These tree-specific out-of-bag (OOB) samples are unknown to the respective tree, and therefore can be unambiguously used for evaluation (Archer and Kimes, 2008; Altmann et al., 2010; Auret and Aldrich, 2011). The tree-specific OOB error is the average misclassification rate obtained by classifying all OOB samples, and is roughly equivalent to a regular three-fold cross validation (cf. Janitza and Hornung, 2018).

The MDA is premised on generating, for each tree and feature, an OOB data replica in which all values for a variable j are randomly permuted. The MDA is then derived by calculating the ensemble average of the difference of the OOB error before and after permutation, the rationale being that permuting a variable should void their numerical association with the response variable y (Breiman, 2001; Louppe et al., 2013; Gregorutti et al., 2016).

While both variable importance measures are recognized to be sensible means for variable evaluation, they are not reliable in cases where predictor variables show a strong mutual correlation or vary in their number of categorical values (cf. e.g., Strobl et al., 2007; Archer and Kimes, 2008; Louppe, 2014). In this study, we use continua only, so that our workflow is not affected by the split selection bias occurring when the number of categorical values differs between predictor variables (cf. Janitza, 2016). Conversely, non-negligible product-moment correlation coefficients between the morphometric variables (cf. Suppl. C.2–C.7) indicate that predictor correlation needs to be addressed.

MDI scores are strongly correlated with the frequencies by which features are selected as split variable. If two or more correlated variables are selected at a node, the competition over the selection as split variable results in a partial masking of the potential impurity decrease inherent to group-correlated variables (Toloşi and Lengauer, 2011; Louppe, 2014). While predictor correlation thus exerts a negative bias on MDI scores for correlated variables in the majority of cases (cf. Nicodemus and Malley, 2009; Nicodemus et al., 2010; Toloşi and Lengauer, 2011), masking effects can also result in an overestimated importance score for a variable. This counterintuitive effect is attributable to the fact that if a variable has a substantially higher explanatory potential than a group of variables with which it is strongly correlated, the draw of this variable and one or more members of the correlated group as split candidates increases the probability of this highly indicative variable to be selected for splitting (cf. Louppe et al., 2013).

It is readily apparent that the impact of MDI masking strongly depends on the number of randomly selected variables at each split (mtry). Specifically, lowering mtry reduces the likelihood of masking effects, with mtry=1 representing the end-member where masking cannot occur (Nicodemus et al., 2010; Louppe, 2014). Trees being parametrized with mtry=1 are also denoted as fully randomized trees, and ensembles of fully randomized trees have been proposed as viable alternative to conventional random forests (cf. Geurts et al., 2006).

While the impact of predictor correlation on MDA scores has been found to be less pronounced than for MDI scores (cf. e.g., Nicodemus and Malley, 2009; Toloşi and Lengauer, 2011), both positive and negative impacts on MDA scores were found in empirical studies (cf. e.g., Strobl et al., 2008; Genuer et al., 2010; Toloşi and Lengauer, 2011). However, the causal factors for these contradictory results are yet to be fully resolved. Strobl et al. (2008) suggest to use a more robust variant of the MDA which measures a conditional decrease of accuracy, that is, the decrease of accuracy made by a feature which cannot be obtained by other, correlated variables. The conditional MDA is calculated by permuting observations only within the subdomains imposed by the tree-induced partition. Since we are interested in assessing the marginal influence of a variable, this approach was not considered for this study.

With respect to the lacking consensus on the quantitative impact of importance bias, we refrained from using the MDA, and calculated MDI scores for fully randomized ensembles (cf. Geurts et al., 2006). Although these ensembles differ from the random forests parametrized with an optimized mtry,

we expect these MDI values to provide expedient information on dataset partitioning. When evaluating variable importance in the context of a OCRF, however, we must bear in mind that we quantify the potential a variable exhibits for a differentiation between the thematic class and the seeded null class, which does not enable direct conclusions on the relevance of a variable for the differentiation between different thematic classes.

Hence, we will evaluate variable importance by calculating the amount of overlap between empirical density distributions obtained for the alluvial fan and null-class subsets of the evaluation dataset. Conducting univariate kernel density estimation using an Epanechnikov kernel with CVML-optimal bandwidth, we get empirical density distributions of each morphometric feature (cf. Section 6.3.3). Eventually, measures of inter-class heterogeneity were obtained by taking the Bhattacharyya coefficient (BC), which calculates the amount of overlap between the two populations (Bhattacharyya, 1946; Comaniciu et al., 2000; Pratt, 2001):

$$\mathrm{BC}\,(p, q) = \sum_{i=1}^{n} \sqrt{p_i \cdot q_i}, \tag{6.30}$$

where p and q denote two probability distributions satisfying $\sum_{i=1}^{n} = 1$, with p_i and q_i representing two probability values for a feature having a specific value. Inspecting Equation (6.30), it can be seen that the BC yields 1 for a perfect overlap, and gradually decreasing scores for growing differences of corresponding probability values.

6.4 Results

6.4.1 Classification performance

Examining the ROC curves depicted in Fig. 6.7, we note substantial differences between AW3D30 and SRTM1, as well as between different DEM preprocessing variants. With the best AUC obtained for an SRTM1 variant being inferior to the worst-performing AW3D30 version, the ALOS DEM demonstrates a substantially higher classification performance than SRTM1 (cf. Table 6.3). Furthermore, filtered variants display higher classification capabilities than their unfiltered equivalents. In this context, AW3D30 and SRTM1 differ in that SRTM1 shows consistently improving performance with increasing filtering strength. Conversely, AW3D30 performance metrics start to decline for stronger filtering, indicating light over-filtering. Note that the different response of AW3D30 and SRTM1 is in good agreement with the finding of Section 6.2.4, corroborating that while AW3D30 is also characterized by textural grain, its magnitude and, consequently, impact are notably smaller than in the case of SRTM1.

Depicted in Fig. 6.8 are the best-performing one-class random forest (OCRF) variants in comparison with the one-class support vector machine (OCSVM) introduced and evaluated in Pipaud and Lehmkuhl (2017 / Chapter 5). It is clearly apparent that substantial improvements over the OCSVM have been made for both OCRF variants. In this context, recall that the preprocessing of the best-performing SRTM1 version matches the preprocessing used in Chapter 5, allowing for a direct comparison of both SRTM1-based classifiers. With respect to the substantially higher statistical basis, as well as the expanded and improved set of morphometric parameters, the performance enhancement shown by OCRF is, however, to be expected. That said, it must be borne in mind that the OCSVM parametrization

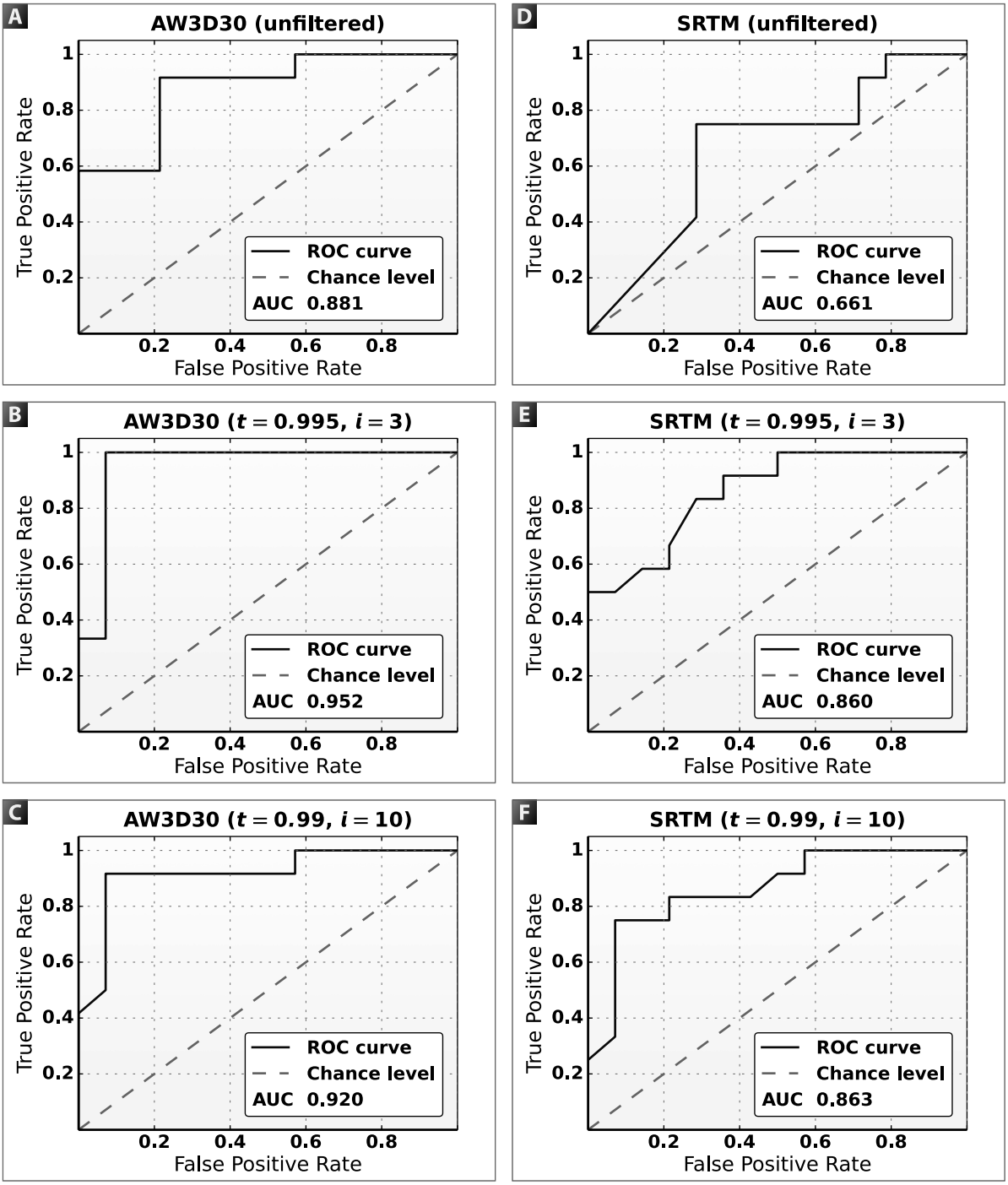


Figure 6.7: Comparison of ROC curves obtained for the evaluation dataset, using the respective hyper-parameter set which maximizes AUC_{EV}. (A) AW3D30 DEM with no filtering applied, (B) AW3D30 DEM with light filtering applied (t=.995, i=3), (C) AW3D30 DEM with strong filtering applied (t=.99, i=10), (D) SRTM1 DEM with no filtering applied, (E) SRTM1 DEM with light filtering applied (t=.995, i=3), (F) SRTM1 DEM with strong filtering applied (t=.99, i=10).

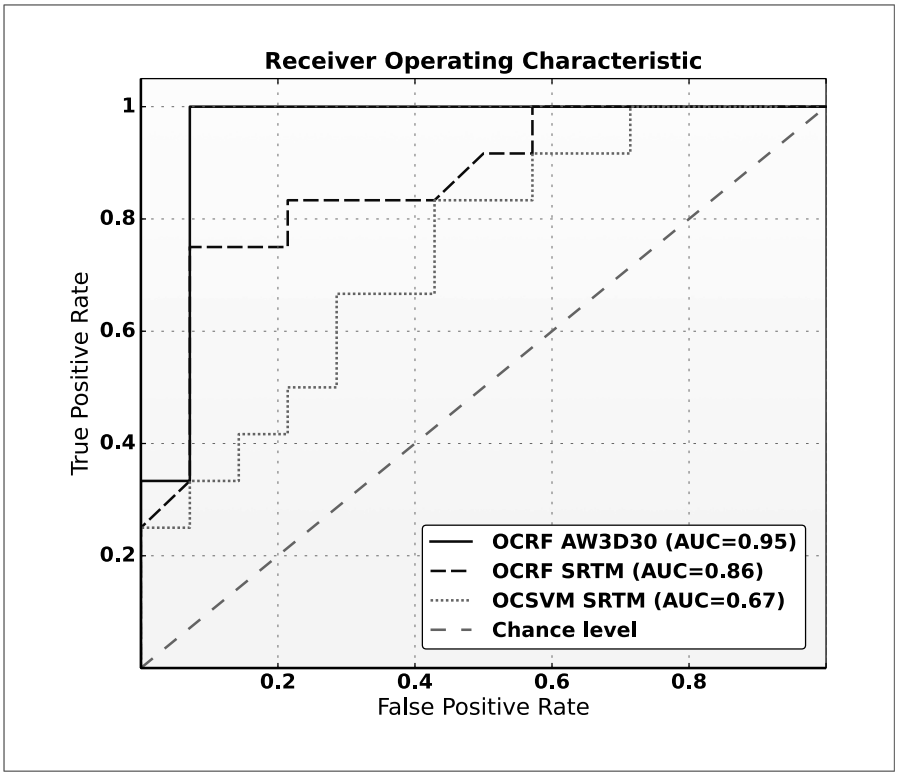


Figure 6.8: Comparison of ROCs obtained from one-class support vector machine (OCSVM) and one-class random forest (OCRF) instances for the evaluation dataset. Depicted are the best-performing AW3D30 (i.e., t=.995, i=3) and SRTM1 (i.e., t=.99, i=10) variant, and the OCSVM as introduced and parametrized in Pipaud and Lehmkuhl (2017 / Chapter 5).

must be chosen via tentative evaluation, so that the OCSVM approach is much less conducive to automated optimization approaches.

For 10-fold cross validation, all datasets display a nearly perfect differentiation between alluvial fans and the seeded null-class (cf. Suppl. C.8). Furthermore, the corresponding threshold-accuracy plots depict very similar curves for all DEMs (cf. Suppl. C.9). Maximum accuracy is obtained for discrimination thresholds between 0.31 and 0.37 (cf. Table 6.3, Suppl. C.9). While these results indicate that alluvial fans can be accurately discriminated from the seeded null class, the area under curve (AUC) and the accuracy (ACC) values obtained for 10-fold cross validation (AUC_{KF} and ACC_{KF}, respectively) bear little practical relevance for the discriminatory potential to be anticipated for alluvial fans and landforms converging into fans.

Inspecting Table 6.3 and Suppl. C.10, we see that owing to sharply rising false positive rate (FPR) values, optimal ACC_{EV} values are obtained by applying discrimination thresholds between 0.79 and 0.97. Calculating the ACC for the cross-validated dataset (ACC_{KF}) by using these threshold values yields ACC_{KF} scores between 0.81 and 0.93, with all AW3D30 variants performing notably better than SRTM1. In this context, recall that all ensemble trees are perfectively balanced, i.e., each tree gets assigned 306 outlier samples. With false positive rates (FPRs; cf. Table 6.2) for the respective thresholds being invariably zero, the potential for alluvial fan discrimination from most similar landforms is revealed by the corresponding true positive rate (TPR) scores. While AW3D30-based classifiers attain solid

Table 6.3: OCRF parameter sets yielding the best performance for the respective DEM versions. Depicted are the area under curve (AUC) obtained for the evaluation dataset (AUC_{EV}) and a 10-fold cross validation of the training dataset (AUC_{KF}), as well as maximum accuracy (ACC) scores and the discrimination thresholds at which the respective maxima are achieved. In the last column, we denote the ACC score for the training dataset which would be achieved if the optimal threshold for the evaluation dataset ($t_{max}(ACC_{EV})$) would be used for a hard classification.

DEM		mtry	Kernel	bw method	AUC_{EV}	max ACC_{EV}	t_{max} ACC_{EV}	AUC_{KF}	max ACC_{KF}	t_{max} ACC_{KF}	ACC_{KF}@ t_{max} ACC_{EV}
AW3D30	unfiltered	1	Epan.	CVML	0.88	0.85	0.79	1.000	1.00	0.34	0.93
AW3D30	t=.995, i=3	9	Gauss.	NR	0.95	0.96	0.89	1.000	0.99	0.31	0.92
AW3D30	t=.99, i=10	5	Gauss.	NR	0.92	0.92	0.87	0.999	0.99	0.35	0.91
SRTM1	unfiltered	8	Gauss.	CVML	0.66	0.73	0.97	0.996	0.98	0.37	0.83
SRTM1	t=.995, i=3	1	Gauss.	CVML	0.86	0.77	0.88	0.999	0.99	0.34	0.84
SRTM1	t=.99, i=10	1	Gauss.	CVML	0.86	0.85	0.95	0.999	1.00	0.35	0.81

TPRs values between 0.82 and 0.86, SRTM variants only achieve values between 0.65 and 0.67 (cf. Suppl. C.9).

Interestingly, highest ACC_{KF} scores for the discrimination threshold maximizing the ACC for the evaluation dataset, $t_{max}(ACC_{EV})$, are obtained for AW3D30 (unfiltered) and SRTM1 (t=.995, i=3). This finding does, however, not indicate that these DEM variants perform best with respect to the set of training fans, because their differentiation potential with respect to alluvial slopes and alluvial plains is inferior to AW3D30 (t=.995, i=3) and SRTM (t=.99, i=10). Overall, the scores indicate that the accuracy values obtained for the evaluation dataset are representative for the basic population of alluvial fans.

Inspecting Fig. 6.9, we see that AW3D30 (t=.995, i=3) achieves perfect discrimination with the exception of a single alluvial slope (Evaluation ID 23, Evaluation ID denoted EID hereafter), which exhibits a strikingly high OCRF score of 0.996 (cf. Suppl. C.11). Significantly, this membership likelihood is higher than the arithmetic mean of the training dataset of 306 fans (0.942). Evaluating the corresponding Z-transformed morphometric data shows that the landform displays surprisingly low values for all gradient–apex divergence (GAD) and radial approximation divergence (RAD) variants, indicating that its geomorphometry largely complies with a radial sedimentation model. As expected for alluvial slopes, substantially above-average Z-standardized values for slope (+1.83) are associated with below-average values for cross-sectional curvature (−0.34), a combination which is atypical with respect to a positive correlation (+0.66) between both parameters in the training dataset (cf. Suppl. C.3). Visually examining the location of the landform in further detail, we observe that it is located at the point where the Tsagaan-Shuvuut fault system and the mountain range turn northwestward (cf. Pipaud and Lehmkuhl, 2017 / Section 5.3), so that the cross-sectional convexity of the landform is tightly related to the morphotectonic situation. Since this peculiar setting mimics the morphometric signature of radial sedimentation, alluvial slope EID 23 can be considered a worst case for the discrimination of alluvial fans from most similar landforms.

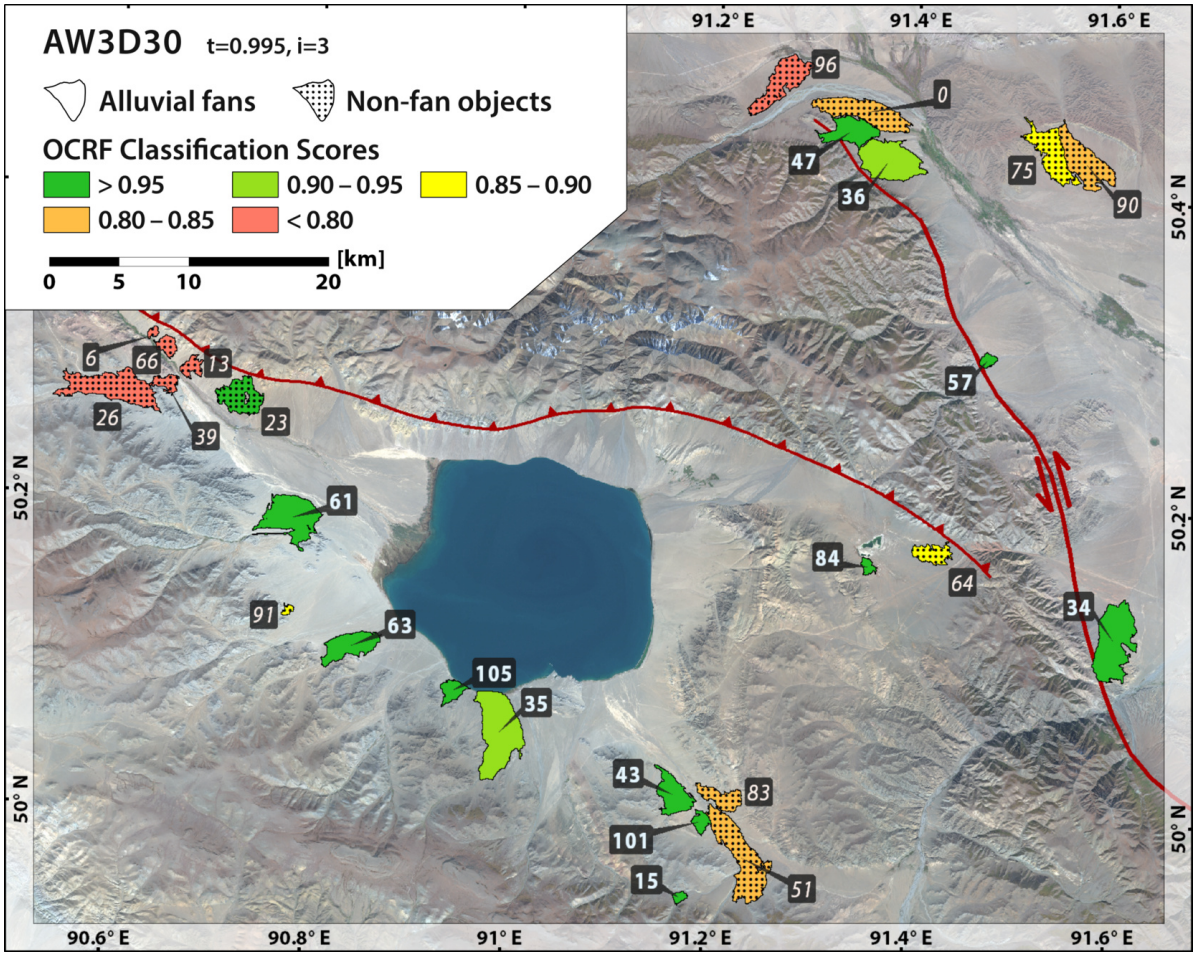


Figure 6.9: OCRF membership likelihoods obtained for the evaluation dataset, which encompasses 12 alluvial fans (EIDs denoted in bold font), and 14 null-class members (EIDs denoted in italics). Here, the OCRF was trained with morphometric data derived from the AW3D30 DEM with light mesh denoising applied (t=.995, i=3). With the exception of alluvial slope EID 23, a perfect discrimination between alluvial fans and landforms grading into fans is achieved. (Imagery source: Sentinel 2a)

Apart from alluvial slope EID 23, the OCRF trained with the AW3D30 DEM with light filtering applied (t=.995, i=3) shows substantial improvements over the OCSVM introduced in Pipaud and Lehmkuhl (2017 / Chapter 5), in particular with respect to alluvial fans which have been identified as challenging to classify (e.g., alluvial fan EID 36; cf. Section 5.3). In the case of the OCRF estimator trained with morphometric data derived from the SRTM1 DEM with strong filtering applied (t=.99, i=10), we observe, however, that the ability to discriminate between fans and null-class members starts to deteriorate for fans diverging from the idealistic conical shape (EID 36), as well as small fans (alluvial fan EID 15 with a planimetric area of 0.62 km^2; cf. Suppl. C.12 and C.13). To facilitate visual comparison, the results of the OCSVM workflow employed in Pipaud and Lehmkuhl (2017 / Chapter 5) are redrawn in Suppl. C.14.

To provide an estimate of how the OCRF scales with the size of the training dataset, let us turn to quality indicators obtained for a reverse 10-fold cross validation, i.e., a k-fold cross validation where one fold is utilized to train the estimator, whereas the remaining folds are used to evaluate the training

data. For the training set of fans at hand, this is equivalent to 30 to 31 samples being used for training. Inspecting Suppl. C.15, it is apparent that the diagnostic ability declines substantially, with TPRs values falling below 0.6 for the significant range of discrimination thresholds (0.79 to 0.95).

6.4.2 OCRF parametrization

As shown by the area under curves (AUCs) calculated with respect to the evaluation dataset, optimal performance is achieved using different combinations of mtry and kernel density parametrizations (cf. Table 6.3), and the impact of classifier parametrization appears to be minor in comparison to DEM selection and DEM filtering. Inspecting Suppl. C.16, we see that the differences between AUCs obtained for the considered parametrizations tend to decrease for better-performing DEM variants, signifying diminishing marginal returns. Significantly, no clear trend is given for any OCRF parameter. While instances utilizing bandwidth optimization (CVML) and a Gaussian kernel yield optimal results in the majority of cases, the differences in AUC scores to the next best instances are marginal. Indicating that equivalent results can be obtained using the normal reference (NR) method with a Gaussian kernel, the computationally intensive cross-validation can be dispensed with.

A remarkable result is that the unfiltered AW3D30 DEM and both filtered SRTM1 variants yield optimal results for a fully randomized tree ensemble. Conversely, such a trend is lacking for the other DEMs, which tend to show higher AUC scores for greater mtry values. With respect to the filtered AW3D30 variants, the result must be interpreted with caution, because performance differences between the instances are low. With mtry controlling the degree of feature-level randomization, this peculiarity still indicates that entropies within the OCRF exhibit varying significance for the differentiation of alluvial fans from most similar landforms. While full randomization enforces the use of all variables in the case of the most performant SRTM1 variants, differences in feature entropy as given by the filtered AW3D30 versions seem to be somewhat informative.

6.4.3 Attribution analysis

Feature importance

Inspecting Fig. 6.10, we observe substantial differences in the patterns of mean decrease of impurity (MDI) values (with mtry=1) and Bhattacharyya coefficients (BCs) across the considered DEM products and preprocessing variants. Interestingly, differences between filtering strengths are more pronounced than the differences across AW3D30 and SRTM, with an increase in filtering strength manifesting itself in an average increase of MDI scores and a diminution of the differences between morphometric variables. In this context, note that in the proposed one-class classification workflow, the achievable feature-specific reduction in impurity is not only governed by the dispersion of feature values, but also depends on how well the empirical density distribution can be reproduced by a single-bandwidth kernel density estimation.

The data provides evidence that several variables are affected by non-informative high-frequency components of the altitude field. Specifically, morphometric variables which are highly sensitive to high-frequency undulations tend to receive low MDI scores in the case of unfiltered DEM data. This particularly applies to gradient–apex divergence (GAD) calculated with the global and zonal gradient

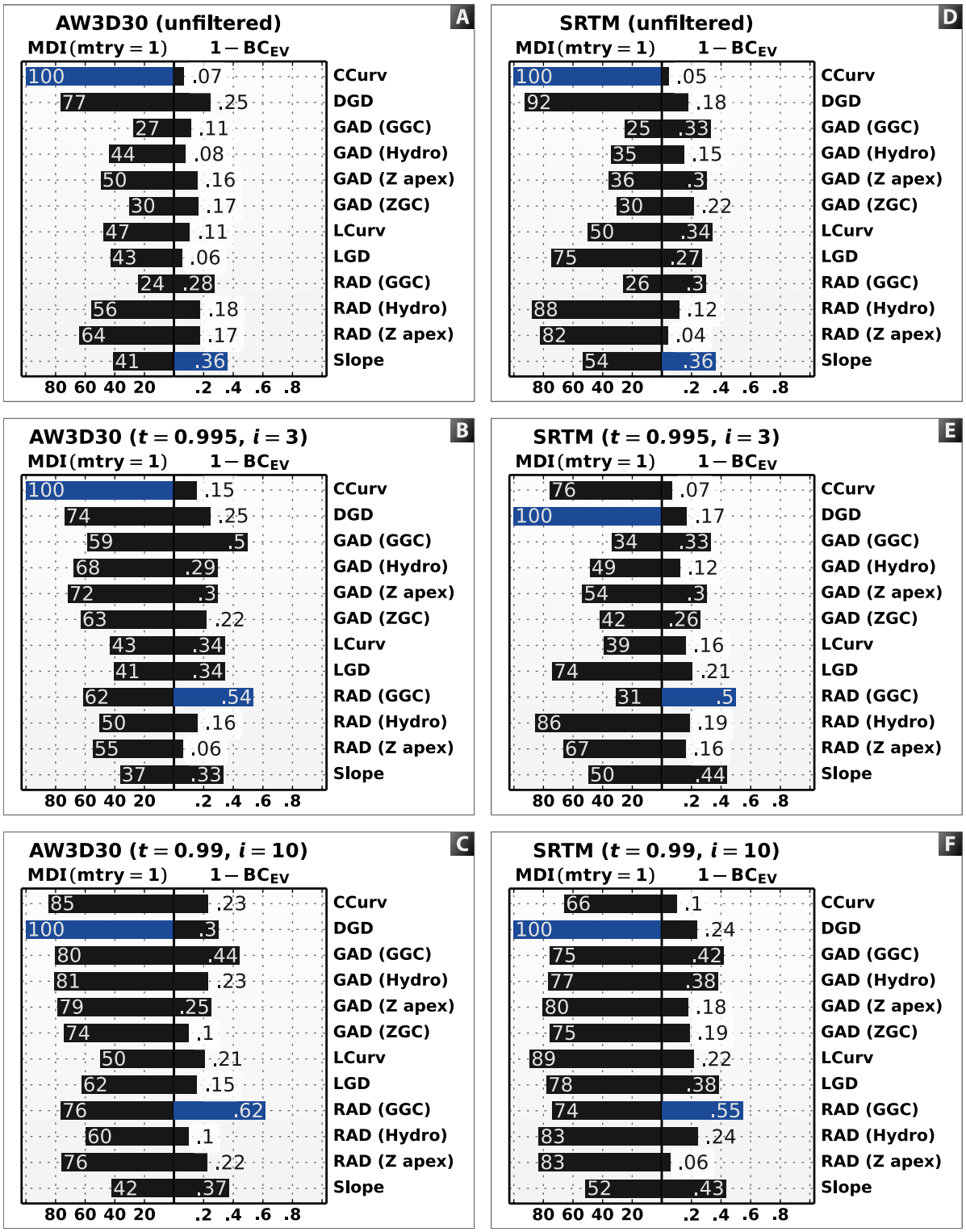


Figure 6.10: MDI scores obtained for OCRF instances which were configured to fully randomize feature selection (mtry=1), and inverse Bhattacharyya coefficients obtained for the evaluation dataset. (A) AW3D30 DEM with no filtering applied, (B) AW3D30 DEM with light filtering applied (t=.995, i=3), (C) AW3D30 DEM with strong filtering applied (t=.99, i=10), (D) SRTM1 DEM with no filtering applied, (E) SRTM1 DEM with light filtering applied (t=.995, i=3), (F) SRTM1 DEM with strong filtering applied (t=.99, i=10).

convergence (GGC and ZGC, respectively), which are susceptible to high-frequency signals both with respect to the apex localization, and the final angular measure. Although the unfiltered AW3D30 surpasses the unfiltered SRTM1 DEM in terms of classifier performance (cf. Section 6.4.1), it shows Bhattacharyya coefficients scores which are lower than those given for SRTM1. With light filtering (t=.995, i=3) applied, most morphometric variables display a considerable boost in terms of both MDI and BC values, and in particular GAD (GGC) and radial approximation divergence (RAD GGC) show increased values.

In the case of stronger filtering (t=.99, i=10), this trend continues for MDI scores, but mostly gets reversed for BC values. Significantly, GAD and RAD evolve in opposite directions. Specifically, RAD shows a further increase of the BC, presumably benefiting from a leveling of microscale features on the fan surfaces. Conversely, GAD (GGC) shows a light and GAD calculated with zonal gradient convergence (ZGC) displays a substantial decrease in BC scores, signifying a deterioration of gradient convergence by incipient over-filtering. In total, BC scores obtained for the AW3D30 are congruent with the findings of Sections 6.2.4 and 6.4.1, corroborating that the lightly filtered (t=.995, i=3) dataset provides most informative morphometric parameters for the discrimination of alluvial fans and consequently enables the corresponding OCRF to achieve best performance. In contrast to AW3D30, SRTM1 MDI scores and Bhattacharyya coefficients tend to continuously raise with increasing filtering strength, giving support to the finding of Section 6.4.1 that optimal performance is achieved by applying a stronger filtering (t=.99, i=10).

BC values of both the lightly filtered AW3D30 and the more heavily filtered SRTM1 DEM point to GGC-based morphometric variables as the most significant variables for *critical cases* in an alluvial fan classification context, that is, the discrimination of fans from alluvial slopes and plains. The difference in statistical separation between GGC-based RAD and GAD measures with those calculated with a hydrological or topographic apex is quite substantial, and is especially pronounced for the RAD. This finding emphasizes that the existence of an alluvial fan necessitates that the calculated global convergence point is, in fact, a good approximation of the initiation point of radial sedimentation, rendering the GGC-based variants of the GAD and RAD the morphometric variables with the highest discriminatory potential.

In contrast to the GGC-based parameters, GAD ZGC falls substantially short in BC values, indicating that zonal gradient convergence points are susceptible to internal alluvial fan differentiation to a point where the statistical separation between alluvial fans and similar landforms is negatively affected. With respect to the both highest-performing classifiers, differences in statistical separability are, for the most part, moderate among the other morphometric variables involved.

An exception is surface slope, which exhibits relatively high Bhattacharyya coefficients particularly in the case of SRTM1-based classifiers. The empirical density for the evaluation null-class exhibits a flat and wide-tailed distribution (cf. Suppl. C.17–C.22), thereby meeting the anticipation that the characteristic gradient range for alluvial fans is situated between those given for alluvial plains and alluvial slopes. Note, however, that the set of training fans shows a lower statistical separability, implying that the evaluation case overestimates the explanatory potential of surface slope. This conspicuity can be attributed to the fact that the evaluation dataset lacks very large fans which display low fan gradients as part of system-intrinsic scaling effects (cf. Chapter 7). Significantly, MDI values of surface gradient

do not benefit from DEM filtering, signifying that substantial variations in surface slope are inherent to alluvial fan datasets (cf. Chapter 2 and 7).

In contrast to surface slope, cross-sectional curvature (CCurv) displays a poor statistical separation. In view of the fact that Bhattacharyya coefficients (BCs) for CCurv consistently improve with filtering strength, we can suspect this finding to be due to the impact of non-informative high-frequency undulations evident in both datasets. Importantly, low BC are associated with very high MDI values. In conjunction with the Bhattacharyya coefficient, this conspicuous feature indicates that the CCurv signal is dominated by high-frequency components of the altitude field which are non-informative for the classification task. Furthermore, it is noteworthy that lateral gradient difference provides more statistical separation than distal gradient difference in the majority of cases, showing that the gradient convergence pattern resulting from the coalescence of radial sedimentation bodies helps in differentiating fans from alluvial slopes and plains. Overall, however, both variables do not show a higher informative value than generic morphometric parameters.

Membership likelihoods

In what follows, we will be concerned with an identification of causal factors for the distribution of membership likelihoods obtained for the training set of 306 alluvial fans via 10-fold cross-validation. An inspection of the empirical density curves obtained for the top 20th percentile (Q80) and the bottom 20th percentile of the classification scores (Q20; cf. Suppl. C.17–C.22) emphasizes that appropriate filtering is quintessential to retain the informative value of morphometric parameters and, consequently, for a reasonable distribution of membership likelihoods within the training dataset. If we consider, for instance, the empirical density curves estimated for the GGC-based variants of the RAD and GAD, we observe that in both OCRF classifiers trained with unfiltered data, the Q80 subset displays similar or even higher parameter values than the Q20 quintile, indicating that both variables are in fact non-informative for the classification task. In the case of the unfiltered SRTM1 DEM, higher values for the Q80 quintile can also be observed for all GAD variables, corroborating that these morphometric parameters are susceptible to textural grain (cf. Section 6.4.3).

These findings are also reflected in the variation of product-moment correlation coefficients across the different classifiers (cf. Suppl. C.2–C.7). With the exception of radial approximation divergence (RAD) calculated with the hydrological apex and RAD (Z apex), whose calculations do not involve the local gradient field, all RAD and GAD parameters exhibit low negative (AW3D30) or even positive (SRTM1) correlation coefficients with membership scores. Another peculiar aspect is that all classifiers show considerable negative correlation coefficients of membership likelihoods with surface slope and cross-sectional curvature, indicating that steep fans tend to exhibit lower scores. In accordance, positive correlation coefficients are shown for distal gradient difference and lateral gradient difference. In the case of surface slope, it can be deduced from the low MDI scores that feature distribution in the high value spectrum of aspect slope is more sparse and less constraint, placing the respective samples at marginal positions in the alluvial fan property space.

Turning to the set of auxiliary parameters, a striking characteristic is that the apex distance factor (ADF) displays high product-moment correlation coefficients with both GGC-based morphometric variables, and, to a lesser extent, with all other GAD versions (cf. Suppl. C.2–C.7). Significantly,

this finding indicates that all RAD and GAD variants except RAD (Hydro) and RAD (Z apex) are fundamentally affected by fan progradation. In cases where the former morphometric parameters contribute substantially to membership likelihoods—i.e., all filtered variants of both AW3D30 and SRTM1—this statistical relationship has the adverse effect that fans affected by progradation exhibit in average lower classification scores. Consequently, a weak positive positive correlation between ADF and classification score can be observed for these DEMs (cf. Suppl. C.3, C.4, C.6, and C.7).

Furthermore, we note that considerable negative correlation coefficients are given for classification scores with vector ruggedness measure (VRM), identifying local terrain ruggedness as a primary external control factor. Importantly, the degree of correlation is not affected by filtering, indicating that undulation of the altitude field is present at magnitudes which are sufficiently high to be preserved by the mesh-denoising routine (cf. Sun et al., 2007; Stevenson et al., 2010; Pipaud and Lehmkuhl, 2017 / Chapter 5). Note that while the influence of local terrain ruggedness might be alleviated via stronger filtering, the results discussed in Sections 6.4.1 and 6.4.3 indicate that this is unfeasible with respect to the overall classification performance. Inspecting the empirical density plots for fans falling into the Q80 and Q20 quintiles of the classification scores (cf. Suppl. C.17–C.22), it can be observed that the empirical density distribution of the Q80 subset considerably narrows from the unfiltered towards the filtered DEM variants, whereas the distribution given for the Q20 quintile stays largely constant. With respect to the response shown by the Q80 cohort, we can infer that the accentuated ruggedness shown by the Q20 percentile is *not* related to the background textural grain inherent to the incorporated DEM products (cf. Fig. 6.1; Chapter 3), but to a deterioration of terrain rendition, e.g., due to DEM blunders, or actual microscale topographic features.

In this context, it should be noted with regard to AW3D30 that while the unfiltered DEM variant displays a considerable inverse product-moment correlation between the number of processed scene stacks (STK) and VRM (-0.41), the statistical relationships between both variables weakens with increasing filtering strength, and is negligible for AW3D30 filtered with stronger mesh denoising (cf. Suppl. C.2–C.4). Even for the unfiltered AW3D30, however, membership likelihoods display only a marginal response to STK numbers, indicating that other factors outweigh the impact of STK numbers (cf. Suppl. C.2 and C.17).

Inspecting Suppl. C.2–C.7, we also observe a considerable inverse relationship between membership likelihoods with slope and cross-sectional curvature (CCurv), which, however, decreases for stronger filtering. With respect to the positive relationship of VRM values with slope and CCurv, it can be assumed that high-frequency components contribute to the inverse relationship of classification scores with these two variables (cf. Suppl. C.2–C.7).

Owing to the scaling relationships of alluvial fan morphology (cf. Section 2.3.1), the inverse relation between classification scores and surface slope involves below-average classification scores for small fans. The statistical relationship between planimetric fan area and membership scores is, however, very weak, so that all classifiers can be considered robust with respect to fan size (cf. Suppl. C.2–C.7). In this context, it is noteworthy that small fans tend to show low values for all RAD and GAD variants, which presumably counteracts the negative effect imposed by above-average surface ruggedness. This effect can be related to the fact that comparably small fans exhibit a higher variability to be built be simple vertical aggradation, as indicated by the negative correlation between apex distance factor and

planimetric fan area.

6.5 Discussion

6.5.1 Classifier assessment

Using a lightly filtered AW3D30 dataset and a one-class random forest with a parametrization optimized for the discrimination of alluvial fans from alluvial slopes and plains, we obtain a high-performant classifier. After elimination of a single outlier, a perfect discrimination of fans from alluvial slopes and plains could be achieved for the evaluation dataset, and approximately 83 % of the training dataset exhibit higher scores than the highest-scoring null-class member. While a material contribution to improved classification accuracy is made by AW3D30 performing better than SRTM1, a direct comparison via the more heavily filtered SRTM1 variant still indicates that the performance of the proposed OCRF workflow is superior to the one-class support vector machine introduced in Pipaud and Lehmkuhl (2017 / Chapter 5). Furthermore, substantial performance differences between unfiltered and filtered DEM variants demonstrate the significance of an adequate filtering, which needs to be tailored towards the DEM product in use and the classification task at hand. Providing a robust data-driven approach whose parametrization is important in the context of performance optimization only, and eliminating the need for data standardization techniques and all kinds of manual user involvement, the suggested OCRF workflow enables the unbiased comparison of different DEM products and variations in DEM preprocessing.

While these are major advances over the results obtained in Pipaud and Lehmkuhl (2017 / Chapter 5), the substantially reduced performance obtained for the reverse 10-fold cross-validation runs elucidates that these enhancements partly rely on the training dataset at hand being substantially larger than that used in Pipaud and Lehmkuhl (2017 / Chapter 5). For small datasets, a classification algorithm involving a user-adaptable level of generalization is thus still expected to yield better performance (Schölkopf et al., 2001; Pipaud and Lehmkuhl, 2017 / Chapter 5).

The influence of OCRF parameters is generally dwarfed by the impact imposed by the DEM and the filtering applied, with only mtry displaying a non-negligible impact on classification scores. Hence, it is feasible to use a Gaussian kernel for the integrated KDE instance and to set feature-specific bandwidths according to the normal reference method. Foregoing the computationally intensive cross-validation of bandwidth improves overall computation speed and facilitates cross-validation in particular. Significantly, three of six DEM variants show optimal performance for mtry = 1, and merely the classifier using the unfiltered SRTM1 displays a non-negligible performance difference between the best parametrization and a tree ensemble with full randomization on feature-level. This observation indicates that feature impurities bear little connection with the discrimination of alluvial fans from most similar landforms. Therefore, feature-randomized one-class random forests (cf. Geurts et al., 2006) appear as a viable alternative to deterministic OCRFs. Full feature randomization is appealing also from a conceptual viewpoint, because it is the most consequent implementation of a one-class classification approach. Specifically, full randomization ensures a high generalization potential, i.e., the classifier should provide robust classification performance for discrimination tasks it has not been optimized for. While this is not vital for the classification of alluvial fans—where discrimination from other alluvial

landforms is undoubtedly most critical and optimization for this specific problem is indicated—it can be a beneficial characteristic for the classification of landforms where critical differentiation cases are less well established.

6.5.2 DEM assessment

The results of our study clearly demonstrate that the classification accuracy attainable with AW3D30 (version 1.1) is superior to the accuracy provided by SRTM1, indicating that the improvements observed with respect to terrain rendition (cf. Boulton and Stokes, 2018; Li and Zhao, 2018) are also reflected in the classification of geomorphometric data. Note, however, that being concerned with landforms of gentle relief, our study does not enable assessments on whether the issues with high-relief terrain rendition noted by Hu et al. (2017) and Purinton and Bookhagen (2017) have been resolved with version 1.1 of the dataset (cf. Boulton and Stokes, 2018).

DEMs derived from stereometric processing of optical stereo pairs are susceptible to undulation wavelengths spanning multiple pixels, because the correlation window applied for parallax estimation entails that topographic information can only be derived at a resolution below that of the posting of the optical imagery (cf. Gallay, 2009; Tachikawa et al., 2011a,b,c; Pipaud et al., 2015 / Chapter 3). Owing to the pixel aggregation applied to derive AW3D30 data from the AW3D5 DEM (cf. Section 6.2.2), however, multi-pixel undulations are condensed into single points and induce a high-frequency noise signal with moderate magnitude. The fact that noise propagates into the AW3D30 DEM corroborates the results of Purinton and Bookhagen (2017), who state that AW3D elevation data is intrinsically noisy. In this study, weak filtering proves to be an optimal compromise between noise dampening and terrain rendition. For the lightly filtered DEM, the number of stacked scenes (STK) is still correlated with terrain ruggedness (VRM), confirming the results of Hu et al. (2017). Then again, the fact that all AW3D30-based classifiers show no direct linkage between STK and classification scores indicates that high VRM numbers relate to deteriorations of terrain rendition which are not reflected in STK numbers, so that the metric cannot be used as a quality control metric.

SAR interferometry involves pixel-wise altitude calculation via interferometric phase unwrapping, but is affected by pixel-specific phase noise (cf. Bamler and Hartl, 1998; Rodríguez et al., 2006; Stevenson et al., 2010). In the case of SRTM1, the DEM posting roughly corresponds to the spatial resolution of the raw interferometric SIR-C imagery, indicating that noise compulsorily propagates into the final DEM product (cf. Jordan et al., 1995). Postprocessing the DEM by a low pass filter fails in completely suppressing this noise. Conversely, it alters the noise signal into an autocorrelated grainy texture which interferes with topographic information on wavelengths being significant for alluvial fan classification (cf. Rodríguez et al., 2006; Pipaud et al., 2015 / Chapter 3). As reflected by both visual analysis and classification scores, SRTM1 yields optimal performance with a stronger filtering than AW3D30.

6.5.3 Assessment of morphometric parameters

A close match with an ideal radial sedimentation pattern emerges as the principal morphometric signature of alluvial fans (Troeh, 1965; Pipaud and Lehmkuhl, 2017 / Chapter 5). Consequently, an appropriate quantification of the level of agreement with a radially symmetric conical surface turns out to be pivotal for the discrimination between alluvial fans and landforms grading into them.

Deriving the origin of the imposed radial model directly from the gradient field, the variants of the gradient–apex divergence (GAD) and radial approximation divergence (RAD) which utilize the global gradient convergence (GGC) method for apex estimation display superior discriminatory potential across all filtered DEM, but are susceptible to high-frequency undulations of the altitude field. In contrast, parameters relying on hydrological or topographical apex localization fall substantially short in statistical separation between alluvial fans and alluvial slopes and plains. From a general viewpoint, no definitive assertion can be made as to whether radial approximation divergence or gradient–apex divergence provide more informative value for alluvial fan discrimination. Relying on the gradient field only for apex localization, RAD (GGC) is more resilient towards DEM noise, and consequently displays higher statistical separation in this study.

In contrast to the results obtained by using the GGC method, the GAD based on the zonal gradient convergence method provides relatively little informative value, casting doubt on the utility of the ZGC approach for alluvial fan discrimination based on AW3D30 or SRTM1 elevation data. Generic morphometric parameters as well as lateral gradient difference and distal gradient difference generally display a reduced explanatory potential, with a notable exception being surface slope. This finding reflects the fact that a substantial part of the alluvial fan population exhibits surface gradients that lie in between those of alluvial plains and alluvial slopes. The observation contradicts, however, the results obtained by Pipaud and Lehmkuhl (2017 / Chapter 5), who ascertained that slope could not be incorporated into a one-class support vector machine-based classification due to its high intra-class variability. In this context, the example of surface slope showcases the robustness of the presented OCRF classification approach with respect to the statistical distribution and the discriminatory potential of features. That said, it must be taken into account that the greatly larger training dataset enhances the delimitation of morphometric parameters in the alluvial fan property space, which contributes substantially to the utility of variables showing a high intra-class variance.

6.5.4 Feature importance metrics

Our findings indicate that average BC values do not directly translate into classifier performance. This result is to be expected, because the univariate BCs do not consider sample-specific combinations of morphometric parameter values and, consequently, cannot reflect the distribution of samples within the alluvial fan feature space. While BC values thus cannot be used to compare different DEM products, they show strong interrelationships with variations in classifier performance achieved with different filtering strengths applied to the same DEM product.

In contrast to MDI values obtained for a conventional binary random forest, MDI values calculated for a OCRF bear no relationship with variable importance sensu stricto, but quantify the variable-specific intra-class homogeneity. Specifically, complex distribution patterns with variations in univariate feature density affect the statistical representation via kernel density estimation. In this context, the increases in MDI observed for filtered DEM variants indicate a substantial impact of textural grain on achievable impurity decreases. However, intra-class heterogeneity can result in a lacking improvement of MDI values, and ensemble classifiers which are not fully randomized on a feature level are therefore forced to underweight this variable. If such a variable is important for a binary classification problem performed using a OCRF, a parameter optimization might identify a full randomization of feature-selection as an

optimal approach to solving the classification problem.

6.5.5 Perspectives and incentives

Geomorphological phenomena are characterized by a unique combination of morphometric properties, and consequently exhibit unique indicative feature sets. By not imposing any constraints on data distribution, and being tolerant towards irrelevant features, OCRFs enable a data-driven ad hoc identification of indicative morphometric parameters and optimal approaches to DEM preparation and classifier setup. As a consequence, an OCRF-based classification framework allows to dispense with tentative feature selection approaches, which are tedious to set up and susceptible to yielding non-optimal solutions due to potential user-bias, e.g., a user choosing allegedly indicative features. Owing to these properties, OCRFs offer a reliable approach to the discrimination of landforms of interest from the spectrum of geomorphological phenomena.

Major performance differences between the original and the filtered versions of both DEMs demonstrate the relevance of appropriate filtering for the classification of object-based datasets. In the study at hand, variations in DEM selection and filtering come with substantial changes with respect to statistical properties and significance of morphometric parameters, which in conventional rule-based workflows would have required error-prone manual adjustments of thresholds (cf. e.g., Gerçek et al., 2011; Saha et al., 2011; Eisank, 2013; Pedersen, 2016; Argyridis and Argialas, 2017). In this context, the findings of our study emphasize that due to the additional level of complexity imposed by the impact of DEM characteristics on terrain rendition, and morphometric parametrization acting as an interface to digital elevation data (cf. Eisank et al., 2014; Pipaud and Lehmkuhl, 2017 / Section 5.1), object-based morphometric analysis (OBMA) in particular benefits from robust data-driven approaches.

Since the classification scores of the respective highest performing variants of both AW3D30 and SRTM1 show only a minor dependence on planimetric area, the intrinsic resolutions of both datasets seem to provide sufficient morphometric detail to enable a robust classification of small fans. Then again, the substantial correlation between terrain ruggedness and membership likelihoods—which persists even for the more heavily filtered variants—poses the question to what extent classification performance can be improved with superior near-global digital elevation data. The analysis performed within the scope of this thesis (Pipaud et al., 2015 / Chapter 3) as well as recent research (Boulton and Stokes, 2018) indicate that TanDEM-X provides the most consistent landscape representation among all near-global medium resolution DEM products for areas of gentle to moderate relief. Incorporating TanDEM-X thus has the potential to improve the classification, but might also provide valuable insights into the source of high VRM values in AW3D30 and SRTM1 data.

With a key finding being that a close match with a radial sedimentation pattern is the principal morphometric signature of alluvial fans, a compulsory consequence is that alluvial fans displaying a considerable amount of progradation obtain below-average membership likelihoods. Since progradation is an integral part of many fan–catchment systems (cf. Chapter 2; Clevis et al., 2003; Viseras et al., 2003; Densmore et al., 2007; Bahrami, 2013), future research should seek to alleviate this issue by considering, for instance, only those pixels which are located downstream of a GGC point.

6.6 Conclusions

Rule-based object-based frameworks exhibit limited potential with respect to the formalization of complex feature spaces and transferability between different study areas and source datasets, impairing their applicability in the context of object-based morphometric analysis. Since multi-class machine learning classifiers are trained to differentiate within a specific set of thematic classes specified by the study area, they lack in adaptability as well. Building upon the robust properties of multi-class random forests, we introduce a one-class variant which differentiates the training data from a synthetic null class seeded via kernel density estimation. The proposed one-class random forest provides a high-performing classification workflow conducting a fully data-driven identification of morphometric signatures. Being robust towards irrelevant features, the algorithm allows for an ad hoc identification of indicative morphometric parameters.

Substantial performance differences between original and filtered variants of AW3D30 and SRTM1 illustrate the demand for a data-driven selection and optimization of incorporated DEMs. OCRFs enable the comparison of different source datasets without requiring any manual interaction, thereby avoiding user-induced bias. Owing to an autocorrelated grainy texture shown by SRTM1, the AW3D30 DEM shows superior performance and requires less intense filtering.

While the parametrization can be optimized to handle critical classification tasks, the susceptibility of OCRFs to their parametrization is generally low. As a consequence, one-class random forest with a full randomization on feature level can be used with no or little performance deficit. Since this variant offers the closest adherence to the idea of formalizing a universal morphometric signature for a landform, and therefore ensures optimal transferability, we encourage to consider feature-randomized OCRFs for future research.

7 The expression of environmental controls in alluvial fan geomorphometry – An exploratory statistical analysis

7.1 Introduction

The problem to which extent environmental controls affect the formation of alluvial fans is subject to a longstanding debate (cf. Lecce, 1990). In research done hitherto, this question has been tackled predominantly from a morphodynamic point of view, with the general consensus being that climate dynamics trigger phases of alluvial activity (cf. Chapter 4), whereas tectonic activity controls alluvial fan morphogenesis on substantially longer time scales—particularly by inducing and maintaining topographic contrast and providing accommodation space (cf. Section 2.2). In contrast, the issue how differences in environmental controls manifest themselves in the geomorphometry of alluvial fans received relatively little emphasis. The hypothetical existence of morphometric signatures of environmental controls entails that the alluvial fan problem can be inverted (Tarantola, 2005), with full invertibility implying that a *unique* set of boundary conditions can be deduced for all fan surfaces and their corresponding unique sets of morphometric sample statistics.

With regard to the study of alluvial fan geomorphometry, three major branches of research can be differentiated. (1.) *Classic* approaches to alluvial fan geomorphometry involve the investigation of bivariate relationships of alluvial fan planimetric area and fan gradient with the planimetric area of the corresponding catchment (cf. Section 2.3.1). Emphasizing the role of scaling relationships, these contributions are undeniably important to the field. A largely unaddressed problem is, however, that the incorporation of catchment area introduces an additional element of uncertainty. Catchment-level controls, like differences in sediment connectivity, can substantially alter the allometric relationship between fan and catchment area and may thus hamper the thematic inversion of fan geomorphometry (cf. Roehl, 1962; Fryirs et al., 2007; Church, 2017; Mather and Stokes, 2018). Until now, approaches to consider scaling relationships of fan planimetric area with morphometric variables gained little emphasis and are limited to a consideration of fan gradient (cf., e.g. Al-Farraj and Harvey, 2005; Saito and Oguchi, 2005; Hashimoto et al., 2008).

(2.) Multivariate morphometric approaches have been successfully used to evaluate the impact of tectonic activity via provision of accommodation space (cf. Silva et al., 1992; Calvache et al., 1997; Sorriso-Valvo et al., 1998; Viseras et al., 2003; Bahrami, 2013; Šilhán, 2014). In cases where sediment flux is balanced by generation of accommodation space, fans build up proximal to the mountain front by simple vertical stacking. These *aggradational* fans display simple conical shapes with large splay angles and exhibit comparably high slopes and cross-sectional curvatures. If the generation of accommodation space cannot keep pace with sediment supply, the alluvial fan is forced to prograde into the depositional basin. The concomitant increase in areal expansion raises the probability of fans to adjoin, resulting in comparably gentle sloping fans with elongated footprints (cf. Section 2.2).

In contrast to tectonic activity, the situation for climatic activity is far less constrained. As

comprehensively discussed in section Section 2.1.1, equifinal solutions can be obtained for different grain size distributions and sediment load factors. Both factors are controlled by catchment lithology, tectonic fracturing, sediment connectivity, climatic conditions, and vegetation density, with the latter two being closely intertwined. (cf. Vandenberghe, 2002; Thompson et al., 2010). Affecting fan gradient and cross-sectional curvature alike, the morphometric imprints of these environmental boundary conditions and the rate of tectonic offset interfere. The climatic impact on fan-building processes can clearly be identified when comparing alluvial fans of (semi-) arid and humid regions, with fans located in humid regions exhibiting *in average* lower gradients than fans built up under more arid conditions (cf. Saito and Oguchi, 2005; Hashimoto et al., 2008). With respect to semi-arid and arid environments, Löhrer (2008) found, however, that fan gradients and fan–catchment relationships do not enable a differentiation on the basis of the relative importance of tectonic and climatic control.

(3.) While supervised classification approaches have been successfully used for the differentiation between streamflow- and debris flow-dominated fan–catchment systems (cf. de Scally and Owens, 2004; de Scally et al., 2010; Bertrand et al., 2013), equifinality and deficient information on in-situ environmental controls cast doubt on the applicability of supervised classification methods for a thematic differentiation of alluvial fans. Approaches to cluster the alluvial fan feature space received little attention so far, with research being restricted to agglomerative clustering (cf. Crosta and Frattini, 2004) and the generation of self-organizing maps—a subtype of artificial neural networks which yields a two-dimensional topology-preserving discrete representation of a Euclidean ($\mathbb{R}^p$) feature space (cf. Kohonen, 1982, 2001; Karymbalis et al., 2010; Mokarram et al., 2014; Seif et al., 2014; Karymbalis et al., 2018). Furthermore, the exploratory data analysis of the alluvial fan feature space can be facilitated via dimensionality reduction methods (cf. Crosta and Frattini, 2004).

Using a restricted set of morphometric variables, Karymbalis et al. (2018) were able to verify the result of conventional multivariate analysis—i.e., that fan gradient and relative fan size are fundamentally related to the rate of tectonic uplift—but did not provide any further insights. Crosta and Frattini (2004) found that alluvial fan feature space is fundamentally governed by scaling relationships, but also delineated the impact of differing fan-building processes. Regrettably, the authors did not validate the obtained clustering result, and their study thus does not allow assertions on whether the alluvial feature space is amenable to a semantically significant hard partition.

A fundamental issue of all previous research performing multivariate statistical analysis, dimensionality reduction, or clustering is that analysis is conducted on the raw morphometric data, and thus also depicts variability being related to scaling relationships. Since this impedes the application to a large and diverse set of alluvial fans, all studies exhibit a local scope of analysis.

Adhering to the fan-oriented morphometric approach followed throughout this thesis, we will conduct an exploratory statistical analysis to assess whether the alluvial fan feature space as defined by the set of 306 fans introduced in Chapter 4 shows a tendency to cluster into different semantically significant groups. Using mean-shift clustering, we are able to flexibly test different bandwidths and evaluate the consistency of yielded clusters via silhouette coefficients (Rousseeuw, 1987; Handl and Kuhlenkasper, 2017). Furthermore, we will assess the impact of scaling effects on the thematic differentiation of alluvial fans by considering alluvial fan planimetric area as the controlling variable and de-trending all morphometric parameters according to their bivariate relationship with fan area. A principal component

analysis is conducted to evaluate if morphometric signatures attributable to single controlling factors or a set of controlling factors are identifiable within the feature space. By explicitly quantifying the degree of progradation, we provide an independent indicator for tectonic activity which facilitates the differentiation of controlling factors in the dataset.

7.2 Data and Methods

7.2.1 Geomorphometric Analysis

In Chapter 6, the ALOS World-3D DEM with 1″ (~30 m) posting (AW3D30) and light mesh denoising (cf. Section 6.2) applied provided the best performance, and was consequently selected for this study. Furthermore, we build upon the morphometric parameters introduced in Section 6.3, and the reader is referred to this section for further information. In order to keep the number of dimensions as low as possible, we only used a subset of the morphometric parameters presented in Chapter 6.

Specifically, we omitted morphometric variables which show redundancy and inferior explanatory potential to their respective equivalents. This applies to all variants of the radial approximation divergence (RAD) and the gradient–apex divergence (GAD) basing the calculation on the hydrological apex and the Z apex. In addition, the zonal gradient convergence (ZGC) variant of the GAD was omitted for the same reason. Conversely, we kept both RAD and GAD calculated with the global gradient convergence (GGC) technique, respectively, even though both variants are strongly correlated with each other (cf. Suppl. D.1). This decision was motivated by both parameters showing equivalent performance in Section 6.4, and the ensuing objective to evaluate whether a performance difference exists from the perspective of alluvial fan feature space differentiation. We augmented this subset of the classification features with variables which were not considered in the classification scenario of Chapter 6 because they were expected to show large intra-class variability, or because their behavior in a diverse set of landforms is insufficiently constrained. In a sub-classification scenario, however, inter-class variability is not relevant, and the explanatory potential of features is exclusively defined by its intra-class variability, given that disparities have a thematic meaning.

Specifically, we included the apex distance factor (ADF) as introduced in Section 6.3.2. Furthermore, we propose a robust metric to measure the elongation of an alluvial fan footprint. The presented approach first requires the derivation of a rectangular fan envelope, where one side is given by the mean gradient of the alluvial fan ($\bar{\nabla}$; cf. Section 6.3). The aspect ratio (AR) can now be simply defined as:

$$\text{Aspect Ratio} = \frac{L}{W}, \tag{7.1}$$

where L and W are envelope length and width, respectively, and L is defined as the envelope edge running parallel to $\bar{\nabla}$.

Furthermore, we introduce an enhanced variant of the half-splay angle (HSA) algorithm introduced in Chapter 5. Recall that the HSA is defined as the angle of the respective mean gradient vectors of two split segments, obtained by splitting the alluvial fan surface along a line given by the (hydrological)

apex and the mean gradient vector of the full surface:

$$\bar{\nabla}_{S_1} = \frac{1}{n} \cdot \sum_{i=1}^{n} \nabla_i \,, \quad \bar{\nabla}_{S_2} = \frac{1}{m} \cdot \sum_{j=1}^{m} \nabla_j \,,$$
$$\text{Half-splay Angle} = \arccos \frac{\bar{\nabla}_{S_1} \cdot \bar{\nabla}_{S_2}}{\left\|\bar{\nabla}_{S_1}\right\| \cdot \left\|\bar{\nabla}_{S_2}\right\|} \cdot \frac{180}{\pi}, \qquad \text{(5.16 revisited)}$$

where S_1 and S_2 denote the surface patches resulting from the split, ∇i and ∇j denote the gradients of points i and j, respectively, and n and m denote the pixel count of the split segment considered. In the case of alluvial fans, the HSA can be expected to be approximately half of the aperture angle. Iterative HSA calculations can be performed on the outermost two split segments of the true left and right side, respectively, eventually yielding a value for the full splay angle (SA) of the fan. To maintain a sufficiently large calculation basis for taking the mean of the gradient vectors, we stopped iteration at each orographic side when the respective slice of the fan surface became smaller than five percent of the full planimetric area. In Chapter 5, it was found that the HSA falls significantly short in terms of its explanatory value for alluvial fan identification in an object-based morphometric context, i.e., in a diverse set of landforms yielded by a segmentation algorithm. Since abundance or lack of accommodation space generation is linked with high and small SAs, respectively, we expect the SA to be valuable for alluvial fan differentiation. A summary of all incorporated morphometric parameters and their supposed significance for alluvial fan differentiation is provided in Table 7.1.

7.2.2 Trend removal

Removal of the trend induced by the statistical relationships of morphometric variables with fan area was performed by conducting either linear or non-linear bivariate regression. We performed a pre-selection between linear or non-linear regression based on a visual examination backed up by kernel regression. Kernel regression is a non-parametric technique to estimate the local (non-linear) relation between a pair of variables, and is based on calculating a locally weighted average by using a kernel K with bandwidth h as weighting function (Watson, 1964; Nadaraya, 1965; Härdle et al., 2004; Hastie et al., 2009):

$$\hat{f}(x) = \frac{\sum_{i=1}^{n} K\left(\frac{x-x_i}{h}\right) \cdot y_i}{\sum_{i=1}^{n} K\left(\frac{x-x_i}{h}\right)}, \qquad (7.2)$$

where $\hat{f}$ is the estimator function yielding estimates of the dependent variable y (a morphometric variable), x is a query point for which an estimate for y is desired, and x_i and y_i are the observations at hand for the independent (planimetric area) and the dependent variable, respectively. We performed kernel regression applying a Gaussian kernel and estimated the bandwidth via likelihood optimization (CVML; cf. Section 6.3). For those morphometric parameters that were selected to be subjected to a non-linear de-trending, we performed bivariate regression for the set of monotonic functions denoted in Table 7.2 (cf. Daniel et al., 1999), and selected the function yielding the minimum mean squared error (MSE).

Table 7.1: Morphometric variables used for alluvial fan feature space analysis. Both GAD and RAD were calculated utilizing the GGC method. Impacts on the respective morphometric variable are summarized with respect to an increase of the considered influencing factor.

Morphometric variable	Influencing factors & impact on variable
Radial approximation divergence (RAD)	Accommodation space − Internal differentiation +
Gradient–apex divergence (GAD)	Accommodation space − Internal differentiation +
Lateral gradient difference (LGD)	Lateral coalescence + Fan slope −
Distal gradient difference (DGD)	Relevance of streamflow deposits + Relevance of mass flow deposits − Distal secondary mobilization + Fan slope −
Slope	Relevance of streamflow deposits − Relevance of mass flow deposits + Sediment load factor + Accommodation space +
Cross-sectional curvature (CCurv)	Lateral coalescence − Fan slope +
Longitudinal curvature (LCurv)	Relevance of streamflow deposits + Relevance of mass flow deposits − Grain size distribution width −
Apex distance factor (ADF)	Accommodation space − Distal secondary remobilization +
Aspect ratio (AR)	Accommodation space − Lateral coalescence +
Splay angle (SA)	Accommodation space + Lateral coalescence −

7.2.3 Mean-shift clustering

As discussed in detail in Chapter 5, mean-shift is a single-parametric algorithm for locating the modes of a density function, with clusters being implicitly defined by the set of all data points converging to the same density mode—the attraction basin (Fukunaga and Hostetler, 1975; Cheng, 1995; Comaniciu and Meer, 2002; Carreira-Perpinan, 2006). The advantageous property of not requiring any constraints on the number of clusters or cluster shape (cf. Duong et al., 2016) renders mean-shift clustering an ideal method for exploratory statistical analysis, because clustering into more than a single class is, by design, not imposed on the feature space.

In this study, we use the exclusively feature-space-related variant of the mean-shift algorithm as provided by scikit-learn (Pedregosa et al., 2011), and conduct clustering using a Gaussian kernel. Being parametrized by a single bandwidth value, the algorithm implicitly presupposes that all incorporated features exhibit equivalent value ranges, so that distance is reflected equally in all dimensions of the feature space. For the incorporated set of morphometric variables, this assumption is clearly violated (cf. Fig. 7.1), hence indicating the need to scale the data into a common value domain.

Table 7.2: The set of non-linear regression functions considered for trend removal (cf. Daniel et al., 1999). The function yielding the minimum MSE was used for area de-trending.

Type	Equation
Exponential	$a \cdot \exp(b \cdot x)$
Logarithmic	$a + b \cdot \ln x$
Power	$a \cdot x^b$
Asymptotic	$a + \frac{b}{x}$
Growth	$a \cdot (1+x)^b$

In Chapter 5 (Pipaud and Lehmkuhl, 2017), we implicitly considered different feature bandwidths by conducting an iterative rescaling of variables, based on a tentative visual pre-examination. In this study, however, we lack such independent control, and are thus concerned with stipulating appropriate bandwidth values to be used as starting point of our analysis. Since the mean-shift approach is equivalent to performing a gradient ascent on the kernel density estimate for each sample until convergence (Arias-Castro et al., 2016), it is reasonable to assume that a feasible bandwidth estimate can be deduced from those bandwidth values yielding cross-validated optimal density estimates (Chacón and Duong, 2013), and that these bandwidth values can thus be used for rescaling the datasets prior to performing clustering. Hence, we calculated variable-specific optimal bandwidth values applying the cross-validated maximum likelihood (CVML) approach as introduced in Section 6.3 (cf. Stone, 1974; Geisser, 1975; Rudemo, 1982; Racine, 2008; Li and Racine, 2009) and used the obtained bandwidths to rescale the incorporated features for mean-shift clustering.

For the consistency evaluation of the obtained clusters, we calculated mean silhouette scores for each cluster and the full ensemble. The silhouette coefficient quantifies the cohesion of a sample with respect to other members of the cluster A in relation to their separation from the most adjacent cluster B by calculating the mean intra-cluster distance and the mean nearest-cluster distance. The silhouette coefficient is given by (Rousseeuw, 1987; Kaufman and Rousseeuw, 1990):

$$\mathrm{SC}_i = \begin{cases} 0 & \text{if } \mathrm{dist}(A,i) = \mathrm{dist}(B,i) = 0, \\ 0 & \text{if } n = 1, \\ \dfrac{\mathrm{dist}(B,i) - \mathrm{dist}(A,i)}{\max\left(\mathrm{dist}(A,i),\ \mathrm{dist}(B,i)\right)} & \text{otherwise,} \end{cases} \tag{7.3}$$

where $\mathrm{dist}(A,i)$ denotes the average distance of an object i to all objects of its own cluster A, $\mathrm{dist}(B,i)$ denotes the average distance to the objects of the neighboring cluster B, n defines the size of cluster A, and SC_i connotes the sample-specific silhouette score. Silhouette coefficients were calculated with

Euclidean distance metric, so that dist is defined by:

$$\mathrm{dist}(C,i) = \frac{1}{n}\sum_{\substack{j\in C\\ j\neq i}}^{n} \left\| \vec{p}_i - \vec{p}_j \right\|_2 , \tag{7.4}$$

where $\vec{p}$ are the feature vectors, and n is the number of samples j in cluster C. According to Kaufman and Rousseeuw (1990), reasonable structuring necessitates SC to exhibit values greater than 0.5, whereas a strong structure is indicated if large clusters exhibit average silhouette coefficients of greater than 0.7.

7.2.4 Principal component analysis

Principal component analysis (PCA) is a multivariate statistical method used to restructure a dataset. By applying an orthogonal linear transformation to maximize the variance between all dimensions, a PCA yields uncorrelated principal components (Hotelling, 1933; Jackson, 1991; Jolliffe, 2002; Abdi and Williams, 2010). Note that in the following, we refer exclusively to a PCA performed on correlation matrices.

Besides its common use for dimensionality reduction, PCA exposes what kind of feature combinations bear the most variance within the dataset, making it a valuable tool for exploratory data analysis (Abdi and Williams, 2010). The principal components are obtained from an eigendecomposition of the correlation matrix of the dataset (cf. Cuppen, 1980), yielding the eigenvalues and eigenvectors of the matrix. Here, the eigenvectors are unit vectors indicating the direction of the obtained principal components within the feature space spanned by the incorporated morphometric parameters. The eigenvalues define the corresponding scalars by which this eigenvector is scaled, and, consequently, show how much variance is reflected in this component (Jolliffe, 2002; Strang, 2009). The transformation is performed in such a way that the first principal component (PC) bears the largest possible variance, with each subsequent component exhibiting the highest variance possible under the constraint of being orthogonal to the preceding PCs. Performing variance maximization, an unbiased PCA requires features to be centered at zero and to exhibit equal variances if these features are measured in different units (Jolliffe, 2002; Abdi and Williams, 2010; Lever et al., 2017). We therefore applied a Z-standardization on the data (cf. Pipaud and Lehmkuhl, 2017 / Section 5.5) prior to conducting the PCA. PC scores for all features can then be derived by:

$$\mathrm{PCS} = Z \cdot V, \tag{7.5}$$

where Z denotes an $n \times p$ matrix of all Z-standardized feature vectors, V is the $p \times k$ matrix of all feature eigenvectors, and n, p, and k denote the number of features, the number of morphometric parameters, and the number of eigenvectors used for transformation. Note that performing an eigendecomposition of a covariance matrix of Z-standardized data is equivalent to conducting an eigendecomposition of the respective correlation matrix (cf. Jolliffe, 2002), but yields PC scores which are straightforward to interpret (cf. Legendre and Legendre, 2012). While clustering tendencies within the dataset can be revealed by PCA, the strictly variance-focused approach of the method does not guarantee that the obtained principal components reveal data structures conducive to a thematic interpretation. Furthermore, an underlying structure is only precisely reflected if it is linear (Lever et al., 2017), an assumption that is generally not met for the morphometric data at hand (cf. Suppl. D.1).

The variance-oriented approach entails that outliers can have a substantial impact on the direction of the principal component vectors (Jolliffe, 2002; Handl and Kuhlenkasper, 2017). Therefore, we propose to conduct outlier detection and removal prior to computing the covariance matrix. In this study, we used the local outlier factor (LOF) algorithm available in scikit-learn (Pedregosa et al., 2011). The LOF is a density-oriented technique suggested by Breunig et al. (2000), which is essentially based on using a k-nearest neighbor algorithm to evaluate and compare the distances of samples to each other. Defining local density as the distance of a sample to the k-nearest neighbor—the k-distance, the algorithm has the valuable property of being adaptive to different average densities within the feature space. Sample-specific density values are obtained by first calculating the reachability distance (RD) between a sample A and its k-nearest neighbors B:

$$\mathrm{RD}_k(A, B) = \max\Big(k\text{-distance}(B),\ \mathrm{dist}(A, B)\Big) \tag{7.6}$$

Then, the local reachability density (LRD) is defined as the reciprocal of the average RD of object A:

$$\mathrm{LRD}_k = 1 / \left(\frac{\sum_{B \in N_k(A)} \mathrm{RD}_k(A, B)}{|N_k(A)|}\right), \tag{7.7}$$

where $N_k(A)$ is the k-neighborhood of A. Eventually, the LOF for a sample A is defined as the average LRD of the neighbors B divided by the sample's own LRD:

$$\mathrm{LOF}_k(A) = \frac{\sum_{B \in N_k(A)} \mathrm{LRD}_k(B)}{|N_k(A)| \cdot \mathrm{LRD}_k(A)} \tag{7.8}$$

An LOF value below 1 indicates that the sample considered exhibits a higher density than its surroundings, implying that it is an inlier of a clustered region of the feature space. Conversely, while values significantly larger than 1 indicate that the considered points are outliers, there is no objective rule for setting a cutoff value (Schubert et al., 2014). Since the LOF algorithm is subject to the same variable scaling issues as already discussed in the context of Mean-Shift clustering (cf. Section 5.5), we performed the LOF calculation on data which was rescaled by kernel density estimation (KDE)-derived density estimates. Subsequently, arithmetic mean and standard deviation for a regular Z-standardization are computed from the subset of data samples remaining after the outlier detection. Whereas the Z-transformed subset of remainders is subsequently used for determining the covariance matrix, the component scores are still computed for the full dataset with Z-standardization being applied with the mean and standard deviation from the remainder subset. Note that PCA was exclusively performed for the de-trended dataset. The number of neighbors defining the local density domain was set to 20, and the LOF threshold was set to a value of 1.5.

7.3 Results

7.3.1 Scaling relationships with alluvial fan area

As clearly depicted in Fig. 7.1, a majority of morphometric variables exhibit a statistical relationship with area. Positive trends are given for radial approximation divergence (RAD), gradient–apex divergence (GAD), and both lateral and distal gradient difference (DGD). Conversely, strong negative trends are

Table 7.3: Regression functions and function coefficients applied to remove the relationship with fan planimetric area (km^2), as depicted in Fig. 7.1. In cases where the type of statistical relationship did not differ clearly from a linear relationship, linear de-trending was stipulated. For all non-linear functions, those yielding the minimal MSE were selected.

Morphometric variable	Selected function	*a*	*b*
RAD (GGC)	Linear	1.737	0.043
GAD (GGC)	Linear	13.670	0.308
LGD	Growth	–0.061	–0.327
DGD	Logarithmic	–0.049	0.005
Slope	Logarithmic	3.916	–0.596
CCurv	Power	0.516	–0.659
LCurv	Linear	–0.022	0.000
ADF	Logarithmic	–0.040	–0.052
AR	Linear	0.996	–0.001
SA	Linear	79.467	–0.004

given for slope and cross-sectional curvature (CCurv), and a weaker negative trend can be observed for the apex distance factor (ADF) and aspect ratio (AR). Splay angle (SA) values seem to be unaffected by fan area with the exception of the largest fan sizes, for which statistical support is very low. Finally, an overall trend is clearly absent in the case of longitudinal curvature. Based on visual inspection and kernel regression trends, a linear regression model was chosen for RAD, GAD, LCurv, AR, as well as SA, because these variables show either a linear relationship, no relationship, or allow no conclusive assessment of the nature of their statistical relationship with alluvial fan area. For the remaining morphometric parameters, best fits were most often provided by using a logarithmic regression. Growth and power function have each been selected once (cf. Table 7.3).

Note that some of the variables, such as cross-sectional curvature, exhibit constant upper or lower value bounds, and consequently, the aforementioned trends do only apply with respect to central tendency. These bounds are imposed by radial deposition and the concomitant radially symmetric conical morphology, thus reconfirming that these variables are valuable for alluvial fan recognition within a diverse geomorphological inventory. Despite the presence of hard upper or lower limits, it is, however, still indicated to apply regression on these samples. Specifically, if we are aiming to differentiate between dominance of sediment transport over generation of accommodation space, and vice versa, we are required to evaluate where alluvial fans are located in the feature space in comparison to other alluvial fans with similar planimetric areas.

RAD and GAD measure the derivation from an idealistic radial deposition from the apex (cf. Chapters 5 and 6). In this context, the linear increase with fan area shown by both morphometric parameters is quite striking, since it essentially signifies that the level of agreement with this fundamental model of alluvial fan geomorphometry gradually deteriorates with growing fan sizes. The positive scaling relationship for RAD and GAD is concomitant with a decrease of the ADF, indicating an increasing trend for progradation (cf. Chapter 6). Progradation compulsorily leads to a deviation from the radial sedimentation model, thus being inversely correlated with both RAD and GAD (cf.

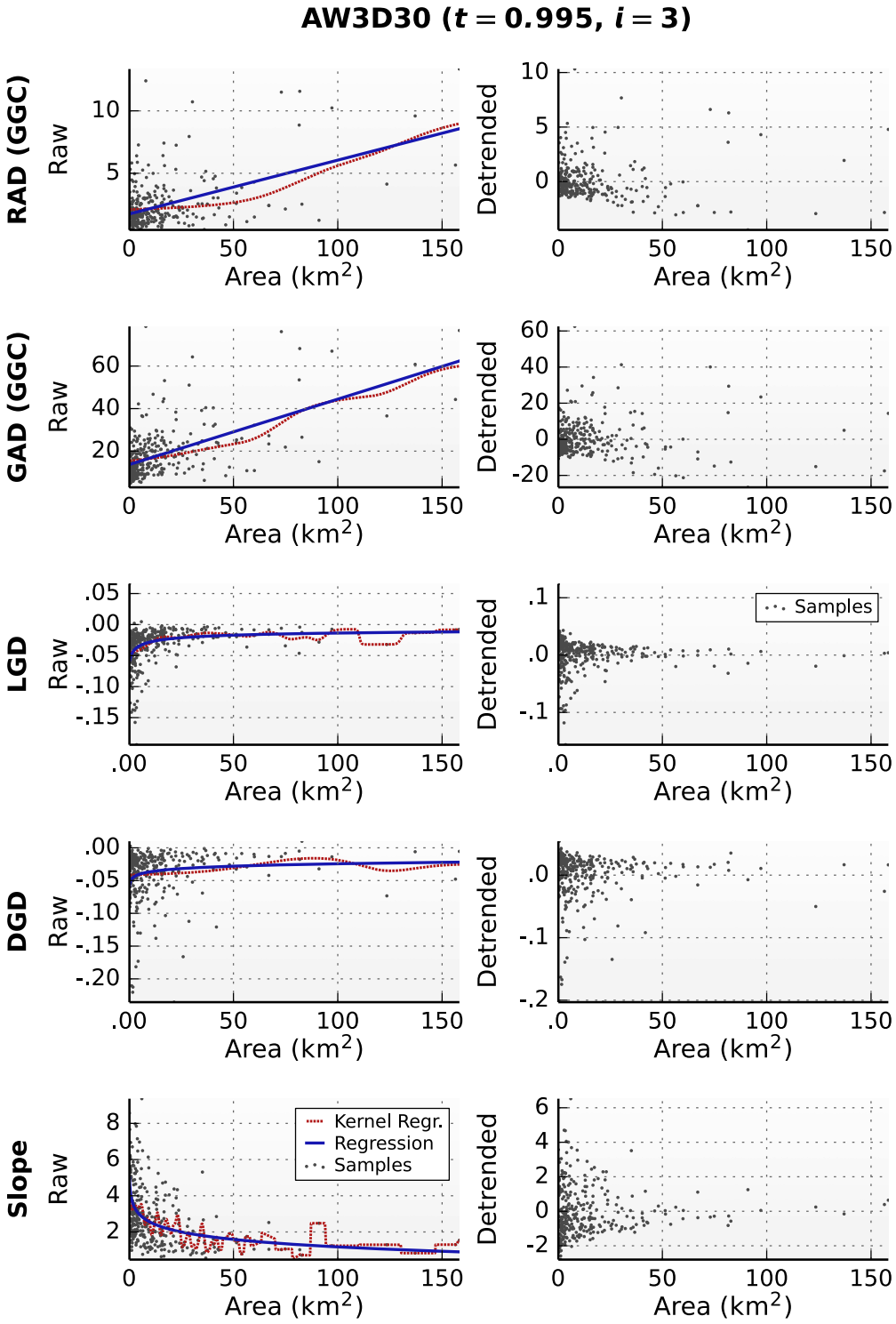


Figure 7.1: Scatter plots of the incorporated morphometric variables prior and after de-trending, and the corresponding regression function yielding the minimal MSE, or the stipulated linear regression function, respectively. Also depicted are the kernel regression functions obtained by using a Gaussian kernel parametrized with a CVML-optimal bandwdith.

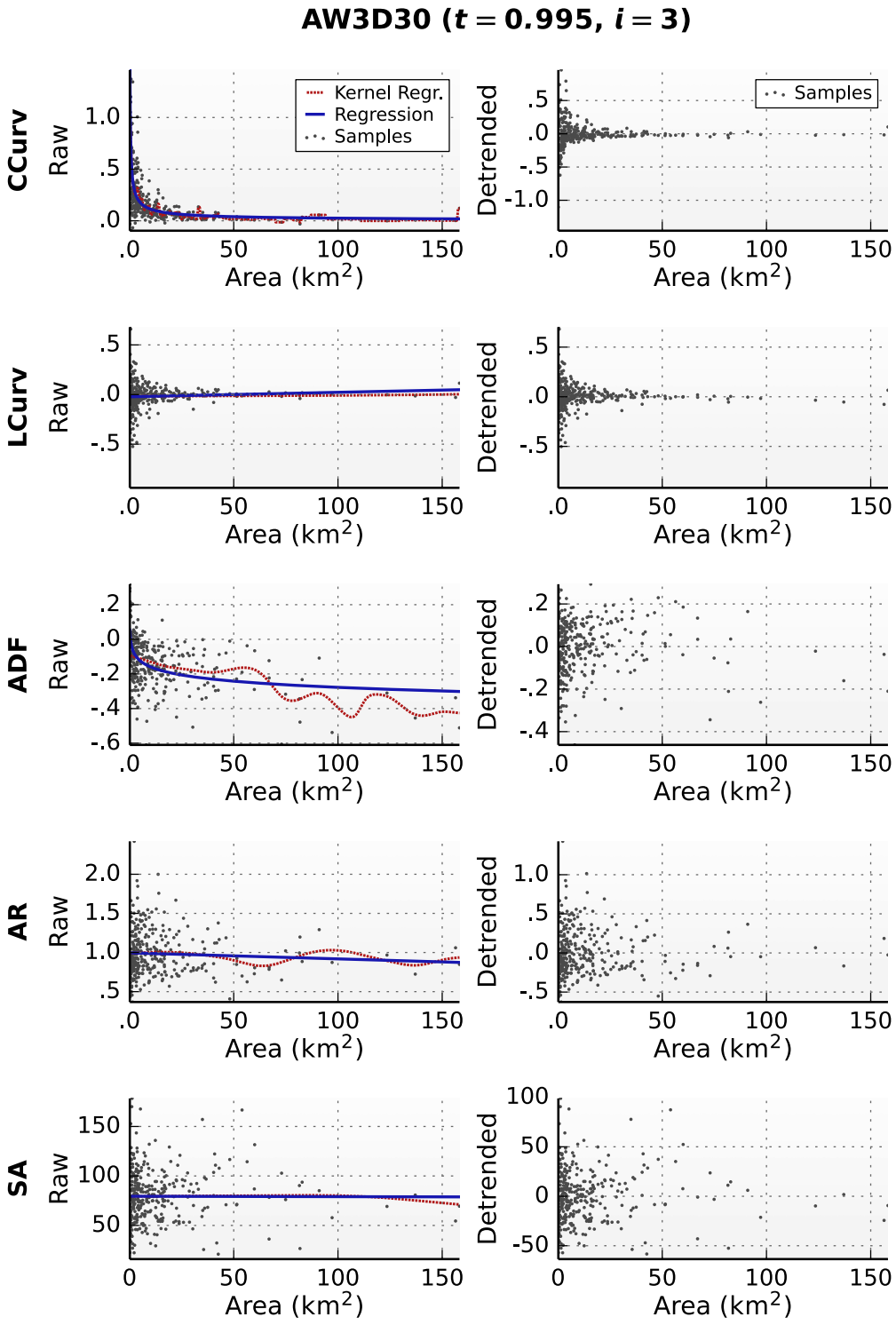


Figure 7.1 (cont.)

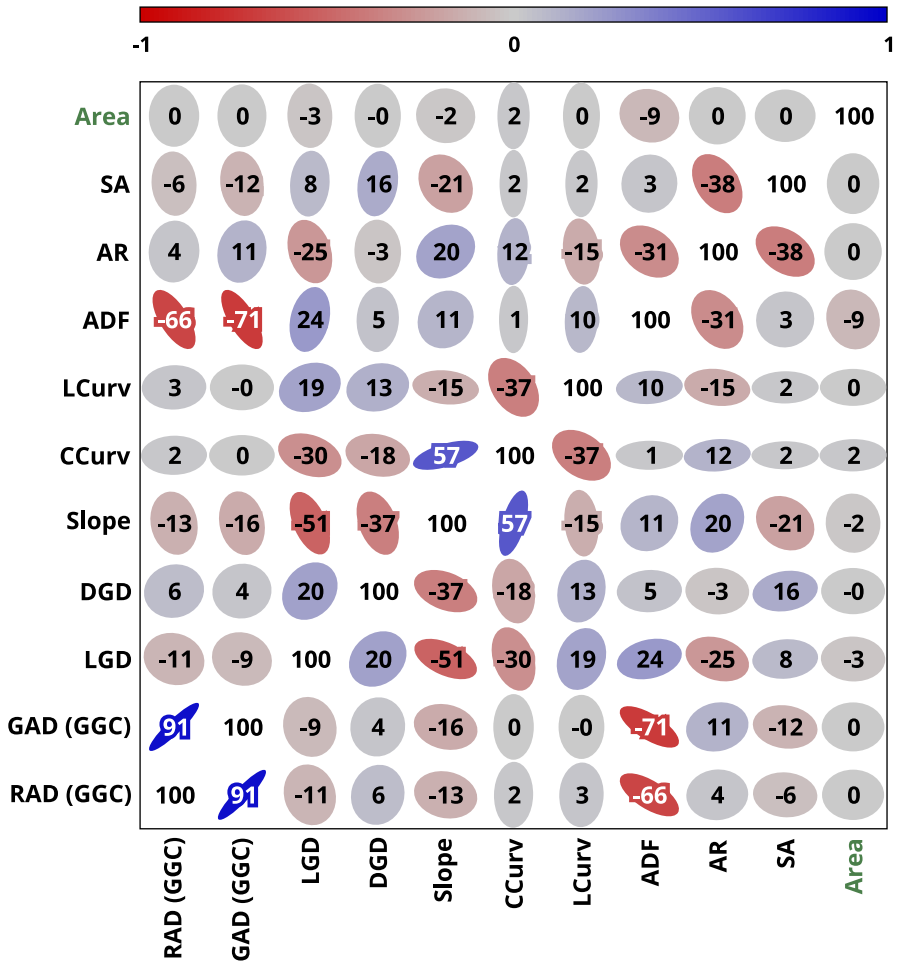


Figure 7.2: Product-moment correlation matrix of the de-trended dataset. Auxiliary variables are denoted in green letters.

Suppl. D.1). Besides, the positive trend for GAD and RAD may also be related to a pronounced internal differentiation by multi-lobation and large parts of the fan surface being inactive for extended periods of time—characteristics which are considered inherent to large alluvial fans (cf. Stanistreet and McCarthy, 1993), and which compellingly emerge from supply dominance and the resulting promotion of sediment bypassing the proximal fan areas.

Another important characteristic depicted in Fig. 7.1 is that the considered morphometric parameters partly display a strong decrease of variance with increasing planimetric fan area. Sharply declining variances are present in the case of Slope, cross-sectional curvature (CCurv), longitudinal curvature (LCurv), lateral gradient difference (LGD), and distal gradient difference (DGD), i.e., all variables representing or being dependent on fan gradient (cf. Suppl. D.1). Furthermore, a smaller negative trend for variance of feature values is given in the case of the apex distance factor (ADF) and aspect ratio (AR), substantiating an increasing relevance of progradation for large fans. Conversely, no decreasing variability is shown by gradient–apex divergence (GAD), radial approximation divergence (RAD), and splay angle (SA).

In general terms, removing the variance imposed by planimetric fan area moderately reduces product-moment correlation coefficients. A notable decrease in correlation coefficients is given in the case

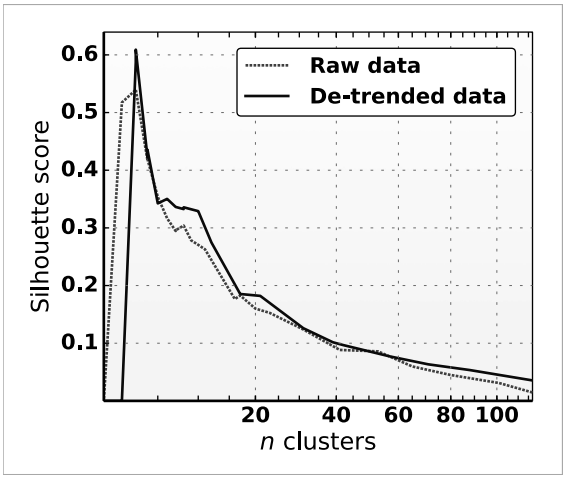


Figure 7.3: Average silhouette values in relation to the number of clusters, obtained via mean-shift clustering and iterative increase of bandwidths.

Table 7.4: Obtained clusters from mean-shift clustering of the raw morphometric data with silhouette-optimal bandwidth selection.

ID	n	Silh.	Area (km^2)	RAD	GAD	LGD	DGD	Slope	CCurv	LCurv	ADF	AR	SA
C0	**289**	**0.54**	12.50	2.04	16.22	−0.03	−0.04	2.86	0.23	−0.01	−0.12	0.99	80.18
C1	**15**	**0.52**	61.21	8.90	58.05	−0.02	−0.02	1.29	0.04	−0.00	−0.42	0.97	67.17
C2	**2**	**0.26**	0.31	1.67	9.06	−0.07	−0.08	7.40	2.59	−1.12	0.07	0.56	60.35

of ADF, RAD and GAD, which all lose their statistical relationship with lateral gradient difference (LGD), Slope, and CCurv (cf. Fig. 7.2). Three groups with distinct statistical relationships emerge in the de-trended dataset. (1.) The closest statistical relationship is given for RAD, GAD and ADF, which corroborates progradation as primary controlling factor for these variables. This group is followed by (2.) LGD, DGD, and CCurv, whose dependency on fan gradient (Slope) compulsorily results from radial sedimentation. In addition, (3.) a weak but distinct correlation is shown between SA and AR, which is in line with the thematic significances of both variables (cf. Table 7.1). It is noteworthy, however, that despite the similar informative value of these two variables and the first group, SA and AR are entirely uncorrelated with fan area (cf. Suppl. D.1).

7.3.2 Clustering

Conducting mean-shift clustering with a bandwidth estimated by the KDE-based density estimation yields 117 classes for both the raw and the de-trended dataset (cf. Suppl. D.2 and Suppl. D.3), indicating strong data sparsity related to the relatively high-dimensional feature space (cf. *curse of dimensionality*; Bellman, 1984; Aggarwal and Yu, 2001).

Both runs return a single dominant *bulk* class with 95 and 94 fans, respectively. Conversely, most other classes are either singletons or exhibit a single digit number of fans. We performed an iterative search for parametrizations yielding maximal average silhouette scores by multiplying the sample data

Table 7.5: Obtained clusters from mean-shift clustering of the de-trended morphometric data with silhouette-optimal bandwidth selection.

ID	n	Silh.	Area (km^2)	RAD	GAD	LGD	DGD	Slope	CCurv	LCurv	ADF	AR	SA
C0	**301**	**0.61**	14.41	−0.10	−0.55	0.00	0.00	−0.00	0.03	0.00	0.00	0.00	0.43
C1	**4**	**0.58**	48.27	7.73	43.31	−0.01	0.00	−0.86	0.00	0.01	−0.34	0.10	−23.52
C2	**1**	**0**	0.16	−0.00	−8.23	−0.03	−0.03	4.39	2.81	−0.92	0.17	−0.50	−34.65

with a successively increasing factor, which is equivalent to an increase in bandwidth. As shown in Fig. 7.3, three clusters denoted by C0 to C2 are obtained as optimal result for both raw morphometric data and the de-trended dataset, and both clusterings contain a very large bulk cluster with 289 and 301 members, respectively (cf. Tables 7.4 and 7.5). Maximum average silhouette scores are 0.54 and 0.61, respectively, which according to Kaufman and Rousseeuw (1990) corresponds to a *reasonable*, but still not strong clustering.

With C2 being a singleton and two-member cluster, respectively, C1 is the only considerable cluster besides the bulk class C0. In the case of the raw dataset clustering, C1 consists of 15 exceptionally large fans showing a characteristic morphometric signature of sediment delivery dominance, i.e., a very low ADF, which corresponds to strong progradation, and correspondingly large values for RAD and GAD. Applying mean-shift clustering to the de-trended dataset results in an enlarged bulk cluster at the expense of cluster C1, which has only four samples left. These findings indicate that a slight clustering tendency is only given with respect to scaling relationships, i.e., the variable relationships between morphometric parameters and fan area result in scale-dependent combinations of morphometric parameter values. It facilitates the delineation of large fans in the alluvial fan feature space, as long as clustering is conducted without area de-trending.

In a further step, we manually setup the bandwidth to yield 10 classes each, thereby deliberately accepting a subpar clustering consistency. Ten clusters where obtained by applying bandwidth scaling factors of 2.2 and 2.0, resulting in average silhouette scores amounting to 0.27 and 0.34, respectively. The manual bandwidth reduction lessens the member count of the main cluster moderately to 257 and 275 members, respectively, but does not yield any thematic split of the bulk class (cf. Suppl. D.4 and D.5). This result implies that even with bandwidth manipulated to be smaller than the optimal value, a majority of samples still converge to a common density center, falsifying the hypothesis of distinct morphometric sub-classes in the alluvial fan property space. In this context, a decreasing sample density towards peripheral regions of the feature domain entails multiple local mean-shift trajectories and convergence points, but these detached small clusters do not thematically translate into distinct fan types. Conversely, the result is in agreement with the notion of a single property cluster exhibiting a decreasing density and increasing variability towards its peripheral regions. Furthermore, note that in the case of the de-trended dataset, the detached singletons and small clusters are mostly characterized by small fans.

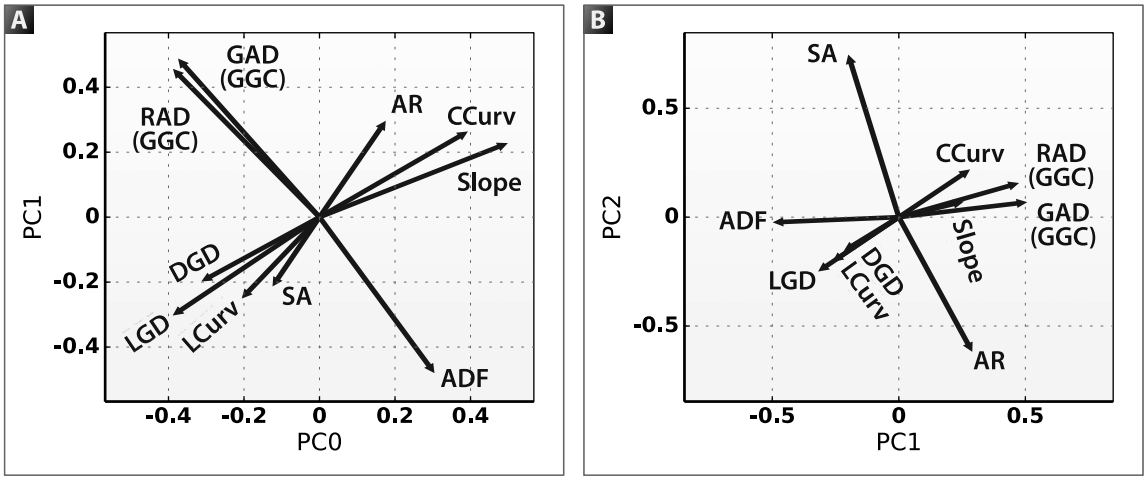


Figure 7.4: Projections of morphometric variables on principal components. (A) Projections for the two-dimensional space spanned by PC0 and PC1, (B) projections for the two-dimensional space spanned by PC1 and PC2.

7.3.3 Principal Component Analysis

Local Outlier Factor

Conducting LOF calculation with a threshold value of 1.5, the algorithm identified 26 fans as outliers. For these fans, the median of the planimetric area amounts to approximately 1.5 km^2, corroborating that the morphometric feature space is most diverse in the cohort of small fans (cf. Suppl D.8). In contrast, 41 alluvial fans exhibit a LOF score below 1 and are thus to be interpreted as inliers of relatively dense regions within the property space. Moreover, 97 fans exhibit LOF values between 1 and 1.1. From a general perspective, the LOF curve depicted in Suppl. D.6 signifies a relatively gradual decrease of density towards more marginal regions, with prominent outliers being given for LOF greater than ~1.6. This finding is well in line with the results obtained from mean-shift clustering.

PCA Eigenvalues and Eigenvectors

Applying principal component analysis on the de-trended and Z-standardized dataset yields a set of eigenvalues with a low decrease of explained variance, indicating complex relationships within the alluvial fan property space. Specifically, while PC0 and PC1 explain ~29 and ~24 % of the total variance, the percentage share of eigenvalues decreases abruptly to ~13 % for PC2 (cf. Supp. D.7). Beyond PC2, however, eigenvalues decrease only gradually.

Inspecting Fig. 7.4, it becomes apparent that all projections of morphometric variables into the PCA space (denoted feature importance vectors hereafter) form bundles along two nearly independent lines which are rotated by ~45° with respect to the coordinate system. This structure is presumably imposed by the complexity of the feature space and the orthogonality constraint of PCA. As already indicated by product-moment correlation coefficients, RAD, GAD and ADF form a thematic bundle quantifying the degree of progradation (called direction 0 hereafter).

A second nearly orthogonal and therefore statistically almost independent direction is taken by AR, CCurv, slope, and—in opposite direction—DGD, LGD, SA, and LCurv (denoted direction 1 hereafter).

While the direction of the feature importance vector given for DGD and LGD is clearly related to their relationship with fan gradients (cf. Fig. 7.2), the direction of the vector given for longitudinal curvature corroborates that this direction jointly reflects the impact of fan-building processes, as well as tectonic controls on fan gradient and related morphometric variables. By considering both PCs in conjunction, however, a qualitative differentiation between tectonic and non-tectonic controls should be feasible.

This assertion conflicts, however, with the fact that positive values of fan slope and CCurv are associated with positive and negative values for AR and SA, respectively, spuriously implying that specifically steep fans tend to be elongated (cf. Chapter 2). Notably, both vectors are oriented towards direction 0, implying that both morphometric variables are significant for both axes. Taking PC2 into account, we observe that this PC exhibits highly positive and negative values for SA and AR, supposedly counterbalancing the vector components given for PC0 and PC1. With respect to the impact of tectonic activity and the degree of accommodation space generation, PC2 also has to be interpreted as a complement to PC0 with a focus on unconfined lateral expansion, which is notably lacking in PC0.

Starting from PC3, the principal components have a gradually increasing tendency to show entry combinations which are allegedly contradictory and lack straightforward geomorphological interpretations. In the case of PC3, a markedly negative value for longitudinal curvature is associated with a moderately negative component for fan slope, as well as positive values for DGD, AR, and SA (cf. Suppl. D.7). Conflictingly, PC3 shows divergent vector components for DGD and longitudinal curvature, implying that alluvial fans with smooth transitions into the adjacent foreland tend to exhibit longitudinal convexity. An extreme example is PC9, which exclusively quantifies contradictory evidence between RAD and GAD (cf. Suppl. D.7). Notably, this PC is disproportionately represented in larger fans, again indicating the tendency of GAD to show higher values in the case of large fans. These components are thus best interpreted as modifiers of the fundamental morphometric relationships which are relatively clearly represented within the first three principal components. They thereby reflect morphometric diversity and non-linearity emerging from the specific geomorphic context of alluvial fans, as well as the specific susceptibility of morphometric parameters to digital elevation model characteristics.

In what follows, we will be concerned with testing the assertions we made so far by examining the projections of the fan dataset within the first three PCs. Based on their representativeness for juxtapositions of tectonic and climatic control, three of the considered study areas were selected to be examined in more detail. As discussed in-depth in Chapter 4, Region 2 (northern parts of the Numic subtaphrogen of the Basin and Range region) is characterized by ample generation of accommodation space along normal-fault-bounded horsts and half-horsts. Fan formation is related to extratropical precipitation, and fans are predominantly built-up by streamflows. Furthermore, Region 3 (Walker Lane Fault Zone) was selected based on its generally very high but variable subsidence rates and the facilitation of debris flow instigation by monsoonal high-intensity rainfall during the late Pleistocene-Holocene transition phase. Eventually, Region 7 (Gobi Altai) was incorporated, because it exhibits generally limited and variable accommodation space, depending on the position of fans with respect to the range front and the presence of foreberg zones. Here, formation phases are related to extratropical circulation, and evidence for both streamflow and debris flow-deposition is reported.

Inspecting the two-dimensional plot given for the full dataset in Fig. 7.5A, we observe that large fans are plotted along direction0 within the PC0–PC1 feature space. This finding corroborates the results of

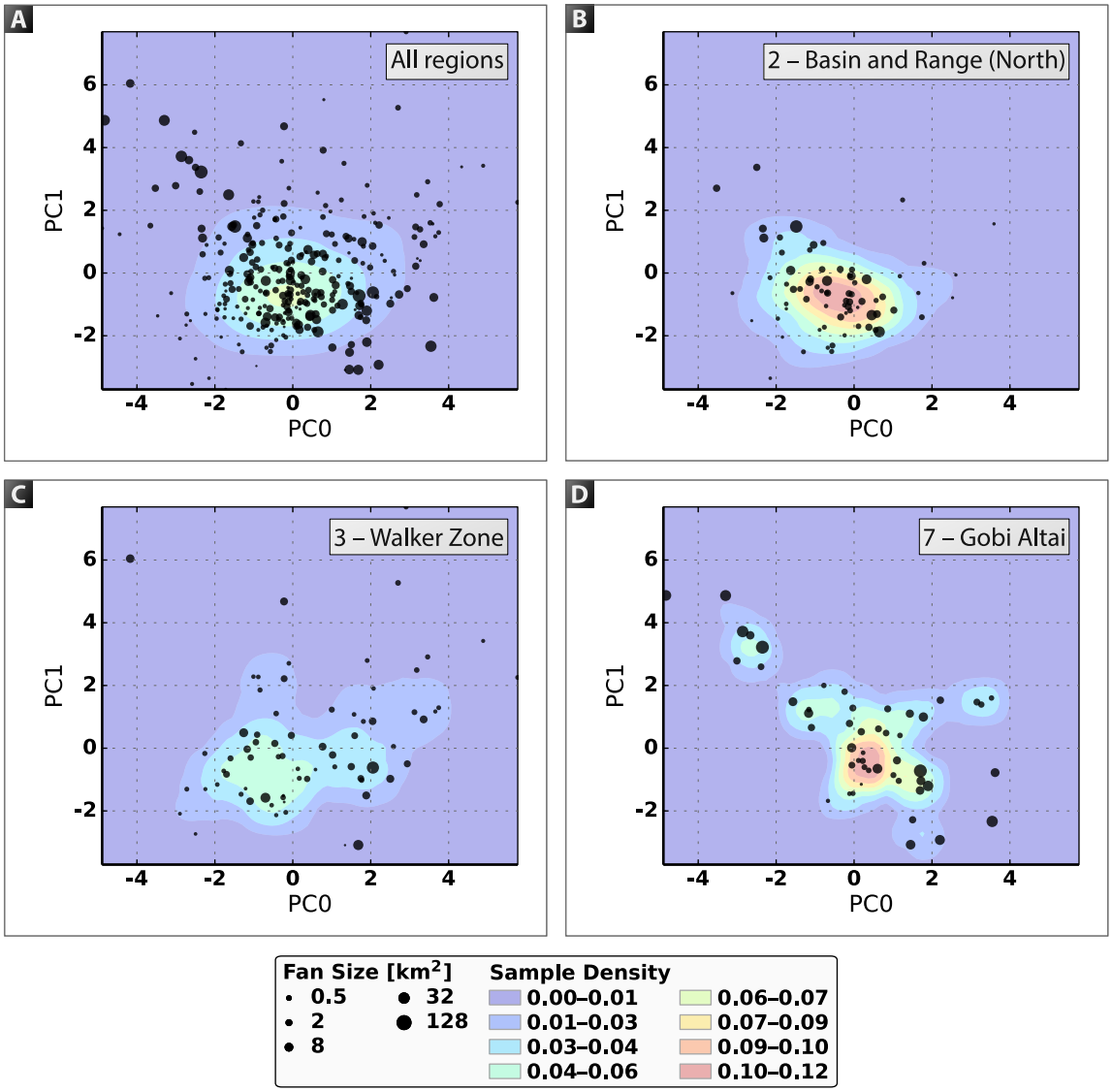


Figure 7.5: Scatter plots of component scores in the two-dimensional space spanned by PC0 and PC1. (A) All regions, (B) Northern Great Basin, (C) Walker Lane Fault Zone, (D) Gobi Altai.

the trend analysis by showing that varying degrees of progradation are the major differentiating factor of the feature space for large fans, whereas differentiation is small with respect to other morphometric aspects. Smaller fans, in contrast, show less variability with respect to progradation. Conversely, they display a pronounced differentiation along the second major direction of feature importance vectors—indicating differences with respect to specific steepness and longitudinal concavity. Turning to the bivariate plots provided for the selected regions (Fig. 7.5B–D), it must first be noted that the empirical distributions of all regions show substantial overlaps, again falsifying the hypothesis that differences in environmental conditions are reflected in distinct clusters. However, some notable trends can still be observed.

In line with theoretical considerations and reported in-field research, Region 2 (northern Basin and Range) exhibits a compact distribution with only moderate values in the direction of both thematic bundles, signifying little variability of environmental boundary conditions and mostly lacking evidence

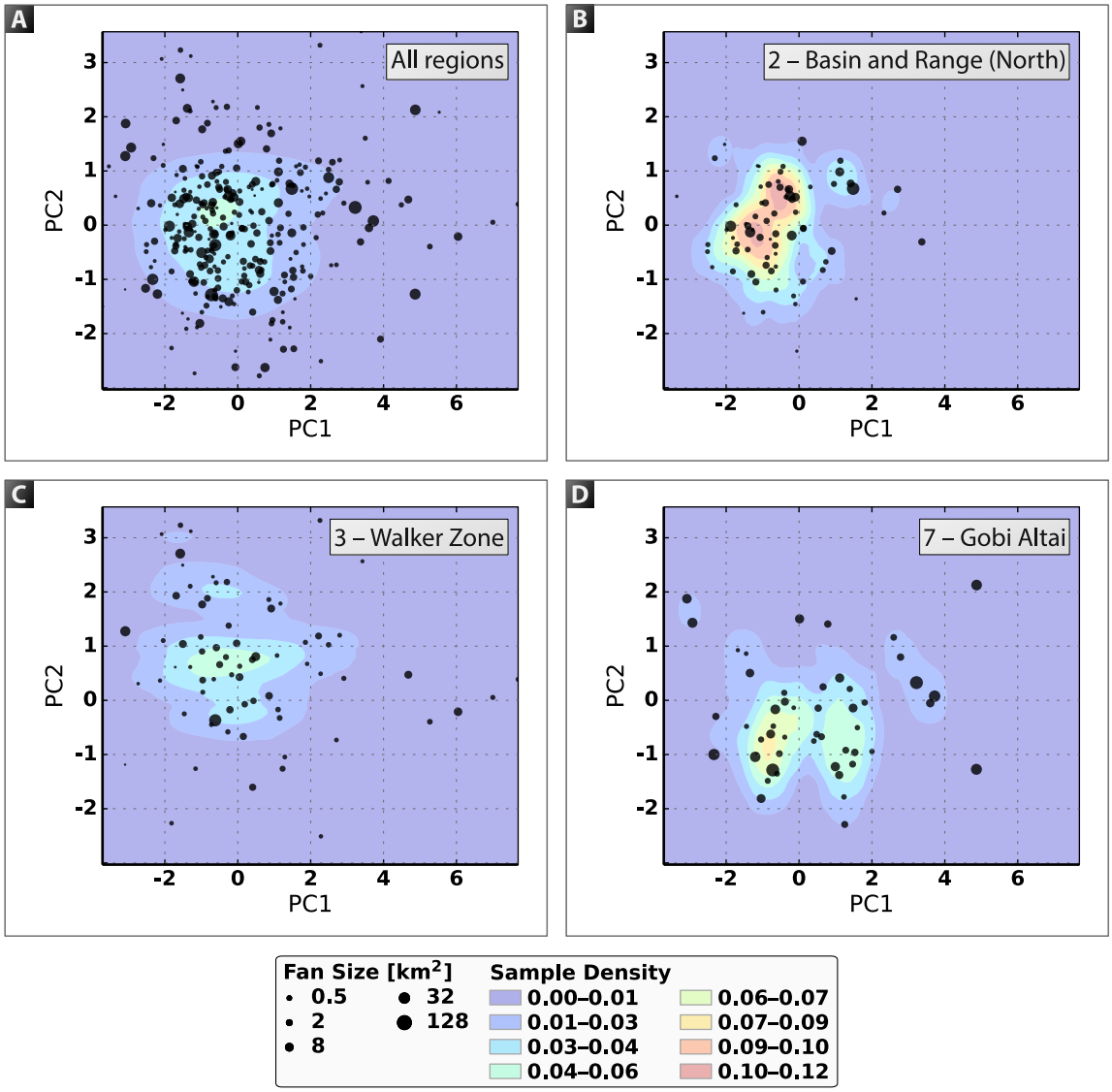


Figure 7.6: Scatter plots of component scores in the two-dimensional space spanned by PC1 and PC2. (A) All regions, (B) Northern Great Basin, (C) Walker Lane Fault Zone, (D) Gobi Altai.

for progradation. In contrast to the northern core areas of the Numic subtaphrogen, the Walker Lane Fault Zone (Region 3) is characterized by a substantially larger variability with respect to direction 1. In order to produce fans primarily built by non-Newtonian flow, geologic boundary conditions must be conducive for debris flow instigation as well (cf. Section 2.1.1). Consequently, spatially extensive regions with a climatic susceptibility for debris flow-generation should be characterized by a larger variability with respect to specific steepness and longitudinal curvature—a conjecture which is nicely reflected in the dataset. Considering the empirical distribution given for the Gobi Altai (Region 7), we observe that fan morphometry of this region is predominantly characterized by variability along the first thematic direction, illustrating variable degrees of progradation attributable to the local tectonic setting.

As depicted in Fig. 7.6, no trends are discernible in the bivariate plot provided for the full dataset, and the empirical distributions of all three regions are again characterized by a significant amount of overlap. For the three regions, however, trends are apparent which are well in line with theoretical expectations.

Specifically, fans of the Walker Lane Fault Zone (Region 3) tend to exhibit the highest PC2 scores, signifying a low relevance of lateral coalescence. Region 3 once more displays a larger variability than Region 2 (northern Basin and Range), indicating that the Walker Lane Fault Zone provides greater internal differentiation with respect to the tectonic generation of accommodation space. In contrast to both other regions, the Gobi Altai dataset (Region 7) as a whole exhibits considerably lower PC2 values, indicating an increased role of lateral coalescence resulting from limited accommodation space.

7.4 Discussion

7.4.1 Scaling relationships

The study at hand extends the approach of relating planimetric fan area with fan gradient (cf. e.g., Al-Farraj and Harvey, 2005; Saito and Oguchi, 2005; Hashimoto et al., 2008) by putting fan area into relation with a comprehensive set of morphometric variables. Our results indicate that inverse non-linear relationships apply in the case of fan slope and variables correlated with slope, i.e., cross-sectional curvature, LGD, and DGD, as well as ADF. Decreasing magnitudes for the aforementioned morphometric variables are accompanied by a decreasing variance of feature values, indicating a *narrowing* of morphometric variance for increasing fan areas. By contrast, RAD and GAD display a trend for linearly increasing values with growing fan sizes, signifying a growing relevance of progradation.

As comprehensively discussed in Chapter 2, scaling relationships between alluvial fans and their corresponding catchments are characterized by negative surface allometries and decreasing fan gradients (cf. e.g. Blissenbach, 1952; Bull, 1962, 1964), instigated by sediment retention and decreasing sediment load factors. Catchment-related scaling effects also cause a gradual transition into streamflow-derived sediment supply in geomorphic settings with generally favorable conditions for mass flow deposition (cf. Stanistreet and McCarthy, 1993, Section 2.1.1).

The findings of this study imply, however, that these scale-related effects are also accompanied by a changing relevance of the tectonic imprint in alluvial fan geomorphometry. Specifically, scale-related change also involves ADF values decreasing with a logarithmic trend, which cannot be explained neither by a dominance of streamflows, nor decreasing sediment load factors. Conversely, this decline in ADF compulsorily points to a tendency towards progradation, signaling a change towards sediment-overloaded accommodation systems. In this context, note that distal remobilization—which might be expected for large streamflow-derived fans (cf. Stanistreet and McCarthy, 1993)—would cause a deviation from the radial deposition pattern and therefore shift the convergence point towards the mountain front, rather than inducing a spurious progradation signal.

While alluvial fan area has an inverse power law relationship with the planimetric area of the corresponding catchment, fan areas are still monotonically increasing, which equates to a continuously growing sediment delivery per feeder channel. Consequently, the enhanced focus of sediment supply along the mountain range presumably facilitates accommodation capacities along the mountain front to become exceeded. Then again, the increasing tendency for progradation is not reflected by SA and AR, which jointly indicate only a slight tendency for elongated fan footprints. This conspicuous feature indicates that large fans are only moderately affected by lateral coalescence even in the case of substantial progradation. The informative value of both morphometric parameters is therefore inferior

to RAD, GAD, and ADF.

Although asymptotically converging geomorphometric properties restrict the thematic interpretation of large fans with respect to their environmental boundary conditions, these fans still show differences enabling a differentiation with respect to the relevance of tectonic control. With RAD, GAD and ADF mostly retaining their variance throughout the spectrum of fan sizes, variations of the degree of progradation can be reliably detected. Conversely, morphometric proxies for the rheology of fan-building processes are not reliably discernible in the cohort of large fans. In this context, it needs to be kept in mind that slight differences might well be masked by the limited accuracy of DEMs (cf. Pipaud et al., 2015 / Chapter 3; Purinton and Bookhagen, 2017). Further, note that with respect to the low amount of fans with planimetric areas above ~50 km^2, the statistical support for large fans is low in the study at hand, and further research is encouraged.

7.4.2 Feature space structure

The results obtained from mean-shift clustering clearly indicate that alluvial fans are distributed within the property space in a largely even manner, confirming a continuous character of alluvial fan morphometry as postulated by Saito and Oguchi (2005), and rendering any attempts to obtain semantically significant clusters unfeasible. When the mean-shift algorithm is parameterized with KDE-derived optimal bandwidths, the clustering yields a large bulk cluster and a large number of small clusters and singletons, signifying a decreasing feature density towards the peripheral regions of the alluvial fan property space. The only thematically related clustering tendency found applies to very large fans and emanates from scaling relationships of morphometric variables against planimetric fan area. Consistent therewith, de-trending the data mostly diminishes clustering trends.

Applying PCA on the de-trended data yields a gradual decrease of eigenvalues, signaling the complexity of the property space and the underlying geomorphic settings. Still, the first three PCs display plausible patterns of vector components which are conducive to a thematic interpretation. As a result of feature space complexity, these PCs are, however, intermingled with respect to their thematic implications, and therefore must be considered together. In the two-dimensional space spanned by PC0 and PC1, feature vector components bundle along two directions rotated by about 45° relative to the coordinate system. With these directions indicating the relevance of progradation and the specific steepness and longitudinal concavity, respectively, tectonic signals and indicators for fan-building processes are both represented within the dataset. The scale-dependent convergence of values of geomorphometric properties represented in PC1 entails, however, that variability along this direction is first and foremost shown by smaller fans.

Empirical density distributions of fans in the PC0–PC1 space as well as in the PC1–PC2 space show substantial intra-region variability, which manifests itself in regions with clearly differing boundary conditions showing substantial amounts of overlap. While emphasizing that the alluvial fan feature space is not conducive to a thematic subdivision, general trends can be observed which are in agreement with theoretical considerations and research done hitherto (cf. Viseras et al., 2003; Crosta and Frattini, 2004; Bahrami, 2013).

Intra-region variability can be plausibly related to variation in the generation of accommodation space and differences in fan-building processes. It is particularly noteworthy that variability along the

second thematic direction is larger in the case of regions for which sediment supply by debris flows has been reported. This result stresses that debris flow instigation is affected by various boundary conditions, including climatic conditions, topographic contrasts, readily transportable sediment, grain size distribution, conveyor path length, and sediment connectivity (cf. Chapter 2). While a distinct climatic signature therefore cannot exist, the combined impact of these factors can be identified within the data. It needs to be emphasized that the joint representation of tectonic controls and signals for fan-building processes by the second feature vector group in the PC0–PC1 space entails that the consideration of proxies for progradation greatly improves the differentiation between tectonic and non-tectonic signals.

7.5 Conclusions

This study evaluated the internal differentiation of the alluvial fan property space, and examined the dataset for signatures which can be linked to environmental control factors. Scaling relationships were found to fundamentally govern the distribution of fan samples within the feature space spanned by the non-de-trended morphometric variables. This result entails that fan populations with substantially differing planimetric areas cannot be juxtaposed without involving substantial bias. Our findings thus highlight a significant gap in research done hitherto. Specifically, while scaling relationships are well established in alluvial fan research, they have so far only been considered in the context of bivariate regression, but not in a multivariate context.

After removing the influence induced by planimetric area, the alluvial fan feature space is characterized by a disperse distribution of fans and lacks any predominant intervening spaces. When study areas with different environmental boundary controls are considered, thematically significant trends can, however, be identified within the first three principal components, with morphometric patterns being in agreement with theoretical considerations, as well as prior research.

While a distinct morphometric signature for climatic impacts does not exist, a combined signal expressing the specific steepness and longitudinal concavity of fans jointly reflects tectonic, climatic, and other environmental influences in the two-dimensional space spanned by the first two principal components. Proxies for progradation are statistically independent from these group of morphometric variables, thereby greatly improving the differentiation between tectonic and non-tectonic control on alluvial fan morphology.

The scale-dependent change of the dominant fan-building process towards streamflow-derived sediment supply involves that geomorphometric expressions of alluvial fans become successively more similar with increasing planimetric area. It is thus indicated to focus thematic research of alluvial fan geomorphology on fans with planimetric areas below $50\,km^2$, for which morphometric differentiation is still given for all morphometric variables. With the alluvial fan property space not being conducive to a thematic clustering, we encourage to apply scaling-adjusted multivariate morphometric data to self-organizing maps. Yielding topology-preserving discrete representations of the alluvial fan feature space, we envisage this approach to improve our understanding of morphometric expressions of environmental controls.

8 Synthesis

The application of object-based image analysis (OBIA) frameworks offers great potential for the field of specific geomorphometry. In research done hitherto, object-based techniques have been adapted from the field of remote sensing in a straightforward manner, using tools geared towards remote sensing use cases. In this context, it is mostly neglected that the geomorphometric formalization of digital elevation data functions as an interface to the altitude field as depicted by a DEM. Consequently, the selection of variables is pivotal for both segmentation and classification. In the case of object-based analysis of alluvial fans, this deficiency is manifested in a lacking ability to discriminate adjoining alluvial fans (cf. e.g., Norini et al., 2016; Argyridis and Argialas, 2017)—a setting which is common for piedmonts under (semi-) arid conditions.

With in-situ geomorphometric information being derived from the local altitude field as modeled by a DEM, the terrain rendition characteristics of the DEM product in use strongly affect the spectrum of parameter values for the landform of interest. This insight casts serious doubt on the utility of classification approaches based on rule-sets, which are the de facto standard in OBIA workflows.

The principal objective of this doctoral dissertation was to improve this situation by introducing a data-driven object-based framework for the robust and flexible delineation and classification of alluvial fans. A secondary objective was to assess whether the set of specific geomorphometric variables developed within the scope of this thesis can be used to foster our understanding of how environmental controls on alluvial fan formation are reflected in alluvial fan geomorphometry. To set the stage and gain insight into the terrain rendition characteristics of DEM products, a visual and geomorphometric analysis of the consistency of terrain rendition of medium-resolution near-global DEM data was performed.

In what follows, we will readdress the research questions (RQs) and objectives as defined in Chapter 1, and deduce incentives for future research.

Objective 1

RQs How do near-global DEM products compare to each other with respect to their intrinsic resolution and consistency of terrain rendition?
What improvements are made by the recently released DEM products TanDEM-X and AW3D30?

In Chapter 1, we asserted that the little attention given to DEM characteristics is a major deficiency in object-based geomorphometric research performed hitherto (Challenge 1). The comprehensive analysis conducted in Pipaud et al. (2015 / Chapter 3) emphasizes that available near-global medium-resolution DEM products strongly differ with respect to their depiction of high-frequency components of the terrain. Discrepancies in rendition of local relief can be traced back to both source data, i.e., optical and SAR imagery, as well as the respective stereometric and interferometric processing workflows.

The multi-pixel autocorrelated undulation pattern displayed by ASTER GDEM clearly points to the issue that the 15 m-resolution of the ASTER NIR imagery is insufficient both for a target DEM resolution of 1″, as well as with respect to the attainable co-registration precision of the image matching performed for parallax estimation. Although both DEM products are derived from base data with

roughly equivalent resolutions, SRTM1 displays substantially improved performance. Terrain rendition is, however, compromised in that the resolution difference between SIR-C imagery and the DEM is too small to allow for a substantial attenuation of DEM phase noise. In conjunction with the moderate-baseline across-track geometry of SRTM, this entails that phase noise propagates into 1″ elevation data.

Both fundamental approaches to near-global DEM generation saw substantial improvements with the TanDEM-X and ALOS missions, respectively. In the case of ALOS World-3D, stereo-triplet imagery with a posting of 2.5 m provides substantial leeway to process a 1″ DEM with an intrinsic resolution equivalent to its nominal one. While the author of this thesis concurs with, e.g., Purinton and Bookhagen (2017) in that noise is still evident in AW3D30 data, the analysis performed within the scope of Chapter 6 shows that this non-autocorrelated low-magnitude noise is more conducive to filtering techniques being effective than the autocorrelated textural pattern shown by SRTM1. In accordance, AW3D30 performed substantially better than SRTM1.

SAR interferometry provides per-pixel elevation information. Subject to the condition that source data have equivalent spatial resolution, SAR interferometry yields terrain information at an intrinsically higher resolution than optical stereometry. Hence, it comes at no surprise that based on the studies presented in Chapters 3 and 6, we can assert that for gentle to moderate relief, already a single TanDEM-X CoSSC scene enables the generation of a DEM which is superior to AW3D30 both with respect to its intrinsic resolution, as well as DEM noise.

Without the operative TanDEM-X DEM being available for the studies presented in Chapters 5 and 6, this finding poses the question whether TanDEM-X elevation data offers potential to foster advances in the object-based delineation and classification of alluvial fans. Based upon the results obtained in Pipaud and Lehmkuhl (2017 / Chapter 5), we can expect the highest potential for improvement to be given with respect to the delineation of alluvial fans displaying indistinct lateral boundaries. The findings of Chapter 6 in turn indicate that for the classification of alluvial fans, the improvements made with respect to DEM noise are presumably more important than the progress made with respect to intrinsic resolution.

From a more general perspective, it must be stressed that mountainous relief poses challenging conditions for interferometric processing, with attainable accuracy and resolution being considerably reduced. Interferometric processing of high-accuracy elevation data requires sufficiently high across-track baselines to inhibit inherent noise sources such as thermal (sensor) noise, geometric decorrelation, and SAR compression. In conjunction with the geometric distortion imposed by the slant range geometry of radar data, large baselines adversely affect, however, phase unwrapping in mountainous terrain.

Acknowledging this fundamental issue, DLR envisaged novel techniques such as multibaseline phase unwrapping for the generation of the operational TanDEM-X DEM (cf. Lachaise et al., 2008). While the thesis at hand does not allow inferences to be drawn on the quality of the final DEM product, the recent study of Boulton and Stokes (2018) indicates that the operational DEM is still affected by artifacts in mountainous terrain.

With respect to object-based geomorphometry, the corollary of these findings is that DEM selection has a strong impact on the range of values that can be expected for geomorphometric variables for a specific landform. This situation in turn emphasizes the pivotal role that near-global DEM products

exhibit for unbiased approaches to geomorphometric studies with a supra-regional scope. In this context, the author of this thesis deems it unfortunate that operational TanDEM-X elevation data is not freely available for scientific research, but is charged for at a per-scene (1°) basis resulting in substantial expenses for geomorphometric studies with a large spatial scope (cf. DLR, 2011a).

Objective 2

RQs Which combination of morphometric variables allows for an accurate delineation and classification of alluvial fans, including adjoining fans?
Can the problem of bandwidth selection for segmentation be addressed on a per-feature basis and in an objective, data-driven manner?
How can machine learning approaches facilitate the object-based analysis of landforms? What are the advantages over rule-based techniques and which challenges need to be addressed?
What inferences can be drawn for the future development of object-based geomorphometry?

In this doctoral dissertation, the adoption of OBIA methods for object-based workflows in the field of geomorphometry is subject to a critical examination. For a segmentation routine to yield semantically meaningful objects, a set of geomorphometric variables that depicts peripheries of objects of interest, as selectively as possible, must be provided. A fundamental issue affecting remote sensing and geomorphometry alike is that segmentation is an ill-structured problem, entailing that the quality of segmentation can only be asserted a-posteriori (cf. Challenge 2). In addition to the susceptibility of generic morphometric variables to the rendition of local relief in digital elevation data, landforms can exhibit complex feature spaces. In the case of alluvial fans, Chapters 2 and 7 emphasize, from a theoretical and statistical viewpoint, that intra-class heterogeneity is caused by (1.) a variety of environmental conditions controlling sediment conveyance and accommodation of sedimentary bodies, as well as (2.) fan size-related changes to environmental controls.

With respect to classification, these considerations point to the fact that (1.) the property space of alluvial fans cannot be appropriately reflected via rule sets. Furthermore, (2.) the identification of a *geomorphometric signature* with low intra-class variability stipulates the development of geomorphometric parameters which quantify quintessential morphometric characteristics. Specifically, morphometric parameters are required to be valid across the full spectrum of fan sizes and environmental conditions (cf. Challenge 4). For segmentation, these framework conditions entail that a globally optimal parametrization of a segmentation algorithm cannot exist.

All things considered, it becomes clearly apparent that object-based geomorphometry faces specific challenges distinguishing it from OBIA, motivating the use of the term object-based morphometric analysis (OBMA) to emphasize this differentiation (cf. Fig. 8.1). In this doctoral thesis, an innovative OBMA framework is introduced, which tackles the aforementioned issues via data-driven segmentation and the incorporation of machine learning algorithms for classification. A tenet of the presented approach is that both segmentation and classification are addressed in a landform-specific way. As a consequence, this thesis pursues the use of supervised one-class classification algorithms, thereby formalizing the morphometric signature of a landform rather than morphometric disparities within a diverse geomorphological inventory.

Acknowledging the ill-structured nature of the segmentation problem, we propose to perform

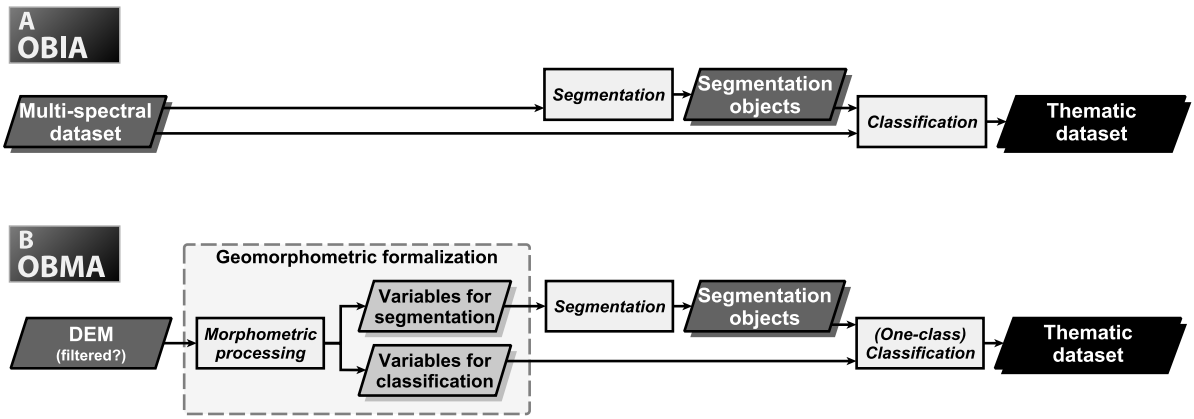


Figure 8.1: Fundamental differences between object-based image analysis (OBIA) and object-based morphometric analysis (OBMA). In geomorphometry, informative values emerges from spatial context, which needs to be formalized via geomorphometric processing. Segmentation and classification have different objective functions with regard to which terrain properties are to be represented in the multi-variate geomorphometric dataset, and thus require a tailored compilation of morphometric variables. It follows that single OBMA instances are feature-specific, and, consequently, a one-class estimator should be used to derive membership scores for the landform under consideration.

segmentation for a range of parameters, and to control the subsequent selection of final objects via fuzzy membership scores obtained from a one-class classification algorithm. Notably, this approach essentially mimics the strategy of an expert performing a tentative estimation of viable parameters, but of course offers much greater potential with regard to the complexity of the parametrization that can be included into the analysis. In this context, the investigation performed in Pipaud and Lehmkuhl (2017 / Chapter 5) corroborates that for the segmentation of alluvial fans, optimal segments are actually obtained from a wide spectrum of parameter sets. While this approach is computationally intensive, single segmentation runs are independent from each other, rendering the approach fully parallelizable.

In the dissertation at hand, fuzzy membership scores have been derived from a one-class support vector machine (OCSVM; Pipaud and Lehmkuhl, 2017 / Chapter 5), using the implementation of Schölkopf et al. (2001) with a radial basis function (RBF) kernel. For the study presented in Chapter 6, a new one-class random forest (OCRF) algorithm was developed. While building upon the ideas of Désir et al. (2013), we propose to derive outliers from a kernel density estimation (KDE), thereby making the approach suitable for smaller training datasets. Although the OCRF displays a considerably higher performance than the OCSVM, it must be stressed that both algorithms tackle different case scenarios.

Bearing in mind that the OCSVM is trained with merely eleven samples (from Region 6), its performance is very promising. The quality of the algorithm of yielding a sound classification with little statistical support stems from the fact that the generalization of the separating boundary can be flexibly adjusted. Performance optimization thus involves a careful adjustment of the two parameters γ, which controls the distance dependence of the RBF kernel in use, and ν, which adjusts the allowed amount of *slack* of the separating boundary. Owing to the low number of training samples, this presupposed a manual tentative evaluation in this thesis. OCSVM performance optimization might, however, be more

conducive to unsupervised cross-validation procedures if more statistical support is provided.

A fundamental problem inherent to all support vector machines is, however, that the algorithm is not robust towards features of little explanatory potential, and that it is susceptible to variances in probability density distributions of input variables. Importantly, the latter is a condition which is regularly given for a set of geomorphometric variables, with changes to feature density distributions potentially also emerging from a change of the DEM product in use. As a consequence, OCSVMs do not meet all demands imposed on a data-driven OBMA framework.

Owing to its non-parametric nature, as well as its robustness towards irrelevant features and density distributions, the OCRF introduced in Chapter 6 of this thesis resolves this issue. Specifically, the study demonstrates that the proposed algorithm does not require any kind of data standardization, and that its setup is not performance-critical and amenable to an optimization via cross-validation (cf. Fig. 8.2). Cross-validation involves a hybrid approach where the parametrization of the estimator is optimized against an evaluation dataset consisting of alluvial fans and null-class members for which discrimination was deemed most critical. In this context, the analysis performed in Chapter 6 shows only moderate differences across the full range of parameter sets tested. Significantly, OCRF with full randomization on feature level regularly display optimal or near-optimal performance. This trait offers no benefit for the object-based analysis of alluvial fans where the discrimination from other alluvial landforms is most critical. Fully randomized tree ensembles can, however, be expected to be a robust approach for the classification of landforms for which most similar landforms are less well constrained.

In Chapter 6, we exploited the potential of OCRFs by classifying—without any user interaction—variants of SRTM1 and AW3D30 differing in the degree of filtering applied to the base DEM. Obtaining substantial discrepancies in classification performance for different variants of the same base DEMs, this work demonstrates the significance of data-driven classification approaches for progress in the field of object-based geomorphometry.

By emphasizing the data-driven delimitation of the alluvial fan property space over explicit formalizations by a researcher, the dissertation at hand contrasts with the work of Eisank (2013), who asserts that the assembly of feature signature libraries is a major challenge for progress in the field. It must be noted, however, that feature signature libraries are still significant for an accurate definition of the property space of landforms. In contrast to prior research, the author of the dissertation at hand proposes that landform ontologies should emerge from the process of object-based modeling, rather than being imposed by explicit definitions.

Due to their robustness towards irrelevant features, random forests support the operative use of object-based geomorphic frameworks by facilitating a strategy where the explanatory value of variables is *deduced* from the classifier, rather than being *induced* by a human interpreter. Then again, feature importance metrics inherent to bivariate random forest classifiers cannot be readily adopted to measure variable importance in a one-class classification scenario. Instead, the evaluation of variable importance requires recourse to techniques established for the validation of training datasets, such as Bhattacharyya coefficients (cf. Pratt, 2001). Variable importance metrics such as the mean decrease of impurity still provide valuable information on variable-specific intra-class heterogeneities, which can be utilized to evaluate different DEM filtering intensities.

Turning to the morphometric variables selected for the object-based processing of alluvial fans, we

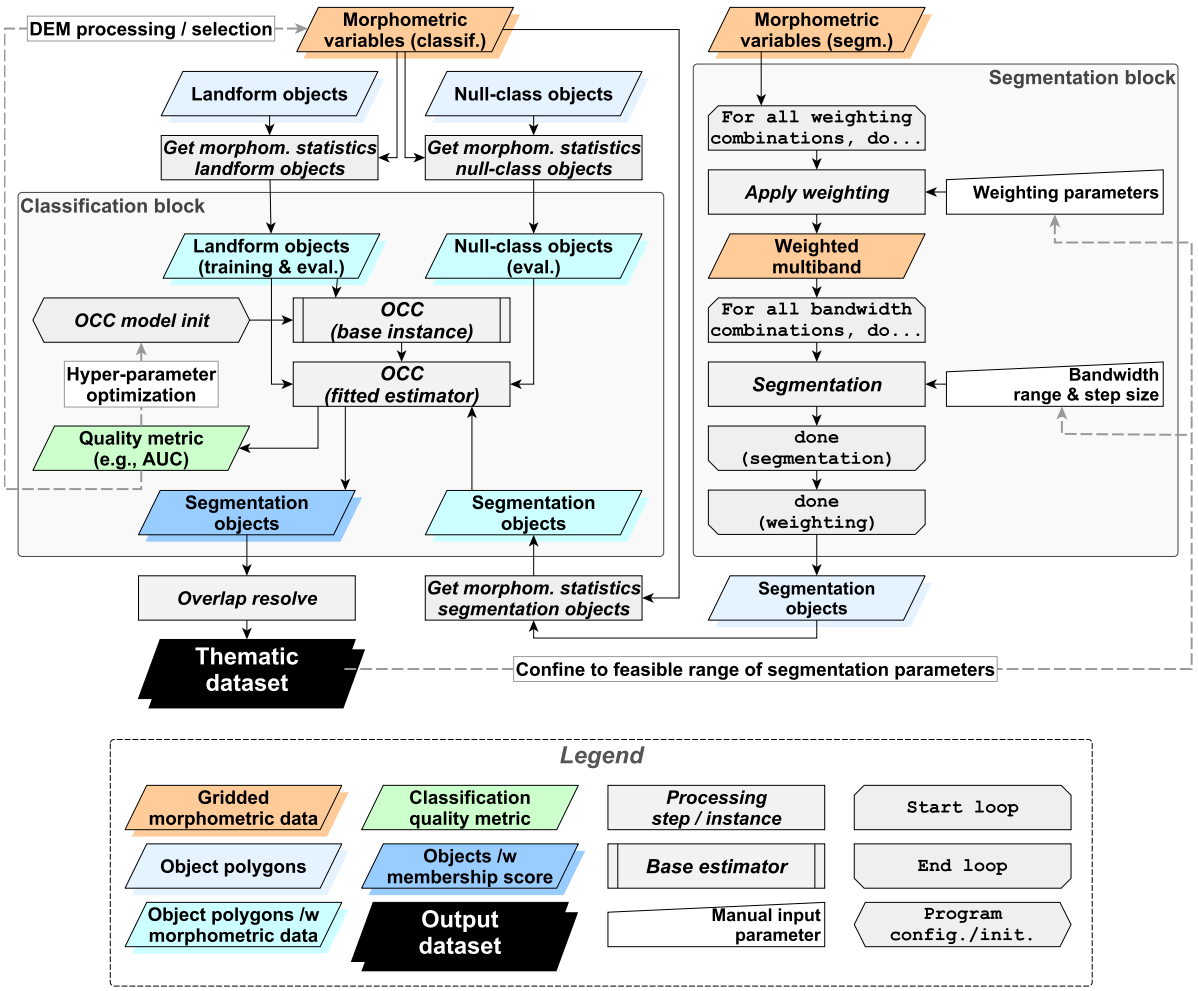


Figure 8.2: Synopsis of the OBMA workflow developed in this doctoral dissertation. The approach is based on guiding the segmentation process via classification scores. Classification scores are calculated for multiple raw segmentation sets, which are obtained by varying the parametrization of the segmentation algorithm. By incorporating a one-class classifier, the classification process formalizes the morphometric signature of a landform, rather than discrepancies between landforms. Utilizing a robust classifier such as OCRF, and a moderately sized evaluation dataset, a fully data-driven optimization can be performed (see dashed arrows).

can conclude that a robust segmentation of solitary and coalescing fan bodies can be obtained by using directional curvatures and the sine and cosine of slope aspect in addition to fan slope. With regard to classification, the pioneering work of Troeh (1964, 1965) already emphasized that a morphometric signature of alluvial fans emerges from formalizing the radial nature of fan bodies. In this thesis, it was shown that the apex is most appropriately modeled as the global convergence point of the gradient field (GGC), defined as the point which minimizes the distance to all gradient lines. The GGC apex can then be utilized to derive a measure of the angular deviation from an ideal cone shape (the gradient–apex divergence, GAD). Alternatively, the convergence point can be utilized to derive a radial approximation surface, where the mean absolute deviation from this surface serves as a measure for the degree of similarity (the radial approximation divergence, RAD). The empirical studies performed in Chapters 5 and 6 indicate that the difference between both metrics with respect to their explanatory potential is generally minor. As a measure of angular discrepancy, the GAD shows, however, a higher susceptibility to high-frequency undulations of the modeled terrain surface, as induced by actual terrain ruggedness and the statistical uncertainty inherent to DEM products.

In summary, the doctoral thesis at hand demonstrates that prospects of successfully applying object-based geomorphometry are closely linked to the ability to design landform-specific segmentation and classification workflows. Robust and flexible algorithms like OCRFs facilitate the design of such frameworks. For the automated mapping of larger portions of the geomorphological inventory of a study area, the author envisages a *stratified* approach (cf. Anders et al., 2011) where different landform types are identified and delineated in a serial manner, applying OBMA instances tailored towards each geomorphic feature of interest.

Objective 3

RQ To which extent is variability in environmental controls reflected in the geomorphometry of fan surfaces?

As elaborated in Chapter 2, the consideration of fan–catchment relationships dates back to the mid of the 20th century (cf. e.g., Blissenbach, 1952; Bull, 1962, 1964; Hooke, 1968b). It has been shown comprehensively that across the spectrum of fan sizes, alluvial fan geomorphometry is fundamentally governed by sediment load factor and average grain size, which decrease with increasing planimetric fan area. Both factors are chiefly induced by the growth in average sediment conveyor path length, and the concomitant increase in sediment retention, as well as enhanced sediment reworking. In the doctoral dissertation at hand, we complement this fundamental insight by showing that large fans tend to focus sediment evacuation along the mountain front. In all probability, they thereby exceed the accommodation capabilities of the mountain front and display substantial amounts of progradation. In contrast to smaller fans showing progradation, however, they tend to be comparably little constrained by laterally adjoining fans or other geomorphological phenomena.

In research performing multi-variate analysis of fan and catchment parameters, this scale-related change of morphometric expression is, however, mostly neglected (cf. Challenge 5). Utilizing the training dataset of 306 fans acquired within the scope of Objective 2, this thesis closes this gap by de-trending all morphometric parameters according to their relationship with planimetric fan area. In this context, opting for planimetric fan area instead of catchment area was motivated by theoretical

considerations and empirical support pointing to the pronounced impact of differences in sediment connectivity (cf. Fryirs et al., 2007; Mather and Stokes, 2018). As a result, we consider planimetric fan area to be the more suitable reference for de-trending, but need to stress that this assertion should be substantiated by future research performing a juxtaposition of de-trended data using both variables as a basis for de-trending.

The results obtained in Chapter 7 confirm the proposition of Saito and Oguchi (2005) that the alluvial fan property space is gradual in nature. Given a study record of considerable size and diversity in environmental boundary conditions, the feature space is thus not conducive to a hard clustering. While clustering can be evident in cases where disparate environmental settings are provided within a smaller study area, the obtained clusters must always be subjected to a critical evaluation of cluster consistency, e.g., via silhouette scores (cf. Rousseeuw, 1987). Regrettably, the issue of cluster consistency has been ignored in previous studies performing multi-variate analysis of fan–catchment geomorphometry (cf. Crosta and Frattini, 2004; Karymbalis et al., 2018). For future research, these findings encourage the use of techniques like self-organizing maps (SOMs), which facilitate geomorphic analysis by providing a topology-preserving two-dimensional mapping of a high-dimensional feature space (cf. e.g., Karymbalis et al., 2010, 2018), but do not impose a clustering on the data.

Although feature spaces of study areas with differing environmental conditions show substantial amounts of overlap, indicative trends can be traced back to environmental boundary conditions, and are in agreement with research done hitherto (cf. e.g., Viseras et al., 2003; Bahrami, 2013). For the de-trended dataset, the first three principal components (PCs) display three thematically significant bundles of feature projection vectors. Importantly, two of these projection bundles depict the amount of progradation and splay angle size, respectively, thereby functioning as proxies for the footprint of accommodation space generation in alluvial fan geomorphometry. While a third vector bundle quantifies the influence of fan-formative sedimentary processes on fan geomorphometry, this vector bundle jointly reflects the impact of tectonic and sedimentological processes on specific steepness and longitudinal curvature. As a consequence, the consideration of proxies for accommodation space generation greatly improves the differentiation between tectonic and non-tectonic signals.

In this context, the computation of the GGC enables us, for the first time, to directly measure the amount of progradation. With apex distance factors (ADFs) displaying comparably large product-moment correlation coefficients with both radial approximation divergence and gradient–apex divergence, ADF values signify that from an intra-class perspective, the former geomorphometric variables are first and foremost indicators for the amount of progradation. This fact should be taken into account in future OBMA processing of alluvial fan data by, for instance, taking into consideration only those pixels for the calculation of the RAD and GAD which are located downstream of the GGC apex. However, it must be stressed that this approach might come with potential adverse effects, because it can result in a reduction in inter-class separation.

Significantly, scale-related changes in fan-building processes have a formative influence on sample distribution in the dataset *even after* de-trending. As can be expected from theoretical considerations and the huge body of research on alluvial fan morphodynamics, large alluvial fans show little variability with respect to their fan-building processes. Therefore, they predominantly plot along the bundle of feature projection vectors which is formed by RAD, GAD, and ADF. This is particularly reflected in

the dataset of the Gobi Altai (Region 7), where accommodation space along the mountain front chiefly varies according to the different degree of foreberg zone development.

Conversely, smaller fans show more variation along the second major projection vector bundle in the PC0–PC1 space, signaling stronger variations in sedimentary processes. Differences in the degree of spatial dispersion can be attributed to regional particularities of environmental boundary conditions. Specifically, the alluvial fan inventory of the Walker Lane Fault Zone (Region 3) displays a larger variability along this direction than the main segment of the northern (Numic) Basin and Range region (Region 2). In this context, the morphometric data nicely reflects that study areas with climatic boundary conditions that promote the generation of debris flows should show larger internal variability, because debris flow instigation is constrained by bedrock lithology and sediment connectivity (cf. e.g., Blair, 1999b).

With small fans partly being designated as outliers by their local outlier factors, even a dataset of 306 alluvial fans was insufficient to precisely delimit the property space of small fans. In essence, the findings obtained in this thesis thus illustrate a case where extensive mapping and geomorphometric analysis via unattended OBMA frameworks offer substantial prospects for geomorphological research.

In this dissertation, the balance between tectonic activity and sediment supply was assessed by ascertaining whether the generation of accommodation space matches the supply of sediment. For future research, we suggest to put emphasis on measures which quantify the capability of the catchment to evacuate sediment. In doing so, cases can be identified where low tectonic activity and little sediment evacuation induce the backfilling (also denoted *retrogradation*) of feeder channels into the catchment (cf. Bull, 1978; Viseras et al., 2003; Harvey, 2011; Bowman, 2018), thereby rendering it possible to identify the reasons for the absence of progradation indicators. Identification and quantification of feeder channel backfilling involve a measurement of the position of the alluvial fan relative to the mountain front, as well as an evaluation of feeder channel cross profiles (cf. Bahrami, 2013). Finally, further insight can be provided by considering mountain front sinuosity, thereby providing a complementary measure for tectonic activity (cf. Bull, 1978; Roberts and Cunningham, 2008).

Future research

RQ What are the prospects for object-based geomorphometry with respect to the continuous advancement of deep learning techniques?

As exemplified in this doctoral dissertation, the application of conventional machine learning algorithms depends on hand-crafted feature descriptors which are inferred from domain-specific knowledge. The formalization of such metrics can be particularly challenging in cases where object semantics emerge from complex spatial patterns and on multiple scale levels, as is the case with high-resolution imagery and digital elevation data (cf. Zhang et al., 2018). As a consequence, semantic functions and spatial configuration inherent to the data might not be fully exploited if the classification is performed using engineered feature descriptors (cf. Längkvist et al., 2016). Deep learning frameworks—machine learning frameworks using artificial neural networks—are able to perform *representation learning*, i.e., they possess the ability to mine semantic characteristics of raw data in a hierarchical manner, without any human intervention (Bengio et al., 2013; LeCun et al., 2015). Since the early 2010s, convolutional neural networks (CNNs) have achieved breakthrough performance in the field of computer vision

(Krizhevsky et al., 2012; Deng, 2014; Guo et al., 2016). Originally proposed by LeCun et al. (1998), the success of CNNs was instigated by the introduction of GPU-based implementations (Krizhevsky et al., 2012; Russakovsky et al., 2015). In recent years, deep learning techniques received increasing attention in the geosciences, including their adoption for object-based analysis (Zhu et al., 2017; Ma et al., 2019; Hoeser and Kuenzer, 2020). To conclude this doctoral dissertation, we will evaluate recent developments of deep learning techniques from the perspective of object-based geomorphometry, and identify demands for future research.

MLPs (multilayer perceptrons, also called stacked autoencoders) are the base architecture of feed-forward networks. They are comprised of a series of fully connected layers with artificial neurons, i.e., all neurons within one layer are connected to each neuron of the upstream layer via linear operations (Hoeser and Kuenzer, 2020). These connections pass excitations of all neurons of an upstream layer to each neuron of the downstream layer. The neural excitation is evaluated by computing a weighted sum of all incoming excitations, and passing the sum to a non-linear activation function. This value is then passed as excitation to the following layer. At the head of the network, a softmax activation function is used to obtain categorical values encoded as one-hot vectors (Goodfellow et al., 2016; Aggarwal, 2018). The summation weights are evaluated in the training phase of the network. Supervised learning is conducted by initializing all weights at random, passing a set of known input values through the network, and calculating the loss by comparing the network return with the expected outcome (Atkinson and Tatnall, 1997). Learning is conducted by minimizing the classification loss in an iterative manner. To this end, backpropagation is repeatedly applied to compute the gradient of the loss function in weight space, and to shift all weights in direction of the gradient descent (stochastic gradient descent; Rumelhart et al., 1986; Schmidhuber, 2015; Goodfellow et al., 2016).

According to the *universal approximation theorem*, a neural network is able to approximate any continuous target function, with the quality of approximation only being dependent on the complexity of the neural network in relation to the complexity of the target function (Aggarwal, 2018). The theorem has been proven for bounded (cf. Cybenko, 1989) as well as some unbounded activation functions such as the popular rectified linear unit function (cf. Sonoda and Murata, 2017). Although fully connected neural networks have found use for geoscientific applications since the 1990s (cf. Paola and Schowengerdt, 1995), they did not receive much emphasis until recently for two main reasons: (1.) Full connectivity implies that the number of trainable parameters grows rapidly with increasing network depth (cf. Dixit et al., 2017). As a consequence, deeper MLPs tend to overfit to the training data (Bishop, 1995; Guo et al., 2016). Furthermore, the large number of unknowns entails that training of MLPs is computationally expensive (Goodfellow et al., 2016).

Due to continuous improvements in processing power, readily available implementations for training on GPUs, and instigated by the successful application of CNNs in the field of computer vision (Deng, 2014; Guo et al., 2016), however, a resurgence of interest in the application of MLPs for geoscientific problems has occurred (cf. e.g., Behrens et al., 2018; Zhang et al., 2019; Middleton et al., 2020). That said, studies comparing MLPs with conventional machine learning algorithms such as support vector machines and random forests report mixed results, with MLPs either yielding worse performance than shallow learners (cf. e.g., Fernández-Delgado et al., 2014; Ghorbanzadeh et al., 2019; Alifu et al., 2020; Liu et al., 2021), or showing minor improvements (cf. e.g., Behrens et al., 2018; Nhu et al., 2020).

Importantly, MLPs are permutation-invariant, i.e., they do not exploit the underlying (spatial) structure of the input data (cf. Goodfellow et al., 2016; Hoeser and Kuenzer, 2020).

CNNs are inspired by the organization of the visual cortex of mammals (Olshausen and Field, 1996; LeCun et al., 2015; Aggarwal, 2018). They extend MLPs in two fundamental aspects:

Firstly, these networks exhibit a convolutional backbone, that is, most layers except the most downstream ones perform convolution operations on the image or intermediate feature maps. Since any activation in a particular layer is the function of only a small spatial region in the previous layer, inter-layer connections in CNNs are sparse. With the weights of the convolution kernel being learned by the network, convolutional layers encode a specific pattern of local contextual relation. It follows that an encoded pattern triggers neuronal excitation wherever it is encountered in the image layer or intermediate feature map, causing CNNs to be translation-equivariant (Goodfellow et al., 2016; Guo et al., 2016; Yang et al., 2017; Ghosh et al., 2019; Bazgir et al., 2020). Following common nomenclature, let us denote the area covered by a convolutional kernel as the *receptive field* (Goodfellow et al., 2016; Ma et al., 2019).

Secondly, CNNs incorporate pooling, which creates, via non-overlapping pixel aggregation, condensed feature maps by reducing the array size by a specified stride factor (Krizhevsky et al., 2012; Hoeser and Kuenzer, 2020). While various aggregation functions can be used, the maximum operator is the de facto standard for the summary statistic (Guo et al., 2016; Ma et al., 2019). Convolution and pooling layers are commonly used in an alternating fashion (Zhu et al., 2017; Hoeser and Kuenzer, 2020). The rationale for pooling is that high-level semantic properties are more abstract and can be expected to be representative on lower spatial resolutions (Cadieu et al., 2014; LeCun et al., 2015; Du et al., 2019). Via downscaling, the condensed feature becomes insensitive to small spatial translations occurring on smaller scales, and the computational load can be kept on feasible levels (Goodfellow et al., 2016; Hafiz and Bhat, 2020; Hoeser and Kuenzer, 2020). In comparison to MLPs, convolution and pooling layers in conjunction greatly reduce the number of model parameters, making CNNs somewhat easier to train (Goodfellow et al., 2016; Längkvist et al., 2016). While discriminative contextual and hierarchical relationships are self-learned end-to-end, the pattern of spatial relationships to be considered is hard-coded into the network by the designer (Goodfellow et al., 2016).

Since conventional CNNs still exhibit a fully connected network head, these networks also return single one-hot encoded classification vectors and are thus *scene classifiers* (Zhu et al., 2017). Furthermore, the link between a convolutional backbone and a conventional fully connected head entails that these neural nets only process raster data of a fixed size—a trait which they share with multilayer perceptrons. To address this limitation, conventional CNNs are often used with a sliding-window or non-overlapping (superpixel segmentation) processing setup (Guirado et al., 2017; Liu et al., 2017a; Csillik et al., 2018; Kemker et al., 2018; Liu et al., 2018; Lv et al., 2018). In a naive implementation, a patch processor scans over the input data, yielding classification results representative for fixed-sized extents (cf. Brendel and Bethge, 2019). During recent years, this approach to CNN-based raster analysis has gained considerable emphasis for the integration of convolutional neural networks into object-based classification frameworks, both as a full replacement for the classification with shallow learners and engineered features (Zhang et al., 2018; Ghorbanzadeh et al., 2019), or to yield auxiliary classification metrics which are used in conjunction with hand-crafted feature descriptors (Liu et al.,

2017b; Ghorbanzadeh et al., 2020). In conjunction with OBIA, an object-level categorical vote can be retrieved by a simple majority vote of all patches covered by the respective object (cf. Lv et al., 2018). Alternatively, a single patch or a small number of patches can be positioned within each object (cf. Fu et al., 2018; Zhang et al., 2018; Robson et al., 2020; Wang et al., 2020).

Patch-based CNNs are, however, limited in two main aspects: (1.) In cases where a feature class displays a wide spectrum of sizes, multi-scale adaptability must be realized by using a set of CNNs with varying input patch sizes (Lv et al., 2018; Zhang et al., 2018; Ghorbanzadeh et al., 2019). It follows that further logic must be implemented to obtain the final classification scores, i.e., the classification cannot be performed end-to-end. If object candidates exhibit diverse shapes and occur in varied environments, (2.) a statically sized rectangular processing area covers the adjoining environment to varying degrees, which can have adverse effects on classification performance (Sun et al., 2018; Ghorbanzadeh et al., 2019). In this context, Wang et al. (2020) propose adaptive image patch sampling along principal axes, obtained via shape skeletonization, in order to minimize boundary overlaps. An alternative approach to control boundary overlaps is to keep the patch area small in relation to the average size of target objects (cf. e.g., Zhao et al., 2017; Sameen and Pradhan, 2019; Ghorbanzadeh et al., 2020). Opting for small patch sizes is also appealing in that the fully connected head can be less complex, hence making the model amenable to training from scratch and reducing the risk of overfitting (cf. Cogswell et al., 2016; Längkvist et al., 2016).

While applying small patch sizes reduces the possible contextual richness of the deployed CNN, the viability of combining deep learning with object-based analysis in such a way is corroborated by the study of Brendel and Bethge (2019). Via permutation of optical imagery on a tile level, the authors demonstrated that substantial parts of the inherent semantic conceptualization of convolutional neural networks are encoded in the lowermost layers. Specifically, a bag of local patch classifiers yielded a performance comparable to deeper networks which were applied to the full scene. For the usage of CNNs in conjunction with segmentation algorithms, however, it must be borne in mind that the resolution of a superpixel classification map does not provide sufficient detail to guide the parametrization of the segmentation algorithm, leaving a fundamental problem of object-based analysis unaddressed (cf. Pipaud and Lehmkuhl, 2017 / Chapter 5). In research performed to this date, little attention has been given to empirical comparisons between conventional object-based analysis and CNN-enhanced OBIA. Zhang et al. (2018) compared OBIA using multi-scale patch-CNN with an SVM-based workflow, obtaining ~10 % better overall accuracy with the CNN-enhanced setup. Ghorbanzadeh et al. (2019) compared CNN-based classification setups with classification via random forests, and improved F1 scores by approximately 5 % when making use of the best-performing CNN classifier. At the time of writing, studies applying CNN-OBIA solely on digital elevation models are lacking.

In the field of computer vision, the term *semantic segmentation* defines the categorical labeling of every image pixel (Hafiz and Bhat, 2020; Hoeser and Kuenzer, 2020). Even more so than patch-based scene classification, semantic segmentation is confronted with a trade-off between location accuracy and the possible contextual depth (Shelhamer et al., 2017; Ma et al., 2019). Since fully connected neuronal layers discard the spatial structure of the data, they must be avoided. As a replacement for the fully connected head of conventional CNNs, fully convolutional neural networks (FCNs) thus feature an encoder-decoder structure (Ronneberger et al., 2015; Badrinarayanan et al., 2017). Specifically,

an encoder is a conventional convolutional backbone performing alternating convolution and pooling. The decoder subnetwork replaces the fully connected network head and performs stepwise upscaling, using transposed convolutions with learned weights (deconvolution; Ronneberger et al., 2015; Liu et al., 2017a,b; Shelhamer et al., 2017). In order to preserve spatial detail, state-of-the-art architectures such as the U-Net (Ronneberger et al., 2015) incorporate *skip connections*, i.e., feature layers of the encoder path are concatenated to upscaled feature maps in order to re-introduce high-resolution detail into the decoder path. Although FCNs considerably improve on the resolution-context trade-off, their incorporation into object-based workflows received little attention so far (cf., however, Liu et al., 2017b, 2018). Specifically, only Liu et al. (2018) benchmarked FCN-based implementations against OBIA frameworks applying patch-based CNN, obtaining ~5 % improvements in overall accuracy for the FCN-based design. It must be emphasized, however, that the intrinsic resolution (cf. Pipaud et al., 2015 / Chapter 3) of the feature map is still notably lower than the input raster data, leading to a blurry appearance of category boundaries (Zhao et al., 2017; Fu et al., 2018).

Current research in the field of computer vision puts strong emphasis on *instance segmentation*, which is defined as the integrated identification, categorization, and fine delineation of object instances (Hafiz and Bhat, 2020). Operating at the intersection of the subdomains object detection and semantic segmentation, instance segmentation is considered particularly challenging (Cheng et al., 2016; Arnab and Torr, 2017; He et al., 2020). While all recently proposed techniques for instance segmentation are CNN-based, two general approaches exist: (1.) Segmentation-first algorithms first perform semantic segmentation and then extract object instances from the category patch (cf. Bai and Urtasun, 2017; Kirillov et al., 2017). Conversely, (2.) detection-first approaches first identify object candidates and subsequently perform categorical classification, bounding box refinement, and object delineation (Girshick et al., 2016; Ren et al., 2017; He et al., 2020).

In research done hitherto, the detection-first technique Mask R-CNN (region-based convolutional neural network) received the most attention, and is considered current state-of-the-art (Kirillov et al., 2017; Cheng et al., 2020; Hafiz and Bhat, 2020). Mask R-CNN expands the Faster R-CNN object detection architecture by adding a semantic segmentation network head (Ren et al., 2017; He et al., 2020). Put briefly, Faster R-CNN uses a *region proposal* backbone to identify object candidates and to pass intermediate feature maps and preliminary bounding boxes to a network head (Ren et al., 2017; Hafiz and Bhat, 2020). To this end, a binary classifier is used to assert whether an object candidate is a member of a target category. Subsequently, the cropped feature map is passed over to a network head which splits into two branches independently performing bounding box regression and categorical classification (Lin et al., 2017). Here, Mask R-CNN adds a third branch performing semantic segmentation on the cropped feature layer (He et al., 2020). Furthermore, Faster R-CNN leverages the multi-scale capabilities of *feature pyramid networks* for its region proposal backbone (Cheng et al., 2020; Hafiz and Bhat, 2020; Hoeser and Kuenzer, 2020). Analogously to fully convolutional neural networks, feature pyramid networks exhibit a top-down path where high-level feature maps are iteratively upscaled via learned deconvolution kernels and merged with intermediate feature maps of the encoder stage (Lin et al., 2017). After training, the region proposal network then applies a selective search algorithm on the feature maps of multiple pyramid levels, thus being able to extract objects on multiple scales (Guo et al., 2016).

In geoscientific research, the Mask R-CNN architecture recently received consideration as a potential end-to-end substitute of OBIA (cf. Zhang et al., 2018; Chen et al., 2020; Maxwell et al., 2020; Bonhage et al., 2021; Guirado et al., 2021). It must be borne in mind, however, that Mask R-CNN faces the same limitations as semantic segmentation, that is, the intrinsic resolution is substantially below pixel level. A major reason for this deficiency in detail is that current implementations for semantic and instance segmentation do not learn boundaries explicitly. Note, however, that the enhancement of Mask R-CNN with explicit boundary learning is a field of active research (cf. Huang et al., 2019; Cheng et al., 2020). It also follows that it might be beneficial to combine conventional segmentation algorithms with Mask R-CNN, as has been exemplified by Guirado et al. (2021).

Although CNNs place lower demands on the size of the training dataset than MLPs, the minimum viable number of training samples is in most cases still prohibitively large for geoscientific applications (cf. Cheng et al., 2016; Zhao and Du, 2016; Liu et al., 2017b, 2018; Xie et al., 2020). Transfer learning is a popular technique to enable weakly supervised learning by transferring knowledge acquired for a domain to a problem in a different domain (Pan and Yang, 2010; Shin et al., 2016). In the context of deep learning, transfer learning is usually understood as the application of pre-trained neural networks to a different classification problem, and always involves the adaption of the final layer to the topic of interest (cf. Yosinski et al., 2014; Wang et al., 2019). The amount of knowledge transfer can vary greatly between using transferred weights only for network initialization, or keeping all weights except those of the uppermost layer(s) constant (cf. e.g., Guirado et al., 2017; Zhang et al., 2018; Trier et al., 2019; Cheng et al., 2020; Maxwell et al., 2020; Bonhage et al., 2021). The rationale for transfer learning is that the learned filters of the lowermost convolutional layers display generic patterns like edges, textures and color patterns (Aggarwal, 2018). Notably, they resemble Gabor filters, that is, bandpass filters indicating—for a localized region—the presence of a specific frequency content in a specific direction (Gabor, 1946; Yosinski et al., 2014; Brendel and Bethge, 2019).

For optical imagery, the availability of neural nets pre-trained on large reference datasets such as ImageNet (more than 14 M images, 1000 categories; Deng et al., 2009; Russakovsky et al., 2015) and MS COCO (Microsoft Common Objects in Context, 2.5 M instances in 328 000 images; Lin et al., 2014) was a major impetus for the increasing popularity of CNN-based deep learning in the field of remote sensing (cf. e.g., Guirado et al., 2017; Zhang et al., 2018; Trier et al., 2019; Cheng et al., 2020; Maxwell et al., 2020; Bonhage et al., 2021). Importantly, the fact that non-nadir datasets such as ImageNet and MS COCO were successfully used to pre-train neural networks for their application on remotely sensed optical imagery substantiates the general potential of this technique (cf. Zhu et al., 2017).

While digital elevation data found some popularity as complementary data for very high resolution imagery (cf. e.g., Längkvist et al., 2016; Zhang et al., 2018; Ghorbanzadeh et al., 2019; Kattenborn et al., 2019; Sameen and Pradhan, 2019; Li et al., 2020; Robson et al., 2020; Xie et al., 2020), the exclusive usage of DEMs for CNN-based raster analysis has only very recently received attention (cf. Abolt et al., 2019; Du et al., 2019; Trier et al., 2019; Chen et al., 2020; Maxwell et al., 2020; Shumack et al., 2020; Bonhage et al., 2021). There is a wide spectrum of how digital elevation data is preprocessed before passing it to a convolutional neural network, with implementations ranging from using relative elevation (Längkvist et al., 2016; Ghorbanzadeh et al., 2019; Kattenborn et al., 2019; Robson et al., 2020; Xie et al., 2020), applying metrics emphasizing local relief such as the topographic position index (Abolt

et al., 2019; Trier et al., 2019) or high-pass filters (Shumack et al., 2020), to calculating morphometric variables such as aspect slope (Du et al., 2019; Sameen and Pradhan, 2019; Li et al., 2020; Maxwell et al., 2020; Xie et al., 2020), curvature metrics (Ghorbanzadeh et al., 2019; Sameen and Pradhan, 2019; Robson et al., 2020; Xie et al., 2020), hillshading (Du et al., 2019; Bonhage et al., 2021), and topographic openness (Bonhage et al., 2021). In this context, it must be stressed that CNNs are, in principle, capable of learning all significant signals directly from the input data. Preprocessing the DEM entails that a-priori knowledge is used to pre-condition the learning process, i.e., the incorporation of DEM derivatives is a partial departure from the principle of representation learning.

In research done hitherto, two studies performed instance segmentation using solely digital terrain data, both implementing Mask R-CNN with initial weights taken from MS COCO (Maxwell et al., 2020; Bonhage et al., 2021). A concession resulting from making use of a neural network pre-trained on MS COCO is that input data is required to exhibit three bands. In this context, Maxwell et al. (2020) decided to use aspect slope for all three bands, whereas Bonhage et al. (2021) took three different DEM derivatives, specifically, sky-view factor, openness, and hillshading. The proposed workflows yielded overall accuracies of ~0.77 and ~0.81, obtained by using 1105 and 5470 training samples, respectively. While these results are encouraging, further research is warranted to assess to which extent knowledge obtained from optical imagery can be transferred to digital elevation data and whether DEM preprocessing facilitates transfer learning. As pointed out by Yosinski et al. (2014), intermediate convolutional layers often encode co-adaptions, that is, complex interactions on multiple scale levels. Recalling the distinct spatial autocorrelation of DEM data (Pipaud et al., 2015 / Chapter 3), it must be assumed that the significance of receptive fields differs from that given for optical imagery, i.e., the pattern of spatial relationships hard-coded into the neural network is most likely suboptimal for elevation data (cf. Zhu et al., 2017).

While CNN-based methods can outperform conventional machine learning, performance levels reported in the field of computer vision rely on comprehensive object ontologies. Hence, they should not create inflated expectations for the adoption of CNN-based techniques for geomorphological applications involving digital elevation data. Specifically, the utilization of CNN-based instance segmentation frameworks in the field of geomorphometry is contingent upon the development of morphometric databases (cf. Trier et al., 2019; Maxwell et al., 2020). Future research therefore might pursue a staggered approach where reference datasets are incrementally built by compiling the output of object-based frameworks using shallow learners.

Future research will also have to critically address the problem that the decision process of deeper CNNs is not conducive to human interpretation (cf. Hutson, 2018; Brendel and Bethge, 2019; Xie et al., 2020). In the field of geomorphology, the interpretability of classification results is key to their utility (cf. Chapter 1). The abandonment of hand-crafted metrics in CNN-based processing thus involves that feature descriptors must be formalized for an ex-post analysis, thereby nullifying a fundamental advantage of deep learning. Since domain-specific knowledge is an important prior to geomorphometric processing, it should be incorporated in all cases where an explicit formalization is feasible (cf. Zhu et al., 2017).

According to these considerations, further emphasis should be given to hybrid approaches involving both conventional machine learning and deep learning (cf. Guo et al., 2016). Patch-based CNNs or

FCNs with moderate depths are an accessible approach to exploit the ability of CNNs to mine inherent semantic characteristics from raster data. Since microscale detail can be challenging to comprehensively formalize as morphometric variables, incentives to make use of CNNs in object-based geomorphometry are especially given with regard to high-resolution elevation models (cf. Ma et al., 2019). In the context of alluvial fan research, CNNs might help in incorporating microscale features such as levées (cf. Volker et al., 2007; Pipaud and Lehmkuhl, 2017 / Chapter 5; de Haas et al., 2018) into the decision process and thus have the potential to facilitate the differentiation of alluvial fans with respect to environmental controls.

Acknowledgments

Still during my time as an undergraduate student, my scientific objective became to exploit the potential of geomorphometric methods beyond what is offered by geographic information systems. This led me to a scientific journey, during which I have been accompanied and supported by many people—by sharing thoughts, knowledge, but also by having the occasional laugh along the way.

First, I am grateful to my supervisor Frank Lehmkuhl for giving me the opportunity to do a doctorate and to pursue my research aims, for taking his time to improve the articles and this dissertation, for offering me a position at his chair, and for always being approachable for support and feedback. I am also thankful to Florian Wellmann for his willingness to act as referee for this thesis and the time involved. Besides, I want to express my gratitude to Georg Stauch, for reviewing this work, for providing helpful internal reviews of manuscripts on multiple occasions, but even more so for constantly offering scientific and non-scientific support, leading to many fruitful talks. I also want to thank my co-author of the article presented in Chapter 3, David Loibl, for his valuable contribution to this study. Furthermore, I am indebted to Wolfgang Römer for his valuable feedback on manuscripts, and for having constructive in-depth discussions on the methodological aspects of this thesis.

I am thankful to all my Ph.D. colleagues in Aachen, especially the *first floor bunch*—Bernhard, Janina, Jörg, Igor, Lydia, Michael, and Verena Esser—for the mutual support and good company. In particular, I want to express my thanks to my former office colleagues, Bernhard and Michael, for the constructive and productive working atmosphere, for keeping the good spirit during stressful times, and for putting up with my sometimes nerdy humor ☺.

This thesis makes heavy use of freely available DEM data and free and open source software (FOSS), without which this work would not have been possible. I am grateful to everyone who contributed to the generation of the DEM products ASTER GDEM, AW3D30, SRTM1, and TanDEM-X, as well as to the FOSS projects GDAL, Orfeo Toolbox, scikit-learn, SAGA GIS, SciPy, and statsmodels. Dear reader, if you happen to be a contributor to these projects: Thank You!

Furthermore, I want to thank my family and friends, my mom in particular, for their unconditional support, for believing in me, and for their understanding on the various occasions when I did not have any spare time.

Finally, but most importantly, I am thankful to Hannah, for many things, but ultimately, for being always on my side throughout the years.

Thank You! Dankeschön!

Acknowledgments with regard to published articles

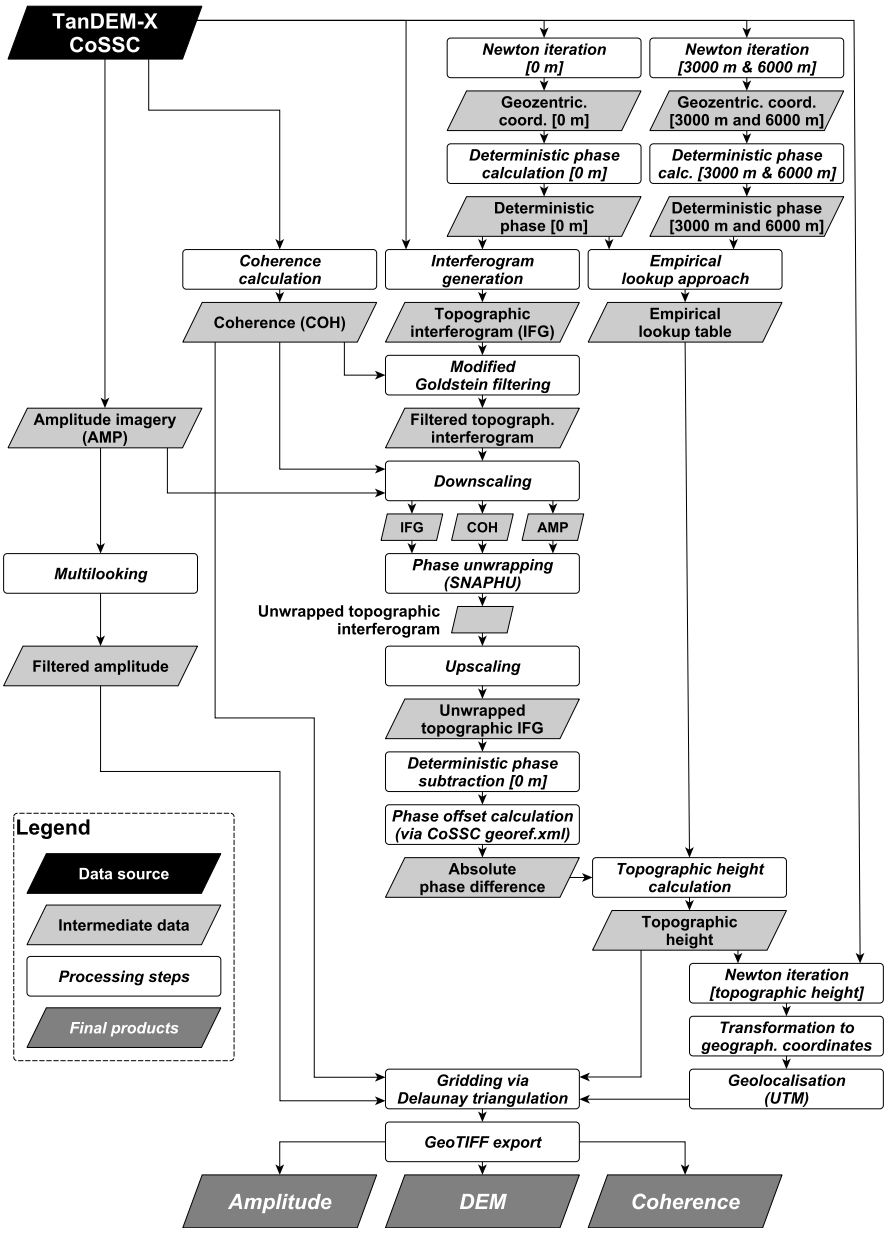
Chapter 3

This research has been conducted within the scope of the project 'Monsoonal variations and climate change during the late Holocene derived from tree rings and glacier fluctuations' funded by the DFG (Deutsche Forschungsgemeinschaft) as part of the SPP 1372: Tibetan Plateau – Formation, Climate, Ecosystems (grant LE 730/28-1). The TanDEM-X CoSSC data were provided by the German Aerospace Center (Deutsches Zentrum für Luft- und Raumfahrt, DLR, grant XTI_GLAC0535). We thank Wolfgang Römer, Georg Stauch, Irena Hajnsek, Florian Kugler and Thomas Busche for helpful comments and discussions. Journal editor Takashi Oguchi and two anonymous reviewers helped greatly to improve the manuscript.

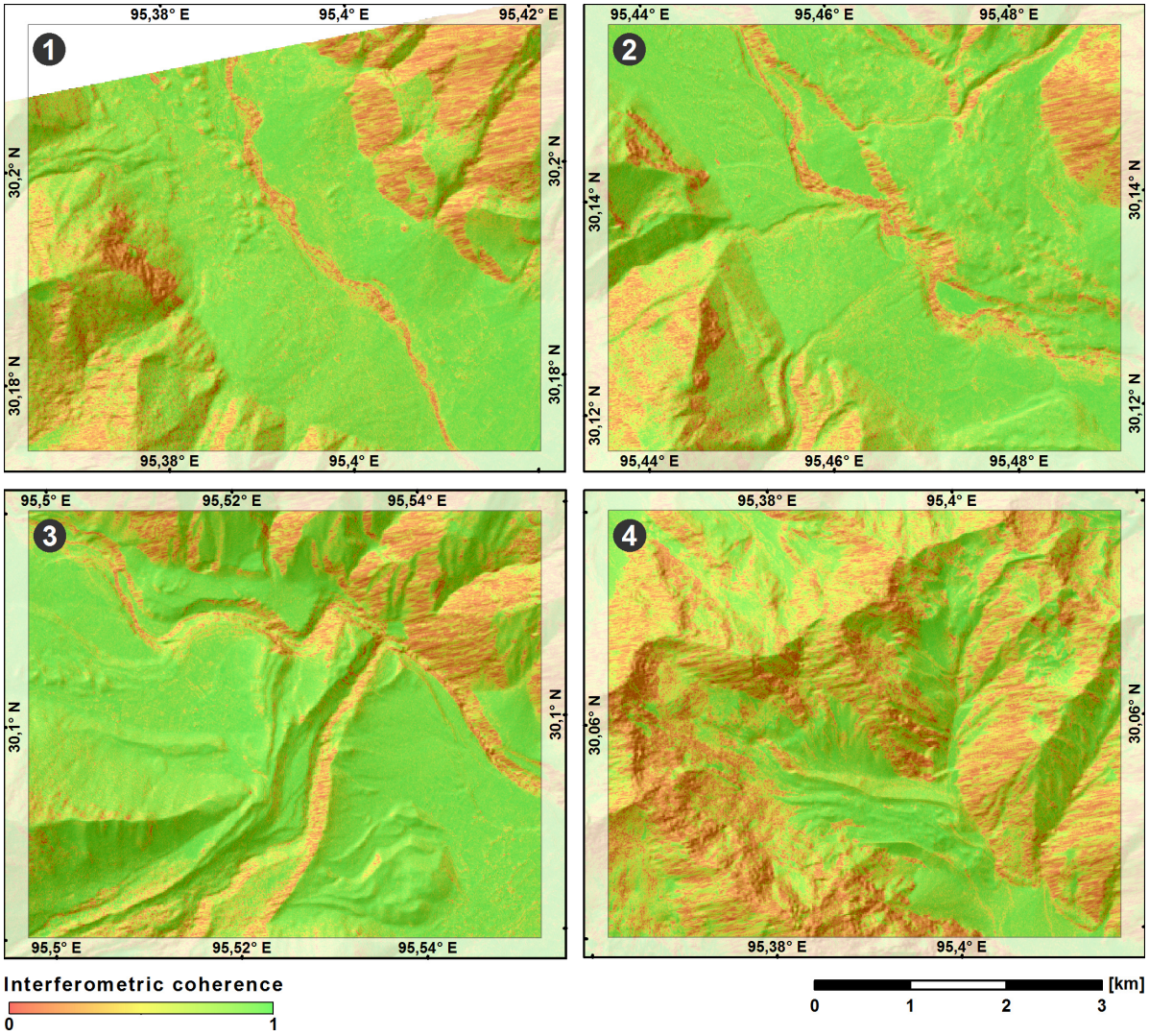
Chapter 5

We thank Hannah Rittich, Wolfgang Römer and Georg Stauch for helpful comments and discussions. Ian Evans is thanked for his constructive review comments, which helped greatly to improve the manuscript.

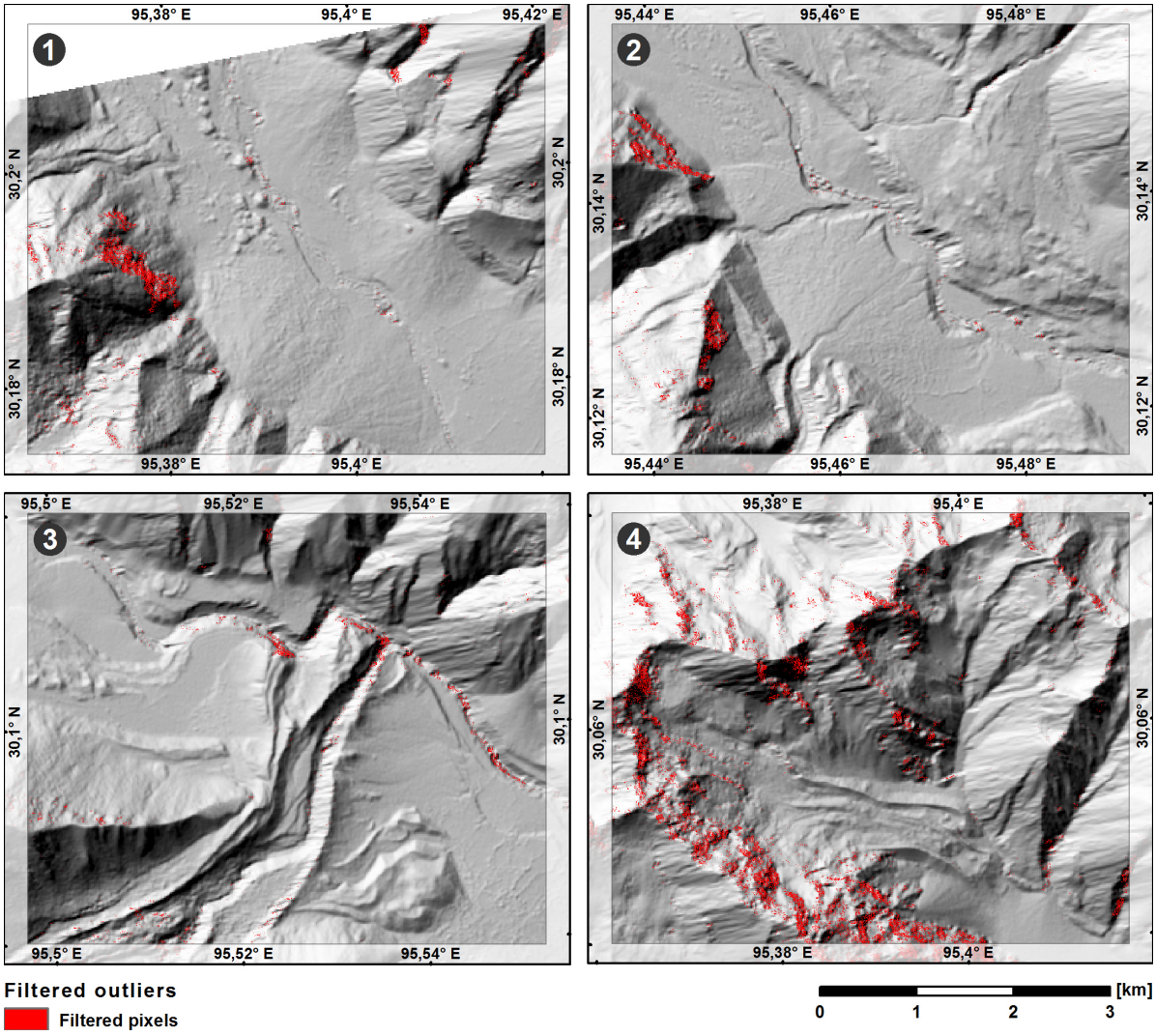
A Supplements, Evaluation of TanDEM-X elevation data for geomorphological mapping and interpretation in high mountain environments – A case study from SE Tibet, China



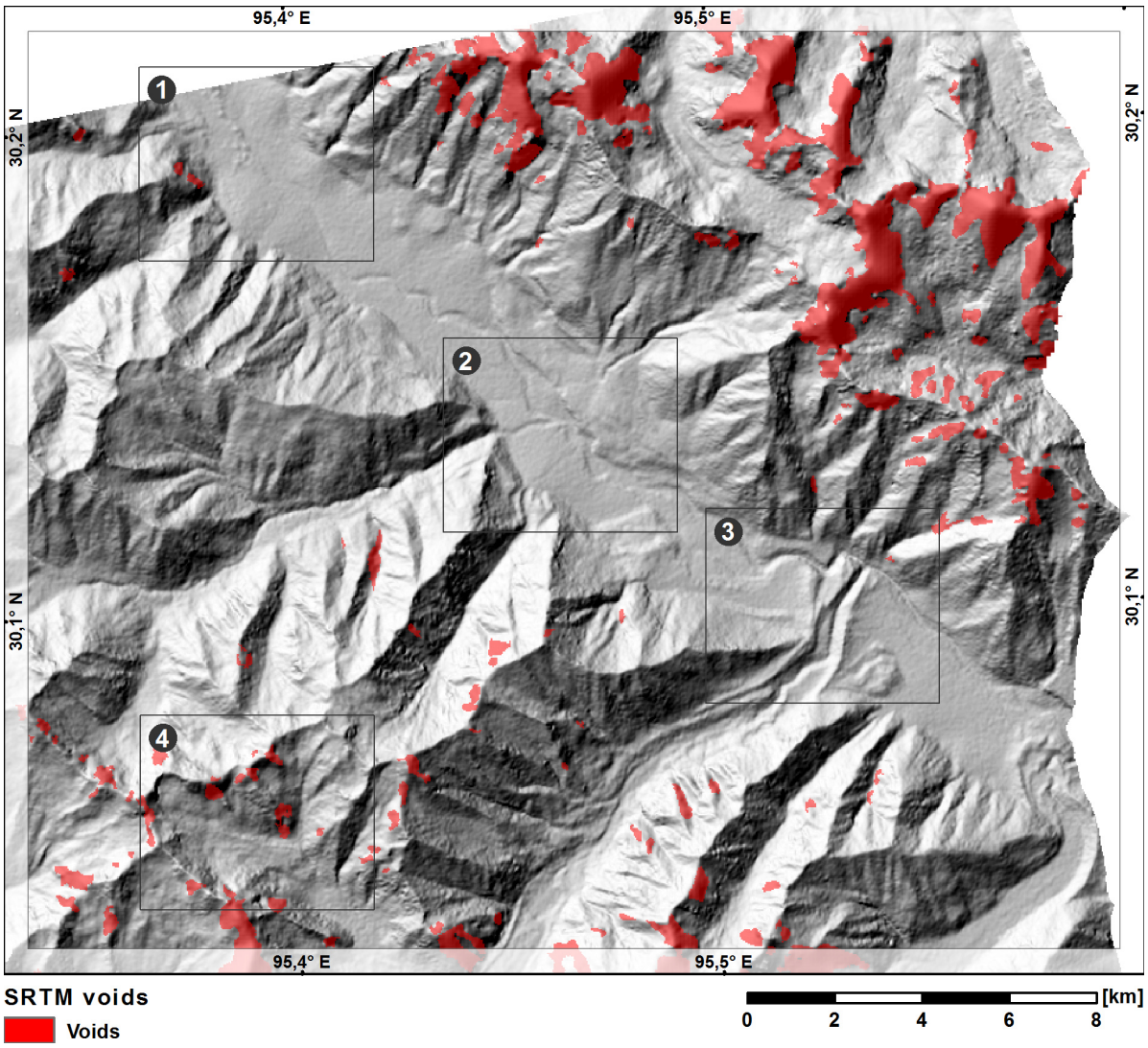
Supplement A.1: Workflow conducted to process the experimental DEM, geocoded SAR amplitude, and geocoded interferometric coherence from TanDEM-X CoSSC data.



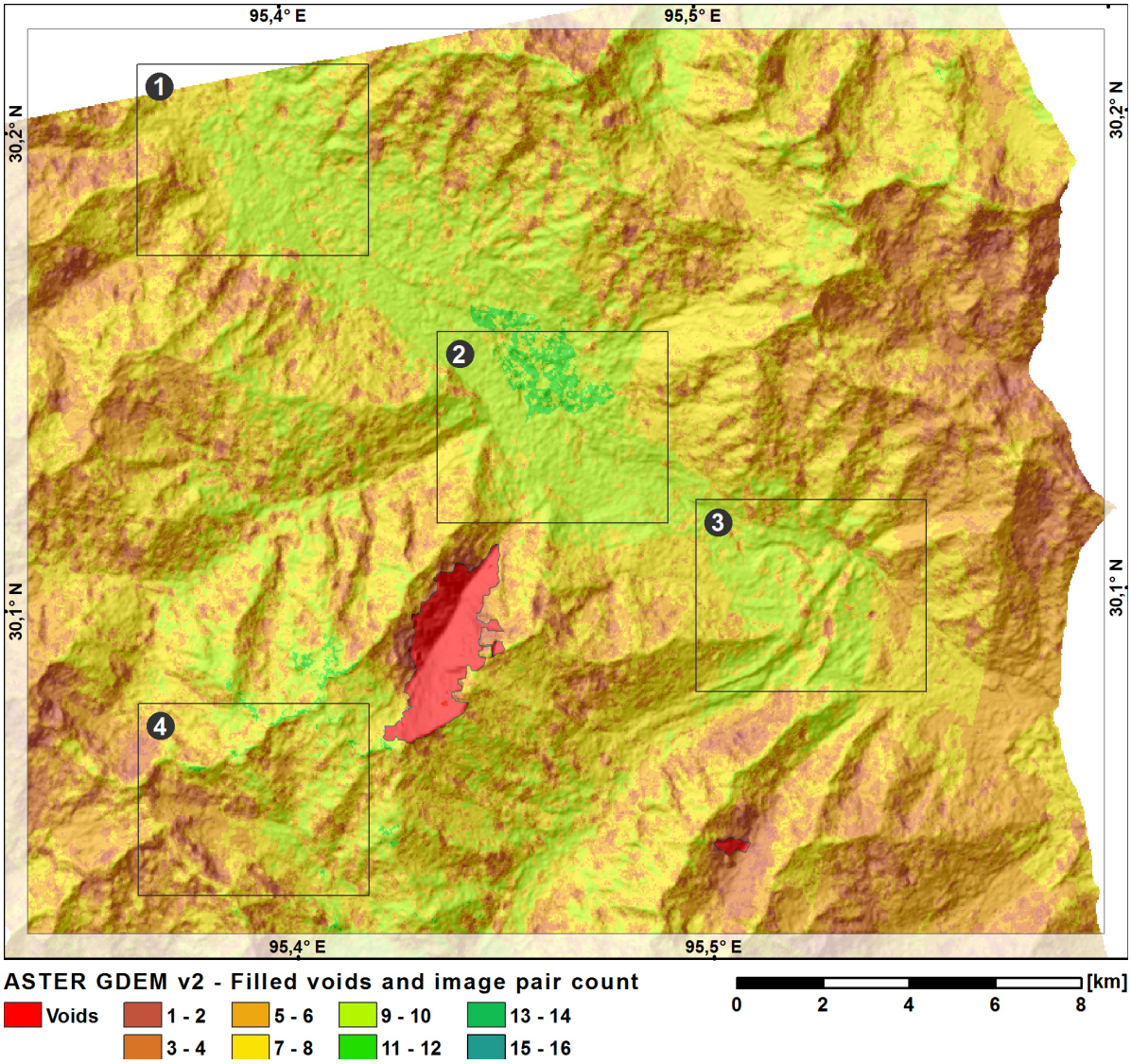
Supplement A.2: Interferometric coherence depicted for the four Details.



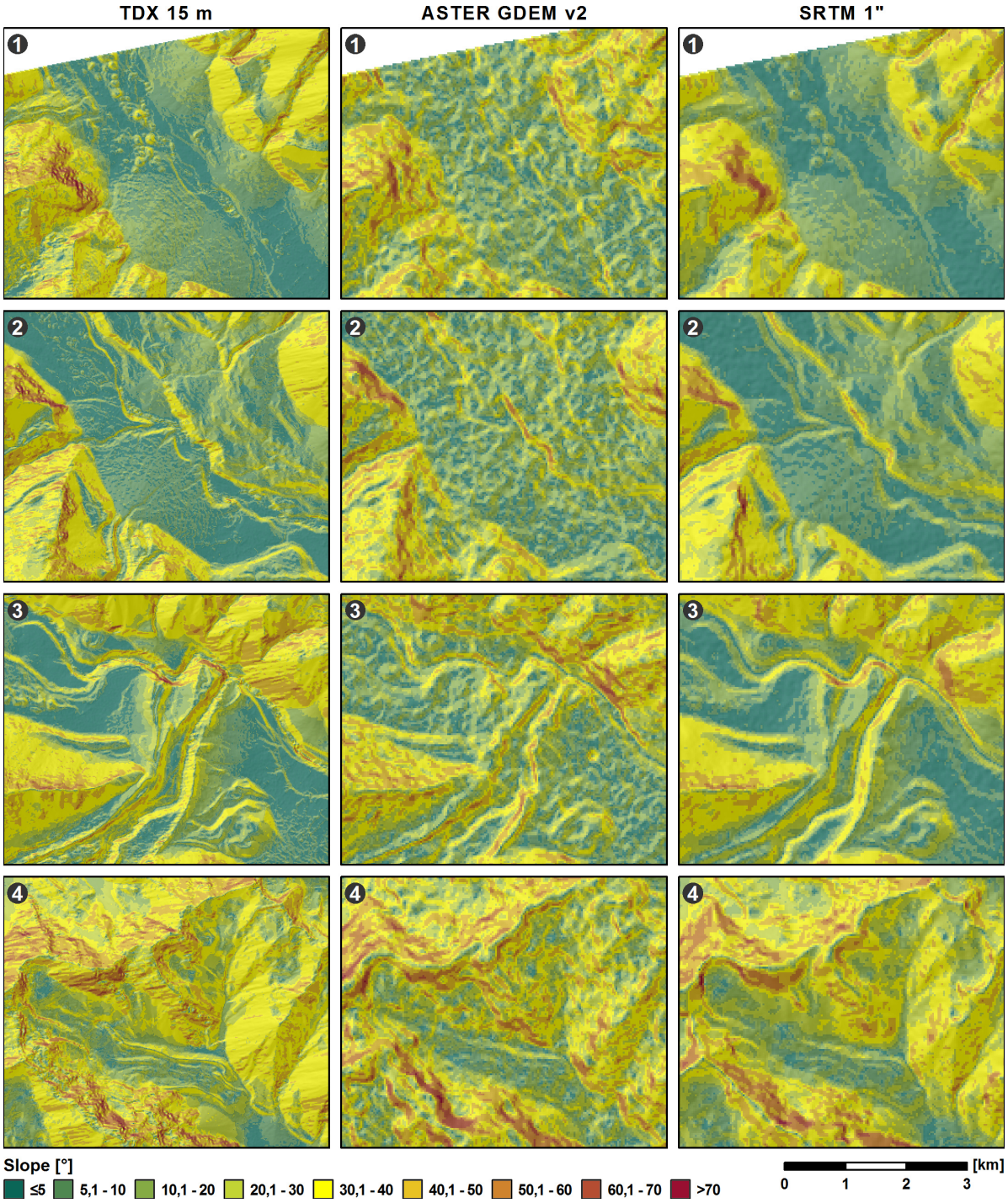
Supplement A.3: Position of pixels which were identified as outliers in the intermediate 1.5 m DEM. Prior to downsampling to a final posting of 15 m, these pixels were substituted by a weighted average of their 5×5 neighborhood.



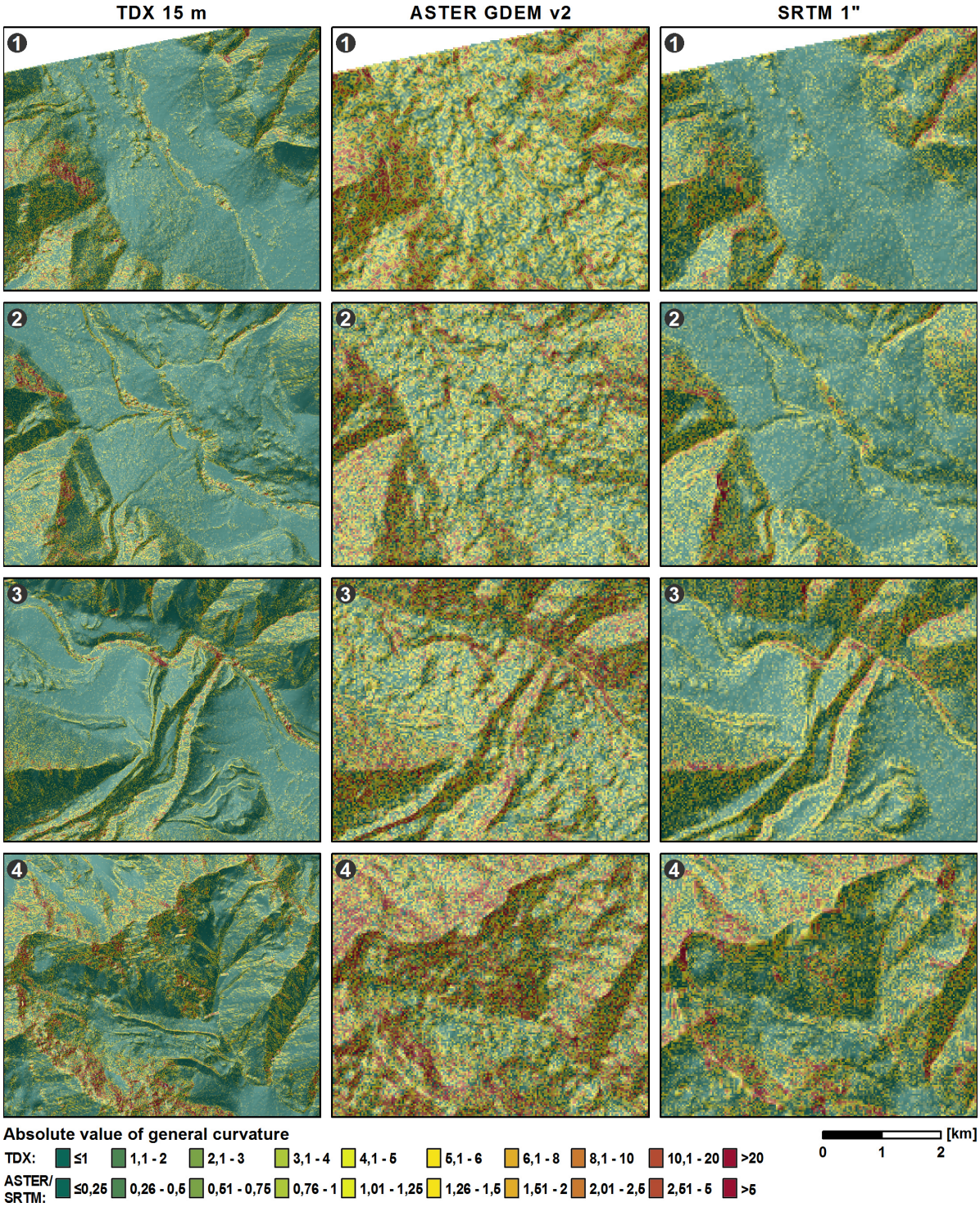
Supplement A.4: Data voids present in the SRTM1 product. Voids were filled using void-free SRTM3 data provided by CGIAR-CSI. To account for the different resolutions and data inaccuracies, both datasets were blended into each other by applying a bicubic spline interpolation.



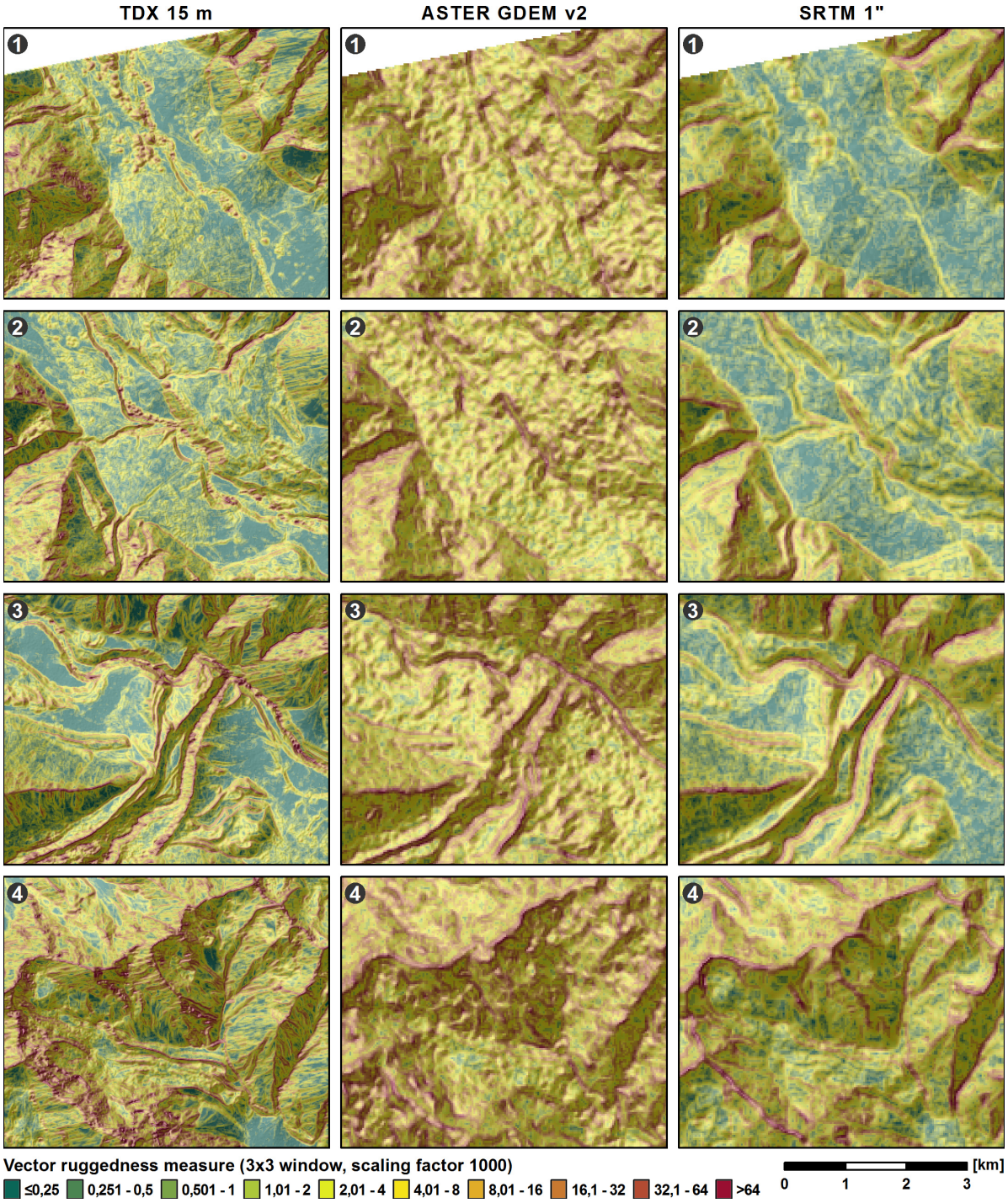
Supplement A.5: Filled voids in ASTER GDEM v2 data and number of stereometric scene pairs incorporated into the generation of the DEM.



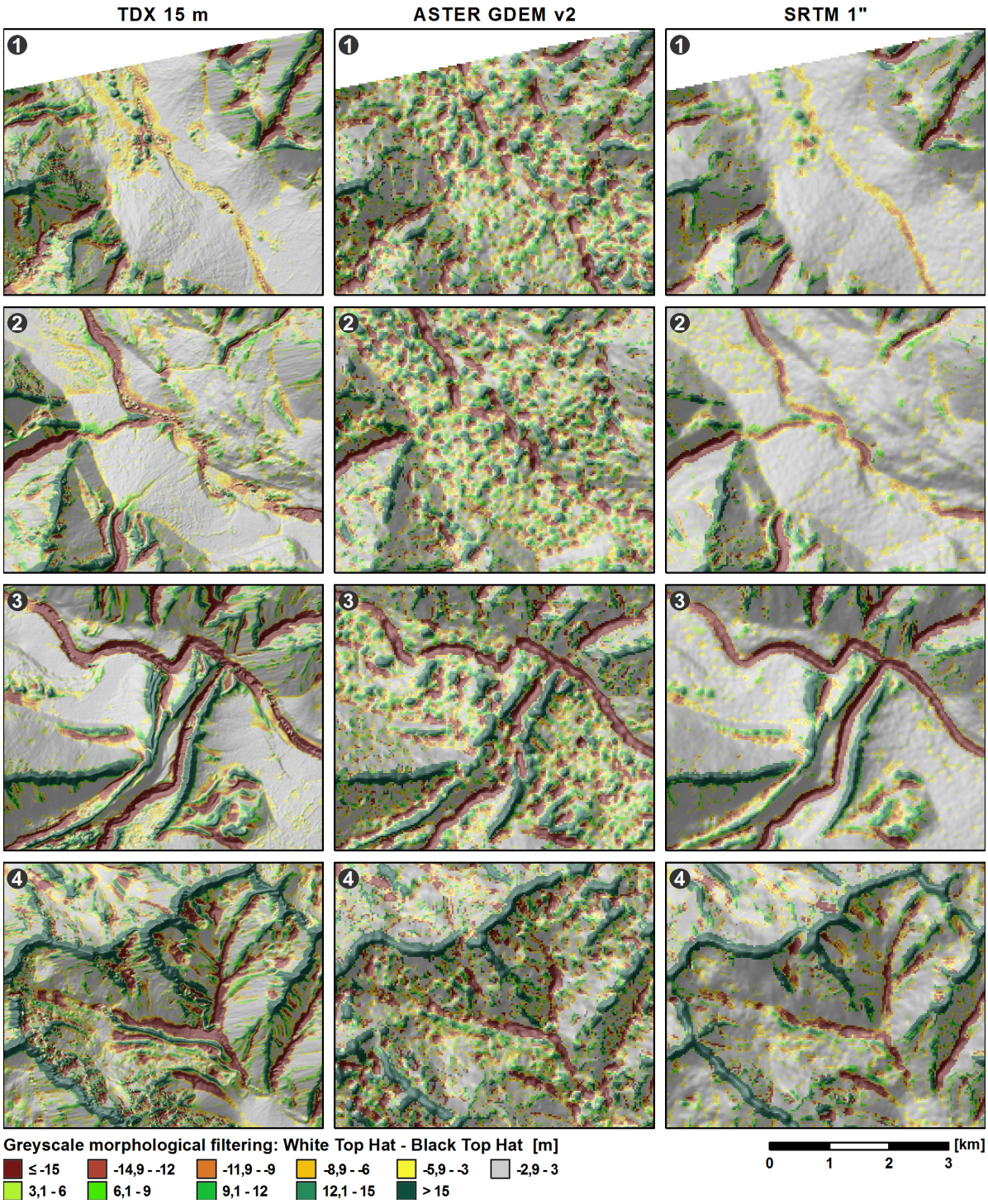
Supplement A.6: Classified values of aspect slope in the four Details, as depicted by TDX (15 m), ASTER GDEM v2, and SRTM1.



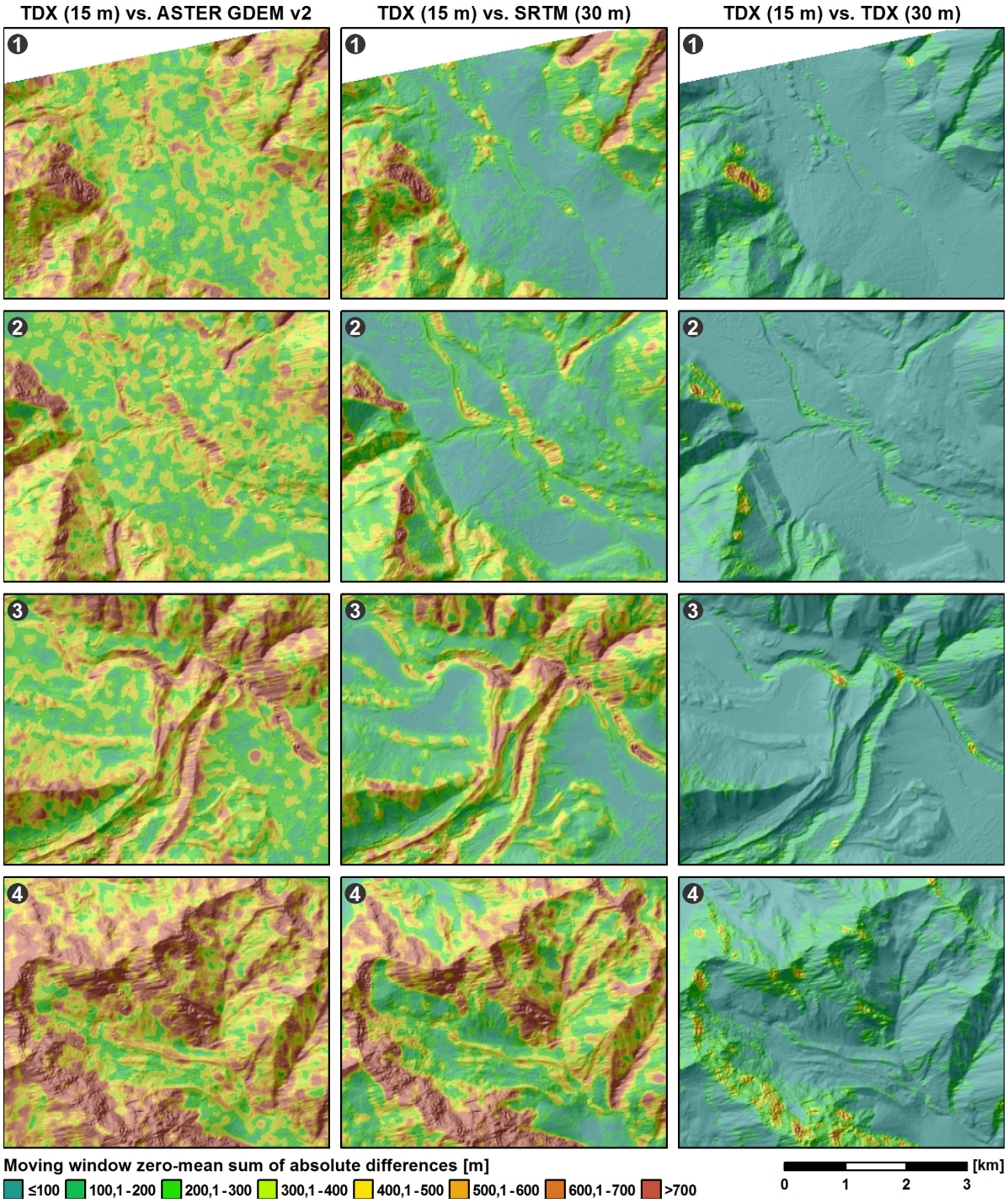
Supplement A.7: Classified absolute values of general curvature in the four Details, as depicted by TDX (15 m), ASTER GDEM v2, and SRTM1.



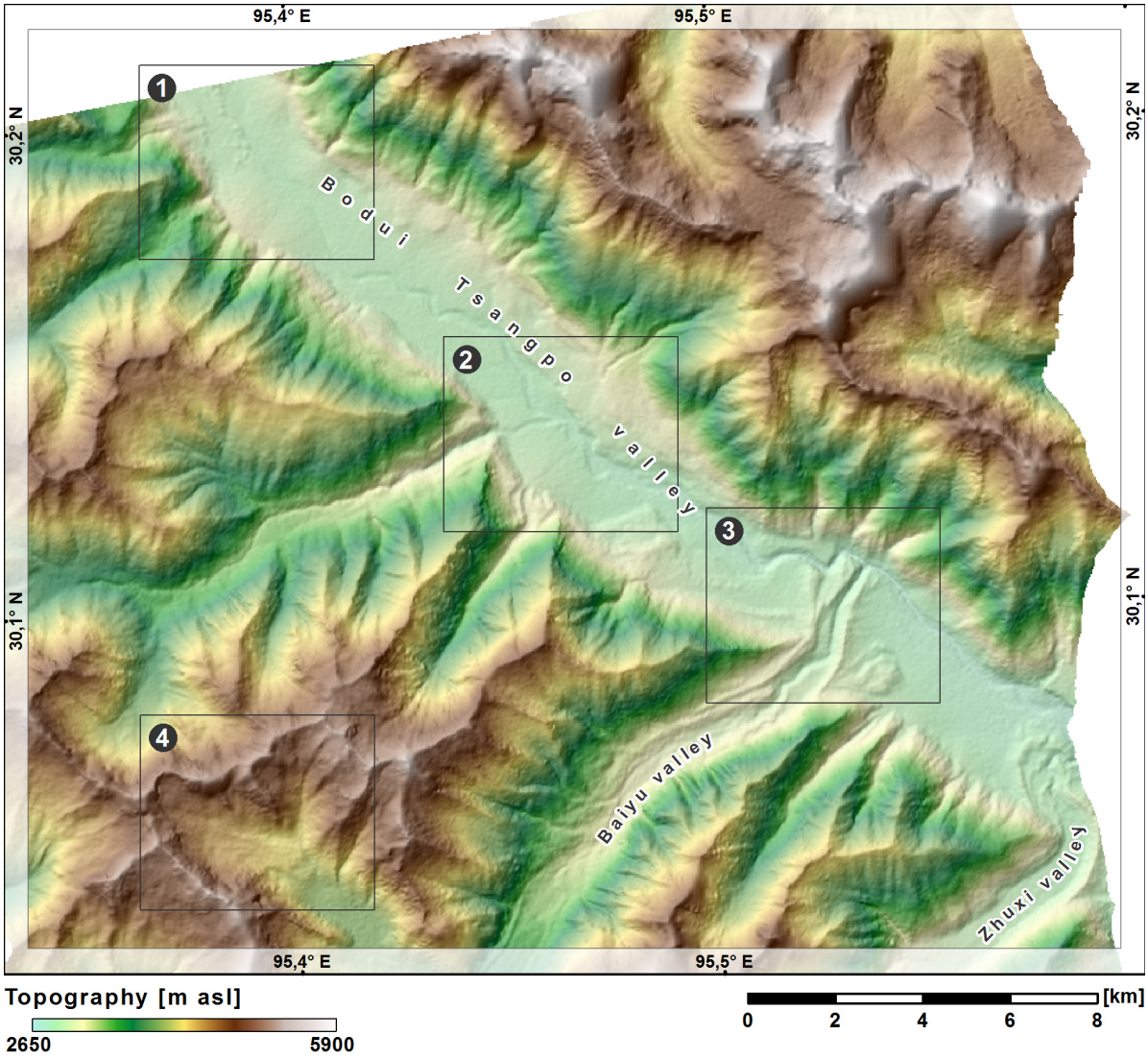
Supplement A.8: Classified values of VRM (3×3 kernel) in the four Details, as given by TDX (15 m), ASTER GDEM v2, and SRTM1.



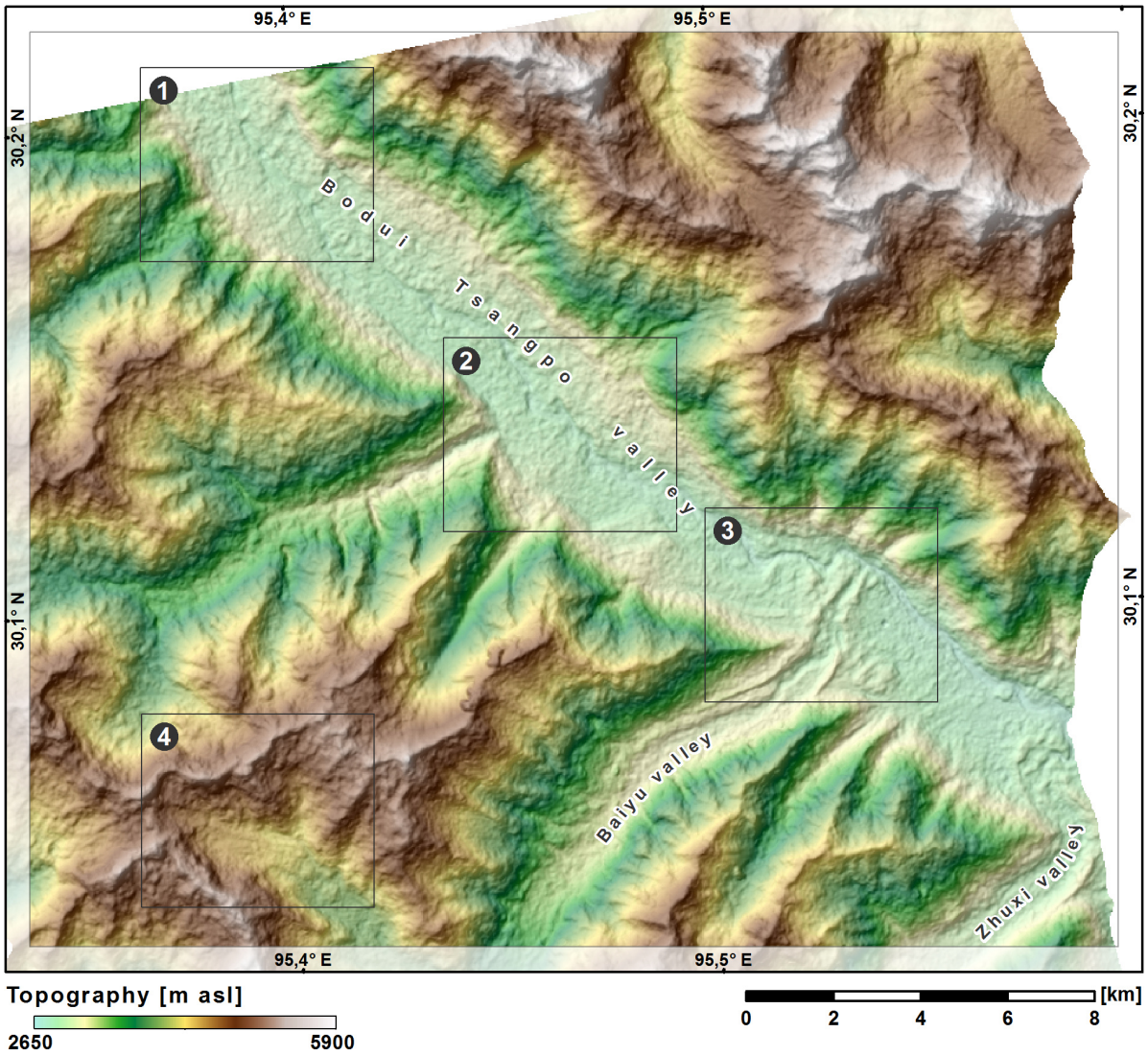
Supplement A.9: Classified values of the BTH-WTH filter obtained for TDX (15 m), ASTER GDEM v2, and SRTM1. The size of the circular structuring element was 19 pixels (equivalent to 285 m) in the case of TDX DEM, and nine pixels (equivalent to 270 m) in the case of both ASTER GDEM and SRTM1.



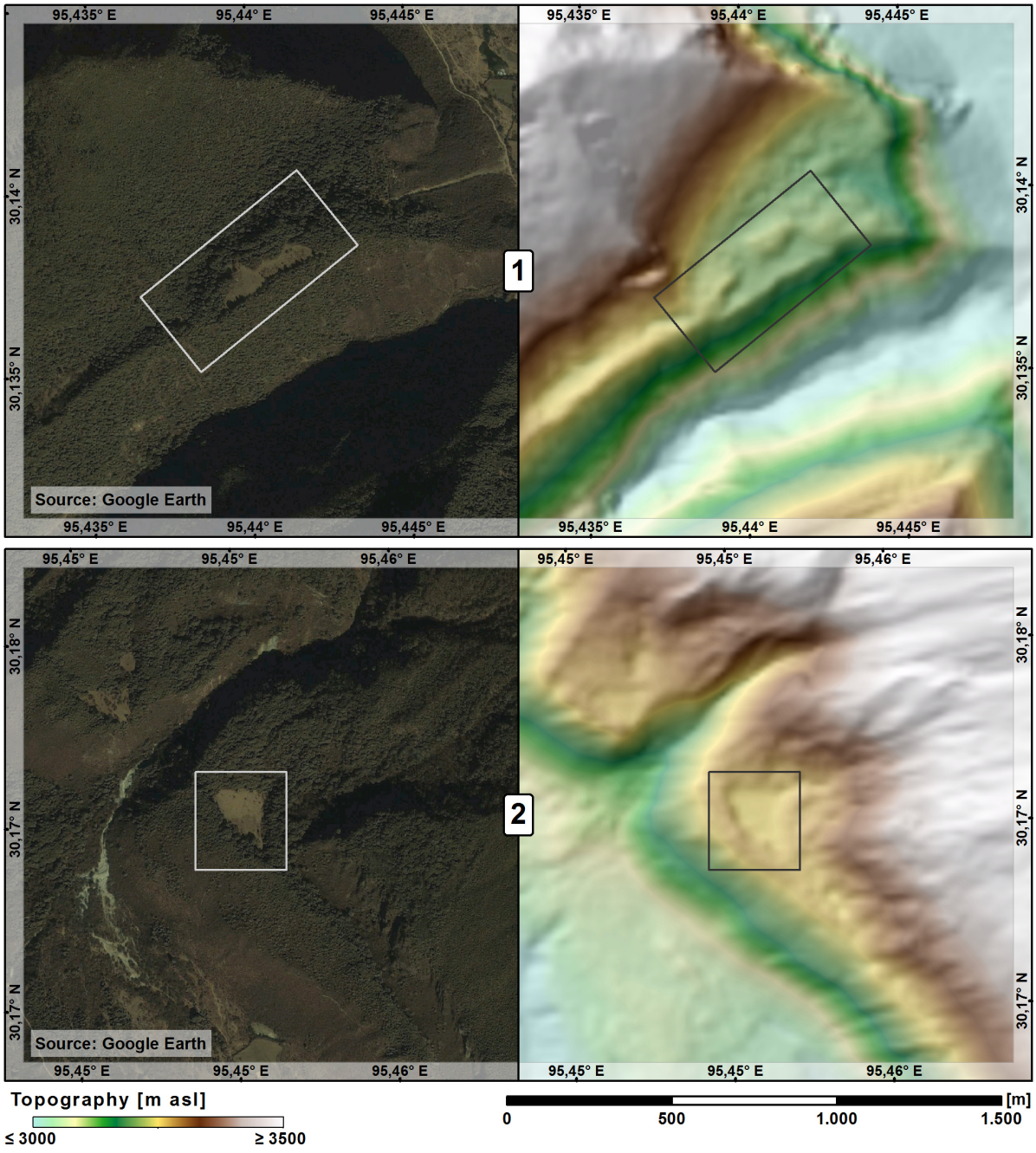
Supplement A.10: Values yielded by the moving window zero-mean sum of absolute differences algorithm (MWZSAD) using juxtapositions of TDX (15 m) with ASTER GDEM v2, SRTM1, and TDX30. A circular neighborhood of 150 m was used for the processing.



Supplement A.11: Topographical overview of the study area in the Bodui Tsangpo valley, as depicted by SRTM1. Black outlines indicate the locations of the Details.

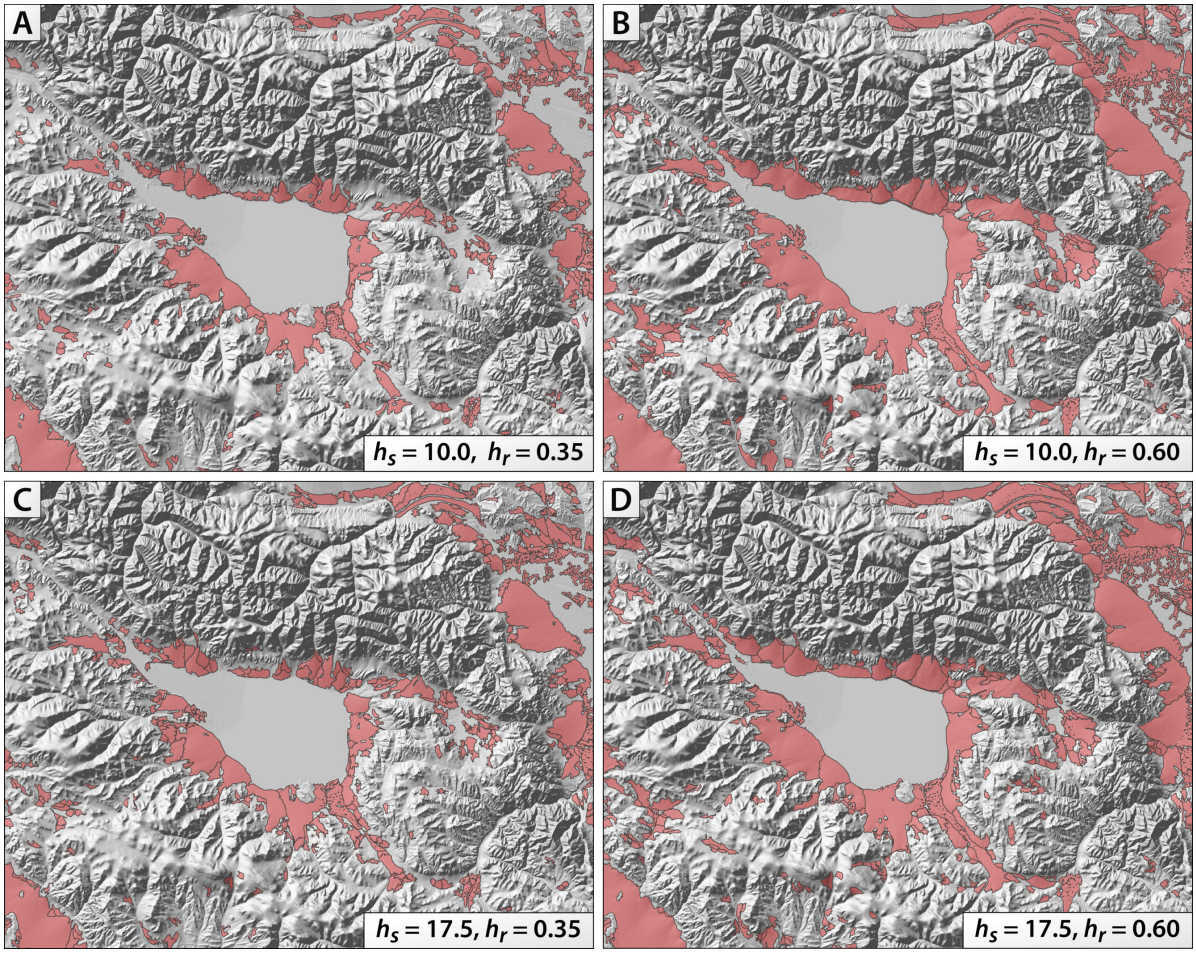


Supplement A.12: Topographical overview of the study area in the Bodui Tsangpo valley, as depicted by ASTER GDEM v2. Black outlines indicate the locations of the Details.

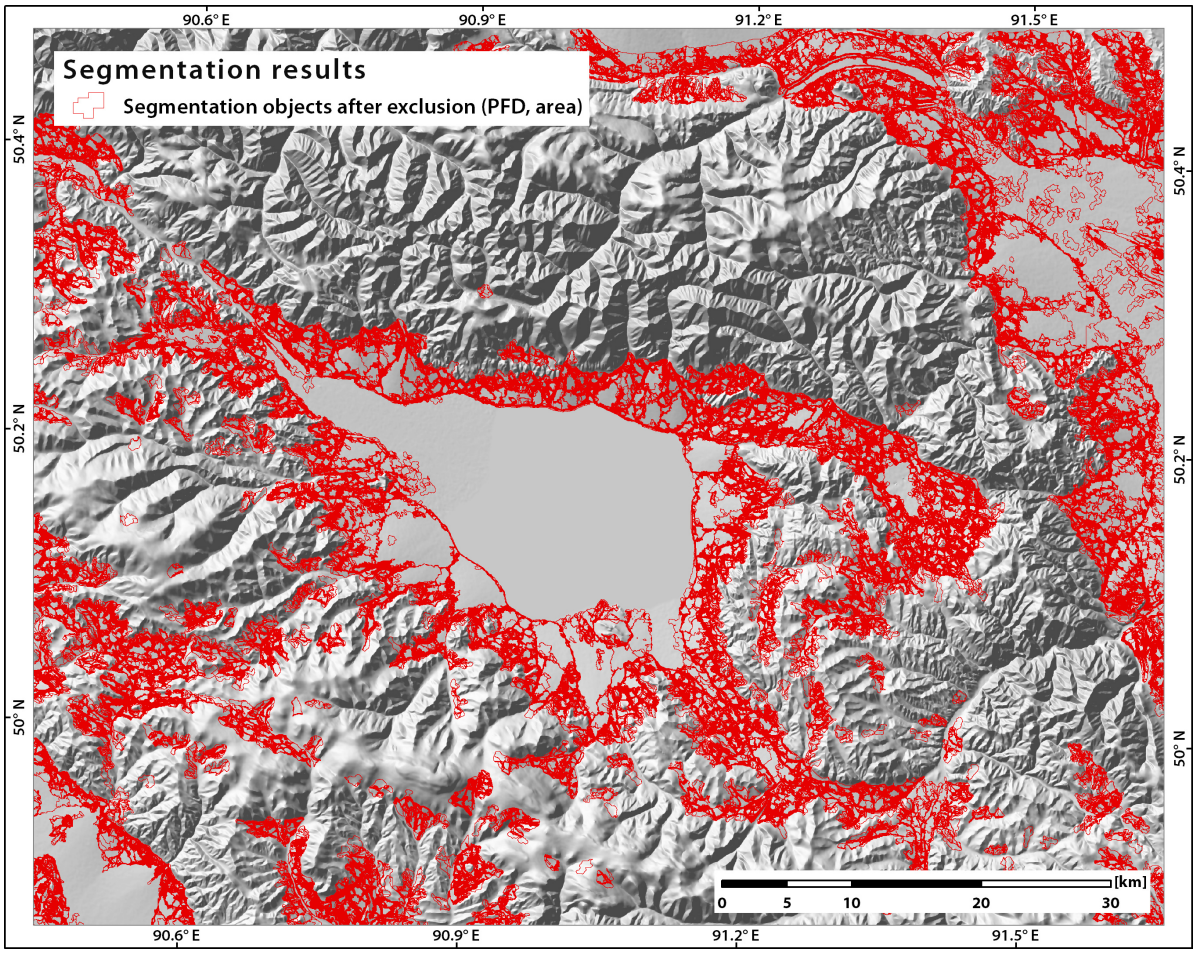


Supplement A.13: Rendition of forest clearings in the self-processed TanDEM-X DEM.

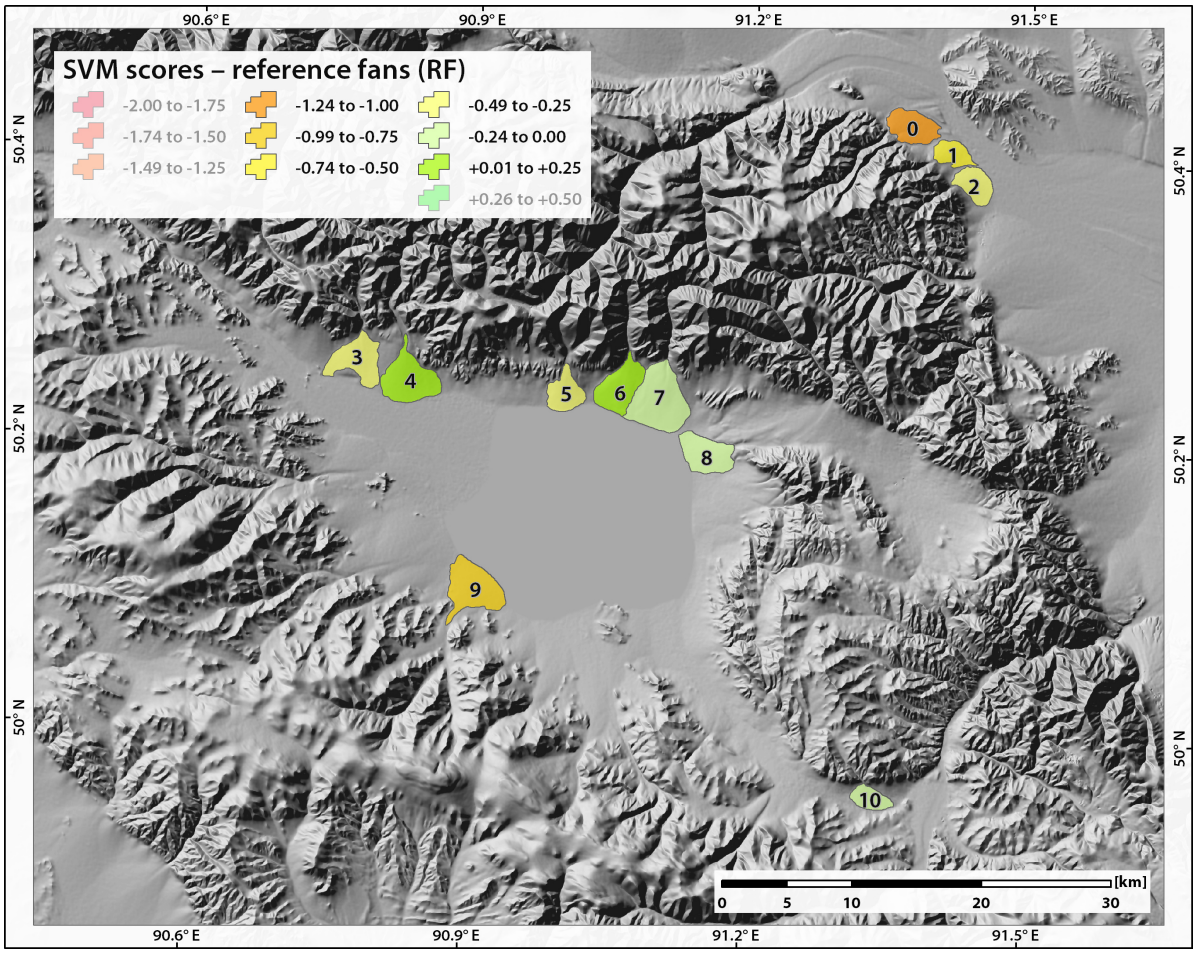
B Supplements, Object-based delineation and classification of alluvial fans by application of mean-shift segmentation and support vector machines



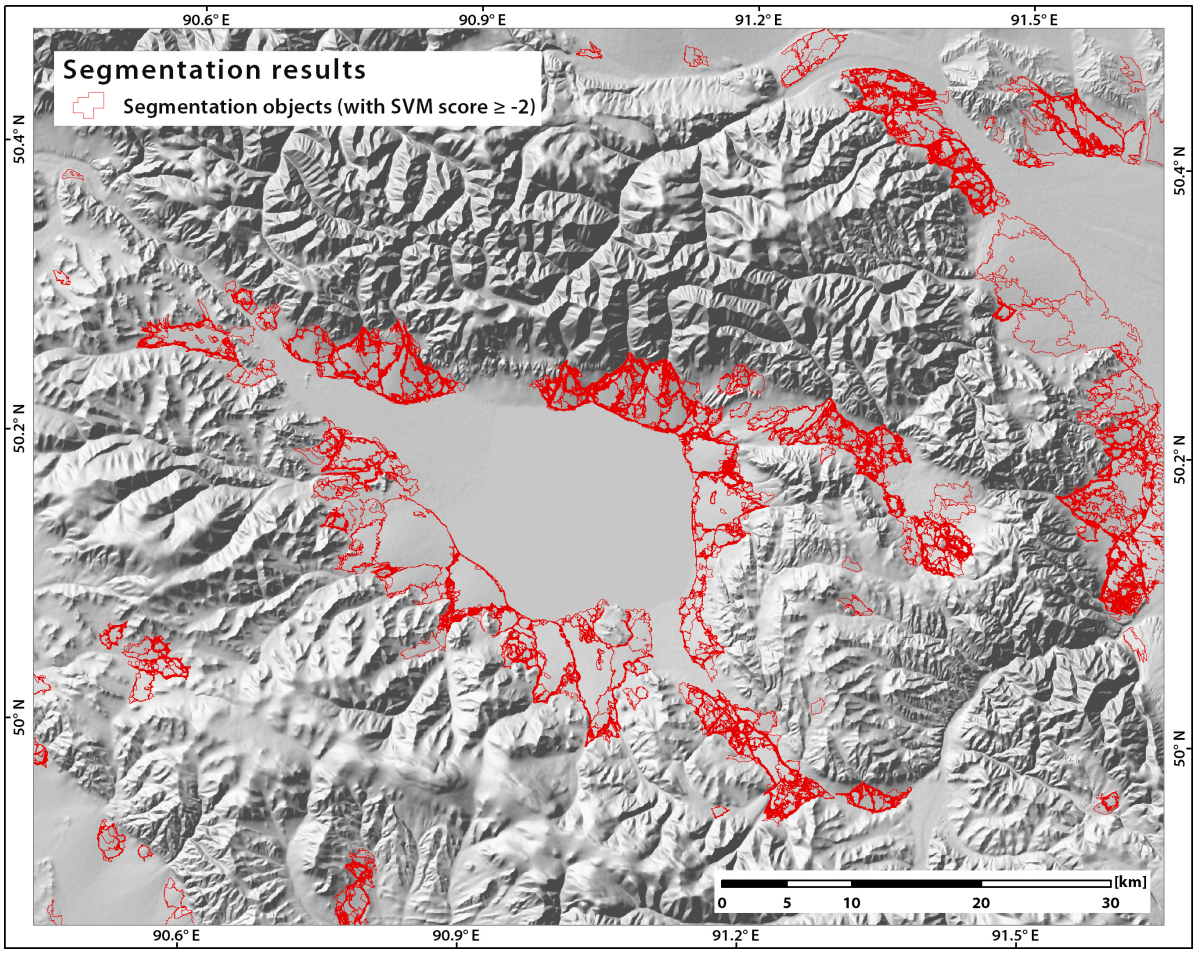
Supplement B.1: Effects of the selection of *hs* and *hr* on object delineation. All depicted segmentation results were obtained with a constant slope area weighting (SAW) and cross-sectional curvature weighting (CCW) of 1.0 and 0.2, respectively. For display reasons, objects exhibiting an area below 6 ha are not shown.



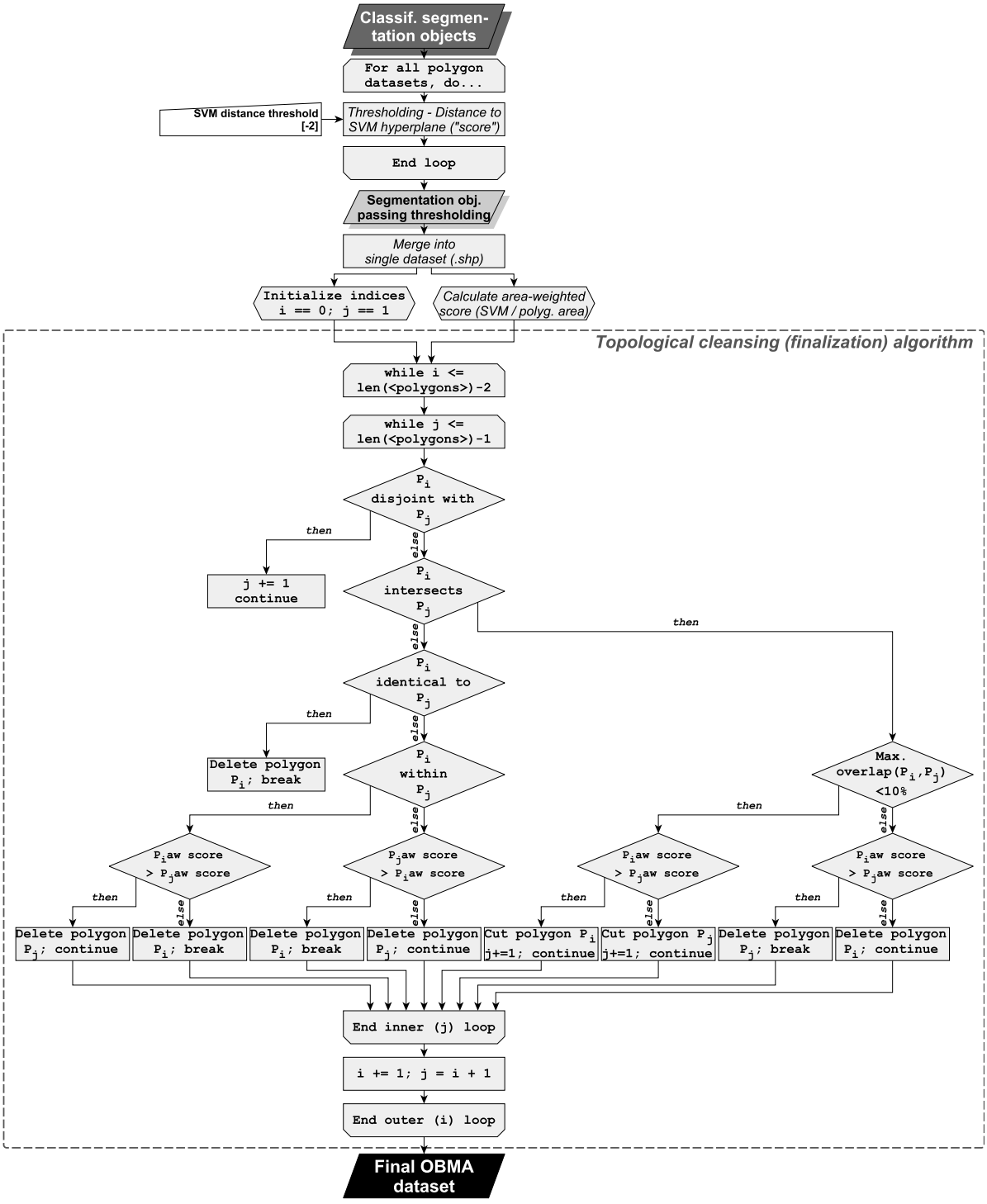
Supplement B.2: Outlines of all segmentation objects passing the exclusion routine described in Section 5.5.2.



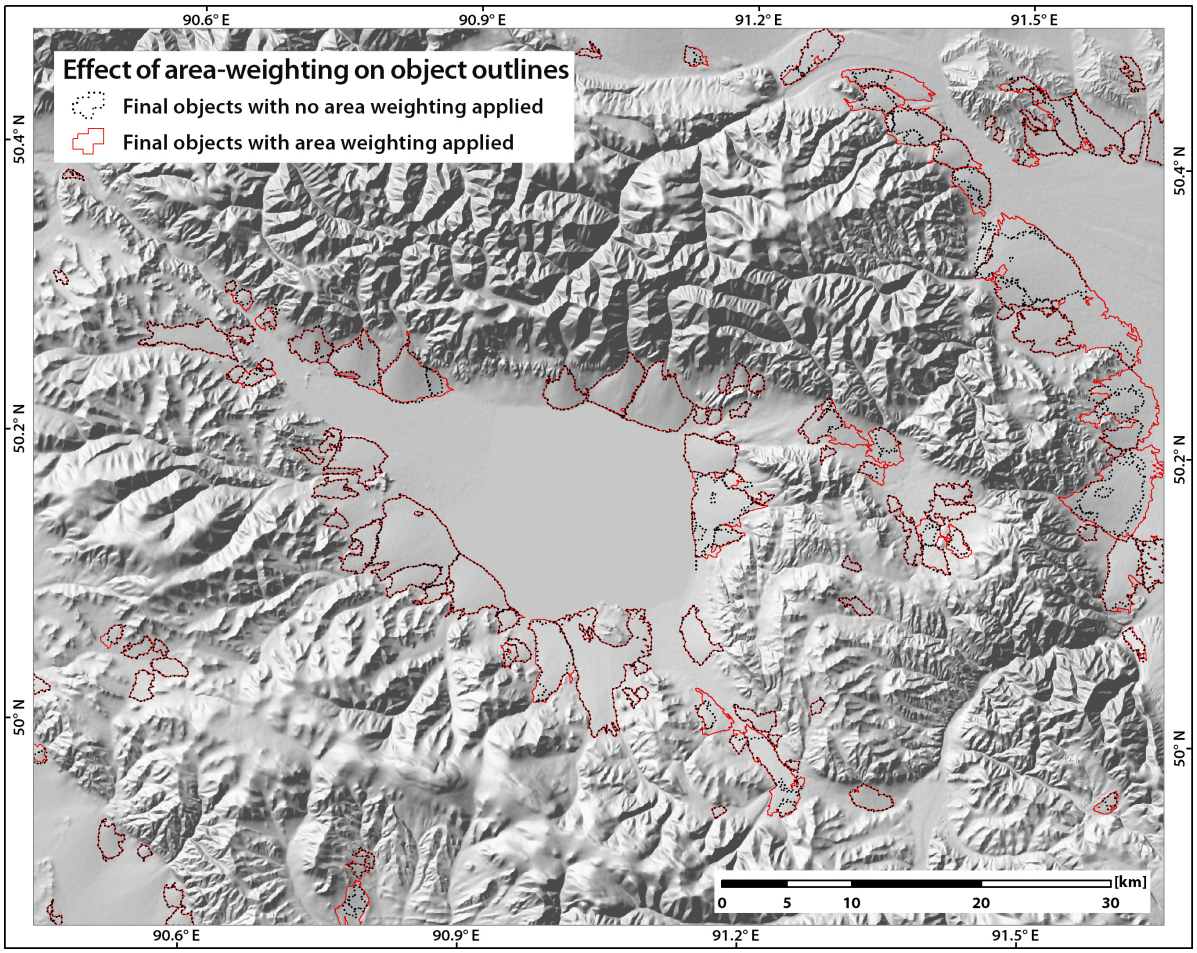
Supplement B.3: Reference fan (manual delineation) SVM scores. SVM score classes not occupied by any reference fan are grayed out.



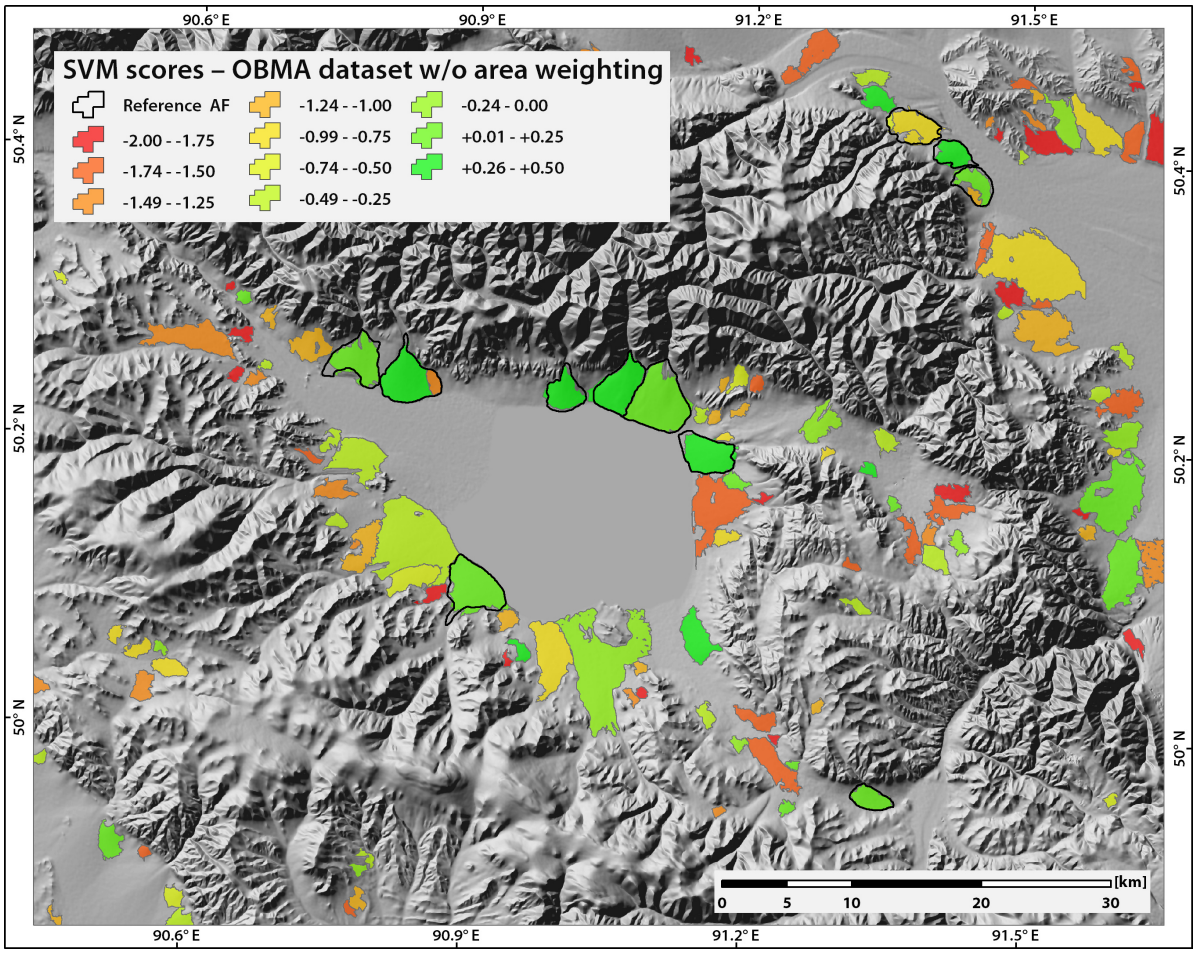
Supplement B.4: Outlines of all OBMA objects exhibiting a SVM score of −2 or better. It becomes apparent that a subset of the OBMA objects exhibits considerable internal differentiation, which are captured by alteration of the segmentation parameters. Other objects, in contrast, display a nearly identical delineation throughout the full range of segmentation parametrization applied, indicating that their surfaces exhibit no considerable internal differentiation.



Supplement B.5: Workflow conducted for all classified polygons to yield a final OBMA dataset. Initially, thresholding is applied to all datasets, and the objects passing the thresholding are merged into a single shapefile. A topological cleansing algorithm is then applied to all polygons to resolve topology violations of the discrete object model, i.e., overlapping polygons. For a legend, please refer to Fig. 5.2.



Supplement B.6: Final OBMA dataset computed with area weighting, compared to the final OBMA objects produced with no area weighting applied. In case of alluvial fans exhibiting minor internal differentiation, area weighting can help in delineating the full fan body.



Supplement B.7: SVM scores of the OBMA dataset which was computed without area weighting (NAW dataset).

Supplement B.8: Morphometric parametrization (Z-standardized values) and classification results for the final OBMA dataset (with area-weighting applied). OBMA objects (OID) are sorted by their SVM score in descending order. Objects best matching reference fan delineations (i.e., exhibiting the greatest degree of overlap) are denoted in bold font.

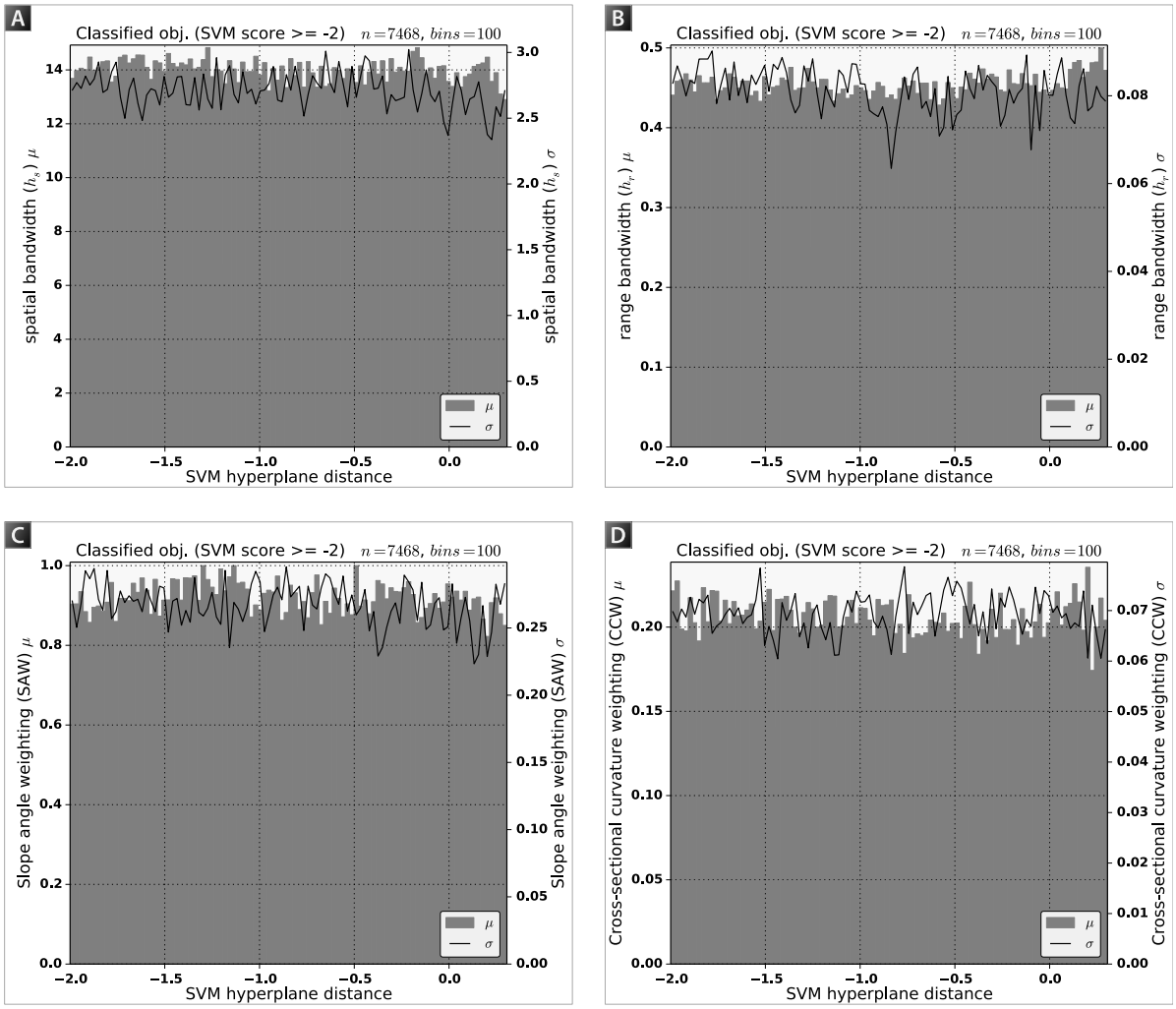
OID	SAW	CCW	h_s	h_r	z skewness	LCurv	CCurv	GAD	BAS	HSA	SVM score
28	**0.50**	**0.30**	**17.5**	**0.55**	**−0.50**	**−0.05**	**−0.07**	**−0.15**	**−0.08**	**−0.44**	**0.43**
71	**1.00**	**0.25**	**10.0**	**0.40**	**0.78**	**0.12**	**0.37**	**−0.24**	**−0.01**	**0.09**	**0.39**
41	0.75	0.25	12.5	0.35	0.01	−0.09	−0.61	−0.29	−0.61	0.14	0.37
110	**1.25**	**0.30**	**10.0**	**0.55**	**0.80**	**0.22**	**−0.25**	**0.36**	**−0.46**	**−0.13**	**0.36**
18	**0.50**	**0.20**	**15.0**	**0.45**	**−0.24**	**−0.74**	**0.38**	**−0.54**	**−0.18**	**0.53**	**0.35**
42	**0.75**	**0.25**	**12.5**	**0.45**	**−0.21**	**−0.04**	**−0.52**	**−0.66**	**−0.34**	**−0.20**	**0.34**
100	1.25	0.10	17.5	0.45	0.58	−0.13	0.00	0.70	0.76	−0.21	0.26
58	**0.75**	**0.30**	**17.5**	**0.35**	**0.77**	**−0.48**	**−0.60**	**0.17**	**−0.55**	**−0.65**	**0.18**
24	**0.50**	**0.30**	**12.5**	**0.45**	**−0.07**	**0.09**	**−0.51**	**0.52**	**0.34**	**−1.22**	**0.17**
84	1.00	0.30	12.5	0.40	−0.03	0.19	0.84	0.56	−0.06	−1.15	0.16
34	0.75	0.10	12.5	0.50	−0.94	−0.33	−0.94	0.56	−0.41	−0.41	0.13
1	**0.50**	**0.15**	**12.5**	**0.35**	**−0.57**	**−0.17**	**−0.78**	**0.58**	**0.55**	**−1.10**	**0.06**
82	1.25	0.25	12.5	0.50	−1.21	−0.31	−0.33	0.47	−0.43	−1.02	0.06
72	**1.00**	**0.25**	**12.5**	**0.55**	**−0.42**	**1.13**	**−0.20**	**0.25**	**0.79**	**0.96**	**0.06**
87	1.00	0.30	17.5	0.35	−0.97	0.13	−0.26	0.79	0.54	−1.11	0.04
47	0.75	0.20	10.0	0.40	0.39	1.11	−1.00	−0.44	−0.73	−0.62	0.01
92	1.25	0.15	12.5	0.60	0.18	1.28	−1.24	0.18	0.10	0.80	−0.06
29	0.75	0.15	10.0	0.40	0.42	−0.55	−1.38	0.72	−0.94	−0.38	−0.09
50	0.75	0.30	12.5	0.35	−0.80	0.13	1.09	0.89	0.11	−1.41	−0.15
66	1.00	0.10	15.0	0.60	−0.79	−1.06	−0.25	1.14	−0.82	−1.03	−0.17
33	**0.75**	**0.10**	**12.5**	**0.40**	**0.26**	**1.14**	**−0.40**	**0.43**	**0.28**	**1.76**	**−0.18**
101	1.25	0.10	17.5	0.55	−0.11	0.18	−0.55	0.40	−0.83	−1.96	−0.20
22	0.50	0.30	10.0	0.50	−0.19	0.82	−0.18	1.32	−1.36	−1.11	−0.21
2	0.50	0.15	15.0	0.35	0.61	−0.50	−1.51	0.30	−0.63	−1.14	−0.22
75	1.00	0.20	10.0	0.40	−1.23	−0.43	−0.30	1.11	−0.84	−1.33	−0.23
61	1.00	0.15	17.5	0.35	−0.03	−1.22	−0.76	1.45	−0.03	−1.04	−0.26
113	1.25	0.30	17.5	0.45	−0.48	−0.92	−0.25	1.50	−1.43	−0.30	−0.27
102	1.25	0.25	15.0	0.55	−0.59	0.43	0.38	0.45	0.20	−2.10	−0.28
73	1.00	0.25	15.0	0.45	−0.44	−0.21	0.01	0.04	−0.52	−2.26	−0.32
103	1.25	0.25	15.0	0.60	0.28	1.03	−1.66	0.83	0.05	−1.24	−0.37
98	1.25	0.15	17.5	0.45	−2.20	0.64	−0.01	0.86	−0.09	−0.70	−0.40
70	1.00	0.25	10.0	0.45	−0.55	0.13	2.20	1.08	−0.54	−0.17	−0.41
108	1.25	0.20	15.0	0.40	−0.22	−1.08	−0.54	0.62	0.27	1.93	−0.42
38	0.75	0.25	10.0	0.35	−0.33	0.53	−0.10	0.34	−1.31	−2.16	−0.44
0	0.50	0.15	10.0	0.55	−0.89	−1.60	−0.42	1.61	−0.42	0.31	−0.44
107	1.25	0.20	12.5	0.45	−0.73	0.56	−1.28	0.71	0.08	−1.94	−0.45
10	0.50	0.25	10.0	0.60	0.76	1.14	−0.24	1.58	1.38	−0.48	−0.46
62	1.00	0.15	17.5	0.35	0.51	−0.99	−1.21	0.73	−1.34	−1.35	−0.49
57	0.75	0.30	17.5	0.35	−1.29	1.66	1.05	0.10	−0.82	−1.14	−0.50
51	0.75	0.30	12.5	0.40	−1.80	−0.60	−1.34	1.31	−0.21	−0.20	−0.52

Supplement B.8 (cont.)

OID	SAW	CCW	h_s	h_r	z skewness	LCurv	CCurv	GAD	BAS	HSA	SVM score
3	0.50	0.15	17.5	0.35	−0.90	1.39	−0.04	0.85	−0.63	−1.96	−0.53
63	1.00	0.15	17.5	0.35	−1.11	−1.20	−0.79	−0.32	0.81	−1.52	−0.53
16	0.50	0.20	17.5	0.50	−2.02	0.17	−0.80	1.34	−0.73	−1.04	−0.58
59	0.75	0.30	17.5	0.45	−0.15	0.59	−0.09	1.61	−1.73	−1.67	−0.63
40	0.75	0.25	10.0	0.40	−1.15	1.12	0.34	0.65	0.35	−2.21	−0.64
60	1.00	0.15	10.0	0.40	−1.36	1.91	0.13	0.44	−0.11	−2.04	−0.85
43	0.75	0.25	15.0	0.45	−1.19	−0.18	1.00	1.07	1.42	−2.00	−0.88
88	1.00	0.30	17.5	0.45	−0.62	−0.21	−2.43	1.34	−0.03	−1.41	−0.89
31	0.75	0.15	12.5	0.50	1.26	2.93	0.74	0.22	−0.44	0.23	−0.89
14	0.50	0.20	10.0	0.50	−0.42	0.11	−1.53	1.20	0.32	−2.48	−0.90
20	0.50	0.20	17.5	0.35	−0.77	0.88	−0.40	2.03	0.02	−2.29	−0.91
90	1.25	0.15	12.5	0.35	−0.86	−1.26	−1.74	0.00	−0.08	−2.17	−0.96
77	1.00	0.20	12.5	0.60	−2.26	−0.28	0.16	0.82	−0.21	−2.30	−1.00
104	1.25	0.25	17.5	0.35	−1.22	−1.74	−0.48	1.07	−1.58	−1.75	−1.02
23	0.50	0.30	12.5	0.35	0.89	1.53	0.09	1.83	1.80	−1.01	−1.02
12	0.50	0.20	10.0	0.35	−0.05	2.64	−0.57	1.61	−0.87	−1.13	−1.04
35	0.75	0.10	15.0	0.35	0.29	−0.39	−1.91	0.77	1.29	−2.13	−1.04
93	1.25	0.15	15.0	0.35	−1.43	−0.27	−1.00	1.97	1.00	−1.92	−1.05
27	0.50	0.30	17.5	0.40	−1.23	0.27	1.08	−0.77	−0.01	−2.78	−1.10
21	0.50	0.30	10.0	0.55	−0.75	0.83	−0.49	1.55	−1.05	−2.77	−1.11
105	1.25	0.25	17.5	0.35	0.18	0.13	−1.87	0.42	0.04	−2.87	−1.16
65	1.00	0.10	12.5	0.60	−0.87	2.76	1.29	1.42	0.03	−0.86	−1.17
111	1.25	0.30	10.0	0.60	−0.08	0.41	−1.14	2.80	−1.40	−1.41	−1.17
112	1.25	0.30	12.5	0.45	0.61	−2.79	0.91	1.48	−0.40	−0.54	−1.18
55	0.75	0.30	15.0	0.45	−1.87	−1.44	1.16	−0.11	−1.52	−1.81	−1.22
81	1.00	0.20	17.5	0.60	−1.24	1.53	2.06	1.25	0.18	−1.80	−1.22
49	0.75	0.30	10.0	0.50	−0.80	0.38	−1.13	3.07	1.27	−0.27	−1.25
13	0.50	0.20	10.0	0.40	−1.35	−0.80	1.78	2.21	−0.60	−1.79	−1.31
69	1.00	0.30	15.0	0.55	−2.01	−0.53	1.35	1.25	−0.72	−2.41	−1.31
46	0.75	0.20	10.0	0.45	−1.30	1.42	0.38	1.47	0.51	−2.75	−1.32
91	1.25	0.30	10.0	0.40	−0.79	−0.21	−0.75	0.25	−1.73	−3.12	−1.33
4	0.50	0.10	10.0	0.35	−0.73	−0.99	−0.83	1.78	0.64	−2.92	−1.35
15	0.50	0.20	12.5	0.35	−0.88	1.71	−1.68	1.48	0.56	−2.31	−1.38
11	0.50	0.25	15.0	0.40	−0.18	−0.10	−1.23	0.74	2.15	−2.62	−1.41
26	0.50	0.30	17.5	0.40	−0.69	−0.43	−1.87	0.67	0.88	−2.97	−1.43
30	0.75	0.15	12.5	0.35	−0.92	−0.58	−1.12	0.71	0.05	−3.42	−1.43
32	0.75	0.15	17.5	0.55	−1.00	−1.07	−1.35	2.80	−0.38	−1.94	−1.43
37	0.75	0.10	15.0	0.60	−1.15	−1.85	−1.03	1.94	1.22	−1.93	−1.43
80	1.00	0.20	17.5	0.55	−1.11	−0.17	−1.00	0.69	−0.27	−3.54	−1.49
76	1.00	0.20	10.0	0.50	0.01	0.83	−1.26	0.65	−0.17	−3.52	−1.50
45	0.75	0.25	17.5	0.50	−1.15	−1.47	−1.20	0.74	0.29	−3.17	−1.55
67	1.00	0.10	15.0	0.60	−1.94	−1.15	−0.51	1.34	0.43	−2.97	−1.56
83	1.00	0.30	10.0	0.60	−1.33	1.38	−2.35	1.60	0.51	−2.02	−1.57

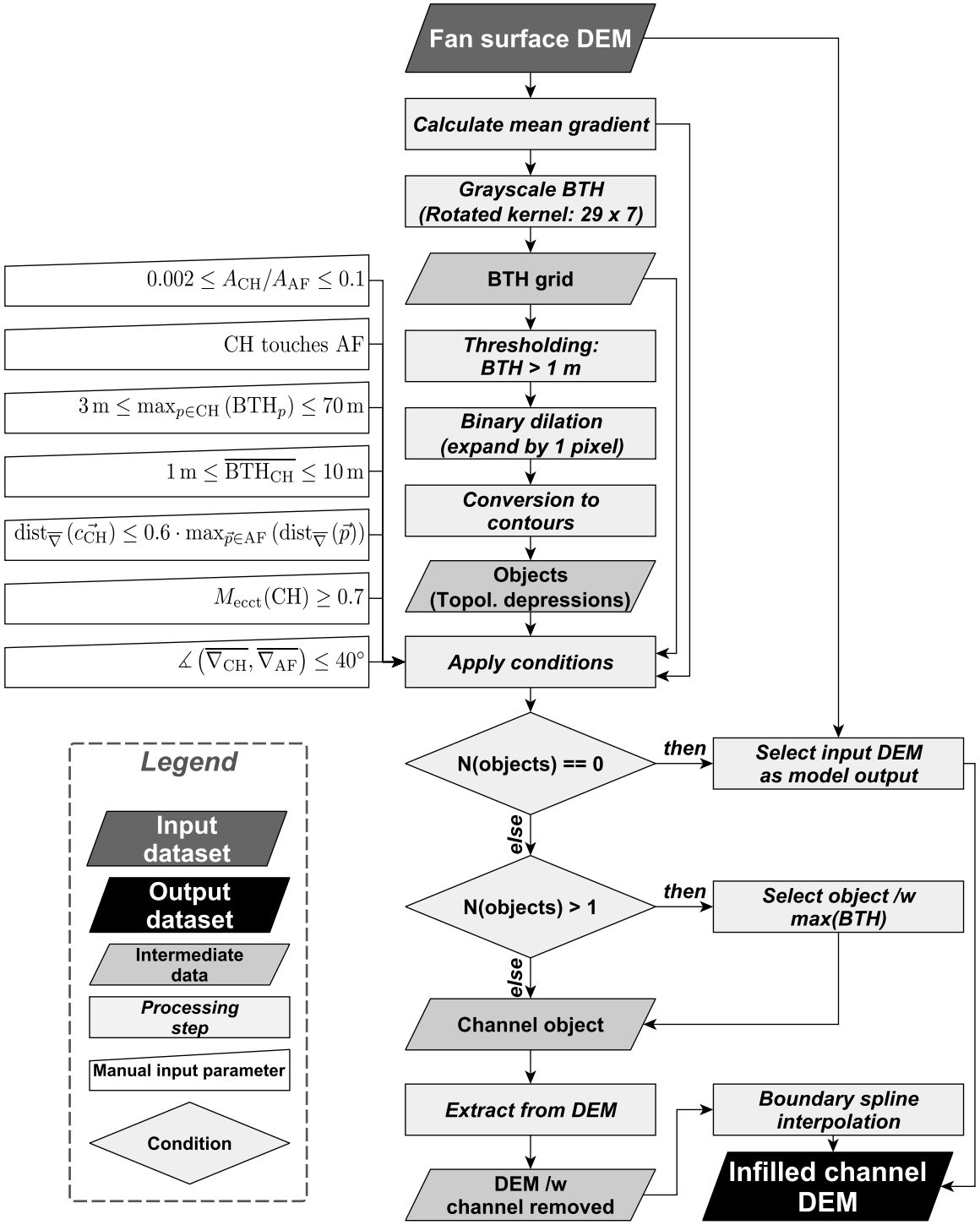
Supplement B.8 (cont.)

OID	SAW	CCW	h_s	h_r	z skewness	LCurv	CCurv	GAD	BAS	HSA	SVM score
48	0.75	0.30	10.0	0.40	0.29	−0.78	−1.58	1.62	1.44	−2.79	−1.57
52	0.75	0.30	12.5	0.50	−0.93	1.43	−1.81	2.72	0.75	−1.59	−1.61
95	1.25	0.15	15.0	0.50	−0.46	1.55	−2.02	2.87	0.01	−1.50	−1.65
68	1.00	0.10	17.5	0.60	−1.26	3.42	1.88	0.85	−0.04	−0.05	−1.68
36	**0.75**	**0.10**	**15.0**	**0.45**	**−1.45**	**2.00**	**−1.89**	**2.27**	**0.41**	**−1.53**	**−1.68**
9	0.50	0.25	10.0	0.40	0.05	3.76	−1.24	1.04	−0.72	−0.55	−1.69
74	1.00	0.25	15.0	0.40	−0.43	−1.12	0.45	3.56	−0.43	−1.86	−1.70
8	0.50	0.25	10.0	0.40	0.29	0.06	−1.28	1.24	1.98	−3.05	−1.71
56	0.75	0.30	15.0	0.45	1.54	0.14	−1.39	2.49	−1.29	−2.34	−1.73
89	1.25	0.15	10.0	0.40	−0.66	−1.12	−0.61	0.77	0.45	−3.78	−1.73
17	0.50	0.20	12.5	0.60	−0.48	−3.55	0.69	1.70	0.35	0.18	−1.73
97	1.25	0.30	15.0	0.45	−0.66	1.26	0.71	1.92	0.06	−3.41	−1.75
54	0.75	0.30	15.0	0.35	−2.08	−0.03	−2.09	2.04	−1.21	−2.18	−1.78
44	0.75	0.25	17.5	0.35	−1.55	−0.35	−1.60	1.96	−0.99	−3.05	−1.79
5	0.50	0.10	10.0	0.40	−0.98	−0.31	1.37	3.44	−0.11	−2.02	−1.80
85	1.00	0.30	12.5	0.50	0.16	−0.61	−1.53	2.37	0.50	−3.18	−1.82
99	1.25	0.10	10.0	0.40	−1.11	−1.59	−0.75	1.42	−1.04	−3.42	−1.83
86	1.00	0.30	17.5	0.35	2.24	0.61	−0.57	1.49	−1.84	−2.67	−1.86
7	0.50	0.25	10.0	0.35	0.53	0.10	−0.37	2.71	−1.67	−3.00	−1.87
94	1.25	0.30	12.5	0.45	−0.21	0.26	−1.94	1.63	2.40	−2.41	−1.87
96	1.25	0.15	17.5	0.35	−0.20	−2.79	0.05	0.96	2.48	−1.71	−1.90
19	0.50	0.20	17.5	0.35	−0.80	0.86	2.36	2.00	0.78	−2.70	−1.91
109	1.25	0.20	15.0	0.55	−0.30	3.56	2.31	1.08	−1.00	0.16	−1.92
79	1.00	0.20	15.0	0.40	−1.98	2.30	0.51	0.86	−0.97	−2.96	−1.95
106	1.25	0.25	17.5	0.35	−1.52	−1.39	−0.96	1.52	3.28	−0.01	−1.95
64	1.00	0.10	10.0	0.45	−0.16	1.37	−2.09	1.89	1.53	−2.66	−1.95
53	0.75	0.30	12.5	0.60	−1.44	0.90	−2.07	2.32	0.27	−2.80	−1.96
6	0.50	0.25	12.5	0.40	−2.05	−0.20	0.84	1.48	−0.81	−3.58	−1.98
25	0.50	0.30	12.5	0.60	−0.59	−2.69	0.33	0.61	0.72	−3.23	−1.98
78	1.00	0.20	15.0	0.45	−1.32	−0.53	−2.22	2.40	−0.37	−2.89	−2.00
39	0.75	0.25	10.0	0.45	−0.67	−0.03	−1.21	2.86	−0.15	−3.33	−2.00

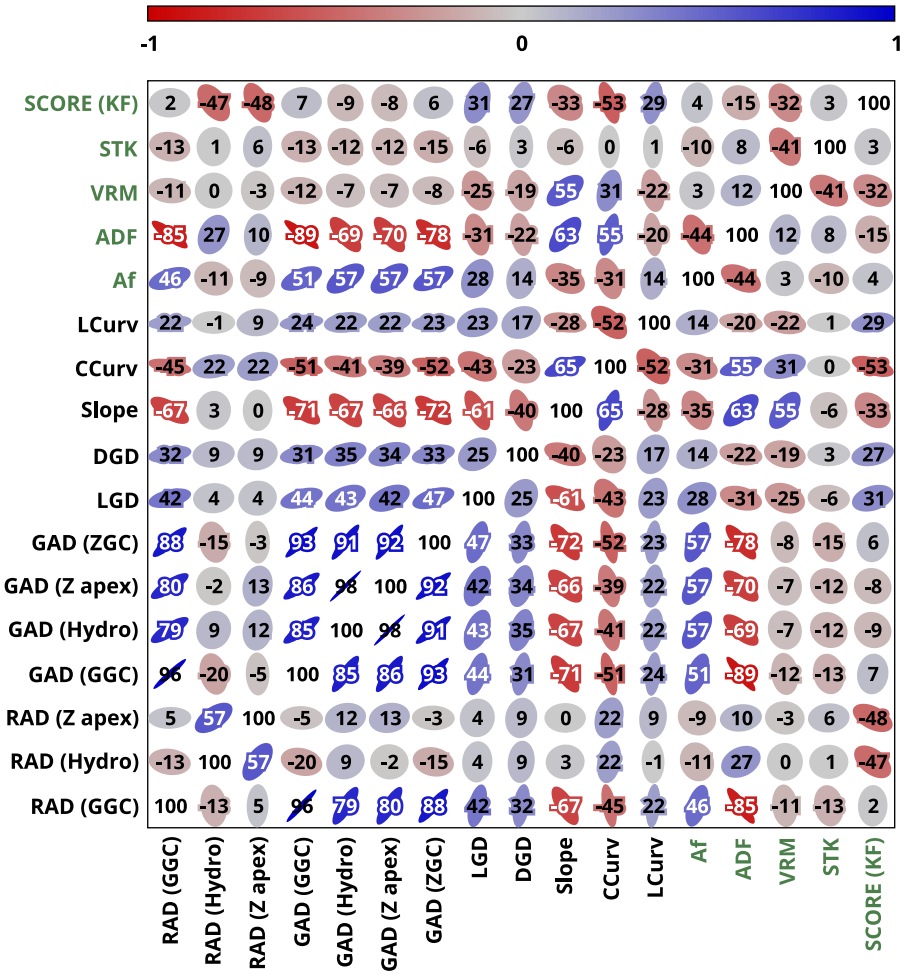


Supplement B.9: Arithmetic means and standard deviations of the segmentation parameters for bins of the SVM score (data basis: OBMA objects yielding SVM scores of −2 or better). (A) Spatial bandwidth h_s. (B) Range bandwidth h_r. (C) Slope area weighting (SAW). (D) Cross-sectional curvature weighting (CCW).

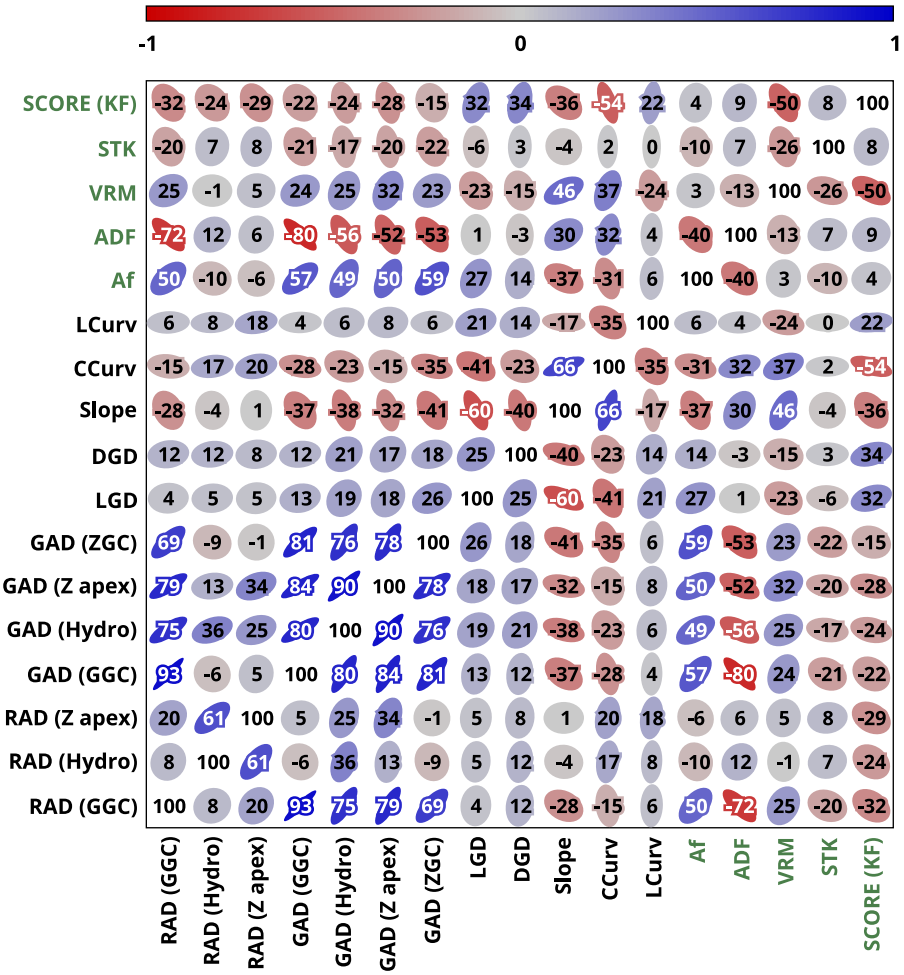
C Supplements, One-Class Random Forests as a robust approach to alluvial fan discrimination: A comparison of SRTM and ALOS World 3D



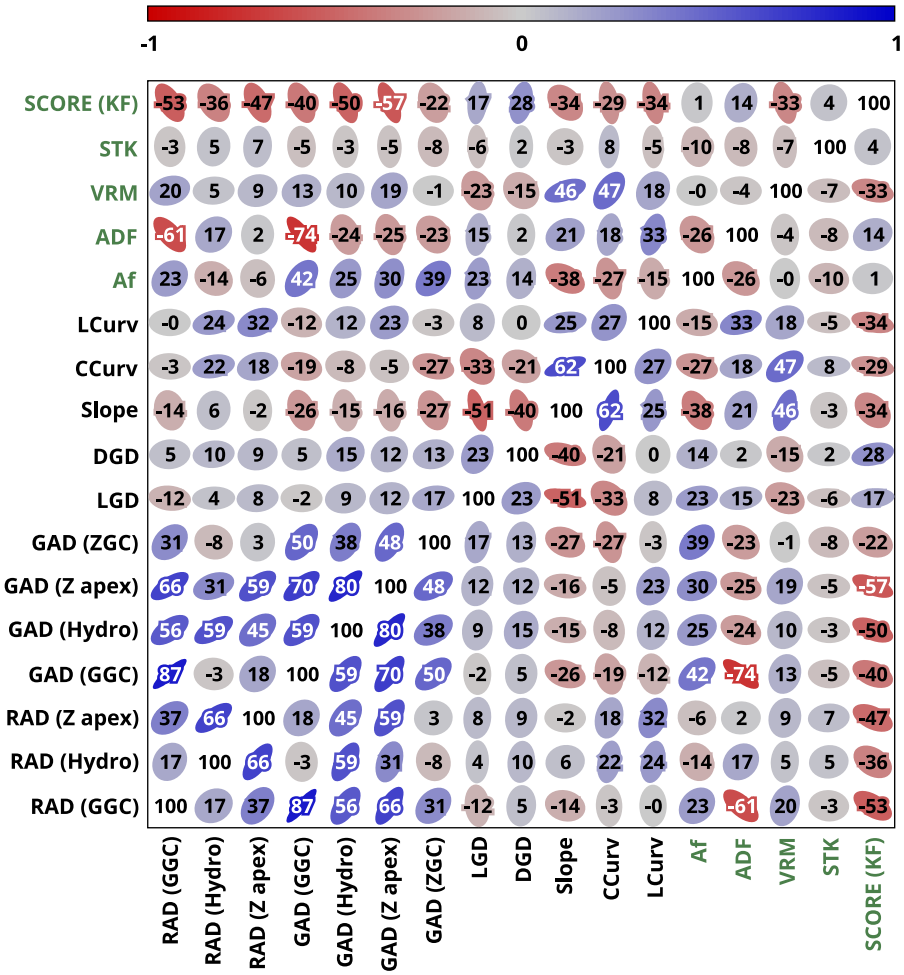
Supplement C.1: Workflow conducted to infill prominent incised channels.



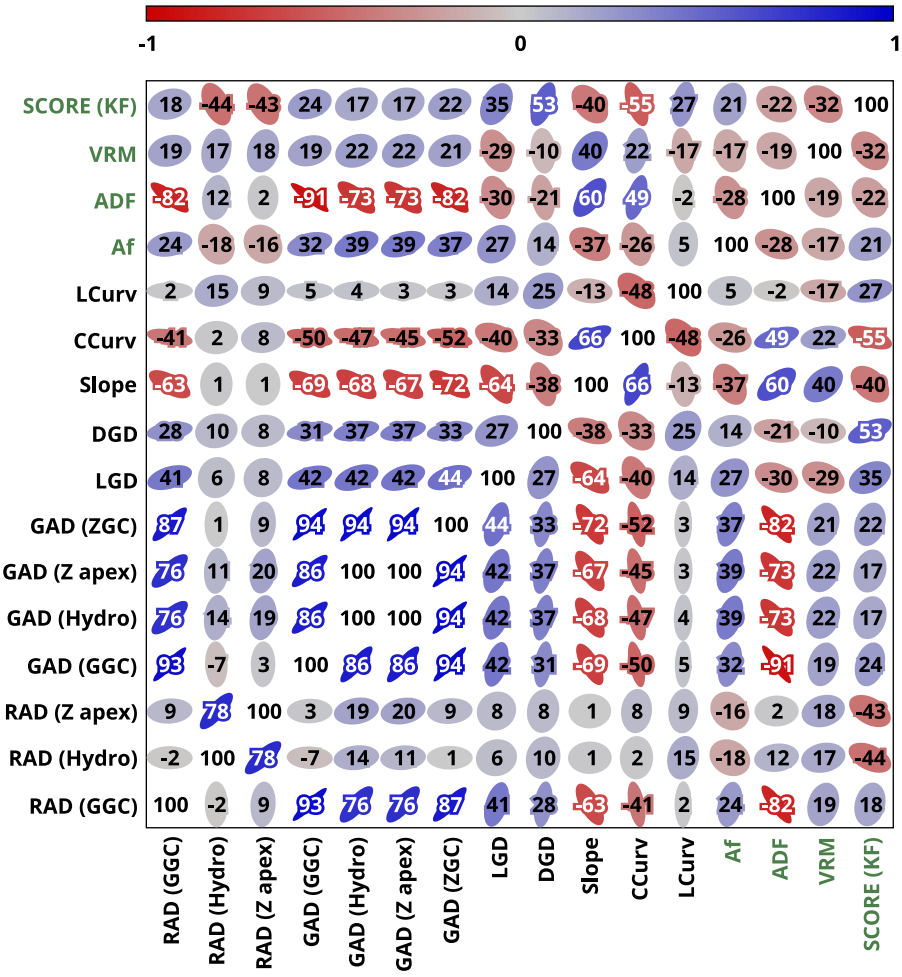
Supplement C.2: Matrix of product-moment correlation coefficients for the AW3D30 DEM with no filtering applied. Auxiliary variables and membership scores obtained via 10-fold (KF) cross-validation are denoted in green letters.



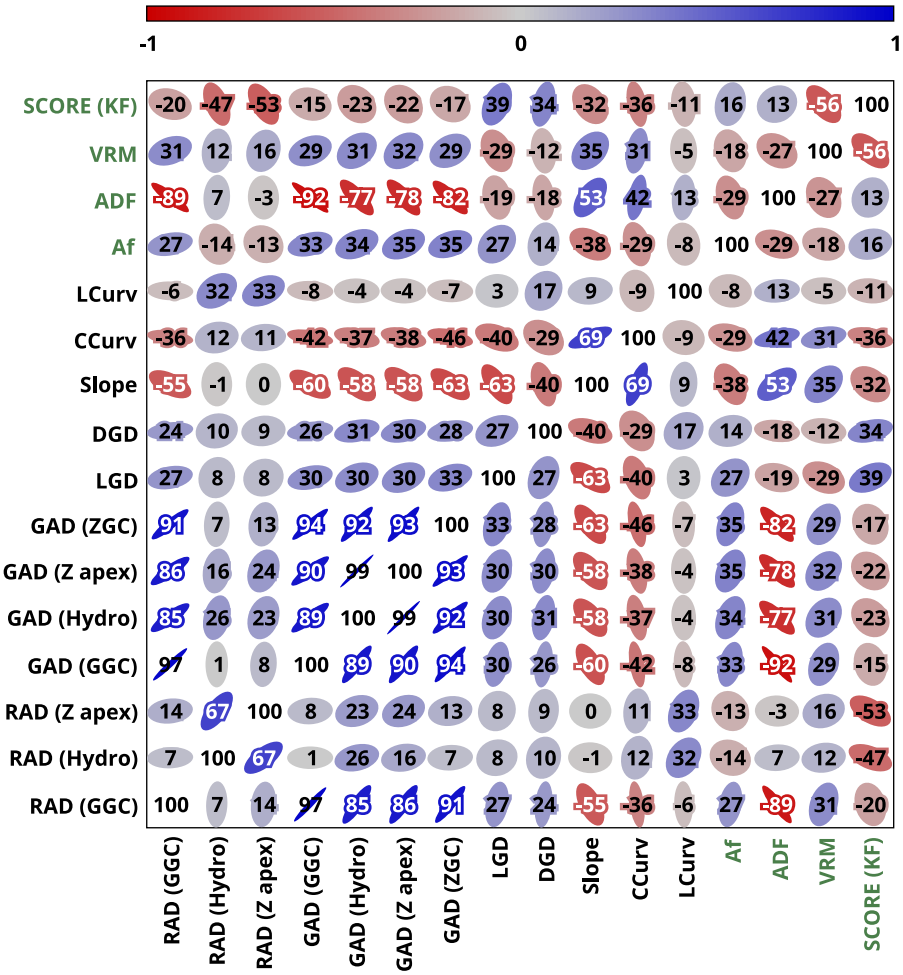
Supplement C.3: Matrix of product-moment correlation coefficients for the AW3D30 DEM with light filtering applied (t=.995, i=3). Auxiliary variables and membership scores obtained via 10-fold (KF) cross-validation are denoted in green letters.



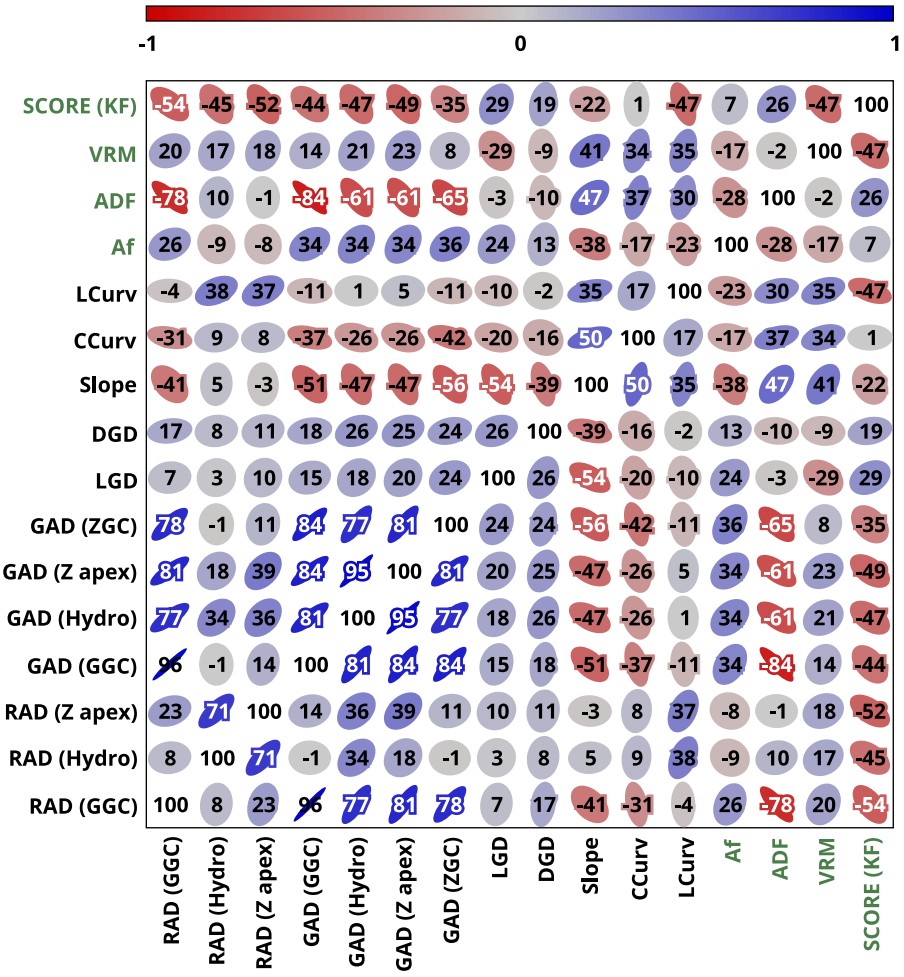
Supplement C.4: Matrix of product-moment correlation coefficients for the AW3D30 DEM with strong filtering applied (t=.99, i=10). Auxiliary variables and membership scores obtained via 10-fold (KF) cross-validation are denoted in green letters.



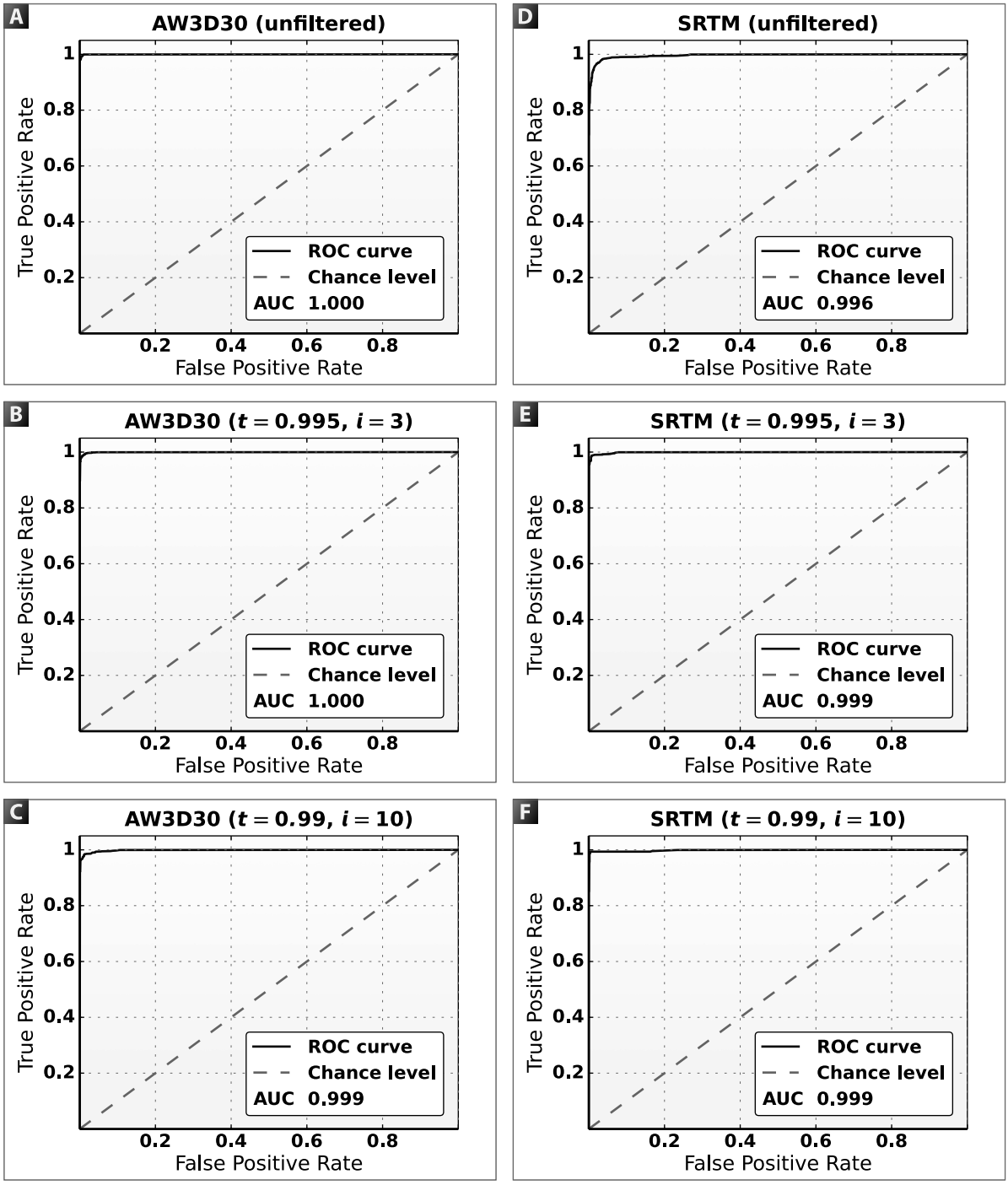
Supplement C.5: Matrix of product-moment correlation coefficients for the SRTM1 DEM with no filtering applied. Auxiliary variables and membership scores obtained via 10-fold (KF) cross-validation are denoted in green letters.



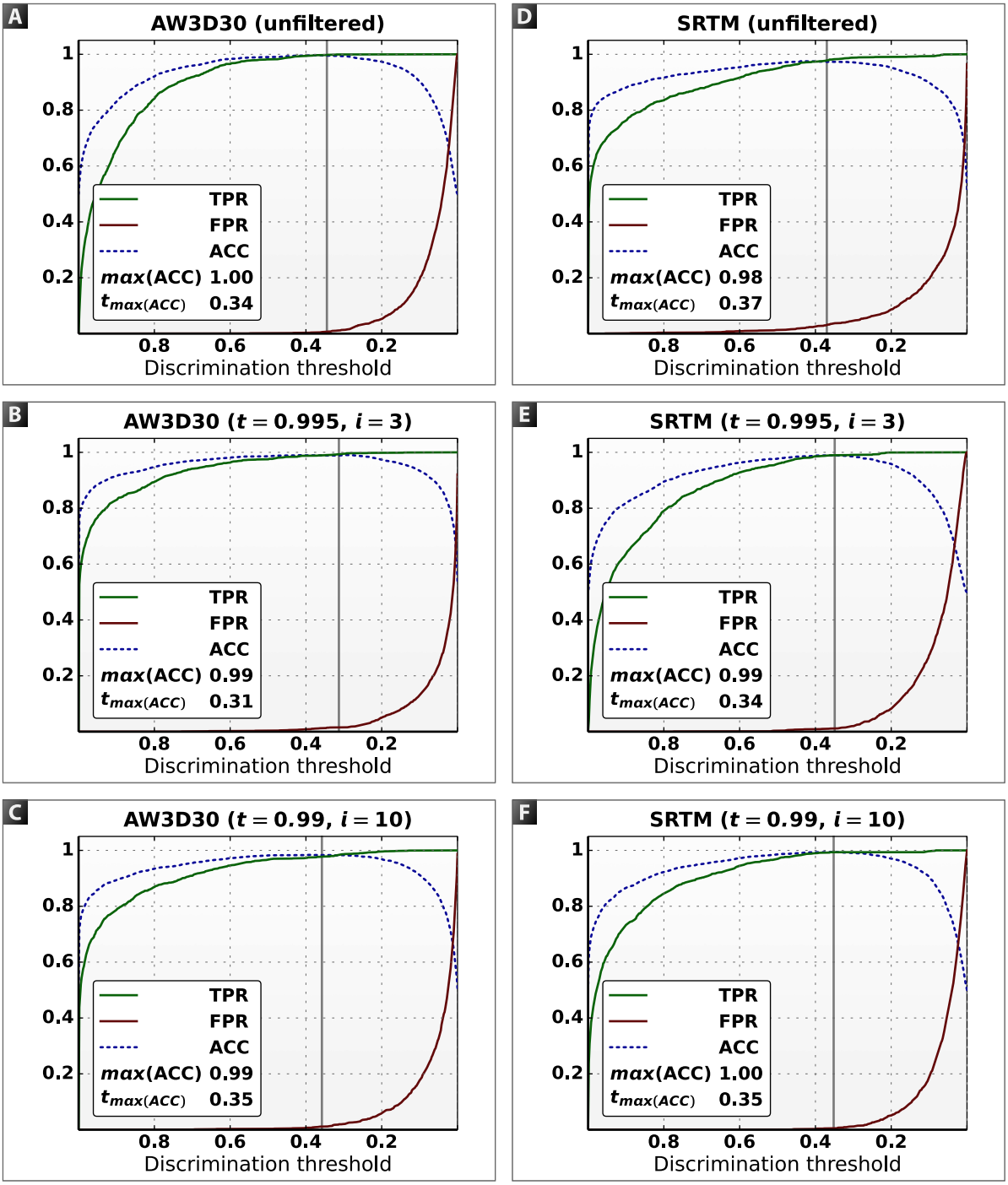
Supplement C.6: Matrix of product-moment correlation coefficients for the SRTM1 DEM with light filtering applied (t=.995, i=3). Auxiliary variables and membership scores obtained via 10-fold (KF) cross-validation are denoted in green letters.



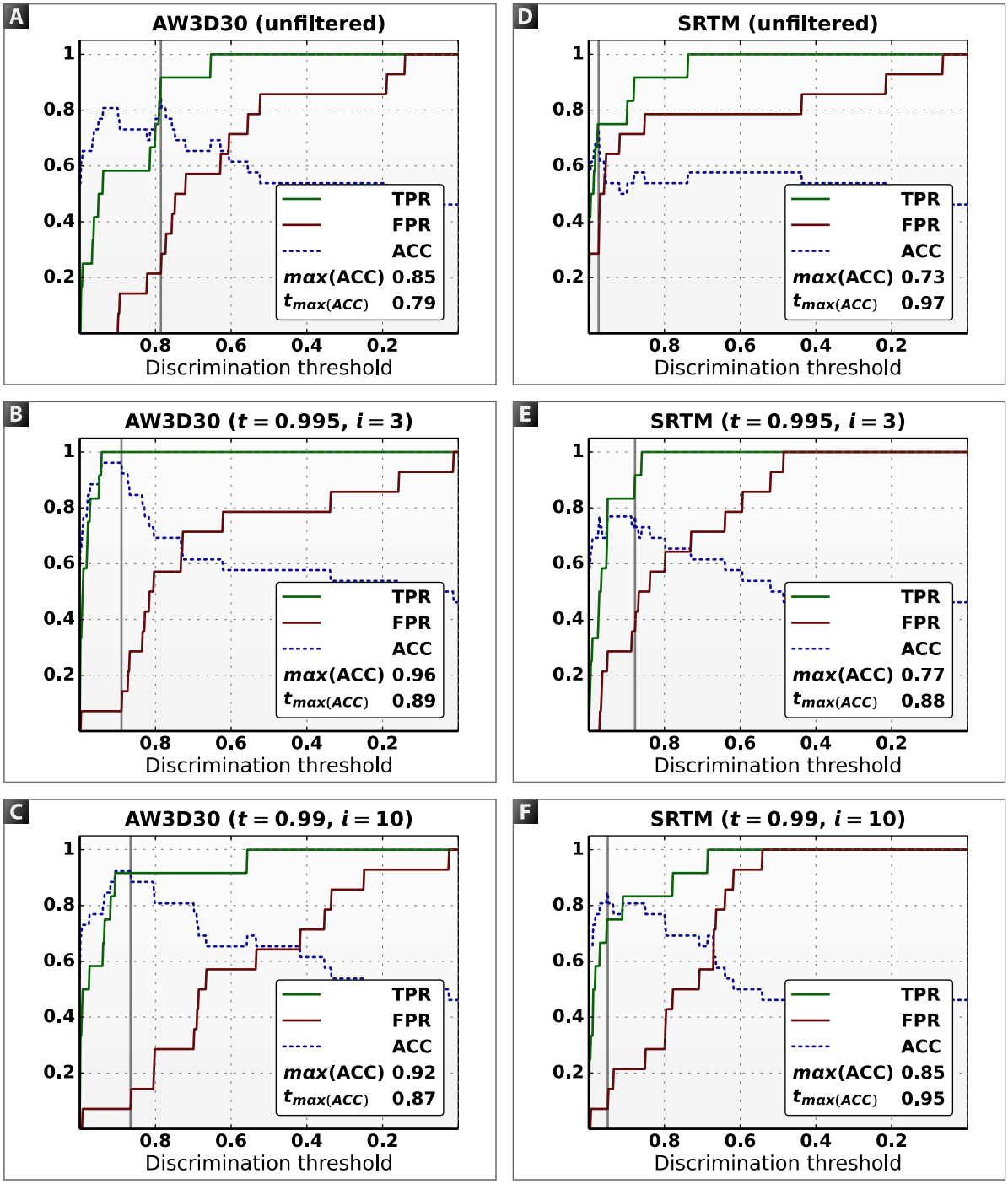
Supplement C.7: Matrix of product-moment correlation coefficients for the SRTM1 DEM with strong filtering applied (t=.99, i=10). Auxiliary variables and membership scores obtained via 10-fold (KF) cross-validation are denoted in green letters.



Supplement C.8: Receiver operating characteristic (ROC) plots obtained for the *training dataset* via 10-fold cross-validation. (A) AW3D30 DEM with no filtering applied, (B) AW3D30 DEM with light filtering applied (t=.995, i=3), (C) AW3D30 DEM with strong filtering applied (t=.99, i=10), (D) SRTM1 DEM with no filtering applied, (E) SRTM1 DEM with light filtering applied (t=.995, i=3), (F) SRTM1 DEM with strong filtering applied (t=.99, i=10).



Supplement C.9: True positive rates (TPRs), false positive rates (FPRs), and corresponding accuracy (ACC) scores, as obtained for the *training dataset* via 10-fold cross-validation. Variables are plotted against the threshold value used for binary discrimination. (A) AW3D30 DEM with no filtering applied, (B) AW3D30 DEM with light filtering applied (t=.995, i=3), (C) AW3D30 DEM with strong filtering applied (t=.99, i=10), (D) SRTM1 DEM with no filtering applied, (E) SRTM1 DEM with light filtering applied (t=.995, i=3), (F) SRTM1 DEM with strong filtering applied (t=.99, i=10).



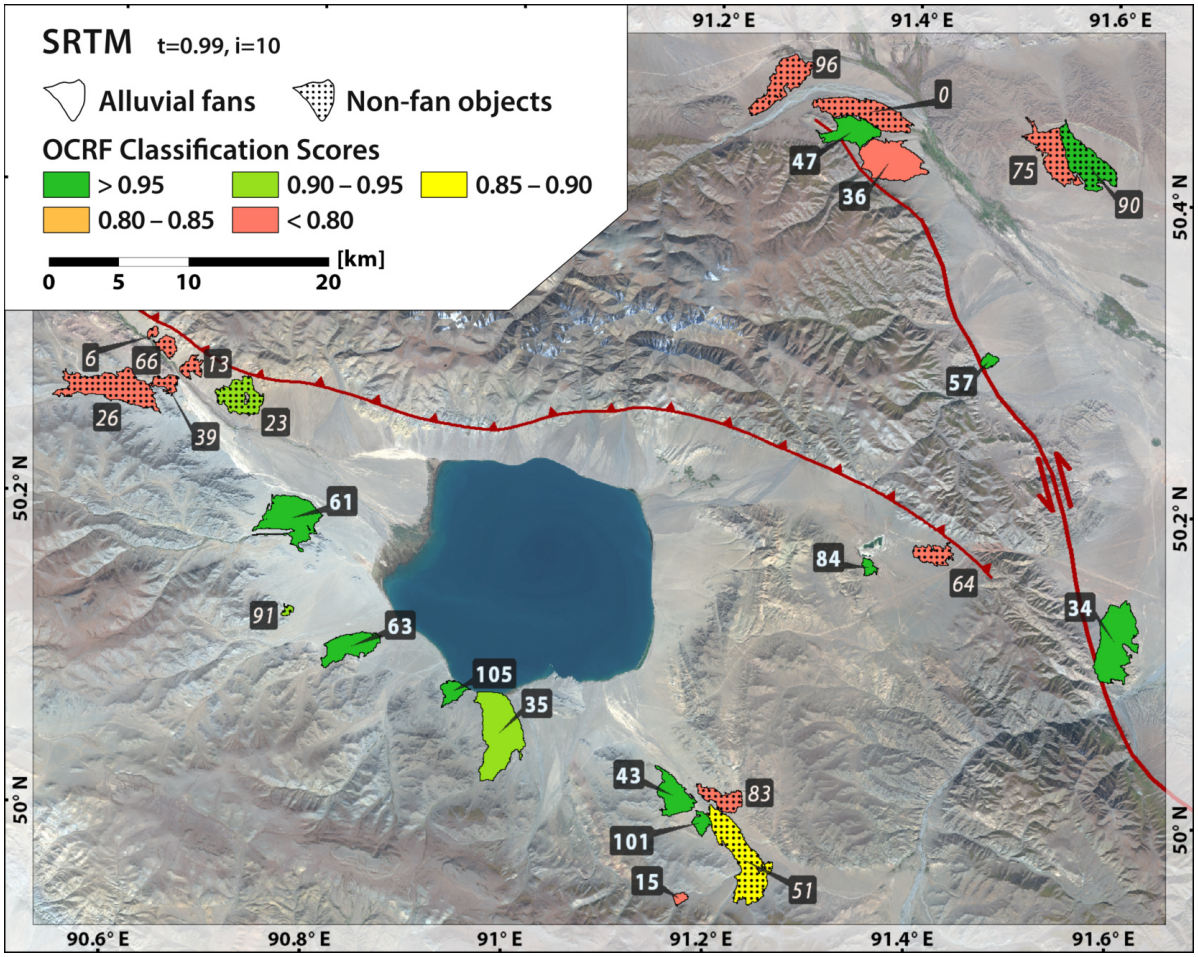
Supplement C.10: TPRs, FPRs, and corresponding ACC scores, as obtained for the *evaluation dataset*. Variables are plotted against the threshold value used for binary discrimination. (A) AW3D30 DEM with no filtering applied, (B) AW3D30 DEM with light filtering applied (t=.995, i=3), (C) AW3D30 DEM with strong filtering applied (t=.99, i=10), (D) SRTM1 DEM with no filtering applied, (E) SRTM1 DEM with light filtering applied (t=.995, i=3), (F) SRTM1 DEM with strong filtering applied (t=.99, i=10).

Supplement C.11: OCRF scores and morphometric parameter values (*Z*-standardized) for the *evaluation dataset*, as yielded by the best-performing AW3D30 variant (t=.995, i=3). Note that the evaluation dataset IDs (EID) are equivalent to the object IDs (OID) denoted in Pipaud and Lehmkuhl (2017 / Chapter 5). For a comparison with membership scores obtained by the OCSVM workflow employed in the aforementioned study, please refer to Suppl. B.8. (AF=Alluvial fans, AP=Alluvial plains, AS=Alluvial slopes)

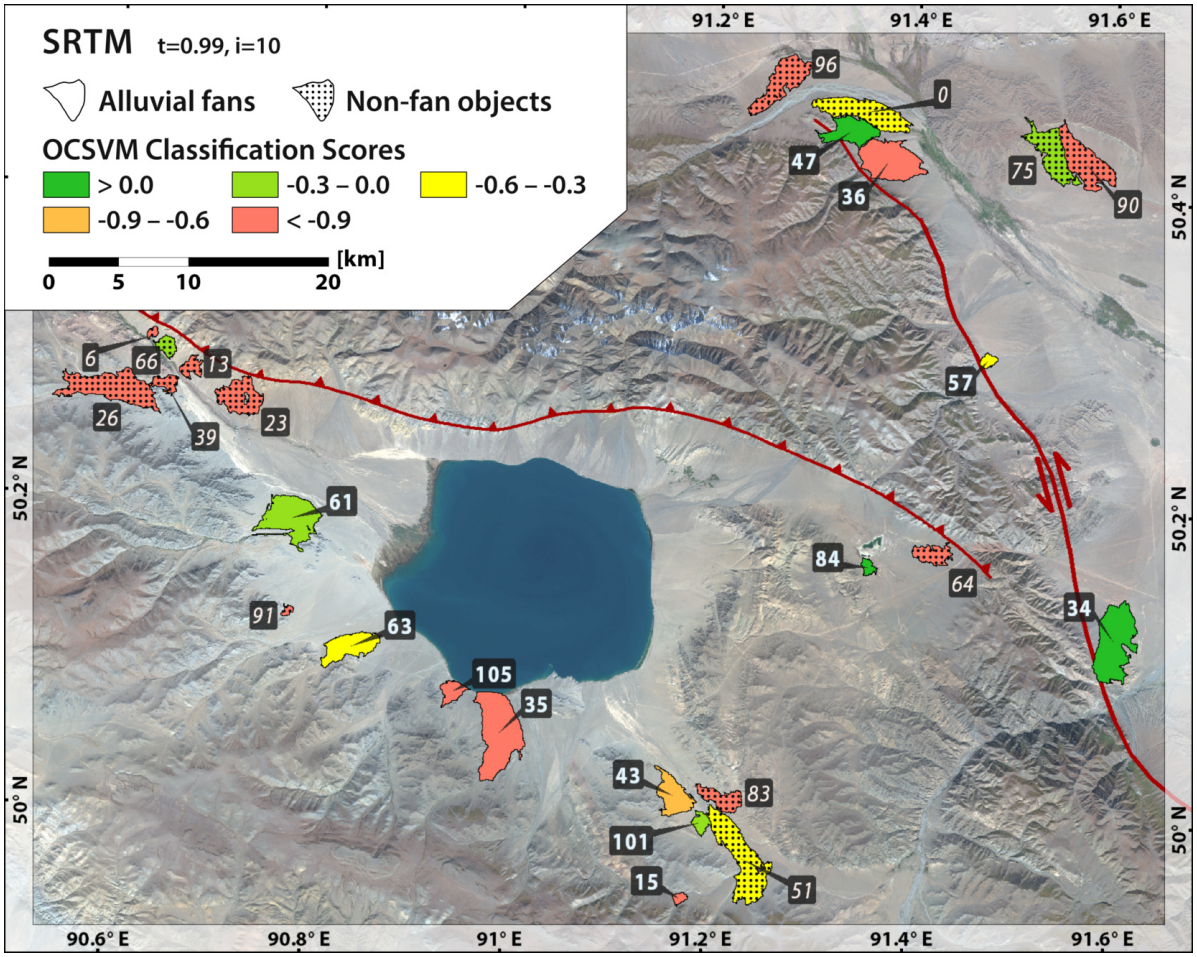
EID	Land-form	**OCRF Score**	RAD (GGC)	RAD (Hydro)	RAD (Z apex)	GAD (GGC)	GAD (Hydro)	GAD (Z apex)	GAD (ZGC)	LGD	DGD	Slope	CCurv	LCurv	Area	ADF	VRM	STK
15	AF	**0.99**	−0.53	1.74	0.87	−0.74	0.33	0.23	0.38	0.32	−0.31	0.30	−0.23	−1.20	−0.63	1.72	−0.48	−0.64
34	AF	**0.98**	−0.08	−0.11	−0.13	−0.02	0.18	0.32	1.59	−0.05	0.46	0.30	−0.91	0.48	−0.11	0.51	0.35	−0.32
35	AF	**0.95**	0.54	0.03	−0.64	0.99	0.93	−0.07	2.56	0.25	0.30	−0.17	−0.68	0.60	−0.03	−0.74	−0.31	−0.28
36	AF	**0.94**	−0.26	2.84	2.40	−0.46	1.36	1.34	1.34	−0.50	0.94	0.39	−0.59	0.46	−0.21	1.64	−0.31	−0.18
43	AF	**0.98**	−0.02	0.44	1.10	0.03	0.54	0.67	1.35	0.31	−0.61	0.34	0.40	−0.21	−0.43	0.54	0.76	−0.71
47	AF	**1.00**	−0.36	−0.88	−1.05	−0.18	−0.63	−0.78	−0.05	−0.15	0.47	0.20	−0.26	−0.66	−0.42	−0.26	−0.19	−0.54
57	AF	**1.00**	−0.89	−0.53	−0.51	−0.99	−0.59	−0.30	−0.82	0.05	0.48	0.49	0.50	0.41	−0.62	1.93	−0.43	−0.29
61	AF	**1.00**	0.01	−0.45	−1.21	0.61	−0.08	−0.17	0.40	0.94	0.59	−0.80	−0.58	−0.46	−0.22	−0.81	−0.40	−0.37
63	AF	**0.99**	−0.66	−1.15	−1.39	−0.27	−1.24	−1.18	−0.25	0.05	0.66	0.09	−0.31	−0.54	−0.40	0.04	−0.55	−0.50
84	AF	**0.97**	−0.45	0.19	0.53	−0.70	0.16	0.34	−0.41	1.26	0.05	−0.08	−0.73	−1.16	−0.62	2.18	−0.45	−0.82
101	AF	**1.00**	−0.53	−0.82	−0.87	−0.31	−0.75	−0.43	−0.54	0.28	0.48	0.11	−0.38	1.06	−0.60	0.35	−0.44	−0.60
105	AF	**1.00**	0.15	−0.58	−0.64	0.44	−0.17	−0.12	1.83	−0.16	−0.06	−0.24	−0.46	−0.11	−0.57	−0.40	−0.01	−0.52
0	AP	**0.82**	8.36	−0.47	−0.71	5.16	1.80	1.57	1.43	0.14	0.09	−0.54	−0.49	−0.21	−0.26	−2.75	0.28	−0.72
6	AS	**0.01**	1.89	−0.16	0.30	2.39	0.90	1.27	1.93	0.31	−6.33	2.59	1.99	−5.86	−0.64	−0.65	10.56	−1.28
13	AS	**0.16**	5.00	1.21	1.14	3.30	2.18	2.01	2.02	1.27	−1.69	2.24	−0.09	−3.42	−0.59	−1.57	14.54	−0.72
23	AS	**1.00**	−0.36	0.19	0.47	−0.45	0.22	0.41	−0.42	0.87	−0.62	1.83	−0.34	1.50	−0.39	1.73	1.25	−0.71
26	AP	**0.73**	5.44	−0.58	−0.96	3.86	0.99	0.43	3.68	−1.12	1.92	−0.31	−0.23	0.85	−0.17	−2.55	0.89	−1.49
39	AP	**0.62**	7.83	0.06	0.38	5.94	1.13	1.22	8.88	0.23	0.61	−0.33	−0.58	1.63	−0.59	−3.35	0.60	−0.85
51	AP	**0.83**	3.43	−0.13	0.57	3.51	1.39	1.74	1.33	−0.32	−0.81	−0.41	−0.51	0.23	−0.12	−1.13	−0.17	−0.63
64	AS	**0.89**	−0.40	−0.08	−0.17	−0.27	0.64	0.37	2.84	0.58	0.23	0.53	−1.14	−0.25	−0.53	0.52	−0.11	−0.90
66	AS	**0.34**	0.83	−0.31	0.53	1.03	0.37	0.96	0.34	0.02	−5.03	2.39	−0.48	−1.78	−0.59	−0.07	7.56	−1.09
75	AS	**0.87**	4.29	−0.76	−0.84	3.61	0.67	0.81	1.54	0.59	0.59	−0.35	−0.55	0.14	−0.33	−2.14	0.49	−0.10
83	AS	**0.83**	0.33	−0.29	−0.02	0.65	0.76	0.99	3.01	1.33	−0.42	0.55	−0.93	−0.05	−0.51	0.11	0.51	−0.47
90	AS	**0.81**	6.08	−0.88	−1.06	4.43	0.83	0.94	2.50	0.58	0.50	−0.56	−0.42	−0.24	−0.28	−2.67	0.85	−0.07
91	AS	**0.87**	2.90	−0.10	1.58	2.58	0.20	1.37	2.02	1.03	0.80	0.43	−0.32	0.85	−0.64	−1.38	0.04	−0.81
96	AP	**0.73**	5.09	−0.63	−0.76	3.55	0.87	0.53	2.67	1.75	0.43	−0.85	−0.64	−0.28	−0.32	−2.25	−0.52	−0.28

Supplement C.12: OCRF scores and morphometric parameter values (Z-standardized) for the *evaluation dataset*, as yielded by the best-performing SRTM1 variant (t=.99, i=10). Note that the evaluation dataset IDs (EID) are equivalent to the object IDs (OID) denoted in Pipaud and Lehmkuhl (2017 / Chapter 5). For a comparison with membership scores obtained by the OCSVM workflow employed in the aforementioned study, please refer to Suppl. B.8. (AF=Alluvial fans, AP=Alluvial plains, AS=Alluvial slopes)

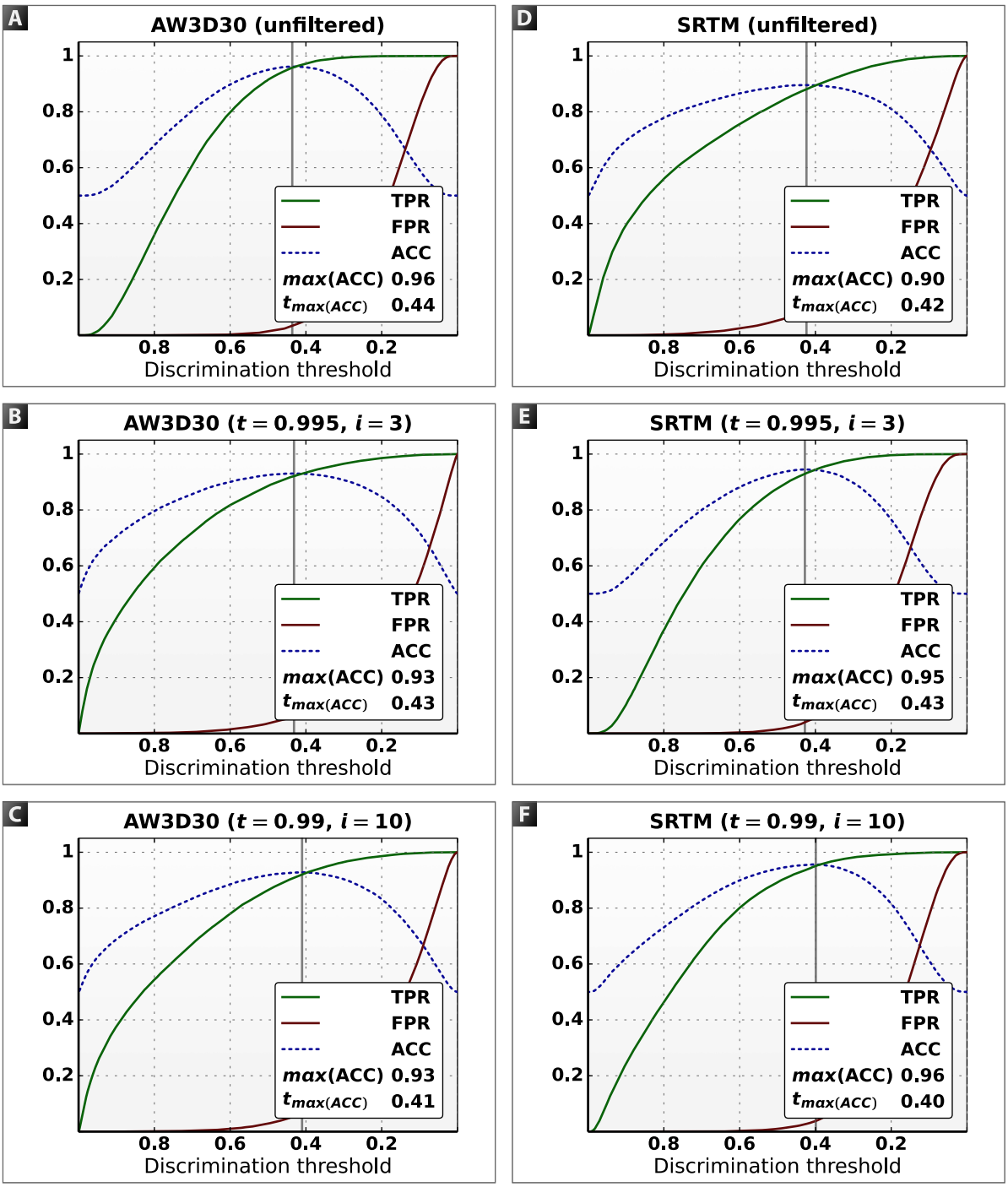
EID	Land-form	**OCRF Score**	RAD (GGC)	RAD (Hydro)	RAD (Z apex)	GAD (GGC)	GAD (Hydro)	GAD (Z apex)	GAD (ZGC)	LGD	DGD	Slope	CCurv	LCurv	Area	ADF	VRM
15	AF	**0.69**	−0.75	3.10	1.07	−0.96	1.37	<−0.01	0.46	−0.10	−1.13	0.27	0.24	−0.81	−0.63	2.17	−0.53
34	AF	**0.99**	−0.58	−0.01	−0.19	−0.69	−0.21	−0.19	0.74	−0.09	0.44	0.29	−0.51	−0.37	−0.11	0.86	−0.43
35	AF	**0.91**	−0.50	−0.48	−0.59	−0.23	−0.41	−0.46	1.78	0.18	0.29	−0.18	−0.65	−0.15	−0.03	0.15	−0.64
36	AF	**0.78**	−0.45	1.87	0.98	−0.61	1.19	0.38	0.89	−0.74	0.83	0.42	−1.00	−0.11	−0.21	1.81	−0.27
43	AF	**0.95**	−0.40	0.67	1.05	−0.54	−0.01	−0.01	0.61	0.23	−0.58	0.30	0.84	−0.81	−0.43	1.10	0.13
47	AF	**1.00**	−0.62	−0.89	−1.05	−0.53	−0.82	−1.02	−0.81	−0.23	0.42	0.20	−0.23	−0.45	−0.42	0.13	−0.49
57	AF	**0.97**	−0.89	−0.58	−0.40	−1.06	−0.69	−0.40	−1.14	−0.01	0.45	0.46	2.03	0.06	−0.62	2.12	−0.54
61	AF	**0.99**	−0.48	−0.48	−1.15	−0.18	−0.56	−0.61	−0.39	1.04	0.57	−0.84	−0.10	−0.55	−0.22	−0.35	−0.61
63	AF	**1.00**	−0.74	−0.77	−1.26	−0.51	−0.78	−1.14	−0.79	<−0.01	0.65	0.10	−0.06	−0.66	−0.40	0.24	−0.66
84	AF	**0.98**	−0.62	−0.14	0.47	−0.92	−0.51	−0.03	−0.99	1.03	−0.06	−0.10	−0.22	−1.16	−0.62	2.65	−0.59
101	AF	**1.00**	−0.65	−0.68	−0.58	−0.79	−0.86	−0.52	−0.90	0.36	0.41	0.11	0.56	−0.10	−0.60	1.13	−0.45
105	AF	**1.00**	−0.84	−0.71	−0.82	−0.96	−0.85	−0.80	−0.55	−0.11	−0.01	−0.27	−0.53	−0.29	−0.57	2.22	−0.67
0	AP	**0.64**	5.77	−0.76	−0.76	3.39	0.58	0.69	0.27	0.21	−0.11	−0.62	0.39	−0.59	−0.26	−2.13	−0.39
6	AS	**0.67**	−0.72	−0.19	0.30	−0.97	0.01	0.24	−1.22	0.41	−4.93	2.43	0.71	−2.56	−0.64	3.54	−0.34
13	AS	**0.62**	0.48	1.20	1.04	0.05	0.78	0.35	−0.68	1.40	−1.51	1.90	0.94	−2.12	−0.59	0.32	−0.27
23	AS	**0.93**	−0.76	0.77	0.53	−0.94	0.01	−0.12	−1.00	1.04	−0.66	1.83	0.34	0.63	−0.39	3.30	−0.59
26	AP	**0.67**	1.80	−0.87	−1.02	1.50	−0.36	−0.33	1.89	−1.54	2.08	−0.36	−0.40	−0.12	−0.17	−1.28	−0.45
39	AP	**0.54**	3.80	0.21	0.19	5.23	0.64	0.32	8.52	3.18	0.42	−0.38	−1.78	−0.11	−0.59	−2.99	−0.39
51	AP	**0.85**	0.99	−0.20	0.38	1.45	0.62	0.90	−0.07	−0.57	−0.84	−0.44	−0.23	−0.22	−0.12	−0.47	−0.56
64	AS	**0.80**	−0.69	−0.22	−0.27	−0.69	0.24	0.03	2.01	0.76	0.26	0.54	−1.34	−0.42	−0.53	1.35	−0.34
66	AS	**0.71**	−0.76	−0.31	0.57	−0.91	−0.47	0.01	−0.99	−0.10	−5.21	2.26	0.53	−2.00	−0.59	2.50	0.07
75	AS	**0.80**	2.11	−0.72	−0.83	1.97	−0.06	−0.02	0.51	0.48	0.57	−0.42	−0.25	−0.38	−0.33	−1.53	−0.46
83	AS	**0.67**	−0.64	−0.24	−0.11	−0.62	0.17	0.25	2.57	1.46	−0.38	0.52	−1.07	<−0.01	−0.51	1.70	−0.40
90	AS	**1.00**	−0.14	−0.94	−1.12	0.22	−0.77	−0.72	−0.30	0.49	0.49	−0.66	−0.36	−0.41	−0.28	−0.65	−0.61
91	AS	**0.95**	−0.72	−0.43	0.91	−0.90	−0.32	0.54	0.63	0.83	0.63	0.41	0.67	−1.26	−0.64	2.12	−0.53
96	AP	**0.78**	2.70	−0.65	−0.74	2.05	−0.08	−0.07	1.21	2.04	0.43	−0.87	−0.18	−0.84	−0.32	−1.52	−0.59



Supplement C.13: Membership likelihoods obtained for the evaluation dataset, using a OCRF being trained with morphometric data derived from the SRTM1 DEM with strong filtering applied (t=.99, i=10). Also depicted are the EIDs, with alluvial fans denoted in bold font, and null-class members EIDs denoted in italics. In comparison to the OCRF instance trained with AW3D30 DEM with light filtering applied (t=.995, i=3), the diagnostic ability is notably reduced. (Imagery source: Sentinel 2a)



Supplement C.14: Membership likelihoods obtained for the evaluation dataset, using a OCSVM being trained with morphometric data derived from the SRTM1 DEM with strong filtering applied (t=.99, i=10). Also depicted are the EIDs, with alluvial fans denoted in bold font, and null-class members EIDs denoted in italics. For the parametrization of the algorithm, please refer to Section 5.5. (Imagery source: Sentinel 2a)



Supplement C.15: TPRs, FPRs, and corresponding ACC scores, as obtained for the training dataset via reverse 10-fold cross-validation, that is, a k-fold cross-validation where one fold is used for training and all remaining folds are used for evaluation. Variables are plotted against the threshold value used for binary discrimination. (A) AW3D30 DEM with no filtering applied, (B) AW3D30 DEM with light filtering applied (t=.995, i=3), (C) AW3D30 DEM with strong filtering applied (t=.99, i=10), (D) SRTM1 DEM with no filtering applied, (E) SRTM1 DEM with light filtering applied (t=.995, i=3), (F) SRTM1 DEM with strong filtering applied (t=.99, i=10).

Supplement C.16: AUC scores obtained for all evaluated OCRF instances, sorted in descending order.

DEM		mtry	Kernel	Bandwidth estimation	AUC_{EV}
AW3D30	t=.995, i=3	9	Gaussian	NR	**0.952**
AW3D30	t=.995, i=3	8	Epanechnikov	CVML	**0.952**
AW3D30	t=.995, i=3	8	Gaussian	NR	**0.952**
AW3D30	t=.995, i=3	3	Gaussian	NR	**0.952**
AW3D30	t=.995, i=3	4	Gaussian	NR	**0.952**
AW3D30	t=.995, i=3	5	Gaussian	NR	**0.952**
AW3D30	t=.995, i=3	7	Gaussian	NR	**0.952**
AW3D30	t=.995, i=3	8	Gaussian	CVML	**0.952**
AW3D30	t=.995, i=3	9	Gaussian	CVML	**0.952**
AW3D30	t=.995, i=3	9	Epanechnikov	CVML	**0.952**
AW3D30	t=.995, i=3	6	Gaussian	NR	**0.950**
AW3D30	t=.995, i=3	3	Gaussian	CVML	**0.950**
AW3D30	t=.995, i=3	4	Gaussian	CVML	**0.950**
AW3D30	t=.995, i=3	5	Gaussian	CVML	**0.950**
AW3D30	t=.995, i=3	6	Gaussian	CVML	**0.950**
AW3D30	t=.995, i=3	7	Gaussian	CVML	**0.950**
AW3D30	t=.995, i=3	3	Epanechnikov	CVML	**0.950**
AW3D30	t=.995, i=3	4	Epanechnikov	CVML	**0.950**
AW3D30	t=.995, i=3	6	Epanechnikov	CVML	**0.950**
AW3D30	t=.995, i=3	7	Epanechnikov	CVML	**0.950**
AW3D30	t=.995, i=3	1	Gaussian	CVML	**0.943**
AW3D30	t=.995, i=3	1	Epanechnikov	CVML	**0.940**
AW3D30	t=.995, i=3	2	Epanechnikov	CVML	**0.940**
AW3D30	t=.995, i=3	5	Epanechnikov	CVML	**0.940**
AW3D30	t=.995, i=3	1	Gaussian	NR	**0.938**
AW3D30	t=.995, i=3	2	Gaussian	NR	**0.935**
AW3D30	t=.995, i=3	2	Gaussian	CVML	**0.935**
AW3D30	t=.99, i=10	5	Gaussian	NR	**0.920**
AW3D30	t=.99, i=10	5	Gaussian	CVML	**0.920**
AW3D30	t=.99, i=10	4	Epanechnikov	CVML	**0.920**
AW3D30	t=.99, i=10	5	Epanechnikov	CVML	**0.920**
AW3D30	t=.99, i=10	6	Gaussian	NR	**0.920**
AW3D30	t=.99, i=10	7	Gaussian	NR	**0.920**
AW3D30	t=.99, i=10	6	Gaussian	CVML	**0.920**
AW3D30	t=.99, i=10	6	Epanechnikov	CVML	**0.920**
AW3D30	t=.99, i=10	1	Epanechnikov	CVML	**0.917**
AW3D30	t=.99, i=10	4	Gaussian	NR	**0.917**
AW3D30	t=.99, i=10	9	Gaussian	NR	**0.917**
AW3D30	t=.99, i=10	4	Gaussian	CVML	**0.917**
AW3D30	t=.99, i=10	8	Gaussian	NR	**0.914**
AW3D30	t=.99, i=10	7	Gaussian	CVML	**0.914**
AW3D30	t=.99, i=10	8	Epanechnikov	CVML	**0.914**
AW3D30	t=.99, i=10	2	Gaussian	NR	**0.911**

Supplement C.16 (cont.)

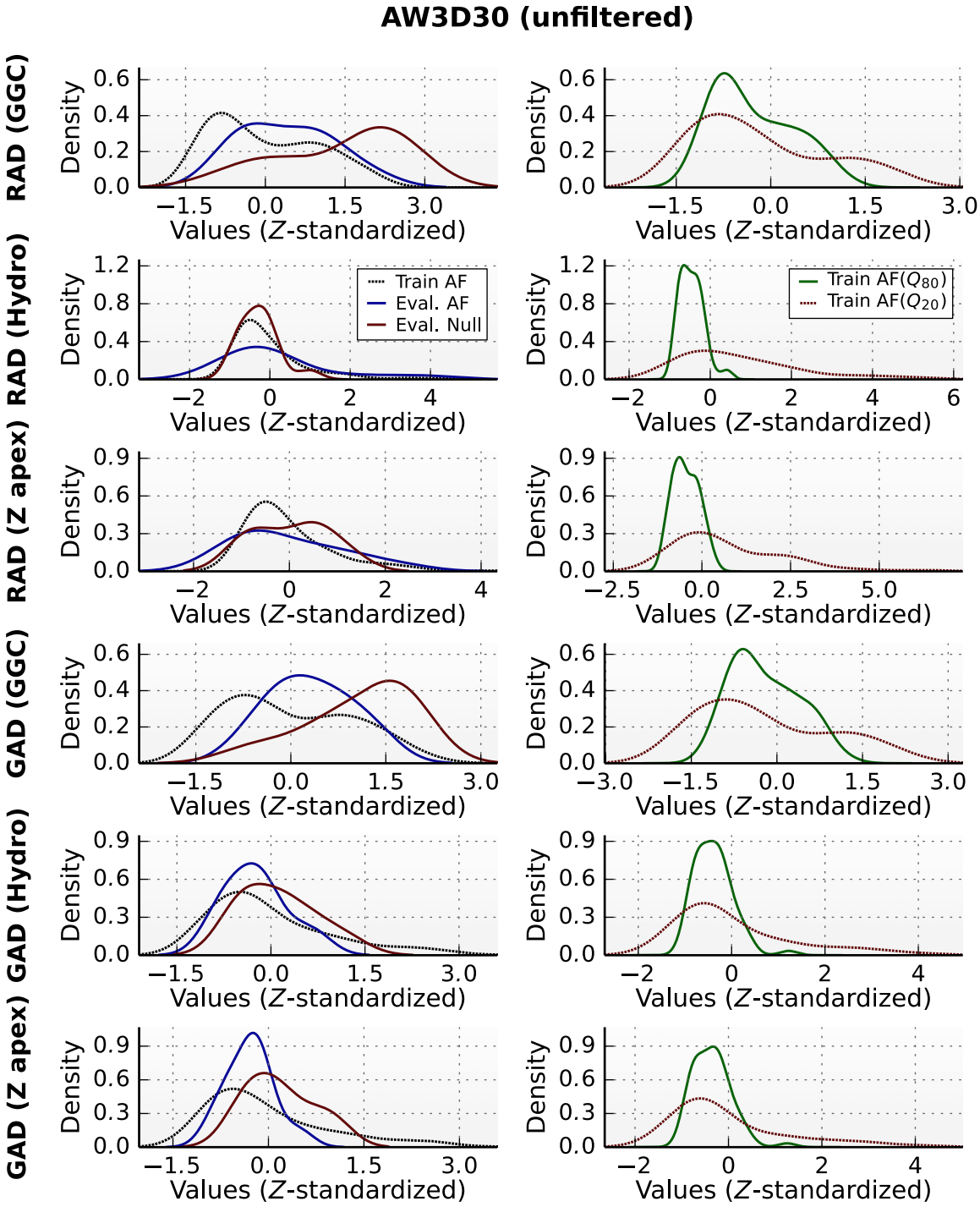
DEM		mtry	Kernel	Bandwidth estimation	AUC_{EV}
AW3D30	t=.99, i=10	3	Gaussian	NR	**0.911**
AW3D30	t=.99, i=10	2	Gaussian	CVML	**0.911**
AW3D30	t=.99, i=10	2	Epanechnikov	CVML	**0.911**
AW3D30	t=.99, i=10	3	Epanechnikov	CVML	**0.911**
AW3D30	t=.99, i=10	7	Epanechnikov	CVML	**0.911**
AW3D30	t=.99, i=10	1	Gaussian	NR	**0.905**
AW3D30	t=.99, i=10	1	Gaussian	CVML	**0.905**
AW3D30	t=.99, i=10	3	Gaussian	CVML	**0.905**
AW3D30	t=.99, i=10	8	Gaussian	CVML	**0.899**
AW3D30	t=.99, i=10	9	Gaussian	CVML	**0.899**
AW3D30	t=.99, i=10	9	Epanechnikov	CVML	**0.899**
AW3D30	unfiltered	1	Epanechnikov	CVML	**0.881**
AW3D30	unfiltered	1	Gaussian	CVML	**0.869**
AW3D30	unfiltered	1	Gaussian	NR	**0.866**
SRTM1	t=.99, i=10	1	Gaussian	CVML	**0.863**
SRTM1	t=.99, i=10	1	Epanechnikov	CVML	**0.863**
SRTM1	t=.995, i=3	1	Gaussian	CVML	**0.861**
SRTM1	t=.99, i=10	1	Gaussian	NR	**0.857**
SRTM1	t=.995, i=3	1	Epanechnikov	CVML	**0.851**
SRTM1	t=.995, i=3	1	Gaussian	NR	**0.845**
AW3D30	unfiltered	2	Gaussian	CVML	**0.839**
AW3D30	unfiltered	2	Epanechnikov	CVML	**0.839**
AW3D30	unfiltered	2	Gaussian	NR	**0.839**
SRTM1	t=.99, i=10	3	Gaussian	NR	**0.836**
SRTM1	t=.99, i=10	3	Gaussian	CVML	**0.833**
SRTM1	t=.99, i=10	4	Gaussian	CVML	**0.833**
SRTM1	t=.99, i=10	3	Epanechnikov	CVML	**0.830**
SRTM1	t=.99, i=10	4	Gaussian	NR	**0.830**
SRTM1	t=.99, i=10	5	Gaussian	CVML	**0.830**
SRTM1	t=.99, i=10	2	Gaussian	NR	**0.827**
SRTM1	t=.99, i=10	2	Epanechnikov	CVML	**0.827**
SRTM1	t=.99, i=10	5	Gaussian	NR	**0.827**
SRTM1	t=.99, i=10	4	Epanechnikov	CVML	**0.827**
SRTM1	t=.99, i=10	2	Gaussian	CVML	**0.824**
SRTM1	t=.99, i=10	5	Epanechnikov	CVML	**0.824**
SRTM1	t=.99, i=10	7	Gaussian	NR	**0.818**
SRTM1	t=.99, i=10	8	Gaussian	NR	**0.818**
SRTM1	t=.99, i=10	8	Epanechnikov	CVML	**0.818**
SRTM1	t=.99, i=10	7	Gaussian	CVML	**0.815**
SRTM1	t=.99, i=10	6	Gaussian	CVML	**0.815**
SRTM1	t=.99, i=10	8	Gaussian	CVML	**0.813**
SRTM1	t=.99, i=10	6	Gaussian	NR	**0.813**
SRTM1	t=.99, i=10	6	Epanechnikov	CVML	**0.810**

Supplement C.16 (cont.)

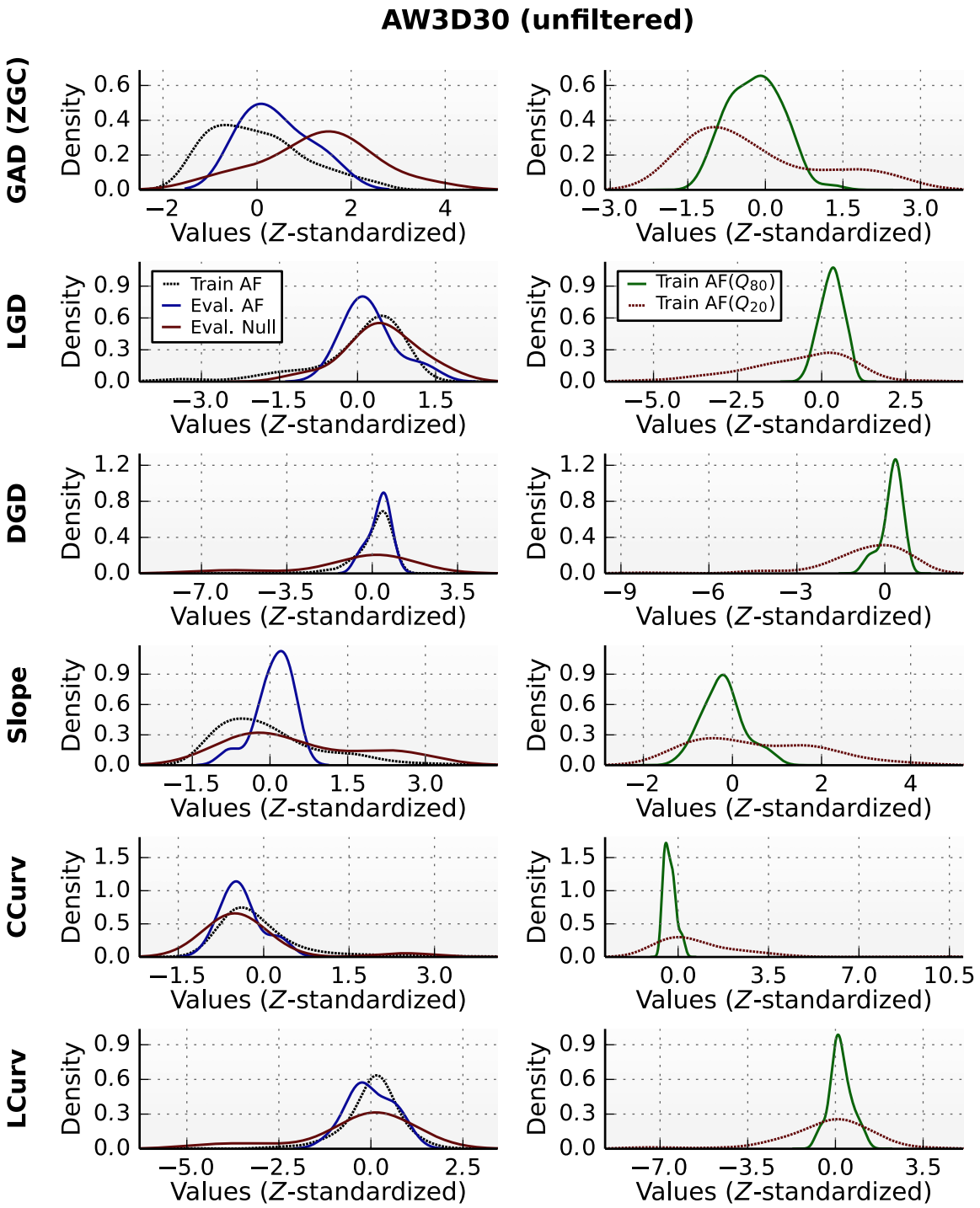
DEM		mtry	Kernel	Bandwidth estimation	AUC_{EV}
SRTM1	t=.99, i=10	7	Epanechnikov	CVML	**0.807**
AW3D30	unfiltered	3	Gaussian	NR	**0.804**
SRTM1	t=.99, i=10	9	Gaussian	CVML	**0.804**
SRTM1	t=.99, i=10	9	Epanechnikov	CVML	**0.804**
AW3D30	unfiltered	3	Epanechnikov	CVML	**0.801**
SRTM1	t=.995, i=3	2	Gaussian	CVML	**0.801**
SRTM1	t=.99, i=10	9	Gaussian	NR	**0.801**
AW3D30	unfiltered	3	Gaussian	CVML	**0.798**
SRTM1	t=.995, i=3	2	Gaussian	NR	**0.798**
SRTM1	t=.995, i=3	2	Epanechnikov	CVML	**0.798**
AW3D30	unfiltered	4	Gaussian	CVML	**0.792**
AW3D30	unfiltered	4	Gaussian	NR	**0.789**
AW3D30	unfiltered	4	Epanechnikov	CVML	**0.783**
SRTM1	t=.995, i=3	3	Gaussian	CVML	**0.777**
SRTM1	t=.995, i=3	4	Epanechnikov	CVML	**0.777**
SRTM1	t=.995, i=3	3	Gaussian	NR	**0.765**
SRTM1	t=.995, i=3	4	Gaussian	NR	**0.762**
SRTM1	t=.995, i=3	4	Gaussian	CVML	**0.762**
SRTM1	t=.995, i=3	8	Gaussian	CVML	**0.762**
SRTM1	t=.995, i=3	3	Epanechnikov	CVML	**0.762**
AW3D30	unfiltered	6	Epanechnikov	CVML	**0.759**
AW3D30	unfiltered	8	Epanechnikov	CVML	**0.756**
SRTM1	t=.995, i=3	8	Epanechnikov	CVML	**0.756**
AW3D30	unfiltered	9	Epanechnikov	CVML	**0.753**
AW3D30	unfiltered	6	Gaussian	CVML	**0.753**
AW3D30	unfiltered	9	Gaussian	CVML	**0.750**
AW3D30	unfiltered	5	Epanechnikov	CVML	**0.750**
SRTM1	t=.995, i=3	9	Gaussian	NR	**0.750**
AW3D30	unfiltered	8	Gaussian	CVML	**0.750**
AW3D30	unfiltered	9	Gaussian	NR	**0.747**
AW3D30	unfiltered	5	Gaussian	CVML	**0.747**
SRTM1	t=.995, i=3	6	Gaussian	NR	**0.747**
SRTM1	t=.995, i=3	5	Gaussian	CVML	**0.747**
SRTM1	t=.995, i=3	6	Gaussian	CVML	**0.747**
SRTM1	t=.995, i=3	7	Gaussian	CVML	**0.747**
SRTM1	t=.995, i=3	7	Epanechnikov	CVML	**0.747**
SRTM1	t=.995, i=3	5	Gaussian	NR	**0.747**
SRTM1	t=.995, i=3	5	Epanechnikov	CVML	**0.747**
SRTM1	t=.995, i=3	6	Epanechnikov	CVML	**0.747**
SRTM1	t=.995, i=3	9	Epanechnikov	CVML	**0.747**
AW3D30	unfiltered	5	Gaussian	NR	**0.744**
SRTM1	t=.995, i=3	9	Gaussian	CVML	**0.744**
AW3D30	unfiltered	7	Epanechnikov	CVML	**0.744**

Supplement C.16 (cont.)

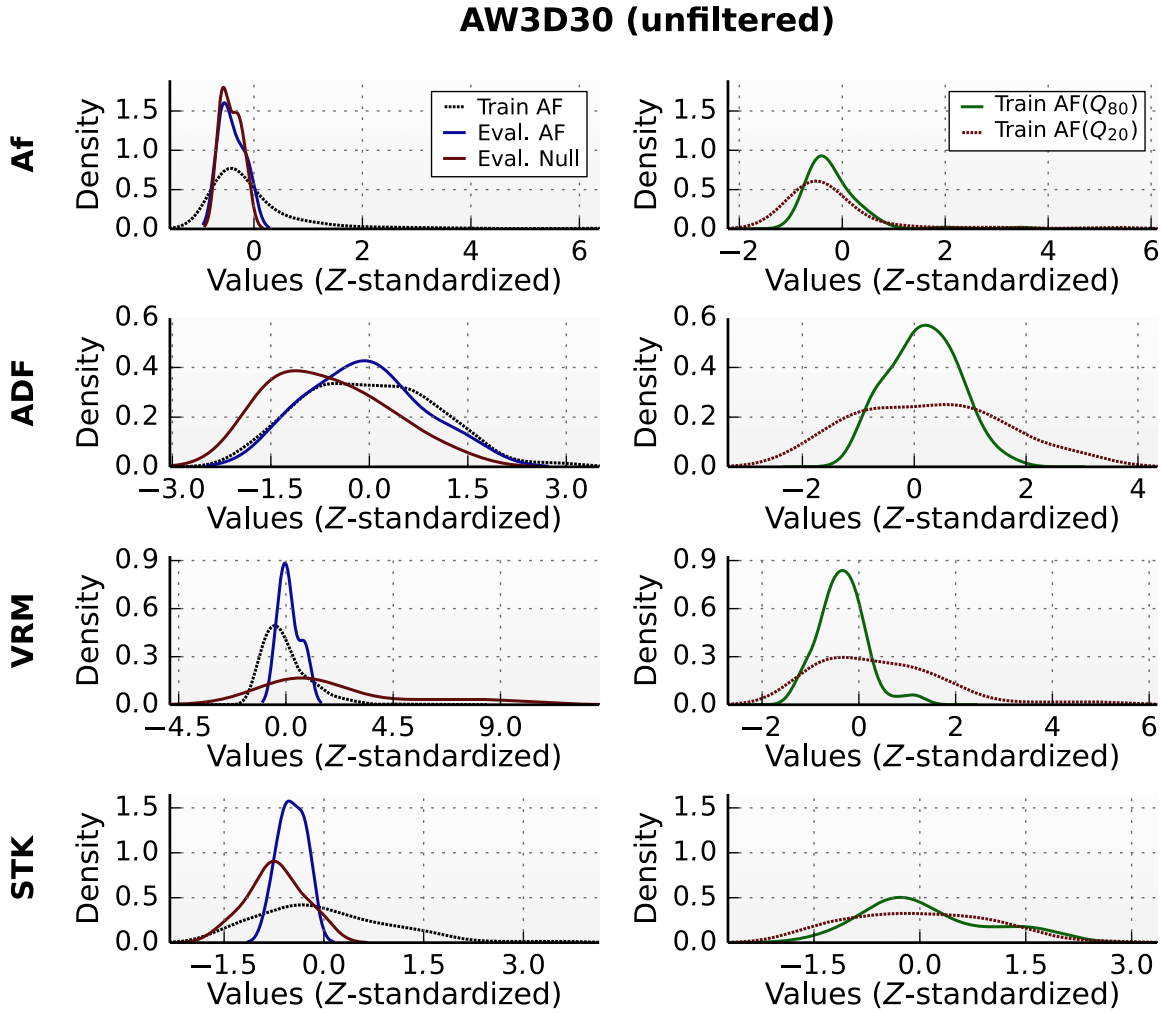
DEM		mtry	Kernel	Bandwidth estimation	AUC_{EV}
SRTM1	t=.995, i=3	7	Gaussian	NR	**0.744**
AW3D30	unfiltered	7	Gaussian	CVML	**0.741**
SRTM1	t=.995, i=3	8	Gaussian	NR	**0.741**
AW3D30	unfiltered	8	Gaussian	NR	**0.732**
AW3D30	unfiltered	6	Gaussian	NR	**0.729**
AW3D30	unfiltered	7	Gaussian	NR	**0.726**
SRTM1	unfiltered	8	Gaussian	CVML	**0.661**
SRTM1	unfiltered	6	Gaussian	CVML	**0.661**
SRTM1	unfiltered	6	Gaussian	NR	**0.658**
SRTM1	unfiltered	8	Gaussian	NR	**0.658**
SRTM1	unfiltered	7	Gaussian	NR	**0.655**
SRTM1	unfiltered	5	Gaussian	CVML	**0.652**
SRTM1	unfiltered	7	Epanechnikov	CVML	**0.652**
SRTM1	unfiltered	9	Gaussian	NR	**0.649**
SRTM1	unfiltered	8	Epanechnikov	CVML	**0.649**
SRTM1	unfiltered	6	Epanechnikov	CVML	**0.646**
SRTM1	unfiltered	7	Gaussian	CVML	**0.646**
SRTM1	unfiltered	4	Epanechnikov	CVML	**0.646**
SRTM1	unfiltered	9	Epanechnikov	CVML	**0.640**
SRTM1	unfiltered	2	Gaussian	CVML	**0.640**
SRTM1	unfiltered	9	Gaussian	CVML	**0.637**
SRTM1	unfiltered	3	Epanechnikov	CVML	**0.637**
SRTM1	unfiltered	5	Epanechnikov	CVML	**0.634**
SRTM1	unfiltered	3	Gaussian	NR	**0.628**
SRTM1	unfiltered	2	Epanechnikov	CVML	**0.628**
SRTM1	unfiltered	5	Gaussian	NR	**0.625**
SRTM1	unfiltered	1	Epanechnikov	CVML	**0.622**
SRTM1	unfiltered	1	Gaussian	CVML	**0.619**
SRTM1	unfiltered	2	Gaussian	NR	**0.616**
SRTM1	unfiltered	4	Gaussian	CVML	**0.616**
SRTM1	unfiltered	1	Gaussian	NR	**0.613**
SRTM1	unfiltered	4	Gaussian	NR	**0.610**
SRTM1	unfiltered	3	Gaussian	CVML	**0.604**



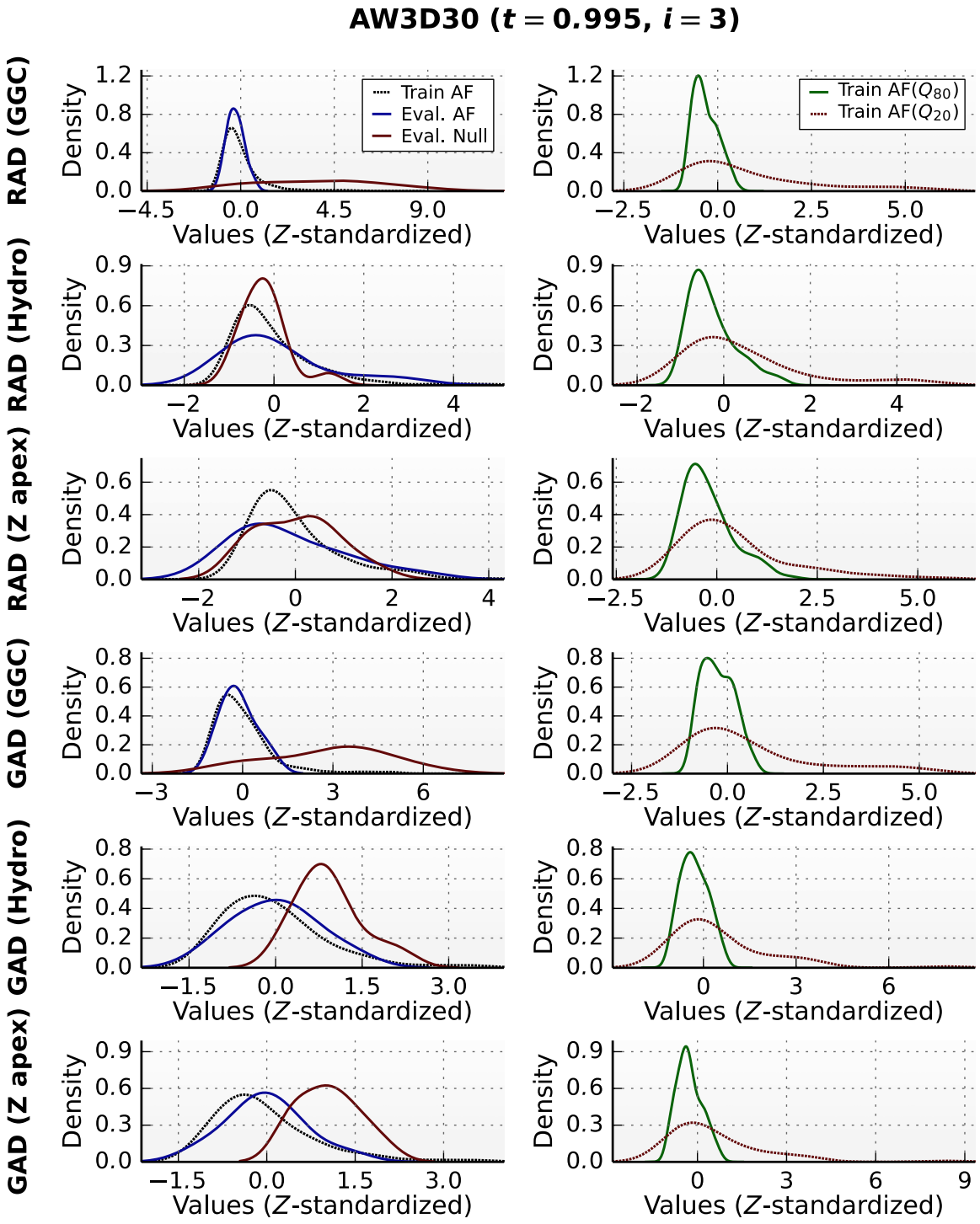
Supplement C.17: Empirical probability density plots for all morphometric variables used to train the OCRF, as well as auxiliary parameters considered for evaluation purposes. All KDE instances use a Gaussian kernel and the normal reference (NR) method for bandwidth estimation. Z-standardization was carried out using the respective arithmetic mean and standard deviation of the training dataset. Depicted are the density curves as obtained by using AW3D30 DEM with no filtering applied.



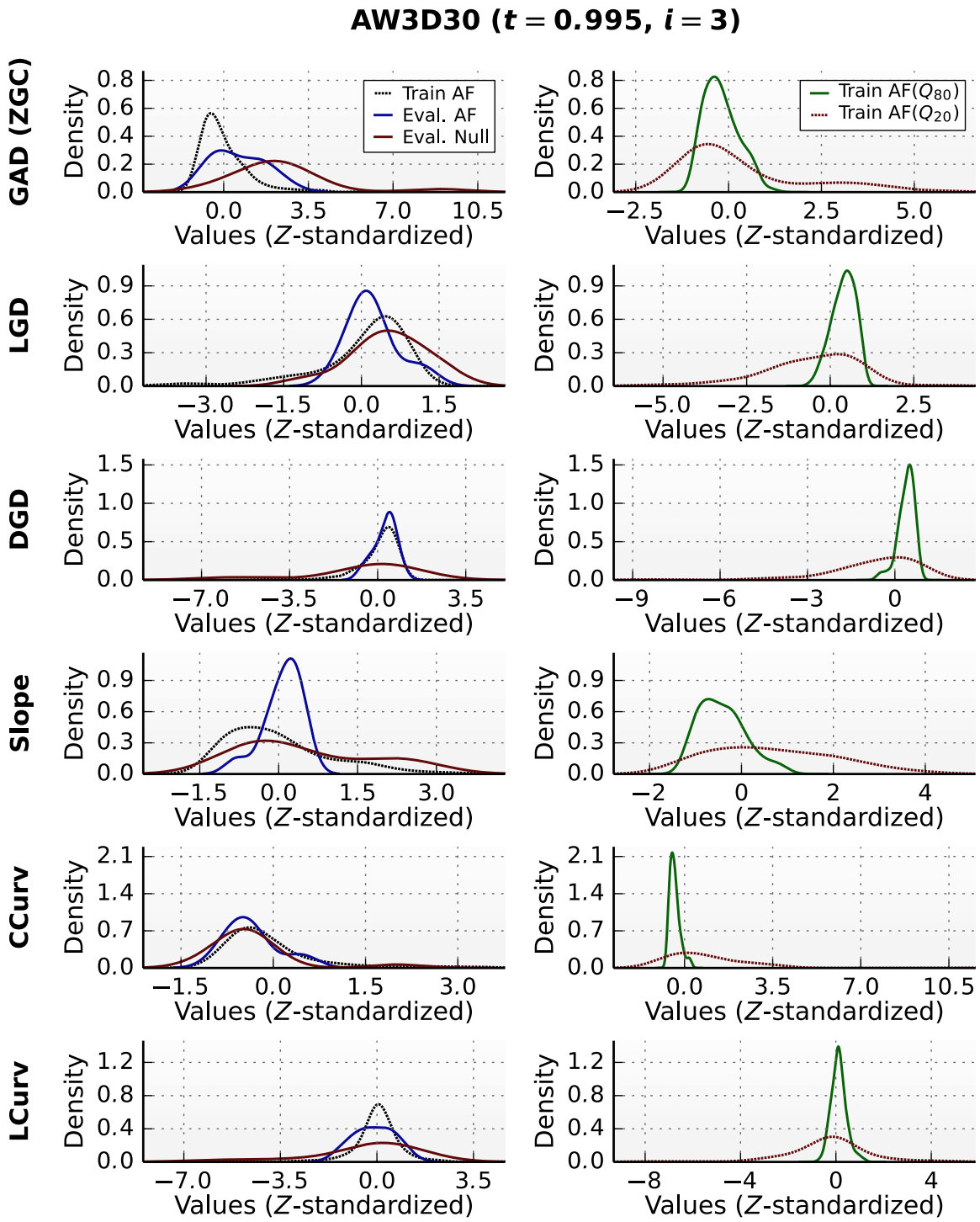
Supplement C.17 (cont.)



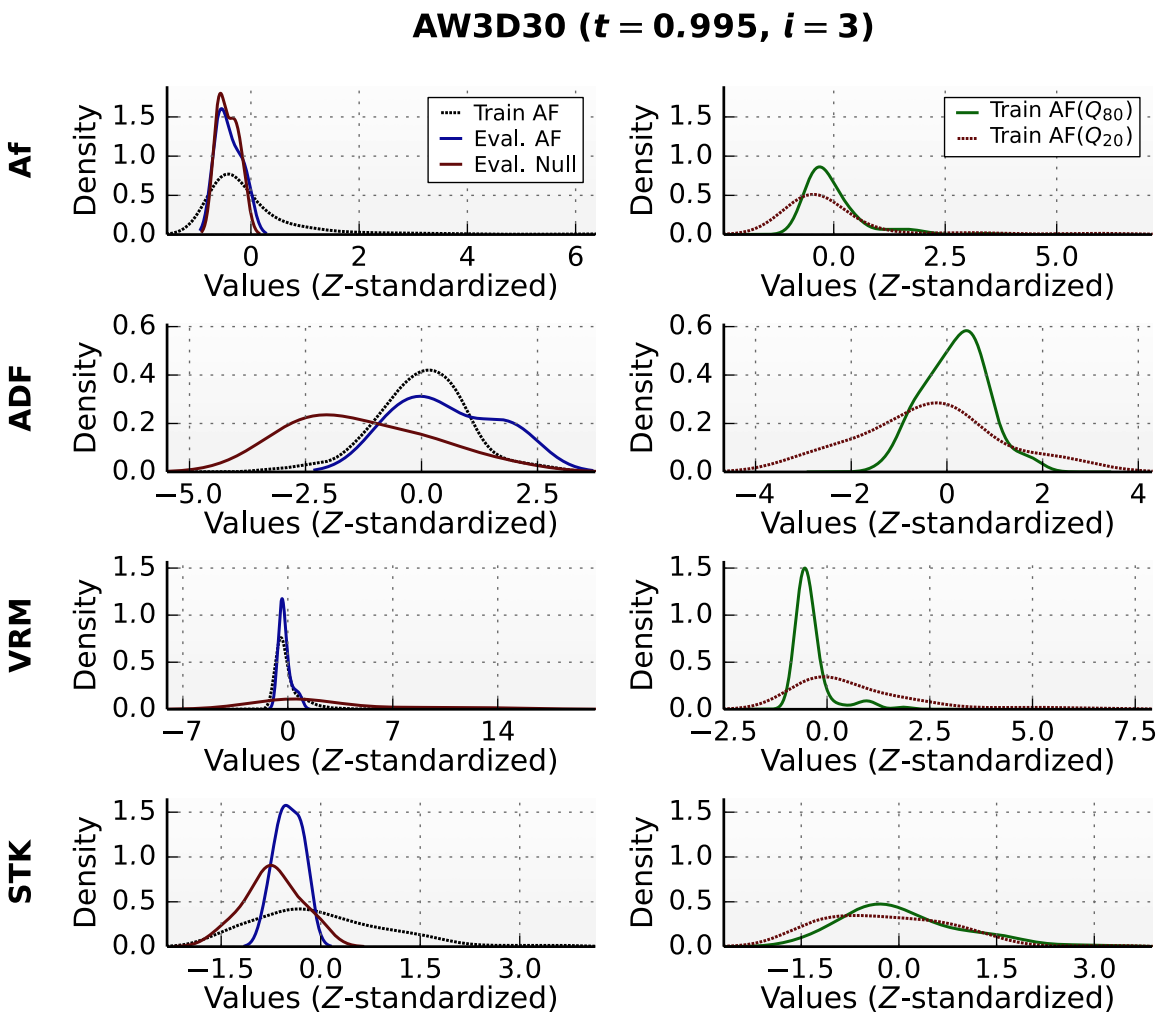
Supplement C.17 (cont.)



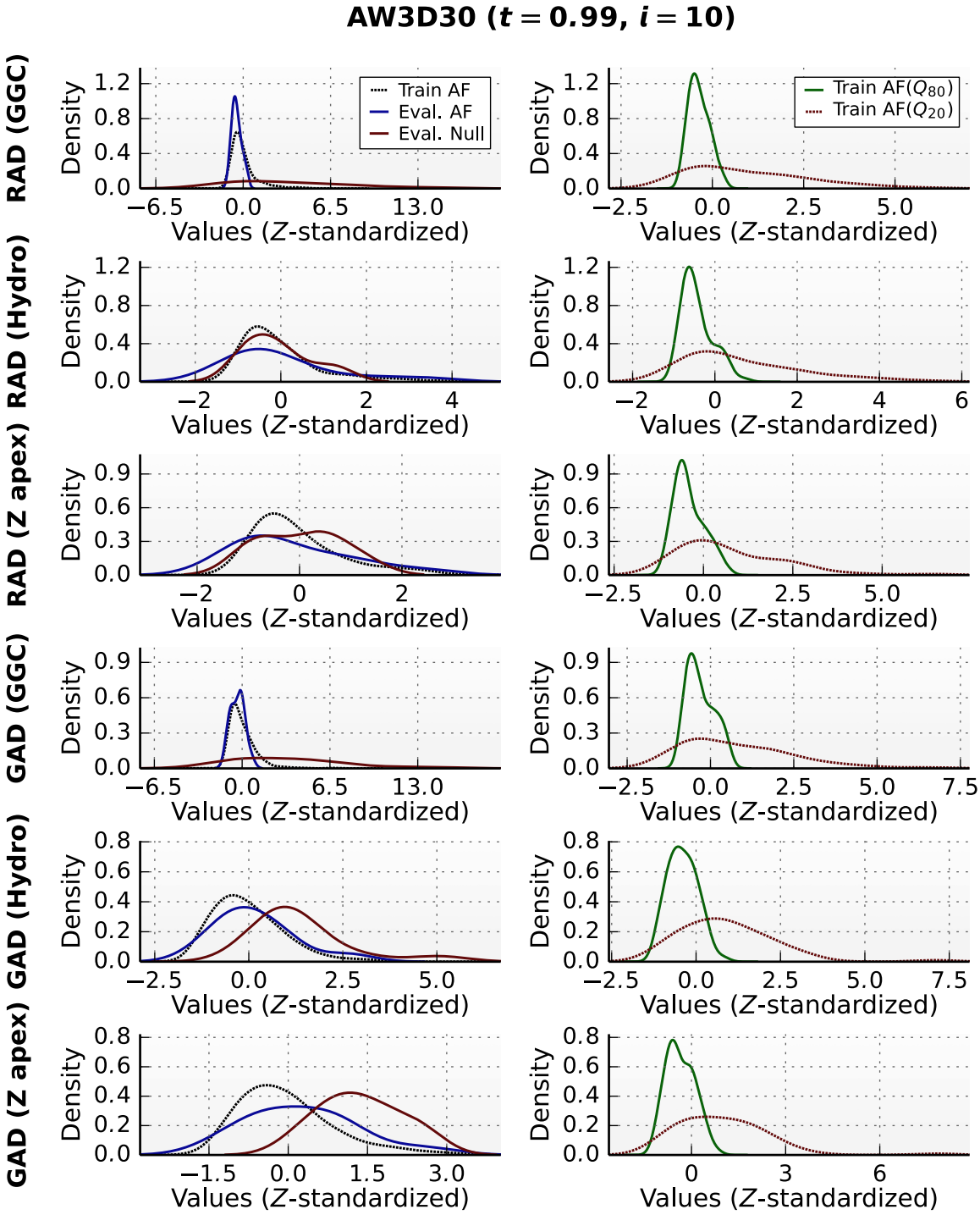
Supplement C.18: Empirical probability density plots for all morphometric variables used to train the OCRF, as well as auxiliary parameters considered for evaluation purposes. All KDE instances use a Gaussian kernel and the NR method for bandwidth estimation. Z-standardization was carried out using the respective arithmetic mean and standard deviation of the training dataset. Depicted are the density curves as obtained by using AW3D30 DEM with light filtering applied (t=.995, i=3).



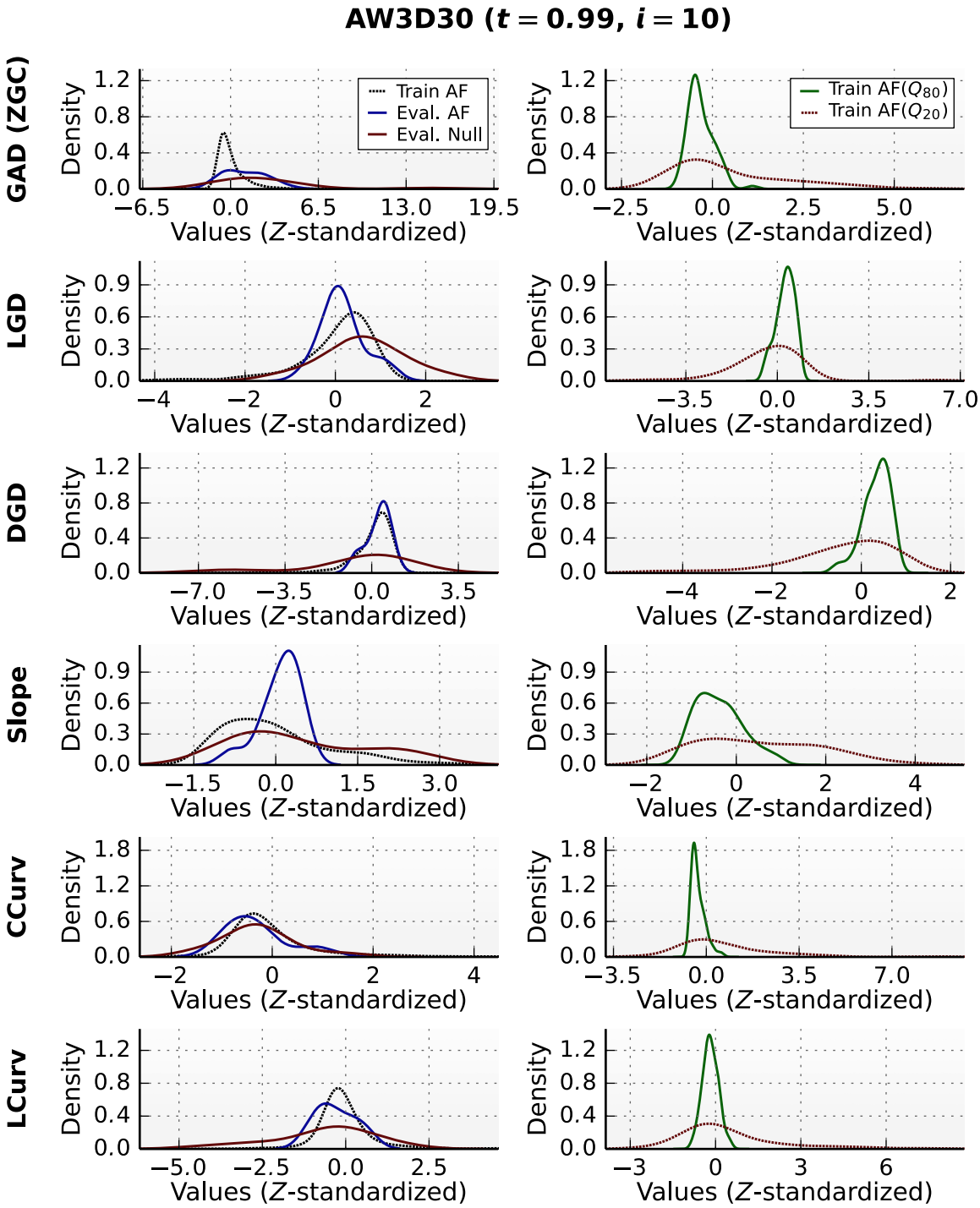
Supplement C.18 (cont.)



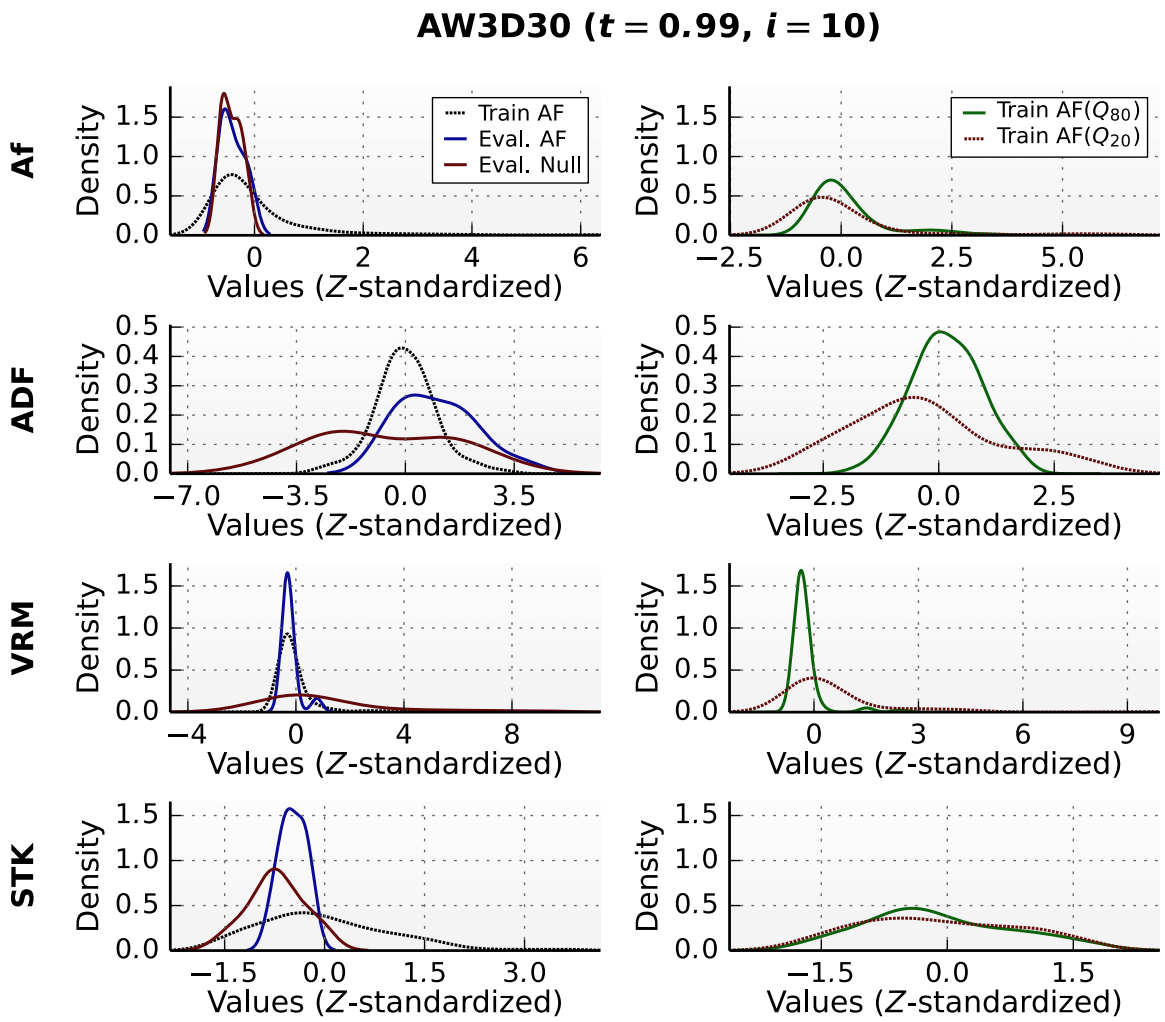
Supplement C.18 (cont.)



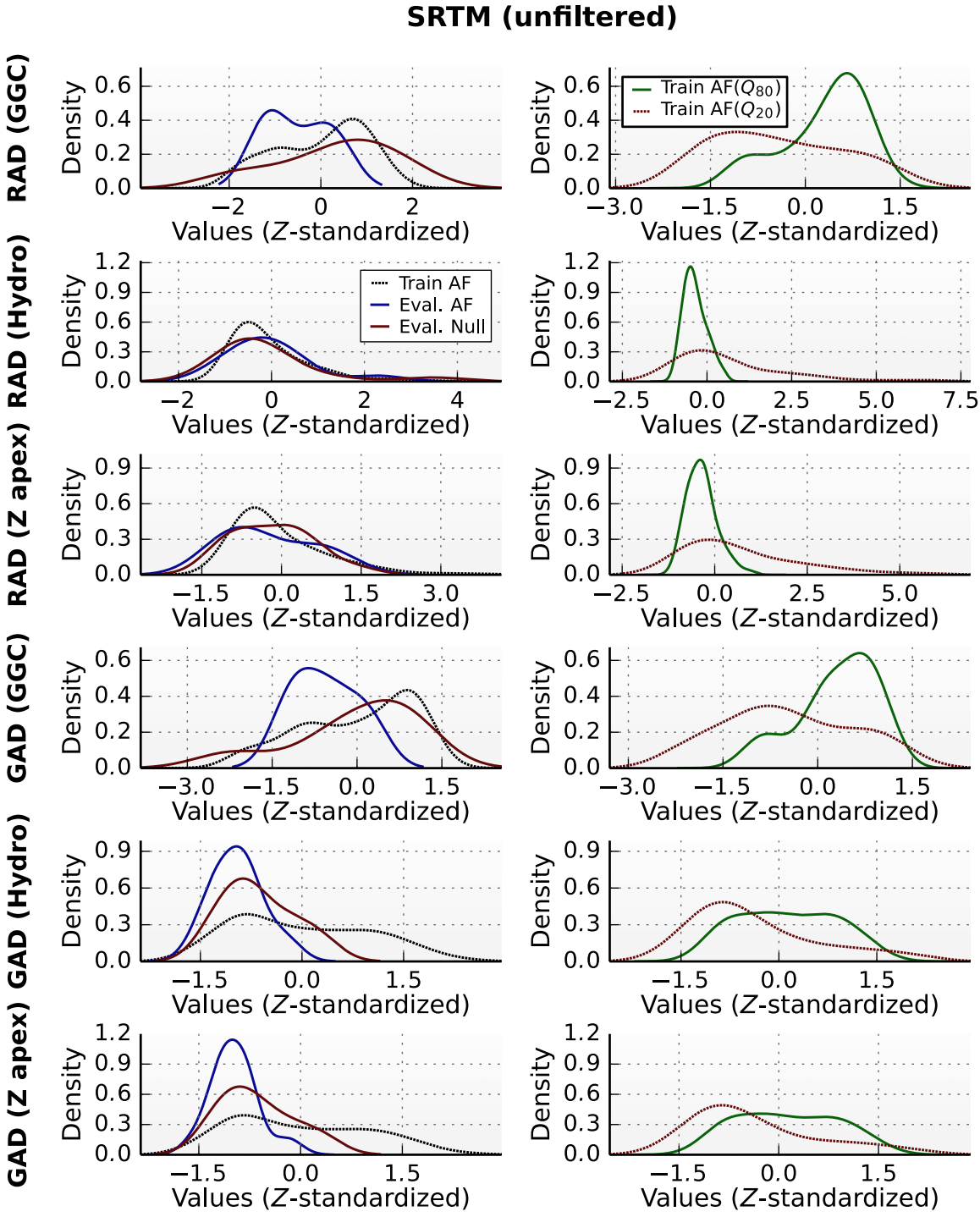
Supplement C.19: Empirical probability density plots for all morphometric variables used to train the OCRF, as well as auxiliary parameters considered for evaluation purposes. All KDE instances use a Gaussian kernel and the NR method for bandwidth estimation. Z-standardization was carried out using the respective arithmetic mean and standard deviation of the training dataset. Depicted are the density curves as obtained by using AW3D30 DEM with strong filtering applied (t=.99, i=10).



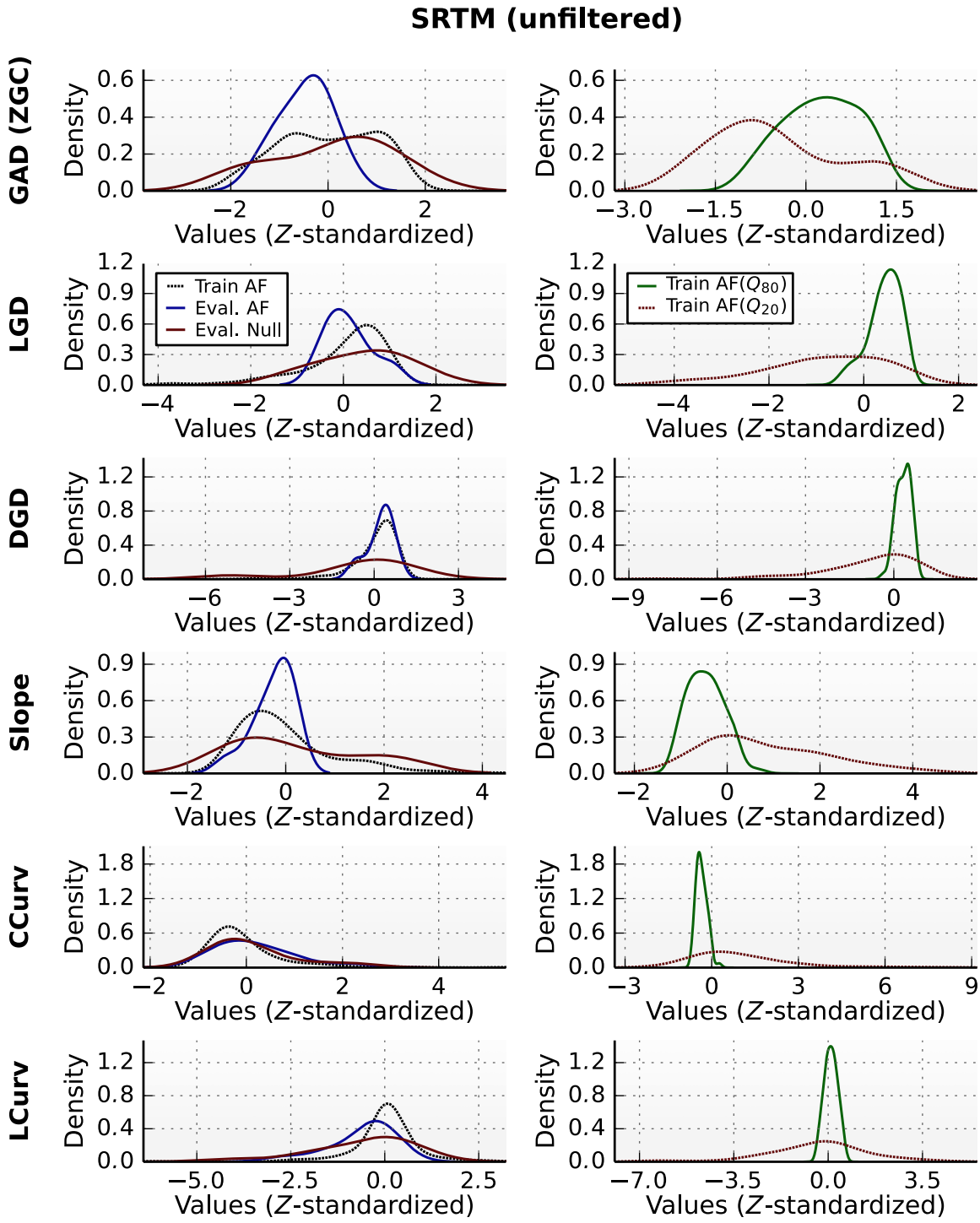
Supplement C.19 (cont.)



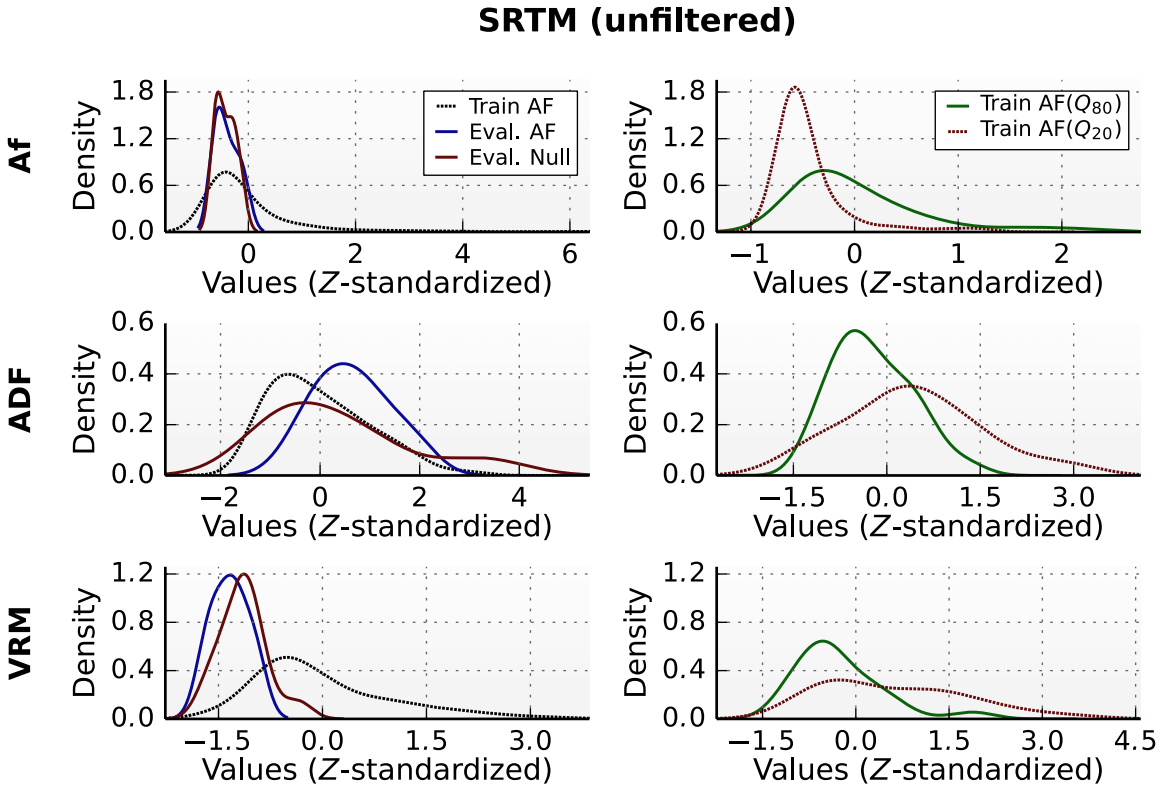
Supplement C.19 (cont.)



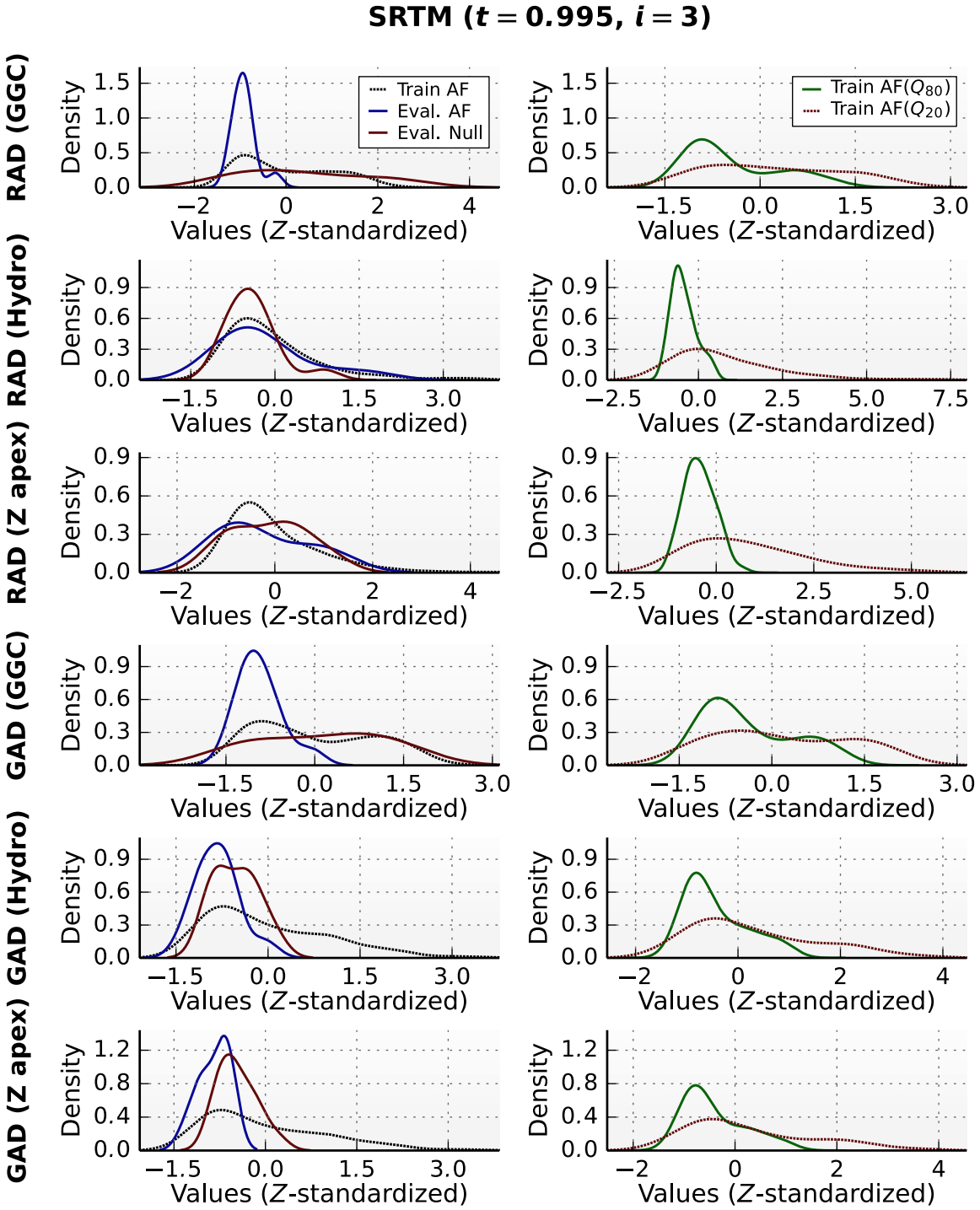
Supplement C.20: Empirical probability density plots for all morphometric variables used to train the OCRF, as well as auxiliary parameters considered for evaluation purposes. All KDE instances use a Gaussian kernel and the NR method for bandwidth estimation. Z-standardization was carried out using the respective arithmetic mean and standard deviation of the training dataset. Depicted are the density curves as obtained by using SRTM1 DEM with no filtering applied.



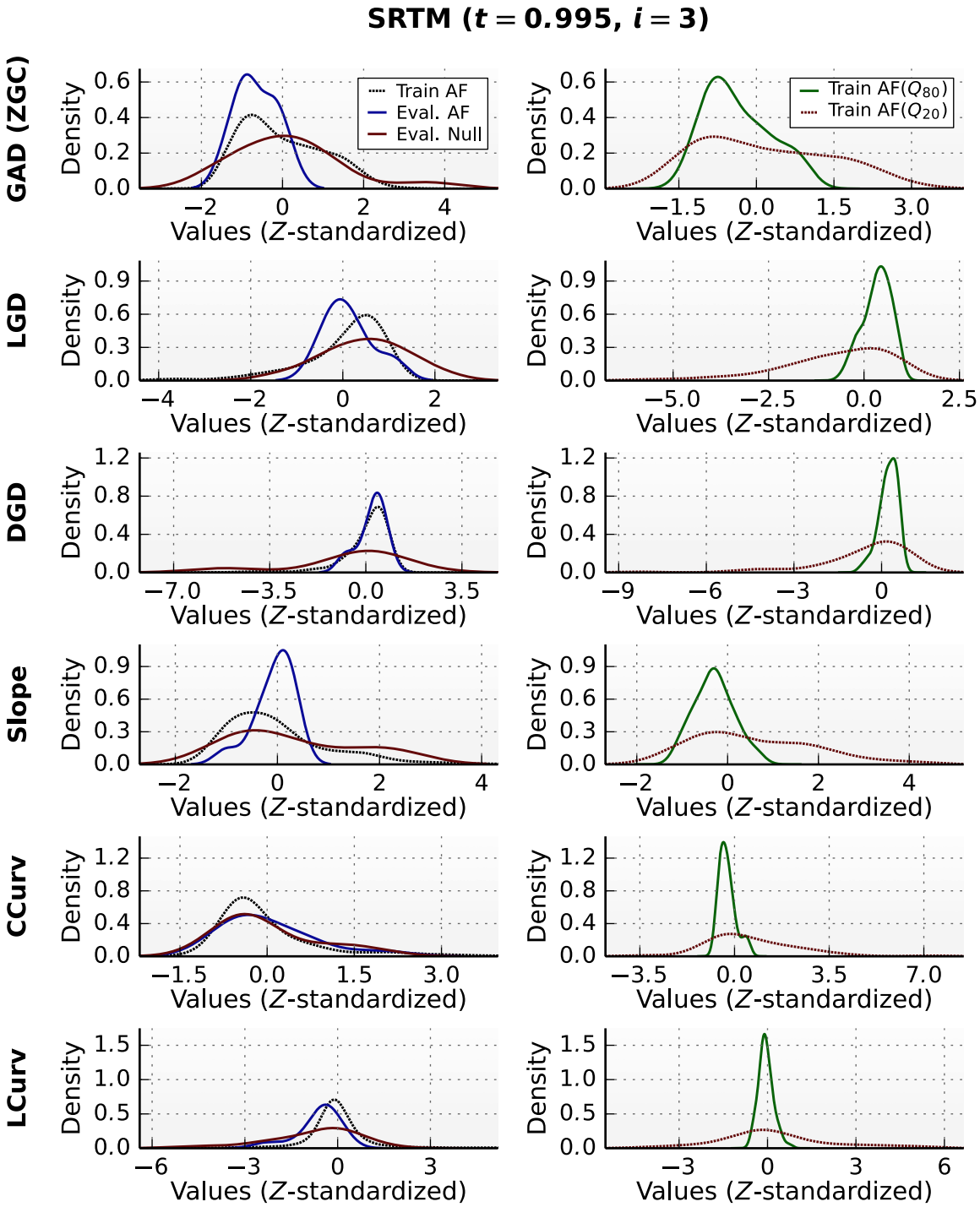
Supplement C.20 (cont.)



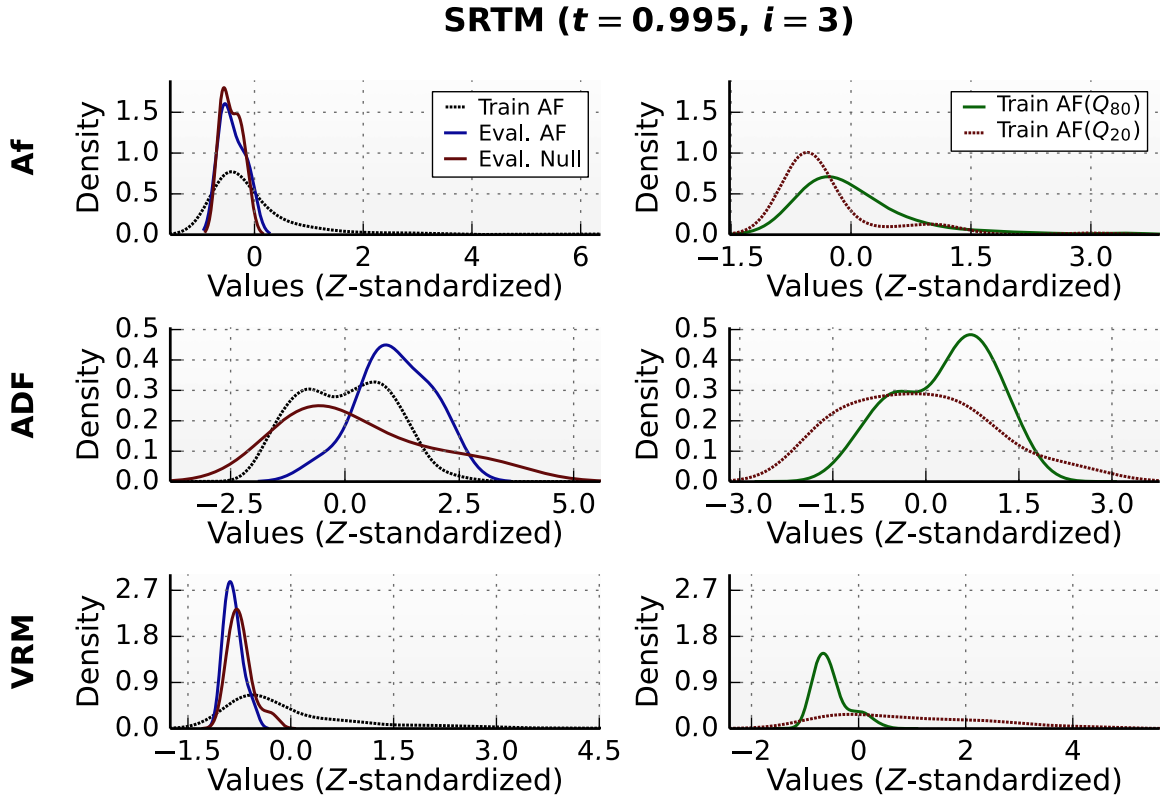
Supplement C.20 (cont.)



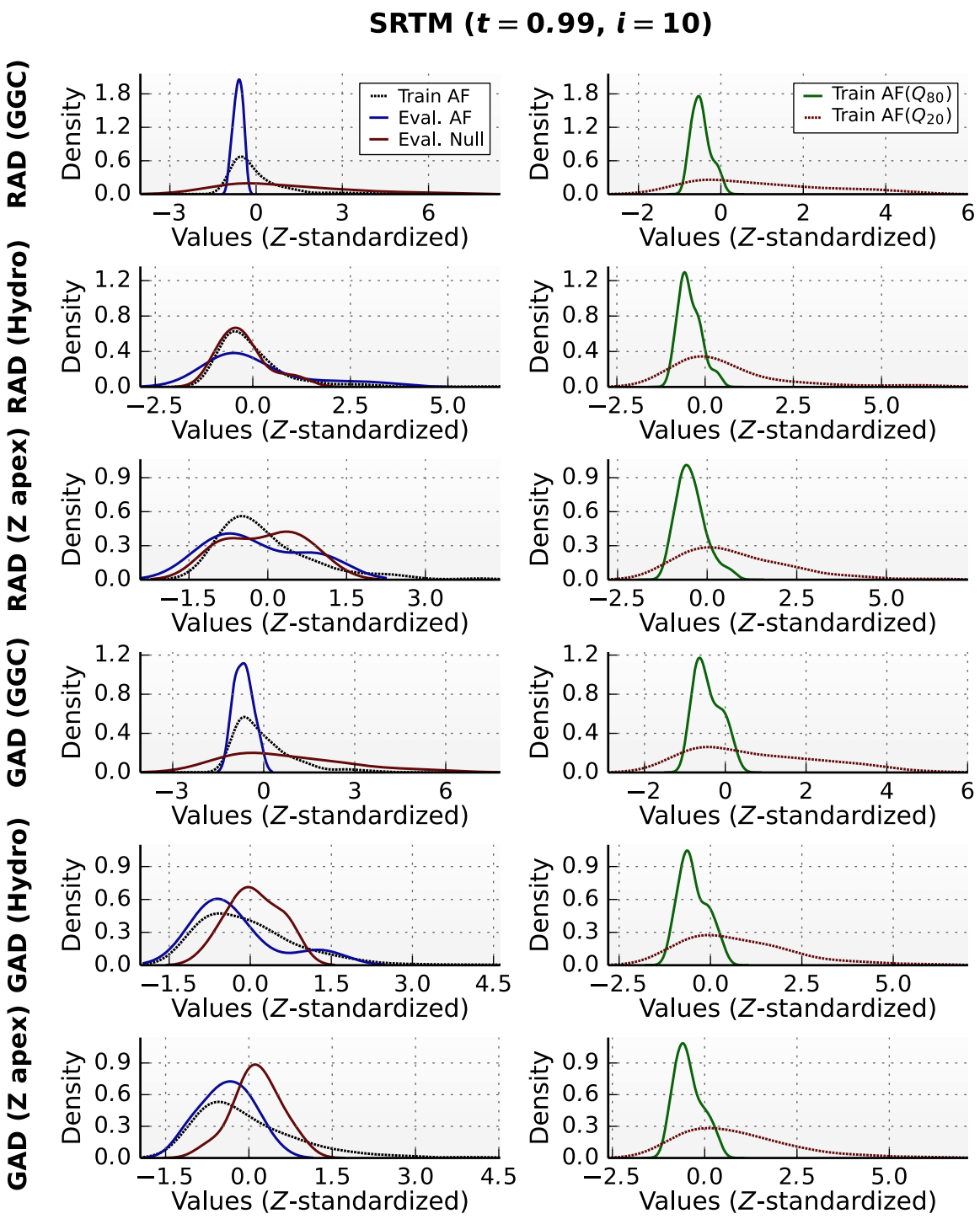
Supplement C.21: Empirical probability density plots for all morphometric variables used to train the OCRF, as well as auxiliary parameters considered for evaluation purposes. All KDE instances use a Gaussian kernel and the NR method for bandwidth estimation. Z-standardization was carried out using the respective arithmetic mean and standard deviation of the training dataset. Depicted are the density curves as obtained by using SRTM1 DEM with light filtering applied (t=.995, i=3).



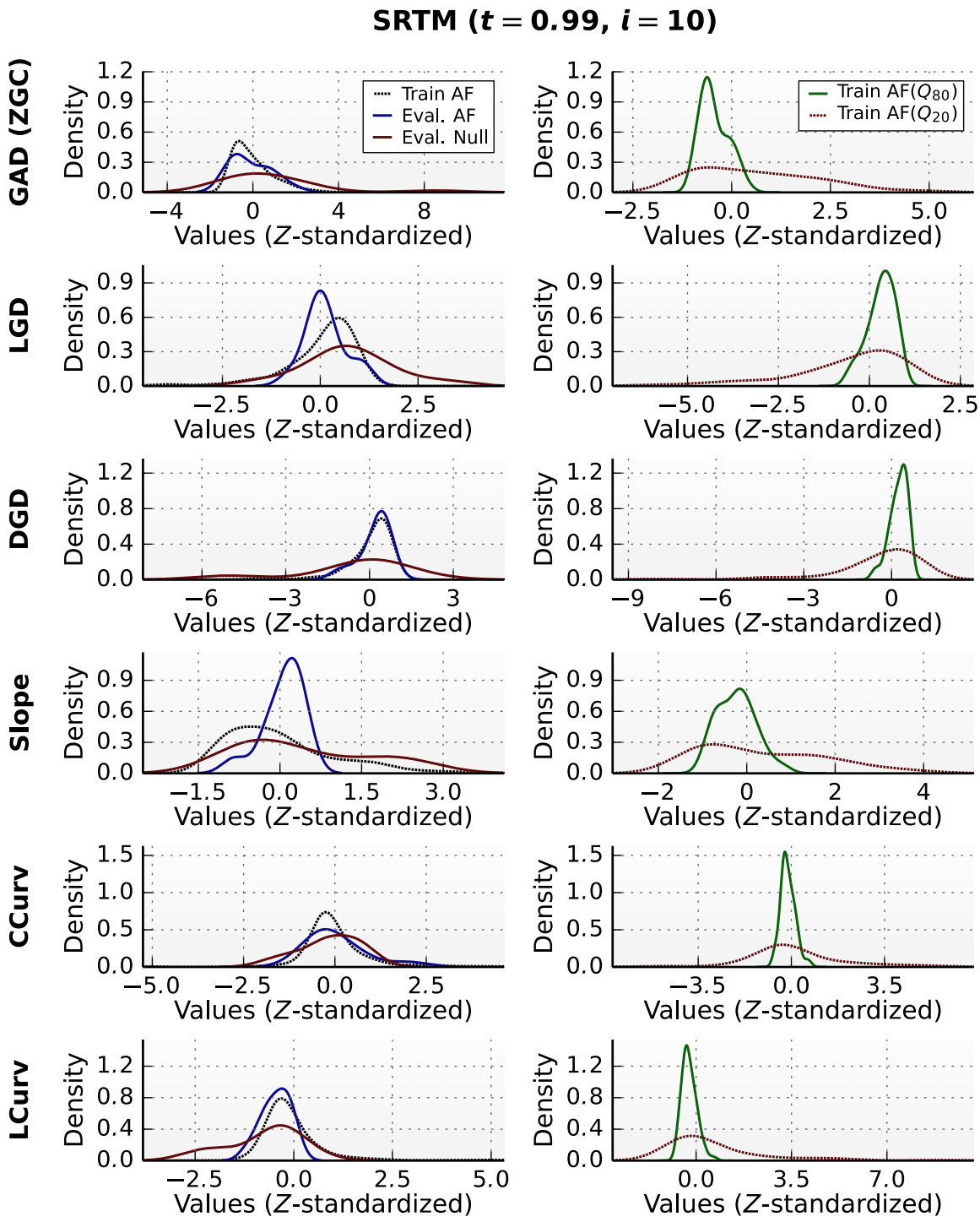
Supplement C.21 (cont.)



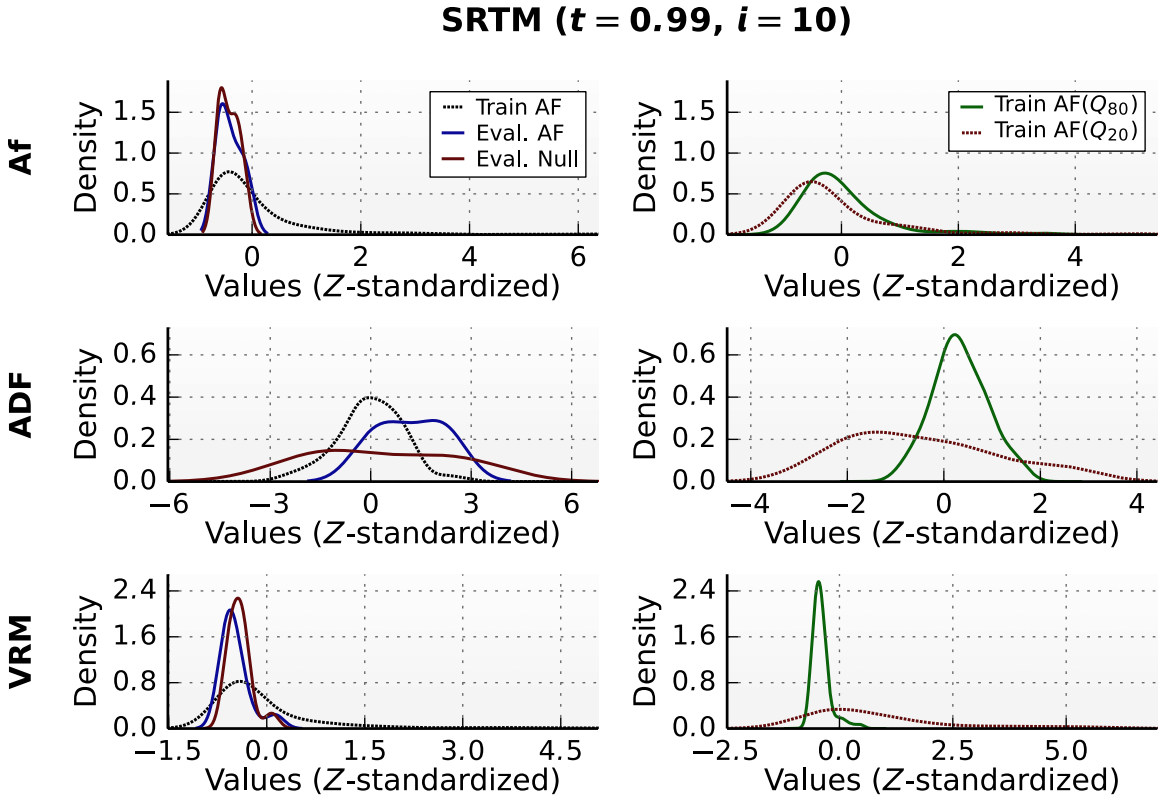
Supplement C.21 (cont.)



Supplement C.22: Empirical probability density plots for all morphometric variables used to train the OCRF, as well as auxiliary parameters considered for evaluation purposes. All KDE instances use a Gaussian kernel and the NR method for bandwidth estimation. Z-standardization was carried out using the respective arithmetic mean and standard deviation of the training dataset. Depicted are the density curves as obtained by using SRTM1 DEM with strong filtering applied (t=.99, i=10).

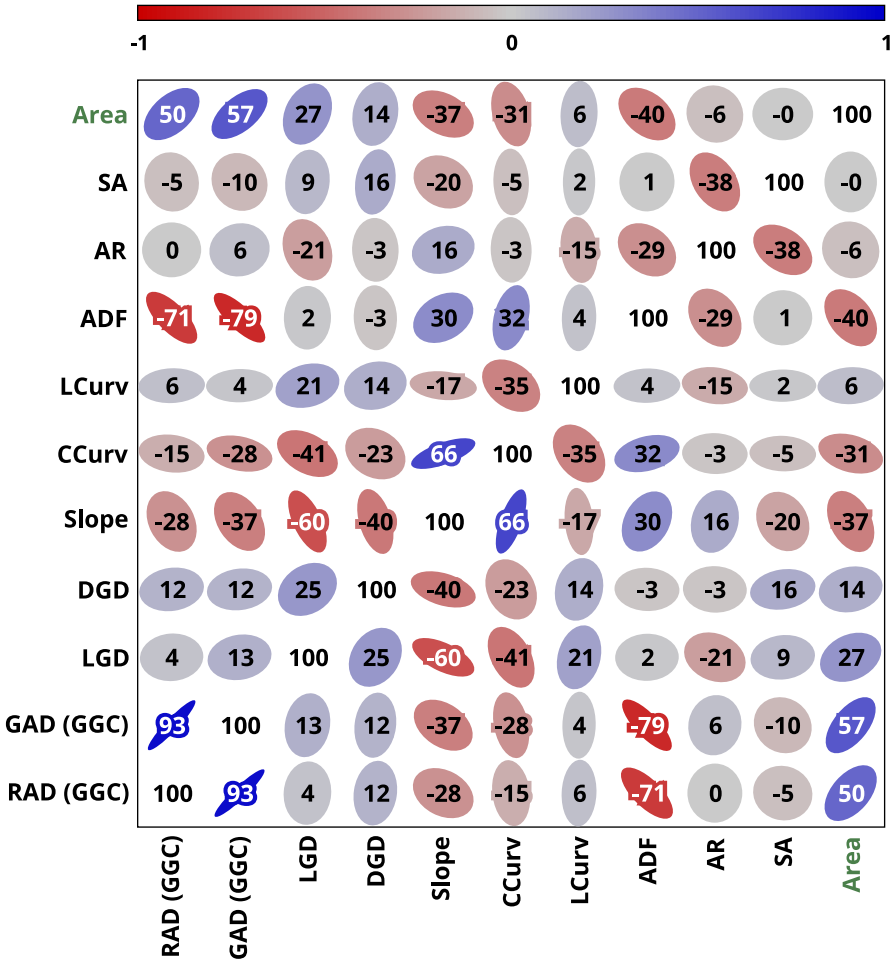


Supplement C.22 (cont.)



Supplement C.22 (cont.)

D Supplements, The expression of environmental controls in alluvial fan geomorphometry – An exploratory statistical analysis



Supplement D.1: Product-moment correlation matrix of the raw dataset. Auxiliary variables are denoted in green letters.

Supplement D.2: Clustering result obtained for the raw dataset and feature-specific bandwidth values estimated via cross-validated maximum likelihood (CVML) bandwidth estimation. Singletons are not shown.

ID	n	Silh.	Area (km^2)	RAD (GGC)	GAD (GGC)	LGD	DGD	Slope	CCurv	LCurv	ADF	AR	SA
C0	**95**	**−0.09**	12.94	1.44	12.79	−0.02	−0.02	2.17	0.11	0.01	−0.07	0.92	80.65
C1	**5**	**−0.01**	15.46	1.77	16.18	−0.03	−0.05	3.76	0.10	−0.02	−0.19	1.20	79.19
C2	**3**	**0.09**	14.82	2.13	20.76	−0.03	−0.04	3.54	0.16	0.08	−0.19	1.11	51.27
C3	**5**	**0.01**	2.13	1.11	8.84	−0.05	−0.02	3.51	0.35	−0.12	−0.02	0.91	93.09
C4	**8**	**−0.02**	15.65	1.78	18.97	−0.02	−0.01	1.88	0.11	−0.01	−0.15	1.47	79.27
C5	**5**	**0.20**	8.14	2.36	20.06	−0.02	−0.04	2.53	0.16	−0.04	−0.27	1.06	66.79
C6	**3**	**0.13**	0.70	1.97	10.99	−0.02	−0.01	2.29	0.50	−0.15	−0.11	0.77	103.57
C7	**9**	**0.08**	23.54	2.71	23.76	−0.02	−0.02	1.76	0.13	0.00	−0.24	0.82	85.90
C8	**6**	**−0.08**	33.17	2.87	26.07	−0.02	−0.02	1.76	0.06	−0.04	−0.22	1.12	83.89
C9	**2**	**0.45**	1.85	1.70	13.27	−0.02	−0.04	4.19	0.37	0.29	−0.18	0.96	60.26
C10	**3**	**0.34**	4.30	0.88	8.08	−0.03	−0.02	3.02	0.22	−0.07	−0.02	1.42	72.55
C11	**2**	**0.04**	7.66	1.77	17.97	−0.05	−0.03	3.41	0.18	−0.13	−0.20	1.44	85.95
C12	**5**	**0.19**	22.34	2.95	25.85	−0.02	−0.04	3.04	0.07	0.03	−0.17	0.92	51.26
C13	**9**	**0.02**	14.48	2.73	22.34	−0.01	−0.01	1.54	0.08	−0.01	−0.21	1.21	49.24
C14	**2**	**0.16**	13.34	1.85	12.34	−0.05	−0.07	4.84	0.28	−0.05	−0.05	0.77	108.24
C15	**2**	**−0.11**	18.25	3.24	24.48	−0.01	−0.01	1.58	0.08	0.01	−0.28	1.28	102.62
C17	**3**	**−0.04**	6.39	0.91	8.88	−0.05	−0.04	5.00	0.41	0.05	−0.02	0.84	79.55
C18	**3**	**0.01**	9.68	3.72	21.06	−0.03	−0.03	2.34	0.17	−0.02	−0.17	0.94	85.74
C19	**4**	**0.19**	12.86	0.97	10.88	−0.03	−0.08	3.06	0.18	−0.04	−0.13	0.82	99.72
C20	**6**	**0.14**	1.97	1.39	7.55	−0.03	−0.02	2.85	0.28	0.05	−0.06	0.67	128.09
C21	**3**	**0.09**	4.18	0.54	5.72	−0.04	−0.05	4.65	0.42	−0.08	−0.02	1.00	87.94
C23	**3**	**−0.09**	13.24	3.24	25.60	−0.01	−0.07	1.26	0.05	−0.00	−0.26	0.87	104.12
C24	**2**	**0.08**	4.62	2.54	17.74	−0.08	−0.03	3.15	0.25	−0.11	−0.20	0.99	70.47
C25	**2**	**−0.02**	43.71	2.29	24.03	−0.02	−0.01	1.00	0.01	0.00	−0.35	1.16	52.72
C28	**2**	**0.02**	4.78	0.95	10.75	−0.06	−0.07	4.65	0.04	−0.02	−0.08	0.98	40.55
C30	**4**	**0.16**	29.19	3.06	24.94	−0.01	−0.01	0.88	0.04	0.01	−0.16	0.74	138.40
C31	**2**	**0.03**	12.75	1.19	11.36	−0.04	−0.09	5.12	0.30	−0.14	−0.10	1.40	67.87
C32	**5**	**0.21**	41.39	4.02	31.48	−0.01	−0.02	1.03	0.04	−0.00	−0.25	0.73	98.25
C33	**2**	**−0.07**	4.19	0.69	7.05	−0.04	−0.05	5.26	0.40	0.25	0.02	0.96	65.87
C35	**2**	**0.02**	20.79	1.49	13.20	−0.05	−0.07	5.90	0.17	0.06	−0.01	1.12	58.54
C42	**7**	**0.23**	8.18	3.18	18.24	−0.02	−0.02	2.06	0.13	0.07	−0.10	0.77	118.72
C48	**5**	**0.46**	28.14	5.00	38.91	−0.01	−0.02	1.19	0.03	0.02	−0.31	0.81	84.62
C70	**3**	**0.34**	5.53	0.94	6.71	−0.02	−0.03	2.55	0.06	0.12	0.20	0.74	51.09

Supplement D.3: Clustering result obtained for the de-trended dataset and feature-specific bandwidth values estimated via CVML bandwidth estimation. Singletons are not shown.

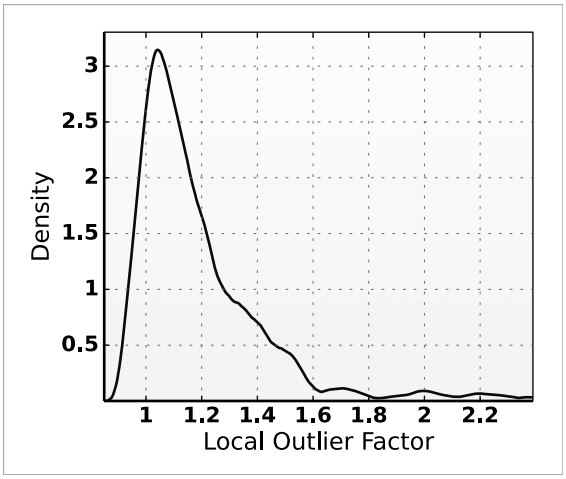
ID	n	Silh.	Area (km^2)	RAD (GGC)	GAD (GGC)	LGD	DGD	Slope	CCurv	LCurv	ADF	AR	SA
C0	**94**	**0.02**	12.34	−0.73	−3.87	0.01	0.02	−0.57	0.01	0.01	0.06	−0.06	3.69
C1	**10**	**0.08**	8.50	0.72	2.37	0.01	0.02	−0.86	−0.03	0.09	−0.03	−0.17	30.10
C2	**9**	**−0.08**	13.49	0.74	6.75	0.00	0.01	−0.28	0.07	−0.00	−0.03	0.14	15.15
C3	**5**	**0.05**	11.08	−0.25	−3.24	−0.01	−0.02	1.61	0.17	−0.00	0.01	−0.12	19.59
C4	**6**	**0.08**	4.40	0.15	3.49	0.02	0.03	−1.70	−0.24	0.10	−0.08	−0.13	−7.91
C5	**3**	**0.10**	1.20	0.15	−1.89	0.03	0.04	−1.68	−0.26	−0.13	−0.06	−0.13	24.42
C6	**6**	**−0.02**	12.92	−0.96	−6.00	−0.02	−0.01	1.99	0.14	0.04	0.11	−0.15	−3.92
C7	**2**	**−0.02**	8.48	0.05	3.26	0.00	0.00	0.26	0.16	−0.11	−0.13	0.29	−0.06
C8	**6**	**−0.01**	39.46	1.39	6.11	0.01	0.02	−0.92	0.02	0.01	−0.06	−0.14	−0.23
C9	**2**	**0.03**	0.87	−0.57	−7.12	0.03	0.03	−1.04	−0.36	0.06	0.02	−0.46	40.97
C10	**3**	**0.24**	1.66	−0.35	−1.20	0.01	0.02	−1.64	−0.42	0.08	0.04	0.02	−42.87
C11	**3**	**−0.02**	8.58	−1.14	−5.84	−0.00	−0.00	1.98	0.13	0.20	0.09	0.01	−6.49
C12	**11**	**0.12**	15.06	−0.56	0.11	0.00	0.01	0.00	0.07	0.00	−0.00	0.49	−17.68
C14	**3**	**0.31**	7.93	−0.17	2.04	0.00	−0.01	1.39	0.20	0.20	−0.06	0.11	−26.50
C15	**2**	**−0.15**	10.00	0.64	9.27	0.01	0.02	−0.49	0.20	−0.05	−0.09	−0.25	1.87
C16	**5**	**0.11**	11.04	−1.37	−7.43	−0.00	−0.02	1.61	0.18	−0.04	0.09	0.17	−16.60
C17	**4**	**−0.09**	9.02	0.14	1.42	−0.03	0.00	0.73	0.10	−0.07	−0.06	0.08	−16.54
C18	**6**	**0.08**	14.93	1.00	10.32	0.01	−0.01	0.13	0.04	0.03	−0.06	−0.01	−19.55
C19	**2**	**−0.03**	4.46	0.80	5.89	0.02	0.03	−1.39	−0.12	−0.05	−0.11	0.44	−22.84
C20	**5**	**−0.11**	6.48	0.50	6.90	0.01	0.02	−1.00	−0.00	−0.01	−0.16	0.20	−24.86
C22	**4**	**0.07**	24.46	−0.61	−4.15	0.00	0.00	−0.41	0.11	−0.01	0.03	−0.27	75.51
C23	**4**	**−0.06**	26.44	−1.46	−10.01	−0.02	−0.01	1.02	0.07	0.06	0.21	−0.25	−22.47
C25	**2**	**0.27**	1.00	−0.76	−8.01	0.02	0.03	−1.67	−0.48	0.09	0.17	−0.09	1.41
C26	**2**	**−0.13**	10.10	0.51	−1.81	0.02	0.02	−0.84	0.16	0.09	0.04	−0.42	70.19
C27	**3**	**0.28**	33.16	1.84	15.84	0.01	0.01	−0.68	0.02	0.03	−0.08	−0.14	11.67
C28	**2**	**0.00**	0.42	−0.91	−8.27	0.00	−0.03	1.29	0.23	−0.20	0.19	−0.24	−27.20
C29	**2**	**0.35**	78.85	−2.81	−13.72	−0.01	0.02	−0.58	0.03	0.00	−0.03	0.02	5.73
C30	**2**	**−0.02**	9.22	0.89	7.17	0.01	−0.03	−1.14	0.03	0.01	−0.12	−0.28	37.22
C31	**4**	**0.02**	9.81	−1.36	−8.58	−0.00	0.02	1.09	0.16	−0.04	0.10	0.38	−30.64
C36	**2**	**0.66**	41.17	−2.84	−18.98	0.01	0.02	−0.15	0.03	−0.00	0.16	0.15	−10.14
C38	**2**	**0.19**	14.33	−0.89	−4.70	−0.03	−0.04	2.48	0.23	−0.13	−0.02	0.39	5.40
C43	**2**	**0.13**	7.84	1.70	4.37	0.02	0.02	−1.25	0.00	0.12	0.04	−0.36	60.25
C48	**3**	**0.10**	35.08	−2.13	−12.81	−0.00	0.00	0.03	0.05	−0.03	0.18	−0.30	19.11
C59	**2**	**0.47**	58.23	−2.94	−20.75	−0.01	0.00	0.09	0.02	0.00	0.19	−0.24	43.75

Supplement D.4: Clustering result obtained for the raw dataset with scaling factors adjusted to yield ten clusters. A scaling factor of 2.20 had to be used for this dataset.

ID	n	Silh.	Area (km^2)	RAD (GGC)	GAD (GGC)	LGD	DGD	Slope	CCurv	LCurv	ADF	AR	SA
C0	**257**	**0.27**	12.57	1.89	15.50	−0.03	−0.03	2.68	0.18	−0.01	−0.12	0.99	81.26
C1	**7**	**0.25**	0.45	1.52	6.73	−0.06	−0.06	5.62	1.17	0.27	0.16	0.75	63.35
C2	**17**	**0.30**	29.79	5.12	36.56	−0.04	−0.04	2.45	0.22	−0.04	−0.32	0.97	77.33
C3	**1**	**0**	6.10	4.00	36.61	−0.11	−0.05	9.36	0.44	0.18	−0.29	1.41	42.85
C4	**3**	**0.22**	7.10	5.38	25.96	−0.11	−0.07	5.44	0.59	−0.09	−0.41	1.92	57.88
C5	**4**	**0.24**	1.48	1.10	8.85	−0.09	−0.07	6.55	1.10	−0.68	0.01	0.86	83.26
C6	**9**	**0.02**	62.59	9.27	59.87	−0.02	−0.02	1.03	0.00	−0.02	−0.43	0.92	68.60
C7	**2**	**0.49**	83.14	12.88	77.68	−0.05	−0.01	1.32	0.10	0.11	−0.56	1.04	58.25
C8	**5**	**0.48**	5.49	1.57	15.29	−0.04	−0.25	3.25	0.36	−0.06	−0.14	0.88	65.89
C9	**1**	**0**	0.16	1.74	5.49	−0.08	−0.08	8.57	3.83	−0.94	0.14	0.49	44.82

Supplement D.5: Clustering result obtained for the de-trended dataset with scaling factors adjusted to yield ten clusters. A scaling factor of 2.00 had to be used for this dataset.

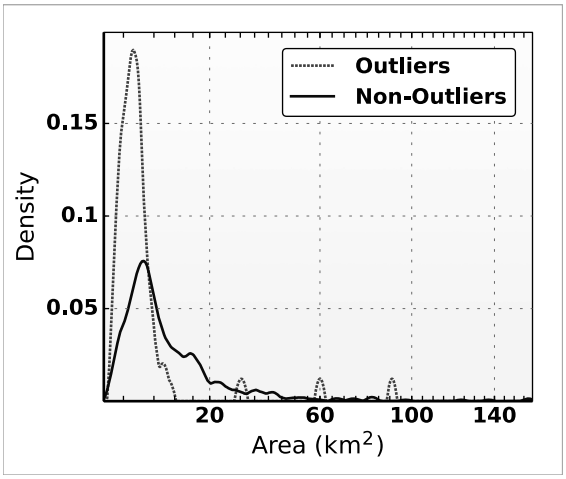
ID	n	Silh.	Area (km^2)	RAD (GGC)	GAD (GGC)	LGD	DGD	Slope	CCurv	LCurv	ADF	AR	SA
C0	**275**	**0.34**	14.12	−0.34	−1.86	0.00	0.00	−0.08	0.02	0.01	0.02	−0.01	1.29
C1	**5**	**0.06**	9.82	3.23	14.56	−0.04	−0.02	1.82	0.31	−0.12	−0.27	0.42	−14.23
C2	**10**	**0.24**	42.96	4.41	26.84	0.00	0.01	−0.64	0.03	−0.00	−0.19	−0.07	−4.00
C3	**2**	**0.28**	56.06	6.99	35.35	0.00	−0.01	−0.70	−0.00	−0.02	−0.26	0.23	−42.65
C4	**2**	**−0.05**	4.35	2.55	18.00	−0.05	−0.01	4.12	0.27	0.27	−0.14	0.13	−21.96
C5	**3**	**0.27**	1.83	−0.60	−4.01	−0.05	−0.03	3.23	0.57	−0.75	0.04	−0.12	14.26
C6	**2**	**−0.10**	3.24	3.29	11.10	−0.14	−0.01	0.25	0.18	−0.05	−0.28	0.57	−10.86
C7	**5**	**0.43**	5.49	−0.40	−0.07	−0.00	−0.21	−0.15	−0.04	−0.04	−0.05	−0.11	−13.56
C8	**1**	**0**	8.00	10.32	62.50	−0.07	0.02	−1.58	0.04	0.13	−0.46	0.24	−32.38
C9	**1**	**0**	0.16	−0.00	−8.23	−0.03	−0.03	4.39	2.81	−0.92	0.17	−0.50	−34.65



Supplement D.6: Empirical density distribution of the local outlier factor. Calculated using an Epanechnikov kernel and bandwidth optimized via the CVML method.

Supplement D.7: Eigenvalues (in percent of total variance) and eigenvectors of the principal component analysis (PCA) applied on the de-trended dataset.

PC	**Eigen-value**	RAD (GGC)	GAD (GGC)	LGD	DGD	Slope	CCurv	LCurv	ADF	AR	SA
PC0	**28.81**	–0.37	–0.36	–0.37	–0.29	0.47	0.37	–0.19	0.29	0.16	–0.11
PC1	**24.16**	0.43	0.47	–0.29	–0.18	0.22	0.25	–0.23	–0.46	0.27	–0.19
PC2	**12.68**	0.14	0.06	–0.22	–0.13	0.06	0.19	–0.18	–0.02	–0.58	0.71
PC3	**10.25**	–0.10	–0.08	0.07	0.55	–0.22	0.21	–0.63	–0.01	0.35	0.24
PC4	**7.76**	0.16	0.13	0.06	0.51	0.27	0.54	0.54	0.18	0.05	0.08
PC5	**5.47**	0.17	0.20	0.53	–0.16	0.00	0.30	–0.37	0.40	–0.34	–0.36
PC6	**5.29**	–0.12	–0.01	0.55	–0.48	–0.05	0.25	0.15	–0.17	0.42	0.42
PC7	**2.61**	0.28	0.27	–0.27	–0.18	–0.24	–0.17	0.04	0.69	0.37	0.21
PC8	**2.16**	0.24	–0.06	0.28	0.14	0.72	–0.49	–0.16	0.09	0.11	0.20
PC9	**0.80**	–0.66	0.72	0.00	0.07	0.16	–0.12	–0.02	0.04	–0.04	0.07



Supplement D.8: Empirical density distribution of planimetric fan area for samples identified as outliers and the remaining alluvial fan dataset.

Bibliography

Abdi, H., Williams, L.J., 2010. Principal component analysis. Wiley Interdisciplinary Reviews: Computational Statistics 2(4), 433–459. doi:10.1002/wics.101.

Abolt, C.J., Young, M.H., Atchley, A.L., Wilson, C.J., 2019. Brief communication: Rapid machine-learning-based extraction and measurement of ice wedge polygons in high-resolution digital elevation models. The Cryosphere 13(1), 237–245. doi:10.5194/tc-13-237-2019.

Abrams, M., 2000. The Advanced Spaceborne Thermal Emission and Reflection Radiometer (ASTER): Data products for the high spatial resolution imager on NASA's Terra platform. International Journal of Remote Sensing 21(5), 847–859. doi:10.1080/014311600210326.

Ackert, R.P., 1998. A Rock Glacier/Debris-Covered Glacier System at Galena Creek, Absaroka Mountains, Wyoming. Geografiska Annaler: Series A, Physical Geography 80(3–4), 267–276. doi:10.1111/j.0435-3676.1998.00042.x.

Adams, D.K., Comrie, A.C., 1997. The North American Monsoon. Bulletin of the American Meteorological Society 78(10), 2197–2214. doi:10.1175/1520-0477(1997)078<2197:TNAM>2.0.CO;2.

Agarwal, P., Skupin, A., 2008. Self-organising maps: applications in geographic information science. Wiley, Chichester.

Aggarwal, C.C., 2018. Neural Networks and Deep Learning. Springer, Cham. doi:10.1007/978-3-319-94463-0.

Aggarwal, C.C., Yu, P.S., 2001. Outlier Detection for High Dimensional Data. In: Proceedings of the ACM SIGMOD International Conference on Management of Data, May 21–24, Santa Barbara. Association for Computing Machinery, New York, pp. 37–46. doi:10.1145/375663.375668.

Al-Farraj, A., Harvey, A.M., 2005. Morphometry and depositional style of Late Pleistocene alluvial fans: Wadi Al-Bih, northern UAE and Oman. In: Harvey, A.M., Mather, A.E., Stokes, M. (Eds.). Alluvial Fans: Geomorphology, Sedimentology, Dynamics. Geological Society, London, Special Publications 251. Geological Society of London, pp. 85–94. doi:10.1144/GSL.SP.2005.251.01.07.

Albani, M., Klinkenberg, B., Andison, D.W., Kimmins, J.P., 2004. The choice of window size in approximating topographic surfaces from Digital Elevation Models. International Journal of Geographical Information Science 18(6), 577–593. doi:10.1080/13658810410001701987.

Alganci, U., Besol, B., Sertel, E., 2018. Accuracy Assessment of Different Digital Surface Models. ISPRS International Journal of Geo-Information 7(3), 114. doi:10.3390/ijgi7030114.

Alifu, H., Vuillaume, J.F., Johnson, B.A., Hirabayashi, Y., 2020. Machine-learning classification of debris-covered glaciers using a combination of Sentinel-1/-2 (SAR/optical), Landsat 8 (thermal) and digital elevation data. Geomorphology 369, 107365. doi:10.1016/j.geomorph.2020.107365.

Allen, P.A., Armitage, J.J., Whittaker, A.C., Michael, N.A., Roda-Boluda, D.C., D'Arcy, M., 2015. Fragmentation Model of the Grain Size Mix of Sediment Supplied to Basins. The Journal of Geology 123(5), 405–427. doi:10.1086/683113.

Allen, P.A., Densmore, A.L., 2000. Sediment flux from an uplifting fault block. Basin Research 12(3–4), 367–380. doi:10.1111/j.1365-2117.2000.00135.x.

Allen, P.A., Hovius, N., 1998. Sediment supply from landslide-dominated catchments: implications for basin-margin fans. Basin Research 10(1), 19–35. doi:10.1046/j.1365-2117.1998.00060.x.

Altmann, A., Toloşi, L., Sander, O., Lengauer, T., 2010. Permutation importance: a corrected feature importance measure. Bioinformatics 26(10), 1340–1347. doi:10.1093/bioinformatics/btq134.

An, C.B., Chen, F.H., Barton, L., 2008. Holocene environmental changes in Mongolia: A review. Global and Planetary Change 63(4), 283–289. doi:10.1016/j.gloplacha.2008.03.007.

Anders, N.S., Seijmonsbergen, A.C., Bouten, W., 2011. Segmentation optimization and stratified object-based analysis for semi-automated geomorphological mapping. Remote Sensing of Environment 115(12), 2976–2985. doi:10.1016/j.rse.2011.05.007.

Anderson, D.E., Wells, S.G., 2003. Latest Pleistocene lake highstands in Death Valley, California. In: Enzel, Y., Wells, S.G., Lancaster, N. (Eds.). Paleoenvironments and paleohydrology of the Mojave and southern Great Basin deserts. Special Paper 368. Geological Society of America, Boulder, pp. 115–128. doi:10.1130/0-8137-2368-X.115.

Antinao, J.L., McDonald, E.V., 2013a. An enhanced role for the Tropical Pacific on the humid Pleistocene–Holocene transition in southwestern North America. Quaternary Science Reviews 78, 319–341. doi:10.1016/j.quascirev.2013.03.019.

Antinao, J.L., McDonald, E.V., 2013b. A reduced relevance of vegetation change for alluvial aggradation in arid zones. Geology 41(1), 11–14. doi:10.1130/G33623.1.

Antinao, J.L., McDonald, E.V., Rhodes, E.J., Brown, N., Barrera, W., Gosse, J.C., Zimmermann, S., 2016. Late Pleistocene-Holocene alluvial stratigraphy of southern Baja California, Mexico. Quaternary Science Reviews 146, 161–181. doi:10.1016/j.quascirev.2016.06.008.

Archer, K.J., Kimes, R.V., 2008. Empirical characterization of random forest variable importance measures. Computational Statistics & Data Analysis 52(4), 2249–2260. doi:10.1016/j.csda.2007.08.015.

Argialas, D.P., Miliaresis, G.C., 1997. Landform Spatial Knowledge Acquisition: Identification, Conceptualization and Representation. In: Proceedings of the ASPRS/ASCM Annual Convention and Exposition, April 7–10, Reno. ASPRS/ASCM, Bethesda, pp. 733–740.

Argialas, D.P., Tzotsos, A., 2004. Automatic Extraction of Aluvial Fans from ASTER L1 Satellite Data and a Digital Elevation Model Using Object-Oriented Image Analysis. In: Geo-Imagery Bridging Continents, XXth ISPRS Congress, July 2–23, Istanbul. ISPRS, Hannover.

Argialas, D.P., Tzotsos, A., 2006. Automatic extraction of physiographic features and alluvial fans in Nevada, USA, from digital elevation models and satellite imagery through multiresolution segmentation and object-oriented classification. In: Proceedings of the ASPRS Annual Conference, May 1–5, Reno. ASPRS, Bethesda.

Argyridis, A., Argialas, D.P., 2017. GEOBIA-based identification of alluvial fans and bajadas through geomorphometry, image analysis and fuzzy ontology. International Journal of Image and Data Fusion 8(4), 309–331. doi:10.1080/19479832.2017.1342707.

Arias-Castro, E., Mason, D., Pelletier, B., 2016. On the Estimation of the Gradient Lines of a Density and the Consistency of the Mean-Shift Algorithm. Journal of Machine Learning Research 17(43), 1–28.

Armijo, R., Tapponnier, P., Han, T., 1989. Late Cenozoic right-lateral strike-slip faulting in southern Tibet. Journal of Geophysical Research 94(B3), 2787–2838. doi:10.1029/JB094iB03p02787.

Armitage, J.J., Duller, R.A., Whittaker, A.C., Allen, P.A., 2011. Transformation of tectonic and climatic signals from source to sedimentary archive. Nature Geoscience 4, 231. doi:10.1038/ngeo1087.

Arnab, A., Torr, P.H.S., 2017. Pixelwise Instance Segmentation with a Dynamically Instantiated Network. In: Proceedings of the IEEE Conference on Computer Vision and Pattern Recognition, July 21–26, Honolulu. IEEE, New York, pp. 879–888. doi:10.1109/CVPR.2017.100.

Arrell, K., Wise, S.M., Wood, J.D., Donoghue, D., 2008. Spectral filtering as a method of visualising and removing striped artefacts in digital elevation data. Earth Surface Processes and Landforms 33(6), 943–961. doi:10.1002/esp.1597.

Arrell, K.E., Fisher, P.F., Tate, N.J., Bastin, L., 2007. A fuzzy c-means classification of elevation derivatives to extract the morphometric classification of landforms in Snowdonia, Wales. Computers & Geosciences 33(10), 1366–1381. doi:10.1016/j.cageo.2007.05.005.

Arvor, D., Durieux, L., Andrés, S., Laporte, M.A., 2013. Advances in Geographic Object-Based Image Analysis with ontologies: A review of main contributions and limitations from a remote sensing perspective. ISPRS Journal of Photogrammetry and Remote Sensing 82, 125–137. doi: 10.1016/j.isprsjprs.2013.05.003.

Aschwanden, P., Guggenbuhl, W., 1992. Experimental results from a comparative study on correlation-type registration algorithms. In: Förster, W., Ruwiedel, S. (Eds.). Robust computer vision: quality of vision algorithms. Wichmann, Karlsruhe, pp. 268–287.

ASTER GDEM Validation Team, 2009. ASTER Global DEM Validation Summary Report. https://lpdaac.usgs.gov/sites/default/files/public/aster/docs/ASTER_GDEM_Validation_Summary_Report.pdf. Last accessed on October 29, 2014.

Atkinson, P.M., Tatnall, A.R.L., 1997. Introduction Neural networks in remote sensing. International Journal of Remote Sensing 18(4), 699–709. doi:10.1080/014311697218700.

Attal, M., Mudd, S.M., Hurst, M.D., Weinman, B., Yoo, K., Naylor, M., 2015. Impact of change in erosion rate and landscape steepness on hillslope and fluvial sediments grain size in the Feather River basin (Sierra Nevada, California). Earth Surface Dynamics 3(1), 201–222. doi:10.5194/esurf-3-201-2015.

Atwater, T., 1970. Implications of Plate Tectonics for the Cenozoic Tectonic Evolution of Western North America. Geological Society of America Bulletin 81(12), 3513. doi:10.1130/0016-7606(1970)81[3513:IOPTFT]2.0.CO;2.

Atwater, T., Stock, J.M., 1998. Pacific-North America Plate Tectonics of the Neogene Southwestern United States: An Update. International Geology Review 40(5), 375–402. doi:10.1080/00206819809465216.

Auret, L., Aldrich, C., 2011. Empirical comparison of tree ensemble variable importance measures. Chemometrics and Intelligent Laboratory Systems 105(2), 157–170. doi:10.1016/j.chemolab.2010.12.004.

Axen, G., 1995. Extensional segmentation of the Main Gulf Escarpment, Mexico and United States. Geology 23(6), 515–518. doi:10.1130/0091-7613(1995)023<0515:ESOTMG>2.3.CO;2.

Baatz, M., Schäpe, A., 2000. Multiresolution Segmentation: an optimization approach for high quality multi-scale image segmentation. In: Strobl, J. (Ed.). Angewandte Geographische Informationsverarbeitung XII. Beiträge zum AGIT-Symposium Salzburg. Wichmann, Karlsruhe, pp. 12–23.

Bacon, S.N., McDonald, E.V., Caldwell, T.G., Dalldorf, G.K., 2010. Timing and distribution of alluvial fan sedimentation in response to strengthening of late Holocene ENSO variability in the Sonoran Desert, Southwestern Arizona, USA. Quaternary Research 73(03), 425–438. doi: 10.1016/j.yqres.2010.01.004.

Badarch, G., Cunningham, W.D., Windley, B.F., 2002. A new terrane subdivision for Mongolia: implications for the Phanerozoic crustal growth of Central Asia. Journal of Asian Earth Sciences 21(1), 87–110. doi:10.1016/S1367-9120(02)00017-2.

Badrinarayanan, V., Kendall, A., Cipolla, R., 2017. SegNet: A Deep Convolutional Encoder-Decoder Architecture for Image Segmentation. IEEE Transactions on Pattern Analysis and Machine Intelligence 39(12), 2481–2495. doi:10.1109/TPAMI.2016.2644615.

Bahrami, S., 2013. Tectonic controls on the morphometry of alluvial fans around Danehkhoshk anticline, Zagros, Iran. Geomorphology 180–181, 217–230. doi:10.1016/j.geomorph.2012.10.012.

Bai, M., Urtasun, R., 2017. Deep Watershed Transform for Instance Segmentation. In: Proceedings of the IEEE Conference on Computer Vision and Pattern Recognition, July 21–26, Honolulu. IEEE, New York, pp. 2858–2866. doi:10.1109/CVPR.2017.305.

Baker, V.R., 1977. Stream-channel response to floods, with examples from central Texas. GSA Bulletin 88(8), 1057–1071. doi:10.1130/0016-7606(1977)88<1057:SRTFWE>2.0.CO;2.

Balescu, S., Ritz, J.F., Lamothe, M., Auclair, M., Todbileg, M., 2007. Luminescence dating of a gigantic palaeolandslide in the Gobi-Altay mountains, Mongolia. Quaternary Geochronology 2(1–4), 290–295. doi:10.1016/j.quageo.2006.05.026.

Baljinnyam, I., Bayasgalan, A., Borisov, B.A., Cisternas, A., Dem'yanovich, M.G., Ganbaatar, L., Kochetkov, V.M., Kurushin, R.A., Molnar, P., Philip, H., Vashchilov, Y.Y., 1993. Ruptures of Major Earthquakes and Active Deformation in Mongolia and Its Surroundings. Geological Society of America Memoir 181. Geological Society of America, Boulder. doi:10.1130/MEM181-p1.

Ballantyne, C.K., 2002. Paraglacial geomorphology. Quaternary Science Reviews 21(18–19), 1935–2017. doi:10.1016/S0277-3791(02)00005-7.

Bamler, R., Hartl, P., 1998. Synthetic aperture radar interferometry. Inverse Problems 14(4), R1–R54. doi:10.1088/0266-5611/14/4/001.

Baran, I., Stewart, M.P., Kampes, B.M., Perski, Z., Lilly, P., 2003. A modification to the Goldstein radar interferogram filter. IEEE Transactions on Geoscience and Remote Sensing 41(9), 2114–2118. doi:10.1109/TGRS.2003.817212.

Barron, J.A., Bukry, D., Dean, W.E., 2005. Paleoceanographic history of the Guaymas Basin, Gulf of California, during the past 15,000 years based on diatoms, silicoflagellates, and biogenic sediments. Marine Micropaleontology 56(3–4), 81–102. doi:10.1016/j.marmicro.2005.04.001.

Barron, J.A., Metcalfe, S.E., Addison, J.A., 2012. Response of the North American monsoon to regional changes in ocean surface temperature. Paleoceanography 27(3), PA3206. doi:10.1029/2011PA002235.

Barsch, D., Fischer, K., Stäblein, G., 1987. Geomorphological Mapping of High Mountain Relief, Federal Republic of Germany. Mountain Research and Development 7(4), 361–374.

Barsch, D., Liedtke, H., 1980. Principles, scientific value and practical applicability of the geomorphological map of the Federal Republic of Germany at the scale of 1:25000 (GMK 25) and 1:100000 (GMK 100). Zeitschrift für Geomorphologie, Supplementband 36, 296–313.

Barsch, D., Stäblein, G., 1978. EDV-gerechter Symbolschlüssel für die geomorphologische Detailaufnahme in der Bundesrepublik Deutschland. In: Stäblein, G. (Ed.). Geomorphologische Detailaufnahme. Berliner geographische Abhandlungen 30. Institut für Physische Geographie der Freien Universität Berlin, Berlin, pp. 7–19.

Barth, C., Boyle, D.P., Hatchett, B.J., Bassett, S.D., Garner, C.B., Adams, K.D., 2016. Late Pleistocene climate inferences from a water balance model of Jakes Valley, Nevada (USA). Journal of Paleolimnology 56(2–3), 109–122. doi:10.1007/s10933-016-9897-z.

Bartlein, P.J., Hostetler, S.W., Alder, J.R., 2014. Paleoclimate. In: Ohring, G. (Ed.). Climate Change in North America. Springer, Cham, pp. 1–51. doi:10.1007/978-3-319-03768-4_1.

Batbaatar, J., Gillespie, A.R., Fink, D., Matmon, A., Fujioka, T., 2018. Asynchronous glaciations in arid continental climate. Quaternary Science Reviews 182, 1–19. doi:10.1016/j.quascirev.2017.12.001.

Bayasgalan, A., Jackson, J., McKenzie, D., 2005. Lithosphere rheology and active tectonics in Mongolia: relations between earthquake source parameters, gravity and GPS measurements. Geophysical Journal International 163(3), 1151–1179. doi:10.1111/j.1365-246X.2005.02764.x.

Bayasgalan, A., Jackson, J., Ritz, J.F., Carretier, S., 1999. 'Forebergs', flower structures, and the development of large intra-continental strike-slip faults: the Gurvan Bogd fault system in Mongolia. Journal of Structural Geology 21(10), 1285–1302. doi:10.1016/S0191-8141(99)00064-4.

Bayburt, S., Kurtak, A.B., Büyüksalih, G., Jacobsen, K., 2017. Geometric Accuracy Analysis of WorldDEM in Relation to AW3D30, SRTM and ASTER GDEM2. ISPRS - International Archives of the Photogrammetry, Remote Sensing and Spatial Information Sciences XLII-1/W1, 211–217. doi:10.5194/isprs-archives-XLII-1-W1-211-2017.

Bayık, Ç., Becek, K., Mekik, Ç., Özendi, M., 2018. On the Vertical Accuracy of the ALOS World

3D-30m Digital Elevation Model. Remote Sensing Letters 9(6), 607–615. doi:10.1080/2150704X.2018.1453174.

Bazgir, O., Zhang, R., Dhruba, S.R., Rahman, R., Ghosh, S., Pal, R., 2020. Representation of features as images with neighborhood dependencies for compatibility with convolutional neural networks. Nature Communications 11(1), 4391. doi:10.1038/s41467-020-18197-y.

Beaty, C.B., 1970. Age and estimated rate of accumulation of an alluvial fan, White Mountains, California, U.S.A. American Journal of Science 268(1), 50–77. doi:10.2475/ajs.268.1.50.

Behrens, T., Schmidt, K., MacMillan, R.A., Viscarra Rossel, R.A., 2018. Multi-scale digital soil mapping with deep learning. Scientific Reports 8(1), 15244. doi:10.1038/s41598-018-33516-6.

Belgiu, M., Drăguţ, L., 2016. Random forest in remote sensing: A review of applications and future directions. ISPRS Journal of Photogrammetry and Remote Sensing 114, 24–31. doi:10.1016/j.isprsjprs.2016.01.011.

Belgiu, M., Tomljenovic, I., Lampoltshammer, T., Blaschke, T., Höfle, B., 2014. Ontology-Based Classification of Building Types Detected from Airborne Laser Scanning Data. Remote Sensing 6(2), 1347–1366. doi:10.3390/rs6021347.

Bellman, R., 1984. Dynamic programming. Princeton University Press, Princeton.

Bengio, Y., Courville, A., Vincent, P., 2013. Representation Learning: A Review and New Perspectives. IEEE Transactions on Pattern Analysis and Machine Intelligence 35(8), 1798–1828. doi:10.1109/TPAMI.2013.50.

Benn, D.I., Owen, L.A., 1998. The role of the Indian summer monsoon and the mid-latitude westerlies in Himalayan glaciation: review and speculative discussion. Journal of the Geological Society 155(2), 353–363. doi:10.1144/gsjgs.155.2.0353.

Benn, D.I., Owen, L.A., Finkel, R.C., Clemmens, S., 2006. Pleistocene lake outburst floods and fan formation along the eastern Sierra Nevada, California: implications for the interpretation of intermontane lacustrine records. Quaternary Science Reviews 25(21), 2729–2748. doi:10.1016/j.quascirev.2006.02.018.

Benson, L.V., 2003. Western lakes. In: Gillespie, A.R., Porter, S.C., Atwater, B.F. (Eds.). The Quaternary period in the United States. Developments in Quaternary Sciences 1. Elsevier, Amsterdam, New York, pp. 185–204. doi:10.1016/S1571-0866(03)01009-1.

Benson, L.V., Currey, D.R., Dorn, R.I., Lajoie, K.R., Oviatt, C.G., Robinson, S.W., Smith, G.I., Stine, S., 1990. Chronology of expansion and contraction of four great Basin lake systems during the past 35,000 years. Palaeogeography, Palaeoclimatology, Palaeoecology 78(3–4), 241–286. doi:10.1016/0031-0182(90)90217-U.

Benson, L.V., Kashgarian, M., Rubin, M., 1995. Carbonate deposition, Pyramid Lake subbasin, Nevada: 2. Lake levels and polar jet stream positions reconstructed from radiocarbon ages and elevations of carbonates (tufas) deposited in the Lahontan basin. Palaeogeography, Palaeoclimatology, Palaeoecology 117(1–2), 1–30. doi:10.1016/0031-0182(94)00103-F.

Benson, L.V., Smoot, J.P., Kashgarian, M., Sarna-Wojcicki, A.M., Burdett, J.W., 1997. Radiocarbon Ages and Environments of Deposition of the Wono and Trego Hot Springs Tephra Layers in the Pyramid Lake Subbasin, Nevada. Quaternary Research 47(3), 251–260. doi:10.1006/qres.1997.1897.

Benz, U.C., Hofmann, P., Willhauck, G., Lingenfelder, I., Heynen, M., 2004. Multi-resolution, object-oriented fuzzy analysis of remote sensing data for GIS-ready information. ISPRS Journal of Photogrammetry and Remote Sensing 58(3–4), 239–258. doi:10.1016/j.isprsjprs.2003.10.002.

Berger, C., McArdell, B.W., Schlunegger, F., 2011. Sediment transfer patterns at the Illgraben catchment, Switzerland: Implications for the time scales of debris flow activities. Geomorphology 125(3), 421–432. doi:10.1016/j.geomorph.2010.10.019.

Berry, P.A.M., Garlick, J.D., Smith, R.G., 2007. Near-global validation of the SRTM DEM using satellite radar altimetry. Remote Sensing of Environment 106(1), 17–27. doi:10.1016/j.rse.2006.07.011.

Bertrand, M., Liébault, F., Piégay, H., 2013. Debris-flow susceptibility of upland catchments. Natural Hazards 67(2), 497–511. doi:10.1007/s11069-013-0575-4.

Beven, K., 2006. A manifesto for the equifinality thesis. Journal of Hydrology 320(1–2), 18–36. doi:10.1016/j.jhydrol.2005.07.007.

Bhattacharyya, A., 1946. On a Measure of Divergence between Two Multinomial Populations. The Indian Journal of Statistics 7(4), 401–406.

Böhner, J., 2006. General climatic controls and topoclimatic variations in Central and High Asia. Boreas 35(2), 279–295. doi:10.1080/03009480500456073.

Bieda, S.W., 2012. Flash Flood Causing Mechanisms of the North American Monsoon System in the Sonoran Desert. Ph.D. thesis, University of Arizona, Tucson.

Binnie, S.A., Phillips, W.M., Summerfield, M.A., Fifield, L.K., 2007. Tectonic uplift, threshold hillslopes, and denudation rates in a developing mountain range. Geology 35(8), 743–746. doi:10.1130/G23641A.1.

Binnie, S.A., Phillips, W.M., Summerfield, M.A., Fifield, L.K., Spotila, J.A., 2008. Patterns of denudation through time in the San Bernardino Mountains, California: Implications for early-stage orogenesis. Earth and Planetary Science Letters 276(1–2), 62–72. doi:10.1016/j.epsl.2008.09.008.

Bishop, C.M., 1995. Neural networks for pattern recognition. Clarendon Press, Oxford University Press, New York, Oxford.

Bishop, M.P., James, L.A., Shroder, J.F., Walsh, S.J., 2012. Geospatial technologies and digital geomorphological mapping: Concepts, issues and research. Geomorphology 137(1), 5–26. doi:10.1016/j.geomorph.2011.06.027.

Bishr, Y., 1998. Overcoming the semantic and other barriers to GIS interoperability. International Journal of Geographical Information Science 12(4), 299–314. doi:10.1080/136588198241806.

Björck, Å., 1996. Numerical methods for least squares problems. Society for Industrial and Applied Mathematics, Philadelphia.

Blair, T.C., 1999a. Alluvial fan and catchment initiation by rock avalanching, Owens Valley, California. Geomorphology 28(3–4), 201–221. doi:10.1016/S0169-555X(98)00111-1.

Blair, T.C., 1999b. Cause of dominance by sheetflood vs. debris-flow processes on two adjoining alluvial fans, Death Valley, California. Sedimentology 46(6), 1015–1028. doi:10.1046/j.1365-3091.1999.00261.x.

Blair, T.C., 1999c. Sedimentary processes and facies of the waterlaid Anvil Spring Canyon alluvial fan, Death Valley, California. Sedimentology 46(5), 913–940. doi:10.1046/j.1365-3091.1999.00259.x.

Blair, T.C., 2001. Outburst Flood Sedimentation on the Proglacial Tuttle Canyon Alluvial Fan, Owens Valley, California, U.S.A. Journal of Sedimentary Research 71(5), 657–679. doi:10.1306/2DC4095E-0E47-11D7-8643000102C1865D.

Blair, T.C., 2003. Features and origin of the giant Cucomungo Canyon alluvial fan, Eureka Valley, California. In: Chan, M.A., Archer, A.W. (Eds.). Extreme depositional environments: mega end members in geologic time. Special Paper 370. Geological Society of America, Boulder, pp. 105–126. doi:10.1130/0-8137-2370-1.105.

Blair, T.C., McPherson, J.G., 1994. Alluvial Fans and their Natural Distinction from Rivers Based on Morphology, Hydraulic Processes, Sedimentary Processes, and Facies Assemblages. SEPM Journal of Sedimentary Research 64A, 450–489. doi:10.1306/D4267DDE-2B26-11D7-8648000102C1865D.

Blair, T.C., McPherson, J.G., 1998. Recent debris-flow processes and resultant form and facies of the

Dolomite alluvial fan, Owens Valley, California. Journal of Sedimentary Research 68(5), 800–818. doi:10.2110/jsr.68.800.

Blair, T.C., McPherson, J.G., 2009. Processes and Forms of Alluvial Fans. In: Parsons, A.J., Abrahams, A.D. (Eds.). Geomorphology of Desert Environments. Springer, Dordrecht, pp. 413–467. doi:10.1007/978-1-4020-5719-9_14.

Blaschke, T., 2003. Object-based contextual image classification built on image segmentation. In: IEEE Workshop on Advances in Techniques for Analysis of Remotely Sensed Data, October 27–28, Greenbelt. IEEE, New York, pp. 113–119. doi:10.1109/WARSD.2003.1295182.

Blaschke, T., 2010. Object based image analysis for remote sensing. ISPRS Journal of Photogrammetry and Remote Sensing 65(1), 2–16. doi:10.1016/j.isprsjprs.2009.06.004.

Blaschke, T., Burnett, C., Pekkarinen, A., 2004. Image Segmentation Methods for Object-based Analysis and Classification. In: van der Meer, F.D., Jong, S.M. (Eds.). Remote Sensing Image Analysis: Including The Spatial Domain. Remote Sensing and Digital Image Processing 5. Springer, Dordrecht, pp. 211–236. doi:10.1007/978-1-4020-2560-0_12.

Blaschke, T., Hay, G.J., Kelly, M., Lang, S., Hofmann, P., Addink, E., Queiroz Feitosa, R., van der Meer, F.D., van der Werff, H., van Coillie, F., Tiede, D., 2014. Geographic Object-Based Image Analysis – Towards a new paradigm. ISPRS Journal of Photogrammetry and Remote Sensing 87, 180–191. doi:10.1016/j.isprsjprs.2013.09.014.

Blaschke, T., Lang, S., Lorup, E., Strobl, J., Zeil, P., 2000. Object-oriented Image Processing in an Integrated GIS/Remote Sensing Environment and Perspectives for Environmental Applications. In: Cremers, A.B., Greve, K. (Eds.). Umweltinformatik '00 Umweltinformation für Planung, Politik und Öffentlichkeit, October 4–6, Bonn. Metropolis, Marburg, pp. 555–570.

Blaschke, T., Strobl, J., 2001. What's wrong with pixels? Some recent developments interfacing remote sensing and GIS. Geo-Informations-Systeme 14(6), 12–17.

Blisniuk, K., Oskin, M., Fletcher, K., Rockwell, T., Sharp, W., 2012. Assessing the reliability of U-series and ^{10}Be dating techniques on alluvial fans in the Anza Borrego Desert, California. Quaternary Geochronology 13, 26–41. doi:10.1016/j.quageo.2012.08.004.

Blissenbach, E., 1952. Relation of surface angle distribution to particle size distribution on alluvial fans. Journal of Sedimentary Research 22(1), 25–28. doi:10.1306/D42694A4-2B26-11D7-8648000102C1865D.

Blum, M.D., Törnqvist, T.E., 2000. Fluvial responses to climate and sea-level change: a review and look forward: Fluvial responses to climate and sea-level change. Sedimentology 47, 2–48. doi:10.1046/j.1365-3091.2000.00008.x.

Blythe, A.E., Burbank, D.W., Farley, K.A., Fielding, E.J., 2000. Structural and topographic evolution of the central Transverse Ranges, California, from apatite fission-track, (U-Th)/He and digital elevation model analyses. Basin Research 12(2), 97–114. doi:10.1046/j.1365-2117.2000.00116.x.

Bogaart, P.W., van Balen, R.T., 2000. Numerical modeling of the response of alluvial rivers to Quaternary climate change. Global and Planetary Change 27(1–4), 147–163. doi:10.1016/S0921-8181(01)00064-9.

Bonhage, A., Eltaher, M., Raab, T., Breuß, M., Raab, A., Schneider, A., 2021. A modified Mask region-based convolutional neural network approach for the automated detection of archaeological sites on high-resolution light detection and ranging-derived digital elevation models in the North German Lowland. Archaeological Prospection pp. 1–10. doi:10.1002/arp.1806.

Bonini, M., Cerca, M., Moratti, G., López-Martínez, M., Corti, G., Gracia-Marroquín, D., 2017. Early Miocene shortening in the lower Comondú Group in Baja California Sur (México). Tectonophysics 719–720, 135–147. doi:10.1016/j.tecto.2017.05.032.

Bonnet, S., Crave, A., 2003. Landscape response to climate change: Insights from experimental

modeling and implications for tectonic versus climatic uplift of topography. Geology 31(2), 123–126. doi:10.1130/0091-7613(2003)031<0123:LRTCCI>2.0.CO;2.

Borga, M., Stoffel, M., Marchi, L., Marra, F., Jakob, M., 2014. Hydrogeomorphic response to extreme rainfall in headwater systems: Flash floods and debris flows. Journal of Hydrology 518, 194–205. doi:10.1016/j.jhydrol.2014.05.022.

Boser, B.E., Guyon, I.M., Vapnik, V.N., 1992. A Training Algorithm for Optimal Margin Classifiers. In: Annual Workshop on Computational Learning Theory, July 27–29, Pittsburgh. Association for Computing Machinery, New York, pp. 144–152. doi:10.1145/130385.130401.

Bostrom, N., 2002. Anthropic bias: observation selection effects in science and philosophy. Studies in philosophy. Routledge, New York.

Boulton, S.J., Stokes, M., 2018. Which DEM is best for analyzing fluvial landscape development in mountainous terrains? Geomorphology 310, 168–187. doi:10.1016/j.geomorph.2018.03.002.

Bovis, M.J., Jakob, M., 1999. The role of debris supply conditions in predicting debris flow activity. Earth Surface Processes and Landforms 24(11), 1039–1054. doi:10.1002/(SICI)1096-9837(199910)24:11<1039::AID-ESP29>3.0.CO;2-U.

Bowman, D., 1978. Determination of intersection points within a telescopic alluvial fan complex. Earth Surface Processes 3(3), 265–276. doi:10.1002/esp.3290030306.

Bowman, D., 2018. Principles of Alluvial Fan Morphology. Springer, Dordrecht.

Bradley, A.P., 1997. The use of the area under the ROC curve in the evaluation of machine learning algorithms. Pattern Recognition 30(7), 1145–1159. doi:10.1016/S0031-3203(96)00142-2.

Bramer, M.A., 2007. Principles of Data Mining. Springer, London.

Brardinoni, F., Church, M.A., Simoni, A., Macconi, P., 2012. Lithologic and glacially conditioned controls on regional debris-flow sediment dynamics. Geology 40(5), 455–458. doi:10.1130/G33106.1.

Breiman, L., 1996. Bagging Predictors. Machine Learning 24(2), 123–140. doi:10.1023/A:1018054314350.

Breiman, L., 2001. Random Forests. Machine Learning 45(1), 5–32. doi:10.1023/A:1010933404324.

Breiman, L., Friedman, J., Olshen, R., Stone, C., 1984. Classification and Regression Trees. Chapman & Hall/CRC, Boca Raton.

Brendel, W., Bethge, M., 2019. Approximating CNNs with Bag-of-local-Features models works surprisingly well on ImageNet. In: Proceedings of the 7th International Conference on Learning Representations, May 6–9, New Orleans. ICLR, La Jolla, pp. 1–15.

Breslow, L.A., Aha, D.W., 1997. Simplifying decision trees: A survey. The Knowledge Engineering Review 12(01), 1–40. doi:10.1017/S0269888997000015.

Breunig, M.M., Kriegel, H.P., Ng, R.T., Sander, J., 2000. LOF: identifying density-based local outliers. In: Proceedings of the ACM SIGMOD international conference on Management of data, May 16–18, Dallas. Association for Computing Machinery, Dallas, pp. 93–104. doi:10.1145/342009.335388.

Brunsden, D., 1993. Barriers to geomorphological change. In: Thomas, D.S.G., Allison, R.J. (Eds.). Landscape sensitivity. British Geomorphological Research Group symposia series. Wiley, Chichester, New York, pp. 7–12.

Brunsden, D., 1996. Geomorphological events and landform change. Zeitschrift für Geomorphologie 40, 273–288.

Bryant, M., Falk, P., Paola, C., 1995. Experimental study of avulsion frequency and rate of deposition. Geology 23(4), 365–368. doi:10.1130/0091-7613(1995)023<0365:ESOAFA>2.3.CO;2.

Bubenzer, O., Bolten, A., 2008. The use of new elevation data (SRTM/ASTER) for the detection and morphometric quantification of Pleistocene megadunes (draa) in the eastern Sahara and the southern Namib. Geomorphology 102(2), 221–231. doi:10.1016/j.geomorph.2008.05.003.

Bull, W.B., 1962. Relations of alluvial fan size and slope to drainage basin size and lithology in western Fresno County, California. In: USGS (Ed.). Short papers in geology, hydrology, and topography; Articles 1-59: Geological Survey Research 1962. United States Geological Survey Professional Paper 450-B. United States Government Printing Office, Washington, D.C., pp. 51–53. doi:10.3133/pp450B.

Bull, W.B., 1964. Geomorphology of segmented alluvial fans in western Fresno County, California. United States Geological Survey Professional Paper 352-E, United States Government Printing Office, Washington, D.C. doi:10.3133/pp352E.

Bull, W.B., 1972. Recognition of Alluvial-Fan Deposits in the Stratigraphic Record. In: Rigby, J.K., Hamblin, W.K. (Eds.). Recognition of Ancient Sedimentary Environments. SEPM Special Publication 16. SEPM Society for Sedimentary Geology. doi:10.2110/pec.72.02.0063.

Bull, W.B., 1977. The alluvial-fan environment. Progress in Physical Geography 1(2), 222–270. doi:10.1177/030913337700100202.

Bull, W.B., 1978. Geomorphic tectonic activity classes of the south front of the San Gabriel Mountains, California. Contract Report 14-08-001-G-394, USGS, Menlo Park.

Bull, W.B., 1979. Threshold of critical power in streams. GSA Bulletin 90(5), 453–464. doi:10.1130/0016-7606(1979)90<453:TOCPIS>2.0.CO;2.

Bull, W.B., 1991. Geomorphic responses to climatic change. Oxford University Press, New York.

Bull, W.B., 2000. Correlation of Fluvial Aggradation Events to Times of Global Climate Change. In: Noller, J.S., Sowers, J.M., Lettis, W.R. (Eds.). Quaternary geochronology methods and applications. American Geophysical Union, Washington, D.C., pp. 456–464. doi:10.1029/RF004p0456.

Burg, J.P., Nievergelt, P., Oberli, F., Seward, D., Davy, P., Maurin, J.C., Diao, Z., Meier, M., 1998. The Namche Barwa syntaxis: evidence for exhumation related to compressional crustal folding. Journal of Asian Earth Sciences 16(2–3), 239–252. doi:10.1016/S0743-9547(98)00002-6.

Burnett, A.W., 1994. Regional-Scale Troughing Over the Southwestern United States: Temporal Climatology, Teleconnections, and Climatic Impact. Physical Geography 15(1), 80–98. doi:10.1080/02723646.1994.10642506.

Burnett, C., Blaschke, T., 2003. A multi-scale segmentation/object relationship modelling methodology for landscape analysis. Ecological Modelling 168(3), 233–249. doi:10.1016/S0304-3800(03)00139-X.

Burrough, P.A., 1986. Principles of geographical information systems for land resources assessment. Geocarto International 1(3), 54–54. doi:10.1080/10106048609354060.

Burrough, P.A., van Gaans, P.F.M., MacMillan, R.A., 2000. High-resolution landform classification using fuzzy k-means. Fuzzy Sets and Systems 113(1), 37–52. doi:10.1016/S0165-0114(99)00011-1.

Cadieu, C.F., Hong, H., Yamins, D.L.K., Pinto, N., Ardila, D., Solomon, E.A., Majaj, N.J., DiCarlo, J.J., 2014. Deep Neural Networks Rival the Representation of Primate IT Cortex for Core Visual Object Recognition. PLOS Computational Biology 10(12), 1–18. doi:10.1371/journal.pcbi.1003963.

Cai, Y., Zhang, H., Cheng, H., An, Z., Edwards, R.L., Wang, X., Tan, L., Liang, F., Wang, J., Kelly, M., 2012. The Holocene Indian monsoon variability over the southern Tibetan Plateau and its teleconnections. Earth and Planetary Science Letters 335–336, 135–144. doi:10.1016/j.epsl.2012.04.035.

Calais, E., Vergnolle, M., San'kov, V., Lukhnev, A., Miroshnitchenko, A., Amarjargal, S., Déverchère, J., 2003. GPS measurements of crustal deformation in the Baikal-Mongolia area (1994-2002): Implications for current kinematics of Asia. Journal of Geophysical Research: Solid Earth 108(B10), 2501. doi:10.1029/2002JB002373.

Calmus, T., Aguillón-Robles, A., Maury, R.C., Bellon, H., Benoit, M., Cotten, J., Bourgois, J., Michaud, F., 2003. Spatial and temporal evolution of basalts and magnesian andesites ("bajaites")

from Baja California, Mexico: the role of slab melts. Lithos 66(1–2), 77–105. doi:10.1016/S0024-4937(02)00214-1.

Calvache, M.L., Viseras, C., Fernández, J., 1997. Controls on fan development — evidence from fan morphometry and sedimentology; Sierra Nevada, SE Spain. Geomorphology 21(1), 69–84. doi:10.1016/S0169-555X(97)00035-4.

Carabajal, C.C., Harding, D.J., 2006. SRTM C-Band and ICESat Laser Altimetry Elevation Comparisons as a Function of Tree Cover and Relief. Photogrammetric Engineering & Remote Sensing 72(3), 287–298.

Carleton, A.M., Carpenter, D.A., Weser, P.J., 1990. Mechanisms of Interannual Variability of the Southwest United States Summer Rainfall Maximum. Journal of Climate 3(9), 999–1015. doi:10.1175/1520-0442(1990)003<0999:MOIVOT>2.0.CO;2.

Carlson, C.W., Pluhar, C.J., Glen, J.M.G., Farner, M.J., 2013. Kinematics of the west-central Walker Lane: Spatially and temporally variable rotations evident in the Late Miocene Stanislaus Group. Geosphere 9(6), 1530–1551. doi:10.1130/GES00955.1.

Carreira-Perpinan, M.A., 2006. Acceleration Strategies for Gaussian Mean-Shift Image Segmentation. In: Proceedings of the IEEE Computer Society Conference on Computer Vision and Pattern Recognition, June 17–22, New York. IEEE, New York, pp. 1160–1167. doi:10.1109/CVPR.2006.44.

Carretier, S., Lucazeau, F., Ritz, J.F., 1998. Approche numérique des interactions entre faille active, climat et érosion: exemple de la faille de Bogd, Gobi Altay, Mongolie. Comptes Rendus de l'Académie des Sciences - Series IIA - Earth and Planetary Science 326(6), 391–397. doi:10.1016/S1251-8050(98)80061-X.

Carretier, S., Ritz, J.F., Jackson, J., Bayasgalan, A., 2002. Morphological dating of cumulative reverse fault scarps: examples from the Gurvan Bogd fault system, Mongolia. Geophysical Journal International 148(2), 256–277. doi:10.1046/j.1365-246X.2002.01599.x.

Castilla, G., Hay, G.J., 2008. Image objects and geographic objects. In: Blaschke, T., Lang, S., Hay, G.J. (Eds.). Object-Based Image Analysis: Spatial Concepts for Knowledge-Driven Remote Sensing Applications. Springer, Berlin, Heidelberg, pp. 91–110. doi:10.1007/978-3-540-77058-9_5.

Cavalli, M., Marchi, L., 2008. Characterisation of the surface morphology of an alpine alluvial fan using airborne LiDAR. Natural Hazards and Earth System Science 8(2), 323–333. doi:10.5194/nhess-8-323-2008.

Caves, J.K., Sjostrom, D.J., Mix, H.T., Winnick, M.J., Chamberlain, C.P., 2014. Aridification of Central Asia and uplift of the Altai and Hangay Mountains, Mongolia: Stable isotope evidence. American Journal of Science 314(8), 1171–1201. doi:10.2475/08.2014.01.

Cerezo-Mota, R., Allen, M., Jones, R., 2011. Mechanisms Controlling Precipitation in the Northern Portion of the North American Monsoon. Journal of Climate 24(11), 2771–2783. doi:10.1175/2011JCLI3846.1.

Cesta, J.M., Ward, D.J., 2016. Timing and nature of alluvial fan development along the Chajnantor Plateau, northern Chile. Geomorphology 273, 412–427. doi:10.1016/j.geomorph.2016.09.003.

Chacón, J.E., Duong, T., 2013. Data-driven density derivative estimation, with applications to nonparametric clustering and bump hunting. Electronic Journal of Statistics 7, 499–532. doi:10.1214/13-EJS781.

Chan, J.C.W., Beckers, P., Spanhove, T., Borre, J.V., 2012. An evaluation of ensemble classifiers for mapping Natura 2000 heathland in Belgium using spaceborne angular hyperspectral (CHRIS/Proba) imagery. International Journal of Applied Earth Observation and Geoinformation 18, 13–22. doi:10.1016/j.jag.2012.01.002.

Chan, J.C.W., Paelinckx, D., 2008. Evaluation of Random Forest and Adaboost tree-based ensemble

classification and spectral band selection for ecotope mapping using airborne hyperspectral imagery. Remote Sensing of Environment 112(6), 2999–3011. doi:10.1016/j.rse.2008.02.011.

Chapin, C.E., Cather, S.M., 1994. Tectonic setting of the axial basins of the northern and central Rio Grande rift. In: Keller, G.R., Cather, S.M. (Eds.). Basins of the Rio Grande rift: structure, stratigraphy, and tectonic setting. Special Paper 291. Geological Society of America, Boulder, pp. 5–26. doi:10.1130/SPE291-p5.

Chen, A., Darbon, J., Morel, J.M., 2014. Landscape evolution models: A review of their fundamental equations. Geomorphology 219, 68–86. doi:10.1016/j.geomorph.2014.04.037.

Chen, C.W., 2001. Statistical-cost Network-flow Approaches to Two-dimensional Phase Unwrapping for Radar Interferometry. Ph.D. thesis, Stanford University, Stanford.

Chen, C.W., Zebker, H.A., 2000. Two-dimensional phase unwrapping with statistical models for nonlinear optimization. In: Proceedings of the IEEE International Geoscience and Remote Sensing Symposium, July 24–28, Honolulu. IEEE, New York, pp. 3213–3215. doi:10.1109/IGARSS.2000.860386.

Chen, F.H., Chen, J.H., Holmes, J., Boomer, I., Austin, P., Gates, J.B., Wang, N.L., Brooks, S.J., Zhang, J.W., 2010. Moisture changes over the last millennium in arid central Asia: a review, synthesis and comparison with monsoon region. Quaternary Science Reviews 29(7–8), 1055–1068. doi:10.1016/j.quascirev.2010.01.005.

Chen, Z., Scott, T.R., Bearman, S., Anand, H., Keating, D., Scott, C., Arrowsmith, J.R., Das, J., 2020. Geomorphological Analysis Using Unpiloted Aircraft Systems, Structure from Motion, and Deep Learning. In: Proceedings of the IEEE/RSJ International Conference on Intelligent Robots and Systems, October 24–January 24 2021, Las Vegas. IEEE, New York, pp. 1276–1283. doi:10.1109/IROS45743.2020.9341354.

Cheng, G., Zhou, P., Han, J., 2016. Learning Rotation-Invariant Convolutional Neural Networks for Object Detection in VHR Optical Remote Sensing Images. IEEE Transactions on Geoscience and Remote Sensing 54(12), 7405–7415. doi:10.1109/TGRS.2016.2601622.

Cheng, T., Wang, X., Huang, L., Liu, W., 2020. Boundary-Preserving Mask R-CNN. In: Proceedings of the 16th European Conference on Computer Vision, August 23–28, Glasgow. Springer, Cham, pp. 660–676. doi:10.1007/978-3-030-58568-6_39.

Cheng, Y., 1995. Mean shift, mode seeking, and clustering. IEEE Transactions on Pattern Analysis and Machine Intelligence 17(8), 790–799. doi:10.1109/34.400568.

Christiansen, R.L., Lipman, P.W., 1972. Cenozoic Volcanism and Plate-Tectonic Evolution of the Western United States. II. Late Cenozoic. Philosophical Transactions of the Royal Society A: Mathematical, Physical and Engineering Sciences 271(1213), 249–284. doi:10.1098/rsta.1972.0009.

Chrysoulakis, N., Abrams, M., Kamarianakis, Y., Stanislawski, M., 2011. Validation of ASTER GDEM for the Area of Greece. Photogrammetric Engineering & Remote Sensing 77(2), 157–165. doi:10.14358/PERS.77.2.157.

Chudzian, P., 2011. Radial Basis Function Kernel Optimization for Pattern Classification. In: Kacprzyk, J., Burduk, R., Kurzyński, M., Woźniak, M., Żołnierek, A. (Eds.). Computer Recognition Systems 4. Advances in Intelligent and Soft Computing 95. Springer, Berlin, Heidelberg, pp. 99–108. doi:10.1007/978-3-642-20320-6_11.

Church, M.A., 2006. Bed Material Transport and the Morphology of Alluvial River Channels. Annual Review of Earth and Planetary Sciences 34(1), 325–354. doi:10.1146/annurev.earth.33.092203.122721.

Church, M.A., 2017. Interpreting sediment yield scaling. Earth Surface Processes and Landforms 42(12), 1895–1898. doi:10.1002/esp.4165.

Church, M.A., Mark, D.M., 1980. On size and scale in geomorphology. Progress in Physical Geography 4(3), 342–390. doi:10.1177/030913338000400302.

Church, M.A., Ryder, J.M., 1972. Paraglacial Sedimentation: A Consideration of Fluvial Processes Conditioned by Glaciation. GSA Bulletin 83(10), 3059–3072. doi:10.1130/0016-7606(1972)83[3059:PSACOF]2.0.CO;2.

Clark, M.K., Schoenbohm, L.M., Royden, L.H., Whipple, K.X., Burchfiel, B.C., Zhang, X., Tang, W., Wang, E., Chen, L., 2004. Surface uplift, tectonics, and erosion of eastern Tibet from large-scale drainage patterns. Tectonics 23(1), 1–20. doi:10.1029/2002TC001402.

Clarke, K.C., 1995. Analytical and Computer Cartography. Prentice Hall series in geographic information science. Prentice Hall, Englewood Cliffs, 2nd ed.

Clarke, L.E., 2015. Experimental alluvial fans: Advances in understanding of fan dynamics and processes. Geomorphology 244, 135–145. doi:10.1016/j.geomorph.2015.04.013.

Clarke, L.E., Quine, T.A., Nicholas, A.P., 2010. An experimental investigation of autogenic behaviour during alluvial fan evolution. Geomorphology 115(3), 278–285. doi:10.1016/j.geomorph.2009.06.033.

Clevis, Q., de Boer, P.L., Wachter, M., 2003. Numerical modelling of drainage basin evolution and three-dimensional alluvial fan stratigraphy. Sedimentary Geology 163(1–2), 85–110. doi:10.1016/S0037-0738(03)00174-X.

Cogswell, M., Ahmed, F., Girshick, R.B., Zitnick, L., Batra, D., 2016. Reducing Overfitting in Deep Networks by Decorrelating Representations. In: Proceedings of the 4th International Conference on Learning Representations, May 2–4, San Juan. ICLR, La Jolla.

Colgan, J.P., Dumitru, T.A., Reiners, P.W., Wooden, J.L., Miller, E.L., 2006. Cenozoic Tectonic Evolution of the Basin and Range Province in Northwestern Nevada. American Journal of Science 306(8), 616–654. doi:10.2475/08.2006.02.

Comaniciu, D., 2003. An algorithm for data-driven bandwidth selection. IEEE Transactions on Pattern Analysis and Machine Intelligence 25(2), 281–288. doi:10.1109/TPAMI.2003.1177159.

Comaniciu, D., Meer, P., 1999. Mean shift analysis and applications. In: Proceedings of the IEEE International Conference on Computer Vision, September 20–27, Kerkyra. IEEE, New York, pp. 1197–1203. doi:10.1109/ICCV.1999.790416.

Comaniciu, D., Meer, P., 2002. Mean shift: a robust approach toward feature space analysis. IEEE Transactions on Pattern Analysis and Machine Intelligence 24(5), 603–619. doi:10.1109/34.1000236.

Comaniciu, D., Ramesh, V., Meer, P., 2000. Real-time tracking of non-rigid objects using mean shift. In: Proceedings of the IEEE Conference on Computer Vision and Pattern Recognition, June 15, Hilton Head Island. IEEE, New York, pp. 142–149. doi:10.1109/CVPR.2000.854761.

Comaniciu, D., Ramesh, V., Meer, P., 2001. The variable bandwidth mean shift and data-driven scale selection. In: Proceedings of the IEEE International Conference on Computer Vision, July 7–14, Vancouver. IEEE, New York, pp. 438–445. doi:10.1109/ICCV.2001.937550.

Comrie, A.C., Glenn, E.C., 1998. Principal components-based regionalization of precipitation regimes across the southwest United States and Northern Mexico, with an application to monsoon precipitation variability. Climate Research 10, 201–215. doi:10.3354/cr010201.

Conn, D., Ramirez, C.M., 2016. Random Forests and Fuzzy Forests in Biomedical Research. In: Alvarez, R.M. (Ed.). Computational Social Science. Cambridge University Press, Cambridge, pp. 168–196. doi:10.1017/CBO9781316257340.008.

Conrad, O., Bechtel, B., Bock, M., Dietrich, H., Fischer, E., Gerlitz, L., Wehberg, J., Wichmann, V., Böhner, J., 2015. System for Automated Geoscientific Analyses (SAGA) v. 2.1.4. Geoscientific Model Development 8(7), 1991–2007. doi:10.5194/gmd-8-1991-2015.

Corrigan, P., Fenn, D.D., Kluck, D.R., Vogel, J.L., 1999. Probable maximum precipitation for California. Hydrometeorological Report 59, National Weather Service, Silver Spring.

Cortes, C., Vapnik, V.N., 1995. Support-vector networks. Machine Learning 20(3), 273–297. doi: 10.1007/BF00994018.

Costa, J.E., 1984. Physical Geomorphology of Debris Flows. In: Costa, J.E., Fleisher, P.J. (Eds.). Developments and Applications of Geomorphology. Springer, Berlin, Heidelberg, pp. 268–317. doi:10.1007/978-3-642-69759-3_9.

Costa, J.E., 1988. Rheologic, geomorphic and sedimentologic differentiation of water floods, hyperconcentrated flows and debris flows. In: Baker, V.R., Kochel, R.C., Patton, P.C. (Eds.). Flood geomorphology. Wiley, New York, pp. 113–122.

Cracknell, M.J., Reading, A.M., 2014. Geological mapping using remote sensing data: A comparison of five machine learning algorithms, their response to variations in the spatial distribution of training data and the use of explicit spatial information. Computers & Geosciences 63, 22–33. doi:10.1016/j.cageo.2013.10.008.

Cristianini, N., Shawe-Taylor, J., 2000. An introduction to support vector machines and other kernel-based learning methods. Cambridge University Press, Cambridge, New York.

Crosta, G.B., Frattini, P., 2004. Controls on modern alluvial fan processes in the central Alps, northern Italy. Earth Surface Processes and Landforms 29(3), 267–293. doi:10.1002/esp.1009.

Csillik, O., Cherbini, J., Johnson, R., Lyons, A., Kelly, M., 2018. Identification of Citrus Trees from Unmanned Aerial Vehicle Imagery Using Convolutional Neural Networks. Drones 2(4), 39. doi:10.3390/drones2040039.

Csillik, O., Evans, I.S., Drăguţ, L., 2015. Transformation (normalization) of slope gradient and surface curvatures, automated for statistical analyses from DEMs. Geomorphology 232, 65–77. doi:10.1016/j.geomorph.2014.12.038.

Cumming, I.G., Wong, F.H., 2005. Digital Processing of Synthetic Aperture Radar Data: Algorithms and Implementation. Artech House, Boston.

Cunningham, W.D., 2005. Active intracontinental transpressional mountain building in the Mongolian Altai: Defining a new class of orogen. Earth and Planetary Science Letters 240(2), 436–444. doi:10.1016/j.epsl.2005.09.013.

Cunningham, W.D., 2007. Structural and topographic characteristics of restraining bend mountain ranges of the Altai, Gobi Altai and easternmost Tien Shan. In: Cunningham, W.D., Mann, P. (Eds.). Tectonics of Strike-Slip Restraining and Releasing Bends. Geological Society, London, Special Publications 290. Geological Society of London, London, pp. 219–237. doi:10.1144/SP290.7.

Cunningham, W.D., 2010. Tectonic setting and structural evolution of the Late Cenozoic Gobi Altai orogen. In: Kusky, T.M., Zhai, M.G., Xiao, W. (Eds.). The Evolving Continents: Understanding Processes of Continental Growth. Geological Society, London, Special Publications 338. Geological Society of London, London, pp. 361–387. doi:10.1144/SP338.17.

Cunningham, W.D., Windley, B.F., Dorjnamjaa, D., Badamgarov, G., Saandar, M., 1996. A structural transect across the Mongolian Western Altai: Active transpressional mountain building in central Asia. Tectonics 15(1), 142–156. doi:10.1029/95TC02354.

Cunningham, W.D., Windley, B.F., Owen, L.A., Barry, T., Dorjnamjaa, D., Badamgarov, J., 1997. Geometry and style of partitioned deformation within a late Cenozoic transpressional zone in the eastern Gobi Altai Mountains, Mongolia. Tectonophysics 277(4), 285–306. doi:10.1016/S0040-1951(97)00034-6.

Cuppen, J.J.M., 1980. A divide and conquer method for the symmetric tridiagonal eigenproblem. Numerische Mathematik 36(2), 177–195. doi:10.1007/BF01396757.

Curlander, J.C., 1982. Location of Spaceborne SAR Imagery. IEEE Transactions on Geoscience and Remote Sensing GE-20(3), 359–364. doi:10.1109/TGRS.1982.350455.

Cybenko, G., 1989. Approximation by superpositions of a sigmoidal function. Mathematics of Control, Signals, and Systems 2(4), 303–314. doi:10.1007/BF02551274.

Dade, W.B., Verdeyen, M.E., 2007. Tectonic and climatic controls of alluvial-fan size and source-catchment relief. Journal of the Geological Society 164(2), 353–358. doi:10.1144/0016-76492006-039.

Daniel, C., Wood, F.S., Gorman, J.W., 1999. Fitting equations to data: computer analysis of multifactor data. Wiley classics library. Wiley, New York, 2nd ed.

Danielson, J.J., Gesch, D.B., 2011. Global multi-resolution terrain elevation data 2010 (GMTED2010). Open-File Report 2011-1073, U.S. Geological Survey and Earth Resources Observation and Science Center, Sioux Falls. doi:10.3133/ofr20111073.

D'Arcy, M., Roda-Boluda, D.C., Whittaker, A.C., 2017. Glacial-interglacial climate changes recorded by debris flow fan deposits, Owens Valley, California. Quaternary Science Reviews 169, 288–311. doi:10.1016/j.quascirev.2017.06.002.

Dasgupta, P., 2003. Sediment gravity flow—the conceptual problems. Earth-Science Reviews 62(3–4), 265–281. doi:10.1016/S0012-8252(02)00160-5.

Davi, N.K., Jacoby, G.C., Curtis, A.E., Baatarbileg, N., 2006. Extension of Drought Records for Central Asia Using Tree Rings: West-Central Mongolia. Journal of Climate 19(2), 288–299. doi:10.1175/JCLI3621.1.

Davies, T.R., McSaveney, M.J., 2008. Principles of sustainable development on fans. Journal of Hydrology (New Zealand) 47(1), 43–65.

Davis, J., Goadrich, M., 2006. The Relationship between Precision-Recall and ROC Curves. In: Proceedings of the 23rd International Conference on Machine Learning, June 25–29, Pittsburgh. Association for Computing Machinery, New York, pp. 233—240. doi:10.1145/1143844.1143874.

Davis, R.E., Walker, D.R., 1992. An Upper-Air Synoptic Climatology of the Western United States. Journal of Climate 5(12), 1449–1467. doi:10.1175/1520-0442(1992)005<1449:AUASCO>2.0.CO;2.

Davis, W.M., 1905. The Geographical Cycle in an Arid Climate. The Journal of Geology 13(5), 381–407. doi:10.1086/621241.

Díaz-Uriarte, R., Alvarez de Andrés, S., 2006. Gene selection and classification of microarray data using random forest. BMC Bioinformatics 7(1), 3. doi:10.1186/1471-2105-7-3.

de Haas, T., Braat, L., Leuven, J.R.F.W., Lokhorst, I.R., Kleinhans, M.G., 2015a. Effects of debris flow composition on runout, depositional mechanisms, and deposit morphology in laboratory experiments: Experimental Debris Flows. Journal of Geophysical Research: Earth Surface 120(9), 1949–1972. doi:10.1002/2015JF003525.

de Haas, T., Densmore, A.L., Stoffel, M., Suwa, H., Imaizumi, F., Ballesteros-Cánovas, J.A., Wasklewicz, T.A., 2018. Avulsions and the spatio-temporal evolution of debris-flow fans. Earth-Science Reviews 177, 53–75. doi:10.1016/j.earscirev.2017.11.007.

de Haas, T., Kleinhans, M.G., Carbonneau, P.E., Rubensdotter, L., Hauber, E., 2015b. Surface morphology of fans in the high-Arctic periglacial environment of Svalbard: Controls and processes. Earth-Science Reviews 146, 163–182. doi:10.1016/j.earscirev.2015.04.004.

de Haas, T., van den Berg, W., Braat, L., Kleinhans, M.G., 2016. Autogenic avulsion, channelization and backfilling dynamics of debris-flow fans. Sedimentology 63(6), 1596–1619. doi:10.1111/sed.12275.

de Scally, F.A., Owens, I.F., 2004. Morphometric controls and geomorphic responses on fans in the Southern Alps, New Zealand. Earth Surface Processes and Landforms 29(3), 311–322. doi:10.1002/esp.1022.

de Scally, F.A., Owens, I.F., Louis, J., 2010. Controls on fan depositional processes in the schist ranges of the Southern Alps, New Zealand, and implications for debris-flow hazard assessment. Geomorphology 122(1–2), 99–116. doi:10.1016/j.geomorph.2010.06.002.

de Scally, F.A., Slaymaker, O., Owens, I.F., 2001. Morphometric controls and basin response in the cascade mountains. Geografiska Annaler: Series A, Physical Geography 83(3), 117–130. doi:10.1111/j.0435-3676.2001.00148.x.

De Smith, M.J., Goodchild, M.F., Longley, P., 2007. Geospatial analysis: a comprehensive guide to principles, techniques and software tools. Troubador, Leicester.

de Vries, J.J., 1994. Dynamics of the interface between streams and groundwater systems in lowland areas, with reference to stream net evolution. Journal of Hydrology 155(1–2), 39–56. doi:10.1016/0022-1694(94)90157-0.

Deangeli, C., Paltrinieri, E., Tiranti, D., 2013. Debris Flow Analysis: From Lithological Classification of the Basin to Deposition. In: Margottini, C., Canuti, P., Sassa, K. (Eds.). Landslide Science and Practice. Springer, Berlin, Heidelberg, pp. 301–307. doi:10.1007/978-3-642-31310-3_40.

DeCelles, P.G., 2004. Late Jurassic to Eocene evolution of the Cordilleran thrust belt and foreland basin system, western U.S.A. American Journal of Science 304(2), 105–168. doi:10.2475/ajs.304.2.105.

Dehn, M., Gärtner, H., Dikau, R., 2001. Principles of semantic modeling of landform structures. Computers & Geosciences 27(8), 1005–1010. doi:10.1016/S0098-3004(00)00138-2.

Delorme, P., 2017. Morphologie des cônes alluviaux. Ph.D. thesis, Université Sorbonne Paris Cité, Paris.

Delorme, P., Devauchelle, O., Barrier, L., Métivier, F., 2018. Growth and shape of a laboratory alluvial fan. Physical Review E 98(1), 012907. doi:10.1103/PhysRevE.98.012907.

Delorme, P., Voller, V., Paola, C., Devauchelle, O., Lajeunesse, É., Barrier, L., Métivier, F., 2017. Self-similar growth of a bimodal laboratory fan. Earth Surface Dynamics 5(2), 239–252. doi:10.5194/esurf-5-239-2017.

Deng, J., Dong, W., Socher, R., Li, L., Kai Li, Li Fei-Fei, 2009. ImageNet: A large-scale hierarchical image database. In: Proceedings of the IEEE Conference on Computer Vision and Pattern Recognition, June 20–25, Miami. IEEE, New York, pp. 248–255. doi:10.1109/CVPR.2009.5206848.

Deng, L., 2014. A tutorial survey of architectures, algorithms, and applications for deep learning. APSIPA Transactions on Signal and Information Processing 3, e2. doi:10.1017/atsip.2013.9.

Denny, C.S., 1965. Alluvial fans in the Death Valley region, California and Nevada. Professional Paper 466, United States Government Printing Office, Washington, D.C. doi:10.3133/pp466.

Denny, C.S., 1967. Fans and pediments. American Journal of Science 265(2), 81–105. doi:10.2475/ajs.265.2.81.

Densmore, A.L., Allen, P.A., Simpson, G., 2007. Development and response of a coupled catchment fan system under changing tectonic and climatic forcing. Journal of Geophysical Research 112(F1). doi:10.1029/2006JF000474.

Dewey, J.F., Shackleton, R.M., Chengfa, C., Yiyin, S., 1988. The Tectonic Evolution of the Tibetan Plateau. Philosophical Transactions of the Royal Society A: Mathematical, Physical and Engineering Sciences 327(1594), 379–413. doi:10.1098/rsta.1988.0135.

Dickinson, W.R., 2002. The Basin and Range Province as a Composite Extensional Domain. International Geology Review 44(1), 1–38. doi:10.2747/0020-6814.44.1.1.

Dickinson, W.R., 2004. Evolution of the North American Cordillera. Annual Review of Earth and Planetary Sciences 32(1), 13–45. doi:10.1146/annurev.earth.32.101802.120257.

Dickinson, W.R., 2006. Geotectonic evolution of the Great Basin. Geosphere 2(7), 353–368. doi:10.1130/GES00054.1.

Dickinson, W.R., Snyder, W.S., 1979. Geometry of triple junctions related to San Andreas Transform. Journal of Geophysical Research 84(B2), 561. doi:10.1029/JB084iB02p00561.

Dikau, R., 1989. The application of a digital relief model to landform analysis. In: Raper, J.F. (Ed.). Three Dimensional Applications in Geographical Information Systems. Taylor & Francis, London, New York, pp. 51–77.

Dittman, D.J., Khoshgoftaar, T.M., Napolitano, A., 2015. The Effect of Data Sampling When Using Random Forest on Imbalanced Bioinformatics Data. In: Proceedings of the IEEE International Conference on Information Reuse and Integration, August 13–15, Redwood City. IEEE, New York, pp. 457–463. doi:10.1109/IRI.2015.76.

Dixit, M., Kwitt, R., Niethammer, M., Vasconcelos, N., 2017. AGA: Attribute-Guided Augmentation. In: Proceedings of the IEEE Conference on Computer Vision and Pattern Recognition, July 21–26, Honolulu. IEEE, New York, pp. 3328–3336. doi:10.1109/CVPR.2017.355.

Dixon, J.L., Hartshorn, A.S., Heimsath, A.M., DiBiase, R.A., Whipple, K., 2012. Chemical weathering response to tectonic forcing: A soils perspective from the San Gabriel Mountains, California. Earth and Planetary Science Letters 323–324, 40–49. doi:10.1016/j.epsl.2012.01.010.

Dixon, T.H., Miller, M., Farina, F., Wang, H., Johnson, D., 2000. Present-day motion of the Sierra Nevada block and some tectonic implications for the Basin and Range province, North American Cordillera. Tectonics 19(1), 1–24. doi:10.1029/1998TC001088.

DLR (Deutsches Zentrum für Luft- und Raumfahrt), 2010. TanDEM-X Ground Segment TanDEM-X Science Service System Manual. https://tandemx-science.dlr.de/pdfs/TD-GS-UM-0115-TanDEM-X-Science-Service-System-Manual_V1.0.pdf. Last accessed on October 28, 2014.

DLR (Deutsches Zentrum für Luft- und Raumfahrt), 2011a. COFUR Prices for scientific TanDEM-X products. https://tandemx-science.dlr.de/pdfs/cofur_list_tdx_20110331.pdf. Last accessed on November 28, 2019.

DLR (Deutsches Zentrum für Luft- und Raumfahrt), 2011b. TanDEM-X Ground Segment DEM Products Specification Document. https://tandemx-science.dlr.de/pdfs/TD-GS-PS-0021_DEM-Product-Specification_v3.0.pdf. Last accessed on October 29, 2014.

DLR (Deutsches Zentrum für Luft- und Raumfahrt), 2012. TanDEM-X Ground Segment TanDEM-X Experimental Product Description. https://tandemx-science.dlr.de/pdfs/TD-GS-PS-3028_TanDEM-X-Experimental-Product-Description_1.2.pdf. Last accessed on October 28, 2014.

Dobretsov, N.L., Buslov, M.M., 2007. Late Cambrian-Ordovician tectonics and geodynamics of Central Asia. Russian Geology and Geophysics 48(1), 71–82. doi:10.1016/j.rgg.2006.12.006.

Dohrenwend, J.C., 1984. Nivation Landforms in the Western Great Basin and Their Paleoclimatic Significance. Quaternary Research 22(3), 275–288. doi:10.1016/0033-5894(84)90022-X.

Dolan, J.F., Bowman, D.D., Sammis, C.G., 2007. Long-range and long-term fault interactions in Southern California. Geology 35(9), 855–858. doi:10.1130/G23789A.1.

Domrös, M., Peng, G., 1988. The Climate of China. Springer, Berlin, Heidelberg, New York.

Dorn, R.I., 2009. The Role of Climatic Change in Alluvial Fan Development. In: Parsons, A.J., Abrahams, A.D. (Eds.). Geomorphology of Desert Environments. Springer, Dordrecht, pp. 723–742. doi:10.1007/978-1-4020-5719-9_24.

Dorsey, R.J., Housen, B.A., Janecke, S.U., Fanning, C.M., Spears, A.L.F., 2011. Stratigraphic record of basin development within the San Andreas fault system: Late Cenozoic Fish Creek-Vallecito basin, southern California. Geological Society of America Bulletin 123(5–6), 771–793. doi:10.1130/B30168.1.

Dowding, S., Kuuskivi, T., Li, X., 2004. Void fill of SRTM elevation data - principles, processes and performance. In: Proceedings of the ASPRS Conference on Images to Decision: Remote Sensing Foundation for GIS Applications, September 12–16, Kansas City. ASPRS, Bethesda.

Drew, F., 1873. Alluvial and Lacustrine Deposits and Glacial Records of the Upper-Indus Basin. Quarterly Journal of the Geological Society 29(1–2), 441–471. doi:10.1144/GSL.JGS.1873.029.01-02.39.

Drăguţ, L., Blaschke, T., 2006. Automated classification of landform elements using object-based image analysis. Geomorphology 81(3–4), 330–344. doi:10.1016/j.geomorph.2006.04.013.

Drăguţ, L., Blaschke, T., 2008. Terrain Segmentation and Classification using SRTM Data. In: Zhou, Q., Lees, B., Tang, G.a. (Eds.). Advances in Digital Terrain Analysis. Springer, Berlin, Heidelberg, pp. 141–158. doi:10.1007/978-3-540-77800-4_8.

Drăguţ, L., Csillik, O., Eisank, C., Tiede, D., 2014. Automated parameterisation for multi-scale image segmentation on multiple layers. ISPRS Journal of Photogrammetry and Remote Sensing 88, 119–127. doi:10.1016/j.isprsjprs.2013.11.018.

Drăguţ, L., Eisank, C., 2011. Object representations at multiple scales from digital elevation models. Geomorphology 129(3–4), 183–189. doi:10.1016/j.geomorph.2011.03.003.

Drăguţ, L., Eisank, C., 2012. Automated object-based classification of topography from SRTM data. Geomorphology 141–142, 21–33. doi:10.1016/j.geomorph.2011.12.001.

Drăguţ, L., Eisank, C., Strasser, T., 2011. Local variance for multi-scale analysis in geomorphometry. Geomorphology 130(3–4), 162–172. doi:10.1016/j.geomorph.2011.03.011.

Drăguţ, L., Schauppenlehner, T., Muhar, A., Strobl, J., Blaschke, T., 2009. Optimization of scale and parametrization for terrain segmentation: An application to soil-landscape modeling. Computers & Geosciences 35(9), 1875–1883. doi:10.1016/j.cageo.2008.10.008.

Drummond, C., Holte, R.C., 2003. C4.5, Class Imbalance, and Cost Sensitivity: Why Under-Sampling beats Over-Sampling. In: Workshop on Learning from Imbalanced Datasets II, August 21, Washington, D.C. ICML, Washington, D.C., pp. 1–8.

Désir, C., Bernard, S., Petitjean, C., Heutte, L., 2013. One class random forests. Pattern Recognition 46(12), 3490–3506. doi:10.1016/j.patcog.2013.05.022.

Du, L., You, X., Li, K., Meng, L., Cheng, G., Xiong, L., Wang, G., 2019. Multi-modal deep learning for landform recognition. ISPRS Journal of Photogrammetry and Remote Sensing 158, 63–75. doi:10.1016/j.isprsjprs.2019.09.018.

Du, P., Samat, A., Waske, B., Liu, S., Li, Z., 2015. Random Forest and Rotation Forest for fully polarized SAR image classification using polarimetric and spatial features. ISPRS Journal of Photogrammetry and Remote Sensing 105, 38–53. doi:10.1016/j.isprsjprs.2015.03.002.

Duong, T., Beck, G., Azzag, H., Lebbah, M., 2016. Nearest neighbour estimators of density derivatives, with application to mean shift clustering. Pattern Recognition Letters 80, 224–230. doi:10.1016/j.patrec.2016.06.021.

Dymond, J.R., De Rose, R., 2011. Modelling landscape evolution in the Waipaoa catchment, New Zealand — A phenomenalogical approach. Geomorphology 132(1–2), 29–34. doi:10.1016/j.geomorph.2011.04.032.

Efron, B., 1979. Bootstrap Methods: Another Look at the Jackknife. The Annals of Statistics 7(1), 1–26. doi:10.1214/aos/1176344552.

Efron, B., Tibshirani, R., 1997. Improvements on Cross-Validation: The 632+ Bootstrap Method. Journal of the American Statistical Association 92(438), 548–560. doi:10.1080/01621459.1997.10474007.

Ehlschlaeger, C.R., 1998. The Stochastic Simulation Approach: Tools for Representing Spatial Application Uncertainty. Ph.D. thesis, University of California, Santa Barbara.

Einbeck, J., 2011. Bandwidth Selection for Mean-shift based Unsupervised Learning Techniques: a Unified Approach via Self-coverage. Journal of Pattern Recognition Research 6(2), 175–192. doi:10.13176/11.288.

Eisank, C., 2013. An object-based workflow for integrating spatial scale and semantics to derive landforms from digital elevation models. Ph.D. thesis, Paris-Lodron-Universität Salzburg, Salzburg.

Eisank, C., Smith, M.J., Hillier, J., 2014. Assessment of multiresolution segmentation for delimiting drumlins in digital elevation models. Geomorphology 214, 452–464. doi:10.1016/j.geomorph.2014.02.028.

Ellis, M.A., Densmore, A.L., Anderson, R.S., 1999. Development of mountainous topography in the Basin Ranges, USA. Basin Research 11(1), 21–41. doi:10.1046/j.1365-2117.1999.00087.x.

Emanov, A.F., Emanov, A.A., Leskova, E.V., Kolesnikov, Y.I., Yankaitis, V., Filina, A.G., 2012. The Ms = 7.0 Uureg Nuur earthquake of 15.05.1970 (Mongolian Altai): the aftershock process and current seismicity in the epicentral area. Russian Geology and Geophysics 53(10), 1090–1099. doi:10.1016/j.rgg.2012.08.009.

Endo, N., Kadota, T., Matsumoto, J., Ailikun, B., Yasunari, T., 2006. Climatology and Trends in Summer Precipitation Characteristics in Mongolia for the Period 1960-98. Journal of the Meteorological Society of Japan 84(3), 543–551. doi:10.2151/jmsj.84.543.

English, J.M., Johnston, S.T., 2004. The Laramide Orogeny: What Were the Driving Forces? International Geology Review 46(9), 833–838. doi:10.2747/0020-6814.46.9.833.

Enzmann, R.D., 1966. Introduction to the Section on Signatures. Annals of the New York Academy of Sciences 140(1), 154–156. doi:10.1111/j.1749-6632.1966.tb50955.x.

EORC (Earth Observation Research Center), JAXA (Japan Aerospace Exploration Agency), 2018. AW3D30 Version 2.1 Product Description. http://www.eorc.jaxa.jp/ALOS/en/aw3d30/aw3d30v21_format_e.pdf. Last accessed on June 22, 2018.

Epanechnikov, V.A., 1969. Non-Parametric Estimation of a Multivariate Probability Density. Theory of Probability & Its Applications 14(1), 153–158. doi:10.1137/1114019.

Eppes, M.C., McFadden, L.D., 2008. The influence of bedrock weathering on the response of drainage basins and associated alluvial fans to Holocene climates, San Bernardino Mountains, California, USA. The Holocene 18(6), 895–905. doi:10.1177/0959683608093526.

EROS (Earth Resources Observation and Science Center), USGS (U.S. Geological Survey), USDOI (U.S. Department of the Interior), 1997. USGS 30 ARC-second Global Elevation Data, GTOPO30. doi:10.5065/A1Z4-EE71. Last accessed on December 5, 2019.

Evans, I.S., 1972. General geomorphometry, derivatives of altitude, and descriptive statistics. In: Chorley, R.J. (Ed.). Spatial Analysis in Geomorphology. Harper & Row, New York, pp. 17–90.

Evans, I.S., 1980. An integrated system of terrain analysis and slope mapping. Zeitschrift für Geomorphologie, Supplementband 36, 274–295.

Evans, I.S., 1987. The morphometry of specific Landforms. In: Gardiner, V. (Ed.). International Geomorphology 1986 Part II. Wiley, Chichester, pp. 105–124.

Evans, I.S., 2003. Scale-Specific Landforms and Aspects of the Land Surface. In: Evans, I.S., Dikau, R., Tokunaga, E., Ohmori, H., Hirano, M. (Eds.). Concepts and Modelling in Geomorphology: International Perspectives. Terrapub, Tokyo, pp. 61–84.

Evans, I.S., 2010. Allometry, Scaling and Scale-Specificity of Cirques, Landslides and Other Landforms. Transactions, Japanese Geomorphological Union 31(2), 133–153.

Evans, I.S., 2012. Geomorphometry and landform mapping: What is a landform? Geomorphology 137(1), 94–106. doi:10.1016/j.geomorph.2010.09.029.

Evans, I.S., Cox, N.J., 1974. Geomorphometry and the Operational Definition of Cirques. Area 6(2), 150–153.

Evans, I.S., Cox, N.J., 1999. Relations between land surface properties: Altitude, slope and curvature. In: Hergarten, S., Neugebauer, H.J. (Eds.). Process Modelling and Landform Evolution. Lecture Notes in Earth Sciences 78. Springer, Berlin, Heidelberg, pp. 13–45. doi:10.1007/BFb0009718.

Evans, I.S., Hengl, T., Gorsevski, P., 2009. Applications in Geomorphology. In: Hengl, T., Reuter, H.I. (Eds.). Geomorphometry. Concepts, Software, Applications. Developments in Soil Science 33. Elsevier, Amsterdam, Boston, Heidelberg, pp. 497–525. doi:10.1016/S0166-2481(08)00022-6.

Exelis, DLR (Deutsches Zentrum für Luft- und Raumfahrt), 2012. TerraSAR-X/TanDEM-X SSC/CoSSC Reader for IDL and ENVI. Tech. Rep. 2011-ITT-DLR-0001, Exelis Visual Information Solutions, Deutsches Zentrum für Luft- und Raumfahrt, Oberpfaffenhofen.

Fang, J.Y., Ohsawa, M., Kira, T., 1996. Vertical vegetation zones along 30° N latitude in humid East Asia. Vegetatio 126(2), 135–149. doi:10.1007/BF00045600.

Farr, T.G., 1995. Use of TOPSAR digital elevation data to determine the 3-dimensional shape of an alluvial fan. NASA Technical Reports 19950027383, National Aeronautics and Space Administration, Pasadena.

Farr, T.G., Rosen, P.A., Caro, E., Crippen, R., Duren, R., Hensley, S., Kobrick, M., Paller, M., Rodríguez, E., Roth, L., Seal, D., Shaffer, S., Shimada, J., Umland, J., Werner, M., Oskin, M., Burbank, D.W., Alsdorf, D., 2007. The Shuttle Radar Topography Mission. Reviews of Geophysics 45(2), 1–33. doi:10.1029/2005RG000183.

Fawcett, T., 2006. An introduction to ROC analysis. Pattern Recognition Letters 27(8), 861–874. doi:10.1016/j.patrec.2005.10.010.

Felauer, T., 2011. Jungquartäre Landschafts- und Klimageschichte der Südmongolei. Ph.D. thesis, Rheinisch-Westfälische Technische Hochschule Aachen, Aachen.

Felauer, T., Schlütz, F., Murad, W., Mischke, S., Lehmkuhl, F., 2012. Late Quaternary climate and landscape evolution in arid Central Asia: A multiproxy study of lake archive Bayan Tohomin Nuur, Gobi desert, southern Mongolia. Journal of Asian Earth Sciences 48, 125–135. doi:10.1016/j.jseaes.2011.12.002.

Felicísimo, A.M., 1994. Parametric statistical method for error detection in digital elevation models. ISPRS Journal of Photogrammetry and Remote Sensing 49(4), 29–33. doi:10.1016/0924-2716(94)90044-2.

Fernández-Delgado, M., Cernadas, E., Barro, S., Amorim, D., 2014. Do We Need Hundreds of Classifiers to Solve Real World Classification Problems? Journal of Machine Learning Research 15(1), 3133–3181.

Ferrari, L., López-Martínez, M., Orozco-Esquivel, T., Bryan, S.E., Duque-Trujillo, J., Lonsdale, P., Solari, L., 2013. Late Oligocene to Middle Miocene rifting and synextensional magmatism in the southwestern Sierra Madre Occidental, Mexico: The beginning of the Gulf of California rift. Geosphere 9(5), 1161–1200. doi:10.1130/GES00925.1.

Field, J., 2001. Channel avulsion on alluvial fans in southern Arizona. Geomorphology 37(1), 93–104. doi:10.1016/S0169-555X(00)00064-7.

Fisher, P.F., Tate, N.J., 2006. Causes and consequences of error in digital elevation models. Progress in Physical Geography 30(4), 467–489. doi:10.1191/0309133306pp492ra.

Flanders, D., Hall-Beyer, M., Pereverzoff, J., 2003. Preliminary evaluation of eCognition object-based software for cut block delineation and feature extraction. Canadian Journal of Remote Sensing 29(4), 441–452. doi:10.5589/m03-006.

Florinsky, I.V., 1998. Accuracy of local topographic variables derived from digital elevation models. International Journal of Geographical Information Science 12(1), 47–62. doi:10.1080/136588198242003.

Florinsky, I.V., 2012. Digital terrain analysis in soil science and geology. Elsevier/Academic Press, Amsterdam, Boston, Heidelberg.

Florinsky, I.V., Eilers, R.G., Manning, G.R., Fuller, L.G., 2002. Prediction of soil properties by digital

terrain modelling. Environmental Modelling & Software 17(3), 295–311. doi:10.1016/S1364-8152(01)00067-6.

Florinsky, I.V., Skrypitsyna, T.N., Luschikova, O.S., 2018. Comparative accuracy of the AW3D30 DSM, ASTER GDEM, and SRTM1 DEM: A case study on the Zaoksky testing ground, Central European Russia. Remote Sensing Letters 9(7), 706–714. doi:10.1080/2150704X.2018.1468098.

Florinsky, I.V., Skrypitsyna, T.N., Trevisani, S., Romaikin, S.V., 2019. Statistical and visual quality assessment of nearly-global and continental digital elevation models of Trentino, Italy. Remote Sensing Letters 10(8), 726–735. doi:10.1080/2150704X.2019.1602790.

Frankel, K.L., Brantley, K.S., Dolan, J.F., Finkel, R.C., Klinger, R.E., Knott, J.R., Machette, M.N., Owen, L.A., Phillips, F.M., Slate, J.L., Wernicke, B.P., 2007. Cosmogenic ^{10}Be and ^{36}Cl geochronology of offset alluvial fans along the northern Death Valley fault zone: Implications for transient strain in the eastern California shear zone. Journal of Geophysical Research 112(B6), B06407. doi:10.1029/2006JB004350.

Frankel, K.L., Dolan, J.F., 2007. Characterizing arid region alluvial fan surface roughness with airborne laser swath mapping digital topographic data. Journal of Geophysical Research 112(F2). doi:10.1029/2006JF000644.

Frankel, K.L., Wegmann, K.W., Bayasgalan, A., Carson, R.J., Bader, N.E., Adiya, T., Bolor, E., Durfey, C.C., Otgonkhuu, J., Sprajcar, J., Sweeney, K.E., Walker, R.T., Marstellar, T.L., Gregory, L., 2010. Late Pleistocene slip rate of the Höh Serh-Tsagaan Salaa fault system, Mongolian Altai and intracontinental deformation in central Asia: Mongolian Altai late Pleistocene slip rate. Geophysical Journal International 183(3), 1134–1150. doi:10.1111/j.1365-246X.2010.04826.x.

Fraser, C.S., Baltsavias, E., Gruen, A., 2002. Processing of Ikonos imagery for submetre 3D positioning and building extraction. ISPRS Journal of Photogrammetry and Remote Sensing 56(3), 177–194. doi:10.1016/S0924-2716(02)00045-X.

Freeman, A., Zink, M., Caro, E., Moreira, A., Veilleux, L., Werner, M., 2019. The legacy of the SIR-C/X-SAR radar system: 25 years on. Remote Sensing of Environment 231, 111255. doi:10.1016/j.rse.2019.111255.

French, R.H. (Ed.), 1987. Hydraulic processes on alluvial fans. Developments in water science 31. Elsevier, Amsterdam, New York.

Frey, H., Paul, F., 2012. On the suitability of the SRTM DEM and ASTER GDEM for the compilation of topographic parameters in glacier inventories. International Journal of Applied Earth Observation and Geoinformation 18, 480–490. doi:10.1016/j.jag.2011.09.020.

Friedman, J.H., 2001. Greedy Function Approximation: A Gradient Boosting Machine. The Annals of Statistics 29(5), 1189–1232. doi:10.1214/aos/1013203451.

Fryirs, K.A., Brierley, G.J., Preston, N.J., Kasai, M., 2007. Buffers, barriers and blankets: The (dis)connectivity of catchment-scale sediment cascades. CATENA 70(1), 49–67. doi:10.1016/j.catena.2006.07.007.

Fu, T., Ma, L., Li, M., Johnson, B.A., 2018. Using convolutional neural network to identify irregular segmentation objects from very high-resolution remote sensing imagery. Journal of Applied Remote Sensing 12(2), 1–21. doi:10.1117/1.JRS.12.025010.

Fuchs, M., Reverman, R., Owen, L.A., Frankel, K.L., 2015. Reconstructing the Timing of Flash Floods Using ^{10}Be Surface Exposure Dating at Leidy Creek Alluvial Fan and Valley, White Mountains, California–Nevada, USA. Quaternary Research 83(01), 178–186. doi:10.1016/j.yqres.2014.08.006.

Fujisada, H., Bailey, G.B., Kelly, G.G., Hara, S., Abrams, M.J., 2005. ASTER DEM performance. IEEE Transactions on Geoscience and Remote Sensing 43(12), 2707–2714. doi:10.1109/TGRS.2005.847924.

Fukunaga, K., Hostetler, L., 1975. The estimation of the gradient of a density function, with

applications in pattern recognition. IEEE Transactions on Information Theory 21(1), 32–40. doi: 10.1109/TIT.1975.1055330.

Gabor, D., 1946. Theory of communication. Part 1: The analysis of information. Journal of the Institution of Electrical Engineers - Part III: Radio and Communication Engineering 93(26), 429–441. doi:10.1049/ji-3-2.1946.0074.

Gallant, J.C., Dowling, T.I., 2003. A multiresolution index of valley bottom flatness for mapping depositional areas. Water Resources Research 39(12). doi:10.1029/2002WR001426.

Gallant, J.C., Wilson, J.P., 2000. Primary Topographic Attributes. In: Wilson, J.P., Gallant, J.C. (Eds.). Terrain analysis: principles and applications. Wiley, New York, pp. 51–85.

Gallay, M., 2009. Assessing alternative methods for acquiring and processing digital elevation data. Ph.D. thesis, Queen's University, Belfast.

Geisser, S., 1975. The Predictive Sample Reuse Method with Applications. Journal of the American Statistical Association 70(350), 320–328.

Genuer, R., Poggi, J.M., Tuleau-Malot, C., 2010. Variable selection using random forests. Pattern Recognition Letters 31(14), 2225–2236. doi:10.1016/j.patrec.2010.03.014.

Gerçek, D., Toprak, V., Strobl, J., 2011. Object-based classification of landforms based on their local geometry and geomorphometric context. International Journal of Geographical Information Science 25(6), 1011–1023. doi:10.1080/13658816.2011.558845.

Gerelchuluun, B., Ahn, J.B., 2014. Air temperature distribution over Mongolia using dynamical downscaling and statistical correction. International Journal of Climatology 34(7), 2464–2476. doi:10.1002/joc.3853.

Gesch, D.B., 2018. Best Practices for Elevation-Based Assessments of Sea-Level Rise and Coastal Flooding Exposure. Frontiers in Earth Science 6, 230. doi:10.3389/feart.2018.00230.

Geudtner, D., 1995. Die interferometrische Verarbeitung von SAR-Daten des ERS-1. DLR-Mitteilungen 95-28. Deutsches Zentrum für Luft- und Raumfahrt, Oberpfaffenhofen.

Geurts, P., Ernst, D., Wehenkel, L., 2006. Extremely randomized trees. Machine Learning 63(1), 3–42. doi:10.1007/s10994-006-6226-1.

Ghimire, B., Rogan, J., Galiano, V.R., Panday, P., Neeti, N., 2012. An Evaluation of Bagging, Boosting, and Random Forests for Land-Cover Classification in Cape Cod, Massachusetts, USA. GIScience & Remote Sensing 49(5), 623–643. doi:10.2747/1548-1603.49.5.623.

Ghorbanzadeh, O., Blaschke, T., Gholamnia, K., Meena, S., Tiede, D., Aryal, J., 2019. Evaluation of Different Machine Learning Methods and Deep-Learning Convolutional Neural Networks for Landslide Detection. Remote Sensing 11(2), 196. doi:10.3390/rs11020196.

Ghorbanzadeh, O., Tiede, D., Wendt, L., Sudmanns, M., Lang, S., 2020. Transferable instance segmentation of dwellings in a refugee camp - integrating CNN and OBIA. European Journal of Remote Sensing 54(sup1), 127–140. doi:10.1080/22797254.2020.1759456.

Ghosh, A., Joshi, P.K., 2014. A comparison of selected classification algorithms for mapping bamboo patches in lower Gangetic plains using very high resolution WorldView 2 imagery. International Journal of Applied Earth Observation and Geoinformation 26, 298–311. doi:10.1016/j.jag.2013.08.011.

Ghosh, R., Gupta, A.K., Motani, M., 2019. Investigating Convolutional Neural Networks using Spatial Orderness. In: IEEE/CVF International Conference on Computer Vision Workshops, October 27–28, Seoul. IEEE, New York, pp. 2053–2056. doi:10.1109/ICCVW.2019.00259.

Ghosh, S., Stepinski, T.F., Vilalta, R., 2010. Automatic Annotation of Planetary Surfaces With Geomorphic Labels. IEEE Transactions on Geoscience and Remote Sensing 48(1), 175–185. doi: 10.1109/TGRS.2009.2027113.

Giachetti, A., 2000. Matching techniques to compute image motion. Image and Vision Computing 18(3), 247–260. doi:10.1016/S0262-8856(99)00018-9.

Giles, P.T., 1998. Geomorphological signatures: classification of aggregated slope unit objects from digital elevation and remote sensing data. Earth Surface Processes and Landforms 23(7), 581–594. doi:10.1002/(SICI)1096-9837(199807)23:7<581::AID-ESP863>3.0.CO;2-S.

Giles, P.T., 2010. Investigating the use of alluvial fan volume to represent fan size in morphometric studies. Geomorphology 121(3–4), 317–328. doi:10.1016/j.geomorph.2010.05.001.

Giles, P.T., Whitehouse, B.M., Karymbalis, E., 2018. Interactions between alluvial fans and axial rivers in Yukon, Canada and Alaska, USA. In: Ventra, D., Clarke, L.E. (Eds.). Geology and Geomorphology of Alluvial and Fluvial Fans: Terrestrial and Planetary Perspectives. Geological Society, London, Special Publications 440. Geological Society of London, London, pp. 23–43. doi:10.1144/SP440.3.

Girshick, R.B., Donahue, J., Darrell, T., Malik, J., 2016. Region-Based Convolutional Networks for Accurate Object Detection and Segmentation. IEEE Transactions on Pattern Analysis and Machine Intelligence 38(1), 142–158. doi:10.1109/TPAMI.2015.2437384.

Gislason, P.O., Benediktsson, J.A., Sveinsson, J.R., 2006. Random Forests for land cover classification. Pattern Recognition Letters 27(4), 294–300. doi:10.1016/j.patrec.2005.08.011.

Glazner, A.F., Walker, J.D., Bartley, J.M., Fletcher, J.M., 2002. Cenozoic evolution of the Mojave block of southern California. In: Glazner, A.F., Walker, J.D., Bartley, J.M. (Eds.). Geologic Evolution of the Mojave Desert and Southwestern Basin and Range. GSA Memoir 195. Geological Society of America, Boulder, pp. 19–41. doi:10.1130/0-8137-1195-9.19.

Gloaguen, R., Ratschbacher, L., 2011. Growth and collapse of the Tibetan Plateau: introduction. In: Gloaguen, R., Ratschbacher, L. (Eds.). Growth and Collapse of the Tibetan Plateau. Geological Society, London, Special Publications 353. Geological Society of London, London, pp. 1–8. doi:10.1144/SP353.1.

Gómez-Villar, A., Álvarez Martínez, J., García-Ruiz, J.M., 2006. Factors influencing the presence or absence of tributary-junction fans in the Iberian Range, Spain. Geomorphology 81(3), 252–264. doi:10.1016/j.geomorph.2006.04.011.

Goes, S., 2013. Western North America's jigsaw. Nature 496(7443), 35–37. doi:10.1038/496035a.

Gohain, K., Parkash, B., 1990. Morphology of the Kosi Megafan. In: Rachocki, A., Church, M.A.A. (Eds.). Alluvial fans: A Field Approach. Wiley, Chichester, New York, pp. 151–178.

Goldstein, R.M., Werner, C.L., 1998. Radar interferogram filtering for geophysical applications. Geophysical Research Letters 25(21), 4035–4038. doi:10.1029/1998GL900033.

Goldstein, R.M., Zebker, H.A., Werner, C.L., 1988. Satellite radar interferometry: Two-dimensional phase unwrapping. Radio Science 23(4), 713–720. doi:10.1029/RS023i004p00713.

Gong, D.Y., Ho, C.H., 2002. The Siberian High and climate change over middle to high latitude Asia. Theoretical and Applied Climatology 72(1–2), 1–9. doi:10.1007/s007040200008.

Gonga-Saholiariliva, N., Gunnell, Y., Petit, C., Mering, C., 2011. Techniques for quantifying the accuracy of gridded elevation models and for mapping uncertainty in digital terrain analysis. Progress in Physical Geography 35(6), 739–764. doi:10.1177/0309133311409086.

Gonzalez, R.C., Woods, R.E., 2008. Digital image processing. Prentice Hall, Upper Saddle River, New Jersey, 3rd ed.

Goode, J.R., Wohl, E., 2010. Substrate controls on the longitudinal profile of bedrock channels: Implications for reach-scale roughness. Journal of Geophysical Research 115(F3), F03018. doi:10.1029/2008JF001188.

Goodfellow, I., Bengio, Y., Courville, A., 2016. Deep learning. Adaptive computation and machine learning. Massachusetts Institute of Technology Press, Cambridge.

Gorokhovich, Y., Voustianiouk, A., 2006. Accuracy assessment of the processed SRTM-based elevation data by CGIAR using field data from USA and Thailand and its relation to the terrain characteristics. Remote Sensing of Environment 104(4), 409–415. doi:10.1016/j.rse.2006.05.012.

Goswami, P.K., Pant, C.C., Pandey, S., 2009. Tectonic controls on the geomorphic evolution of alluvial fans in the Piedmont Zone of Ganga Plain, Uttarakhand, India. Journal of Earth System Science 118(3), 245–259. doi:10.1007/s12040-009-0012-y.

Goudie, A.S. (Ed.), 1990. Geomorphological techniques. Routledge, London.

Goudie, A.S., Viles, H., 2008. Weathering processes and forms. In: Chorley, R.J., Burt, T.P., Brunsden, D., Cox, N.J., Goudie, A.S. (Eds.). Quaternary and Recent Processes and Forms (1890-1965) and the Mid-century Revolutions. The history of the study of landforms, or the development of geomorphology 4. Geological Society, London, London, pp. 129–164.

Gray, H.J., Owen, L.A., Dietsch, C., Beck, R.A., Caffee, M.A., Finkel, R.C., Mahan, S.A., 2014. Quaternary landscape development, alluvial fan chronology and erosion of the Mecca Hills at the southern end of the San Andreas Fault zone. Quaternary Science Reviews 105, 66–85. doi:10.1016/j.quascirev.2014.09.009.

Grayson, D.K., 2011. The great basin: a natural prehistory. University of California Press, Berkeley, 2nd ed.

Gregorutti, B., Michel, B., Saint-Pierre, P., 2016. Correlation and variable importance in random forests. Statistics and Computing 27(3), 659–678. doi:10.1007/s11222-016-9646-1.

Gregory, L.C., Thomas, A.L., Walker, R.T., Garland, R., Mac Niocaill, C., Fenton, C.R., Bayasgalan, A., Amgaa, T., Gantulga, B., Xu, S., Schnabel, C., West, A.J., 2014. Combined uranium series and ^{10}Be cosmogenic exposure dating of surface abandonment: A case study from the Ölgiy strike-slip fault in western Mongolia. Quaternary Geochronology 24, 27–43. doi:10.1016/j.quageo.2014.07.005.

Griffiths, P.G., 2004. Frequency and initiation of debris flows in Grand Canyon, Arizona. Journal of Geophysical Research 109(F4), F04002. doi:10.1029/2003JF000077.

Grohmann, C.H., 2018. Evaluation of TanDEM-X DEMs on selected Brazilian sites: Comparison with SRTM, ASTER GDEM and ALOS AW3D30. Remote Sensing of Environment 212, 121–133. doi:10.1016/j.rse.2018.04.043.

Grohmann, C.H., Smith, M.J., Riccomini, C., 2011. Multiscale Analysis of Topographic Surface Roughness in the Midland Valley, Scotland. IEEE Transactions on Geoscience and Remote Sensing 49(4), 1200–1213. doi:10.1109/TGRS.2010.2053546.

Gruber, F.E., Baruck, J., Geitner, C., 2017. Algorithms vs. surveyors: A comparison of automated landform delineations and surveyed topographic positions from soil mapping in an Alpine environment. Geoderma 308, 9–25. doi:10.1016/j.geoderma.2017.08.017.

Gruber, T.R., 1995. Toward principles for the design of ontologies used for knowledge sharing? International Journal of Human-Computer Studies 43(5–6), 907–928. doi:10.1006/ijhc.1995.1081.

Grunert, J., Lehmkuhl, F., Walther, M., 2000. Paleoclimatic evolution of the Uvs Nuur basin and adjacent areas (Western Mongolia). Quaternary International 65–66, 171–192. doi:10.1016/S1040-6182(99)00043-9.

Guan, H., Li, J., Chapman, M., Deng, F., Ji, Z., Yang, X., 2013. Integration of orthoimagery and lidar data for object-based urban thematic mapping using random forests. International Journal of Remote Sensing 34(14), 5166–5186. doi:10.1080/01431161.2013.788261.

Guerit, L., Métivier, F., Devauchelle, O., Lajeunesse, E., Barrier, L., 2014. Laboratory alluvial fans in one dimension. Physical Review E 90(2). doi:10.1103/PhysRevE.90.022203.

Guirado, E., Blanco-Sacristán, J., Rodríguez-Caballero, E., Tabik, S., Alcaraz-Segura, D., Martínez-Valderrama, J., Cabello, J., 2021. Mask R-CNN and OBIA Fusion Improves the Segmentation of

Scattered Vegetation in Very High-Resolution Optical Sensors. Sensors 21(1), 320. doi:10.3390/s21010320.

Guirado, E., Tabik, S., Alcaraz-Segura, D., Cabello, J., Herrera, F., 2017. Deep-learning Versus OBIA for Scattered Shrub Detection with Google Earth Imagery: Ziziphus lotus as Case Study. Remote Sensing 9(12), 1220. doi:10.3390/rs9121220.

Gunin, P.D., Vostokova, E.A., Dorofeyuk, N.I., Tarasov, P.E., Black, C.C., 1999. Vegetation Dynamics of Mongolia. Geobotany 26. Springer, Dordrecht. doi:10.1007/978-94-015-9143-0.

Guo, Y., Liu, Y., Oerlemans, A., Lao, S., Wu, S., Lew, M.S., 2016. Deep learning for visual understanding: A review. Neurocomputing 187, 27–48. doi:10.1016/j.neucom.2015.09.116.

Guth, P.L., 2006. Geomorphometry from SRTM: Comparison to NED. Photogrammetric Engineering & Remote Sensing 72(3), 269–277.

Hack, J.T., 1960. Interpretation of erosional topography in humid temperate regions. American Journal of Science 258-A, 80–97.

Hafiz, A.M., Bhat, G.M., 2020. A survey on instance segmentation: state of the art. International Journal of Multimedia Information Retrieval 9(3), 171–189. doi:10.1007/s13735-020-00195-x.

Haining, R.P., Kerry, R., Oliver, M.A., 2010. Geography, Spatial Data Analysis, and Geostatistics: An Overview. Geographical Analysis 42(1), 7–31. doi:10.1111/j.1538-4632.2009.00780.x.

Hancock, G.R., Coulthard, T.J., Martinez, C., Kalma, J.D., 2011. An evaluation of landscape evolution models to simulate decadal and centennial scale soil erosion in grassland catchments. Journal of Hydrology 398(3–4), 171–183. doi:10.1016/j.jhydrol.2010.12.002.

Hancock, G.R., Martinez, C., Evans, K.G., Moliere, D.R., 2006. A comparison of SRTM and high-resolution digital elevation models and their use in catchment geomorphology and hydrology: Australian examples. Earth Surface Processes and Landforms 31(11), 1394–1412. doi:10.1002/esp.1335.

Handl, A., Kuhlenkasper, T., 2017. Multivariate Analysemethoden: Theorie und Praxis mit R. Statistik und ihre Anwendungen. Springer Spektrum, Berlin, 3rd ed.

Hannah, M.J., 1981. Error Detection and Correction in Digital Terrain Models. Photogrammetric Engineering and Remote Sensing 47(1), 63–69.

Harvey, A.M., 1987. Alluvial fan dissection: relationships between morphology and sedimentation. In: Frostick, L.E., Reid, I. (Eds.). Desert sediments: Ancient and Modern. Geological Society, London, Special Publications 35. Blackwell Scientific Publications, Oxford, Boston, pp. 87–103. doi:10.1144/GSL.SP.1987.035.01.07.

Harvey, A.M., 1992. The influence of sedimentary style on the morphology and development of alluvial fans. Israel Journal of Earth Sciences 41, 123–137.

Harvey, A.M., 2002a. Effective timescales of coupling within fluvial systems. Geomorphology 44(3–4), 175–201. doi:10.1016/S0169-555X(01)00174-X.

Harvey, A.M., 2002b. The relationship between alluvial fans and fan channels within Mediterranean mountain fluvial systems. In: Bull, L.J., Kirkby, M.J. (Eds.). Dryland Rivers: Processes and Management in Mediterranean Climates. Wiley, Chichester, pp. 205–226.

Harvey, A.M., 2002c. The role of base-level change in the dissection of alluvial fans: case studies from southeast Spain and Nevada. Geomorphology 45(1–2), 67–87. doi:10.1016/S0169-555X(01)00190-8.

Harvey, A.M., 2003a. Alluvial Fans. In: Middleton, G.V. (Ed.). Encyclopedia of sediments & sedimentary rocks. Kluwer Academic encyclopedia of earth sciences series. Kluwer Academic Publishers, Dordrecht, Boston, pp. 5–9.

Harvey, A.M., 2003b. The response of dry region alluvial fans to quaternary climatic change. In:

Alsharhan, A.S., Wood, W.W., Goudie, A.S., Fowler, A., Abdellatif, E.M. (Eds.). Desertification in the Third Millenium. Balkema, Lisse, Abingdon, Exton, Tokyo, pp. 75–90.

Harvey, A.M., 2005. Differential effects of base-level, tectonic setting and climatic change on Quaternary alluvial fans in the northern Great Basin, Nevada, USA. In: Harvey, A.M., Mather, A.E., Stokes, M. (Eds.). Alluvial Fans: Geomorphology, Sedimentology, Dynamics. Geological Society, London, Special Publications 251. Geological Society of London, London, pp. 117–131. doi:10.1144/GSL.SP.2005.251.01.09.

Harvey, A.M., 2011. Dryland Alluvial Fans. In: Thomas, D.S.G. (Ed.). Arid Zone Geomorphology. Wiley, Chichester, pp. 333–371. doi:10.1002/9780470710777.ch14.

Harvey, A.M., 2018. Alluvial Fans. In: Reference Module in Earth Systems and Environmental Sciences. Elsevier. doi:10.1016/B978-0-12-409548-9.11066-8.

Harvey, A.M., Mather, A.E., Stokes, M., 2005. Alluvial fans: geomorphology, sedimentology, dynamics – introduction. A review of alluvial-fan research. In: Harvey, A.M., Mather, A.E., Stokes, M. (Eds.). Alluvial Fans: Geomorphology, Sedimentology, Dynamics. Geological Society, London, Special Publications 251. Geological Society of London, London, pp. 1–7. doi:10.1144/GSL.SP.2005.251.01.01.

Harvey, A.M., Silva, P.G., Mather, A.E., Goy, J.L., Stokes, M., Zazo, C., 1999a. The impact of Quaternary sea-level and climatic change on coastal alluvial fans in the Cabo de Gata ranges, southeast Spain. Geomorphology 28(1–2), 1–22. doi:10.1016/S0169-555X(98)00100-7.

Harvey, A.M., Wells, S.G., 1994. Late Pleistocene and Holocene Changes in Hillslope Sediment Supply to Alluvial Fan Systems: Zzyzx, California. In: Millington, A.C., Pye, K. (Eds.). Environmental change in drylands: biogeographical and geomorphological perspectives. British Geomorphological Research Group symposia series 9. Wiley, Chichester, New York, pp. 66–84.

Harvey, A.M., Wells, S.G., 2003. Late Quaternary variations in alluvial fan sedimentologic and geomorphic processes, Soda Lake basin, eastern Mojave Desert, California. In: Enzel, Y., Wells, S.G., Lancaster, N. (Eds.). Paleoenvironments and paleohydrology of the Mojave and southern Great Basin deserts. Special Paper 368. Geological Society of America, Boulder, pp. 207–230. doi:10.1130/0-8137-2368-X.207.

Harvey, A.M., Wigand, P.E.E., Wells, S.G., 1999b. Response of alluvial fan systems to the late Pleistocene to Holocene climatic transition: contrasts between the margins of pluvial Lakes Lahontan and Mojave, Nevada and California, USA. CATENA 36(4), 255–281. doi:10.1016/S0341-8162(99)00049-1.

Hashimoto, A., Oguchi, T., Hayakawa, Y.S., Lin, Z., Saito, K., Wasklewicz, T.A., 2008. GIS analysis of depositional slope change at alluvial-fan toes in Japan and the American Southwest. Geomorphology 100(1–2), 120–130. doi:10.1016/j.geomorph.2007.10.027.

Hastie, T., Tibshirani, R., Friedman, J., 2009. The Elements of Statistical Learning. Springer Series in Statistics. Springer, New York. doi:10.1007/978-0-387-84858-7.

Hastings, J.R., Turner, R.M., 1965. Seasonal Precipitation Regimes in Baja California, Mexico. Geografiska Annaler: Series A, Physical Geography 47(4), 204–223. doi:10.1080/04353676.1965.11879720.

Hay, G.J., Castilla, G., 2008. Geographic Object-Based Image Analysis (GEOBIA): A new name for a new discipline. In: Blaschke, T., Lang, S., Hay, G.J. (Eds.). Object-Based Image Analysis: Spatial Concepts for Knowledge-Driven Remote Sensing Applications. Springer, Berlin, Heidelberg, pp. 75–89. doi:10.1007/978-3-540-77058-9_4.

Hay, G.J., Marceau, D.J., Dubé, P., Bouchard, A., 2001. A multiscale framework for landscape analysis: Object-specific analysis and upscaling. Landscape Ecology 16(6), 471–490. doi:10.1023/A:1013101931793.

He, K., Gkioxari, G., Dollár, P., Girshick, R.B., 2020. Mask R-CNN. IEEE Transactions on Pattern Analysis and Machine Intelligence 42(2), 386–397. doi:10.1109/TPAMI.2018.2844175.

Hebeler, F., Purves, R.S., 2009. The influence of elevation uncertainty on derivation of topographic indices. Geomorphology 111(1–2), 4–16. doi:10.1016/j.geomorph.2007.06.026.

Heller, P.L., Burns, B.A., Marzo, M., 1993. Stratigraphic solution sets for determining the roles of sediment supply, subsidence, and sea level on transgressions and regressions. Geology 21(8), 747–750. doi:10.1130/0091-7613(1993)021<0747:SSSFDT>2.3.CO;2.

Henry, C.D., McGrew, A.J., Colgan, J.P., Snoke, A.W., Brueseke, M.E., 2011. Timing, distribution, amount, and style of Cenozoic extension in the northern Great Basin. In: Lee, J., Evans, J.P. (Eds.). Geologic Field Trips to the Basin and Range, Rocky Mountains, Snake River Plain, and Terranes of the U.S. Cordillera. Geological Society of America, pp. 27–66. doi:10.1130/2011.0021(02).

Hensley, S., Munjy, R., Rosen, P.A., 2007. Interferometric Synthetic Aperture Radar (IFSAR). In: Maune, D.F. (Ed.). Digital elevation model technologies and applications: the DEM users manual. American Society for Photogrammetry and Remote Sensing, Bethesda, pp. 141–198. 2nd ed.

Hereford, R., 2004. Precipitation History of the Mojave Desert Region, 1893–2001. https://pubs.usgs.gov/fs/fs117-03/. Last accessed on October 15, 2019.

Hevesi, J.A., Flint, A.L., Flint, L.E., 2003. Simulation of net infiltration and potential recharge using a distributed-parameter watershed model of the Death Valley region, Nevada and California. Water-Resources Investigations Report 2003-4090, USGS, Sacramento. doi:10.3133/wri034090.

Heward, A.P., 1978. Alluvial fan and lacustrine sediments from the Stephanian A and B (La Magdalena, Ciñera—Matallana and Sabero) coalfields, northern Spain. Sedimentology 25(4), 451–488. doi:10.1111/j.1365-3091.1978.tb02076.x.

Hilbig, W., 1995. The Vegetation of Mongolia. SPB Academic Publishers, Amsterdam.

Hill, S., 1995. The differential weathering of granitic rocks in Victoria, Australia. AGSO Journal of Australian Geology & Geophysics 16(3), 271–276.

Hinderer, M., 2001. Late Quaternary denudation of the Alps, valley and lake fillings and modern river loads. Geodinamica Acta 14(4), 231–263. doi:10.1080/09853111.2001.11432446.

Hirt, C., Filmer, M.S., Featherstone, W.E., 2010. Comparison and validation of the recent freely available ASTER-GDEM ver1, SRTM ver4.1 and GEODATA DEM-9S ver3 digital elevation models over Australia. Australian Journal of Earth Sciences 57(3), 337–347. doi:10.1080/08120091003677553.

Ho, T.K., 1998. The random subspace method for constructing decision forests. IEEE Transactions on Pattern Analysis and Machine Intelligence 20(8), 832–844. doi:10.1109/34.709601.

Hodges, J.L., Lehmann, E.L., 1956. The Efficiency of Some Nonparametric Competitors of the t-Test. The Annals of Mathematical Statistics 27(2), 324–335. doi:10.1214/aoms/1177728261.

Hoeser, T., Kuenzer, C., 2020. Object Detection and Image Segmentation with Deep Learning on Earth Observation Data: A Review-Part I: Evolution and Recent Trends. Remote Sensing 12(10), 1667. doi:10.3390/rs12101667.

Hofton, M., Dubayah, R., Blair, J.B., Rabine, D., 2006. Validation of SRTM elevations over vegetated and non-vegetated terrain using medium footprinting lidar. Photogrammetric Engineering and Remote Sensing 72(3), 279–285.

Holbrook, J., Schumm, S.A., 1999. Geomorphic and sedimentary response of rivers to tectonic deformation: a brief review and critique of a tool for recognizing subtle epeirogenic deformation in modern and ancient settings. Tectonophysics 305(1–3), 287–306. doi:10.1016/S0040-1951(99)00011-6.

Holland, P.W., Welsch, R.E., 1977. Robust regression using iteratively reweighted least-squares. Communications in Statistics - Theory and Methods 6(9), 813–827. doi:10.1080/03610927708827533.

Holmgren, C.A., Betancourt, J.L., Rylander, K.A., 2011. Vegetation history along the eastern, desert escarpment of the Sierra San Pedro Mártir, Baja California, Mexico. Quaternary Research 75(3), 647–657. doi:10.1016/j.yqres.2011.01.008.

Hooke, R.B., 1967. Processes on Arid-Region Alluvial Fans. The Journal of Geology 75(4), 438–460. doi:10.1086/627271.

Hooke, R.B., 1968a. Model Geology: Prototype and Laboratory Streams: Discussion. GSA Bulletin 79(3), 391–394. doi:10.1130/0016-7606(1968)79[391:MGPALS]2.0.CO;2.

Hooke, R.B., 1968b. Steady-state relationships on arid-region alluvial fans in closed basins. American Journal of Science 266(8), 609–629. doi:10.2475/ajs.266.8.609.

Hooke, R.B., Rohrer, W.L., 1979. Geometry of alluvial fans: Effect of discharge and sediment size. Earth Surface Processes 4(2), 147–166. doi:10.1002/esp.3290040205.

Horton, B.K., DeCelles, P.G., 2001. Modern and ancient fluvial megafans in the foreland basin system of the central Andes, southern Bolivia: implications for drainage network evolution in fold-thrust belts. Basin Research 13(1), 43–63. doi:10.1046/j.1365-2117.2001.00137.x.

Hostetler, S.W., Benson, L.V., 1990. Paleoclimatic implications of the high stand of Lake Lahontan derived from models of evaporation and lake level. Climate Dynamics 4(3), 207–217. doi:10.1007/BF00209522.

Hotelling, H., 1933. Analysis of a complex of statistical variables into principal components. Journal of Educational Psychology 24(6), 417–441. doi:10.1037/h0071325.

Härdle, W., Werwatz, A., Müller, M., Sperlich, S., 2004. Nonparametric and Semiparametric Models. Springer Series in Statistics. Springer, Berlin, Heidelberg. doi:10.1007/978-3-642-17146-8.

Hsü, K.J., Chen, H., 1999. Geologic atlas of China: an application of the tectonic facies concept to the geology of China. Elsevier, Amsterdam, Lausanne, New York.

Hu, Z., Peng, J., Hou, Y., Shan, J., 2017. Evaluation of Recently Released Open Global Digital Elevation Models of Hubei, China. Remote Sensing 9(3), 262. doi:10.3390/rs9030262.

Huang, Z., Huang, L., Gong, Y., Huang, C., Wang, X., 2019. Mask Scoring R-CNN. In: Proceedings of the IEEE/CVF Conference on Computer Vision and Pattern Recognition, June 15–20, Long Beach. IEEE, New York, pp. 6402–6411. doi:10.1109/CVPR.2019.00657.

Hunter, G.J., Goodchild, M.F., 1997. Modeling the Uncertainty of Slope and Aspect Estimates Derived from Spatial Databases. Geographical Analysis 29(1), 35–49. doi:10.1111/j.1538-4632.1997.tb00944.x.

Hutson, M., 2018. Has artificial intelligence become alchemy? Science 360(6388), 478. doi:10.1126/science.360.6388.478.

Ibarra, D.E., Oster, J.L., Winnick, M.J., Caves Rugenstein, J.K., Byrne, M.P., Chamberlain, C.P., 2018. Warm and cold wet states in the western United States during the Pliocene–Pleistocene. Geology 46(4), 355–358. doi:10.1130/G39962.1.

Igarashi, T., 2001. ALOS Mission Requirement and Sensor Specifications. Advances in Space Research 28(1), 127–131. doi:10.1016/S0273-1177(01)00316-7.

Šilhán, K., 2014. Chronology of processes in high-gradient channels of medium-high mountains and their influence on the properties of alluvial fans. Geomorphology 206, 288–298. doi:10.1016/j.geomorph.2013.09.032.

Ingersoll, R.V., Cavazza, W., Baldridge, W.S., Shafiqullah, M., 1990. Cenozoic sedimentation and paleotectonics of north-central New Mexico: Implications for initiation and evolution of the Rio Grande rift. GSA Bulletin 102(9), 1280–1296. doi:10.1130/0016-7606(1990)102<1280:CSAPON>2.3.CO;2.

Ingersoll, R.V., Rumelhart, P.E., 1999. Three-stage evolution of the Los Angeles basin, southern California. Geology 27(7), 593–596. doi:10.1130/0091-7613(1999)027<0593:TSEOTL>2.3.CO;2.

Inglada, J., Christophe, E., 2009. The Orfeo Toolbox remote sensing image processing software. In: Proceedings of the IEEE International Geoscience and Remote Sensing Symposium, July 12–17, Cape Town. IEEE, New York, pp. IV–733–IV–736. doi:10.1109/IGARSS.2009.5417481.

IOGP (International Association of Oil and Gas Producers), 2014. Coordinate Conversions and Transformations including Formulas. IOGP Report 373-7-2.

Irvin, B.J., Ventura, S.J., Slater, B.K., 1997. Fuzzy and isodata classification of landform elements from digital terrain data in Pleasant Valley, Wisconsin. Geoderma 77(2–4), 137–154. doi:10.1016/S0016-7061(97)00019-0.

Iverson, R.M., 1997. The physics of debris flows. Reviews of Geophysics 35(3), 245–296. doi:10.1029/97RG00426.

Iverson, R.M., 2004. Debris flow. In: Goudie, A.S. (Ed.). Encyclopedia of Geomorphology. Routledge, London, p. 225. doi:10.4324/9780203381137.

Ivezić, Ž., Connolly, A., VanderPlas, J.T., Gray, A. (Eds.), 2014. Statistics, data mining, and machine learning in astronomy: a practical Python guide for the analysis of survey data. Princeton series in modern observational astronomy. Princeton University Press, Princeton.

Iwahashi, J., Pike, R.J., 2007. Automated classifications of topography from DEMs by an unsupervised nested-means algorithm and a three-part geometric signature. Geomorphology 86(3–4), 409–440. doi:10.1016/j.geomorph.2006.09.012.

Jackson, J.E., 1991. A User's Guide to Principal Components. Wiley Series in Probability and Statistics. Wiley, Hoboken. doi:10.1002/0471725331.

Jackson, L.E., Kostaschuk, R.A., MacDonald, G.M., 1987. Identification of debris flow hazard on alluvial fans in the Canadian Rocky Mountains. In: Debris flows/avalanches process, recognition, and mitigation. Reviews in Engineering Geology 7. Geological Society of America, Boulder, pp. 115–124. doi:10.1130/REG7-p115.

Jacobsen, K., 2010. Comparison of ASTER GDEMs with SRTM Height Models. In: Proceedings of the 30th EARSeL Symposium, May 31–July 3, Paris. European Association of Remote Sensing Laboratories, Strasbourg, pp. 521–526.

Jain, A., 1989. Fundamentals of digital image processing. Prentice Hall information and system sciences series. Prentice-Hall, Englewood Cliffs, New Jersey.

Jain, A.O., Thaker, T., Chaurasia, A., Patel, P., Singh, A.K., 2017. Vertical accuracy evaluation of SRTM-GL1, GDEM-V2, AW3D30 and CartoDEM-V3.1 of 30-m resolution with dual frequency GNSS for lower Tapi Basin India. Geocarto International pp. 1–20. doi:10.1080/10106049.2017.1343392.

Jain, M.K., Kothyari, U.C., Ranga Raju, K.G., 2004. A GIS based distributed rainfall–runoff model. Journal of Hydrology 299(1–2), 107–135. doi:10.1016/j.jhydrol.2004.04.024.

James, G., Witten, D., Hastie, T., Tibshirani, R., 2013. An Introduction to Statistical Learning. Springer Texts in Statistics 103. Springer, New York. doi:10.1007/978-1-4614-7138-7.

Janitza, S., 2016. Resampling approaches in biometrical applications. Ph.D. thesis, Ludwig-Maximilians-Universität München, München.

Janitza, S., Hornung, R., 2018. On the overestimation of random forest's out-of-bag error. PLOS ONE 13(8), e0201904. doi:10.1371/journal.pone.0201904.

Janowicz, K., 2012. Observation-Driven Geo-Ontology Engineering. Transactions in GIS 16(3), 351–374. doi:10.1111/j.1467-9671.2012.01342.x.

Jansson, P., Jacobson, D., Hooke, R.B., 1993. Fan and playa areas in southern California and adjacent parts of Nevada. Earth Surface Processes and Landforms 18(2), 109–119. doi:10.1002/esp.3290180203.

Jarvis, A., Guevara, E., Reuter, H.I., Nelson, A.D., 2008. Hole-filled SRTM for the globe: version 4: data grid. http://srtm.csi.cgiar.org/. Last accessed on October 12, 2019.

Jensen, J.R., 1986. Introductory Digital Image Processing: A Remote Sensing Perspective. Prentice-Hall, Englewood Cliffs.

Jhonnerie, R., Siregar, V.P., Nababan, B., Prasetyo, L.B., Wouthuyzen, S., 2015. Random forest classification for mangrove land cover mapping using Landsat 5 TM and ALOS PALSAR imageries. Procedia Environmental Sciences 24, 215–221. doi:10.1016/j.proenv.2015.03.028.

Johnson, C.L., Constenius, K.C., Graham, S.A., Mackey, G., Menotti, T., Payton, A., Tully, J., 2015. Subsurface evidence for late Mesozoic extension in western Mongolia: tectonic and petroleum systems implications. Basin Research 27(3), 272–294. doi:10.1111/bre.12073.

Jolivet, M., Ritz, J.F., Vassallo, R., Larroque, C., Braucher, R., Todbileg, M., Chauvet, A., Sue, C., Arnaud, N., De Vicente, R., Arzhanikova, A., Arzhanikov, S., 2007. Mongolian summits: An uplifted, flat, old but still preserved erosion surface. Geology 35(10), 871. doi:10.1130/G23758A.1.

Jolliffe, I.T., 2002. Principal component analysis. Springer series in statistics. Springer, New York, 2nd ed.

Jones, A.F., Brewer, P.A., Johnstone, E., Macklin, M.G., 2007. High-resolution interpretative geomorphological mapping of river valley environments using airborne LiDAR data. Earth Surface Processes and Landforms 32(10), 1574–1592. doi:10.1002/esp.1505.

Jones, C.H., Unruh, J.R., Sonder, L.J., 1996a. The role of gravitational potential energy in active deformation in the southwestern United States. Nature 381(6577), 37–41. doi:10.1038/381037a0.

Jones, M.C., Marron, J.S., Sheather, S.J., 1996b. A Brief Survey of Bandwidth Selection for Density Estimation. Journal of the American Statistical Association 91(433), 401. doi:10.2307/2291420.

Joo, Y.J., Elwood Madden, M.E., Soreghan, G.S., 2016. Chemical and physical weathering in a hot-arid, tectonically active alluvial system of Anza Borrego Desert, California. Sedimentology 63(5), 1065–1083. doi:10.1111/sed.12249.

Jordan, R.L., Huneycutt, B.L., Werner, M., 1995. The SIR-C/X-SAR Synthetic Aperture Radar system. IEEE Transactions on Geoscience and Remote Sensing 33(4), 829–839. doi:10.1109/36.406669.

Juel, A., Groom, G.B., Svenning, J.C., Ejrnæs, R., 2015. Spatial application of Random Forest models for fine-scale coastal vegetation classification using object based analysis of aerial orthophoto and DEM data. International Journal of Applied Earth Observation and Geoinformation 42, 106–114. doi:10.1016/j.jag.2015.05.008.

Kamp, U., McManigal, K.G., Dashtseren, A., Walther, M., 2013. Documenting glacial changes between 1910, 1970, 1992 and 2010 in the Turgen Mountains, Mongolian Altai, using repeat photographs, topographic maps, and satellite imagery. The Geographical Journal 179(3), 248–263. doi:10.1111/j.1475-4959.2012.00486.x.

Kamp, U., Owen, L.A., 2013. Polygenetic Landscapes. In: Shroder, J.F. (Ed.). Treatise on Geomorphology. Academic Press, San Diego, pp. 370–393. doi:10.1016/B978-0-12-374739-6.00097-X.

Kapp, J.L.D., Harrison, T.M., Kapp, P., Grove, M., Lovera, O.M., Lin, D., 2005. Nyainqentanglha Shan: A window into the tectonic, thermal, and geochemical evolution of the Lhasa block, southern Tibet. Journal of Geophysical Research 110(B8), B08413. doi:10.1029/2004JB003330.

Karymbalis, E., Ferentinou, M., Giles, P.T., 2018. Use of morphometric variables and self-organizing maps to identify clusters of alluvial fans and catchments in the north Peloponnese, Greece. In: Ventra, D., Clarke, L.E. (Eds.). Geology and Geomorphology of Alluvial and Fluvial Fans: Terrestrial and Planetary Perspectives. Geological Society, London, Special Publications 440. Geological Society of London, pp. 45–64. doi:10.1144/SP440.7.

Karymbalis, E., Gaki-Papanastassiou, K., Ferentinou, M., 2010. Fan deltas classification coupling morphometric analysis and artificial neural networks: The case of NW coast of Gulf of Corinth, Greece. Hellenic Journal of Geosciences 45, 133–146.

Katsube, K., Oguchi, T., 1999. Altitudinal Changes in Slope Angle and Profile Curvature in the Japan

Alps: A Hypothesis Regarding a Characteristic Slope Angle. Geographical review of Japan, Series B. 72(1), 63–72. doi:10.4157/grj1984b.72.63.

Kattenborn, T., Eichel, J., Fassnacht, F.E., 2019. Convolutional Neural Networks enable efficient, accurate and fine-grained segmentation of plant species and communities from high-resolution UAV imagery. Scientific Reports 9(1), 17656. doi:10.1038/s41598-019-53797-9.

Katz, I.N., Vogl, S.R., 2010. A Weiszfeld algorithm for the solution of an asymmetric extension of the generalized Fermat location problem. Computers & Mathematics with Applications 59(1), 399–410. doi:10.1016/j.camwa.2009.07.007.

Kaufman, L., Rousseeuw, P.J., 1990. Finding groups in data: an introduction to cluster analysis. Wiley series in probability and mathematical statistics. Wiley, New York.

Keefer, W.R., Whitney, J.W., Buesch, D.C., 2007. Geology of the Yucca Mountain site area, southwestern Nevada. In: Stuckless, J.S., Levich, R.A. (Eds.). The Geology and Climatology of Yucca Mountain and Vicinity, Southern Nevada and California. Memoir 199. Geological Society of America, Boulder, pp. 53–103. doi:10.1130/2007.1199(03).

Kemker, R., Salvaggio, C., Kanan, C., 2018. Algorithms for semantic segmentation of multispectral remote sensing imagery using deep learning. ISPRS Journal of Photogrammetry and Remote Sensing 145, 60–77. doi:https://doi.org/10.1016/j.isprsjprs.2018.04.014.

Kenworthy, M.K., Rittenour, T.M., Pierce, J.L., Sutfin, N.A., Sharp, W.D., 2014. Luminescence dating without sand lenses: An application of OSL to coarse-grained alluvial fan deposits of the Lost River Range, Idaho, USA. Quaternary Geochronology 23, 9–25. doi:10.1016/j.quageo.2014.03.004.

Kervyn, M., Ernst, G.G.J., Goossens, R., Jacobs, P., 2008. Mapping volcano topography with remote sensing: ASTER vs. SRTM. International Journal of Remote Sensing 29(22), 6515–6538. doi:10.1080/01431160802167949.

Kesel, R.H., Spicer, B.E., 1985. Geomorphologic relationships and ages of soils on alluvial fans in the Rio General Valley, Costa Rica. CATENA 12(1), 149–166. doi:10.1016/S0341-8162(85)80014-X.

Khrutsky, V., Golubeva, E., 2008. Dynamics of the glaciers of the Turgen-Kharkhira mountain range (Western Mongolia). Geography and Natural Resources 29(3), 278–287. doi:10.1016/j.gnr.2008.09.014.

Kirby, M.E., Knell, E.J., Anderson, W.T., Lachniet, M.S., Palermo, J., Eeg, H., Lucero, R., Murrieta, R., Arevalo, A., Silveira, E., Hiner, C.A., 2015. Evidence for insolation and Pacific forcing of late glacial through Holocene climate in the Central Mojave Desert (Silver Lake, CA). Quaternary Research 84(2), 174–186. doi:10.1016/j.yqres.2015.07.003.

Kirillov, A., Levinkov, E., Andres, B., Savchynskyy, B., Rother, C., 2017. InstanceCut: From Edges to Instances with MultiCut. In: Proceedings of the IEEE Conference on Computer Vision and Pattern Recognition, July 21–26, Honolulu. IEEE, New York, pp. 7322–7331. doi:10.1109/CVPR.2017.774.

Kneisel, C., Lehmkuhl, F., Winkler, S., Tressel, E., Schröder, H., 1998. Legende für geomorphologische Kartierungen in Hochgebirgen (GMK Hochgebirge). Trierer Geographische Studien 18. Trierer Geographische Gesellschaft, Trier.

Knighton, D., 2014. Fluvial Forms and Processes: A New Perspective. Routledge, London, New York, 2nd ed. doi:10.4324/9780203784662.

Knox, J.C., 1984. Responses of River Systems to Holocene Climates. In: Wright, H.E. (Ed.). Late Quaternary Environments of the United States Volume 2: The Holocene. University of Minnesota Press, Minneapolis, pp. 26–41.

Koehler, P.A., Anderson, R.S., Spaulding, W.G., 2005. Development of vegetation in the Central Mojave Desert of California during the late Quaternary. Palaeogeography, Palaeoclimatology, Palaeoecology 215(3–4), 297–311. doi:10.1016/j.palaeo.2004.09.010.

Kohonen, T., 1982. Self-organized formation of topologically correct feature maps. Biological Cybernetics 43(1), 59–69. doi:10.1007/BF00337288.

Kohonen, T., 2001. Self-organizing maps. Springer series in information sciences 30. Springer, Berlin, New York, 3rd ed.

Kolb, C.R., 1984. Alluvial plains, Engineering geology. In: Finkl, C.W. (Ed.). Applied Geology. Encyclopedia of Earth Sciences Series 3. Kluwer Academic Publishers, Dordrecht, pp. 1–2. doi: 10.1007/0-387-30842-3_1.

Korup, O., 2008. Rock type leaves topographic signature in landslide-dominated mountain ranges. Geophysical Research Letters 35(11). doi:10.1029/2008GL034157.

Korup, O., Montgomery, D.R., Hewitt, K., 2010. Glacier and landslide feedbacks to topographic relief in the Himalayan syntaxes. Proceedings of the National Academy of Sciences 107(12), 5317–5322. doi:10.1073/pnas.0907531107.

Kostaschuk, R.A., Macdonald, G.M., Putnam, P.E., 1986. Depositional process and alluvial fan-drainage basin morphometric relationships near Banff, Alberta, Canada. Earth Surface Processes and Landforms 11(5), 471–484. doi:10.1002/esp.3290110502.

Kostrova, S.S., Meyer, H., Chapligin, B., Tarasov, P.E., Bezrukova, E.V., 2014. The last glacial maximum and late glacial environmental and climate dynamics in the Baikal region inferred from an oxygen isotope record of lacustrine diatom silica. Quaternary International 348, 25–36. doi: 10.1016/j.quaint.2014.07.034.

Krieger, G., Fiedler, H., Hajnsek, I., Eineder, M., Werner, M., Moreira, A., 2005. TanDEM-X: mission concept and performance analysis. In: Proceedings of the IEEE International Geoscience and Remote Sensing Symposium, July 29, Seoul. IEEE, New York, pp. 4890–4893. doi:10.1109/IGARSS.2005. 1526770.

Krieger, G., Moreira, A., Fiedler, H., Hajnsek, I., Werner, M., Younis, M., Zink, M., 2007. TanDEM-X: A Satellite Formation for High-Resolution SAR Interferometry. IEEE Transactions on Geoscience and Remote Sensing 45(11), 3317–3341. doi:10.1109/TGRS.2007.900693.

Krizhevsky, A., Sutskever, I., Hinton, G.E., 2012. ImageNet Classification with Deep Convolutional Neural Networks. In: Proceedings of the 25th International Conference on Neural Information Processing Systems, December 3–8, Lake Tahoe. Curran Associates, New York, p. 1097–1105.

Kutzbach, J.E., 1981. Monsoon Climate of the Early Holocene: Climate Experiment with the Earth's Orbital Parameters for 9000 Years Ago. Science 214(4516), 59–61. doi:10.1126/science.214.4516.59.

Lachaise, M., Fritz, T., Eineder, M., 2008. A new dual baseline phase unwrapping algorithm for the TanDEM-X Mission. In: Proceedings of the 7th European Conference on Synthetic Aperture Radar, June 2–5, Friedrichshafen. VDE, Berlin, pp. 1–4.

Lachniet, M.S., Denniston, R.F., Asmerom, Y., Polyak, V.J., 2014. Orbital control of western North America atmospheric circulation and climate over two glacial cycles. Nature Communications 5(1), 3805. doi:10.1038/ncomms4805.

Lang, S., 2008. Object-based image analysis for remote sensing applications: modeling reality – dealing with complexity. In: Blaschke, T., Lang, S., Hay, G.J. (Eds.). Object-Based Image Analysis. Springer, Berlin, Heidelberg, pp. 3–27. doi:10.1007/978-3-540-77058-9_1.

Larson, J., Zhou, Y., Higgins, R.W., 2005. Characteristics of Landfalling Tropical Cyclones in the United States and Mexico: Climatology and Interannual Variability. Journal of Climate 18(8), 1247–1262. doi:10.1175/JCLI3317.1.

Lawson, C.L., Hanson, R.J., 1995. Solving Least Squares Problems. Society for Industrial and Applied Mathematics. doi:10.1137/1.9781611971217.

Le Bris, R., Paul, F., 2013. An automatic method to create flow lines for determination of glacier

length: A pilot study with Alaskan glaciers. Computers & Geosciences 52, 234–245. doi: 10.1016/j.cageo.2012.10.014.

Lecce, S.A., 1990. The Alluvial Fan Problem. In: Rachocki, A., Church, M.A.A. (Eds.). Alluvial fans: A Field Approach. Wiley, Chichester, New York, pp. 3–24.

Lecce, S.A., 1991. Influence of Lithologic Erodibility on Alluvial Fan Area, Western White Mountains, California and Nevada. Earth Surface Processes and Landforms 16(1), 11–18. doi:10.1002/esp.3290160103.

LeCun, Y., Bengio, Y., Hinton, G.E., 2015. Deep learning. Nature 521(7553), 436–444. doi: 10.1038/nature14539.

LeCun, Y., Bottou, L., Bengio, Y., Haffner, P., 1998. Gradient-based learning applied to document recognition. Proceedings of the IEEE 86(11), 2278–2324. doi:10.1109/5.726791.

Lee, M.K., Lee, Y.I., Lim, H.S., Lee, J.I., Yoon, H.I., 2013. Late Pleistocene-Holocene records from Lake Ulaan, southern Mongolia: implications for east Asian palaeomonsoonal climate changes. Journal of Quaternary Science 28(4), 370–378. doi:10.1002/jqs.2626.

Leeder, M.R., 1982. Sedimentology. Springer, Dordrecht. doi:10.1007/978-94-009-5986-6.

Leeder, M.R., Mack, G.H., 2001. Lateral erosion ('toe-cutting') of alluvial fans by axial rivers: implications for basin analysis and architecture. Journal of the Geological Society 158(6), 885–893. doi:10.1144/0016-760000-198.

Legendre, P., Legendre, L., 2012. Numerical ecology. Developments in environmental modelling 24. Elsevier, Amsterdam, 3rd ed.

Lehmkuhl, F., 1998. Quaternary Glaciations in Central and Western Mongolia. In: Owen, L.A. (Ed.). Mountain Glaciations. Quaternary Proceedings 6. Wiley, Chichester, pp. 153–167.

Lehmkuhl, F., 2000. Alluvial fans and pediments in Western Mongolia and their implications for neotectonic events and climatic change. Berliner geowissenschaftliche Abhandlungen A(205), 14–21.

Lehmkuhl, F., Grunert, J., Hülle, D., Batkhishig, O., Stauch, G., 2018a. Paleolakes in the Gobi region of southern Mongolia. Quaternary Science Reviews 179, 1–23. doi:10.1016/j.quascirev.2017.10.035.

Lehmkuhl, F., Haselein, F., 2000. Quaternary paleoenvironmental change on the Tibetan Plateau and adjacent areas (Western China and Western Mongolia). Quaternary International 65–66, 121–145. doi:10.1016/S1040-6182(99)00040-3.

Lehmkuhl, F., Klinge, M., Rother, H., Hülle, D., 2016. Distribution and timing of Holocene and late Pleistocene glacier fluctuations in western Mongolia. Annals of Glaciology 57(71), 169–178. doi:10.3189/2016AoG71A030.

Lehmkuhl, F., Klinge, M., Stauch, G., 2011. The Extent and Timing of Late Pleistocene Glaciations in the Altai and Neighbouring Mountain Systems. In: Ehlers, J., Gibbard, P.L., Hughes, P.D. (Eds.). Quaternary glaciations - extent and chronology: a closer look. Developments in Quaternary Sciences 15. Elsevier, Amsterdam, Boston, Heidelberg, pp. 967–979. doi:10.1016/B978-0-444-53447-7.00069-6.

Lehmkuhl, F., Nottebaum, V., Hülle, D., 2018b. Aspects of late Quaternary geomorphological development in the Khangai Mountains and the Gobi Altai Mountains (Mongolia). Geomorphology 312, 24–39. doi:10.1016/j.geomorph.2018.03.029.

Leier, A.L., DeCelles, P.G., Pelletier, J.D., 2005. Mountains, monsoons, and megafans. Geology 33(4), 289. doi:10.1130/G21228.1.

Leopold, L.B., Bull, W.B., 2008. Base level, aggradation, and grade. Proceedings of the American Philosophical Society 123(3), 168–202.

Lever, J., Krzywinski, M., Altman, N., 2017. Principal component analysis. Nature Methods 14, 641.

Levson, V.M., Rutter, N.W., 2000. Influence of bedrock geology on sedimentation in Pre-Late Wisconsinan alluvial fans in the Canadian Rocky Mountains. Quaternary International 68–71, 133–146. doi:10.1016/S1040-6182(00)00039-2.

Löhrer, R., 2008. Reliefanalyse an Schwemmfächern und Fußflächen im Südwesten der USA. Ph.D. thesis, Rheinisch-Westfälische Technische Hochschule Aachen, Aachen.

Li, H., Zhao, J., 2018. Evaluation of the Newly Released Worldwide AW3D30 DEM Over Typical Landforms of China Using Two Global DEMs and ICESat/GLAS Data. IEEE Journal of Selected Topics in Applied Earth Observations and Remote Sensing 11(11), 4430–4440. doi:10.1109/JSTARS.2018.2874361.

Li, J., Cook, E.R., D'arrigo, R., Chen, F., Gou, X., 2009. Moisture variability across China and Mongolia: 1951–2005. Climate Dynamics 32(7–8), 1173–1186. doi:10.1007/s00382-008-0436-0.

Li, J., Lowenstein, T.K., Brown, C.B., Ku, T.L., Luo, S., 1996. A 100 ka record of water tables and paleoclimates from salt cores, Death Valley, California. Palaeogeography, Palaeoclimatology, Palaeoecology 123(1–4), 179–203. doi:10.1016/0031-0182(95)00123-9.

Li, M., Ma, L., Blaschke, T., Cheng, L., Tiede, D., 2016. A systematic comparison of different object-based classification techniques using high spatial resolution imagery in agricultural environments. International Journal of Applied Earth Observation and Geoinformation 49, 87–98. doi:10.1016/j.jag.2016.01.011.

Li, P., Shi, C., Li, Z., Muller, J.P., Drummond, J., Li, X., Li, T., Li, Y., Liu, J., 2013. Evaluation of ASTER GDEM using GPS benchmarks and SRTM in China. International Journal of Remote Sensing 34(5), 1744–1771. doi:10.1080/01431161.2012.726752.

Li, Q., Racine, J.S. (Eds.), 2009. Nonparametric econometric methods. Advances in econometrics 25. Emerald, Bingley.

Li, S., Xiong, L., Tang, G., Strobl, J., 2020. Deep learning-based approach for landform classification from integrated data sources of digital elevation model and imagery. Geomorphology 354, 107045. doi:10.1016/j.geomorph.2020.107045.

Li, X., Cheng, X., Chen, W., Chen, G., Liu, S., 2015. Identification of Forested Landslides Using LiDar Data, Object-based Image Analysis, and Machine Learning Algorithms. Remote Sensing 7(8), 9705–9726. doi:10.3390/rs70809705.

Liang, E.Y., Shao, X.M., Xu, Y., 2009. Tree-ring evidence of recent abnormal warming on the southeast Tibetan Plateau. Theoretical and Applied Climatology 98(1–2), 9–18. doi:10.1007/s00704-008-0085-6.

Lillesand, T.M., Kiefer, R.W., Chipman, J.W., 2004. Remote Sensing and Image Interpretation. Wiley, New York, 5th ed.

Lin, T.Y., Dollár, P., Girshick, R.B., He, K., Hariharan, B., Belongie, S., 2017. Feature Pyramid Networks for Object Detection. In: Proceedings of the IEEE Conference on Computer Vision and Pattern Recognition, July 21–26, Honolulu. IEEE, New York, pp. 936–944. doi:10.1109/CVPR.2017.106.

Lin, T.Y., Maire, M., Belongie, S., Hays, J., Perona, P., Ramanan, D., Dollár, P., Zitnick, C.L., 2014. Microsoft COCO: Common Objects in Context. In: Proceedings of the 13th European Conference on Computer Vision, September 6–12, Zürich. Springer, Cham, vol. 8693, pp. 740–755. doi:10.1007/978-3-319-10602-1_48.

Lin, Z., Oguchi, T., Chen, Y.G., Saito, K., 2009. Constant-slope alluvial fans and source basins in Taiwan. Geology 37(9), 787–790. doi:10.1130/G25675A.1.

Lioubimtseva, E., Cole, R., Adams, J.M., Kapustin, G., 2005. Impacts of climate and land-cover changes in arid lands of Central Asia. Journal of Arid Environments 62(2), 285–308. doi:10.1016/j.jaridenv.2004.11.005.

Liu, L., Gurnis, M., Seton, M., Saleeby, J., Müller, R.D., Jackson, J.M., 2010. The role of oceanic plateau subduction in the Laramide orogeny. Nature Geoscience 3(5), 353–357. doi:10.1038/ngeo829.

Liu, M., Shen, Y., 1998. Crustal collapse, mantle upwelling, and Cenozoic extension in the North American Cordillera. Tectonics 17(2), 311–321. doi:10.1029/98TC00313.

Liu, T., Abd-Elrahman, A., Morton, J., Wilhelm, V.L., 2018. Comparing fully convolutional networks, random forest, support vector machine, and patch-based deep convolutional neural networks for object-based wetland mapping using images from small unmanned aircraft system. GIScience & Remote Sensing 55(2), 243–264. doi:10.1080/15481603.2018.1426091.

Liu, X., 2008. Airborne LiDAR for DEM generation: some critical issues. Progress in Physical Geography 32(1), 31–49. doi:10.1177/0309133308089496.

Liu, Y., Minh Nguyen, D., Deligiannis, N., Ding, W., Munteanu, A., 2017a. Hourglass-ShapeNetwork Based Semantic Segmentation for High Resolution Aerial Imagery. Remote Sensing 9(6), 522. doi:10.3390/rs9060522.

Liu, Y., Piramanayagam, S., Monteiro, S.T., Saber, E., 2017b. Dense Semantic Labeling of Very-High-Resolution Aerial Imagery and LiDAR with Fully-Convolutional Neural Networks and Higher-Order CRFs. In: IEEE Conference on Computer Vision and Pattern Recognition Workshops, July 21–26, Honolulu. IEEE, New York, pp. 1561–1570. doi:10.1109/CVPRW.2017.200.

Liu, Z., Gilbert, G., Cepeda, J.M., Lysdahl, A.O.K., Piciullo, L., Hefre, H., Lacasse, S., 2021. Modelling of shallow landslides with machine learning algorithms. Geoscience Frontiers 12(1), 385–393. doi:10.1016/j.gsf.2020.04.014.

Livaccari, R.F., Burke, K., Şengör, A.M.C., 1981. Was the Laramide orogeny related to subduction of an oceanic plateau? Nature 289(5795), 276–278. doi:10.1038/289276a0.

Längkvist, M., Kiselev, A., Alirezaie, M., Loutfi, A., 2016. Classification and Segmentation of Satellite Orthoimagery Using Convolutional Neural Networks. Remote Sensing 8(4), 329. doi:10.3390/rs8040329.

Loibl, D., Hochreuther, P., Schulte, P., Hülle, D., Zhu, H., Bräuning, A., Lehmkuhl, F., 2015. Toward a late Holocene glacial chronology for the eastern Nyainqêntanglha Range, southeastern Tibet. Quaternary Science Reviews 107, 243–259. doi:10.1016/j.quascirev.2014.10.034.

Loibl, D., Lehmkuhl, F., 2013. High-resolution geomorphological map of a low mountain range near Aachen, Germany. Journal of Maps 9(2), 245–253. doi:10.1080/17445647.2013.771291.

Loibl, D., Lehmkuhl, F., 2015. Glaciers and equilibrium line altitudes of the eastern Nyainqêntanglha Range, SE Tibet. Journal of Maps 11(4), 1–14. doi:10.1080/17445647.2014.933451.

Loibl, D., Lehmkuhl, F., Grießinger, J., 2014. Reconstructing glacier retreat since the Little Ice Age in SE Tibet by glacier mapping and equilibrium line altitude calculation. Geomorphology 214, 22–39. doi:10.1016/j.geomorph.2014.03.018.

Louppe, G., 2014. Understanding Random Forests: From Theory to Practice. Ph.D. thesis, University of Liege, Liege.

Louppe, G., Wehenkel, L., Sutera, A., Geurts, P., 2013. Understanding variable importances in forests of randomized trees. In: Proceedings of the 26th International Conference on Neural Information Processing Systems, December 5–10, Lake Tahoe. Curran Associates, New York, pp. 431–439.

Louw, G., van Niekerk, A., 2019. Object-based land surface segmentation scale optimisation: An ill-structured problem. Geomorphology 327, 377–384. doi:10.1016/j.geomorph.2018.11.021.

Lustig, L.K., 1965. Clastic sedimentation in Deep Springs Valley, California. In: USGS (Ed.). Erosion and sedimentation in a semiarid environment. Professional Paper 352F. USGS, pp. 131–192. doi:10.3133/pp352F.

Lv, X., Ming, D., Lu, T., Zhou, K., Wang, M., Bao, H., 2018. A New Method for Region-Based

Majority Voting CNNs for Very High Resolution Image Classification. Remote Sensing 10(12), 1946. doi:10.3390/rs10121946.

Lyle, M., Heusser, L., Ravelo, C., Yamamoto, M., Barron, J., Diffenbaugh, N.S., Herbert, T., Andreasen, D., 2012. Out of the Tropics: The Pacific, Great Basin Lakes, and Late Pleistocene Water Cycle in the Western United States. Science 337(6102), 1629–1633. doi:10.1126/science.1218390.

Ma, L., Liu, Y., Zhang, X., Ye, Y., Yin, G., Johnson, B.A., 2019. Deep learning in remote sensing applications: A meta-analysis and review. ISPRS Journal of Photogrammetry and Remote Sensing 152, 166–177. doi:10.1016/j.isprsjprs.2019.04.015.

Mack, G.H., Leeder, M.R., 1999. Climatic and tectonic controls on alluvial-fan and axial-fluvial sedimentation in the Plio-Pleistocene Palomas half graben, southern Rio Grande Rift. Journal of Sedimentary Research 69(3), 635–652. doi:10.2110/jsr.69.635.

MacMillan, R.A., Jones, R.K., McNabb, D.H., 2004. Defining a hierarchy of spatial entities for environmental analysis and modeling using digital elevation models (DEMs). Computers, Environment and Urban Systems 28(3), 175–200. doi:10.1016/S0198-9715(03)00019-X.

MacMillan, R.A., Pettapiece, W., Nolan, S.C., Goddard, T.W., 2000. A generic procedure for automatically segmenting landforms into landform elements using DEMs, heuristic rules and fuzzy logic. Fuzzy Sets and Systems 113(1), 81–109. doi:10.1016/S0165-0114(99)00014-7.

MacMillan, R.A., Shary, P.A., 2009. Landforms and Landform Elements in Geomorphometry. In: Hengl, T., Reuter, H.I. (Eds.). Geomorphometry. Concepts, Software, Applications. Developments in Soil Science 33. Elsevier, Amsterdam, Boston, Heidelberg, pp. 227–254. doi:10.1016/S0166-2481(08)00009-3.

Mahan, S.A., Miller, D.M., Menges, C.M., Yount, J.C., 2007. Late Quaternary stratigraphy and luminescence geochronology of the northeastern Mojave Desert. Quaternary International 166(1), 61–78. doi:10.1016/j.quaint.2006.12.010.

Major, J.J., 2003. Debris flow. In: Middleton, G.V. (Ed.). Encyclopedia of sediments & sedimentary rocks. Kluwer Academic encyclopedia of earth sciences series. Kluwer Academic Publishers, Dordrecht, Boston, pp. 295–300. doi:10.1007/978-1-4020-3609-5_58.

Major, J.J., Iverson, R.M., 1999. Debris-flow deposition: Effects of pore-fluid pressure and friction concentrated at flow margins. GSA Bulletin 111(10), 1424–1434. doi:10.1130/0016-7606(1999)111<1424:DFDEOP>2.3.CO;2.

Mann, P., 2007. Global catalogue, classification and tectonic origins of restraining- and releasing bends on active and ancient strike-slip fault systems. In: Cunningham, W.D., Mann, P. (Eds.). Tectonics of Strike-Slip Restraining and Releasing Bends. Geological Society, London, Special Publications 290. Geological Society of London, London, pp. 13–142. doi:10.1144/SP290.2.

Marchi, B., Pasuto, A., Tecca, P.R., 1993. Flow processes on alluvial fans in the Eastern Italian Alps. Zeitschrift für Geomorphologie 37(4), 447–458.

Marchi, L., Brochot, S., 2000. Les cônes de déjection torrentiels dans les Alpes françaises. Morphométrie et processus de transport solide torrentiel. Revue de géographie alpine 88(3), 23–38. doi:10.3406/rga.2000.2999.

Marchi, L., D'Agostino, V., 2004. Estimation of debris-flow magnitude in the Eastern Italian Alps. Earth Surface Processes and Landforms 29(2), 207–220. doi:10.1002/esp.1027.

Marchi, L., Tecca, P.R., 1995. Alluvial fans of the Eastern Italian Alps: morphometry and depositional processes. Geodinamica Acta 8(1), 20–27. doi:10.1080/09853111.1995.11105270.

Mark, D.M., 1975. Geomorphometric Parameters: A Review and Evaluation. Geografiska Annaler. Series A, Physical Geography 57(3–4), 165–177.

Mark, D.M., Smith, B., 2004. A science of topography: From qualitative ontology to digital represen-

tations. In: Bishop, M.P., Shroder, J.F. (Eds.). GIS & Mountain Geomorphology. Springer, Berlin, New York, pp. 75–100.

Markham, C.G., 1972. Baja California's Climate. Weatherwise 25(2), 64–101. doi:10.1080/00431672.1972.9931578.

Marron, J.S., 1988. Automatic smoothing parameter selection: A survey. Empirical Economics 13(3), 187–208. doi:10.1007/BF01972448.

Marshall, J.A., Sklar, L.S., 2012. Mining soil databases for landscape-scale patterns in the abundance and size distribution of hillslope rock fragments. Earth Surface Processes and Landforms 37(3), 287–300. doi:10.1002/esp.2241.

Martin, J., Sheets, B., Paola, C., Hoyal, D., 2009. Influence of steady base-level rise on channel mobility, shoreline migration, and scaling properties of a cohesive experimental delta. Journal of Geophysical Research 114(F3), F03017. doi:10.1029/2008JF001142.

Martin, Y., Church, M.A., 2004. Numerical modelling of landscape evolution: geomorphological perspectives. Progress in Physical Geography 28(3), 317–339. doi:10.1191/0309133304pp412ra.

Mashimbye, Z.E., de Clercq, W.P., van Niekerk, A., 2014. An evaluation of digital elevation models (DEMs) for delineating land components. Geoderma 213, 312–319. doi:10.1016/j.geoderma.2013.08.023.

Mason, C.C., Romans, B.W., 2018. Climate-driven unsteady denudation and sediment flux in a high-relief unglaciated catchment–fan using ^{26}Al and ^{10}Be: Panamint Valley, California. Earth and Planetary Science Letters 492, 130–143. doi:10.1016/j.epsl.2018.03.056.

Mather, A.E., Harvey, A.M., Stokes, M., 2000. Quantifying long-term catchment changes of alluvial fan systems. Geological Society of America Bulletin 112(12), 1825–1833. doi:10.1130/0016-7606(2000)112<1825:QLTCCO>2.0.CO;2.

Mather, A.E., Stokes, M., 2018. Bedrock structural control on catchment-scale connectivity and alluvial fan processes, High Atlas Mountains, Morocco. In: Ventra, D., Clarke, L.E. (Eds.). Geology and Geomorphology of Alluvial and Fluvial Fans: Terrestrial and Planetary Perspectives. Geological Society, London, Special Publications 440. Geological Society of London, London, pp. 103–128. doi:10.1144/SP440.15.

Matsubara, Y., Howard, A.D., 2009. A spatially explicit model of runoff, evaporation, and lake extent: Application to modern and late Pleistocene lakes in the Great Basin region, western United States. Water Resources Research 45(6). doi:10.1029/2007WR005953.

Maussion, F., Scherer, D., Mölg, T., Collier, E., Curio, J., Finkelnburg, R., 2014. Precipitation Seasonality and Variability over the Tibetan Plateau as Resolved by the High Asia Reanalysis. Journal of Climate 27(5), 1910–1927. doi:10.1175/JCLI-D-13-00282.1.

Maxwell, A.E., Pourmohammadi, P., Poyner, J.D., 2020. Mapping the Topographic Features of Mining-Related Valley Fills Using Mask R-CNN Deep Learning and Digital Elevation Data. Remote Sensing 12(3), 547. doi:10.3390/rs12030547.

Mayor, Á.G., Bautista, S., Small, E.E., Dixon, M., Bellot, J., 2008. Measurement of the connectivity of runoff source areas as determined by vegetation pattern and topography: A tool for assessing potential water and soil losses in drylands. Water Resources Research 44(10), W10423. doi:10.1029/2007WR006367.

McDonald, E.V., McFadden, L.D., Wells, S.G., 2003. Regional response of alluvial fans to the Pleistocene-Holocene climatic transition, Mojave Desert, California. In: Enzel, Y., Wells, S.G., Lancaster, N. (Eds.). Paleoenvironments and paleohydrology of the Mojave and southern Great Basin deserts. Special Paper 368. Geological Society of America, Boulder, pp. 189–205. doi:10.1130/0-8137-2368-X.189.

McGlone, C.J., 2007. Photogrammetry. In: Maune, D.F. (Ed.). Digital elevation model technologies and

applications: the DEM users manual. American Society for Photogrammetry and Remote Sensing, Bethesda, pp. 119–139. 2nd ed.

Melton, M.A., 1965. The Geomorphic and Paleoclimatic Significance of Alluvial Deposits in Southern Arizona. The Journal of Geology 73(1), 1–38.

Messenzehl, K., Meyer, H., Otto, J.C., Hoffmann, T., Dikau, R., 2017. Regional-scale controls on the spatial activity of rockfalls (Turtmann Valley, Swiss Alps) — A multivariate modeling approach. Geomorphology 287, 29–45. doi:10.1016/j.geomorph.2016.01.008.

Metcalfe, S.E., Barron, J.A., Davies, S.J., 2015. The Holocene history of the North American Monsoon: 'known knowns' and 'known unknowns' in understanding its spatial and temporal complexity. Quaternary Science Reviews 120, 1–27. doi:10.1016/j.quascirev.2015.04.004.

Michaud, F., Calmus, T., Royer, J.Y., Sosson, M., Bandy, B., Mortera-Gutiérrez, C., Dyment, J., Bigot-Cormier, F., Chabert, A., Bourgois, J., 2007. Right-lateral active faulting between southern Baja California and the Pacific plate: The Tosco-Abreojos fault. In: Alaniz-Álvarez, S.A., Nieto-Samaniego, Á.F., Mexicana, S.G. (Eds.). Geology of México: Celebrating the Centenary of the Geological Society of México. Special Paper 422. Geological Society of America, Boulder, pp. 287–300. doi:10.1130/2007.2422(09).

Middleton, M., Heikkonen, J., Nevalainen, P., Hyvönen, E., Sutinen, R., 2020. Machine learning-based mapping of micro-topographic earthquake-induced paleo-Pulju moraines and liquefaction spreads from a digital elevation model acquired through laser scanning. Geomorphology 358, 107099. doi:10.1016/j.geomorph.2020.107099.

Milana, J.P., Ruzycki, L., 1999. Alluvial-fan slope as a function of sediment transport efficiency. Journal of Sedimentary Research 69(3), 553–562. doi:10.2110/jsr.69.553.

Miliaresis, G.C., 1999. Automated Segmentation of Alluvial Fans to Regions of High to Intermediate Flood Hazard from Landsat Thematic Mapper Imagery. In: Proceedings of the 2nd International Symposium on Operationalization of Remote Sensing, August 16–20, Enschede. ITC, Enschede. doi:10.6084/m9.figshare.1004664.

Miliaresis, G.C., 2001. Extraction of bajadas from digital elevation models and satellite imagery. Computers & Geosciences 27(10), 1157–1167. doi:10.1016/S0098-3004(01)00032-2.

Miliaresis, G.C., Argialas, D.P., 2000. Extraction and delineation of alluvial fans from digital elevation models and Landsat thematic mapper images. Photogrammetric Engineering & Remote Sensing 66(9), 1093–1101.

Miliaresis, G.C., Paraschou, C.V.E., 2011. An evaluation of the accuracy of the ASTER GDEM and the role of stack number: a case study of Nisiros Island, Greece. Remote Sensing Letters 2(2), 127–135. doi:10.1080/01431161.2010.503667.

Miller, D.M., Schmidt, K.M., Mahan, S.A., McGeehin, J.P., Owen, L.A., Barron, J.A., Lehmkuhl, F., Löhrer, R., 2010. Holocene landscape response to seasonality of storms in the Mojave Desert. Quaternary International 215(1–2), 45–61. doi:10.1016/j.quaint.2009.10.001.

Miller, K.L., Reitz, M.D., Jerolmack, D.J., 2014. Generalized sorting profile of alluvial fans. Geophysical Research Letters 41(20), 7191–7199. doi:10.1002/2014GL060991.

Millman, J., Vaught, T., 2008. The State of SciPy. In: Varoquaux, G., Vaught, T., Millman, J. (Eds.). Proceedings of the 7th Python in Science Conference, August 19–24, Pasadena. pp. 5–10.

Mills, H.H., 2000. Controls on form, process, and sedimentology of alluvial fans in the Central and Southern Appalachians, Southeastern U.S.A. Southeastern Geology 39, 281–313.

Ming, D., Ci, T., Cai, H., Li, L., Qiao, C., Du, J., 2012. Semivariogram-Based Spatial Bandwidth Selection for Remote Sensing Image Segmentation With Mean-Shift Algorithm. IEEE Geoscience and Remote Sensing Letters 9(5), 813–817. doi:10.1109/LGRS.2011.2182604.

Ming, D., Li, J., Wang, J., Zhang, M., 2015. Scale parameter selection by spatial statistics for GeOBIA:

Using mean-shift based multi-scale segmentation as an example. ISPRS Journal of Photogrammetry and Remote Sensing 106, 28–41. doi:10.1016/j.isprsjprs.2015.04.010.

Minár, J., Evans, I.S., 2008. Elementary forms for land surface segmentation: The theoretical basis of terrain analysis and geomorphological mapping. Geomorphology 95(3–4), 236–259. doi:10.1016/j.geomorph.2007.06.003.

Minár, J., Evans, I.S., Krcho, J., 2013. Geomorphometry: Quantitative Land-Surface Analysis. In: Shroder, J.F. (Ed.). Treatise on Geomorphology. Academic Press, San Diego, pp. 22–34. doi:10.1016/B978-0-12-374739-6.00370-5.

Mitchell, D.L., Ivanova, D., Rabin, R., Brown, T.J., Redmond, K., 2002. Gulf of California Sea Surface Temperatures and the North American Monsoon: Mechanistic Implications from Observations. Journal of Climate 15(17), 2261–2281. doi:10.1175/1520-0442(2002)015<2261:GOCSST>2.0.CO;2.

Möller, M., Volk, M., Friedrich, K., Lymburner, L., 2008. Placing soil-genesis and transport processes into a landscape context: A multiscale terrain-analysis approach. Journal of Plant Nutrition and Soil Science 171(3), 419–430. doi:10.1002/jpln.200625039.

Mock, C.J., 1996. Climatic Controls and Spatial Variations of Precipitation in the Western United States. Journal of Climate 9(5), 1111–1125. doi:10.1175/1520-0442(1996)009<1111:CCASVO>2.0.CO;2.

Mock, C.J., Bartlein, P.J., 1995. Spatial Variability of Late-Quaternary Paleoclimates in the Western United States. Quaternary Research 44(3), 425–433. doi:10.1006/qres.1995.1087.

Mokarram, M., Seif, A., Sathyamoorthy, D., 2014. Use of morphometric analysis and self-organizing maps for alluvial fan classification: case study on Ostorankooh altitudes, Iran. IOP Conference Series: Earth and Environmental Science 20, 012003. doi:10.1088/1755-1315/20/1/012003.

Molnar, P., Anderson, R.S., Anderson, S.P., 2007. Tectonics, fracturing of rock, and erosion. Journal of Geophysical Research 112(F3), F03014. doi:10.1029/2005JF000433.

Molnar, P., Boos, W.R., Battisti, D.S., 2010. Orographic Controls on Climate and Paleoclimate of Asia: Thermal and Mechanical Roles for the Tibetan Plateau. Annual Review of Earth and Planetary Sciences 38, 77–102. doi:10.1146/annurev-earth-040809-152456.

Molnar, P., Tapponnier, P., 1975. Cenozoic Tectonics of Asia: Effects of a Continental Collision: Features of recent continental tectonics in Asia can be interpreted as results of the India-Eurasia collision. Science 189(4201), 419–426. doi:10.1126/science.189.4201.419.

Montgomery, D.R., 2003. Predicting landscape-scale erosion rates using digital elevation models. Comptes Rendus Geoscience 335(16), 1121–1130. doi:10.1016/j.crte.2003.10.005.

Moore, I.D., Gessler, P.E., Nielsen, G.A., Peterson, G.A., 1993. Soil Attribute Prediction Using Terrain Analysis. Soil Science Society of America Journal 57(2), 443–452. doi:10.2136/sssaj1993.572NPb.

Moore, I.D., Grayson, R.B., Ladson, A.R., 1991. Digital terrain modelling: A review of hydrological, geomorphological, and biological applications. Hydrological Processes 5(1), 3–30. doi:10.1002/hyp.3360050103.

Morinaga, Y., Tian, S.F., Shinoda, M., 2003. Winter snow anomaly and atmospheric circulation in Mongolia. International Journal of Climatology 23(13), 1627–1636. doi:10.1002/joc.961.

Mouratidis, A., Briole, P., Katsambalos, K., 2010. SRTM 3″ DEM (versions 1, 2, 3, 4) validation by means of extensive kinematic GPS measurements: a case study from North Greece. International Journal of Remote Sensing 31(23), 6205–6222. doi:10.1080/01431160903401403.

Mueller, K., Kier, G., Rockwell, T., Jones, C.H., 2009. Quaternary rift flank uplift of the Peninsular Ranges in Baja and southern California by removal of mantle lithosphere. Tectonics 28(5), TC5003. doi:10.1029/2007TC002227.

Mukherjee, S., Joshi, P.K., Mukherjee, S., Ghosh, A., Garg, R.D., Mukhopadhyay, A., 2013. Evaluation

of vertical accuracy of open source Digital Elevation Model (DEM). International Journal of Applied Earth Observation and Geoinformation 21, 205–217. doi:10.1016/j.jag.2012.09.004.

Muto, T., Steel, R.J., 2004. Autogenic response of fluvial deltas to steady sea-level fall: Implications from flume-tank experiments. Geology 32(5), 401. doi:10.1130/G20269.1.

Nadaraya, É.A., 1965. On Non-Parametric Estimates of Density Functions and Regression Curves. Theory of Probability & Its Applications 10(1), 186–190. doi:10.1137/1110024.

Nandintsetseg, B., Shinoda, M., 2011. Seasonal change of soil moisture in Mongolia: its climatology and modelling. International Journal of Climatology 31(8), 1143–1152. doi:10.1002/joc.2134.

Negrini, R.M., 2002. Pluvial Lake Sizes in the Northwestern Great Basin throughout the Quaternary Period. In: Hershler, R., Madsen, D.B., Currey, D.R. (Eds.). Great Basin Aquatic Systems History. Smithsonian Contributions to the Earth Sciences 33. Smithsonian Institution Press, Washington, D.C., pp. 11–52.

Negrini, R.M., Erbes, D., Faber, K., Herrera, A., Roberts, A., Cohen, A., Wigand, P.E., Foit, F., 2000. A paleoclimate record for the past 250,000 years from Summer Lake, Oregon, USA. 1. chronology and magnetic proxies for lake level. Journal of Paleolimnology 24(2), 125–149. doi:10.1023/A:1008144025492.

Nelder, J.A., Mead, R., 1965. A Simplex Method for Function Minimization. The Computer Journal 7(4), 308–313. doi:10.1093/comjnl/7.4.308.

Nelson, A.D., Reuter, H.I., Gessler, P., 2009. DEM Production Methods and Sources. In: Hengl, T., Reuter, H.I. (Eds.). Geomorphometry: concepts, software, applications. Developments in Soil Science 33. Elsevier, Amsterdam, Boston, Heidelberg, pp. 65–85. 1st ed.

Nguyen, T.T., Huang, J.Z., Nguyen, T.T., 2015. Unbiased Feature Selection in Learning Random Forests for High-Dimensional Data. The Scientific World Journal 2015, 1–18. doi:10.1155/2015/471371.

Nhu, V.H., Hoang, N.D., Nguyen, H., Ngo, P.T.T., Thanh Bui, T., Hoa, P.V., Samui, P., Tien Bui, D., 2020. Effectiveness assessment of Keras based deep learning with different robust optimization algorithms for shallow landslide susceptibility mapping at tropical area. CATENA 188, 104458. doi:10.1016/j.catena.2020.104458.

Nicholas, A.P., Clarke, L.E., Quine, T.A., 2009. A numerical modelling and experimental study of flow width dynamics on alluvial fans. Earth Surface Processes and Landforms 34(15), 1985–1993. doi:10.1002/esp.1839.

Nichols, G.J., 2005. Tertiary alluvial fans at the northern margin of the Ebro Basin: a review. In: Harvey, A.M., Mather, A.E., Stokes, M. (Eds.). Alluvial Fans: Geomorphology, Sedimentology, Dynamics. Geological Society, London, Special Publications 251. Geological Society of London, London, pp. 187–206. doi:10.1144/GSL.SP.2005.251.01.13.

Nicholson, C., Sorlien, C.C., Atwater, T., Crowell, J.C., Luyendyk, B.P., 1994. Microplate capture, rotation of the western Transverse Ranges, and initiation of the San Andreas transform as a low-angle fault system. Geology 22(6), 491–495. doi:10.1130/0091-7613(1994)022<0491:MCROTW>2.3.CO;2.

Nicholson, S.E., 2011. Dryland Climatology. Cambridge University Press, Cambridge. doi:10.1017/CBO9780511973840.

Nicodemus, K.K., Malley, J.D., 2009. Predictor correlation impacts machine learning algorithms: implications for genomic studies. Bioinformatics 25(15), 1884–1890. doi:10.1093/bioinformatics/btp331.

Nicodemus, K.K., Malley, J.D., Strobl, C., Ziegler, A., 2010. The behaviour of random forest permutation-based variable importance measures under predictor correlation. BMC Bioinformatics 11(1), 110. doi:10.1186/1471-2105-11-110.

Nikolakopoulos, K.G., Kamaratakis, E.K., Chrysoulakis, N., 2006. SRTM vs ASTER elevation

products. Comparison for two regions in Crete, Greece. International Journal of Remote Sensing 27(21), 4819–4838. doi:10.1080/01431160600835853.

Nixon, M.S., Aguado, A.S., 2002. Feature extraction and image processing. Newnes, Oxford, Boston, 1st ed.

Norini, G., Zuluaga, M.C., Ortiz, I.J., Aquino, D.T., Lagmay, A.M.F., 2016. Delineation of alluvial fans from Digital Elevation Models with a GIS algorithm for the geomorphological mapping of the Earth and Mars. Geomorphology 273, 134–149. doi:10.1016/j.geomorph.2016.08.010.

North, C.P., Davidson, S.K., 2012. Unconfined alluvial flow processes: Recognition and interpretation of their deposits, and the significance for palaeogeographic reconstruction. Earth-Science Reviews 111(1–2), 199–223. doi:10.1016/j.earscirev.2011.11.008.

Oguchi, T., Ohmori, H., 1994. Analysis of relationships among alluvial fan area, source basin area, basin slope, and sediment yield. Zeitschrift für Geomorphologie 38(4), 405–420.

Oksanen, J., 2006. Digital Elevation Model Error in Terrain Analysis. Ph.D. thesis, University of Helsinki, Helsinki.

Olaya, V., 2009. Basic Land-Surface Parameters. In: Hengl, T., Reuter, H.I. (Eds.). Geomorphometry. Concepts, Software, Applications. Developments in Soil Science 33. Elsevier, Amsterdam, Boston, Heidelberg, pp. 141–169. doi:10.1016/S0166-2481(08)00006-8.

Oldroyd, D.R., 2013. Geomorphology in the First Half of the Twentieth Century. In: Shroder, J.F. (Ed.). Treatise on Geomorphology. Academic Press, San Diego, pp. 64–85. doi:10.1016/B978-0-12-374739-6.00005-1.

Olshausen, B.A., Field, D.J., 1996. Emergence of simple-cell receptive field properties by learning a sparse code for natural images. Nature 381(6583), 607–609. doi:10.1038/381607a0.

Orme, A.R., 2008. Pleistocene pluvial lakes of the American West: a short history of research. In: Grapes, R.H., Grigelis, A., Oldroyd, D.D. (Eds.). History of geomorphology and Quaternary geology. Geological Society, London, Special Publications 301. Geological Society of London, London, pp. 51–78. doi:10.1144/SP301.4.

Orme, A.R., 2013. The Scientific Roots of Geomorphology before 1830. In: Shroder, J.F. (Ed.). Treatise on Geomorphology. Academic Press, San Diego, pp. 11–36. doi:10.1016/B978-0-12-374739-6.00002-6.

Orme, A.R., Orme, A.J., 2008. Late Pleistocene shorelines of Owens Lake, California, and their hydroclimatic and tectonic implications. In: Reheis, M.C., Hershler, R., Miller, D.M. (Eds.). Late Cenozoic Drainage History of the Southwestern Great Basin and Lower Colorado River Region: Geologic and Biotic Perspectives. Special Paper 439. Geological Society of America, Boulder, pp. 207–225. doi:10.1130/2008.2439(09).

Osborn, G., 2004. Great Basin of the western United States. In: Ehlers, J., Gibbard, P.L. (Eds.). Quaternary glaciations: extent and chronology - Part II: North America. Developments in Quaternary Sciences 2B. Elsevier, Amsterdam, San Diego, pp. 63–67. doi:10.1016/S1571-0866(04)80186-6.

Osborn, G., Bevis, K., 2001. Glaciation in the Great Basin of the Western United States. Quaternary Science Reviews 20(13), 1377–1410. doi:10.1016/S0277-3791(01)00002-6.

Ouellet, M.A., Germain, D., 2014. Hyperconcentrated flows on a forested alluvial fan of eastern Canada: geomorphic characteristics, return period, and triggering scenarios. Earth Surface Processes and Landforms 39(14), 1876–1887. doi:10.1002/esp.3581.

Owen, L.A., Clemmens, S.J., Finkel, R.C., Gray, H.J., 2014. Late Quaternary alluvial fans at the eastern end of the San Bernardino Mountains, Southern California. Quaternary Science Reviews 87, 114–134. doi:10.1016/j.quascirev.2014.01.003.

Owen, L.A., Cunningham, W.D., Richards, B.W.M., Rhodes, E.J., Windley, B.F., Dorjnamjaa, D., Badamgarov, J., 1999a. Timing of formation of forebergs in the northeastern Gobi Altai, Mongolia:

implications for estimating mountain uplift rates and earthquake recurrence intervals. Journal of the Geological Society 156(3), 457–464. doi:10.1144/gsjgs.156.3.0457.

Owen, L.A., Cunningham, W.D., Windley, B.F., Badamgarov, J., Dorjnamjaa, D., 1999b. The landscape evolution of Nemegt Uul: a late Cenozoic transpressional uplift in the Gobi Altai, southern Mongolia. In: Smith, B.J., Whalley, W.B., Warke, P.A. (Eds.). Uplift, erosion and stability: perspectives on long-term landscape development. Geological Society, London, Special Publications 162. Geological Society of London, London, pp. 201–218. doi:10.1144/GSL.SP.1999.162.01.16.

Owen, L.A., Richards, B., Rhodes, E.J., Cunningham, W.D., Windley, B.F., Badamgarov, J., Dorjnamjaa, D., 1998. Relic permafrost structures in the Gobi of Mongolia: age and significance. Journal of Quaternary Science 13(6), 539–547. doi:10.1002/(SICI)1099-1417(1998110)13:6<539::AID-JQS390>3.0.CO;2-N.

Owen, L.A., Windley, B.F., Cunningham, W.D., Badamgarov, J., Dorjnamjaa, D., 1997. Quaternary alluvial fans in the Gobi of southern Mongolia: evidence for neotectonics and climate change. Journal of Quaternary Science 12(3), 239–252. doi:10.1002/(SICI)1099-1417(199705/06)12:3<239::AID-JQS293>3.0.CO;2-P.

Pahlavan Rad, M.R., Toomanian, N., Khormali, F., Brungard, C.W., Komaki, C.B., Bogaert, P., 2014. Updating soil survey maps using random forest and conditioned Latin hypercube sampling in the loess derived soils of northern Iran. Geoderma 232–234, 97–106. doi:10.1016/j.geoderma.2014.04.036.

Pan, S.J., Yang, Q., 2010. A Survey on Transfer Learning. IEEE Transactions on Knowledge and Data Engineering 22(10), 1345–1359. doi:10.1109/TKDE.2009.191.

Panagiotopoulos, F., Shahgedanova, M., Hannachi, A., Stephenson, D.B., 2005. Observed Trends and Teleconnections of the Siberian High: A Recently Declining Center of Action. Journal of Climate 18(9), 1411–1422. doi:10.1175/JCLI3352.1.

Panov, P., Džeroski, S., 2007. Combining Bagging and Random Subspaces to Create Better Ensembles. In: R. Berthold, M., Shawe-Taylor, J., Lavrač, N. (Eds.). Proceedings of IDA 2007: Advances in Intelligent Data Analysis VII, September 6–8, Ljubljana. Springer, Berlin, Heidelberg, pp. 118–129.

Paola, C., Heller, P.L., Angevine, C.L., 1992a. The large-scale dynamics of grain-size variation in alluvial basins, 1: Theory. Basin Research 4(2), 73–90. doi:10.1111/j.1365-2117.1992.tb00145.x.

Paola, C., Parker, G., Seal, R., Sinha, S.K., Southard, J.B., Wilcock, P.R., 1992b. Downstream Fining by Selective Deposition in a Laboratory Flume. Science 258(5089), 1757–1760. doi:10.1126/science.258.5089.1757.

Paola, J.D., Schowengerdt, R.A., 1995. A review and analysis of backpropagation neural networks for classification of remotely-sensed multi-spectral imagery. International Journal of Remote Sensing 16(16), 3033–3058. doi:10.1080/01431169508954607.

Parker, G., Paola, C., Whipple, K., Mohrig, D., 1998. Alluvial Fans Formed by Channelized Fluvial and Sheet Flow. I: Theory. Journal of Hydraulic Engineering 124(10), 985–995. doi:10.1061/(ASCE)0733-9429(1998)124:10(985).

Parsons, A.J., Abrahams, A.D., Howard, A.D., 2009. Rock-Mantled Slopes. In: Parsons, A.J., Abrahams, A.D. (Eds.). Geomorphology of Desert Environments. Springer, Dordrecht, pp. 233–263. doi:10.1007/978-1-4020-5719-9_9.

Parzen, E., 1962. On Estimation of a Probability Density Function and Mode. The Annals of Mathematical Statistics 33(3), 1065–1076. doi:10.1214/aoms/1177704472.

Peck, J.A., Khosbayar, P., Fowell, S.J., Pearce, R.B., Ariunbileg, S., Hansen, B.C.S., Soninkhishig, N., 2002. Mid to Late Holocene climate change in north central Mongolia as recorded in the sediments of Lake Telmen. Palaeogeography, Palaeoclimatology, Palaeoecology 183(1–2), 135–153. doi:10.1016/S0031-0182(01)00465-5.

Pedersen, G.B.M., 2016. Semi-automatic classification of glaciovolcanic landforms: An object-based

mapping approach based on geomorphometry. Journal of Volcanology and Geothermal Research 311, 29–40. doi:10.1016/j.jvolgeores.2015.12.015.

Pedregosa, F., Varoquaux, G., Gramfort, A., Michel, V., Thirion, B., Grisel, O., Blondel, M., Prettenhofer, P., Weiss, R., Dubourg, V., VanderPlas, J.T., Passos, A., Cournapeau, D., Brucher, M., Perrot, M., Duchesnay, E., 2011. Scikit-learn: Machine Learning in Python. Journal of Machine Learning Research 12, 2825–2830.

Peinado, M., Macías, M.Á., Delgadillo, J., Aguirre, J.L., 2006. Major plant communities of North America's most arid region: The San Felipe Desert, Baja California, México. Plant Biosystems 140(3), 280–296. doi:10.1080/11263500600947715.

Pelletier, J.D., 2014. The linkages among hillslope-vegetation changes, elevation, and the timing of late-Quaternary fluvial-system aggradation in the Mojave Desert revisited. Earth Surface Dynamics 2(2), 455–468. doi:10.5194/esurf-2-455-2014.

Penck, W., 1924. Die morphologische Analyse: Ein Kapitel der physikalischen Geologie. J. Engelhorns Nachfolger, Stuttgart.

Peng, B., Bao, H., Pu, L., 2000. Ch. 13. Geo-Ecology of Mts. Namjagbarwa Region. In: Zheng, D., Zhang, Q., Wu, Q. (Eds.). Mountain geoecology and sustainable development of the Tibetan Plateau. The GeoJournal library 57. Kluwer Academic Publishers, Dordrecht, Boston, pp. 265–282.

Petit, F., Gob, F., Houbrechts, G., Assani, A.A., 2005. Critical specific stream power in gravel-bed rivers. Geomorphology 69(1–4), 92–101. doi:10.1016/j.geomorph.2004.12.004.

Pierce, K.L., 2003. Pleistocene glaciations of the Rocky Mountains. In: Gillespie, A.R., Porter, S.C., Atwater, B.F. (Eds.). The Quaternary period in the United States. Developments in Quaternary Sciences 1. Elsevier, Amsterdam, New York, pp. 63–76. doi:10.1016/S1571-0866(03)01004-2.

Pierce, K.L., Scott, W., 1982. Pleistocene Episodes of Alluvial-Gravel Deposition, Southeastern Idaho. In: Bonnichsen, B., Breckenridge, R.M. (Eds.). Cenozoic Geology of Idaho. Bulletin B-26. Idaho Department of Lands, Bureau of Mines and Geology, Moscow, Idaho, pp. 685–702.

Pierson, F.B., Bates, J.D., Svejcar, T.J., Hardegree, S.P., 2007. Runoff and Erosion After Cutting Western Juniper. Rangeland Ecology and Management 60(3), 285–292. doi:10.2111/1551-5028(2007)60[285:RAEACW]2.0.CO;2.

Pierson, T.C., 2005. Hyperconcentrated flow — transitional process between water flow and debris flow. In: Jakob, M., Hungr, O. (Eds.). Debris-flow Hazards and Related Phenomena. Springer, Berlin, Heidelberg, pp. 159–202. doi:10.1007/3-540-27129-5_8.

Pike, R.J., 1988. The geometric signature: Quantifying landslide-terrain types from digital elevation models. Mathematical Geology 20(5), 491–511. doi:10.1007/BF00890333.

Pike, R.J., 1995. Geomorphometry – Progress, practice, and prospect. Zeitschrift für Geomorphologie, Supplementband 101, 221–238.

Pike, R.J., 2000. Geomorphometry - diversity in quantitative surface analysis. Progress in Physical Geography: Earth and Environment 24(1), 1–20. doi:10.1177/030913330002400101.

Pike, R.J., Evans, I.S., Hengl, T., 2009. Geomorphometry: A Brief Guide. In: Hengl, T., Reuter, H.I. (Eds.). Geomorphometry. Developments in Soil Science 33. Elsevier, Amsterdam, Boston, Heidelberg, pp. 3–30. 1st ed. doi:10.1016/S0166-2481(08)00001-9.

Pipaud, I., Lehmkuhl, F., 2017. Object-based delineation and classification of alluvial fans by application of mean-shift segmentation and support vector machines. Geomorphology 293A, 178–200. doi:10.1016/j.geomorph.2017.05.013.

Pipaud, I., Loibl, D., Lehmkuhl, F., 2015. Evaluation of TanDEM-X elevation data for geomorphological mapping and interpretation in high mountain environments — A case study from SE Tibet, China. Geomorphology 246, 232–254. doi:10.1016/j.geomorph.2015.06.025.

Plattner, C., Malservisi, R., Govers, R., 2009. On the plate boundary forces that drive and resist Baja California motion. Geology 37(4), 359–362. doi:10.1130/G25360A.1.

Pohjola, J., Turunen, J., Lipping, T., Ikonen, A.T.K., 2014. Landscape development modeling based on statistical framework. Computers & Geosciences 62, 43–52. doi:10.1016/j.cageo.2013.09.013.

Pope, G.A., Dorn, R.I., Dixon, J.C., 1995. A New Conceptual Model for Understanding Geographical Variations in Weathering. Annals of the Association of American Geographers 85(1), 38–64. doi:10.1111/j.1467-8306.1995.tb01794.x.

Pope, R.J.J., Wilkinson, K.N., 2005. Reconciling the roles of climate and tectonics in Late Quaternary fan development on the Spartan piedmont, Greece. In: Harvey, A.M., Mather, A.E., Stokes, M. (Eds.). Alluvial Fans: Geomorphology, Sedimentology, Dynamics. Geological Society, London, Special Publications 251. Geological Society of London, London, pp. 133–152. doi:10.1144/GSL.SP.2005.251.01.10.

Portenga, E.W., Bierman, P.R., 2011. Understanding Earth's eroding surface with ^{10}Be. GSA Today 21(8), 4–10. doi:10.1130/G111A.1.

Powell, E.J., Kim, W., Muto, T., 2012. Varying discharge controls on timescales of autogenic storage and release processes in fluvio-deltaic environments: Tank experiments. Journal of Geophysical Research: Earth Surface 117(F2), F02011. doi:10.1029/2011JF002097.

Powell, R.E., Weldon, R.J., 1992. Evolution of the San Andreas Fault. Annual Review of Earth and Planetary Sciences 20(1), 431–468. doi:10.1146/annurev.ea.20.050192.002243.

Pratt, W.K., 2001. Digital image processing: PIKS inside. Wiley, New York, 3rd ed.

Purinton, B., Bookhagen, B., 2017. Validation of digital elevation models (DEMs) and comparison of geomorphic metrics on the southern Central Andean Plateau. Earth Surface Dynamics 5(2), 211–237. doi:10.5194/esurf-5-211-2017.

Péwé, T.L., 1983. The Periglacial Environment in North America during Wisconsin Time. In: Wright, H.E., Porter, S.C. (Eds.). Late-Quaternary environments of the United States. University of Minnesota Press, Minneapolis, pp. 157–189.

Pyankov, V.I., Gunin, P.D., Tsoog, S., Black, C.C., 2000. C_4 plants in the vegetation of Mongolia: their natural occurrence and geographical distribution in relation to climate. Oecologia 123(1), 15–31. doi:10.1007/s004420050985.

Pye, K., 1995. The nature, origin and accumulation of loess. Quaternary Science Reviews 14(7–8), 653–667. doi:10.1016/0277-3791(95)00047-X.

Pye, K., Goudie, A.S., Watson, A., 1986. Petrological influence on differential weathering and inselberg development in the Kora area of central Kenya. Earth Surface Processes and Landforms 11(1), 41–52. doi:10.1002/esp.3290110106.

Quigley, M.C., Sandiford, M., Cupper, M.L., 2007. Distinguishing tectonic from climatic controls on range-front sedimentation. Basin Research 19(4), 491–505. doi:10.1111/j.1365-2117.2007.00336.x.

Quinlan, J.R., 1986. Induction of decision trees. Machine Learning 1(1), 81–106. doi:10.1007/BF00116251.

Rabus, B., Eineder, M., Roth, A., Bamler, R., 2003. The shuttle radar topography mission - a new class of digital elevation models acquired by spaceborne radar. ISPRS Journal of Photogrammetry and Remote Sensing 57(4), 241–262. doi:10.1016/S0924-2716(02)00124-7.

Racine, J.S., 2008. Nonparametric econometrics: a primer. Foundations and Trends in Econometrics 3(1). doi:10.1561/0800000009.

Rahmati, O., Tahmasebipour, N., Haghizadeh, A., Pourghasemi, H.R., Feizizadeh, B., 2017a. Evaluating the influence of geo-environmental factors on gully erosion in a semi-arid region of Iran: An integrated framework. Science of The Total Environment 579, 913–927. doi:10.1016/j.scitotenv.2016.10.176.

Rahmati, O., Tahmasebipour, N., Haghizadeh, A., Pourghasemi, H.R., Feizizadeh, B., 2017b. Evaluation of different machine learning models for predicting and mapping the susceptibility of gully erosion. Geomorphology 298, 118–137. doi:10.1016/j.geomorph.2017.09.006.

Rasemann, S., Schmidt, J., Schrott, L., Dikau, R., 2004. Geomorphometry in mountain terrain. In: Bishop, M.P., Shroder, J.F. (Eds.). GIS & Mountain Geomorphology. Springer, Berlin, New York, pp. 101–145.

Regmi, N.R., McDonald, E.V., Bacon, S.N., 2014. Mapping Quaternary alluvial fans in the southwestern United States based on multiparameter surface roughness of lidar topographic data. Journal of Geophysical Research: Earth Surface 119(1), 12–27. doi:10.1002/2012JF002711.

Reheis, M.C., 1987. Soils in granitic alluvium in humid and semiarid climates along Rock Creek, Carbon County, Montana. U.S. Geological Survey Bulletin 1590D, United States Government Publishing Office, Washington, D.C. doi:10.3133/b1590D.

Reheis, M.C., Adams, K.D., Oviatt, C.G., Bacon, S.N., 2014. Pluvial lakes in the Great Basin of the western United States—a view from the outcrop. Quaternary Science Reviews 97, 33–57. doi:10.1016/j.quascirev.2014.04.012.

Reheis, M.C., Slate, J.L., Throckmorton, C.K., McGeehin, J.P., Sarna-Wojcicki, A.M., Dengler, L., 1996. Late Quaternary sedimentation on the Leidy Creek fan, Nevada-California: geomorphic responses to climate change. Basin Research 8(3), 279–299. doi:10.1046/j.1365-2117.1996.00205.x.

Reid, K.D., Wilcox, B.P., Breshears, D.D., MacDonald, L., 1999. Runoff and Erosion in a Piñon–Juniper Woodland. Soil Science Society of America Journal 63(6), 1869–1879. doi:10.2136/sssaj1999.6361869x.

Reitz, M.D., Jerolmack, D.J., 2012. Experimental alluvial fan evolution: Channel dynamics, slope controls, and shoreline growth. Journal of Geophysical Research: Earth Surface 117(F2), 1–19. doi:10.1029/2011JF002261.

Reitz, M.D., Jerolmack, D.J., Swenson, J.B., 2010. Flooding and flow path selection on alluvial fans and deltas. Geophysical Research Letters 37(6), L06401. doi:10.1029/2009GL041985.

Ren, S., He, K., Girshick, R.B., Sun, J., 2017. Faster R-CNN: Towards Real-Time Object Detection with Region Proposal Networks. IEEE Transactions on Pattern Analysis and Machine Intelligence 39(6), 1137–1149. doi:10.1109/TPAMI.2016.2577031.

Reuter, H.I., Hengl, T., Gessler, P.E., Soille, P., 2009. Preparation of DEMs for Geomorphometric Analysis. In: Hengl, T., Reuter, H.I. (Eds.). Geomorphometry: concepts, software, applications. Developments in Soil Science 33. Elsevier, Amsterdam, Boston, Heidelberg, pp. 87–120. doi:10.1016/S0166-2481(08)00004-4.

Reuter, H.I., Nelson, A.D., Jarvis, A., 2007. An evaluation of void-filling interpolation methods for SRTM data. International Journal of Geographical Information Science 21(9), 983–1008. doi:10.1080/13658810601169899.

Richards, J.A., 2009. Remote sensing with imaging radar. Springer, Heidelberg, Dordrecht, London.

Rickenmann, D., 2005. Runout prediction methods. In: Jakob, M., Hungr, O. (Eds.). Debris-flow Hazards and Related Phenomena. Springer, Berlin, Heidelberg, pp. 305–324. doi:10.1007/3-540-27129-5_13.

Rickenmann, D., Scheidl, C., 2013. Debris-Flow Runout and Deposition on the Fan. In: Schneuwly-Bollschweiler, M., Stoffel, M., Rudolf-Miklau, F. (Eds.). Dating Torrential Processes on Fans and Cones. Advances in Global Change Research 47. Springer, Dordrecht, pp. 75–93. doi:10.1007/978-94-007-4336-6_5.

Riebe, C.S., Kirchner, J.W., Finkel, R.C., 2004. Sharp decrease in long-term chemical weathering rates along an altitudinal transect. Earth and Planetary Science Letters 218(3–4), 421–434. doi:10.1016/S0012-821X(03)00673-3.

Riebe, C.S., Sklar, L.S., Lukens, C.E., Shuster, D.L., 2015. Climate and topography control the size and flux of sediment produced on steep mountain slopes. Proceedings of the National Academy of Sciences 112(51), 15574–15579. doi:10.1073/pnas.1503567112.

Ritter, J.B., Miller, J.R., Enzel, Y., Wells, S.G., 1995. Reconciling the roles of tectonism and climate in Quaternary alluvial fan evolution. Geology 23(3), 245. doi:10.1130/0091-7613(1995)023<0245:RTROTA>2.3.CO;2.

Ritter, J.B., Miller, J.R., Husek-Wulforst, J., 2000. Environmental controls on the evolution of alluvial fans in Buena Vista Valley, North Central Nevada, during late Quaternary time. Geomorphology 36(1–2), 63–87. doi:10.1016/S0169-555X(00)00048-9.

Ritz, J.F., Bourlès, D., Brown, E.T., Carretier, S., Chéry, J., Enhtuvshin, B., Galsan, P., Finkel, R.C., Hanks, T.C., Kendrick, K.J., Philip, H., Raisbeck, G., Schlupp, A., Schwartz, D.P., Yiou, F., 2003. Late Pleistocene to Holocene slip rates for the Gurvan Bulag thrust fault (Gobi-Altay, Mongolia) estimated with ^{10}Be dates. Journal of Geophysical Research: Solid Earth 108(B3), 8–1–8–16. doi:10.1029/2001JB000553.

Ritz, J.F., Brown, E.T., Bourlès, D.L., Philip, H., Schlupp, A., Raisbeck, G.M., Yiou, F., Enkhtuvshin, B., 1995. Slip rates along active faults estimated with cosmic-ray–exposure dates: Application to the Bogd fault, Gobi-Altaï, Mongolia. Geology 23(11), 1019–1022. doi:10.1130/0091-7613(1995)023<1019:SRAAFE>2.3.CO;2.

Ritz, J.F., Vassallo, R., Braucher, R., Brown, E.T., Carretier, S., Bourlès, D.L., 2006. Using in situ–produced ^{10}Be to quantify active tectonics in the Gurvan Bogd mountain range (Gobi-Altay, Mongolia). In: Alonso-Zarza, A.M., Tanner, L.H. (Eds.). In Situ-Produced Cosmogenic Nuclides and Quantification of Geological Processes. Special Paper 415. Geological Society of America, pp. 87–110. doi:10.1130/2006.2415(06).

Rizzoli, P., Martone, M., Gonzalez, C., Wecklich, C., Borla Tridon, D., Bräutigam, B., Bachmann, M., Schulze, D., Fritz, T., Huber, M., Wessel, B., Krieger, G., Zink, M., Moreira, A., 2017. Generation and performance assessment of the global TanDEM-X digital elevation model. ISPRS Journal of Photogrammetry and Remote Sensing 132, 119–139. doi:10.1016/j.isprsjprs.2017.08.008.

Roberts, N., Cunningham, W.D., 2008. Automated alluvial fan discrimination, Quaternary fault identification, and the distribution of tectonically reactivated crust in the Gobi Altai region, southern Mongolia. International Journal of Remote Sensing 29(23), 6957–6969. doi:10.1080/01431160802220227.

Robinson, G.J., 1994. The Accuracy of Digital Elevation Models Derived from Digitised Contour Data. The Photogrammetric Record 14(83), 805–814. doi:10.1111/j.1477-9730.1994.tb00793.x.

Robinson, R.A.J., Spencer, J.Q.G., Strecker, M.R., Richter, A., Alonso, R.N., 2005. Luminescence dating of alluvial fans in intramontane basins of NW Argentina. In: Harvey, A.M., Mather, A.E., Stokes, M. (Eds.). Alluvial Fans: Geomorphology, Sedimentology, Dynamics. Geological Society, London, Special Publications 251. Geological Society of London, London, pp. 153–168. doi:10.1144/GSL.SP.2005.251.01.11.

Robson, B.A., Bolch, T., MacDonell, S., Hölbling, D., Rastner, P., Schaffer, N., 2020. Automated detection of rock glaciers using deep learning and object-based image analysis. Remote Sensing of Environment 250, 112033. doi:10.1016/j.rse.2020.112033.

Roda-Boluda, D.C., D'Arcy, M., McDonald, J., Whittaker, A.C., 2018. Lithological controls on hillslope sediment supply: insights from landslide activity and grain size distributions: Lithological controls on hillslope sediment supply. Earth Surface Processes and Landforms 43(5), 956–977. doi:10.1002/esp.4281.

Rodríguez, E., Morris, C.S., Belz, J.E., 2006. A Global Assessment of the SRTM Performance. Photogrammetric Engineering & Remote Sensing 72(3), 249–260.

Rodriguez, F., Maire, E., Courjault-Radé, P., Darrozes, J., 2002. The Black Top Hat function applied to

a DEM: A tool to estimate recent incision in a mountainous watershed (Estibère Watershed, Central Pyrenees). Geophysical Research Letters 29(6), 1–4. doi:10.1029/2001GL014412.

Rodriguez-Galiano, V.F., Ghimire, B., Rogan, J., Chica-Olmo, M., Rigol-Sanchez, J.P., 2012. An assessment of the effectiveness of a random forest classifier for land-cover classification. ISPRS Journal of Photogrammetry and Remote Sensing 67, 93–104. doi:10.1016/j.isprsjprs.2011.11.002.

Roehl, E.J., 1962. Sediment source areas, delivery ratios and influencing morphological factors. In: Proceedings of the IAHS Symposium 59, October 1–8, Bari. IAHS, Bari, pp. 202–213.

Rohais, S., Bonnet, S., Eschard, R., 2012. Sedimentary record of tectonic and climatic erosional perturbations in an experimental coupled catchment-fan system. Basin Research 24(2), 198–212. doi:10.1111/j.1365-2117.2011.00520.x.

Romstad, B., Etzelmüller, B., 2012. Mean-curvature watersheds: A simple method for segmentation of a digital elevation model into terrain units. Geomorphology 139–140, 293–302. doi:10.1016/j.geomorph.2011.10.031.

Ronneberger, O., Fischer, P., Brox, T., 2015. U-Net: Convolutional Networks for Biomedical Image Segmentation. In: Proceedings of the 18th International Conference on Medical Image Computing and Computer-Assisted Intervention, October 5–9, Munich. Springer, Cham, vol. 9351, pp. 234–241. doi:10.1007/978-3-319-24574-4_28.

Rosenblatt, M., 1956. Remarks on Some Nonparametric Estimates of a Density Function. The Annals of Mathematical Statistics 27(3), 832–837. doi:10.1214/aoms/1177728190.

Rossi, C., Rodriguez Gonzalez, F., Fritz, T., Yague-Martinez, N., Eineder, M., 2012. TanDEM-X calibrated Raw DEM generation. ISPRS Journal of Photogrammetry and Remote Sensing 73, 12–20. doi:10.1016/j.isprsjprs.2012.05.014.

Rott, H., 2009. Advances in interferometric synthetic aperture radar (InSAR) in earth system science. Progress in Physical Geography 33(6), 769–791. doi:10.1177/0309133309350263.

Rousseeuw, P.J., 1987. Silhouettes: A graphical aid to the interpretation and validation of cluster analysis. Journal of Computational and Applied Mathematics 20, 53–65. doi:10.1016/0377-0427(87)90125-7.

Rousseeuw, P.J., Leroy, A.M., 1987. Robust Regression and Outlier Detection. Wiley Series in Probability and Statistics. Wiley, Hoboken. doi:10.1002/0471725382.

Roy, P.D., Caballero, M., Lozano, S., Morton, O., Lozano, R., Jonathan, M.P., Sánchez, J.L., Macías, M.C., 2012. Provenance of sediments deposited at paleolake San Felipe, western Sonora Desert: Implications to regimes of summer and winter precipitation during last 50 cal kyr BP. Journal of Arid Environments 81, 47–58. doi:10.1016/j.jaridenv.2012.01.008.

Roy, P.D., Quiroz-Jiménez, J.D., Chávez-Lara, C.M., Sánchez-Zavala, J.L., Pérez-Cruz, L.L., Sankar, G.M., 2014. Humid Pleistocene–Holocene transition and early Holocene in sub-tropical northern Mexico and possible Gulf of California forcing: Pleistocene–Holocene transition and early Holocene, N Mexico. Boreas 43(3), 577–587. doi:10.1111/bor.12062.

Rudemo, M., 1982. Empirical Choice of Histograms and Kernel Density Estimators. Scandinavian Journal of Statistics 9(2), 65–78.

Rumelhart, D.E., Hinton, G.E., Williams, R.J., 1986. Learning representations by back-propagating errors. Nature 323(6088), 533–536. doi:10.1038/323533a0.

Rush, F.E., Katzer, T., 1973. Water-resources appraisal of Fish Lake Valley, Nevada and California. Water resources–reconnaissance series report 58. State of Nevada, Division of Water Resources, Carson City.

Russakovsky, O., Deng, J., Su, H., Krause, J., Satheesh, S., Ma, S., Huang, Z., Karpathy, A., Khosla, A., Bernstein, M., Berg, A.C., Fei-Fei, L., 2015. ImageNet Large Scale Visual Recognition Challenge. International Journal of Computer Vision 115(3), 211–252. doi:10.1007/s11263-015-0816-y.

Ruszkiczay-Rüdiger, Z., Fodor, L., Horváth, E., Telbisz, T., 2009. Discrimination of fluvial, eolian and neotectonic features in a low hilly landscape: A DEM-based morphotectonic analysis in the Central Pannonian Basin, Hungary. Geomorphology 104(3–4), 203–217. doi:10.1016/j.geomorph.2008.08.014.

Ryder, J.M., 1971. Some Aspects of the Morphometry of Paraglacial Alluvial Fans in South-central British Columbia. Canadian Journal of Earth Sciences 8(10), 1252–1264. doi:10.1139/e71-114.

Sack, D., 2013. Geomorphology and Nineteenth-Century Explorations of the American West. In: Shroder, J.F. (Ed.). Treatise on Geomorphology. Academic Press, San Diego, pp. 53–63. doi:10.1016/B978-0-12-374739-6.00004-X.

Saha, K., Wells, N.A., Munro-Stasiuk, M., 2011. An object-oriented approach to automated landform mapping: A case study of drumlins. Computers & Geosciences 37(9), 1324–1336. doi:10.1016/j.cageo.2011.04.001.

Saito, K., Oguchi, T., 2005. Slope of alluvial fans in humid regions of Japan, Taiwan and the Philippines. Geomorphology 70(1–2), 147–162. doi:10.1016/j.geomorph.2005.04.006.

Salcher, B.C., Faber, R., Wagreich, M., 2010. Climate as main factor controlling the sequence development of two Pleistocene alluvial fans in the Vienna Basin (eastern Austria) — A numerical modelling approach. Geomorphology 115(3–4), 215–227. doi:10.1016/j.geomorph.2009.06.030.

Sameen, M.I., Pradhan, B., 2019. Landslide Detection Using Residual Networks and the Fusion of Spectral and Topographic Information. IEEE Access 7, 114363–114373. doi:10.1109/ACCESS.2019.2935761.

Santillan, J.R., Makinano-Santillan, M., 2016. Vertical Accuracy Assessment of 30-m Resolution ALOS, ASTER, and SRTM Global DEMs Over Northeastern Mindanao, Philippines. ISPRS - International Archives of the Photogrammetry, Remote Sensing and Spatial Information Sciences XLI-B4, 149–156. doi:10.5194/isprsarchives-XLI-B4-149-2016.

Sappington, J.M., Longshore, K.M., Thompson, D.B., 2007. Quantifying Landscape Ruggedness for Animal Habitat Analysis: A Case Study Using Bighorn Sheep in the Mojave Desert. Journal of Wildlife Management 71(5), 1419–1426. doi:10.2193/2005-723.

Sato, T., Tsujimura, M., Yamanaka, T., Iwasaki, H., Sugimoto, A., Sugita, M., Kimura, F., Davaa, G., Oyunbaatar, D., 2007. Water sources in semiarid northeast Asia as revealed by field observations and isotope transport model. Journal of Geophysical Research 112(D17), D17112. doi:10.1029/2006JD008321.

Sattler, K., 2016. Periglacial Preconditioning of Debris Flows in the Southern Alps, New Zealand. Springer Theses. Springer, Cham. doi:10.1007/978-3-319-35074-5.

Scarpone, C., Schmidt, M.G., Bulmer, C.E., Knudby, A., 2017. Semi-automated classification of exposed bedrock cover in British Columbia's Southern Mountains using a Random Forest approach. Geomorphology 285, 214–224. doi:10.1016/j.geomorph.2017.02.013.

Scheidl, C., Rickenmann, D., 2010. Empirical prediction of debris-flow mobility and deposition on fans. Earth Surface Processes and Landforms 35(2), 157–173. doi:10.1002/esp.1897.

Schellart, W.P., Stegman, D.R., Farrington, R.J., Freeman, J., Moresi, L., 2010. Cenozoic Tectonics of Western North America Controlled by Evolving Width of Farallon Slab. Science 329(5989), 316–319. doi:10.1126/science.1190366.

Schickhoff, U., 2005. The Upper Timberline in the Himalayas, Hindu Kush and Karakorum: a Review of Geographical and Ecological Aspects. In: Broll, G., Keplin, B. (Eds.). Mountain ecosystems: studies in treeline ecology. Springer, Berlin, Heidelberg, New York, pp. 275–354.

Schölkopf, B., Platt, J.C., Shawe-Taylor, J., Smola, A.J., Williamson, R.C., 2001. Estimating the Support of a High-Dimensional Distribution. Neural Computation 13(7), 1443–1471. doi:10.1162/089976601750264965.

Schlummer, M., Hoffmann, T., Dikau, R., Eickmeier, M., Fischer, P., Gerlach, R., Holzkämper, J., Kalis, A.J., Kretschmer, I., Lauer, F., Maier, A., Meesenburg, J., Meurers-Balke, J., Münch, U., Pätzold, S., Steininger, F., Stobbe, A., Zimmermann, A., 2014. From point to area: Upscaling approaches for Late Quaternary archaeological and environmental data. Earth-Science Reviews 131, 22–48. doi:10.1016/j.earscirev.2014.01.004.

Schmidhuber, J., 2015. Deep learning in neural networks: An overview. Neural Networks 61, 85–117. doi:10.1016/j.neunet.2014.09.003.

Schmidt, J., Andrew, R., 2005. Multi-scale landform characterization. Area 37(3), 341–350. doi: 10.1111/j.1475-4762.2005.00638.x.

Schmidt, J., Dikau, R., 1999. Extracting geomorphometric attributes and objects from digital elevation models – Semantics, methods, future needs. In: Dikau, R., Saurer, H. (Eds.). GIS for Earth Surface Systems – Analysis and Modelling of the Natural Environment. Borntraeger, Berlin, Stuttgart, pp. 153–173.

Schmidt, J., Evans, I.S., Brinkmann, J., 2003. Comparison of polynomial models for land surface curvature calculation. International Journal of Geographical Information Science 17(8), 797–814. doi:10.1080/13658810310001596058.

Schmidt, J., Hewitt, A., 2004. Fuzzy land element classification from DTMs based on geometry and terrain position. Geoderma 121(3–4), 243–256. doi:10.1016/j.geoderma.2003.10.008.

Schneevoigt, N.J., van der Linden, S., Thamm, H.P., Schrott, L., 2008. Detecting Alpine landforms from remotely sensed imagery. A pilot study in the Bavarian Alps. Geomorphology 93(1–2), 104–119. doi:10.1016/j.geomorph.2006.12.034.

Schneider, U., Becker, A., Finger, P., Meyer-Christoffer, A., Rudolf, B., Ziese, M., 2015. GPCC Full Data Reanalysis Version 7.0 at 0.5°: Monthly Land-Surface Precipitation from Rain-Gauges built on GTS-based and Historic Data: Gridded Monthly Totals. doi:10.5676/dwd_gpcc/fd_m_v7_050. https://opendata.dwd.de/climate_environment/GPCC/html/fulldata_v7_doi_download.html. Last accessed on September 9, 2019.

Schubert, E., Zimek, A., Kriegel, H.P., 2014. Local outlier detection reconsidered: a generalized view on locality with applications to spatial, video, and network outlier detection. Data Mining and Knowledge Discovery 28(1), 190–237. doi:10.1007/s10618-012-0300-z.

Schumm, S.A., 1977. The fluvial system. Wiley, New York.

Schumm, S.A., Lichty, R.W., 1965. Time, space, and causality in geomorphology. American Journal of Science 263(2), 110–119. doi:10.2475/ajs.263.2.110.

Schumm, S.A., Mosley, M.P., Weaver, W.E., 1987. Experimental Fluvial Geomorphology. Wiley, New York.

Schwäbisch, M., 1995. Die SAR-Interferometrie zur Erzeugung digitaler Geländemodelle. DLR-Mitteilungen 95-25. Deutsches Zentrum für Luft- und Raumfahrt, Oberpfaffenhofen.

Schwäbisch, M., 1998. A fast and efficient technique for SAR interferogram geocoding. In: Proceedings of the IEEE International Geoscience and Remote Sensing Symposium, July 6–10, Seattle. IEEE, New York, pp. 1100–1102. doi:10.1109/IGARSS.1998.699685.

Scott, D.W. (Ed.), 1992. Multivariate Density Estimation. Wiley Series in Probability and Statistics. Wiley, Hoboken. doi:10.1002/9780470316849.

Scott, K.M., Vallance, J.W., Pringle, P.T., 1995. Sedimentology, Behavior, and Hazards of Debris Flows at Mount Rainier, Washington. Professional Paper 1547, USGS. doi:10.3133/pp1547.

Seager, W.R., 1981. Geology of Organ Mountains and southern San Andres mountains, New Mexico. Memoirs 36. New Mexico Bureau of Mines & Mineral Resources, Socorro.

Sefercik, U.G., Büyüksalih, G., Atalay, C., Jacobsen, K., 2018. Validation of Sentinel-1A and AW3D30

DSMs for the Metropolitan Area of Istanbul, Turkey. PFG – Journal of Photogrammetry, Remote Sensing and Geoinformation Science 86(3–4), 141–155. doi:10.1007/s41064-018-0054-3.

Seif, A., Mokarram, M., Sathyamoorthy, D., 2014. Using Self-Organizing Maps for Alluvial Fan Classification. International Journal of Scientific Research in Knowledge 2(4), 189–198. doi: 10.12983/ijsrk-2014-p0189-0198.

Seiler, C., Fletcher, J.M., Quigley, M.C., Gleadow, A.J.W., Kohn, B.P., 2010. Neogene structural evolution of the Sierra San Felipe, Baja California: Evidence for proto-gulf transtension in the Gulf Extensional Province? Tectonophysics 488(1–4), 87–109. doi:10.1016/j.tecto.2009.09.026.

Selby, M.J., 1980. Rock mass strength classification for geomorphic purposes: with tests from Antarctica and New Zealand. Zeitschrift fur Geomorphologie, N. F. 24, 31–51.

Selby, M.J., 1982. Controls on the stability and inclinations of hillslopes formed on hard rock. Earth Surface Processes and Landforms 7(5), 449–467. doi:10.1002/esp.3290070506.

Şengör, A.M.C., Natal'in, B.A., Burtman, V.S., 1993. Evolution of the Altaid tectonic collage and Palaeozoic crustal growth in Eurasia. Nature 364(6435), 299–307. doi:10.1038/364299a0.

Serra, J., 1986. Introduction to Mathematical Morphology. Computer Vision, Graphics, and Image Processing 35, 283–305.

Seward, D., Burg, J.P., 2008. Growth of the Namche Barwa Syntaxis and associated evolution of the Tsangpo Gorge: Constraints from structural and thermochronological data. Tectonophysics 451(1–4), 282–289. doi:10.1016/j.tecto.2007.11.057.

Shafique, M., van der Meijde, M., Kerle, N., van der Meer, F., 2011. Impact of DEM source and resolution on topographic seismic amplification. International Journal of Applied Earth Observation and Geoinformation 13(3), 420–427. doi:10.1016/j.jag.2010.09.005.

Shary, P.A., 1995. Land surface in gravity points classification by a complete system of curvatures. Mathematical Geology 27(3), 373–390. doi:10.1007/BF02084608.

Shary, P.A., Sharaya, L.S., Mitusov, A.V., 2002. Fundamental quantitative methods of land surface analysis. Geoderma 107(1–2), 1–32. doi:10.1016/S0016-7061(01)00136-7.

Shary, P.A., Sharaya, L.S., Mitusov, A.V., 2005. The problem of scale-specific and scale-free approaches in geomorphometry. Geografia Fisica e Dinamica Quaternaria 28(1), 81–101.

Sheather, S.J., 1992. The performance of six popular bandwidth selection methods on some real data sets (with discussion). Computational Statistics 7, 225–250.

Shelhamer, E., Long, J., Darrell, T., 2017. Fully Convolutional Networks for Semantic Segmentation. IEEE Transactions on Pattern Analysis and Machine Intelligence 39(4), 640–651. doi:10.1109/TP AMI.2016.2572683.

Sheppard, P., Comrie, A.C., Packin, G., Angersbach, K., Hughes, M., 2002. The climate of the US Southwest. Climate Research 21, 219–238. doi:10.3354/cr021219.

Shi, X., Girod, L., Long, R., DeKett, R., Philippe, J., Burke, T., 2012. A comparison of LiDAR-based DEMs and USGS-sourced DEMs in terrain analysis for knowledge-based digital soil mapping. Geoderma 170, 217–226. doi:10.1016/j.geoderma.2011.11.020.

Shields, A., 1936. Anwendung der Ähnlichkeitsmechanik und der Turbulenzforschung auf die Geschiebebewegung. Mitteilungen der Preußischen Versuchsanstalt für Wasserbau und Schiffbau 26. Preußische Versuchsanstalt für Wasserbau und Schiffbau, Berlin.

Shimada, M., Tadono, T., Rosenqvist, A., 2010. Advanced Land Observing Satellite (ALOS) and Monitoring Global Environmental Change. Proceedings of the IEEE 98(5), 780–799. doi:10.1109/ JPROC.2009.2033724.

Shin, H.C., Roth, H.R., Gao, M., Lu, L., Xu, Z., Nogues, I., Yao, J., Mollura, D., Summers, R.M., 2016. Deep Convolutional Neural Networks for Computer-Aided Detection: CNN Architectures, Dataset

Characteristics and Transfer Learning. IEEE Transactions on Medical Imaging 35(5), 1285–1298. doi:10.1109/TMI.2016.2528162.

Shortridge, A., Messina, J., 2011. Spatial structure and landscape associations of SRTM error. Remote Sensing of Environment 115(6), 1576–1587. doi:10.1016/j.rse.2011.02.017.

Shruthi, R.B.V., Kerle, N., Jetten, V., Stein, A., 2014. Object-based gully system prediction from medium resolution imagery using Random Forests. Geomorphology 216, 283–294. doi:10.1016/j.geomorph.2014.04.006.

Shumack, S., Hesse, P., Farebrother, W., 2020. Deep learning for dune pattern mapping with the AW3D30 global surface model. Earth Surface Processes and Landforms 45(11), 2417–2431. doi:10.1002/esp.4888.

Siart, C., Bubenzer, O., Eitel, B., 2009. Combining digital elevation data (SRTM/ASTER), high resolution satellite imagery (Quickbird) and GIS for geomorphological mapping: A multi-component case study on Mediterranean karst in Central Crete. Geomorphology 112(1–2), 106–121. doi:10.1016/j.geomorph.2009.05.010.

Sigloch, K., Mihalynuk, M.G., 2013. Intra-oceanic subduction shaped the assembly of Cordilleran North America. Nature 496(7443), 50–56. doi:10.1038/nature12019.

Silva, P., Harvey, A.M., Zazo, C., Goy, J., 1992. Geomorphology, depositional style and morphometric relationships of Quaternary alluvial fans in the Guadalentin Depression (Murcia, Southeast Spain). Zeitschrift für Geomorphologie 36, 325–341.

Silverman, B.W., 1986. Density Estimation for Statistics and Data Analysis. Springer, Boston. doi:10.1007/978-1-4899-3324-9.

Sinha, R., 2009. The Great avulsion of Kosi on 18 August 2008. Current Science 97(3), 429–433.

Sklar, L.S., Riebe, C.S., Marshall, J.A., Genetti, J., Leclere, S., Lukens, C.L., Merces, V., 2017. The problem of predicting the size distribution of sediment supplied by hillslopes to rivers. Geomorphology 277, 31–49. doi:10.1016/j.geomorph.2016.05.005.

Slater, J.A., Garvey, G., Johnston, C., Haase, J., Heady, B., Kroenung, G., Little, J., 2006. The SRTM Data "Finishing" Process and Products. Photogrammetric Engineering & Remote Sensing 72(3), 237–247.

Slaymaker, O., 2011. Criteria to Distinguish Between Periglacial, Proglacial and Paraglacial Environments. Quaestiones Geographicae 30(1), 85–94. doi:10.2478/v10117-011-0008-y.

Slingerland, R., Smith, N.D., 2004. River Avulsions and Their Deposits. Annual Review of Earth and Planetary Sciences 32(1), 257–285. doi:10.1146/annurev.earth.32.101802.120201.

Small, D., 1998. Generation of Digital Elevation Models Through Spaceborne SAR Interferometry. Remote sensing series 30. Remote Sensing Laboratories, Department of Geography, University of Zürich, Zürich.

Small, D., Pasquali, P., Fuglistaler, S., 1996. A comparison of phase to height conversion methods for SAR interferometry. In: Proceedings of the IEEE International Geoscience and Remote Sensing Symposium, May 31, Lincoln. IEEE, New York, pp. 342–344. doi:10.1109/IGARSS.1996.516334.

Smith, B., Sandwell, D., 2003. Accuracy and resolution of shuttle radar topography mission data. Geophysical Research Letters 30(9), 1–4. doi:10.1029/2002GL016643.

Smith, B.J., Wright, J.S., Whalley, W.B., 2002. Sources of non-glacial, loess-size quartz silt and the origins of "desert loess". Earth-Science Reviews 59(1–4), 1–26. doi:10.1016/S0012-8252(02)00066-1.

Smith, G.H.S., Ferguson, R.I., 1996. The gravel-sand transition: flume study of channel response to reduced slope. Geomorphology 16(2), 147–159. doi:10.1016/0169-555X(95)00140-Z.

Smith, L.C., 2002. Emerging Applications of Interferometric Synthetic Aperture Radar (InSAR)

in Geomorphology and Hydrology. Annals of the Association of American Geographers 92(3), 385–398. doi:10.1111/1467-8306.00295.

Smith, M.J., 2011. Digital Mapping. In: Smith, M.J., Paron, P., Griffiths, J.S. (Eds.). Geomorphological Mapping: Methods and Applications. Developments in Earth Surface Processes 15. Elsevier, Amsterdam, New York, pp. 225–251.

Smith, M.J., Clark, C.D., 2005. Methods for the visualization of digital elevation models for landform mapping. Earth Surface Processes and Landforms 30(7), 885–900. doi:10.1002/esp.1210.

Smith, M.J., Hillier, J., Otto, J.C., Geilhausen, M., 2013. Geovisualization. In: Bishop, M.P. (Ed.). Remote Sensing and GIScience in Geomorphology. 3. Elsevier/Academic Press, London, Oxford, Boston, pp. 299–325. doi:10.1016/B978-0-12-374739-6.00054-3.

Smith, M.J., Pain, C.F., 2009. Applications of remote sensing in geomorphology. Progress in Physical Geography 33(4), 568–582. doi:10.1177/0309133309346648.

Smith, M.J., Rose, J., Booth, S., 2006. Geomorphological mapping of glacial landforms from remotely sensed data: An evaluation of the principal data sources and an assessment of their quality. Geomorphology 76(1–2), 148–165. doi:10.1016/j.geomorph.2005.11.001.

Smith, M.J., Wise, S.M., 2007. Problems of bias in mapping linear landforms from satellite imagery. International Journal of Applied Earth Observation and Geoinformation 9(1), 65–78. doi:10.1016/j.jag.2006.07.002.

Smith, M.W., 2014. Roughness in the Earth Sciences. Earth-Science Reviews 136, 202–225. doi:10.1016/j.earscirev.2014.05.016.

Sánchez-Núñez, J.M., Macías, J.L., Saucedo, R., Zamorano, J.J., Novelo, D., Mendoza, M.E., Torres-Hernández, J.R., 2015. Geomorphology, internal structure and evolution of alluvial fans at Motozintla, Chiapas, Mexico. Geomorphology 230, 1–12. doi:10.1016/j.geomorph.2014.10.003.

Sonder, L.J., Jones, C.H., 1999. Western United States Extension: How the West Was Widened. Annual Review of Earth and Planetary Sciences 27(1), 417–462. doi:10.1146/annurev.earth.27.1.417.

Sonoda, S., Murata, N., 2017. Neural network with unbounded activation functions is universal approximator. Applied and Computational Harmonic Analysis 43(2), 233–268. doi:10.1016/j.acha.2015.12.005.

Sorriso-Valvo, M., Antronico, L., Le Pera, E., 1998. Controls on modern fan morphology in Calabria, Southern Italy. Geomorphology 24(2–3), 169–187. doi:10.1016/S0169-555X(97)00079-2.

Spark, R.N., Williams, P.F., 1996. Digital Terrain Models and the Visualization of Structural Geology. In: De Paor, D.G. (Ed.). Structural geology and personal computers. Computer Methods in the Geosciences 15. Elsevier, Oxford, Tarrytown, New York, pp. 421–446.

Spaulding, W.G., Graumlich, L.J., 1986. The last pluvial climatic episodes in the deserts of southwestern North America. Nature 320(6061), 441–444. doi:10.1038/320441a0.

Speight, J.G., 1971. Log-normality of slope distributions. Zeitschrift für Geomorphologie 15, 290–311.

Speight, J.G., 1974. A parametric approach to landform regions. In: Brown, E.H., Waters, R.S. (Eds.). Progress in Geomorphology. Institute of British Geographers Special Publication 7. Alden Press, Oxford, pp. 213–230.

Spelz, R.M., Fletcher, J.M., Owen, L.A., Caffee, M.W., 2008. Quaternary alluvial-fan development, climate and morphologic dating of fault scarps in Laguna Salada, Baja California, Mexico. Geomorphology 102(3–4), 578–594. doi:10.1016/j.geomorph.2008.06.001.

Staley, D.M., Wasklewicz, T.A., Blaszczynski, J.S., 2006. Surficial patterns of debris flow deposition on alluvial fans in Death Valley, CA using airborne laser swath mapping data. Geomorphology 74(1–4), 152–163. doi:10.1016/j.geomorph.2005.07.014.

Stanistreet, I.G., McCarthy, T.S., 1993. The Okavango Fan and the classification of subaerial fan systems. Sedimentary Geology 85(1–4), 115–133. doi:10.1016/0037-0738(93)90078-J.

Stepinski, T.F., Bagaria, C., 2009. Segmentation-Based Unsupervised Terrain Classification for Generation of Physiographic Maps. IEEE Geoscience and Remote Sensing Letters 6(4), 733–737. doi:10.1109/LGRS.2009.2024333.

Stepinski, T.F., Ghosh, S., Vilalta, R., 2006. Automatic Recognition of Landforms on Mars Using Terrain Segmentation and Classification. In: Todorovski, L., Lavrač, N., Jantke, K.P. (Eds.). Discovery Science. Lecture Notes in Computer Science 4265. Springer, Berlin, Heidelberg, pp. 255–266. doi: 10.1007/11893318_26.

Stepinski, T.F., Ghosh, S., Vilalta, R., 2007. Machine Learning for Automatic Mapping of Planetary Surfaces. In: Proceedings of the 22nd AAAI Conference on Artificial Intelligence, July 22–26, Vancouver. AAAI, Palo Alto. doi:10.13140/2.1.1518.9445.

Sternberg, S.R., 1986. Grayscale Morphology. Computer Vision, Graphics, and Image Processing 35, 333–355.

Stevenson, J.A., Sun, X., Mitchell, N.C., 2010. Despeckling SRTM and other topographic data with a denoising algorithm. Geomorphology 114(3), 238–252. doi:10.1016/j.geomorph.2009.07.006.

Stewart, J.H., 1998. Regional characteristics, tilt domains, and extensional history of the later Cenozoic Basin and Range Province, western North America. In: Faulds, J.E., Stewart, J.H. (Eds.). Accommodation zones and transfer zones; the regional segmentation of the Basin and Range Province. Special Paper 323. Geological Society of America, Boulder, pp. 47–74. doi: 10.1130/0-8137-2323-X.47.

Stock, J.D., 2013. Waters Divided: A History of Alluvial Fan Research and a View of Its Future. In: Shroder, J.F. (Ed.). Treatise on Geomorphology. Academic Press, San Diego, pp. 413–458. doi:10.1016/B978-0-12-374739-6.00249-9.

Stock, J.D., Schmidt, K.M., Miller, D.M., 2008. Controls on alluvial fan long-profiles. Geological Society of America Bulletin 120(5–6), 619–640. doi:10.1130/B26208.1.

Stock, J.M., Hodges, K.V., 1989. Pre-Pliocene Extension around the Gulf of California and the transfer of Baja California to the Pacific Plate. Tectonics 8(1), 99–115. doi:10.1029/TC008i001p00099.

Stokes, M., Mather, A.E., 2015. Controls on modern tributary-junction alluvial fan occurrence and morphology: High Atlas Mountains, Morocco. Geomorphology 248, 344–362. doi:10.1016/j.geom orph.2015.08.003.

Stokes, S., Kocurek, G., Pye, K., Winspear, N.R., 1997. New evidence for the timing of aeolian sand supply to the Algodones dunefield and East Mesa area, southeastern California, USA. Palaeogeography, Palaeoclimatology, Palaeoecology 128(1–4), 63–75. doi:10.1016/S0031-0182(96)00048-X.

Stolle, A., Langer, M., Blöthe, J.H., Korup, O., 2015. On predicting debris flows in arid mountain belts. Global and Planetary Change 126, 1–13. doi:10.1016/j.gloplacha.2014.12.005.

Stolz, C., Hülle, D., Hilgers, A., Grunert, J., Lehmkuhl, F., Dasch, D., 2012. Reconstructing fluvial, lacustrine and aeolian process dynamics in Western Mongolia. Zeitschrift für Geomorphologie 56(3), 267–300. doi:10.1127/0372-8854/2012/0078.

Stone, M., 1974. Cross-Validatory Choice and Assessment of Statistical Predictions. Journal of the Royal Statistical Society. Series B 36(2), 111–147.

Storz-Peretz, Y., Bowman, D., Laronne, J.B., Svoray, T., 2011. Rapid incision of a small, coarse and steep fan-delta in response to base-level fall: the case of Nahal Qedem, the Dead Sea, Israel. Earth Surface Processes and Landforms 36(4), 467–480. doi:10.1002/esp.2066.

Strahler, A.H., Woodcock, C.E., Smith, J.A., 1986. On the nature of models in remote sensing. Remote Sensing of Environment 20(2), 121–139. doi:10.1016/0034-4257(86)90018-0.

Strang, G., 2009. Introduction to linear algebra. Wellesley-Cambridge Press, Wellesley, 4th ed.

Strobl, C., Boulesteix, A.L., Kneib, T., Augustin, T., Zeileis, A., 2008. Conditional Variable Importance for Random Forests. BMC Bioinformatics 9(1), 307. doi:10.1186/1471-2105-9-307.

Strobl, C., Boulesteix, A.L., Zeileis, A., Hothorn, T., 2007. Bias in random forest variable importance measures: Illustrations, sources and a solution. BMC Bioinformatics 8, 25. doi:10.1186/1471-2105-8-25.

Strobl, C., Malley, J.D., Tutz, G., 2009. An introduction to recursive partitioning: Rationale, application, and characteristics of classification and regression trees, bagging, and random forests. Psychological Methods 14(4), 323–348. doi:10.1037/a0016973.

Strobl, J., 2008. Segmentation-based Terrain Classification. In: Zhou, Q., Lees, B., Tang, G. (Eds.). Advances in Digital Terrain Analysis. Lecture Notes in Geoinformation and Cartography. Springer, Berlin, Heidelberg, pp. 125–139. doi:10.1007/978-3-540-77800-4_7.

Stumpf, A., Kerle, N., 2011. Object-oriented mapping of landslides using Random Forests. Remote Sensing of Environment 115(10), 2564–2577. doi:10.1016/j.rse.2011.05.013.

Sun, G., Ranson, K.J., Kharuk, V.I., Auerswald, K., 2003. Validation of surface height from shuttle radar topography mission using shuttle laser altimeter. Remote Sensing of Environment 88(4), 401–411. doi:10.1016/j.rse.2003.09.001.

Sun, X., Rosin, P.L., Martin, R., Langbein, F., 2007. Fast and Effective Feature-Preserving Mesh Denoising. IEEE Transactions on Visualization and Computer Graphics 13(5), 925–938. doi:10.1109/TVCG.2007.1065.

Sun, Y., Zhang, X., Xin, Q., Huang, J., 2018. Developing a multi-filter convolutional neural network for semantic segmentation using high-resolution aerial imagery and LiDAR data. ISPRS Journal of Photogrammetry and Remote Sensing 143, 3–14. doi:10.1016/j.isprsjprs.2018.06.005.

Suwandana, E., Kawamura, K., Sakuno, Y., Kustiyanto, E., Raharjo, B., 2012. Evaluation of ASTER GDEM2 in Comparison with GDEM1, SRTM DEM and Topographic-Map-Derived DEM Using Inundation Area Analysis and RTK-dGPS Data. Remote Sensing 4(12), 2419–2431. doi:10.3390/rs4082419.

Tachikawa, T., Hato, M., Kaku, M., Iwasaki, A., 2011a. Characteristics of ASTER GDEM version 2. In: Proceedings of the IEEE International Geoscience and Remote Sensing Symposium, July 24–29, Vancouver. IEEE, New York, pp. 3657–3660. doi:10.1109/IGARSS.2011.6050017.

Tachikawa, T., Kaku, M., Iwasaki, A., 2011b. ASTER GDEM Version 2 Validation Report. Japan's Validation Report. http://www.jspacesystems.or.jp/ersdac/GDEM/ver2Validation/Appendix_A_ERSDAC_GDEM2_validation_report.pdf. Last accessed on October 29, 2014.

Tachikawa, T., Kaku, M., Iwasaki, A., Gesch, D.B., Oimoen, M., Zhang, Z., Danielson, J.J., Krieger, T., Curtis, B., Haase, J., Abrams, M., Crippen, R., Carabajal, C.C., 2011c. ASTER Global Digital Elevation Model Version 2 – Summary of Validation Results. http://www.jspacesystems.or.jp/ersdac/GDEM/ver2Validation/Summary_GDEM2_validation_report_final.pdf. Last accessed on October 28, 2014.

Tadono, T., Ishida, H., Oda, F., Naito, S., Minakawa, K., Iwamoto, H., 2014. Precise Global DEM Generation by ALOS PRISM. ISPRS Annals of Photogrammetry, Remote Sensing and Spatial Information Sciences II-4, 71–76. doi:10.5194/isprsannals-II-4-71-2014.

Tadono, T., Nagai, H., Ishida, H., Oda, F., Naito, S., Minakawa, K., Iwamoto, H., 2016. Generation of the 30 m-Mesh Global Digital Surface Model by ALOS PRISM. ISPRS - International Archives of the Photogrammetry, Remote Sensing and Spatial Information Sciences XLI-B4, 157–162. doi:10.5194/isprs-archives-XLI-B4-157-2016.

Tadono, T., Shimada, M., Murakami, H., Takaku, J., 2009. Calibration of PRISM and AVNIR-2 Onboard ALOS "Daichi". IEEE Transactions on Geoscience and Remote Sensing 47(12), 4042–4050. doi:10.1109/TGRS.2009.2025270.

Tadono, T., Shimada, M., Watanabe, M., Hashimoto, T., Iwata, T., 2004. Calibration and validation

of PRISM onboard ALOS. International Archives of Photogrammetry, Remote Sensing and Spatial Information Sciences 35(1), 13–18.

Tadono, T., Takaku, J., Tsutsui, K., Oda, F., Nagai, H., 2015. Status of "ALOS World 3D (AW3D)" global DSM generation. In: Proceedings of the IEEE International Geoscience and Remote Sensing Symposium, July 26–31, Milan. IEEE, New York, pp. 3822–3825. doi:10.1109/IGARSS.2015.7326657.

Tagil, S., Jenness, J., 2008. GIS-Based Automated Landform Classification and Topographic, Landcover and Geologic Attributes of Landforms Around the Yazoren Polje, Turkey. Journal of Applied Sciences 8(6), 910–921. doi:10.3923/jas.2008.910.921.

Takahashi, T., 1980. Debris Flow on Prismatic Open Channel. Journal of the Hydraulics Division 106(3), 381–396.

Takaku, J., Futamura, N., Iijima, T., Tadono, T., Shimada, M., 2007. High resolution DSM generation from ALOS PRISM. In: Proceedings of the IEEE International Geoscience and Remote Sensing Symposium, July 23–28, Barcelona. IEEE, New York, pp. 1974–1977. doi:10.1109/IGARSS.2007.4423215.

Takaku, J., Tadono, T., 2017. Quality updates of 'AW3D' global DSM generated from ALOS PRISM. In: Proceedings of the IEEE International Geoscience and Remote Sensing Symposium, July 23–28, Fort Worth. IEEE, New York, pp. 5666–5669. doi:10.1109/IGARSS.2017.8128293.

Takaku, J., Tadono, T., Tsutsui, K., 2014. Generation of High Resolution Global DSM from ALOS PRISM. ISPRS - International Archives of the Photogrammetry, Remote Sensing and Spatial Information Sciences XL-4, 243–248. doi:10.5194/isprsarchives-XL-4-243-2014.

Tapponnier, P., Molnar, P., 1979. Active faulting and cenozoic tectonics of the Tien Shan, Mongolia, and Baykal Regions. Journal of Geophysical Research: Solid Earth 84(B7), 3425–3459. doi:10.1029/JB084iB07p03425.

Tarantola, A., 2005. Inverse problem theory and methods for model parameter estimation. Society for Industrial and Applied Mathematics, Philadelphia.

Thatcher, W., 1999. Present-Day Deformation Across the Basin and Range Province, Western United States. Science 283(5408), 1714–1718. doi:10.1126/science.283.5408.1714.

Thomas, J., Joseph, S., Thrivikramji, K.P., Arunkumar, K.S., 2014. Sensitivity of digital elevation models: The scenario from two tropical mountain river basins of the Western Ghats, India. Geoscience Frontiers 5(6), 893–909. doi:10.1016/j.gsf.2013.12.008.

Thompson, R.S., Whitlock, C., Bartlein, P.J., Harrison, S.P., Spaulding, W.G., 1993. Climatic Changes in the Western United States since 18,000 yr B.P. In: Wright, H.E., Kutzbach, J.E., Webb, T., Ruddiman, W.F., Street-Perrott, F.A., Bartlein, P.J. (Eds.). Global Climates since the Last Glacial Maximum. University of Minnesota Press, Minneapolis, pp. 468–513.

Thompson, S.E., Harman, C.J., Heine, P., Katul, G.G., 2010. Vegetation-infiltration relationships across climatic and soil type gradients. Journal of Geophysical Research 115, G02023. doi:10.1029/2009JG001134.

Thorne, C.R., Zevenbergen, L.W., Burt, T.P., Butcher, D.P., 1987. Terrain analysis for quantitative description of zero-order basins. In: Erosion and Sedimentation in the Pacific Rim. Proceedings of the Corvallis Symposium, August 3–7, Corvallis. IAHS Publications 165, IAHS, Wallingford, pp. 121–130.

Toloşi, L., Lengauer, T., 2011. Classification with correlated features: unreliability of feature ranking and solutions. Bioinformatics 27(14), 1986–1994. doi:10.1093/bioinformatics/btr300.

Trier, Ø.D., Cowley, D.C., Waldeland, A.U., 2019. Using deep neural networks on airborne laser scanning data: Results from a case study of semi-automatic mapping of archaeological topography on Arran, Scotland. Archaeological Prospection 26(2), 165–175. doi:10.1002/arp.1731.

Troeh, F.R., 1964. Landform Parameters Correlated to Soil Drainage. Soil Science Society of America Journal 28(6), 808–812. doi:10.2136/sssaj1964.03615995002800060035x.

Troeh, F.R., 1965. Landform equations fitted to contour maps. American Journal of Science 263(7), 616–627. doi:10.2475/ajs.263.7.616.

Umhoefer, P.J., 2000. Where are the missing faults in translated terranes? Tectonophysics 326(1–2), 23–35. doi:10.1016/S0040-1951(00)00144-X.

Unruh, J.R., Humphrey, J., Barron, A., 2003. Transtensional model for the Sierra Nevada frontal fault system, eastern California. Geology 31(4), 327–330. doi:10.1130/0091-7613(2003)031<0327:TMFTSN>2.0.CO;2.

van Asselen, S., Seijmonsbergen, A.C., 2006. Expert-driven semi-automated geomorphological mapping for a mountainous area using a laser DTM. Geomorphology 78(3–4), 309–320. doi:10.1016/j.geomorph.2006.01.037.

Van Den Eeckhaut, M., Kerle, N., Poesen, J., Hervás, J., 2012. Object-oriented identification of forested landslides with derivatives of single pulse LiDAR data. Geomorphology 173–174, 30–42. doi:10.1016/j.geomorph.2012.05.024.

van Hinsbergen, D.J.J., Straathof, G.B., Kuiper, K.F., Cunningham, W.D., Wijbrans, J., 2008. No vertical axis rotations during Neogene transpressional orogeny in the NE Gobi Altai: coinciding Mongolian and Eurasian early Cretaceous apparent polar wander paths. Geophysical Journal International 173(1), 105–126. doi:10.1111/j.1365-246X.2007.03712.x.

Vandenberghe, J., 2002. The relation between climate and river processes, landforms and deposits during the Quaternary. Quaternary International 91(1), 17–23. doi:10.1016/S1040-6182(01)00098-2.

Vapnik, V.N., 2000. The Nature of Statistical Learning Theory. Springer, New York. doi:10.1007/978-1-4757-3264-1.

Vassallo, R., Ritz, J.F., Braucher, R., Carretier, S., 2005. Dating faulted alluvial fans with cosmogenic ^{10}Be in the Gurvan Bogd mountain range (Gobi-Altay, Mongolia): climatic and tectonic implications. Terra Nova 17(3), 278–285. doi:10.1111/j.1365-3121.2005.00612.x.

Vassallo, R., Ritz, J.F., Braucher, R., Jolivet, M., Carretier, S., Larroque, C., Chauvet, A., Sue, C., Todbileg, M., Bourlès, D., Arzhanikova, A., Arzhanikov, S., 2007. Transpressional tectonics and stream terraces of the Gobi-Altay, Mongolia. Tectonics 26(5), TC5013. doi:10.1029/2006TC002081.

Vassallo, R., Ritz, J.F., Carretier, S., 2011. Control of geomorphic processes on ^{10}Be concentrations in individual clasts: Complexity of the exposure history in Gobi-Altay range (Mongolia). Geomorphology 135(1–2), 35–47. doi:10.1016/j.geomorph.2011.07.023.

Ventra, D., Clarke, L.E., 2018. Geology and geomorphology of alluvial and fluvial fans: current progress and research perspectives. In: Ventra, D., Clarke, L.E. (Eds.). Geology and Geomorphology of Alluvial and Fluvial Fans: Terrestrial and Planetary Perspectives. Geological Society, London, Special Publications 440. Geological Society of London, London, pp. 1–21. doi:10.1144/SP440.16.

Veronesi, F., Hurni, L., 2014. Random Forest with semantic tie points for classifying landforms and creating rigorous shaded relief representations. Geomorphology 224, 152–160. doi:10.1016/j.geomorph.2014.07.020.

Vert, J.P., Tsuda, K., Schölkopf, B., 2004. A Primer on Kernel Methods. In: Schölkopf, B., Tsuda, K., Vert, J.P. (Eds.). Kernel Methods in Computational Biology. Computational molecular biology. Massachusetts Institute of Technology Press, Cambridge, pp. 35–70.

Viseras, C., Calvache, M.L., Soria, J.M., Fernández, J., 2003. Differential features of alluvial fans controlled by tectonic or eustatic accommodation space. Examples from the Betic Cordillera, Spain. Geomorphology 50(1–3), 181–202. doi:10.1016/S0169-555X(02)00214-3.

Volker, H.X., Wasklewicz, T.A., Ellis, M.A., 2007. A topographic fingerprint to distinguish alluvial fan formative processes. Geomorphology 88(1–2), 34–45. doi:10.1016/j.geomorph.2006.10.008.

von Blanckenburg, F., 2005. The control mechanisms of erosion and weathering at basin scale from cosmogenic nuclides in river sediment. Earth and Planetary Science Letters 237(3–4), 462–479. doi:10.1016/j.epsl.2005.06.030.

Walker, J.D., Glazner, A.F., 1999. Tectonic development of the Southern California deserts. In: Moores, E.M., Sloan, D., Stout, D.L. (Eds.). Classic Cordilleran Concepts: A View from California. Special Paper 338. Geological Society of America, Boulder, pp. 375–380. doi:10.1130/0-8137-2338-8.375.

Walker, R.T., Bayasgalan, A., Carson, R.J., Hazlett, R., McCarthy, L., Mischler, J., Molor, E., Sarantsetseg, P., Smith, L., Tsogtbadrakh, B., Tsolmon, G., 2006. Geomorphology and structure of the Jid right-lateral strike-slip fault in the Mongolian Altay mountains. Journal of Structural Geology 28(9), 1607–1622. doi:10.1016/j.jsg.2006.04.007.

Wang, J., Zheng, Y., Wang, M., Shen, Q., Huang, J., 2020. Object-Scale Adaptive Convolutional Neural Networks for High-Spatial Resolution Remote Sensing Image Classification. IEEE Journal of Selected Topics in Applied Earth Observations and Remote Sensing 14, 283–299. doi:10.1109/JSTARS.2020.3041859.

Wang, W., Yang, X., Yao, T., 2012. Evaluation of ASTER GDEM and SRTM and their suitability in hydraulic modelling of a glacial lake outburst flood in southeast Tibet. Hydrological Processes 26(2), 213–225. doi:10.1002/hyp.8127.

Wang, Z., Du, L., Mao, J., Liu, B., Yang, D., 2019. SAR Target Detection Based on SSD With Data Augmentation and Transfer Learning. IEEE Geoscience and Remote Sensing Letters 16(1), 150–154. doi:10.1109/LGRS.2018.2867242.

Wasserman, L., 2010. All of statistics: a concise course in statistical inference. Springer texts in statistics. Springer, New York, 2nd ed.

Watson, G.S., 1964. Smooth Regression Analysis. The Indian Journal of Statistics 26(4), 359–372.

Wechsler, S.P., 2007. Uncertainties associated with digital elevation models for hydrologic applications: a review. Hydrology and Earth System Sciences 11(4), 1481–1500. doi:10.5194/hess-11-1481-2007.

Wechsler, S.P., Kroll, C.N., 2006. Quantifying DEM Uncertainty and its Effect on Topographic Parameters. Photogrammetric Engineering & Remote Sensing 72(9), 1081–1090.

Weibel, R., 1990. Verarbeitung und Anwendung digitaler Geländemodelle im Bereich der Geographie. Geographica Helvetica 45(4), 145–153. doi:10.5194/gh-45-145-1990.

Weibel, R., Heller, M., 1991. Digital Terrain Modelling. In: Maguire, D.J., Goodchild, M.F., Rhind, D. (Eds.). Geographical information systems: principles and applications. Longman, London, pp. 269–297.

Weischet, W., 1996. Regionale Klimatologie Teil 1. Die Neue Welt: Amerika - Neuseeland - Australien. Schweizerbart, Stuttgart.

Weissmann, G.S., Bennett, G.L., Lansdale, A.L., 2005. Factors controlling sequence development on Quaternary fluvial fans, San Joaquin Basin, California, USA. In: Harvey, A.M., Mather, A.E., Stokes, M. (Eds.). Alluvial Fans: Geomorphology, Sedimentology, Dynamics. Geological Society, London, Special Publications 251. Geological Society of London, London, pp. 169–186. doi:10.1144/GSL.SP.2005.251.01.12.

Weiszfeld, E., 1937. Sur le point pour lequel la somme des distances de n points donnés est minimum. Tohoku Mathematical Journal 43, 355–386.

Wells, S.G., Harvey, A.M., 1987. Sedimentologic and geomorphic variations in storm-generated alluvial fans, Howgill Fells, northwest England. Geological Society of America Bulletin 98(2), 182. doi:10.1130/0016-7606(1987)98<182:SAGVIS>2.0.CO;2.

Wells, S.G., McFadden, L.D., Dohrenwend, J.C., 1987. Influence of late Quaternary climatic changes on geomorphic and pedogenic processes on a desert piedmont, Eastern Mojave Desert, California. Quaternary Research 27(2), 130–146. doi:10.1016/0033-5894(87)90072-X.

Welsh, A., Davies, T.R., 2011. Identification of alluvial fans susceptible to debris-flow hazards. Landslides 8(2), 183–194. doi:10.1007/s10346-010-0238-4.

Wendt, K.A., Dublyansky, Y.V., Moseley, G.E., Edwards, R.L., Cheng, H., Spötl, C., 2018. Moisture availability in the southwest United States over the last three glacial-interglacial cycles. Science Advances 4(10), eaau1375. doi:10.1126/sciadv.aau1375.

Wesnousky, S.G., 2005. Active faulting in the Walker Lane. Tectonics 24(3), TC3009. doi:10.1029/2004TC001645.

West, A.J., Galy, A., Bickle, M., 2005. Tectonic and climatic controls on silicate weathering. Earth and Planetary Science Letters 235(1–2), 211–228. doi:10.1016/j.epsl.2005.03.020.

Whipple, K., Parker, G., Paola, C., Mohrig, D., 1998. Channel Dynamics, Sediment Transport, and the Slope of Alluvial Fans: Experimental Study. The Journal of Geology 106(6), 677–694. doi:10.1086/516053.

Whipple, K., Trayler, C.R., 1996. Tectonic control of fan size: the importance of spatially variable subsidence rates. Basin Research 8(3), 351–366. doi:10.1046/j.1365-2117.1996.00129.x.

Whipple, K., Tucker, G.E., 1999. Dynamics of the stream-power river incision model: Implications for height limits of mountain ranges, landscape response timescales, and research needs. Journal of Geophysical Research: Solid Earth 104(B8), 17661–17674. doi:10.1029/1999JB900120.

Whipple, K., Tucker, G.E., 2002. Implications of sediment-flux-dependent river incision models for landscape evolution. Journal of Geophysical Research: Solid Earth 107(B2), 2039. doi:10.1029/2000JB000044.

Whitlock, C., Bartlein, P.J., 1993. Spatial Variations of Holocene Climatic Change in the Yellowstone Region. Quaternary Research 39(2), 231–238. doi:10.1006/qres.1993.1026.

Whittaker, A.C., Attal, M., Cowie, P.A., Tucker, G.E., Roberts, G., 2008. Decoding temporal and spatial patterns of fault uplift using transient river long profiles. Geomorphology 100(3–4), 506–526. doi:10.1016/j.geomorph.2008.01.018.

Wiesmeier, M., Barthold, F., Blank, B., Kögel-Knabner, I., 2011. Digital mapping of soil organic matter stocks using Random Forest modeling in a semi-arid steppe ecosystem. Plant and Soil 340(1), 7–24. doi:10.1007/s11104-010-0425-z.

Wigand, P.E., Rhode, D., 2002. Great Basin Vegetation History and Aquatic Systems: The Last 150,000 Years. In: Hershler, R., Madsen, D.B., Currey, D.R. (Eds.). Great Basin Aquatic Systems History. Smithsonian Contributions to the Earth Sciences 33. Smithsonian Institution Press, Washington, D.C., pp. 309–367. doi:10.5479/si.00810274.33.1.

Wilford, D.J., Sakals, M.E., Innes, J.L., Sidle, R.C., Bergerud, W.A., 2004. Recognition of debris flow, debris flood and flood hazard through watershed morphometrics. Landslides 1(1), 61–66. doi:10.1007/s10346-003-0002-0.

Williams, R.M.E., Zimbelman, J.R., Johnston, A.K., 2006. Aspects of alluvial fan shape indicative of formation process: A case study in southwestern California with application to Mojave Crater fans on Mars. Geophysical Research Letters 33(10), L10201. doi:10.1029/2005GL025618.

Wilson, D., Aster, R., West, M., Ni, J., Grand, S., Gao, W., Baldridge, W.S., Semken, S., Patel, P., 2005. Lithospheric structure of the Rio Grande rift. Nature 433(7028), 851–855. doi:10.1038/nature03297.

Wilson, J.P., 2012. Digital terrain modeling. Geomorphology 137(1), 107–121. doi:10.1016/j.geomorph.2011.03.012.

Wilson, M.F.J., O'Connell, B., Brown, C., Guinan, J.C., Grehan, A.J., 2007. Multiscale Terrain Analysis of Multibeam Bathymetry Data for Habitat Mapping on the Continental Slope. Marine Geodesy 30(1–2), 3–35. doi:10.1080/01490410701295962.

Wobus, C., Whipple, K., Kirby, E., Snyder, N., Johnson, J., Spyropolou, K., Crosby, B., Sheehan, D., 2006. Tectonics from topography: Procedures, promise, and pitfalls. In: Willett, S.D., Hovius, N.,

Brandon, M.T., Fisher, D.M. (Eds.). Tectonics, Climate, and Landscape Evolution. Special Paper 398. Geological Society of America, Boulder, pp. 55–74. doi:10.1130/2006.2398(04).

Wohl, E., 2000. Mountain Rivers. Water Resources Monograph 14. American Geophysical Union, Washington, D.C. doi:10.1029/WM014.

Wood, J.D., 1996. The Geomorphological Characterisation of Digital Elevation Models. Ph.D. thesis, University of Leicester, Leicester.

Woodcock, C.E., Strahler, A.H., 1987. The factor of scale in remote sensing. Remote Sensing of Environment 21(3), 311–332. doi:10.1016/0034-4257(87)90015-0.

Woodhouse, C.A., 1997. Winter climate and atmospheric circulation patterns in the Sonoran desert region, USA. International Journal of Climatology 17(8), 859–873. doi:10.1002/(SICI)1097-0088(19970630)17:8<859::AID-JOC158>3.0.CO;2-S.

Wu, J., 2004. Effects of changing scale on landscape pattern analysis: scaling relations. Landscape Ecology 19(2), 125–138. doi:10.1023/B:LAND.0000021711.40074.ae.

Wu, K.L., Yang, M.S., 2007. Mean shift-based clustering. Pattern Recognition 40(11), 3035–3052. doi:10.1016/j.patcog.2007.02.006.

Xie, Z., Haritashya, U.K., Asari, V.K., Young, B.W., Bishop, M.P., Kargel, J.S., 2020. GlacierNet: A Deep-Learning Approach for Debris-Covered Glacier Mapping. IEEE Access 8, 83495–83510. doi:10.1109/ACCESS.2020.2991187.

Xu, B., Huang, J.Z., Williams, G., Wang, Q., Ye, Y., 2012. Classifying Very High-Dimensional Data with Random Forests Built from Small Subspaces:. International Journal of Data Warehousing and Mining 8(2), 44–63. doi:10.4018/jdwm.2012040103.

Yamaguchi, Y., Kahle, A.B., Tsu, H., Kawakami, T., Pniel, M., 1998. Overview of Advanced Spaceborne Thermal Emission and Reflection Radiometer (ASTER). IEEE Transactions on Geoscience and Remote Sensing 36(4), 1062–1071. doi:10.1109/36.700991.

Yang, B., Bräuning, A., Dong, Z., Zhang, Z., Keqing, J., 2008. Late Holocene monsoonal temperate glacier fluctuations on the Tibetan Plateau. Global and Planetary Change 60(1–2), 126–140. doi:10.1016/j.gloplacha.2006.07.035.

Yang, H.L., Lunga, D., Yuan, J., 2017. Toward country scale building detection with convolutional neural network using aerial images. In: Proceedings of the IEEE International Geoscience and Remote Sensing Symposium, July 23–28, Fort Worth. IEEE, New York, pp. 870–873. doi:10.1109/IGARSS.2017.8127091.

Yin, A., 2010. Cenozoic tectonic evolution of Asia: A preliminary synthesis. Tectonophysics 488(1–4), 293–325. doi:10.1016/j.tecto.2009.06.002.

Yin, A., Harrison, T.M., 2000. Geologic Evolution of the Himalayan-Tibetan Orogen. Annual Review of Earth and Planetary Sciences 28(1), 211–280. doi:10.1146/annurev.earth.28.1.211.

Yosinski, J., Clune, J., Bengio, Y., Lipson, H., 2014. How transferable are features in deep neural networks? In: Proceedings of the 27th International Conference on Neural Information Processing Systems, December 8–13, Montreal. Curran Associates, New York, pp. 3320–3328.

Zani, H., Assine, M.L., McGlue, M.M., 2012. Remote sensing analysis of depositional landforms in alluvial settings: Method development and application to the Taquari megafan, Pantanal (Brazil). Geomorphology 161–162, 82–92. doi:10.1016/j.geomorph.2012.04.003.

Zebker, H.A., Villasenor, J., 1992. Decorrelation in interferometric radar echoes. IEEE Transactions on Geoscience and Remote Sensing 30(5), 950–959. doi:10.1109/36.175330.

Zevenbergen, L.W., Thorne, C.R., 1987. Quantitative analysis of land surface topography. Earth Surface Processes and Landforms 12(1), 47–56. doi:10.1002/esp.3290120107.

Zhang, C., Sargent, I., Pan, X., Li, H., Gardiner, A., Hare, J., Atkinson, P.M., 2018. An object-

based convolutional neural network (OCNN) for urban land use classification. Remote Sensing of Environment 216, 57–70. doi:10.1016/j.rse.2018.06.034.

Zhang, K., Gann, D., Ross, M., Robertson, Q., Sarmiento, J., Santana, S., Rhome, J., Fritz, C., 2019. Accuracy assessment of ASTER, SRTM, ALOS, and TDX DEMs for Hispaniola and implications for mapping vulnerability to coastal flooding. Remote Sensing of Environment 225, 290–306. doi:10.1016/j.rse.2019.02.028.

Zhang, K.J., Zhang, Y.X., Tang, X.C., Xia, B., 2012. Late Mesozoic tectonic evolution and growth of the Tibetan plateau prior to the Indo-Asian collision. Earth-Science Reviews 114(3–4), 236–249. doi:10.1016/j.earscirev.2012.06.001.

Zhao, S., Cheng, W., Zhou, C., Chen, X., Zhang, S., Zhou, Z., Liu, H., Chai, H., 2011. Accuracy assessment of the ASTER GDEM and SRTM3 DEM: an example in the Loess Plateau and North China Plain of China. International Journal of Remote Sensing 32(23), 8081–8093. doi:10.1080/01431161.2010.532176.

Zhao, W., Du, S., 2016. Learning multiscale and deep representations for classifying remotely sensed imagery. ISPRS Journal of Photogrammetry and Remote Sensing 113, 155–165. doi:https://doi.org/10.1016/j.isprsjprs.2016.01.004.

Zhao, W., Du, S., Emery, W.J., 2017. Object-Based Convolutional Neural Network for High-Resolution Imagery Classification. IEEE Journal of Selected Topics in Applied Earth Observations and Remote Sensing 10(7), 3386–3396. doi:10.1109/JSTARS.2017.2680324.

Zhou, S., Li, J., Zhao, J., Wang, J., Zheng, J., 2011. Quaternary Glaciations: Extent and Chronology in China. In: Ehlers, J., Gibbard, P.L., Hughes, P.D. (Eds.). Quaternary glaciations: extent and chronology. Developments in Quaternary Science 15. Elsevier, Amsterdam, Boston, Heidelberg, pp. 981–1002.

Zhou, S., Wang, J., Xu, L., Wang, X., Colgan, P.M., Mickelson, D.M., 2010. Glacial advances in southeastern Tibet during late Quaternary and their implications for climatic changes. Quaternary International 218(1–2), 58–66. doi:10.1016/j.quaint.2009.11.026.

Zhou, S., Xu, L., Colgan, P.M., Mickelson, D.M., Wang, X., Wang, J., Zhong, W., 2007. Cosmogenic ^{10}Be dating of Guxiang and Baiyu Glaciations. Chinese Science Bulletin 52(10), 1387–1393. doi:10.1007/s11434-007-0208-y.

Zhu, H., Xu, P., Shao, X., Luo, H., 2013. Little Ice Age glacier fluctuations reconstructed for the southeastern Tibetan Plateau using tree rings. Quaternary International 283, 134–138. doi:10.1016/j.quaint.2012.04.011.

Zhu, X.X., Tuia, D., Mou, L., Xia, G.S., Zhang, L., Xu, F., Fraundorfer, F., 2017. Deep Learning in Remote Sensing: A Comprehensive Review and List of Resources. IEEE Geoscience and Remote Sensing Magazine 5(4), 8–36. doi:10.1109/MGRS.2017.2762307.

Zink, M., Moreira, A., Bachmann, M., Rizzoli, P., Fritz, T., Hajnsek, I., Krieger, G., Wessel, B., 2017. The global TanDEM-X DEM — A unique data set. In: Proceedings of the IEEE International Geoscience and Remote Sensing Symposium, July 23–28, Fort Worth. IEEE, New York, pp. 906–909. doi:10.1109/IGARSS.2017.8127099.

Summary

Automating the mapping of landforms via digital elevation data is a key research topic in the field of geomorphometry. The acquisition of extensive thematic datasets has the potential to foster scientific progress in geomorphology and related disciplines by enhancing our understanding of how formative processes are reflected in geomorphometric variables and by facilitating the transfer of in-field results to larger study areas.

In the wake of continuously improving spatial resolutions of DEMs, traditional pixel-based classification approaches fail in accounting for the irregular boundaries of landforms. To address this fundamental issue, object-based frameworks developed in the field of remote sensing have been adopted for geomorphometric research. With respect to alluvial fans, all workflows presented hitherto are, however, deficient in delineating laterally adjoining fans as individual landforms. Since coalescing fans represent a common scenario for (semi-) arid mountain ranges, further research is warranted.

Although object-based image analysis (OBIA) gained considerable emphasis during the last two decades, scientific progress is complicated by substantial challenges. (1.) The sensitivity of segmentation algorithms to local discontinuities requires a proper choice of parameters. The appropriate selection of *scaling factors* or *bandwidths* is, however, an issue which is not comprehensively resolved to this date, because segmentation is an ill-structured problem which is not conducive to an a-prori assessment. (2.) Existing adaptions of OBIA in the field of geomorphometry neglect that by formalizing the local altitude field, morphometric variables act (i) as an interface to the land surface characteristics of interest and (ii) are strongly influenced by the terrain rendition characteristics of the DEM in use.

This doctoral dissertation first sets the stage by evaluating freely available near-global DEM data—ASTER GDEM, AW3D30, SRTM1 (30 m posting each), and a self-processed TanDEM-X DEM (15 m posting). Both geomorphological mapping and geomorphometric processing attest TanDEM-X a superior terrain rendition up to moderate relief. In settings of strong topographic contrasts, however, challenges toward interferometric processing result in a deterioration of terrain representation. SRTM1 shows an overall consistent depiction of terrain, but is characterized by an autocorrelated grainy texture of moderate magnitude. The most recent 30 m-DEM product, AW3D30, shows improvements over SRTM1 by displaying only uncorrelated systematic noise of relatively low magnitude, which suitable filtering can remove. In contrast to the aforementioned DEM products, ASTER GDEM displays a striking bumpy texture, and it is strongly discouraged to use the DEM in geomorphometric research.

Since DEM characteristics exert a strong influence on significant ranges of morphometric variables, this doctoral dissertation challenges the de facto standard of utilizing rule-based classification schemes for object-based analysis in the field of geomorphometry. As an alternative, a framework is proposed where both segmentation and classification are controlled by supervised machine learning in the following way:

(1.) The approach recognizes that segmentation and classification need to be addressed with individual compilations of morphometric variables. In the case of alluvial fans, a robust segmentation of laterally adjoining fans can be accomplished by incorporating the sine and cosine of slope aspect in addition to slope and curvature values. For classification, tailored algorithms have been

developed to formalize the morphometric signature of alluvial fans.

(2.) A high-performing object-based workflow is thus compulsorily feature-specific. To formalize the morphometric signature of a landform, one-class estimators are for the first time integrated into an object-based workflow.

(3.) To account for the ill-structured nature of segmentation, the issue of selecting appropriate bandwidths for segmentation is tackled from an a-posteriori perspective. Specifically, segmentation is first performed for a range of parametrizations, and all raw datasets are classified. Subsequently, the final thematic dataset is compiled by applying an overlap resolve algorithm on the raw segmentation data, selecting final objects according to their estimator scores and topological relationships.

The framework was first tested for the delineation and discrimination of alluvial fans situated in a single study area within the Mongolian Altai, using a spatial variant of the mean-shift algorithm for segmentation and a one-class support vector machine (OCSVM) for classification. The framework is able to accurately delineate laterally coalescing fans with the exception of fans grading into a bajada, i.e., fans displaying diffuse and ambiguous lateral delimitations. By successively adapting the feature space representation yielded by the OCSVM estimator, a promising diagnostic ability could be achieved by using just eleven training samples.

The sensitivity of the OCSVM algorithm to the choice of its parameters hampers, however, the transferability of the workflow to different landforms and DEM datasets. To address this issue, this thesis introduces a new one-class random forest (OCRF) and trials the algorithm with a training dataset of 306 fans compiled from seven different study areas. Owing to a high diagnostic ability and a robustness towards its parametrization and morphometric variables with little discriminatory potential, the OCRF improves the delineation and classification of alluvial fans at the expense of requiring a larger training dataset. Furthermore, the non-parametric nature of OCRF can be capitalized on by performing a fully data-driven optimization of parameters and DEM preprocessing.

Eventually, the geomorphometric variables developed in this thesis are utilized to assess whether controlling factors can be inferred from the geomorphometry of alluvial fan surfaces. While the findings demonstrate that scaling relationships exert a dominant influence on the expected range of morphometric parameter values, it could be shown that the differentiation between tectonic activity and the capability of the fan–catchment system in evacuating sediment can be improved by quantifying the degree of fan progradation.

In essence, this doctoral dissertation showcases that object-based analysis in the field of geomorphometry poses different demands on methodological frameworks as is the case in the field of remote sensing, and the term object-based morphometric analysis (OBMA) is suggested to emphasize this difference. The methodological framework developed in this thesis offers excellent prospects for an extensive use of object-based techniques in the fields of geomorphology and geomorphometry. Libraries of feature perimeters and feature signatures can be set up in a staggered, semi-automated manner, by first performing an OBMA analysis using an OCSVM or a comparable algorithm, and switching to an OCRF once sufficient training data has been acquired. For the thematic mapping of larger portions of the geomorphological inventory, it is envisaged to pursue a stratified approach where landform types

are delineated and identified in a serial manner, utilizing OBMA workflows tailored towards each geomorphic feature of interest.

Zusammenfassung

Die automatische Erfassung von Oberflächenformen mittels digitaler Höhendaten ist ein zentrales Forschungsfeld der Geomorphometrie. Die Akquise umfangreicher thematischer Datensätze hat dabei das Potential, den wissenschaftlichen Fortschritt in der Geomorphologie und Nachbarwissenschaften zu forcieren – vor allem im Hinblick auf ein besseres Verständnis der Widerspiegelung formativer Prozesse in geomorphometrischen Variablen, sowie durch die Förderung des Transfers von in-situ gewonnenen Erkenntnissen in die Fläche.

Im Zuge der stetig voranschreitenden Verbesserung der räumlichen Auflösung digitaler Höhenmodelle (DHM) weisen traditionelle, pixelbasierte Klassifikationsverfahren zunehmende Defizite auf. In Anerkennung dieses fundamentalen Problems wurden in der Fernerkundung entwickelte objektbasierte Verfahren auf geomorphologische Fragestellungen übertragen. Sämtliche bisher vorgestellten Verfahren für die Erfassung und Klassifikation von Schwemmfächern führen die Differenzierung von lateral aneinander grenzenden Schwemmfächern allerdings nicht oder nur unzureichend durch, so dass weiterer Forschungsbedarf angezeigt ist.

Wenngleich die objektbasierte Bildanalyse (OBIA) in den letzten zwei Jahrzehnten einen wichtigen Forschungszweig der Geomorphometrie darstellte, verhindern bisher unzureichend adressierte Probleme die operative Verwendung des Verfahrens: (1.) Während die Sensitivität des Segmentationsalgorithmus gegenüber Diskontinuitäten durch geeignete Parameterwahl gesteuert werden muss, kann die Bestimmung eines geeigneten Skalierungsfaktors beziehungsweise einer geeigneten Bandbreite lediglich a-posteriori erfolgen. (2.) Bei den bisher vorgestellten Anpassungen der OBIA für geomorphologische Fragestellungen wird zudem vernachlässigt, dass (i) morphometrische Variablen das lokale Höhenpunktfeld quantifizieren und die Formalisierung geeigneter morphometrischer Metriken daher für sich ein Optimierungsproblem darstellt. Darüber hinaus ist (ii) die thematisch signifikante Bandbreite stark durch die Charakteristiken des verwendeten DHMs beeinflusst.

Als Grundlage für die anschließende Entwicklung eines auf geomorphometrische Fragestellungen spezialisierten objektbasierten Verfahrens werden in der vorliegenden Dissertation zunächst für wissenschaftliche Zwecke frei verfügbare, eine nahezu globale Auflösung aufweisende DHM-Datensätze vergleichend betrachtet. Sowohl die Ergebnisse der durchgeführten geomorphologischen Kartierung als auch die geomorphometrische Prozessierung attestieren dem TanDEM-X DHM eine gegenüber SRTM1 und ASTER GDEM überlegene Geländedarstellung. Lediglich für Bereiche extremen Reliefs treten der interferometrischen Radarprozessierung immanente Probleme zutage. Während das SRTM1 DHM durch eine grundsätzlich konsistente Geländewiedergabe gekennzeichnet ist, weist es eine durchgehend vorhandene, autokorrelierte körnige Textur auf. Im Gegensatz zu SRTM1 ist AW3D30 lediglich durch ein moderates, unkorreliertes Rauschen gekennzeichnet, welches über Filterungsverfahren leicht gedämpft werden kann. Von der Anwendung von ASTER GDEM für geomorphometrische Zwecke ist hingegen abzuraten, da hier eine unzureichende Genauigkeit der Parallaxenbestimmung in einer prominent welligen, Geländemerkmale überprägenden Textur resultiert.

Im Hinblick auf den substantiellen Einfluss des verwendeten DHMs auf die signifikanten Wertebereiche von geomorphometrischen Parametern kritisiert die vorliegende Dissertation den de-facto-Standard

der Anwendung regelbasierter Klassifikationsansätze für geomorphometrische Anwendungen. Als alternativer Ansatz wird ein auf der Anwendung von Methoden des überwachten maschinellen Lernens basierendes Verfahren vorgestellt, welches auf den folgenden Grundsätzen beruht:

(1.) Das Verfahren berücksichtigt, dass die konsistente Segmentation und Klassifikation von Oberflächenformen eine individuelle Zusammenstellung von morphometrischen Variablen erfordert. Im Falle von Schwemmfächern wird eine präzise Differenzierung lateral angrenzender Schwemmfächer durch den Einbezug des Sinus und des Kosinus der Exposition ermöglicht. Für die Klassifikation von Schwemmfächern wurden die Morphologie der Oberflächenform spezifisch adressierende Algorithmen entwickelt, die unter anderem die Abweichung von einer idealen partiellen Kegelform quantifizieren.

(2.) Es folgt, dass ein optimierter objektbasierter Klassifikationsansatz zwingend formspezifisch ausgestaltet werden muss. Um diesen Umstand im Rahmen der Klassifikation zu berücksichtigen, erfolgte die im Kontext der objektbasierten Analyse erstmalige Verwendung von Ein-Klassen-Schätzern.

(3.) Das Problem der Festsetzung einer geeigneten Bandbreite für den Segmentationsalgorithmus wird aus einer A-posteriori-Perspektive betrachtet, indem die Segmentation zunächst für ein Spektrum an unterschiedlichen Parametrisierungen durchgeführt wird, und die erhaltenen Rohdaten zunächst separat klassifiziert werden. Im Anschluss werden die einzelnen Segmentationslayer zu einem thematischen Datensatz vereinigt, indem die unter Berücksichtigung topologischer Beziehungen bestklassifizierten Segmentationsobjekte selektiert werden.

Das postulierte Verfahren wird zunächst auf ein einzelnes, im östlichen Monglischen Altai gelegenes Untersuchungsgebiet angewendet, wobei eine raumbezogene Variante des Mean-Shift Clustering-Verfahrens sowie die Ein-Klassen-Variante des Support Vector Machine-Algorithmus (OCSVM) zur Anwendung kommen. Es wird aufgezeigt, dass der Prozessierungsansatz in der Lage ist, auch lateral aneinander grenzende Schwemmfächer als individuelle Oberflächenformen auszuweisen. Einschränkungen bestehen diesbezüglich lediglich für lateral angrenzende Schwemmfächer mit diffusen und/oder mehrdeutigen Begrenzungen (Bajada). OCSVM weisen eine hohe Suszeptibilität gegenüber ihrer Parametrisierung auf, so dass die Ermittlung einer geeigneten Parameterwahl eine tentative Herangehensweise erfordert. Andererseits ergibt sich hierdurch das Potential, den Generalisierungsgrad spezifisch auf den Umfang des verwendeten Trainingsdatensatzes anzupassen. Die vorliegende Dissertation macht sich diese Eigenschaft zunutze, um trotz des Einbezugs von lediglich elf Stichproben eine vielversprechende Klassifikationsgenauigkeit zu erzielen.

Das erhebliche Ausmaß an erforderlicher Anwenderinteraktion erschwert die Übertragung des Ansatzes auf andere Oberflächenformen und/oder DHM-Produkte, und damit die operative Anwendung von objektbasierten Verfahren. Zur Adressierung dieses Problems wird in der vorliegenden Thesis eine Ein-Klassen-Implementierung des Random Forests-Algorithmus (OCRF) eingeführt, und unter Einbezug eines 306 Stichproben umfassenden Trainingsdatensatzes evaluiert. Aufgrund einer hohen Performanz und einer ausgeprägten Robustheit gegenüber der Parametrisierung sowie potentiell nicht signifikanter morphometrischer Variablen konnte einerseits die Klassifikationsgenauigkeit deutlich verbessert werden, andererseits ergibt sich hieraus das Potential für eine automatisierte Kreuzvalidierung

– zum Beispiel von DHM-Filterungsintensitäten. Diese Fortschritte erfolgen auf Kosten eines deutlich höheren Bedarfs an Stichproben, da der Anwender über die Parametrisierung des Schätzers keinen unmittelbaren Einfluss auf die Umgrenzung des Merkmalsraumes einer thematischen Klasse ausübt.

In einer abschließenden Fallstudie wird unter Anwendung der im Rahmen der Dissertation entwickelten geomorphometrischen Parameter evaluiert, inwieweit die Morphometrie von Schwemmfächern Rückschlüsse auf morphogenetische Randbedingungen ermöglicht. Analog zur klassischen morphometrischen Betrachtung von Schwemmfächer–Einzugsgebiets-Relationen ist auch der morphometrische Eigenschaftsraum von Schwemmfächeroberflächen stark durch Skalenbeziehungen geprägt. In dieser Dissertation konnte unter Nutzung trendbereinigter Daten aufgezeigt werden, dass die Differenzierung zwischen durch tektonische Aktivität dominierten und durch Sedimentzufuhr dominierten Schwemmfächersystemen über die morphometrische Formalisierung der Schwemmfächer-Progradation verbessert werden kann.

In einer Gesamtschau zeigt die vorliegende Arbeit auf, dass sich die Ansprüche an ein objektbasiertes Verfahren in der Geomorphometrie deutlich von den in der Fernerkundung etablierten Verfahren unterscheiden. Als zentralen Punkt stellt sich dabei heraus, dass die Zusammenstellung von morphometrischen Parametern formspezifisch erfolgen sollte. Für die Generierung umfangreicher, verschiedene Oberflächenformen umfassender Datensätze wird daher ein Ansatz vorgeschlagen, bei welchem einzelne Oberflächenformen unter Anwendung von angepassten Prozessierungsketten auf serielle Art und Weise ausgewiesen werden.